Springer Series in Optical Sciences 238

Mário F. S. Ferreira *Editor*

Dissipative Optical Solitons

Springer

Springer Series in Optical Sciences

Volume 238

Springer Series in Optical Sciences is led by Editor-in-Chief William T. Rhodes, Florida Atlantic University, USA, and provides an expanding selection of research monographs in all major areas of optics:

- lasers and quantum optics
- ultrafast phenomena
- optical spectroscopy techniques
- optoelectronics
- information optics
- applied laser technology
- industrial applications and
- other topics of contemporary interest.

With this broad coverage of topics the series is useful to research scientists and engineers who need up-to-date reference books.

Mário F. S. Ferreira
Editor

Dissipative Optical Solitons

Springer

Editor
Mário F. S. Ferreira
I3N-Institute of Nanostructures,
Nanomodelling and Nanofabrication
Department of Physics
University of Aveiro
Aveiro, Portugal

ISSN 0342-4111 ISSN 1556-1534 (electronic)
Springer Series in Optical Sciences
ISBN 978-3-030-97492-3 ISBN 978-3-030-97493-0 (eBook)
https://doi.org/10.1007/978-3-030-97493-0

This Springer imprint is published by the registered company Springer Nature Switzerland AG
The registered company address is: Gewerbestrasse 11, 6330 Cham, Switzerland

Contents

Contributors

Fatkhulla Kh. Abdullaev Physical-Technical Institute, Uzbek Academy of Sciences, Tashkent, Uzbekistan

T. Ackemann SUPA and Department of Physics, University of Strathclyde, Glasgow, Scotland, UK

Mohammed AlAraimi Higher College of Technology, Al-Khuwair, Sultanate of Oman

Sergey A. Babin Institute of Automation and Electrometry SB RAS, Novosibirsk, Russia

Novosibirsk State University, Novosibirsk, Russia

Chengying Bao State Key Laboratory of Precision Measurement Technology and Instruments, Department of Precision Instruments, Tsinghua University, Beijing, China

Anastasia E. Bednyakova Novosibirsk State University, Novosibirsk, Russia

Institute of Computational Technologies SB RAS, Novosibirsk, Russia

Mario Chemnitz INRS-EMT, Quebec, Canada

Ji-Xiang Chen Guangdong Provincial Key Laboratory of Nanophotonic Functional Materials and Devices & Guangzhou Key Laboratory for Special Fiber Photonic Devices and Applications, South China Normal University, Guangzhou, Guangdong, China

Lilong Dai The Key Lab of Specialty Fiber Optics and Optical Access Network, Shanghai University, Shanghai Institute of Communication and Advanced Data Science, Joint International Laboratory of Specialty Fiber Optics and Advanced Communication, Shanghai, China

Vlad D. Efremov Institute of Automation and Electrometry SB RAS, Novosibirsk, Russia

Novosibirsk State University, Novosibirsk, Russia

Margarida V. Facão I3N-Institute of Nanostructures, Nanomodelling and Nanofabrication, Department of Physics, University of Aveiro, Aveiro, Portugal

Mikhail P. Fedoruk Novosibirsk State University, Novosibirsk, Russia

Institute of Computational Technologies SB RAS, Novosibirsk, Russia

Meng-Jun Feng Guangdong Provincial Key Laboratory of Nanophotonic Functional Materials and Devices & Guangzhou Key Laboratory for Special Fiber Photonic Devices and Applications, South China Normal University, Guangzhou, Guangdong, China

Mário F. S. Ferreira I3N-Institute of Nanostructures, Nanomodelling and Nanofabrication, Department of Physics, University of Aveiro, Aveiro, Portugal

Bennet Fischer INRS-EMT, Quebec, Canada

Lei Gao Key Laboratory of Optoelectronic Technology & Systems (Ministry of Education), Chongqing University, Chongqing, China

Philippe Grelu Laboratoire ICB UMR 6303 CNRS, Université Bourgogne – Franche-Comté, Dijon, France

T. Guillet Laboratoire Charles Coulomb (L2C), University Montpellier, CNRS, Montpellier, France

Jiangyong He Institute of Modern Optics, Tianjin Key Laboratory of Micro-scale Optical Information Science and Technology, Nankai University, Tianjin, China

Pan Huang School of Mechanical Engineering and Electronic Information, China University of Geosciences (Wuhan), Wuhan, China

Qianqian Huang The Key Lab of Specialty Fiber Optics and Optical Access Network, Shanghai University, Shanghai Institute of Communication and Advanced Data Science, Joint International Laboratory of Specialty Fiber Optics and Advanced Communication, Shanghai, China

Tianye Huang School of Mechanical Engineering and Electronic Information, China University of Geosciences (Wuhan), Wuhan, China

Wuhan National Laboratory Optoelectronics, Wuhan, China

Zinan Huang The Key Lab of Specialty Fiber Optics and Optical Access Network, Shanghai University, Shanghai Institute of Communication and Advanced Data Science, Joint International Laboratory of Specialty Fiber Optics and Advanced Communication, Shanghai, China

Junjie Jiang The Key Lab of Specialty Fiber Optics and Optical Access Network, Shanghai University, Shanghai Institute of Communication and Advanced Data

Science, Joint International Laboratory of Specialty Fiber Optics and Advanced Communication, Shanghai, China

Denis S. Kharenko Institute of Automation and Electrometry SB RAS, Novosibirsk, Russia

Novosibirsk State University, Novosibirsk, Russia

Andrey Komarov Institute of Automation and Electrometry, Russian Academy of Science, Novosibirsk, Russia

Sofia C. Latas I3N-Institute of Nanostructures, Nanomodelling and Nanofabrication, Department of Physics, University of Aveiro, Aveiro, Portugal

Luigi Di Lauro INRS-EMT, Quebec, Canada

Meng Liu Guangdong Provincial Key Laboratory of Nanophotonic Functional Materials and Devices & Guangzhou Key Laboratory for Special Fiber Photonic Devices and Applications, South China Normal University, Guangzhou, Guangdong, China

Yan-ge Liu Institute of Modern Optics, Tianjin Key Laboratory of Micro-scale Optical Information Science and Technology, Nankai University, Tianjin, China

Ai-Ping Luo Guangdong Provincial Key Laboratory of Nanophotonic Functional Materials and Devices & Guangzhou Key Laboratory for Special Fiber Photonic Devices and Applications, South China Normal University, Guangzhou, Guangdong, China

Zhi-Chao Luo Guangdong Provincial Key Laboratory of Nanophotonic Functional Materials and Devices & Guangzhou Key Laboratory for Special Fiber Photonic Devices and Applications, South China Normal University, Guangzhou, Guangdong, China

Baiwei Mao Institute of Modern Optics, Tianjin Key Laboratory of Micro-scale Optical Information Science and Technology, Nankai University, Tianjin, China

Roberto Morandotti INRS-EMT, Quebec, Canada

David J. Moss Centre for Microphotonics, Swinburne University of Technology, Hawthorn, VIC, Australia

Chengbo Mou The Key Lab of Specialty Fiber Optics and Optical Access Network, Shanghai University, Shanghai Institute of Communication and Advanced Data Science, Joint International Laboratory of Specialty Fiber Optics and Advanced Communication, Shanghai, China

G. -L. Oppo SUPA and Department of Physics, University of Strathclyde, Glasgow, Scotland, UK

Alessia Pasquazi Emergent Photonics (Epic) Laboratory, Department of Physics and Astronomy, University of Sussex, Brighton, UK

Evgeniy V. Podivilov Institute of Automation and Electrometry SB RAS, Novosibirsk, Russia

Novosibirsk State University, Novosibirsk, Russia

H. Pulham SUPA and Department of Physics, University of Strathclyde, Glasgow, Scotland, UK

Cristina Rimoldi INRS-EMT, Quebec, Canada

Aleksey Rozhin Aston Institute of Photonic Technologies (AIPT), Aston University, Birmingham, UK

Mario Salerno Dipartimento di Fisica "E.R. Caianiello", and INFN, Gruppo Collegato di Salerno, Università di Salerno, Salerno, Italy

Mohamed Salhi Laboratoire de Photonique d'Angers, Université d'Angers, Département de Physique, Angers, France

François Sanchez Laboratoire de Photonique d'Angers, Université d'Angers, Département de Physique, Angers, France

Georges Semaan Laboratoire de Photonique d'Angers, Université d'Angers, Département de Physique, Angers, France

Grzegorz Soboń Faculty of Electronics, Photonics and Microsystems, Wrocław University of Science and Technology, Wrocław, Poland

Xiaoqing Wang Institute of Modern Optics, Tianjin Key Laboratory of Micro-scale Optical Information Science and Technology, Nankai University, Tianjin, China

Zhi Wang Institute of Modern Optics, Tianjin Key Laboratory of Micro-scale Optical Information Science and Technology, Nankai University, Tianjin, China

Zhichao Wu School of Mechanical Engineering and Electronic Information, China University of Geosciences (Wuhan), Wuhan, China

Xiaosheng Xiao State Key Laboratory of Information Photonics and Optical Communications, School of Electronic Engineering, Beijing University of Posts and Telecommunications, Beijing, China

Wen-Cheng Xu Guangdong Provincial Key Laboratory of Nanophotonic Functional Materials and Devices & Guangzhou Key Laboratory for Special Fiber Photonic Devices and Applications, South China Normal University, Guangzhou, Guangdong, China

Zhijun Yan School of Optical and Electronic Information, Huazhong University of Science and Technology, Wuhan, China

Bingye Zhan School of Mechanical Engineering and Electronic Information, China University of Geosciences (Wuhan), Wuhan, China

Ze-Yu Zhan Guangdong Provincial Key Laboratory of Nanophotonic Functional Materials and Devices & Guangzhou Key Laboratory for Special Fiber Photonic Devices and Applications, South China Normal University, Guangzhou, Guangdong, China

Dazhong Zhang School of Mechanical Engineering and Electronic Information, China University of Geosciences (Wuhan), Wuhan, China

Luming Zhao Jiangsu Key Laboratory of Advanced Laser Materials and Devices, School of Physics and Electronic Engineering, Jiangsu Normal University, Xuzhou, Jiangsu, China

Innokentiy Zhdanov Institute of Automation and Electrometry SB RAS, Novosibirsk, Russia

Novosibirsk State University, Novosibirsk, Russia

Chapter 1
Dissipative Optical Solitons: An Introduction

Mário F. S. Ferreira

Abstract In this chapter we provide an introduction to the topic of this book. After a brief historical note on solitary waves, a special attention is paid to solitons in optical fiber systems. The complex Ginzburg-Landau equation is presented as a main equation describing different dissipative physical systems, namely optical transmission lines and passively mode-locked fiber lasers. Several types of dissipative optical solitons are commented, as well as the formation of multi-soliton complexes. We conclude with a review of recent experimental results on pulsating optical dissipative solitons.

Keywords Optical solitons · Dissipative solitons · Nonlinear Schrödinger equation · Complex Ginzburg-Landau equation · Dissipative systems · Mode-locked fiber lasers · Nonlinear dynamics · Vector dissipative solitons · Pulsating solitons · Soliton molecules

1.1 Solitary Waves

The history of solitons (or solitary waves) began with the famous physical experiments of the Scottish Engineer and Naval Architect John Scott Russell in the Glasgow–Edinburgh Canal in 1834 [1]. This was followed by the mathematical derivation of the Korteweg-de Vries (KdV) equation in 1895 for the propagation of the great solitary wave of Scott Russell in one direction on the free surface of water in a shallow canal. After that, the solitary wave remained during a long time mainly as a simple curiosity in the area of nonlinear wave theory. The subject revived in 1955, when Fermi, Pasta, and Ulam (FPU) published a Laboratory Report on a numerical model of a discrete nonlinear mass–spring system [2]. The FPU model was described by a system of coupled nonlinear ordinary differential equations that, under certain approximations, can be transformed into the KdV equation. Such work

M. F. S. Ferreira (✉)
I3N-Institute of Nanostructures, Nanomodelling and Nanofabrication, Department of Physics, University of Aveiro, Aveiro, Portugal
e-mail: mfernando@ua.pt

M. F. S. Ferreira (ed.), *Dissipative Optical Solitons*, Springer Series in Optical Sciences 238, https://doi.org/10.1007/978-3-030-97493-0_1

inspired M. Kruskal and N. Zabusky, which solved numerically the KdV equation. They observed the formation of solitary waves that undergo nonlinear interaction, after which they emerge without any change of shape and amplitude, but with only a small change in their phases. Due to the particle-like behaviour of such solitary waves, Kruskal and Zabusky called them for the first time "solitons" in a famous 1965 paper [3].

In 1967, C. Gardner, J Greene, M. Kruskal and R Miura developed an ingenious method for finding the exact solution of the KdV equation [4]. The integration of the nonlinear Schrödinger equation (NLSE) was demonstrated in 1971 by V. Zakharov and A. Shabat [5] using the same method. Since these pioneering theoretical works, scientists tend to use the term "soliton" to describe the modes of nonlinear partial differential equations that happen to be integrable by means of the "inverse scattering technique" [5, 6]. Based on such restrictive definition, solitons were usually attributed, until the beginning of the 1990s, only to integrable systems. However, the soliton concept was subsequently broaden when many physicists understood the limitations of the theory. In fact, they observed that "solitary waves" do exist in a variety of systems, though they do not behave exactly as the classical theory predicts for "true" solitons. Actually, solitary waves have been found in many different fields, including hydrodynamics, nonlinear optics, plasma physics, and biology [7–11]. In optical context, solitonic behaviour can occur in time (temporal solitons) or in space (spatial solitons), both in the simplest case described by a nonlinear Schrödinger equation.

1.2 Solitons in Optical Fibers

Temporal solitons in optical fiber systems have a particularly interesting and successful history. Such history begun in 1973, when A. Hasegawa and F. Tappert suggested the existence of solitons in optical fibers [12]. Their formation was shown to be the result of a balance between the negative (anomalous) group velocity dispersion (GVD) of the glass fiber, which occurs for wavelengths longer than 1.3 μm in a standard fiber, and the Kerr nonlinearity. The soliton appeared as an ideal solution to the problem of pulse spreading caused by fiber dispersion. However, solitons could do nothing against the attenuation that any propagating pulse experiences due to the waveguide loss. In fact, at the time that paper was published, there were no practical methods to solve the fiber loss problem and the soliton idea remained nothing more than an elegant mathematical curiosity.

After many ingenious efforts, L. Mollenauer, R. Stolen and J. Gordon [13] succeeded, in 1980, in observing for the first time the optical soliton in a fiber. The experimental results proved that the properties of a nonlinear pulse propagating in an optical fiber are described, to a remarkable degree, by the NLSE. However, few people expected some practical importance of solitons because there were erroneous beliefs that anything nonlinear would be too complicated.

In spite of such beliefs, A. Hasegawa [14] suggested in 1983 that solitons could be used in all-optical transmission systems based on optical amplifiers instead of regenerative repeaters, which were considered standard until 1990. In particular, he proposed using the Raman effect of transmission fiber itself for optical amplification. In practice, the concept of all-optical transmission using the distributed Raman amplification was changed by the inclusion of erbium-doped fiber amplifiers (EDFAs) developed during the 1990s.

Meanwhile, J. Gordon and H. Haus [15] anticipated that the transmission of a signal made of optical solitons could not be extended an unlimited distance when optical amplification is used. In fact, the amplifiers needed to compensate for the fiber loss generate also amplified spontaneous emission (ASE), and this noise is, in part, incorporated by the soliton, whose mean frequency is then shifted. Due to GVD, the arrival time of the soliton becomes then a random variable, whose variance is proportional to the cube of the propagation distance. This is the so-called Gordon-Haus effect.

In order to extend the limit set by such effect, some research groups have suggested to use frequency filters [16–18]. However, it was observed that, using this technique, the transmission distance was still limited by the growth of narrow-band noise at the center frequency of the filters. Such noise results in a background instability which can affect significantly and even destroy the propagating soliton. To solve this problem, L. Mollenauer and co-workers, developed the sliding-guiding filter concept [19–21]. Other proposals to achieve a stable soliton propagation in fiber transmission links made use of amplitude modulators [22] or nonlinear optical amplification [23–25]. The key property of nonlinear gain is to provide an effective gain to the soliton and a suppression (or very small gain) to the noise.

1.3 The Complex Ginzburg-Landau Equation

The pulse propagation in optical fibers systems where narrow-band filters, linear and nonlinear amplifiers are periodically inserted can be described by the following generalized NLSE [11, 23–29]:

$$i\frac{\partial q}{\partial Z}+\frac{D\partial^2 q}{2\partial T^2}+|q|^2 q=i\delta q+i\beta\frac{\partial^2 q}{\partial T^2}i\varepsilon|q|^2 q+i\mu|q|^4 q-\nu|q|^4 q, \tag{1.1}$$

where Z is the normalized propagation distance, T is the retarded time, q is the normalized envelope of the electric field, β stands for spectral filtering ($\beta > 0$), δ is the linear gain or loss coefficient, ε accounts for nonlinear gain-absorption processes (for example, two-photon absorption), μ represents a higher-order correction to the nonlinear gain-absorption, ν is a higher-order correction term to the nonlinear refractive index and D is the dispersion parameter, with $D > 0$ in the anomalous regime and $D < 0$ in the normal regime.

Equation (1.1) is known as the complex Ginzburg-Landau equation (CGLE) [11, 26, 29] and becomes the standard nonlinear Schrödinger equation when $D = +1$ and the right-hand side is set to zero. The CGLE is rather general, as it includes linear and nonlinear effects, in both conservative and dissipative forms. It is known in many branches of physics and can describe several non-equilibrium phenomena, such as convection instabilities, binary fluid convection and phase transitions [30–32]. In the field of nonlinear optics, besides the area of all-optical transmission lines, it has been used to describe optical parametric oscillators, free-electron laser oscillators, spatial and temporal soliton lasers [26, 29, 33–38].

The CGLE provides also an adequate model do describe the main features of passively mode-locked fiber lasers. Actually, the master equation approach to mode-locked lasers, which was initiated by H. Haus in mid-1970s [39, 40], illustrated the high relevance of Ginzburg-Landau equations and in particular the cubic-quintic CGLE to model universal ultrafast laser dynamics [41–43]. The coefficients that appear in the master equation were related in a phenomenological way to the physical parameters of a mode-locked laser by Haus et al. [44].

Equation (1.1) includes all the main physical effects present in any mode-locked laser. In particular, linear loss and nonlinear gain account for the required saturable absorber effect. On the other hand, even if the correction to the nonlinear refractive index is not imposed by most laser materials under common operation conditions, it can be justified by the discrete nature of the laser cavity [45]. An explicit relation of the cubic-quintic CGLE coefficients with regard to the physical parameters has been derived in the case of fiber lasers mode-locked by means of the nonlinear polarization rotation technique [46–49].

Actually, Eq. (1.1) models the fiber laser as a distributed system, which is reasonable if the pulse shape changes only slightly during each round-trip. There are many advantages in using such distributed model, governed by a continuous equation, since it allows, to some extent, an analytic study. However, when the discrete nature of the laser cavity cannot be ignored, the cubic-quintic CGLE given by Eq. (1.1) can be used such that the various parameters vary periodically with Z, the period corresponding to a cavity round-trip.

In general, Eq. (1.1) is non-integrable, and only particular exact solutions can be obtained. In the case of the cubic CGLE, exact solutions can be obtained using a special ansatz [50], Hirota bilinear method [51] or reduction to systems of linear PDEs [52]. Concerning the quintic CGLE, the existence of soliton-like solutions in the case has been demonstrated both analytically and numerically [11, 26, 27, 53]. Exact solutions of the quintic CGLE, including solitons, sinks, fronts and sources, were obtained in [54], using Painlevé analysis and symbolic computations.

Various techniques have been also applied to obtain approximate soliton solutions of the CGLE. The soliton perturbation theory can be used for small value$\varepsilon > 0$s of the parameters [25, 26]. Moreover, approximate expressions for some localized solutions can be derived for arbitrary values of the CGLE parameters by reducing this equation to finite-dimensional dynamical models. These reduced models can be obtained using the variational approach [55–59] or the method of moments [60–63] and they provide evolution equations for the pulse parameters, such as the peak

amplitude, pulse width, and chirp. A direct correspondence between attractors of the finite-dimensional dynamical systems and localized waves of the dissipative system can be found [63]. Moreover, the stability and other properties of a soliton pulse are linked to the stability and characteristics of its attractor. For example, a stationary soliton is associated to a fixed point. By tuning the system parameters, we can transform such fixed point into a limit cycle, which is an oscillatory attracting state. Thus, a previously stationary soliton becomes a pulsating soliton. Further changing the system parameters may result in irregular and chaotic dynamics.

To fully explore the CGLE, massive numerically simulations must be carried out. Different types of soliton solutions have been obtained in this way, which can be divided in two main classes: localized fixed-shape solutions and localized pulsating solutions [26, 58, 59, 64]. Examples of localized fixed-shape solutions are the plain stationary pulses, the flat-top pulses, the composite pulses and the moving pulses [11]. Among the localized pulsating solutions, we may refer the plain pulsating and the creeping solions, as well as the erupting solitons, which belong to the class of chaotic solutions [65, 66]. Actually, the number of solutions to the CGLE is so large that the sphere of this knowledge by itself has been called "the world of the Ginzburg–Landau equation" [67, 68].

A discrete version of the complex Ginzburg-Landau equation (DCGLE) has been used to model diverse physical systems, including arrays of waveguides with amplification and damping, arrays of semiconductor lasers [69], arrays of exciton-polariton condensates [70], frustrated vortices in hydrodynamics [71], dissipative discrete nonlinear electrical lattices with nearest-neighbour interaction [72], etc. In optics, the DGLE appears in problems of beam propagation in the array of the nonlinear optical waveguides with Kerr and resonance nonlinearities. Chapter 14 of this book, by M. Salerno and F. Abdullaev, provides a review of some recent results on localized and extended solutions of the discrete complex Ginzburg-Landau equation,

1.4 Dissipative Solitons

The soliton solutions of Eq. (1.1) are termed *dissipative solitons* (DSs) and they differ significantly from conventional solitons. The conventional soliton concept implies a single balance between nonlinearity and dispersion, whereas a dissipative soliton arises as a result of a double balance: between nonlinearity and dispersion and also between gain and loss [26, 29]. Concerning the second condition, even the slightest imbalance will result in the solution either growing indefinitely, if gain prevails, or disappearing completely because of the dissipation. One can define the DS as a *localized and stable structure emergent in a non-linear dissipative system far from the thermodynamic equilibrium* [29]. Actually, considering the primitive mathematical definition, a DS is not a 'true' soliton. However, many properties of DSs, in particular, their stable localization, robustness in the processes of scattering and interaction, well-organized internal structure, etc., are similar to those of "true" solitons.

Even if it is a stationary object, a dissipative soliton shows non-trivial energy flows with the environment and between different parts of the pulse. Hence the dissipative soliton is an object which is far from equilibrium and which presents characteristics similar to a living thing. In fact, we can consider animal species in nature as elaborate forms of dissipative solitons. Actually, DSs are abundant in the different natural systems ranging from optics and condensed-matter physics to biology and medicine. In this sense, one may paraphrase that DSs "are around us. In the true sense of the word they are absolutely everywhere" [73]. Chapter 2 of this book, by P. Grelu, provides a conceptual framework of dissipative optical solitons, highlighting their general signatures and dynamics in passively mode-locked lasers. Chapter 3, by Z.-C. Luo et al., presents a review of the recent advances on the dissipative soliton buildup dynamics in fiber lasers, which can be well characterized both in the temporal and spectral domains.

The energy of a CGLE dissipative soliton solution increases indefinitely when the equation parameters converge to a given region of the parameter space [74]. Such set of parameters was called a dissipative soliton resonance (DSR) and has been frequently observed and reported [75–84]. DSR can occur in both anomalous and normal dispersion regimes [75, 76] of a mode-locked fiber laser and enables an almost infinite boost in the pulse energy without wave breaking [79]. The energy of a DSR pulse increases mainly due to the increase of the pulse width, while keeping the amplitude at a constant level. Chapter 4 of this book, by G. Semaan et al., describes the generation and control of DSR pulses in fiber lasers under various mode-locking mechanisms.

A different kind of high-energy ultrashort pulses are the very high amplitude (VHA) soliton solutions of the CGLE found in Refs. [85, 86]. These VHA solutions occur when the nonlinear gain saturation parameter tends to vanish. The increase in energy of such pulses is mainly due to the increase of the pulse amplitude, whereas the pulse width becomes narrower. VHA pulses with high energy were found mainly in the normal dispersion region [86]. Chapter 5 of this book, by S. Latas et al., describes the region of existence, the propagation and the main characteristics of ultrashort VHA solitons both in the normal and anomalous dispersion regimes.

The formation and dynamics of vector dissipative solitons in birefringent single-mode fibers can be described by a set of coupled Ginzburg-Landau equations [26]. The experimental generation of such vector solitons in passively mode-locked fiber lasers has been intensively studied during recent years [87–98]. To generate the vector solitons, all the fibers and passive components of the mode-locked fiber lasers have to be polarization insensitive. The main challenge for achieving this objective is to find an appropriate saturable absorber (SA) that has polarization insensitive saturable absorption. In fiber lasers, semiconductor saturable absorber mirrors (SESAMs), carbon nanotubes, graphene and graphene like 2D materials are SAs which have a polarization independent saturable absorption. Depending on the cavity birefringence and cross-polarization coupling strength, vector solitons formed can be classified as polarization locked vector solitons (PLVS), polarization rotation vector solitons (PRVS), group-velocity locked vector solitons (GVLVS), dark-bright

vector solitons, and so on. Chapter 6 of this book, by L. Zhao, describes various forms of vector dissipative solitons and their real-time dynamics in passively mode-locked fiber lasers.

Actually, dissipative soliton generation has been explored mainly using lasers with rare-earth-doped gain media, namely Yb-doped fiber or Er-doped fiber with optical gain near 1 μm or 1.55 μm, respectively. An alternative approach is based on pump-induced Raman gain in passive fibers, offering operation at almost any wavelength. This configuration provides a novel approach to the generation of high-energy ultrashort dissipative pulses. Chapter 8 of this book, by D. Kharenko et al., offers an overview of recent experimental results on high-energy dissipative solitons generated via stimulated Raman scattering.

The advent of widely wavelength tunable fiber lasers has unlocked diverse applications ranging from fiber sensing, biomedical research, optical signal processing, and high capacity optical transmission system. The wavelength tuning operation is commonly achieved through filter control or by adjusting the effective gain profile. Chapter 9 of this book, by Q. Huang et al., reports on the wavelength tuning capability of fiber lasers when they emit dissipative solitons in the L band.

Among the different types of pulsating dissipative solitons, the erupting soliton exhibits a rather interesting behaviour. It has been found numerically for the first time in Ref. [99] and manifests itself as a chaotic and quasi-periodic process when the dissipative system is in a meta-stable state. The soliton in the meta-stable dissipative system erupts into pieces in temporal domain abruptly and gradually recover its original state after the eruption, which is similar to exploding behavior and thus regarded as the so-called soliton explosion [99, 100]. The erupting soliton was experimentally observed for the first time by Cundiff et al. [101] in a solid-state, Kerr-lens mode-locked Ti:sapphire laser. Later on, spectral and temporal signatures of soliton explosions were experimentally observed in an all-normal dispersion, all-polarization maintaining passively mode-locked Yb-doped fiber laser [102]]. Such explosions were observed when the laser was operating in a transition zone between stable mode-locking [103] and noise-like emission [104, 105].

Dissipative optical solitons can also be found in other dissipative systems besides fiber lasers, namely in vertical-cavity surface-emitting lasers (VCSELs). A VCSEL is a semiconductor laser in which the emission is in the direction of the epitaxial growth, which allows for a large Fresnel number, enabling self-organization and spatial solitons independent from boundary conditions. Chapter 13 of this book, by T. Ackemann et al., provides a review of the properties of vector vortex beams (VVBs) in VCSELs with frequency-selective feedback. VVBs are interpreted as high-order vortex solitons with a spatially non-uniform, but locally linear polarization state.

1.5 Dissipative Soliton Molecules

After finding the conditions for the existence of stable solitary-pulse solutions of the CGLE, the next natural step is to consider their interactions and the eventual formation of bound states. Dissipative soliton molecules correspond to bound states

arising from the interaction of initially separate single solitons. Phase-locked two-soliton molecules were experimentally observed in 2002 using a stretched-pulse fiber laser [106]. After that, they have been found numerically and experimentally considering different laser configurations and dispersion regimes [107–111]. The two-soliton molecule can be assumed as the building block to construct various multi-soliton molecules [111].

There have been during the recent years many reports on soliton molecules in fiber lasers mode-locked with the carbon nanotubes, graphene, black phosphorus, and so on [112–117]. Since these saturable absorbers may be polarization independent, soliton molecules formed by vector solitons were also reported. The experimental observation of tightly and loosely bound states of vector solitons in a carbon nanotube mode-locked fiber laser in the anomalous dispersion regime was reported in 2013 [118]. Localized interactions between vector solitons, vector soliton with bound vector solitons, and vector soliton with a bunch of vector solitons were also observed in a fiber laser passively mode locked by graphene [119]. The first experimental observation of group-velocity-locked vector soliton (GVLVS) molecules has been reported in 2017 in a SESAM mode-locked fiber laser using a birefringence-enhanced fiber [120]. Chapter 11 of this book, by C. Bao and X. Xiao, provides a review of soliton molecules and other multi-soliton complexes in mode-locked fiber lasers and high-Q microcavities. The generation of dissipative solitons and frequency combs in Kerr microresonator-based systems is discussed in Chap. 12, by C. Romoldi et al., which provides also a review of actual applications of these objects.

In order to realize multi-soliton co-existence inside one single mode-locked fiber laser, it is desirable to introduce various multiplexed mechanisms. For example, if there is no unidirectional component such as an isolator inside the laser cavity, it would be a bidirectional oscillation that gives rise to a new dimension of multiplexing. Real mode-locked materials such as SESAMs, graphene, and carbon nanotubes contribute to the direction-multiplexed soliton generation. Chapter 10 of this book, by T. Huang et al., discusses various types of multiplexed dissipative soliton fiber lasers, including bidirectional multiplexing, wavelength multiplexing, and polarization multiplexing, besides some other emerging multiplexed methods.

1.6 Recent Experimental Results on Pulsating Dissipative Solitons

Actually, the mode-locked fiber laser constitutes an ideal test bed for investigating the complex nonlinear dynamics associated to pulsating dissipative solitons. The plain pulsating soliton was observed for the first time in 2004 by Soto-Crespo et al. in a mode-locked fiber ring laser [121]. Nevertheless, the lack of a high-resolution real-time diagnostic method has precluded a detailed characterization of the pulsating behavior of such pulses. This limitation has been broken recently through the development of a novel powerful real-time spectra measurement technique called

dispersive Fourier transform (DFT) [122]. Using this technique, the spectrum of the soliton could be mapped into a temporal waveform by using dispersive element with enough group-velocity dispersion. Thus, the ultrafast spectral signals can be captured by a real-time oscilloscope with a high-speed photodetector. Actually, the DFT technique has enabled the experimental observation in real time of transient dynamics of diverse pulsating solitons and other complex ultrafast nonlinear phenomena in fiber lasers [102, 123–138].

Soliton self-organization and pulsation in a passively mode-locked fiber laser was observed experimentally in 2018 [132]. The soliton pulsation process showed a period corresponding to tens of the cavity round trip time. In another 2018 experiment, pulsating dissipative solitons in a mode-locked fiber laser at normal dispersion were observed for the first time using the DFT technique [133]. In that experiment, the artificial saturable absorbers, as well as the birefringent filter formed by the nonlinear polarization rotation, made the polarization controller an effective component to adjust the laser state from stationary to pulsating. The pulsating dissipative solitons were accompanied with the spectrum breathing and oscillating structures due to the nonlinear pulse propagation. Also in 2018, the first experimental evidence of the pulsating soliton with chaotic behaviour in an ultrafast fiber laser was reported [134]. Using the DFT technique, the chaotic behaviour of soliton pulsation was visualized by the fact that the mode-locked spectrum collapsed abruptly in an unpredictable way during the pulsating process.

In a 2019 experiment, three types of soliton pulsations were observed in an L-band normal-dispersion mode-locked fiber laser via the DFT technique [136]. They were classified as single-periodic pulsating soliton, double-periodic pulsating soliton and soliton explosion. These pulsations exhibited common features such as energy oscillation, bandwidth breathing and temporal shift. However, the pulse was repeated every two oscillations for double-periodic pulsating soliton. In the case of soliton explosions, the spectrum was observed to crack into pieces at a periodic manner. The motion dynamics of a creeping soliton in a passively mode-locked fiber laser was also observed in 2020 using the DFT technique [138]. The periodical variation of pulse width, peak power, and motion range could be observed in real time, while the corresponding spectral evolution exhibited breathing dynamics.

Most phenomena related to soliton pulsations have been observed in mode-locked fiber lasers based on the nonlinear polarization rotation (NPR). Since a polarizer is required for the implementation of the NPR technique, the polarization degree of freedom is frozen, and pulsating solitons formed in these lasers are scalar ones. In a 2020 experiment, the generation of pulsating group-velocity-locked vector solitons (GVLVSs) in a net-normal dispersion fiber laser mode locked by nonlinear multimode interference has been reported [139]. In another 2020 experiment, the vector nature of various pulsating solitons in an ultrafast fiber laser with single-wall carbon nanotubes has been investigated [140]. By virtue of the DFT technique, the polarization-resolved spectral evolution of pulsating vector solitons was measured in real time. Double-periodic pulsation in the cavity was also observed. Also in 2020, the vector features of pulsating solitons were studied in an erbium-doped fiber (EDF)

laser [141]. Three categories of vector solitons with different polarization evolution characteristics could be obtained by adjusting the pump power and polarization controller, namely pulsating polarization-locked vector soliton (PLVS), pulsating polarization-rotation vector soliton (PRVS) and progressive pulsating PRVS.

..

The use of the DFT technique has boosted also the experimental investigations of soliton explosions in mode-locked fibre lasers during recent years [102, 123, 131, 142–144]. The first investigation of soliton explosions in an ultrafast fiber laser in the multi-soliton regime was reported in 2018 [131]. It was demonstrated that explosion of one soliton could be induced by another one through the soliton interaction. In another 2018 experiment, the periodic spectrum changing via soliton explosion in a passively mode-locked fiber laser by a nonlinear polarization evolution was observed for the first time [142]. Soliton collision induced explosions in a mode-locked fibre laser were also reported in 2019 [144]. Up to seven nonlinear regimes were observed successively in the laser by increasing the pump power, including single-pulse mode locking, standard soliton explosions, noise-like mode locking, stable double pulsing, soliton collision induced explosions, soliton molecules, and double-pulse noise-like mode locking.

Weak to strong explosive behaviours of pulsating solitons were reported in another 2019 experiment concerning soliton molecules [145]. The simultaneous pulsations of energy, separation and relative phase difference were observed for solitons inside the molecule, Other recent experiments have enabled the real-time observation of internal motion within ultrafast optical soliton molecules [146–152]. Chapter 7 of this book, by X. Wang et al., describes various kinds of pulsating soliton dynamics, including single-period or double-period pulsating solitons, pulsating soliton molecules, synchronous and asynchronous pulsating solitons in multi-soliton pulsation states.

Noise-like pulses (NLPs) have been observed in mode-locked fiber lasers over two decades ago and still attract the interest of scientists because of its complexity and chaotic nature. In the NLP regime, the laser generates sub-nanosecond-long packets of randomly spaced sub-picosecond pulses, with random and uncontrollable duration and peak power. The packets are equally spaced in time (resulting from the cavity round-trip time), but the internal structure of the bunch is incoherent and unstable. NLPs have been observed in many different types of lasers, regardless of their emission wavelength, cavity net dispersion, or mode-locking mechanism. Chapter 15, by G. Soboń, reviews the most recent research on NLPs, with emphasis on the existing hypotheses explaining their formation, dynamics, and applications.

The generation of optical rogue waves during soliton explosions has been identified in recent years by several groups [153–155]. In two separate 2019 experiments, the excitation of rogue waves resulting from soliton molecule dynamics was also experimentally observed [145, 156]. Chapter 16 of this book, by L. Gao, provides a review of optical rogue waves generation in dissipative systems far away from the thermodynamic equilibrium, including ultrafast fiber lasers, microresonators, and other extended systems.

Aknowledgment We aknowledge FCT – Fundação para a Ciência e a Tecnologia (Project UID/CTM/50025/2020).

References

1. J. S. Russell, *Report of 14th Meeting of the British Association for Advancement of Science*, York, September, 311 (1844).
2. E. Fermi, J. R. Pasta, and S. M. Ulam, *Studies of nonlinear problems*, Los Alamos Sci. Lab. Rep., LA-1940, 1955
3. N. Zabusky and M. Kruskal, *Phys. Rev. Lett*. **15**, 240, 1965.
4. C.S. Gardner, J.M. Greene, M.D. Kruskal, and K. M. Miura, Phys. Rev. Lett. **19**, 109 (1967).
5. V.E. Zakharov and A.B. Shabat, *Sov. Phys. JETP* **34**, 62 (1972); *Zh. Eksp. Teor. Fiz.* **61**, 118 (1971).
6. M.J. Ablowitz and P.A. Clarkson, *Solitons, Nonlinear Evolution Equations and Inverse Scattering*, London Mathematical Society Lecture Notes Series **149**, (Cambridge University Press, Cambridge, 1991).
7. M. J. Ablowitz and P. A. Clarkson, P. A. *Solitons, Nonlinear Evolution Equations, and Inverse Scattering* (Cambridge University Press, New York, 1991).
8. J. T. Taylor, Editor, *Optical Solitons – Theory and Experiment* (Cambridge University Press, New York, 1992).
9. P. G. Drazin, *Solitons: An Introduction* (Cambridge University Press, New York, 1993).
10. C. H. Gu, *Soliton Theory and its Applications*, Springer, New York (1995)
11. N. Akhmediev and A. Ankiewicz, *Solitons: Nonlinear Pulses and Beams* (Chapman and Hall, London, 1997).
12. A. Hasegawa and F. D. Tappert, *Appl. Phys. Lett.* **23**, 142 (1973).
13. L. F. Mollenauer, R. H. Stolen, and J. P. Gordon, *Phys. Rev. Lett*. **45**, 1095 (1980).
14. A. Hasegawa, *Opt. Lett*. **8**, 650 (1983).
15. J. P. Gordon and H. A. Haus, *Opt. Lett*. **11**, 665 (1986).
16. L. F. Mollenauer, M. J. Neubelt, M. Haner, E. Lichtman, S. G. Evangelides, and B. M. Nyman, *Electron. Lett*. **27**, 2055 (1991).
17. A. Mecozzi, J. D. Moores, H. A. Haus, and Y. Lai, *Opt. Lett*. **16**, 1841 (1991).
18. Y. Kodama and A. Hasegawa, *Opt. Lett.* **17**, 31 (1992).
19. L. F. Mollenauer, J. P. Gordon, and S. G. Evangelides, *Opt. Lett*. **17**, 1575 (1992).
20. L. F. Mollenauer, E. Lichtman, M. J. Neubelt, and G. T. Harvey, *Electron. Lett*. **29**, 910 (1993).
21. Y. Kodama and S. Wabnitz, *Opt. Lett*., **19**, 162 (1994).
22. M. Nakazawa, Y. Kamada, H. Kubota, and E. Suzuki, *Electron. Lett*. **27**, 1270 (1991).
23. Y. Kodama, M. Romagnoli, and S. Wabnitz, *Electron. Lett*. **28**, 1981 (1992).
24. M. Matsumoto, H. Ikeda, T. Uda, and A. Hasegawa, *J. Lightwave Technol*. **13**, 658 (1995).
25. M. F. Ferreira, M. V. Facão, and S. V. Latas, *Fiber Integrat. Opt*. **19**, 31 (2000)
26. M. F. Ferreira, *Nonlinear Effects in Optical Fibers* (Hoboken, New Jersey: John Wiley & Sons, 2011)
27. N. Akhmediev, V. Afanasjev, and J. Soto-Crespo, *Phys. Rev. E* **53**, 1190 (1996).
28. M. F. Ferreira, M. V. Facão, S. V. Latas, S. V., and M. H. Sousa, *Fiber Integrated Opt.,* **24**, 287 (2005)
29. N. Akhmediev and A. Ankiewicz (Eds), *Dissipative Solitons* (Spinger, Berlin, 2005).
30. C. Normand and Y. Pomeau, *Rev. Mod. Phys*. **49,** 581 (1977).
31. P. Kolodner, Phys. Rev. A **44**, 6466 (1991)
32. R. Graham, *Fluctuations, Instabilities and Phase Transictions* (Springer, Berlin, 1975)
33. K. Staliunas, *Phys. Rev. A*, **48**, 1573 (1993)

34. P. Jian, W. Torruellas, M. Haelterman, S. Trillo, U. Peschel, and F. Lederer, *Opt. Lett.,* **24**, 400 (1999)
35. A. M. Dunlop, E. M. Wright, and W. J. Firth, *Optics Commun*. **147,** 393 (1998)
36. C. Ng and A. Bhattacharjee, *Phys. Rev. Lett.* **82**, 2665 (1999)
37. N. Akhmediev, A. Rodrigues, and G. Townes, *Opt. Commun*. **187**, 419 (2001).
38. N. Akhmediev, A. Ankiewicz, and J. Soto-Crespo, *J. Opt. Soc. Am. B* **15**, 515 (2001).
39. H. Haus, *J. Appl. Phys.* **46,** 3049 (1975).
40. H. Haus, J. Fujimoto, and E. Ippen, *J. Opt. Soc. Am. B* **8,** 2068 (1991).
41. E. Vanin, A. Korytin, A. Sergeev, D Anderson, M Lisak, L Vázquez, *Phys. Rev. A* **49**, 2806 (1994)
42. J. Moores, *Opt. Commun*. **96**, 65 (1993)
43. A. Akhmediev and V. Afanasjev, *Phys. Rev. Lett*. **75**, 2320 (1995)
44. H. Haus, E. Ippen, and K. Tamura, *IEEE J. Quantum Electron*. **30**, 200 (1994).
45. E. Ding and J. Kutz, *Opt. Soc. Am. B* **26,** 2290 (2009).
46. H. Leblond, M. Salhi, A. Hideur, T. Chartier, M. Brunel, and F. Sanchez, *Phys. Rev. A* **65**, 063811 (2002).
47. M. Salhi, H. Leblond, and F. Sanchez, *Phys. Rev. A* **68**, 033815 (2003).
48. M. Salhi, H. Leblond, F. Sanchez, M. Brunel, and A. Hideur, *J. Opt. A, Pure Appl. Opt*. **6**, 774 (2004).
49. A. Komarov, H. Leblond, and F. Sanchez, *Phys. Rev. E* **72**, 025604R (2005)
50. N. Pereira and L. Stenflo, *Phys. Fluids,* **20**, 1733 (1977).
51. K. Nozaki and N. Bekki, *Phys. Soc. Japan*, **53**, 1581 (1984).
52. R. Conte and M. Musette, *Physica D* **69**, 1 (1993).
53. O. Thual and S. Fauvre, *J. Phys*, **49**, 1829 (1988)..
54. P. Marcq, H. Chaté, and R. Conte, *Physica D*, **73,** 305 (1994).
55. M. Manousakis, P. Papagiannis, N. Moshonas, and K. Hizanidis, *Opt. Commun*. **198**, 351 (2001).
56. A. Ankiewicz, N. Akhmediev, and N. Devine, *Optical Fib. Technol*. **13**, 91 (2007).
57. S. Mancas and S. Choudhury, *Theor. Math. Phys*. **152**, 1160 (2007).
58. S. Mancas and S. Choudhury, *Chaos, Solitons & Fractals*, **40**, 91 (2009).
59. M. Ferreira, *IET Optoelectronics*, **12**, 122 (2018).
60. A. Maimistov, *J. Exp. Theor. Phys*. **77**, 727 (1993).
61. M. Zhuravlev and N. Ostrovskaya, *J. Exp. Theor. Phys*. **99**, 427 (2004).
62. E. Tsoy and N. Akhmediev, *Phys. Lett. A* **343**, 417 (2005).
63. E. Tsoy, A. Ankiewicz, and N. Akhmediev, *Phys. Rev. E*. **73**, 036621-1-10 (2006).
64. W. Chang, A. Ankiewicz, N. Akhmediev, and J. Soto-Crespo, Phys. Rev. E., **76,** 016607 (2007).
65. J. Soto-Crespo, N. Akhmediev, and A. Ankiewicz. Phys. Rev. Lett., **85**, 2937 (2000).
66. N. Akhmediev, J. Soto-Crespo, and G. Town, Phys. Rev. E., **63**, 056602 (2001).
67. I. Aranson and L. Kramer, Rev. Mod. Phys. **74**, 99 (2002)
68. W. Chang, A. Ankiewicz, N. Akhmediev, and J. Soto-Crespo, *Phys. Rev. E.*, **76**, 016607 (2007).
69. S. Wang, and H. Winful, Appl. Phys. Lett. **52**, 1174 (1998).
70. A. Tikhomirov, O. Kanakov, B. Altshuler, M. Ivanchenko, Eur. Phys. J. B **88**, 7 (2015).
71. H. Willaime, O. Cardoso and P. Tabeling, Phys. Rev. Lett. **67**, 3247 (1991).
72. A. Mohamadou, J. Mod. Phys. **3**, 438 (2012).
73. N. Akhmediev and A. Ankiewicz, in: Porsezian K, Kuriakose VC. (Eds.) *Optical Solitons: Theoretical and Experimental Challenges* (Berlin: Springer-Verlag; 2002)
74. N. Akhmediev, J.-M. Soto-Crespo, and P. Grelu, *Phys.Lett. A*, **372**, 3124 (2008)
75. W. Chang, A. Ankiewicz, J. Soto-Crespo, and N. Akhmediev, *J. Opt. Soc. Am. B* **25**, 1972 (2008).
76. W. Chang, J. Soto-Crespo, A. Ankiewicz, and N. Akhmediev, *Phys. Rev. A* **79**, 033840 (2009).

77. X. Wu, D. Tang, H. Zhang, and L. Zhao, *Opt. Express* **17**, 5580 (2009).
78. E. Ding, P. Grelu, and J. N. Kutz, *Opt. Lett*. **36**, 1146 (2011).
79. A. Komarov, F. Amrani, A. Dmitriev, K. Komarov, and F. Sanchez, *Phys. Rev. A* **87**, 023838 (2013).
80. Y. Xu, Y. Song, G. Du; P. Yan; C. Guo; G. Zheng; S. Ruan, *IEEE Photonics J*. **7**, 1502007 (2015).
81. K. Krzempek, J. Sotor, and K. Abramski, *Opt. Lett*. **41**, 4995 (2016).
82. G. Semaan, F. Braham, J. Fourmont, M. Salhi, F. Bahloul, and F. Sanchez, *Opt. Lett*. **41**, 4767 (2016).
83. K. Krzempek, D. Tomaszewska, and K. Abramski, *Opt. Express* **25**, 24853 (2017).
84. T. Du, W. Li, Q. Ruan, K. Wang, N. Chen, and Z. Luo, *Appl. Phys. Express* **11**, 052701 (2018).
85. S. C. Latas, M. F. S. Ferreira, and M. Facão, *J. Opt. Soc. Am. B* **34**, 1033 (2017).
86. S. C. Latas and M. F. Ferreira, *J. Opt. Soc. of Am. B*, **36,** 3016 (2019)
87. H. Zhang, D. Tang, L. Zhao, and N. Xiang, *Opt. Express* **16,** 12618 (2008).
88. L. Zhao, D. Tang, H. Zhang, X. Wu, and N. Xiang, *Opt. Express*, **16**, 9528 (2008).
89. L. Zhao, D. Tang, H. Zhang, and X. Wu, Opt. Express, 16, 10053 (2008).
90. L. Zhao, D. Tang, X. Wu, H. Zhang, and H. Tam, Opt. Lett., 34, 3059 (2009).
91. C. Mou, S. Sergeyev, A. Rozhin, and S. Turistyn, *Opt. Lett*. **36**, 3831 (2011).
92. Y. Song, L. Li, H. Zhang, D. Shen, D. Tang, and K. Loh, *Opt. Express* **21**, 10010 (2013).
93. Y. Song, H. Zhang, L. Zhao, D. Shen, and D. Tang, *Opt. Express* **24**, 1814 (2016).
94. Y. Luo, L. Li, D. Liu, Q. Sun, Z. Wu, Z. Xu, D. Tang, S. Fu, L. Zhao, *Opt. Express* **24**, 18718 (2016).
95. M. Liu, A. Luo, Z. Luo, and W. Xu, *Opt. Lett*. **42**, 330 (2017).
96. A. Akosman, J. Zeng, P. Samolis, and M. Sander, *IEEE J. Sel. Top. Quantum Electron.* **24**, 1101107 (2018).
97. D. Li, D. Shen, L. Li, D. Tang, L. Su, and L. Zhao, *Opt. Lett.* **43**, 1222 (2018).
98. J. Ma, G. Shao, Y. Song, L. Zhao, Y. Xiang, D. Shen, M. Richardson, and D. Tang, *Opt Lett*. **44,** 2185 (2019).
99. J. Soto-Crespo, N. Akhmediev, and A. Ankiewicz. Phys. Rev. Lett., **85**, 2937 (2000).
100. N. Akhmediev, J. Soto-Crespo, and G. Town, Phys. Rev. E., **63**, 056602 (2001).
101. S. Cundiff, J. Soto-Crespo, and N. Akhmediev, Phys. Rev. Lett., **88,** 073903 (2002).
102. A. Runge, N. Broderick, and M. Erkintalo, Optica, **2**, 36 (2015)
103. M. Erkintalo, C. Aguergaray, A. Runge, and N. Broderick, Opt. Express **20**, 22669 (2012).
104. C. Aguergaray, A. Runge, M. Erkintalo, and N. Broderick, Opt. Lett. **38**, 2644 (2013).
105. A. Runge, C. Aguergaray, N. Broderick, and M. Erkintalo, Opt. Lett. **39**, 319 (2014).
106. P. Grelu, F. Belhache, F. Gutty, and J. Soto-Crespo, *Opt. Lett.* **27,** 966 (2002).
107. D. Tang, W. Man, H. Tam, and P. Drummond, *Phys. Rev. A* **64,** 033814 (2001).
108. N. Seong and D. Kim, *Opt. Lett.* **27,** 1321 (2002).
109. P. Grelu, J. Beal, and J. Soto-Crespo, *Opt. Express* **11,** 2238 (2003).
110. G. Martel, C. Chédot, V. Réglier, A. Hideur, B. Ortaç, and Ph. Grelu, *Opt. Lett.* **32,** 343 (2007).
111. S. Latas and M. Ferreira, *Opt. Fiber Technol.* **11**, 292, 2005
112. A. Luo, X. Zheng, M. Liu, H. Liu, N. Zhao, Q. Ning, Z. Luo, and W. Xu, *Appl. Phys. Express* **8**, 042702 (2015).
113. P. Wang, C. Bao, B. Fu, X. Xiao, P. Grelu, and C. Yang, *Opt. Lett*. 41, 2254 (2016).
114. C. Ma, X. Tian, B. Gao and G. Wu, *Laser Phys.* **27,** 065102 (2017).
115. B. Liu, Y. Xiang, Y. Luo, S. Zhu, Z. Yan, Q. Sun, D. Liu, *Appl. Phys. B: Lasers Opt.* **124**, 151 (2018).
116. A. Niknafs, H. Rooholamininejad, and A. Bahrampour, *Laser Phys*. **28**, 045406 (2018).
117. H. Qin, X. Xiao, P. Wang, C. Yang, *Opt. Lett*. **43**, 1982 (2018).
118. C. Mou, S. Sergeyev, A. Rozhin, S. Turitsyn , *Opt. Express* **21,** 26868 (2013).
119. Y. Song, H. Zhang, L. Zhao, D. Shen, and D. Tang, *Opt. Express* **24**, 1814 (2016).

120. Y. Luo, J. Cheng, B. Liu, Q. Sun, L. Li, S. Fu, D. Tang, L. Zhao, and D. Liu, *Sci. Rep*. **7**, 2369 (2017).
121. J. Soto-Crespo, M. Grapinet, P. Grelu, N. Akmediev, *Phys. Rev. E* **70**, 066612 (2004).
122. K. Goda and B. Jalali, *Nat. Photonics* **7**, 102 (2013).
123. A. Runge, N. Broderick, and M. Erkinatalo, *J. Opt. Soc. Am. B* **33**, 46 (2016).
124. G. Herink, B. Jalali, C. Ropers, and D. Solli, *Nat. Photonics* **10**, 321 (2016).
125. X. Wei, B. Li, Y. Yu, C. Zhang, K. Tsia, and K. Wong, *Opt. Express* **25**, 29098 (2017).
126. K. Krupa, K. Nithyanandan, and P. Grelu, *Optica* **4**, 1239 (2017).
127. P. Wang, X. Xiao, H. Zhao, and C. Yang, *IEEE Photonics J*. **9**, 1 (2017).
128. P. Ryczkowski, M. Närhi, C. Billet, J.-M. Merolla, G. Genty, and J. Dudley, *Nat. Photonics* **12**, 221 (2018).
129. H. Chen, M. Liu, J. Yao, S. Hu, J. He, A. Luo, W. Xu, and Z. Luo, *Opt. Express* **26**, 2972 (2018).
130. H. Chen, M. Liu, J. Yao, S. Hu, J. He, A. Luo, Z. Luo, and W. Xu, *IEEE Photonics J.* **10**, 1 (2018).
131. Y. Yu, Z. Luo, J. Kang, and K. Wong, *Opt. Lett*. **43**, 4132 (2018).
132. Z. Wang, Z. Wang, Y. Liu, R. He, J. Zhao, G. Wang, and G. Yang, *Opt. Lett*. **43**, 478 (2018).
133. Y. Du, Z. Xu, and X. Shu, *Opt. Lett*. **43**, 3602 (2018).
134. Z. Wei, M. Liu, S. Ming, A. Luo, W. Xu, and Z. Luo, *Opt. Lett.* **43**, 5965 (2018).
135. G. Wang, G. Chen, W. Li, and C. Zeng, *IEEE J. Sel. Top. Quantum Electron*. **25**, 1 (2019).
136. X. Wang, Y. Liu, Z. Wang, Y. Yue, J. He, B. Mao, R. He, and J. Hu, *Opt. Express* **27**, 17729 (2019).
137. Z. Wei, M. Liu, S. Ming, H. Cui, A. Luo, W. Xu, and Z. Luo, *Opt. Lett*. **45**, 531 (2020)
138. Y. Zhang, Y. Cui, L. Huang, L. Tong, and X. Liu, *Op. Lett.* **45**, 6246 (2020).
139. Y. Luo, Y. Xiang, P. P. Shum, Y. Liu, R. Xia, W. Ni, H. Q. Lam, Q. Sun, and X. Tang, *Opt. Express* **28**, 4216 (2020).
140. W. Du, H. Li, J. Li, Z. Wang, Z. Zhang, S. Zhang, and Y. Liu, *Opt. Lett*. **45,** 5024 (2020)
141. T. Li, M. Liu, A. Luo, Z. Luo, and W. Xu, *Opt. Express* **28**, 32010 (2020
142. M. Suzuki, O. Boyraz, H. Asghari, P. Trinh, H. Kuroda, and B. Jalali, *Opt. Lett.* **43**, 1862 (2018).
143. Z. Wei, M. Liu, S. Ming, H. Cui, A. Luo, W. Xu, and Z. Luo, *Opt. Lett.* **45**, 531 (2019)
144. J. Peng and H. Zeng, *Comm Phys*. **2**, 34 (2019).
145. H. Chen, Y. Tan, J. Long, W. Chen, W. Hong, H. Cui, A. Luo, Z. Luo, and W. Xu, *Opt. Express*, **27,** 28507 (2019).
146. G. Herink, F. Kurtz, B. Jalali, D. Solli, and C. Ropers, *Science* **356**, 50 (2017).
147. K. Krupa, K. Nithyanandan, U. Andral, P. Tchofo-Dinda, and P. Grelul Phys. Rev. Lett. **118**, 243901 (2017).
148. X. Liu, X. Yao, and Y. Cui, *Phys. Rev. Lett*. **121**, 023905 (2018).
149. J. Peng and H. Zeng, *Laser Photonics Rev*. **12**, 1800009 (2018).
150. S. Hamdi, A. Coillet, and P. Grelu, *Opt. Lett*. **43**, 4965 (2018).
151. M. Liu, H. Li, A. Luo, H. Cui, W. Xu, and Z. Luo, *J. Opt.* **20**, 034010 (2018).
152. Z. Wang, K. Nithyanandan, A. Coillet, P. Tchofo-Dinda, and P. Grelu, *Nat. Commun.* **10**, 830 (2019).
153. L. Meng, A.-P. Luo, W.-C. Xu, and Z.-C. Luo Opt. Lett. **41**, 3912 (2016).
154. K. Krupa, K. Nithyanandan and P. Grelu, Optica **4**, 1239 (2017)
155. J. Peng, and H. Zeng, Phys. Rev. Applied, **12**, 034052 (2019).
156. J. Peng, and H. Zeng. Opt. Lett. 2019, **44,** 2899 (2019).

Chapter 2
Dissipative Solitons in Passively Mode-Locked Lasers

Philippe Grelu

Abstract In this chapter, I present the conceptual framework of dissipative optical solitons, shown to be particularly efficient to apprehend the diversity of ultrafast laser dynamics, understand their salient features and stimulate the design of innovative laser architectures. The chapter first unfolds the successive advances that built up soliton and dissipative soliton laser concepts. Then, the general signatures of dissipative soliton dynamics are highlighted. As a vivid illustration, a range of nonlinear dynamics of dissipative soliton molecules is presented, following an overview on the interaction processes among dissipative solitons within a laser cavity. Finally, going beyond mode-locked laser dynamics, a generalization of dissipative soliton concepts to incoherent and chaotic localized optical structures is exposed.

Keywords Optical solitons · Dissipative solitons · Ultrafast lasers · Fiber lasers · Mode locking · Bifurcations · Chaos · Nonlinear dynamics · Pattern formation · Dissipative systems · Attractors · Ultrafast optics · Ultrashort pulse characterization · Artificial intelligence · Complexity

2.1 From Solitons to Dissipative Solitons in Ultrafast Lasers

2.1.1 Early Advances Toward Soliton Lasers

A conventional description of the process of laser mode locking may unfold as follows. Take a relatively long laser cavity endowed with a broadband inhomogeneous gain medium: such laser will generally emit multiple longitudinal modes. These multiple lines will start beating in the time domain, occasionally producing intensity fluctuations significantly higher than the overall noisy background. The highest fluctuations will be promoted by the saturable absorber mechanism, which is

P. Grelu (✉)
Laboratoire ICB UMR 6303 CNRS, Université Bourgogne – Franche-Comté, Dijon, France
e-mail: philippe.grelu@u-bourgogne.fr

M. F. S. Ferreira (ed.), *Dissipative Optical Solitons*, Springer Series in Optical Sciences 238, https://doi.org/10.1007/978-3-030-97493-0_2

at the heart of the design of a mode locked laser. At this crucial step, the Kerr nonlinearity comes into play: four-wave mixing interaction transfers coherence among the laser comb lines, and generates additional comb lines, yielding a significant spectral broadening. That spectral broadening is supportive of shorter pulses of higher intensity, which travel round the cavity with fewer losses, owing to a more favorable transmission through the saturable absorber. Naturally, saturation effects soon come into play. The transmission through the saturable absorber has an optimum – and beyond that optimum, the pulses experience either a plateau or a decreased transmission. The gain medium also saturates. When the relaxation time of the gain medium is longer than the cavity roundtrip time, the overall gain saturation increases the competition between pulse precursors, possibly leading to a single-pulse mode locked regime.

This central scenario has variants, which justifies the renewed interest for experimental investigations of the buildup of mode locked pulses, using the currently available real-time ultrafast measurement techniques, see Sect. 2.4. Nevertheless, it strikes the importance of the optical Kerr nonlinearity in the mode locking process. Whereas the Kerr nonlinearity alone does not alter the pulse temporal profile, pulse shaping takes place through the interplay with other physical effects.

From the above mode locking scenario, we also understand that dissipative effects play a key role, whose magnitude hangs on the way they are emphasized within a given laser architecture. The latter was identified by H. Haus in his seminal 1975 article “Theory of mode locking with a fast saturable absorber” [1]. However, the 1975 paper adopted a perturbative approach, considering small pulse changes per cavity roundtrip, and completely overlooked the roles of the Kerr nonlinearity and that of chromatic dispersion. From the mid 1970s, while reaching sub-picosecond mode-locked pulse durations, laser physicists became aware of the major influence of the dispersive effects of chromatic dispersion and self-phase modulation (SPM). Initially, the impact of chromatic dispersion was considered to be a major nuisance, entailing the subsequent development of dispersion compensation schemes.

However, if the optical pulse propagates in the anomalous dispersion regime, the combined effects of SPM and dispersion lead to a temporal compression of the pulse, which is a contributive step in the mode locking scenario. Furthermore, the concept of the optical soliton was exposed [2, 3], providing an elegant solution to the handling of both anomalous dispersion and SPM that is particularly relevant when the accumulation of these effects becomes large. However, in the mid 1970s, ultrafast lasers were not yet operating in the infrared spectral region where the anomalous dispersion takes place, such as above the wavelength of 1.3 μm in silica. In addition, solitonic pulse shaping becomes significant after a propagation length that is generally orders of magnitude beyond the length of the gain medium used in bulk lasers. Exploiting solitonic propagation in the time domain calls for the use of waveguides to suppress diffraction over the relatively long distances needed to increase the linear and nonlinear dispersive interactions within a transparent propagation medium.

Progress in both infrared ultrafast laser sources and single-mode optical fibers allowed, in 1980, the first experimental demonstration of the optical soliton propagation regime [4]. This soliton propagation experiment employed a complicated

cryogenically cooled color-center laser source to reach the 1.35–1.75 μm spectral region and launch picosecond pulses into a 700-m long single mode fiber. The experiment gave a clear signature of fundamental as well as high-order soliton propagation. It provided incentive for a subsequent experiment that incorporated a piece of optical fiber within the ultrafast laser cavity, to get solitonic pulse shaping assist mode locking: in 1984, the *soliton laser* thus entered the scene [5]. The soliton laser concept met instant success, as it triggered subsequent investigations of coupled cavities enabling additive-pulse mode locking, which considerably eased the generation of shorter pulses [6]. In other words, the effectiveness of nonlinear interferences to create a virtual ultrafast saturable absorber was demonstrated. Such efficient strategy has since matured and diversified into virtual saturable absorbers using various schemes of nonlinear loop mirrors or nonlinear polarization evolution. Most interestingly, the 1984 article from Mollenauer and Stolen predicted that, when a suitable fiber gain medium would become available, *the soliton laser would probably take the form of a single loop of fiber closed upon itself. The simplicity and low cost of such devices would make them most attractive* [5].

In parallel, decisive progress in ultrafast laser sources was made in the mid-1980s with the invention of the titanium-sapphire (Ti:S) laser, and its fast-spreading use in photonics laboratories. In the early 1990s, most mode-locked Ti:S lasers were then operated with a dispersion-compensation scheme that placed the cavity in a slightly anomalous regime, to fit a "solitonic" operation, characterized by a nearly chirp-free hyperbolic-secant pulse profile [7]. The fiber laser revolution anticipated by Mollenauer and Stolen had to wait till the beginning of the 1990s, with the advent of the erbium-doped fiber amplifier that transformed the optical communication industry and generalized fiber-integrated components [8], which could be used to test various ultrafast fiber laser architectures at dwindling costs. The conceptual advances that resulted from the investigations begun for ultrafast fiber lasers operated within the 1.5–1.6 μm wavelength region would then revive and boost the development of their efficient counterparts at ~1 μm – with ytterbium-doped fibers, then ~2 μm – with thulium- or thulium-holmium-doped fibers, for which multiple applications followed.

2.1.2 Reconsidering the Value of Dissipation in Lasers

By the time ultrafast erbium-doped fiber lasers became successful, a few experiments with coupled-cavity mode-locked lasers hinted that stable mode locked operation could be obtained in the normal dispersion regime of the intracavity fiber, thus exploiting SPM but ruling out solitonic pulse shaping within the optical fiber [9, 10]. Such feature was investigated by H. Haus et al. in 1991 through an important extension of the 1975 model, which included self-phase modulation and group-velocity dispersion propagation effects within the cavity roundtrip [11]. This led to a master equation for mode locking that included laser pulse solutions in the normal dispersion regime. Laser pulse solutions in the normal dispersion regime

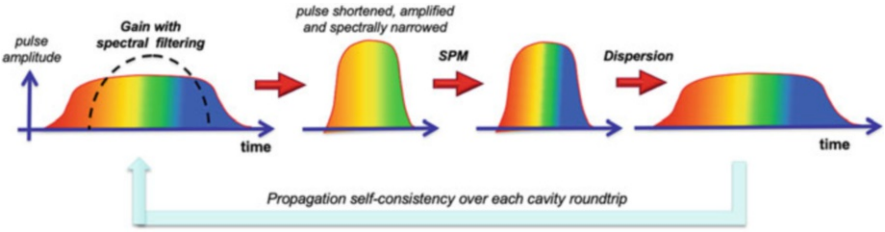

Fig. 2.1 A sequence of optical propagation effects requiring the interplay of strongly dissipative ones to allows a self-consistent laser mode locking in the normal dispersion regime

always require frequency chirping. Interestingly, the authors provided the clue to the existence of such stationary laser pulses within the normal dispersion regime: "*For positive GVD, the chirp parameter can become quite large. (. . .) Gain dispersion, instead of lengthening the pulse, shortens it. At first sight, this may seem paradoxical. However, if a pulse is chirped, then frequency filtering can, in fact, shorten it if it shaves off the high- and low-frequency wings. The pulse is kept in balance by a lengthening that is due to positive GVD. Of course, the gain dispersion also narrows the pulse spectrum. This spectral narrowing is compensated for by SPM*" [11]. Within these few lines, all the key points to establish the concept of a dissipative soliton are set, see Fig. 2.1. We have here the notion of a complex balance where dissipation is crucial and combines with chromatic dispersion and Kerr nonlinearity to enable new types of solitary wave solutions [12]. Such finding was strongly echoed a decade later, with the detailed investigation of dissipative solitons in all-normal dispersion fiber lasers, taking advantage of the large energy of these highly chirped pulses [13]. Indeed, the generation of highly chirped pulses within laser oscillators takes also the essence of chirped-pulse amplification, invented in the mid-1980s by Strickland and Mourou [14].

To fully establish the concept of dissipative solitons for ultrashort laser pulses, additional theoretical and numerical works were required. Indeed, the stability of the pulse solutions under perturbations and their behaviors during collisions needed to be investigated, in order to highlight the relevance of a new soliton concept. These investigations started in the early 1990s, meeting some initial resistance [15]. Indeed, for a few mathematical purists, the soliton terminology should be restricted to the solitary wave solutions of integrable conservative systems. However, it was realized that the solitary wave solutions of non-integrable dissipative systems displayed appealing properties that could find immediate applications in multiple areas in physics and beyond, leading to a wide acceptance of the dissipative soliton terminology at the beginning of the new millennium [16]. Concerning the history of optical soliton concepts, we can also draw two interesting parallels. The optical soliton of the (conservative) nonlinear Schrödinger equation benefitted from a transposition from earlier research in nonlinear plasma physics. Similarly, dissipative optical solitons received a significant theoretical background from the "autosoliton" concept describing reaction–diffusion systems in the field of plasma physics [17].

The dissipative soliton concept was required to solve several puzzles in ultrafast laser dynamics. Besides the case of bright laser pulses generated in the normal dispersion regime, which was discussed above, peculiar features of laser pulses produced by laser cavities in the anomalous dispersion regime could not be explained in the frame of conventional solitons. To understand that, let us first depict the NLS-soliton paradigm used to portrait the dynamics of ultrafast fiber lasers operated at the wavelength around 1.5 μm where standard optical fibers are anomalously dispersive. The NLS-soliton paradigm assumes that the dynamics is dominated by the propagation in passive optical fibers: stable pulses will be close to NLS optical solitons. The pulse duration can be assessed by assuming that the mode-locked pulses use the available gain bandwidth, and that they are sech-profiled chirp-free pulses. Given the fiber dispersion and nonlinearity parameters, knowing the pulse duration fixes the soliton energy. This is also known as the NLS-soliton area theorem: the product of the soliton energy times the soliton duration is a constant determined by the optical fiber. Such description was put forward as a convenient explanation for multiple pulsing that was readily observed in ultrafast fiber lasers [18]. However, the NLS-soliton picture is largely incomplete. Playing with the dissipative cavity parameters such as with linear and nonlinear loss, spectral filtering, etc., laser physicists realized that, within the anomalous dispersion regime, they could generate chirped pulses with a wide range of pulse duration. Moreover, the NLS soliton pulse shaping does not explain why all the pulses going round the cavity should be precisely identical, as generally observed. Indeed, for given fiber parameters, the NLS solitons belong to a family of solutions, see Fig. 2.2a, as reported in passive fiber cavities [19].

Thus, we need to introduce the notion of a dynamical attractor, which provides a fixed pulse profile endowed with robustness and stability. The existence of such attractor requires dissipation. Precisely, this attractor results from the composite balance among dispersive and dissipative interactions and defines the dissipative soliton, see Fig. 2.2b. Whereas the NLS-soliton can depict some features of the ultrafast laser pulses, the latter are always dissipative solitons in essence. The dissipative soliton concept for ultrafast lasers opens up numerous novel possibilities, by allowing a large freedom in handling the balance between the major physical effects, which has been reflected in the diversity of laser architectures and cavity parameter ranges that have been explored since [20].

2.2 Signatures of Dissipative Soliton Dynamics

The concept of dissipative solitons combines several essential physical notions. The *soliton theory* elaborates on the possibility that self-sustaining localized structures arise from a balance between several physical effects, where at least one of these effects should be *nonlinear*. The theory of *self-organization in open systems far from equilibrium* stems from the pioneering works of A. Turing and I. Prigogine and provides a conceptual framework to apprehend the growth and persistence of

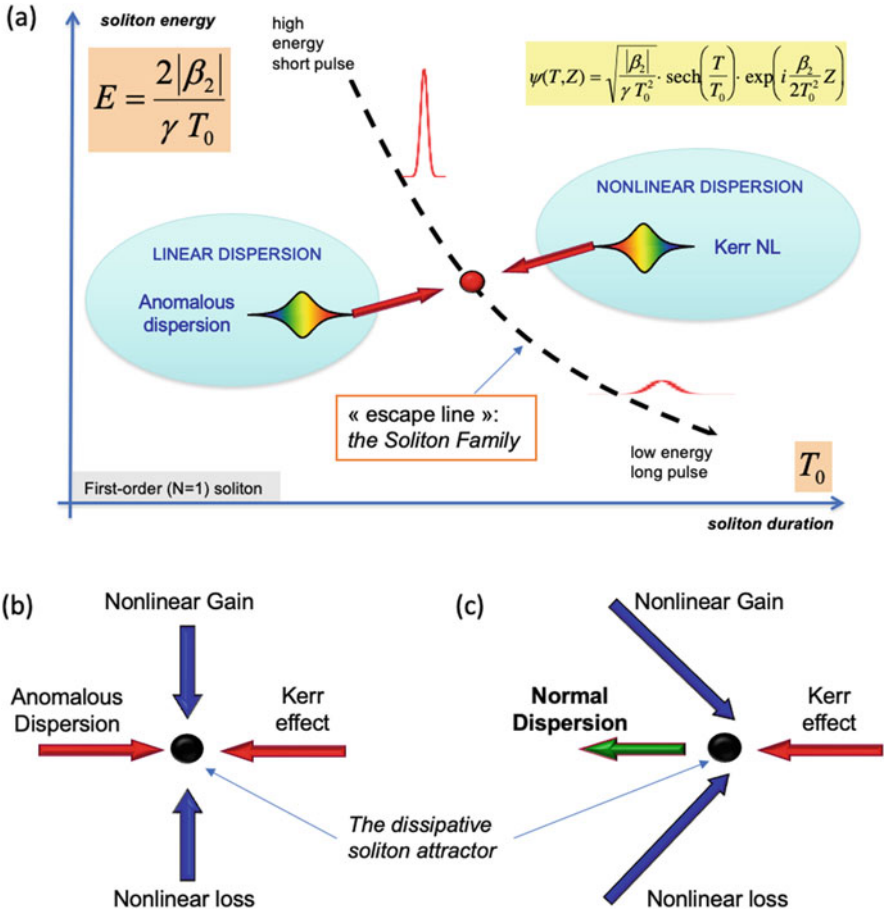

Fig. 2.2 (**a**) Representation of the family of bright fundamental solitons of the nonlinear Schrödinger equation, for propagation medium characterized by an anomalous dispersion coefficient $\beta_2 < 0$ and an effective nonlinearity $\gamma > 0$. (**b**) The addition of dissipative nonlinear effects fixes a unique solution, which is the dissipative soliton attractor characterized by a balance of all dispersive and dissipative effects. (**c**) The dissipative soliton picture works as well in the normal dispersion case, provided that gain/loss dispersion is added, which is represented by tilted vectors

localized structures from energy flow and dissipation [21, 22]. Note that the first implementation of self-organization principles into laser optics dates back to the end of the 1960s, with the theoretical advances made by H. Haken and R. Graham [23]. Finally, the general theory of *nonlinear dynamics* allows to analyze these structures as well as their transformations, through the powerful tools of *attractors* and *bifurcations*. These are the conceptual roots of dissipative solitons [16]. They connect to the specific signatures of dissipative soliton dynamics.

The existence of a dissipative optical soliton is based on that of a dynamical attractor. There are several attractor types. A stable focus attractor guarantees that all initial pulse conditions that belong to the attractor's basin of attraction will converge toward a fixed pulse profile. The convergence time decreases with the strength of dissipation. Therefore, such attractor is by definition a *noise eater*. Indeed, for unchanged system parameters, the focus point attractor dissipates the noise added to the pulse – such as from amplified spontaneous emission – provided that this added noise remains bounded so that it does not quick the pulse out of the basin of attraction. This attractor explains why ultrashort laser pulses can propagate stably for hours round the optical laser cavity, accumulating astronomical distances, a feat beyond the reach of conventional NLS solitons. It also explains why multiple pulses traveling round the laser cavity will generally share an identical profile, since being all carved by the same attractor. As a matter of fact, the stronger the attractor, the less the fluctuations of the dissipative soliton pulses induced by noise. A strong focus attractor thus provides an efficient filtering of noise, bringing stability to the laser pulse regime. It also brings robustness, meaning that it allows some amount of system parameter change without disruption of the pulse regime. This is why ultralow-noise mode locked lasers can be realized without active stabilization. Nevertheless, we note that designing such stable lasers is not straightforward as it requires considering intertwined propagation effects, with for instance a key role acknowledged to the average chromatic dispersion [24, 25].

At this point, one should realize that in real laser cavities, namely composed of a series of components and propagation media, the attracting state is multidimensional. Instead of a single temporal pulse profile, we have a succession of pulse profiles along the cavity spatial coordinate, which are propagated from one to another. Thus, the dissipative soliton attractor consists in the whole internal cavity dynamics, toward which field propagation converges in a self-consistent way over successive cavity roundtrips. The experimental characterization is generally conducted from a single laser output, thus missing this important feature, which can be investigated through numerical simulations.

However, important dissipative optical solitons features can be explored theoretically from averaged propagation equation models. This way, one can gain a general insight more easily than through detailed and specific numerical simulations. Such master equation approach, which was initiated by H. Haus for ultrafast lasers as exposed in the previous section [11], illustrated the high relevance of Ginzburg-Landau equations, with in particular the complex cubic-quintic Ginzburg-Landau equation (CGLE) to model universal ultrafast laser dynamics [15, 26, 27].

The CGLE model shows that dissipative soliton attractors of focus type exist for a wide range of system parameters – namely, effective average parameters – including within the normal dispersion regime [28]. The amplitude pulse profile of the dissipative soliton can vary widely according to the system parameters, spanning for instance from ~hyperbolic-secant to ~gaussian and flat-top profiles. This is in stark contrast with the hyperbolic-secant single shape adopted by stationary fundamental bright solitons within the NLS propagation model, whose duration and peak amplitude depend on both system parameters and input conditions. More, frequency

chirping remains an essential feature of dissipative solitons, as opposed to the constant nonlinear phase lying across the NLS fundamental soliton pulse profile. The essential reason of that non-uniform phase across the dissipative soliton profile is the following. To maintain a stationary pulse profile, dissipative solitons require an internal energy redistribution among their various pulse parts, since due to nonlinear dissipation, some parts will be amplified, whereas others (for instance, pulse tails) will be attenuated. Remembering that energy flows through phase gradients, such energy redistribution therefore maps with a non-uniform phase profile, which will generally combine linear and nonlinear frequency chirping. Dissipative solitons in highly dissipative media will generally feature major linear and nonlinear frequency chirping. This precisely applies, though not exclusively, to the stable bright dissipative solitons found within the normal dispersion regime. It is also possible to find parameter sets in the anomalous dispersion regime where dissipative solitons will bear major frequency chirping, for instance in the so-called dissipative soliton resonance dynamics [29]. Interestingly, since dissipative solitons exist in both anomalous and normal dispersion regimes, we can find dissipative solitons in the absence of linear dispersion, which for example happens within a good approximation in the case of narrowband intense pulses in meter-long laser cavities [30]. Whereas dispersion no longer represents a blocking issue for mode-locked laser operation in general, the whole set of laser parameters needs to be adapted to accommodate a given dispersion range.

Dissipative soliton attractors of focus type also exist for more complex pulse shapes and patterns, such as composite solitons. For instance, two laser pulses, interacting through their pulse tails while they propagate round the laser cavity, can reach a stable equilibrium consisting of a stationary pattern that is defined by a multi-soliton attractor. This complex attractor can be reached from a suitable domain of the two-pulse initial conditions, namely, from within the attractor's basin of attraction. The distributed CGLE model has proved to be particularly useful to yield a common understanding on these multi-soliton attractors [31, 32]. Stable multiple-light-pulse bound states have been dubbed soliton molecules [33], since they allow interesting analogies with matter molecules. The central case for study is that of two interacting pulses, which can form a stable dissipative soliton pair, characterized by a stationary relative separation and a self-locked phase between the two dissipative solitons. The topic of dissipative soliton molecules has driven considerable fundamental interest, with more elements presented in Sect. 2.3.

A stable focus attractor can be subjected to bifurcations, when the laser control parameters (such as pump power, cavity losses, dispersion etc.) are changed. For instance, at a certain point in the parameter space, a Hopf-type bifurcation unfolds, transforming the single focus attractor into a limit cycle attractor. In such as case, the pulse solution will oscillate in time, with oscillation features that depend solely on the system parameters. In the frame of distributed models, such as the CGLE model, this represents an oscillation of the pulse profile with a given period in the spatial coordinate of propagation. If we now consider the ultrashort pulse dynamics within a realistic, non-uniform laser cavity – i.e., modelled by a parameter-managed propagation model – at each location of the laser cavity, the pulse profile will oscillate

from one roundtrip to the next. Therefore, the cavity periodicity implies a discrete oscillation, which can be N-periodic with respect to the cavity roundtrip (the simplest one being a period-2 oscillation), or combine multiple periods, or become incommensurate with the cavity roundtrip [34]. These are main possibilities among others, as the bifurcation options for such nonlinear systems having an infinite number of degrees of freedom appear limitless [35].

In the frame of dissipative soliton dynamics, we can combine the complexity of bifurcations with the multiplicity of pulses within a dissipative soliton pattern, such as a soliton molecule. As a result, various types of pulsating soliton molecules have been predicted numerically and observed in ultrafast laser experiments, see Sect. 2.3.

2.3 Dissipative Soliton Molecules

2.3.1 The Wealth of Soliton Interaction Processes Within a Laser Cavity

As discussed in the previous sections, ultrafast lasers are prone to generate multiple identical dissipative solitons, when driven at high pump power. This tendency is exacerbated in fiber lasers operated in the anomalous dispersion regime, owing to the lower pulse energy limitation: up to thousand pulses can be generated simultaneously within multi-watt pumped ultrafast fiber laser cavities [36, 37]. A handful of dissipative solitons per roundtrip can be easily obtained under ~100 mW pumping of an anomalous fiber laser cavity. These soliton pulses will always interact, as they have virtually an infinite time to do so within the bounded cavity propagation path: even faint interactions can be revealed, leading to specific multi-pulse patterns.

Fundamentally, we can make a distinction between short-range coherent interactions and long-range incoherent interactions. The direct interaction through the pulse tails is phase sensitive and leads to the formation of strongly bound soliton molecules, within suitable domains of system parameters. This interaction range varies according to the pulse specific profile but is typically limited to a few pulse widths: such interaction is taken into account within distributed propagation models such as in the CGLE, where dissipative soliton molecules were theoretically and numerically predicted under the initial denominations of bound states [31] and multisolitons [32]. A number of experimental observations using various laser architectures, wavelengths and parameter ranges soon confirmed the universality of soliton molecules within dissipative nonlinear systems [38–42].

In real laser systems though, the discontinuities and inhomogeneities of the propagation media can lead to an important amount of dispersive wave radiation from the soliton pulses. Combined with the cavity periodicity, relatively coherent dispersive waves can build up in the vicinity of the propagating pulses yielding in the spectral domain the typical Gordon-Kelly sidebands [43, 44]. Such resonant dispersive waves may form an extended pedestal to the soliton pulses, allowing to mediate

phase sensitive interactions through increased pulse separations, up to more than two orders of magnitude beyond the single-pulse width, thus allowing distant soliton molecules [45] and soliton molecular complexes [46]. The numerical modelling of the formation of such light pulse structures requires to take a lumped parameter-managed laser cavity model [46–48].

Long range interactions are not sensitive to the relative optical phase between propagating solitons. Among them, the pulse interaction resulting from gain relaxation dynamics, namely from the depletion of the gain after the passage of a pulse and its subsequent recovery, is usually the most substantial [49]. It yields an effective repulsive force among laser pulses of moderate intensity, which therefore maximizes the separation among all coexisting solitons, hence leading to passive harmonic mode locking. That periodic pattern generally suffers an important timing jitter, as the soliton pulses are not phase-locked one on another.

In between the tight soliton molecules and harmonic mode locking patterns, there are other multi-pulse arrangements characterized by a relative stable pattern, such as pulse bunching, a common phenomenon in ultrafast fiber lasers. Pulse bunching forms packets of ultrashort pulses with an inter-pulse separation in the nanosecond range, typically, which includes non-uniform temporal separations. Whereas the role of gain dynamics cannot be ruled out, pulse bunching requires another type of incoherent pulse interaction. Electrostriction in optical fibers is one possibility, as it drives an optomechanical interaction that modulates the optical index in the wake of an intense pulse, therefore offering the possibility to trap subsequent pulses at specific distances in the moving reference frame [50]. The optomechanical interaction is very weak in standard optical fibers, so that its effects are generally overwhelmed by those of other interaction mechanisms in ultrafast lasers. However, especially designed photonic crystal fibers can enhance the optomechanical interaction by several orders of magnitude, leading to novel possibilities to control multiple soliton patterns in fiber laser cavities, either in the form of multi-soliton complexes [46] or high-harmonic mode locking, the latter obtained by matching cavity harmonics to the optical index oscillation frequency [51].

Besides the optomechanical interaction, another incoherent interaction mechanism was recently unveiled. In some pulsed laser regimes, particularly within fiber lasers, soliton pulses can coexist with quasi-continuous waves, which combine with dispersive waves to form a noisy optical background filling the entire cavity. This is a condition where peculiar multi-pulse dynamics can be observed, such as the *soliton rain* [52]. In such situation, the soliton pulses will undergo a random walk on the fluctuating background. Due to the interplay between gain dynamics and cavity losses, that background will be non-uniform, which leads to a relative pulse drift, which is affected by the presence of other pulses. A weak attractive force results, which bears an analogy with the Casimir effect in quantum electrodynamics [53]. The magnitude of such Casimir-type interaction depends widely on the features of the quasi-cw background, but it can dominate other long-range pulse interactions over pulse separations up to tens of nanoseconds [54].

Therefore, whereas soliton molecules result from short-range coherent interactions, there are numerous scenarios that involve long-range incoherent interactions to get pulses drift toward one another up to the range where coherent interactions

will dominate. It all depends on the specific history of multiple pulse formation: in the early stages of mode locking, multiple pulses can arise from the breakup of an unstable high-energy pulse, or from various pulse precursors that are located far apart within the cavity roundtrip. This justifies the recent interest for the experimental investigation of the self-starting buildup of mode locking, using real time characterization techniques [55–58].

The interplay among interactions is difficult to take into account numerically, considering the large orders of magnitude in time and space that separate them. Nevertheless, such interplay will affect the features of the soliton molecules. For instance, the interplay between coherent short-range interactions and gain relaxation dynamics was observed experimentally and explained theoretically and numerically. For soliton molecules having more than two pulses, it yielded a monotonously varying temporal separation between subsequent pulses, which was dubbed a *chirped soliton molecule* pattern [59].

2.3.2 From Stationary to Pulsating Soliton Molecules

The optical characterization of ultrafast dissipative soliton molecules sets quite a few challenges, which naturally increase along with their dynamical complexity. Early experiments used mainly the output of multi-shot optical autocorrelators and optical spectrum analyzers. The relevance of averaged measurements is assessed with a recording of the integrated pulse energy in real time (via an oscilloscope), possibly complemented with radiofrequency analysis, in order to confirm the observation of stationary molecules. Whereas the photo-detected output pulses do not reveal the picosecond temporal structure of the soliton molecule, a stable stationary soliton molecule produces (i) a (symmetric) multi-peaked second-order autocorrelation trace and (ii) a spectral interferogram containing the information about relative pulse separation and phases within the soliton molecule. Through the processing and comparison of these experimental data, the temporal structure of the soliton molecule can be unveiled.

The two-soliton molecule is the central figure of investigation. Reported within various laser architectures, operating wavelengths, and pulse energy ranges, it illustrates the universal dynamical feature of multisoliton attractors. In the characterization process, we generally make the assumption that the two pulses share the same amplitude profile, being shaped by a common attractor. Thus, the optical spectral intensity $I(\omega)$ of such soliton molecule reads:

$$I(\omega) = 2I_0(\omega)[1 + \cos(\omega\tau - \varphi)],$$

where τ is the temporal separation between the two pulses, φ is their phase difference, ω is the detuning from the central angular frequency ω_0, and $I_0(\omega)$ would be the spectral intensity of a single pulse. Therefore, measuring the spectral interfringe yields the pulse separation, while the offset of the fringe pattern with respect to the

central frequency yields the phase difference. Fourier transforming the spectral intensity allows a more efficient processing of the experimental data, yielding a first-order autocorrelation trace, or temporal coherence function, where τ and φ can be readily extracted. Such procedure can be extended to a higher number of pulse constituents, under some conditions [46].

Highly contrasted spectral fringes are the signature for (i) a stable temporal separation between the pulses constituting the soliton molecule and (ii) self-phase locking of these pulses. Both are attribute of the soliton molecule attractor, seen in a subspace of finite dimension – a tool of visualization and analysis named the Poincaré section. The two-dimensional Poincaré section using both the temporal separation and phase is called the interaction plane, which typically displays the dynamical evolution of ($\tau \cos \varphi$, $\tau \sin \varphi$).

Based on the CGLE model, theoretical and numerical investigations revealed the existence of a limited number of two-soliton molecule fixed-point focus attractors, characterized by the self-locking of the pulses with a relative phase of either π [31], or $\pm\pi/2$, the latter being associated with a high potential stability [32]. These soliton molecule attractors were discovered experimentally [39, 40], but other relative phase locking values have also been found, a fact attributed to the fundamental difference existing between distributed and lumped periodic systems: the latter allow additional focus attractors due to the contribution of dispersive waves in the dissipative soliton interaction [47]. Recently, the high stability of some dissipative soliton molecules was measured by using the technique of balanced optical cross correlation, yielding a relative timing jitter within the two-soliton molecule down to the attosecond level [60].

By changing one or several parameters of the laser cavity, one can move out from the existence domain of fixed-point attractors and meet bifurcations. Among other possibilities, the Hopf bifurcation is a widely spread one: it transforms the fixed-point focus attractor into a limit-cycle. As stated in Sect. 2.2, a stable limit cycle attractor is characterized by a quasi-stationary oscillating pulse feature, whose periodicity can be commensurate or not with the cavity roundtrip time. In the situation of the two-soliton molecule, the first evidence was produced in 2006 [61]: in that related work, the blurring of the experimentally recorded spectral fringes and second-order cross-correlation peaks were attributed to an oscillation of the relative phase and temporal separation between the two solitons, an interpretation supported by numerical simulations. This topic of pulsating soliton molecules gained further consideration a decade later, with the generalization of real-time spectral measurements that provided a strong experimental confirmation [62, 63]. Dispersive Fourier-transform has become the most popular real-time spectral measurement technique. It consists of propagating a short pulse structure through a highly dispersive line in the linear and far-field regime: this way, the pulse stretches considerably to adopt an intensity profile that maps its spectral intensity profile [64]. Several types of pulsating soliton molecule dynamics have therefore been retrieved experimentally and validated numerically, such as oscillating-phase, vibrating (both phase and separation), or sliding-phase soliton molecules [62]. The anharmonic character of some oscillating soliton molecules has also been pointed

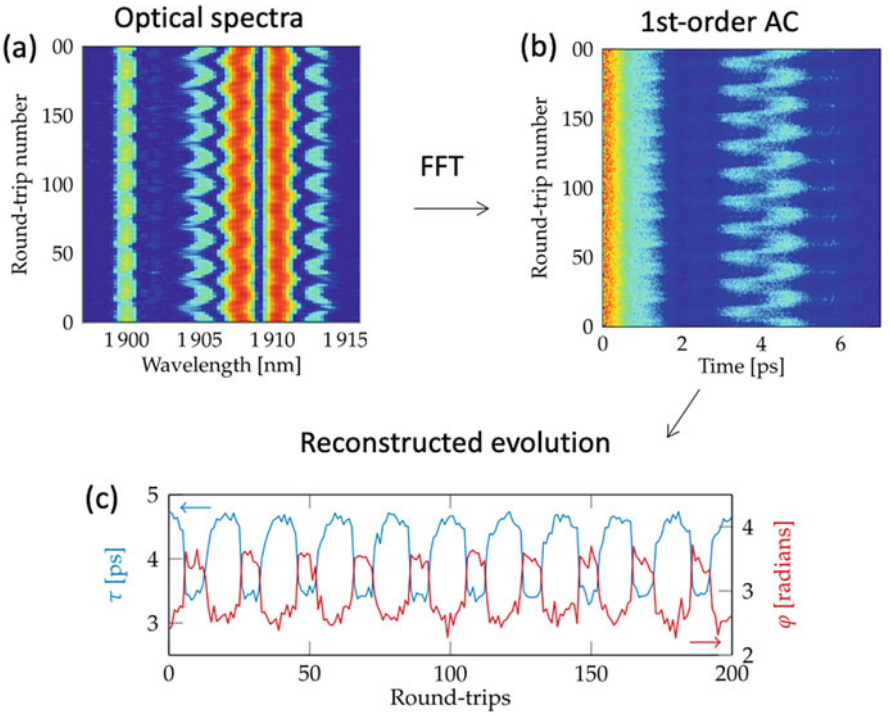

Fig. 2.3 Reconstruction of the oscillations of the relative separation (τ, in ps) and relative phase (φ, in radian) between two dissipative solitons that form a compact soliton molecule self-assembled within a thulium-doped fiber laser (adapted from [65]). (**a**) Recording of optical spectra over 200 successive roundtrips, employing the DFT measurement technique. (**b**) Processing of the spectral data by Fourier transform, which enables (**c**) revealing the anharmonic oscillations of the internal dynamical variables of the soliton molecule

out, see Fig. 2.3 [65]. Finally, the formation and dissociation of unstable soliton molecules was also observed, as well as transient multisoliton states accompanying the formation of stable soliton molecules [56, 65].

Let us remark that the general assumption of identical pulse profiles does not hold true when time-delayed dynamics become important, such as in the case of slow saturable absorber effects [66]. The identical pulse profile assumption may also break for non-stationary soliton molecules, as was recently investigated [67].

Now, considering that two-soliton molecules can behave as units within the ultrafast laser cavity, these molecules will also interact [68]. The long-range repulsive interaction from gain relaxation dynamics will favor harmonic mode locking of two-soliton molecules, which has indeed been confirmed in real-time spectrally resolved experiments. It is also interesting to consider the possible formation of soliton molecular complexes, where several two-soliton molecules bind through attractive forces of intermediate range. This was recently investigated in the elementary case of 2 + 2 optical soliton molecular complexes (SMC) [46]. It consisted in

two identical soliton-pair molecules, each formed through a strong pulse-tail interaction, which were linked through a weaker dispersive wave mediated interaction. Two main SMC dynamics were unveiled: SMC with sliding-phase dynamics and SMC with oscillating-phase dynamics. These dynamics were retrieved from the spectral analysis of successive laser output and confirmed by numerical simulations. This opens up the investigation of the complex dynamics of intricate multiple pulse patterns, whereas the multiple scales involved pose new challenges to the experimental characterization.

2.4 Toward Incoherent Dissipative Solitons

By moving the laser cavity parameters, we cross the successive boundaries of stationary and regularly pulsating dissipative solitons, whose domains of existence are bounded. Moving further will then end up with the complete disruption of the mode-locked pulse operation. For instance, by reducing the pumping power down to some amount, the nonlinearity no longer suffices to maintain the pulse localization, entailing quasi-cw lasing instead. On the other way, by increasing the pumping power, whereas the excess of nonlinearity is generally conducive to multi-pulsing transitions, such excess can also disrupt the mode locking operation as well. However, other abrupt bifurcations can take place, leading for instance to odd chaotic-pulse dynamics. In such cases, a strong competition between instability and localizing physical effects takes place to maintain a short pulse localized in its average moving reference frame. As a matter of fact, despite the persistence of a rather well-defined round trip time for the traveling pulse, the laser regime can no longer be qualified as mode locked. This peculiar situation can take various forms, which we have proposed to encompass within the notion of incoherent dissipative solitons [69, 70]. Indeed, all the situations of long-lived chaotic laser pulses encountered so far are characterized by well-defined averaged features (namely, temporal and spectral intensity profiles as recorded by an averaging instrumentation), which can be measured over times scales that depend on the given chaotic dynamic – say, in a typical range varying from 10^2 to 10^5 cavity roundtrips for most of them. The meaningfulness of averaged pulse features is the clear signature of an underlying chaotic attractor, which employs dissipative processes to limit the pulse excursions inside of the dynamical system that has otherwise infinite dimensions.

Chaotic laser pulse attractors can be categorized by the amount of incoherence attributed to the light pulses, as opposed to the high coherence that is assumed for stable mode locked pulses. Incoherence first refers to the lack of a precise phase relationship between pulses observed at successive cavity roundtrips. Note that even in the case of “stable” mode locked laser regimes, phase noise and timing jitter represent usual limitations of the laser coherence. These limitations are combatted in highly stabilized mode-locked laser schemes by using cavity length stabilization and phase-locked loops to attain, in the best case, the carrier-envelope phase stabilization

required in demanding metrological applications of the frequency comb generated from such stable mode-locked lasers. On the opposite, some applications require pulsed sources with a low degree of coherence, as in free-space communication and lidar applications for dense networks, in order to limit crosstalk. These applications could benefit from the utilization of incoherent dissipative solitons.

Let us now depicts some of the most vivid illustrations of incoherent dissipative solitons. Soliton explosions are defined by intermittent periods of pulse instability followed by recovery, the pulse returning to a quasi-stationary coherent mode locking before the next instability develops. A laser operating in that regime can still be qualified as partially mode locked, since between explosive events, successive output pulses remain relatively close. Soon after being predicted numerically, this unstable pulse regime was observed in a Ti:sapphire pulsed laser [71] and later within fiber laser experiments [72, 73], hence confirming its universality.

Noise-like pulse emission, soliton liquids and dissipative rogue waves are terminologies that relate to chaotic pulse dynamics bearing a large degree of incoherence, since the related internal field structures behave chaotically at all times, from one cavity roundtrip to the next and even within a given cavity roundtrip. A soliton liquid consists in a bunch of dissipative solitons whose interactions induce chaotic relative motions [52, 74]. The characterization of its internal structure requires ultrafast measurements having adequate spectral and/or temporal resolution. It has been observed as one of the three main field components of the soliton rain dynamics [52]. More precisely, in the soliton rain, the presence of a noisy cw background induces fluctuations which, when exceeding a certain threshold, excite the formation of dissipative soliton pulses that subsequently drift toward a condensed liquid soliton phase, the latter aggregating multiple interacting dissipative solitons in ceaseless motions as well as radiating dispersive waves that feed the background. Such laser dynamics illustrates well the amount of complexity which can arise in presence of multiple pulsing and chaos yet displaying a distinct and vivid dynamical picture embedding multiple time scales and field structures. A highly chaotic soliton liquid is also conducive to the observation of dissipative rogue waves, namely, extreme fluctuations of optical intensity or pulse density that occur in the course of multiple pulse interactions and collisions [75].

Noise-like pulse emission in ultrafast lasers is characterized by the complete loss of mutual coherence between successive pulses. It was discovered in 1997 [76], then reported in numerous subsequent experiments [77–80]. This self-starting regime is characterized by (i) a self-generated compact waveform, whose shape and duration strongly depend on the laser scaling parameters (for instance, the duration can vary, accordingly, from a few picoseconds to microseconds); (ii) a complex fine structure consisting in a large collection of sub-picosecond chaotic pulses; (iii) stationary averaged spectral and optical autocorrelation features in the long run, typically over thousand cavity roundtrips. This regime stems from the competition between a strong instability and dissipative processes favoring temporal localization. The statistics of the spectral waveforms can also reveal rare events of extreme amplitude, namely, spectral rogue waves [81].

The features of noise-like pulse emission were revisited in a recent investigation of the buildup dynamics of these incoherent pulses [70]. By combining experimental and numerical approaches, the study brought insight on the similarities and differences of the noise-like pulses developing under either the normal or the anomalous cavity dispersion regime. In the experiment, the laser output was spectrally characterized in real time by using the dispersive Fourier-transform technique. These buildup experiments highlighted the following. In the normal dispersion regime, a few long-lived picosecond pulse precursors compete over a relatively long (thousands of roundtrips) amplification stage, then a winning (largest energy) pulse undergoes an exponential spectral broadening followed by an explosive spectral broadening stage that sets in the chaotic dynamics (within a few tens of roundtrips), while the other pulse precursors vanish. In the anomalous dispersion regime, the pulse precursors propagate in higher numbers and the spectral broadening stage is more gradual (hundreds of roundtrip), associated with a longer coexistence between the growing chaotic pulse and the decaying pulse background. See also Fig. 2.4, which displays the abrupt transitions in both dispersion regimes. In the long run (quasi-stationary regime), the pulse fluctuations are larger in the normal dispersion regime, nevertheless they are associated with a tighter temporal localization than in the anomalous dispersion regime.

A simple parameter-managed numerical laser model was used to interpret the spectral broadening in the buildup phase and the long run features. The normal dispersion regime is indeed characterized by the largest fluctuations, owing to the interplay between gain, self-phase modulation, and dispersion. The waveform growth instability scatters sub-pulses of various magnitude. Inside that chaotic waveform, small amplitude field parts diffuse rapidly and vanish outside the main pulse extension, experiencing mostly the effects of normal dispersion and saturable

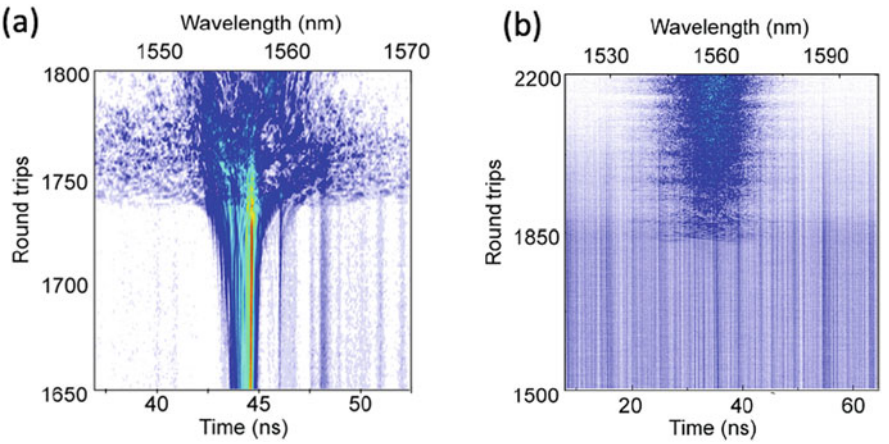

Fig. 2.4 Recording of the buildup of (noise-like) incoherent dissipative solitons, using the real-time DFT measurement under (**a**) the normal cavity dispersion regime, and (**b**) the anomalous cavity dispersion regime. (After Ref. [70])

absorption. In the anomalous dispersion regime, the contribution of a large self-phase modulation favors high-order soliton pulse shaping that is regularized by dissipative processes, hence maintaining the integrity of sub-pulse constituents within the chaotic pulse over much longer times, whereas allowing extended excursions of these sub-pulses within the chaotic pulse bunch. However, frequent pulse collisions entail highly varying amplitudes, which induces a pulse discrimination through the effects of nonlinear gain and loss. The existence of dissimilar physical mechanisms leading to long-lived chaotic-pulse waveforms confirms that these incoherent dissipative localized structures exist in a much wider subspace of cavity parameters than initially anticipated. Akin to the assimilation of a variety of stable ultrashort laser dynamics within the broad concept of dissipative solitons, it is fully justified to include such noise-like pulse generation cases within the terminology of incoherent dissipative solitons of ultrafast lasers. The notion of a chaotic attractor explains why successive laser switch-on will yield the same average features in the long run, though each buildup evolution will be unique.

Observed within a wide range of laser cavity architectures, these chaotic-pulse laser regimes clearly indicate the existence of universal strange attractors, whose properties can be summarized as follows: (i) the dynamics is extremely sensitive to initial conditions, which is the essence of chaos; (ii) the dynamics returns at finite time intervals to similar field realizations, such localization being attribute of an attracting state.

The incoherent dissipative soliton concept is fully applicable to other nonlinear systems, for instance involving additional field dimensions, for instance polarization or multiple transverse modes. Thus, vector dynamics of incoherent dissipative solitons were reported in 2017, bringing additional pieces of nonlinear dynamics complexity. For instance, polarization locking and polarization switching dynamics of the incoherent soliton were reported [69], generalizing locking and switching dynamics previously reported in the case of coherent vector solitons [82, 83]. In the vicinity of polarization switching dynamics, intermittent behaviors were associated with vector rogue waves bearing common features with the soliton explosion effect [69]. Akin to the dissipative soliton concept, the notion of an incoherent dissipative soliton will stimulate research in multiple areas of nonlinear science and favor analogies between them [84].

2.5 Summary and Prospects

We started the journey of dissipative solitons in passively mode-locked lasers with a sort of history capsule of the evolution and mutual enrichment of nonlinear dynamical concepts for ultrafast lasers, which seems to have culminated in the concept of dissipative solitons. Yet, the story is not over, since laser complexity has numerous doors to break in, such as: additional field dimensions, which includes polarization and spatio-temporal complexity [85–87], multiple-pulse interaction dynamics, delayed response and multiple time scales.

In Sect. 2.2, we have seen that the interplay of dissipative nonlinear effects has opened up unsuspected possibilities for stable ultrashort laser pulse generation, found in much wider laser parameter domains than initially anticipated and benefitting from the strength and robustness of dissipative soliton attractors. Basically, dissipative solitons will bear linear and nonlinear frequency chirping. Nevertheless, some cavity designs, such as dispersion managed lasers, can feature nearly chirp-free points where optimal ultrashort output pulses can be extracted. Finally, non-stationary solitons obtained through bifurcations and multi-solitons bring a glimpse of the wealth of nonlinear dynamics that can be generated within ultrafast lasers and apprehended by the general concept of dissipative solitons.

Sections 2.3 and 2.4 developed some recent aspects of complex dissipative dynamics. Optical soliton molecules display interesting analogies with their matter counterparts. The real-time investigation of the two-soliton molecule, highlighting stationary as well as various oscillating dynamics, has expanded the conceptual background: this entices to revisiting soliton molecules comprising larger number of dissipative soliton pulses, up to soliton complexes and macromolecules. We have also exposed the generalization of the notion of dissipative solitons to incoherent and chaotic pulses, which encompasses a variety of short-pulse dynamics that are not mode locked but share the feature of being bound to an attractor of chaotic nature, namely a strange attractor [88].

One upcoming challenge is to control such wealth of ultrafast dynamical behavior with the powerful tools of artificial intelligence. This way, the full-fledged fundamental science of complex ultrafast nonlinear dynamics will travel another loop toward demanding applications [89–92].

References

1. Haus, H A: Theory of mode locking with a fast saturable absorber, J. Appl. Phys. **46**, 3049 (1975)
2. Zakharov V E and Shabat A B: Exact theory of two-dimensional self-focusing and one-dimensional self-modulation of wave in nonlinear media *J. Experim. Theor. Phys.* **34** 62 (1972)
3. Hasegawa A and Tappert F: Transmission of stationary nonlinear optical pulses in dispersive dielectric fibers I—anomalous dispersion *App. Phys. Lett.* **23** 142 (1973)
4. Mollenauer L F, Stolen R H, and Gordon J P: Experimental observation of picosecond pulse narrowing and solitons in optical fibers *Phys. Rev. Lett.* **45** 1095 (1980)
5. Mollenauer L F and Stolen R H: The soliton laser *Opt. Lett.* **9** 13 (1984)
6. Goodberlet J, Wang J, Fujimoto J G, and Schultz P A: Starting dynamics of additive-pulse mode locking in the Ti:Al2O3 laser, *Opt. Lett.* **15** 1300–1302 (1990)
7. Spence D E, Kean P N, and Sibbett W: 60-fsec pulse generation from a self-modelocked Ti: sapphire laser, *Opt. Lett.* **16**, 42–44 (1991)
8. Desurvire E: The golden age of optical amplifiers, *Physics Today* **47** 20–27 (1994)
9. Blow K J and Wood D: Mode-locked lasers with nonlinear external cavities, *J. Opt. Soc. Am. B* **5** 629 (1988)
10. Kean P N, *et al.*: Enhanced mode locking of color-center lasers, *Opt. Lett.* **14**, 39 (1989)

11. Haus H A, Fujimoto J G and Ippen E P: Structures for additive pulse mode locking *J. Opt. Soc. Am. B* **8** 2068 (1991)
12. Picholle E, Montes C, Leycuras C, Legrand O and Botineau J: Observation of dissipative superluminous solitons in a Brillouin fiber ring laser, *Phys. Rev. Lett*. **66**, 1454–1457 (1991).
13. Chong A, Buckley J, Renninger W and Wise F: All-normal-dispersion femtosecond fiber laser *Opt. Express* **14** 10095 (2006)
14. Strickland D and Mourou G: Compression of amplified chirped optical pulses *Opt. Commun.* **56** 219 (1985)
15. Vanin, E V, et al.: Dissipative optical solitons. *Phys. Rev. A* **49**, 2806–2811 (1994)
16. Akhmediev N and Ankiewicz A (Eds.) 2005 *Dissipative solitons* (Springer, Berlin Heidelberg) & 2008 *Dissipative solitons: from Optics to Biology and Medicine* (Springer Verlag, Berlin Heidelberg)
17. Kerner, B S & Osipov V V: *Autosolitons: A new approach to problems of selforganization and turbulence* (Kuwer Academic Publishers, 1994).
18. Grudinin A B, Richardson D J and Payne D N: Energy quantization in figure eight fibre laser *Electron. Lett.* **28** 67 (1992)
19. Schwache A and Mitschke F: Properties of an optical soliton gas *Phys. Rev. E* **55** 7720 (1997)
20. Grelu Ph and Akhmediev N: Dissipative solitons for mode-locked lasers *Nat. Photonics* **6** 84 (2012)
21. Turing A M: The chemical basis of morphogenesis, *Phil. Trans. Roy. Soc. London Series B, Biological Siences* **237** 37–72 (1952)
22. Nicolis G & Prigogine I: *Self-organization in nonequilibrium systems: From dissipative structures to order through fluctuations* (John Wiley & Sons, 1977).
23. Graham R and Haken H: Laserlight — first example of a second-order phase transition far away from thermal equilibrium, *Z. Phys.* **237**, 31–46 (1970)
24. Jones D J et al: Carrier-envelope phase control of femtosecond mode-locked lasers and direct optical frequency synthesis, *Science* **288** 635–639 (2000)
25. Mayer A S et al: Flexible all-PM NALM Yb:fiber laser design for frequency comb applications: operation regimes and their noise properties, *Opt. Express* **28**, 394543 (2020)
26. Moores J D: On the Ginzburg-Landau laser mode-locking model with fifth-order saturable absorber term, *Opt. Commun.* **96**, 65–70 (1993)
27. Akhmediev N and Afanasjev V V: Novel arbitrary-amplitude soliton solutions of the cubic-quintic complex Ginzburg-Landau equation, *Phys. Rev. Lett.* **75**, 2320–2323 (1995)
28. Soto-Crespo J M, Akhmediev N N, Afanasjev V V and Wabnitz S: Pulse solutions of the CQGLE in case of normal dispersion *Phys. Rev. E* **55** 4783 (1997)
29. Grelu Ph, Chang W, Ankiewicz A, Soto-Crespo J M and Akhmediev N: Dissipative soliton resonance as a guideline for high-energy pulse laser oscillators, *J. Opt. Soc. Am. B* **27** 2236 (2010)
30. Deslandes P et al.: Picosecond to femtosecond pulses from high power self-mode–locked ytterbium rod-type fiber laser, *Opt. Express* **21** 10731 (2013)
31. Malomed, B: Bound solitons in the nonlinear Schrödinger–Ginzburg–Landau equation, *Phys. Rev. A* **44**, 6954–6957 (1991)
32. Akhmediev N N, Ankiewicz A & Soto-Crespo J M: Multisoliton solutions of the complex Ginzburg–Landau equation, *Phys. Rev. Lett.* **79**, 4047–4051 (1997)
33. Stratmann M, Pagel T & Mitschke F: Experimental observation of temporal soliton molecules, *Phys. Rev. Lett.* **95,** 143902 (2005)
34. Soto-Crespo J M, Grapinet M, Grelu Ph and Akhmediev N: Bifurcations and multiple-period soliton pulsations in a passively mode-locked fiber laser, *Phys. Rev. E* **70**, 066612 (2004)
35. Akhmediev N, Soto-Crespo J M & Town G: Pulsating solitons, chaotic solitons, period doubling, and pulse coexistence in mode-locked lasers: Complex Ginzburg–Landau equation approach, *Phys. Rev. E* **63**, 056602 (2001)
36. Haboucha A, Leblond H, Salhi M, Komarov A and Sanchez F: Analysis of soliton pattern formation in passively mode-locked fiber lasers, *Phys. Rev. A* **78** 043806 (2008)

37. Lecaplain C and Grelu Ph: Multi-gigahertz repetition-rate-selectable passive harmonic mode locking of a fiber laser, *Opt. Express* **21** 10897 (2013)
38. Gutty F, Grelu Ph, Huot N, Vienne G, and Millot G: Stabilisation of modelocking in fibre ring laser through pulse bunching, *Electron. Lett.* **37** 745 (2001)
39. Tang D Y, Man W S, Tam H Y and Drummond P D: Observation of bound states of solitons in a passively mode-locked fiber laser, *Phys. Rev. A* **64** 033814 (2001)
40. Grelu Ph, Belhache F, Gutty F & Soto-Crespo J M: Phase-locked soliton pairs in a stretched-pulse fiber laser, *Opt. Lett.* **27**, 966–968 (2002)
41. Seong N H and Kim D Y: Experimental observation of stable bound solitons in a figure-eight fiber laser, *Opt. Lett.* **27**, 1321–1323 (2002)
42. Hideur A et al.: Ultra-short bound states generation with a passively modelocked high-power Yb-doped double-clad fiber laser, *Opt. Commun.* **225**, 71–78 (2003)
43. Gordon J P: Dispersive perturbations of solitons of the nonlinear Schrödinger equation, *J. Opt. Soc. Am B* **9** 91 (1992)
44. Kelly S M J: Characteristic sideband instability of periodically amplified average soliton, *Electron. Lett.* **28** 806 (1992)
45. Ortaç B, Hideur A, and Brunel M: Binding widely-separated pulses with a passively mode-locked Yb-doped double-clad fiber laser, *Appl. Phys. B: Lasers and Optics* **79**, 185–192 (2004).
46. Wang Z Q, Nithyanandan K, Coillet A, Tchofo-Dinda P, and Grelu Ph: Optical soliton molecular complexes in a passively mode-locked fiber laser, Nature Commun. **10**, 830 (2019)
47. Soto-Crespo J M, Akhmediev N, Grelu Ph, Belhache F: Quantized separations of phase-locked soliton pairs in fiber lasers, *Opt. Lett.* **28**, 1757 (2003)
48. Tang D Y, Zhao B, Zhao L M, and Tam H Y: Soliton interaction in a fiber ring laser, *Phys. Rev. E* **72**, 016616 (2005)
49. Kutz J N, Collings B C, Bergman K and Knox W H: Stabilized Pulse Spacing in Soliton Lasers Due to Gain Depletion and Recovery, *IEEE J. Quantum Electron.* **34** 1749 (1998)
50. Pilipetskii A N, Golovchenko E A, and Menyuk C R: Acoustic effect in passively mode-locked fiber ring lasers, *Opt. Lett.* **20** 907–909 (1995)
51. Pang M et al.: Stable subpicosecond soliton fiber laser passively mode-locked by gigahertz acoustic resonance in photonic crystal fiber core, *Optica* **2**, 339–342 (2015)
52. Chouli S and Grelu Ph: Soliton rains in a fiber laser: An experimental study, *Phys. Rev. A* **81**, 063829 (2010)
53. R. Weill, A. Bekker, V. Smulakovsky, B. Fischer, and O. Gat: Noise-mediated Casimir-like pulse interaction mechanism in lasers, Optica **3**, 189 (2016).
54. Sulimany K et al.: Bidirectional Soliton Rain Dynamics Induced by Casimir-Like Interactions in a Graphene Mode-Locked Fiber Laser, *Phys. Rev. Lett.* **121**, 133902 (2018)
55. Herink G, Jalali B, Ropers C, and Solli D R: Resolving the build-up of femtosecond mode-locking with single-shot spectroscopy at 90 MHz frame rate, *Nat. Photon.* **10**, 321 (2016)
56. Peng J and Zeng H: Build-up of dissipative optical soliton molecules via diverse soliton interactions, *Laser Photon. Rev.* **12**, 1800009 (2018)
57. Liu X, Yao X, and Cui Y: Real-Time Observation of the Buildup of Soliton Molecules, *Phys. Rev. Lett.* **121**, 023905 (2018)
58. Ryczkowski P et al.: Real-time full-field characterization of transient dissipative soliton dynamics in a mode-locked laser, *Nat. Photon.* **12**, 221 (2018)
59. Zavyalov A, Grelu Ph, and Lederer F: Chirped soliton molecules in mode-locked fiber lasers, *Opt. Lett.* **37**, 175–177 (2012)
60. Shi H, Song Y, Wang C, Zhao L and Hu M: Observation of subfemtosecond fluctuations of the pulse separation in a soliton molecule *Opt. Lett.* **43** 1623 (2018)
61. Grapinet M & Grelu Ph: Vibrating soliton pairs in a mode-locked laser cavity, *Opt. Lett.* **31**, 2115–2117 (2006)
62. Krupa K, Nithyanandan K, Andral U, Tchofo-Dinda P and Grelu P: Real-Time Observation of Internal Motion within Ultrafast Dissipative Optical Soliton Molecules, *Phys. Rev. Lett.* **118** 243901 (2017)

63. Herink G, Kurtz F, Jalali B, Solli D R and Ropers C: Real-time spectral interferometry probes the internal dynamics of femtosecond soliton molecules, *Science* **356** 50 (2017)
64. Goda K and Jalali K B: Dispersive Fourier transformation for fast continuous single-shot measurements, *Nat. Photon.* **7** 102 (2013)
65. Hamdi S, Coillet A, and Grelu Ph: Real-time characterization of optical soliton molecule dynamics in an ultrafast thulium fiber laser, *Opt. Lett.* **43**, 4965–4968 (2018)
66. Lederer M J et al: Multipulse operation of a Ti:sapphire laser mode locked by an ion-implanted semiconductor saturable-absorber mirror, *J. Opt. Soc. Am. B* **16** 895–904 (1999)
67. Igbonacho Y J et al.: Dynamics of distorted and undistorted soliton molecules in a mode-locked fiber laser, *Phys. Rev. A* **99**, 063824 (2019)
68. Zhao L M, Tang D Y, and Liu D: Ultrahigh-repetition-rate bound-soliton fiber laser, *Appl. Phys. B* **99**, 441–447 (2010)
69. Krupa K, Nithyanandan K, and Grelu Ph: Vector dynamics of incoherent dissipative optical solitons, *Optica* **4**, 1239–1244 (2017)
70. Wang Z Q, Nithyanandan K, Coillet A, Tchofo-Dinda P, and Grelu Ph: Buildup of incoherent dissipative solitons in ultrafast fiber lasers, *Phys. Rev. Research* **2**, 013101 (2020)
71. Cundiff S T, Soto-Crespo J M, and Akhmediev N: Experimental Evidence for Soliton Explosions, *Phys. Rev. Lett.* **88** 073903 (2002)
72. Runge A F J, Broderick N G R, and Erkintalo M: Observation of soliton explosions in a passively mode-locked fiber laser, *Optica* **2**, 36 (2015)
73. Liu M et al.: Successive soliton explosions in an ultrafast fiber laser, *Opt. Lett.* **41**, 1181–1184 (2016)
74. Amrani F et al.: Dissipative solitons compounds in a fiber laser: Analogy with the states of the Matter, *Appl. Phys. B*, **99**, 107 (2010)
75. Lecaplain C, Grelu Ph, Soto-Crespo J M, and Akhmediev N: Dissipative rogue waves generated by a mode locked fiber laser, *Phys. Rev. Lett.* **108**, 233901 (2012)
76. Horowitz M, Barad Y and Silberberg Y: Noiselike pulses with a broadband spectrum generated from an erbium-doped fiber laser *Opt. Lett.* **22** 799 (1997)
77. Takushima Y, Yasunaka K, Ozeki Y, and Kikuchi K: 87 nm bandwidth noise-like pulse generation from erbium-doped fiber laser, *Electron. Lett.* **41**, 399 (2005)
78. Zhao L M, Tang D Y, Cheng T H, Tam H Y, and Lu C: 120 nm bandwidth noise-like pulse generation in an erbium-doped fiber laser, *Opt. Commun.* **281**, 157 (2008)
79. Kobtsev S, Kukarin S, Smirnov S, Turitsyn S, and Latkin A: Generation of double-scale femto/pico-second optical lumps in mode-locked fiber lasers, *Opt. Express* **17**, 020707 (2009)
80. Runge A, Aguergaray C, Broderick N G R, and Erkintalo M: Coherence and shot-to-shot spectral fluctuations in noise-like ultrafast fiber lasers, *Opt. Lett.* **38**, 4327 (2013)
81. Lecaplain C and Grelu Ph: Rogue waves among noiselike pulse laser emission: An experimental investigation, *Phys. Rev. A* **90**, 013805 (2014)
82. Cundiff S T, Collings B C, Akhmediev N N, Soto-Crespo J M, Bergman K, and Knox W H: Observation of Polarization-Locked Vector Solitons in an Optical Fiber, Phys. Rev. Lett. **82**, 3988 (1999)
83. Zhang H, Tang D Y, Zhao L M, Bao Q, and Loh K P: Vector dissipative solitons in graphene mode locked fiber lasers, *Opt. Commun.* **283** 3334–3338 (2010)
84. Grelu Ph (Ed.) *Nonlinear optical cavity dynamics: from microresonators to fiber lasers*, Wiley-VCH, Weinheim (2016)
85. Wright L G, Christodoulides D N, and Wise F W: Spatiotemporal modelocking in multimode fiber lasers, *Science* **358**, 94–97 (2017)
86. Qin H, Xiao X, Wang P, and Yang C: Observation of soliton molecules in a spatiotemporal mode-locked multimode fiber laser, *Opt. Lett.* **43**, 1982–1985 (2018)
87. Krupa K et al.: Multimode nonlinear fiber optics, a spatiotemporal avenue, *APL Photonics* **4**, 110901 (2019)
88. Soto-Crespo J M and Akhmediev N: Soliton as Strange Attractor: Nonlinear Synchronization and Chaos, *Phys. Rev. Lett.* **95**, 024101 (2005)

89. Andral U, Si Fodil R, Amrani F, Billard F, Hertz E, and Grelu P: Fiber laser mode locked through an evolutionary algorithm *Optica* **2**, 275 (2015)
90. Woodward R I and Kelleher E J R: Towards 'smart lasers': self-optimisation of an ultrafast pulse source using a genetic algorithm *Sci. Rep.* **6** 37616 (2016)
91. Girardot J, Billard F, Coillet A, Hertz E, and Grelu Ph: Autosetting mode-locked laser using an evolutionary algorithm and time-stretch spectral characterization, *IEEE J. Select. Topics in Quantum Electron*. **26**, 1100108 (2020)
92. Wei X, Jing J C, Shen Y, Wang L: Harnessing a multi-dimensional fibre laser using genetic wavefront shaping, *Light: Sci. & Appl.* **9**, 149 (2020)

Chapter 3
Dissipative Soliton Buildup Dynamics

Zhi-Chao Luo, Ze-Yu Zhan, Meng-Jun Feng, Ji-Xiang Chen, Meng Liu, Ai-Ping Luo, and Wen-Cheng Xu

Abstract The development of ultrafast pulse fiber lasers has great impact on many aspects of our life for their versatile applications in fields ranging from fundamental sciences to industrial purposes. By virtue of passive mode-locking techniques, the ultrashort pulse can be easily obtained from the fiber lasers. In addition to being an ultrashort pulse source for practical applications, the passively mode-locked fiber lasers are also actually the nonlinear optical systems which provide a good platform for investigating various dissipative soliton nonlinear dynamics. As a fundamental but important nonlinear dynamics of ultrafast fiber lasers, the buildup process of the passive mode-locking can be used to describe how to form a soliton in the laser systems. In this chapter, we review the recent advances on the dissipative soliton buildup dynamics in passively mode-locked fiber lasers. The real-time dynamics of dissipative soliton buildup can be well characterized in the temporal and spectral domains based on the advanced experimental methodologies of spatio-temporal reconstruction and dispersive Fourier transform. These findings will give some new insights into the soliton transient dynamics as well as soliton formation dynamics in ultrafast fiber lasers.

Keywords Fiber lasers · Passive mode locking · Ultrashort pulse · Dissipative solitons · Conventional solitons · Soliton transient phenomena · Buildup dynamics · Dispersive Fourier transform · Spatio-temporal reconstruction · Real-time dynamics

Z.-C. Luo (✉) · Z.-Y. Zhan · M.-J. Feng · J.-X. Chen · M. Liu · A.-P. Luo · W.-C. Xu
Guangdong Provincial Key Laboratory of Nanophotonic Functional Materials and Devices & Guangzhou Key Laboratory for Special Fiber Photonic Devices and Applications, South China Normal University, Guangzhou, Guangdong, China
e-mail: zcluo@scnu.edu.cn

M. F. S. Ferreira (ed.), *Dissipative Optical Solitons*, Springer Series in Optical Sciences 238, https://doi.org/10.1007/978-3-030-97493-0_3

3.1 Introduction

Since the physicists discovered the dissipative solitons that widely exist in non-integral and non-conservative systems [1–3], the formation mechanisms and characteristics of dissipative solitons in dissipative systems have attracted much attention. The conventional soliton concept implies that the single balance between nonlinearity and dispersion. But for dissipative soliton, a composite balance among several effects, including nonlinear effect, dispersion, gain and loss, should be taken into account. A notable point here is that the balance between gain and loss plays an important role in the dissipative soliton dynamics [4]. Therefore, the dissipative solitons present more complex dynamics than those of the conventional solitons [2, 5, 6]. The ultrafast fiber lasers are essentially dissipative systems, which are considered as good platforms for exploring the dissipative solitons dynamics [7–11]. Figure 3.1 shows the experimental setup of a common passively mode-locked fiber laser. Revealing the dynamics of dissipative solitons in fiber lasers is of great significance to the investigation of nonlinear dynamics and the practical applications of optical solitons. In recent years, extensive investigations have been conducted on the nonlinear evolution and dynamics of dissipative solitons in passive mode-locked fiber lasers, such as multi-soliton patterns [12–14], dissipative soliton rain [15–17], and dissipative soliton resonance [18–22]. As a fundamental and important nonlinear phenomenon in ultrafast fiber lasers, the investigation of dissipative soliton buildup dynamics would be beneficial for us to understand the physical mechanism of solitons as well as the improvement of laser performance.

Since the 1990s, the buildup dynamics of mode-locked fiber lasers have been reported theoretically and experimentally [23, 24]. To date, the buildup time of dissipative soliton as well as the evolution dynamics in the time domain with a large timescale have been well understood. It has been shown that the buildup time is related to the intracavity soliton power, and large soliton energy is beneficial to the fast self-starting [25]. During the buildup process, the pulses exhibit relaxation oscillations in the temporal domain, similar to the Q-switched mode-locking before achieving the stable mode-locked operation. Since the soliton buildup process in mode-locked fiber lasers can be understood as a non-repetitive and random process,

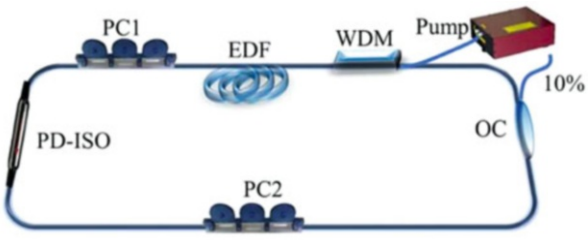

Fig. 3.1 Schematic of passive mode-locked fiber laser

it is actually a transient nonlinear phenomenon. With the great advances in high--temporal-resolution measurement technology of ultrashort pulses, the investigation on the transient dynamics of solitons has reached an unprecedented level. However, the real-time spectral dynamics during the soliton buildup process in ultrafast fiber lasers cannot be captured due to the scanning speed limitations of the conventional optical spectrum analyzer (OSA). To solve this problem, researchers have proposed a simple yet powerful real-time spectral measurement technique, namely the Dispersive Fourier Transform (DFT) technique [26–29], to resolve the buildup dynamics of dissipative soliton in the spectral domain. The DFT method actually utilizes chromatic dispersion to map the optical spectrum of a pulse to a temporal waveform whose intensity envelope mimics its spectrum, allowing real-time spectral dynamics to be measured by an oscilloscope. Therefore, it is expected that the DFT will be a good tool for observing the real-time spectral dynamics of dissipative soliton buildup in fiber lasers. By virtue of DFT technology, some complex soliton transient dynamics have been observed in fiber lasers, such as rogue waves [30–32], soliton explosions [33–36], pulsating solitons [37–39], vector solitons [40, 41], and bound-state solitons [42].

Recently, G. Herink et al. reported a detailed study of soliton buildup in femtosecond Kerr-lens mode-locking (KLM) Ti:sapphire laser by DFT [43]. During the soliton buildup process, several critical phenomena were directly observed in the spectral domain, including the birth of broadband spectrum, the transient interference patterns, and the spectral beating dynamics. However, owing to the different physical mechanisms of pulse formation in the laser cavities, Ti:Sapphire lasers are typically not self-starting ones and their mode-locking operation needs to be triggered by external perturbations [44], while fiber lasers can be self-starting as long as the cavity parameters are properly adjusted [45, 46]. In addition, in fiber lasers, the light propagation is typically limited to the small area of single-mode fiber. When combing the high peak power of mode-locked soliton, it is expected that the soliton will experience more nonlinear effects and fruitful phenomena. Therefore, the exploration of the soliton buildup dynamics in ultrafast fiber lasers will underpin the understanding of soliton dynamics and nonlinear behavior in dissipative optical systems.

In this chapter, we review recent results on the real-time buildup dynamics of different soliton regimes in spectral and temporal domains in fiber lasers. We first outline the buildup dynamics of conventional solitons in fiber lasers operating in the anomalous dispersion regime, and the buildup dynamics of dissipative solitons in the net-normal dispersion fiber lasers. Moreover, the physical mechanisms of spectral beating behavior during the soliton buildup process are also discussed, and the soliton buildup process is further qualitatively reconstructed by the results of numerical simulations. Then we also discuss the buildup process of dissipative solitons in a net-normal dispersion bidirectional fiber laser. Finally, the buildup dynamics of dissipative soliton molecules are introduced to further explore the different properties presented in the soliton buildup dynamics.

3.2 Conventional Soliton Buildup Dynamics in an Anomalous Dispersion Fiber Laser

It is well known that conventional solitons in an anomalous dispersion fiber laser can be formed by balancing group velocity dispersion (GVD) and self-phase modulation (SPM) [47]. This type of soliton features that the Kelly sidebands can be seen on the mode-locked spectrum [48]. Recently, Chen et al. experimentally observed the buildup dynamics of conventional solitons in the fiber laser operating in anomalous dispersion regime. They performed the temporal and spectral analysis of the soliton buildup dynamics based on the experimental methods of spatio-temporal reconstruction and DFT [49].

The schematic diagram of the anomalous dispersion fiber laser used for the experiment is shown in Fig. 3.2, which is a typical fiber ring laser mode-locked by real saturable absorber (SA). A 4.1 m long erbium-doped fiber (EDF) is used as the gain medium, and the carbon nanotube (CNT) is placed in the laser cavity as SA. A mechanical chopper is placed between the pump laser and the wavelength division multiplexer (WDM) to control the start or stop of the mode-locking operation. Two polarization controllers (PCs) are placed in the laser cavity to adjust the polarization state. The polarization-dependent isolator (PD-ISO) is employed for better

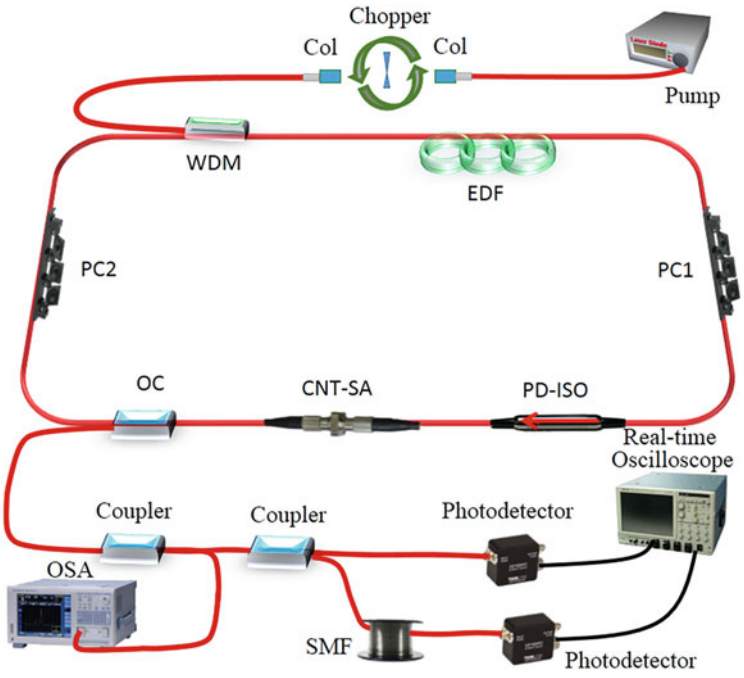

Fig. 3.2 Experimental setup of an anomalous dispersion ultrafast fiber laser. (Adapted from Ref. [49])

optimization of the mode-locking state. By adjusting the PC, the nonlinear loss of the laser cavity can be controlled. In order to measure the buildup dynamics in the spectral domain by DFT method and temporal evolution simultaneously, an additional 10:90 coupler is connected to the laser output. One of the output ports is directly connected to a high-speed real-time oscilloscope with a photodetector. Then the other one is connected to ~14 km long single-mode fiber, which uses the DFT to map the spectrum into a temporal waveform. In this case, the real-time spectral dynamics can be directly recorded by the oscilloscope.

When the fiber laser is operating in mode-locking state, the typical laser performance is shown in Fig. 3.3. Figure 3.3a, b show the mode-locked spectrum centered at 1558 nm and the pulse train with the fundamental repetition rate of 13.06 MHz, respectively. As we can see, there are obvious Kelly sidebands on both sides of the mode-locked spectrum, which is one of the characteristics of conventional solitons in a fiber laser with anomalous dispersion regime. Figure 3.3c shows the autocorrelation trace, indicating the characterized pulse duration is 810 fs. The corresponding radio frequency (RF) spectrum is presented in Fig. 3.3d with a signal-to-noise ratio of ~55 dB, indicating the stability of the laser.

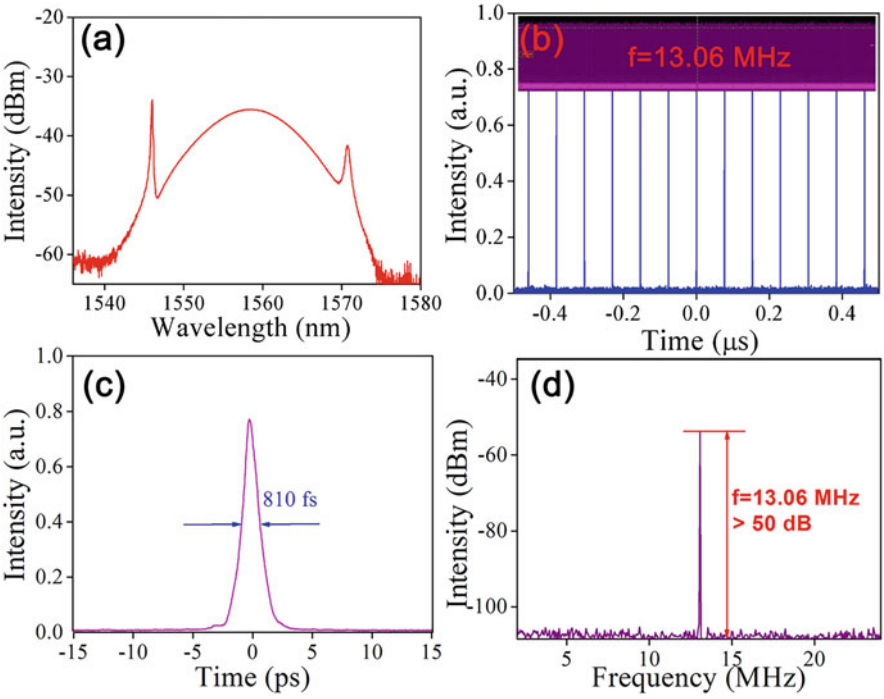

Fig. 3.3 Performance of anomalous dispersion fiber laser in mode locking state. (**a**) Spectrum of conventional soliton. (**b**) Pulse-train. Inset: pulse-train with larger range. (**c**) Autocorrelation trace. (**d**) RF spectrum. (Adapted from Ref. [49])

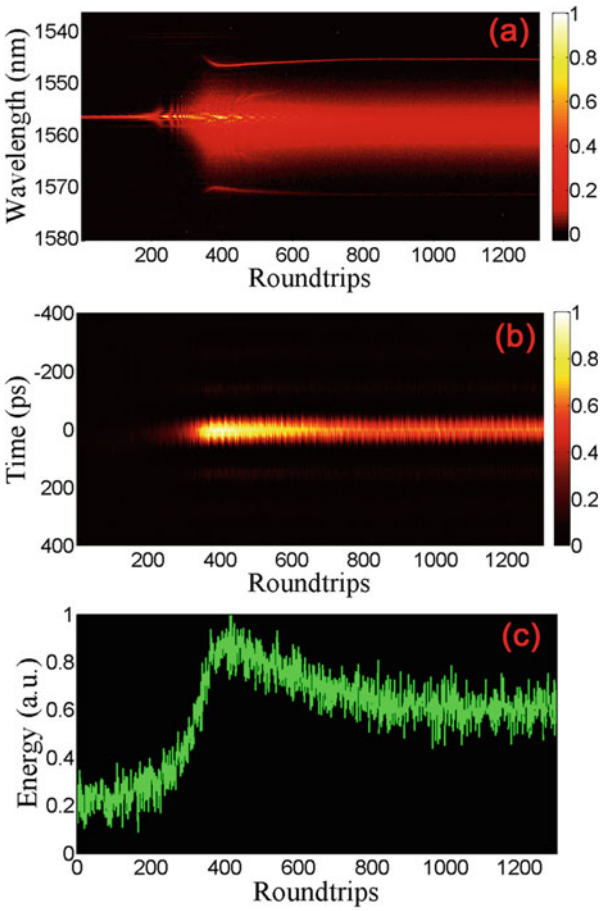

Fig. 3.4 Conventional soliton buildup dynamics in (**a**) the spectral domain and (**b**) the time domain for 1300 consecutive round-trips. (**c**) Pulsed energy evolution. (Adapted from Ref. [49])

When investigating the self-starting process of the conventional soliton, the mechanical chopper was turned on to start or stop the mode locking periodically . Note that if the pump power was too high, the multi-soliton regime could be observed owing to the pulse splitting effect. In this case, the pump power needs to be properly set to keep single-soliton starting. Figure 3.4 shows an overview of the soliton buildup dynamics in the temporal and spectral domains. The temporal dynamics of soliton buildup from the noise background shows a clear intensity oscillation over large time scales of a few microseconds, which is similar to the previous report in [25]. However, in this section, we only discuss the dynamics around the mode-locking transition of the fiber laser.

Figure 3.4a shows the evolution of the lasing spectrum from a quasi-continuous wave with a narrow bandwidth to a mode-locking state with a broadband spectrum. It is worth noting that the real-time spectral dynamics show strong spectral intensity oscillations in the transitional stage of the mode-locking process. At the beginning of the pulse evolution, the duration of the spectral intensity oscillation is about

200 round-trips. When the fiber laser approached the stable mode-locking operation, the period of spectral intensity oscillation tends to decrease. In fact, the initial cavity parameters of the fiber laser system affect the duration of intensity oscillation. However, from the experimental observation, the spectral oscillation behavior of ultrafast fiber lasers operating in anomalous dispersion regime always exists in the pre-mode-locking state. Accordingly, Fig. 3.4b presents the spatio-temporal dynamics, indicating that the pulse intensity increases in the initial pre-mode-locking state. Then the pulse intensity gradually decreases, evolving into the stable mode-locking pulse-train eventually. Only single pulse was detected on the oscilloscope trace during the evolution process. Note that the fine details of the spatio-temporal dynamics measured experimentally is limited by the bandwidth of the oscilloscope, because the pulse width is generally at femtosecond level for anomalous dispersion fiber lasers. To further understand the pulse evolution, the calculated pulse energy is depicted in Fig. 3.4c. It can be seen that the pulse energy first increases and then decreases before approaching stability. Here, a stable mode-locking state was finally reached, which shows a similar dynamic trend in Fig. 3.4b.

However, as mentioned above, the profile and structure of the mode-locked soliton cannot be analyzed experimentally because of the limited bandwidth of the oscilloscope. In order to analyze the soliton buildup process qualitatively, Chen et al. implemented the numerical simulation based on the extended nonlinear Schrödinger equation [50]. The laser cavity is simplified to consist of the EDF, the SMF, a SA and an output coupler (OC), by setting the appropriate parameters (see reference [49] for specific parameter settings). An arbitrary weak pulse is set as the initial lightwave for the simulation. The simulation results of the mode-locking operation of an anomalous fiber laser are briefly shown in Fig. 3.5. Figure 3.5a shows the spectral evolution, and it can be seen that the narrow spectral bandwidth at the beginning evolves to a stable mode-locking spectrum with Kelly sidebands. In agreement with the experimental results, the behavior of strong spectral intensity oscillation could be clearly observed. When approaching the stable mode-locking state, the time period of intensity oscillation decreased accordingly. Figure 3.5b plots the evolution of the corresponding time-domain pulse from quasi-continuous wave to mode-locking, and Fig. 3.5c shows the evolution of the pulse energy. According to the simulation of pulse evolution, it can be seen that the intensity of pulse increases firstly, then tends to stabilize. This process is similar to the pulse evolution measured in Fig. 3.4. The overall features of the soliton buildup dynamics in the simulation results are in good agreement with the experiment in both spectral and temporal domains.

As shown in Fig. 3.4, it is evident that the spectral intensity oscillation behavior is observed before the stable mode-locking state is achieved. In order to analyze the reasons for such oscillations, Chen et al. selected four transient profiles of starting soliton corresponding to different round-trips, as shown in Fig. 3.6. It can be seen that at the center part of the mode-locking spectrum, the number and distribution of the spectral peaks and dips change with the soliton propagation in the laser cavity. Moreover, the spectral interference pattern is also discovered. From the spectral dynamics, it could be inferred that the evolving structural soliton was formed during the soliton buildup process. Because of the pulse shaping effect in the transition regime of passive mode locking, the pulse is not constant and evolves during the

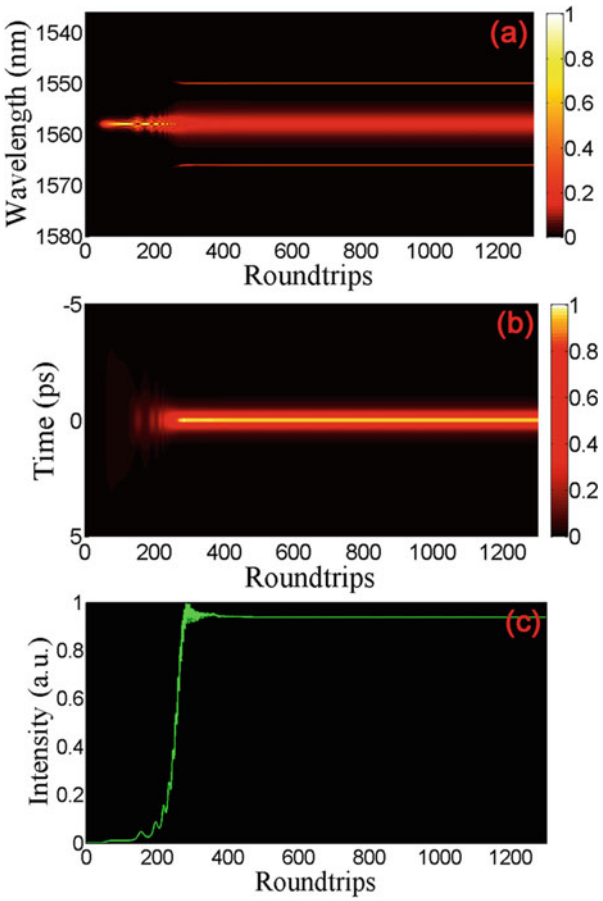

Fig. 3.5 Numerical simulations of conventional soliton buildup dynamics in (**a**) the temporal domain and (**b**) the spectral domain for 1300 consecutive roundtrips. (**c**) Pulse energy evolution. (Adapted from Ref. [49])

buildup process. In this case, a particular structural soliton corresponds to a specific spectral profile. Therefore, strong spectral intensity oscillations can be observed at this stage until the soliton is stably formed.

Correspondingly, the similar dynamics was observed for the simulation results. Figure 3.7 provides the four transient spectra and the corresponding pulse profiles during the soliton buildup process. In the central part of the mode-locked spectrum, the peaks or dips alternately generated, as shown in the upper row of Fig. 3.7. The corresponding pulse profile is plotted in the lower row of Fig. 3.7 to check the pulse evolution in the time domain. During the pulse shaping process, it is evident that there is a pedestal on the evolving pulse. Furthermore, the profile of the pulse pedestal also changed with the cavity roundtrips, meaning that transient structural solitons were observed during the simulations [51]. Thus, the spectral intensity oscillation during the soliton buildup dynamics in an anomalous dispersion fiber laser can be attributed to the formation of transient structural solitons owing to the pulse shaping towards stable mode locking.

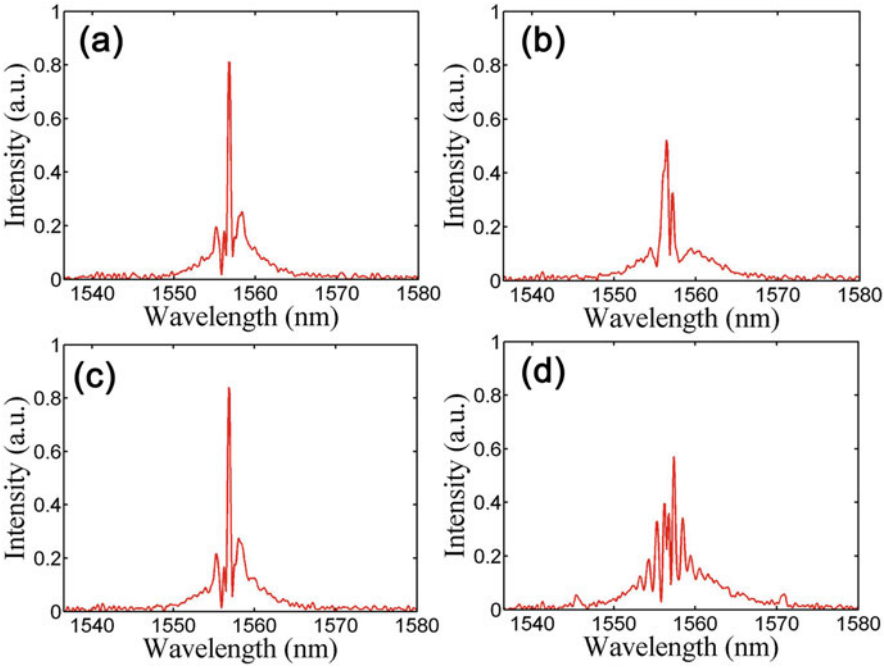

Fig. 3.6 Four transient spectral profiles during soliton buildup process. (**a**) 324th round-trip. (**b**) 326th round-trip. (**c**) 328th round-trip. (**d**) 356th round-trip. (Adapted from Ref. [49])

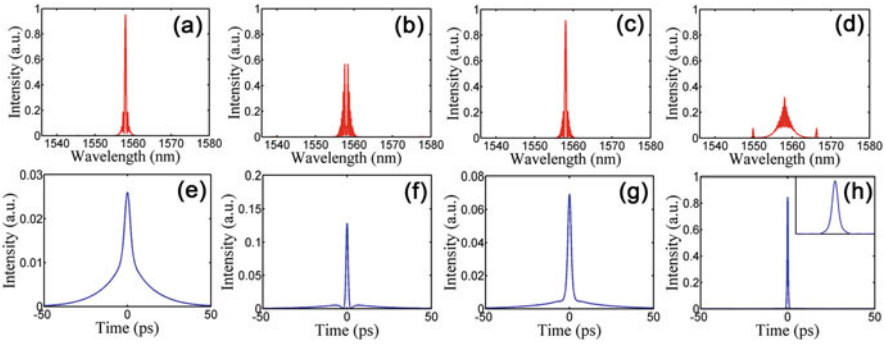

Fig. 3.7 Numerical simulations of four transient spectral and pulse profiles during soliton buildup process. (**a**) and (**e**) 121th round-trip. (**b**) and (**f**) 154th round-trip. (**c**) and (**g**) 174th round-trip. (**d**) and (**h**) 270th round-trip. The upper right inset in (**h**) shows the structural soliton profile. (Adapted from Ref. [49])

3.3 Dissipative Solitons Buildup Dynamics in a Normal Dispersion Fiber Laser

It is well known that the dynamics of pulse shaping is dependent on the cavity dispersion of fiber lasers. Therefore, it is expected that the soliton buildup dynamics in fiber lasers operating in the normal dispersion regime will be different from those of the anomalous dispersion ones. In this case, it is also necessary to unveil the buildup dynamics of dissipative soliton in fiber lasers with the normal dispersion regime. In 2018, the buildup process of dissipative solitons was investigated in a net-normal dispersion fiber laser [52]. Indeed, different soliton buildup dynamics from the anomalous dispersion regime have been observed. Briefly, no spectral intensity oscillation was found during the buildup of dissipative solitons, but there were oscillations of the spectral bandwidth. Moreover, the highest structural peaks are distributed on both sides of spectrum, unlike the conventional solitons whose the highest spectral components are concentrated in the central region.

In order to obtain the dissipative soliton, Chen et al. constructed a net-normal dispersion fiber laser. Being different from the anomalous dispersion fiber laser shown in Fig. 3.2, the EDF gain medium with normal dispersion was increased to 10 m long, and the SMF in the cavity was shortened to 12 m long. Thus, the net cavity dispersion was estimated to be ~0.3 ps^2. Similar to the case of an anomalous dispersion fiber laser, the self-started mode-locking could be easily achieved when the pump power was set to 12.7 mW. To avoid appearing multiple pulses, the pump power only needs to be slightly higher than the mode-locking threshold. The properties of the dissipative soliton are shown in Fig. 3.8. A typical rectangular spectrum centered at 1562 nm of the dissipative soliton is presented in Fig. 3.8a. Figure 3.8b displays the pulse-train with the fundamental repetition rate of 9.27 MHz. The autocorrelation trace in Fig. 3.8c indicates that the pulse duration is 16.21 ps. Besides, >50 dB signal-to-noise ratio of the RF spectrum was obtained, suggesting that the dissipative soliton fiber laser was operating stably.

As mentioned in Sect. 3.1, by virtue of the DFT technique and high-speed oscilloscope, the real-time spectral and temporal evolution of the dissipative soliton buildup dynamics could be observed simultaneously, as shown in Fig. 3.9. Compared to the conventional solitons [53, 54], the same phenomenon of spectral broadening process could be seen during the bulidup process of dissipative solitons. However, the real-time spectral dynamics shown in Fig. 3.9a indicates that the highest structured spectral peaks of the dissipative solitons are distributed along both sides, and oscillations of the spectral bandwidth could also be observed during the dissipative soliton buildup. These oscillations of the spectral bandwidth are due to the incomplete balance among dispersion, nonlinearity, gain and loss before achieving stable mode-locking. Nevertheless, they can be tuned or even eliminated by carefully adjusting the pump power. Figure 3.9b shows the spatio-temporal dynamics of the dissipative soliton buildup process, in which the peak intensity of the pulse has a tendency to increase firstly, with the appearance of an extremely high amplitude, and then decreases sharply. Finally, it becomes a stable mode-locking

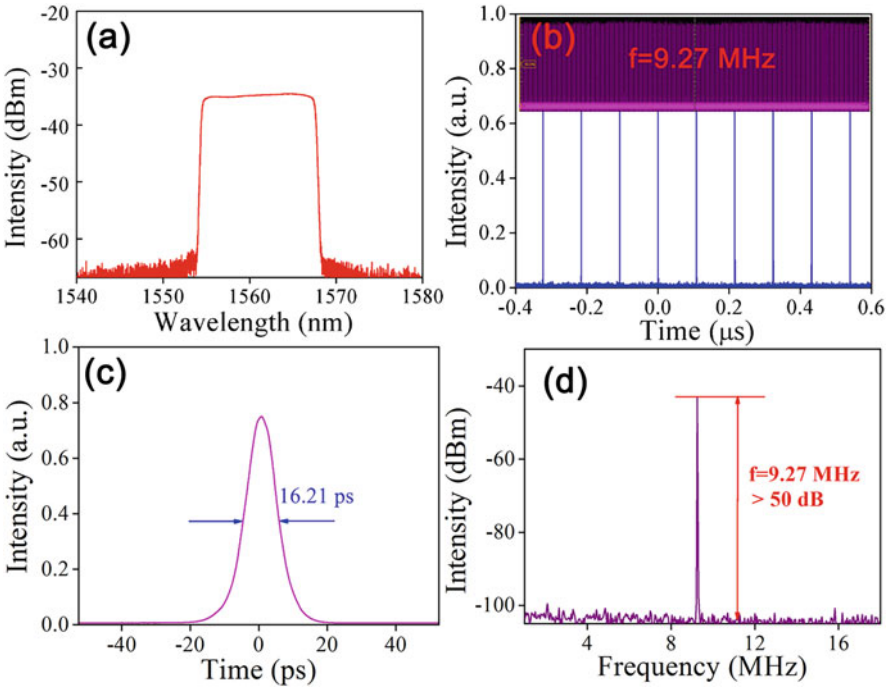

Fig. 3.8 Performance of net-normal dispersion fiber laser in mode locking state. (**a**) Spectrum of dissipative soliton. (**b**) Pulse-train. Inset: pulse-train with larger range. (**c**) Autocorrelation trace. (**d**) RF spectrum. (Adapted from Ref. [52])

state. In addition, Fig. 3.9c provides the corresponding evolution of the pulse energy in the dissipative soliton buildup process.

Again, the buildup dynamics of the dissipative soliton in the net-normal dispersion laser cavity was simulated with the extended nonlinear Schrodinger equation further to reveal the fine details of the pulse profile. Figure 3.10 shows the simulation results. In Fig. 3.10a, it can be seen that the laser first operates in a quasi-continuous wave state, and then the spectral bandwidth broadens as the lightwave propagates through the laser cavity. Similar to the experimental observations, structural peaks at both edges of the mode-locked spectrum were also produced during the broadening process. Figure 3.10b shows the pulse evolution for 2700 round-trips. We can see that the pulse peak intensity first increases rapidly and then decreases until a stable mode-locking operation is achieved. In addition, the energy evolution by integrating the pulse profile is shown in Fig. 3.10c, which is in general agreement with the experimental results.

During the buildup process of the dissipative soliton, the oscillations of the spectral bandwidth can be observed. In order to get insight into the transient dynamics of the dissipative soliton in the fiber laser, Chen et al. selected four typical spectra corresponding to different round-trips during the buildup of the dissipative

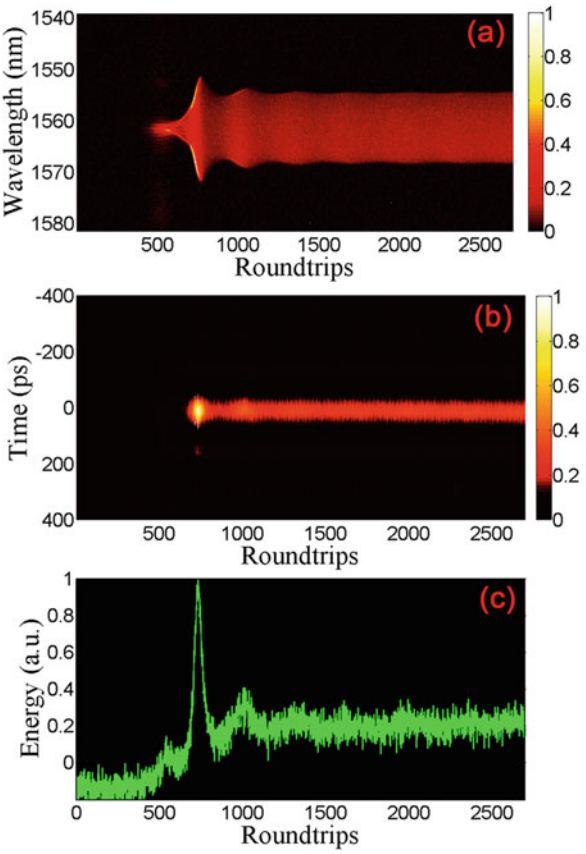

Fig. 3.9 Dissipative soliton buildup dynamics in (**a**) spectral domains and (**b**) time domains for 2700 consecutive round-trips. (**c**) Pulse energy evolution. (Adapted from Ref. [52])

soliton. It can be seen from Fig. 3.11 that the spectral bandwidth increases during the evolution to a stable mode-locking state. At the same time, the spectrum shows an evolving structured profile, where the highest interference peaks are usually located at the two edges of the mode-locked spectrum. Specifically, two spectral spikes with oscillation structures can be seen on both edges of the pulse spectrum near the stable mode-locking state, as shown in Fig. 3.11c. Then, after a certain number of round-trips, the spectral bandwidth still slowly expanded before reaching the stable mode-locked state. Finally, the fiber laser delivered the mode-locked pulse with a rectangular spectrum, which is the typical feature of dissipative solitons [55, 56], as shown in Fig. 3.11d.

Similarly, the numerical simulations were implemented to further investigate the nonlinear behavior during the soliton buildup dynamics in both the spectral and temporal domains. Here, four representative spectra and corresponding pulse profiles are plotted in Fig. 3.12. The upper row of Fig. 3.12 shows that as the number of round-trip increases, the interference peaks appear on both sides of the evolving spectrum. When the stable mode-locked operation was achieved, the interference

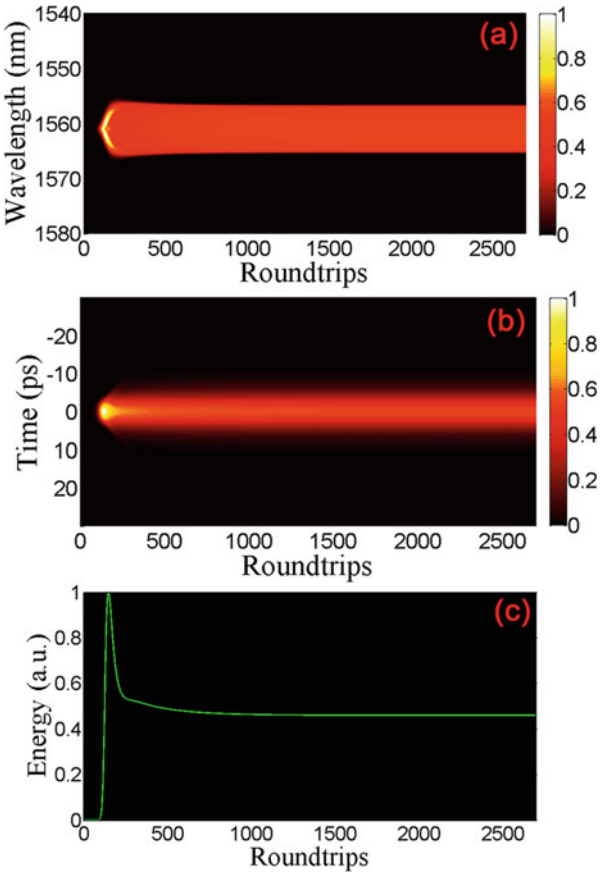

Fig. 3.10 Numerical simulations of dissipative soliton buildup dynamics in (**a**) spectral domains and (**b**) time domains for 2700 consecutive round-trips. (**c**) Pulse energy evolution. (Adapted from Ref. [52])

depth gradually decreased and disappeared. In addition, the spectral peaks with oscillation structures at both edges of the evolution spectrum can be observed in the simulation results before the stable mode-locked operation, which is in agreement with the experimental results. The lower row of Fig. 3.12 shows the pulse profile that varies with the cavity roundtrips in the temporal domain. Owing to the net-normal dispersion regime, the pulse duration increased with the number of roundtrips until it reached the limit of the effective gain bandwidth before stabilizing [3]. In addition, two humps can also be observed at the two edges of the evolving soliton, i.e., in Fig. 3.12g. These properties indicate that the dissipative soliton evolved like a kind of structural soliton in the laser cavity. Here, the spectral pattern appeared on the pulse spectrum [51]. Thus, the transient spectral behavior depends on the pulse evolution in the temporal domain owing to the pulse shaping effect of passive mode-locking.

From the results of experimental and numerical simulations, it could be seen that during the buildup process of the dissipative soliton, the highest spectral peaks were distributed along both sides of the mode-locked spectrum. For the buildup of

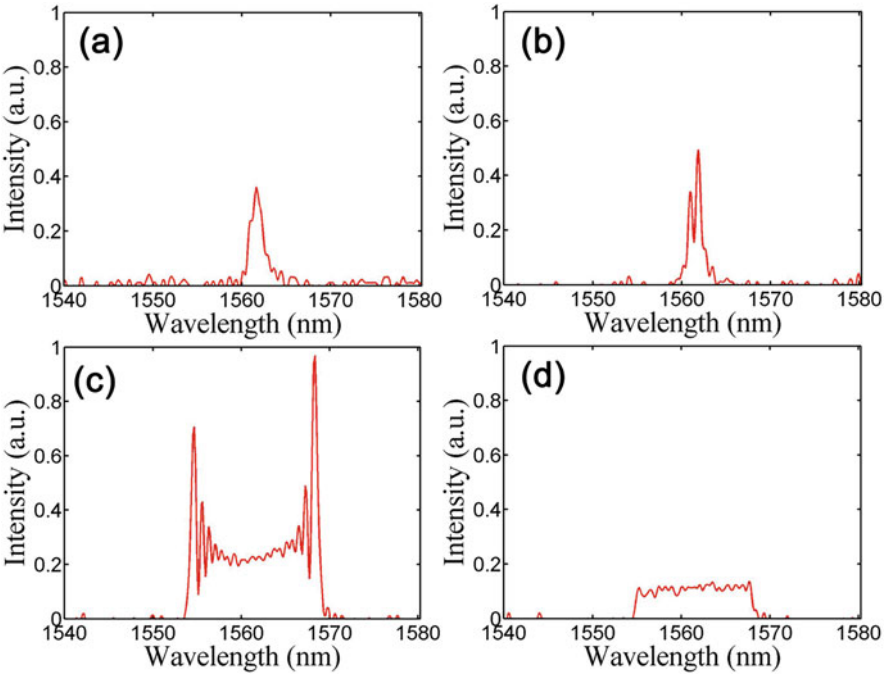

Fig. 3.11 Four transient spectral profiles during dissipative soliton buildup process. (**a**) 535th round-trip. (**b**) 602th round-trip. (**c**) 736th round-trip. (**d**) 965th round-trip. (Adapted from Ref. [52])

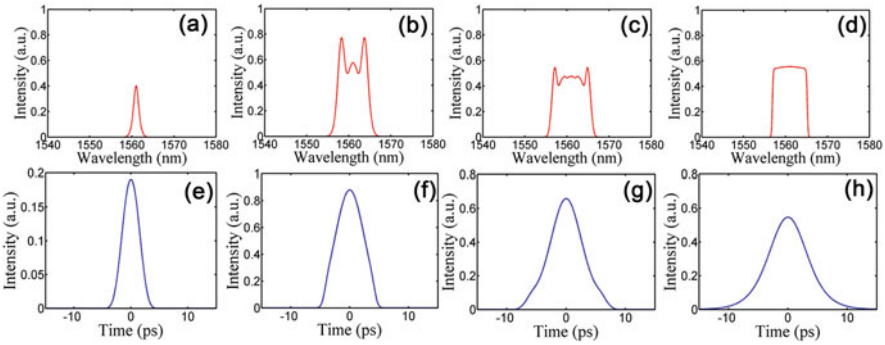

Fig. 3.12 Numerical simulations of four transient spectral and pulse profiles of the dissipative soliton buildup process. (**a**) and (**e**) 104th round-trip. (**b**) and (**f**) 163th round-trip. (**c**) and (**g**) 222th round-trip. (**d**) and (**h**) 1700th round-trip. (Adapted from Ref. [52])

the dissipative soliton, no spectral intensity oscillations were found. However, during the starting process of conventional soliton in the anomalous dispersion regime, the highest spectral components with strong spectral intensity oscillation were concentrated in the central region of the soliton spectrum. The differences in

the spectral evolution of the two types of solitons can be attributed to differences in the pulse shaping mechanisms. In addition, high amplitude waves could also be observed during the buildup process of dissipative soliton, as shown in Fig. 3.9b, which is also different from the buildup of conventional soliton.

So far, we have discussed the soliton buildup process in the anomalous dispersion and net-normal dispersion fiber lasers. However, other operation regimes of mode-locked soliton buildup dynamics in fiber lasers have yet to be studied. For example, the investigation of different operation modes such as bidirectional mode-locked fiber lasers and multi-soliton fiber lasers also helps us to have a more comprehensive exploration of the buildup dynamics of dissipative solitons.

3.4 Dissipative Soliton Buildup Dynamics in a Bidirectional Fiber Laser with Net-Normal Dispersion

Ultrafast fiber lasers can be mode-locked in a bidirectional structure by removing the intracavity isolators [57, 58]. In this case, the lightwave propagates in two opposite directions within the same laser cavity, sharing the same gain medium, saturable absorber, and fiber dispersion. Recently, Yu et al. investigated the behavior of dissipative solitons in a net-normal-dispersion bidirectional ultrafast fiber laser [59]. Even though they may involve transient instabilities, the bidirectional dissipative solitons produced by such a fiber laser will always exhibit similar spectral and temporal characteristics through a common modulation of gain and loss.

Figure 3.13 shows the schematic and measurement equipment of the CNT mode-locked bidirectional fiber laser operating in the net-normal dispersion regime. The gain medium is a segment of EDF. Since no isolator is placed in the cavity, the mode-locked solitons can propagate in both directions. In order to avoid the collisions of dissipative solitons in both directions in the measurement part, the output is combined with a 50:50 coupler with appropriate delays. The two outputs were measured by the same device. The DFT measurement was realized with a long dispersion compensating fiber (DCF).

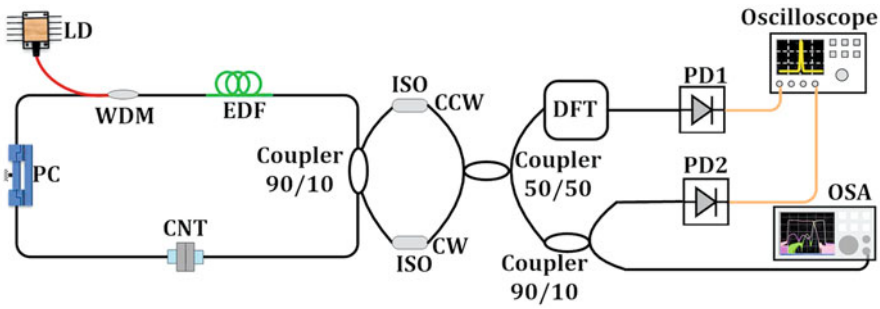

Fig. 3.13 Schematic of the net-normal dispersion bidirectional fiber laser. (Adapted from Ref. [59])

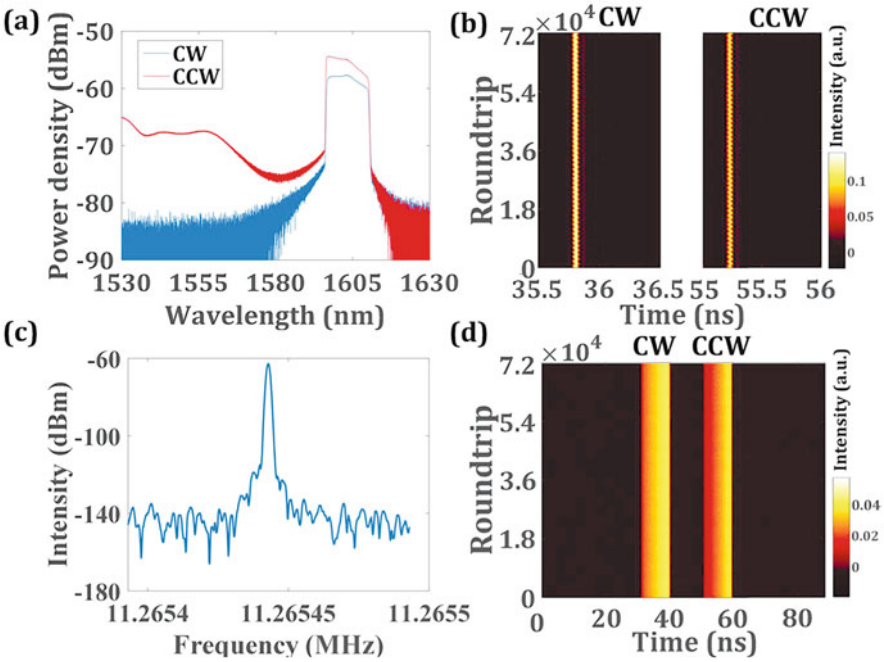

Fig. 3.14 Experimental performance in mode locking state of the net-normal dispersion bidirectional fiber laser. (**a**) Spectrum. (**b**) Temporal evolution. (**c**) RF spectrum. (**d**) Spectral evolution. (Adapted from Ref. [59])

By properly adjusting the pump power, the fiber laser was operating in stable single soliton state in both directions. Interestingly, the dissipative solitons always occur in pairs for both clockwise (CW) and counter-clockwise (CCW) directions. Due to the same gain and loss modulation, both directions could always be mode-locked simultaneously and have very similar characteristics in terms of parameters such as repetition rate and spectral bandwidth. Figure 3.14a shows the spectra measured in both directions. Note that the strong amplified spontaneous emission (ASE) could be seen for the CCW direction pulse (red) with higher energy, which could be attributed to the asymmetric pumping structure of EDF. Figure 3.14b shows the pulse evolution of these two directions in the time domain. The invariable interval between the CW and CCW solitons means that they had the same repetition rates. Only one fundamental frequency was observed in the radio frequency spectrum, which further confirms the synchronization of the two solitons, as shown in Fig. 3.14c. Furthermore, the real-time spectral evolution by DFT in Fig. 3.14d shows that the dissipative solitons keep highly stable in both directions.

In particular, the solitons propagating in opposite directions collided with each other in the laser cavity on each round-trip. Furthermore, it can be calculated that one collision point in the cavity is the position of the CNT. In the stable mode-locking state, the pulses propagating in opposite directions experience the same net

dispersion, nonlinearity, and net gain. The collision inside the CNT implies that the solitons from two directions pass through the CNT at the same time, which leads to equal loss modulation for two directional solitons. Thus, this fiber laser system determines the similar performance of bidirectional dissipative solitons.

To further investigate the features on the behavior of bidirectional dissipative solitons, the DFT technique was employed to measure the real-time spectral dynamics of the mode-locking buildup process, as plotted in Fig. 3.15. Figures 3.15a, b show the pulse evolution in the time domain along with the CW and CCW

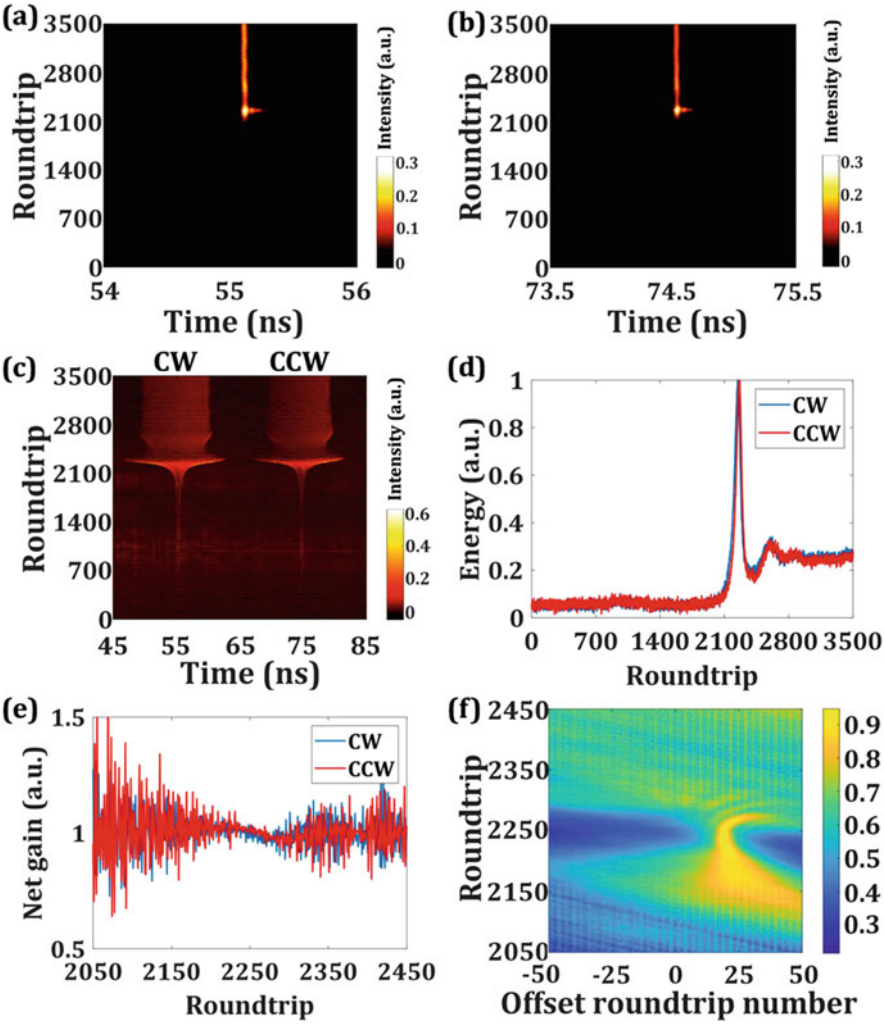

Fig. 3.15 Buildup dynamics of dissipative solitons in CW and CCW directions. Temporal evolution in (**a**) CW and (**b**) CCW directions. (**c**) Spectral evolution. (**d**) Energy evolution. (**e**) Net gain evolution. (f) Spectral cross-correlation map. (Adapted from Ref. [59])

directions, respectively. It is worth noting that owing to the mutual loss modulation of the CNT, once a seed pulse was formed in one direction, another seed pulse would also be generated in the opposite direction. In this case, the temporal separation of bidirectional solitons would be locked, and thus remains invariant. Figure 3.15c shows the real-time spectral evolution in both directions, and it can be seen that they both go through a narrowband noise pulse, an energy-increasing stage, and spectral broadening to a stable mode-locking state. Figure 3.15d, e show the evolution of normalized energy and net gain, respectively. Here, the energy evolution and net gain in both directions follow the same trend. The buildup process in both directions always start almost simultaneously, and bidirectional solitons collide in every roundtrip at the position of the CNT mode locker. In addition, they share the same gain fiber, so the net gain evolves in the same trend. Figure 3.15f calculates the cross-correlation between the single-shot spectra in both directions and further shows their similarity. However, the slight gain difference induced by the different pump directions leads to the bending of the spectral cross-correlation diagram. The above results indicated that the very similar buildup dynamics could be observed in bidirectional mode-locked fiber laser with a net-normal dispersion regime.

3.5 Buildup Dynamics of Dissipative Soliton Molecules

One of the well-known phenomena in ultrafast fiber lasers is that multiple solitons will be generated if the pump power is high enough. Since multiple solitons can exist simultaneously in a laser cavity, they can interact with each other. For example, if several solitons coexist in a laser cavity, they can form the bound state, which is commonly referred to as soliton molecules (SMs). The dynamics of complex soliton interactions and observation of the motions within SM have been revealed by analyzing the real-time spectral dynamics with DFT [42, 60]. Recently, Liu et al. reported the buildup dynamics of SMs in a mode-locked fiber laser [61]. Figures 3.16b and 3.17a show the recorded results of the buildup process of SMs with and without DFT technique, respectively. It was found that the buildup dynamics of stable SM experience five different stages, which are the raised relaxation oscillation stage, spectral intensity oscillation stage, transient single pulse stage, transient bound state, and the stable SM state. From Fig. 3.16, the emergence of a raised relaxation oscillation (RO) stage with six spikes before the 0 round-trip could be observed. During the raised RO stage, multiple pulses were generated in the laser cavity, but only the strong ones eventually survived, and the others finally collapsed.

After the RO stage, the soliton evolution experienced a spectral intensity oscillation stage, a transient single pulse stage with Kelly sidebands, then a transient SM state and finally a stable SM stage, as shown in Fig. 3.17. Figure 3.17 redraws the platform of Fig. 3.16, where Figs. 3.17b, c are enlarged views of regions A and B in Fig. 3.17a, respectively. The apparent oscillation behavior could be observed between the RO and transient single pulse stage. The obvious oscillation behavior

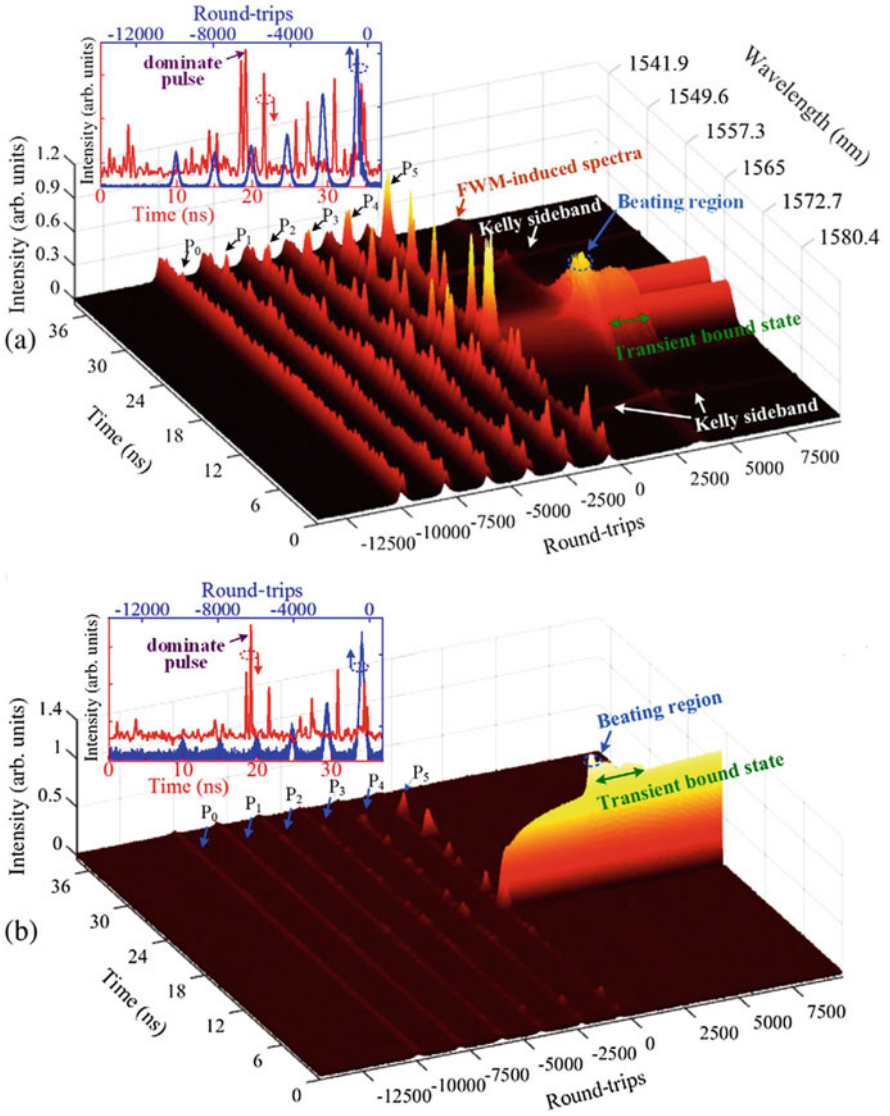

Fig. 3.16 Real-time measurement of the buildup process of a SM in a mode-locked laser (**a**) with TS DFT and (**b**) without the TS DFT technique, respectively. Insets in (**a**), (**b**) are the pulses profiles at the −570th and − 590th round-trip (red curve) and at the time (blue curve) of 34.5 ns, respectively. P_0 to P_5 represent a pulse appearing on six spikes at the time of 34.5 ns. (Adapted from Ref. [61])

was also seen during the evolution of the transient single pulse to the transient SM state. Through the second oscillation process, one soliton was breaking into two solitons. Then the two newly-generated solitons strongly interacted with each other and entered into the bound state, which eventually evolved into a stable SM state.

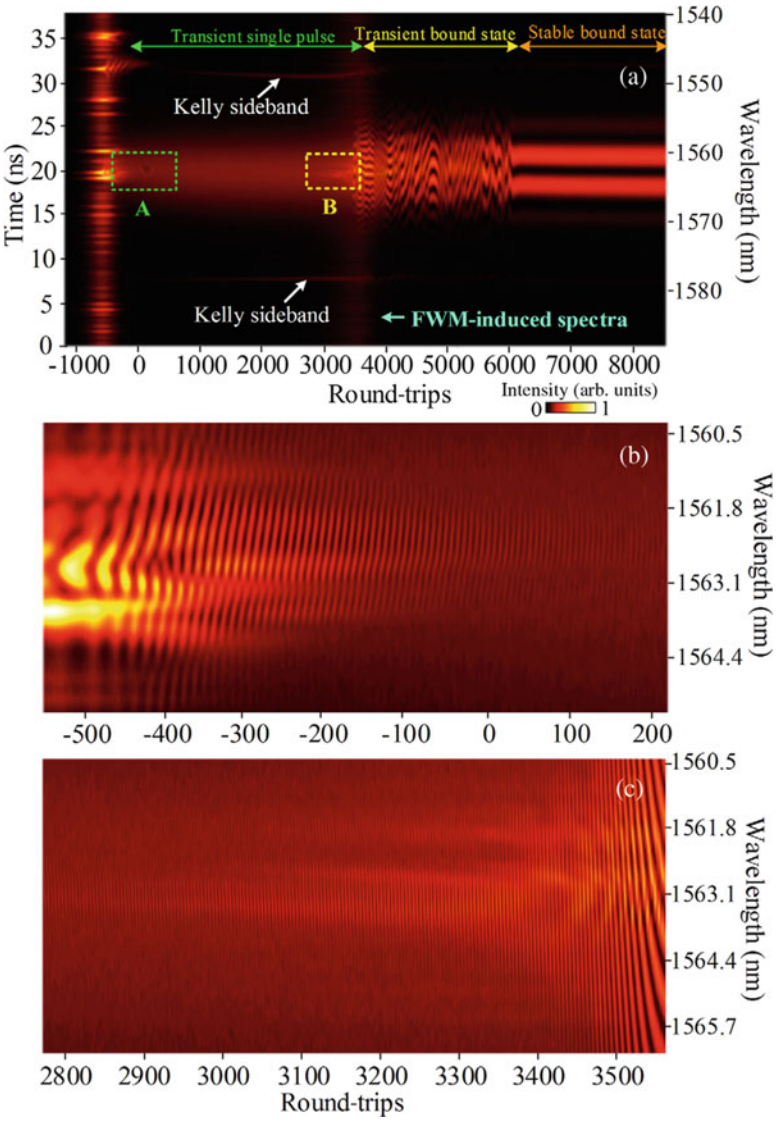

Fig. 3.17 Buildup dynamics of a SM with oscillation. (**a**) Real-time experimental results. (**b**) and (**c**) are enlargement for the A and B regions in (**a**). (Adapted from Ref. [61])

It was found that the process of dissipative soliton buildup was sensitive to external perturbations such as changes of the polarization state and the fluctuation of the pump power. More complex transient process may occur before the buildup of stable SM by using the nonlinear polarization rotation mode-locking technique. Besides, the fluctuating pump power would induce multiple RO stages. More

complex and detailed dynamics are still needed to be investigated. In addition, Peng et al. also investigated the buildup dynamics of dissipative SM through different soliton interactions. They concluded that the buildup process of closely- and well-separated bound solitons consist of three nonlinear stages, including mode locking, soliton splitting, and soliton interactions [62]. The observed results are essential for a better understanding of the buildup dynamics of the localized structures in dissipative systems.

3.6 Conclusion

In this chapter, we review the recent results on the buildup dynamics of solitons in fiber lasers operating in different regimes. Before introducing the dissipative solitons, we presented the buildup process of conventional soliton in an anomalous dispersion fiber laser. From the background noise to a stable mode-locking state, the pulse profile changes periodically and the transient structural solitons appear, corresponding to the intensity oscillations in the spectral domain. Then we described the buildup process of the dissipative soliton in a net-normal dispersion fiber laser. The dissipative soliton buildup is similar to the conventional soliton in some aspects. However, it is important to note that the spectral bandwidth oscillations and high amplitude waves could be seen in the dissipative soliton buildup process, which is different from those of the conventional solitons. In addition, we also briefly discussed the dissipative soliton buildup process of a bidirectional mode-locked fiber laser with net-normal dispersion and buildup dynamics of the dissipative SM in the anomalous dispersion fiber laser.

However, the buildup dynamics in the time domain of the dissipative soliton are not shown in detail in this chapter due to the limitation of measurement methods. Recently, some researchers used time-lens measurement to obtain the fine details of pulse evolution in the time domain. For example, P. Ryczkowski et al. employed the time-lens technology to completely characterize the temporal evolution of ultrashort dissipative solitons [63]. Thus, it is expected that the combination of DFT and time-lens techniques could be employed to reveal the full features of dissipative soliton dynamics in the future. We hope the results shown in this chapter will provide deeper insights into the communities of nonlinear optics and ultrafast lasers dealing with the physical science and industrial applications.

Acknowledgements National Natural Science Foundation of China (11474109, 11874018, 61805084, 61875058); Guangdong. Natural Science Funds for Distinguished Young Scholar. (2014A030306019).

References

1. E.V. Vanin, A.I. Korytin, A.M. Sergeev, D. Anderson, M. Lisak, L. Vázquez, Phys. Rev. A 49, 2806–2811 (1994)
2. N. Akhmediev, A. Ankiewicz, *Dissipative Solitons*, (Springer, Berlin, 2005)
3. F.W. Wise, A. Chong, W.H. Renninger, Laser Photonics Rev. 2, 58–73 (2008)
4. P. Grelu, N. Akhmediev, Nat. Photon. 6, 84–92 (2012)
5. Y.S. Kivshar, B.A. Malomed, Rev. Mod. Phys. 61, 763 (1989)
6. M. Stratmann, T. Pagel, F. Mitschke, Phys. Rev. Lett. 95, 143902 (2005)
7. F.O. Ilday, J.R. Buckley, W.G. Clark, F.W. Wise, Phys. Rev. Lett. 92, 213902 (2004)
8. D.Y. Tang, H. Zhang, L.M. Zhao, X. Wu, Phys. Rev. Lett. 101, 153904 (2008)
9. S.K. Turitsyn, B. Bale, M.P. Fedoruk, Phys. Rep. 521, 135 (2012)
10. C. Bao, W. Chang, C. Yang, N. Akhmediev, S.T. Cundiff, Phys. Rev. Lett. 115, 253903 (2015)
11. K. Sulimany, O. Lib, G. Masri, A. Klein, M. Fridman, P. Grelu, O. Gat, H. Steinberg, Phys. Rev. Lett. 121, 133902 (2018)
12. D.Y. Tang, L.M. Zhao, B. Zhao, A.Q. Liu, Phys. Rev. A 72, 43816 (2005)
13. A. Zavyalov, R. Iliew, O. Egorov, F. Lederer, Phys. Rev. A 80, 43829 (2009)
14. F. Amrani, M. Salhi, P. Grelu, H. Leblond, F. Sanchez, Opt. Lett. 36, 1545–1547 (2011)
15. W. Chang, A. Ankiewicz, J.M. Soto-Crespo, N. Akhmediev, Phys. Rev. A 78, 023830 (2008)
16. S. Chouli, P. Grelu, Opt. Express 17, 11776–11781 (2009)
17. A. Niang, F. Amrani, M. Salhi, P. Grelu, F. Sanchez, Appl. Phys. B 116, 771–775 (2014)
18. X. Wu, D.Y. Tang, H. Zhang, L.M. Zhao, Opt. Express 17, 5580–5584 (2009)
19. S. Chouli, P Grelu, Phys. Rev. A 81, 63829 (2010)
20. X. Liu, Phys. Rev. A 81, 53819 (2010)
21. Z.C. Luo, W.J. Cao, Z.B. Lin, Z.R. Cai, A.P. Luo, W.C. Xu, Opt. Lett. 37, 4777-4779 (2012)
22. W. Lin, S. Wang, S. Xu, Z.C. Luo, Z. Yang, Opt. Express, 23, 14860-14875 (2015)
23. J. Herrmann, Opt. Commun. 98, 111–116 (1993)
24. N.W. Pu, J.M. Shieh, Y. Lai, C.L. Pan, Opt. Lett. 20, 163–165 (1995)
25. H. Li, D.G. Ouzounov, F.W. Wise, Opt. Lett. 35, 2403–2405 (2010)
26. Y.C. Tong, L.Y. Chan, H.K. Tsang, Electron. Lett. 33, 983–985 (1997)
27. K. Goda, B. Jalali, Nat. Photon. 7, 102–112 (2013)
28. M.A. Muriel, J. Azaña, A. Carballar, Opt. Lett. 24, 1–3 (1999).
29. D.R. VSolli, J. Chou, B. Jalali, Nat. Photon. 2, 48–51 (2008)
30. C. Lecaplain, P. Grelu, J.M. Soto-Crespo, N. Akhmediev, Phys. Rev. Lett. 108, 233901 (2012)
31. A.F.J. Runge, C. Aguergaray, N.G.R. Broderick, M. Erkintalo, Opt. Lett. 39, 319–322 (2014)
32. M. Liu, A.P. Luo, W.C. Xu, Z.C. Luo. Opt. Lett. 41, 3912–3915 (2016)
33. A.F.J. Runge, N.G.R. Broderick, M. Erkintalo, Optica 2, 36 (2015)
34. M. Liu, A.P. Luo, Y.R. Yan, S. Hu, Y.C. Liu, H. Cui, Z.C. Luo, W.C. Xu, Opt. Lett. 41, 1181–1184 (2016)
35. Y. Yu, Z.C. Luo, J. Kang, K.K.Y. Wong, Opt. Lett. 43, 4132–4135 (2018)
36. Z.W. Wei, M. Liu, S.X. Ming, H. Cui, A.P. Luo, W.C. Xu, Z.C. Luo, Opt. Lett. 45, 531–534 (2020)
37. Z.W. Wei, M. Liu, S.X. Ming, A.P. Luo, W.C. Xu, Z.C. Luo, Opt. Lett. 43, 5965–5968 (2018)
38. J. Peng, S. Boscolo, Z. Zhao, H. Zeng, Sci. Adv. 5, eaax1110 (2019)
39. M. Liu, Z.W. Wei, H. Li, T.J. Li, A.P. Luo, W.C. Xu, Z.C. Luo, Laser Photonics Rev. 14, 1900317 (2020)
40. M. Liu, A.P. Luo, Z.C. Luo, W.C. Xu, Opt. Lett. 42, 330–333 (2017)
41. K. Krupa, K. Nithyanandan, P. Grelu, Optica 4, 1239–1243 (2017).
42. G. Herink, F. Kurtz, B. Jalali, D.R. Solli, C. Ropers, Science 356, 50–54 (2017)
43. G. Herink, B. Jalali, C. Ropers, D.R. Solli, Nat. Photon. 10, 321–326 (2016)
44. D.E. Spence, P. N. Kean, W. Sibbett, Opt. Lett. 16, 42–44 (1991)
45. V.J. Matsas, T.P. Newson, D.J. Richardson, D.N. Payne, Electron. Lett. 28, 1391–1393 (1992)
46. K. Tamura, H.A. Haus, E.P. Ippen, Electron. Lett. 28, 2226–2228 (1992)

47. I.N. Duling, Opt. Lett. 16, 539–541 (1991)
48. S.M.J. Kelly, Electron. Lett. 28, 806-807 (1992)
49. H.J. Chen, M. Liu, J. Yao, S. Hu, J.B. He, A.P. Luo, Z.C. Luo, W.C. Xu, IEEE Photonics J. 10, 1–9 (2018)
50. A. Cabasse, B. Ortaç, G. Martel, A. Hideur, J. Limpert, Opt. Express 16, 19322–19329 (2008)
51. A. Komarov, F. Sanchez, Phys. Rev. E 77, 066201 (2008)
52. H.J. Chen, M. Liu, J. Yao, S. Hu, J.B. He, A.P. Luo, W.C. Xu, Z.C. Luo, Opt. Express 26, 2972–2982 (2018)
53. X. Wei, C. Zhang, B. Li, K.K.Y. Wong, In 2015 Conference on Lasers and Electro-Optics (CLEO) 1–2 (2015)
54. X. Wei, B. Li, Y. Yu, C. Zhang, K.K. Tsia, K.K.Y. Wong, Opt. Express 25, 29098–29120 (2017)
55. L.M. Zhao, D.Y. Tang, J. Wu, Opt. Lett. 31, 1788–1790 (2006)
56. W.H. Renninger, A. Chong, F.W. Wise, Phys. Rev. A 77, 23814 (2008)
57. K. Kieu, M. Mansuripur, Opt. Lett. 33, 64–66 (2008)
58. X. Zhao, Z. Zheng, Y. Liu, G. Hu, J. Liu, IEEE Photonics J. 26, 1722–1725 (2014)
59. Y. Yu, C. Kong, B. Li, J. Kang, Y.X. Ren, Z.C. Luo, K.K.Y. Wong, Opt. Lett. 44, 4813–4816 (2019)
60. K. Krupa, K. Nithyanandan, U. Andral, P. Tchofo-Dinda, P. Grelu, Phys. Rev. Lett. 118, 243901 (2017)
61. X. Liu, X. Yao, Y. Cui, Phys. Rev. Lett. 121, 023905 (2018)
62. J. Peng, H. Zeng, Laser Photonics Rev. 12, 1800009 (2018)
63. P. Ryczkowski, M. Närhi, C. Billet, J.M. Merolla, G. Genty, J.M. Dudley, Nat. Photonics 12, 221-227 (2018)

Chapter 4
Dissipative Soliton Resonance

Georges Semaan, Andrey Komarov, Mohamed Salhi, and François Sanchez

Abstract Mode-locked fiber lasers capable of producing nanosecond level pulses with high energy have many advantages for various applications. An increase in the mode-locked pulse's energy can be achieved by carefully choosing the cavity parameters. Dissipative soliton resonance (DSR) mechanism leading to high energy mode-locking has been reported in different fiber laser configurations. In the anomalous dispersion regime, this energy is not limited by the soliton area theorem. Under DSR regime, by increasing the pump power, the pulse clamps its peak power while it broadens in the time domain. Since this phenomenon is wave breaking free, it can be useful in designing fiber lasers generating pulses with relatively high energies. In this chapter, we describe the generation and control of DSR pulses in fiber lasers under various mode-locking mechanisms. We also demonstrate that a multi-pulsing can be observed in the form of harmonic generation of square pulses.

Keywords Fiber lasers · Dissipative solitons · Dissipative soliton resonance · Nonlinear optics · Mode-locking · Energy scaling · Erbium · Stretched pulses · Ultrashort pulses · Optical Kerr effect

4.1 Introduction

During the propagation of light in mode-locked fiber lasers, the energy and the temporal profile of the optical soliton-shaped pulses are preserved. Since the laser is characterized by a continuous energy flow, a strong balanced relationship between gain and loss must exist for the soliton formation to occur. Basically, dispersion

G. Semaan (✉) · M. Salhi · F. Sanchez
Laboratoire de Photonique d'Angers, Université d'Angers, Département de Physique, Angers, France
e-mail: georges.semaan@univ-angers.fr; mohamed.salhi@univ-angers.fr; francois.sanchez@univ-angers.fr

A. Komarov
Institute of Automation and Electrometry, Russian Academy of Science, Novosibirsk, Russia
e-mail: komarov@iae.nsk.su

M. F. S. Ferreira (ed.), *Dissipative Optical Solitons*, Springer Series in Optical Sciences 238, https://doi.org/10.1007/978-3-030-97493-0_4

spreads the pulse in the time domain, while nonlinearity broadens it in frequency domain. Thus, to produce stationary state in fiber laser, the balance between gain and loss, dispersion and nonlinearity is needed. This fact exposes the dissipative nature of solitons formed in a fiber laser [1, 2]. As a consequence, the energy dissipation associated to the dispersion and the nonlinearity in the cavity leads to an interaction of solitons and formation of multi-soliton complexes such as bound solitons, bunch of solitons and soliton rains [3–8].

The generation of high-energy pulses from a laser oscillator is a challenging process because the Kerr nonlinearity combined with the dispersion generally lead to a pulse break-up after the accumulated nonlinear phase has exceeded a certain level. Such effects can be circumvented by employing significant temporal stretching of the pulse inside the cavity, thus reducing the peak power while maintaining a large spectral content. This strategy essentially incorporates chirped-pulse amplification inside the laser oscillator [9–12].

In the last decade, alternative cavity designs for achieving stable stretched-pulse operation with higher pulse energies has been explored. This progress allowed, in 2004, the implementation of the self-similar propagation of chirped parabolic pulses in the passive part of the laser cavity, and the report of an increased pulse-energy performance around 10 nJ per pulse [13]. Technically, the incorporation of self-similarity inside a cavity relies on a subtle balance between normal dispersion and nonlinearity. These parameters, acting together in a passive fiber, must be balanced by spectral filtering, nonlinear gain and anomalous dispersion in the laser cavity, thus performing a precise self-consistent pulse reshaping process. Indeed, having unusually large intracavity gain and losses through spectral filtering, is important and seems to be the key to obtain specific pulse regimes e.g. self-similarity. Self-similar pulses or similaritons, are expanding pulses and completely different in nature than solitons. While the transition from similariton to soliton dynamics is performed by a spectral filter, this truncates the pulse in both the spectral and temporal domains. Spectral filtering of a highly chirped pulse has a significant clipping effect on the temporal pulse wings. When the cavity dynamics become dominated by the composite balance between spectral filtering on one side, and nonlinearity, dispersion and gain on the other side, the tendency of emitting pulses with double-lobe optical spectra is confirmed. Ytterbium-doped mode-locked fiber lasers employing such designs can produce pulses with energies above 20 nJ using standard fiber technology [14–16]. In these oscillators, the strong dissipative effects per roundtrip are essential in the pulse's formation and stability. Dissipative solitons are reported in fiber lasers regardless the dispersion sign, revealing dynamics that are unusual to Schrödinger solitons.

Currently, there exists several techniques in the development of high pulse energy mode-locked fiber laser oscillators. Perhaps the most efficient of these relies on the use of micro-structured optical fibers where microjoule-level pulse energies have been achieved [17]. Another trend is to shift mode-locking operation further into the

normal dispersion regime, thereby increasing the pulse chirping effect [18, 19]. To remain compatible with today's interests and available pumping powers, such strategies are usually supplemented with an increased cavity length to reduce the pulse repetition rate.

Recently, an alternative conceptual approach known as DSR was proposed in the context of pulse energy scaling [20–23]. Found initially in the framework of a master equation describing the field evolution in a fiber laser with distributed intracavity medium, complex dispersion, nonlinear refractive index, and nonlinear losses [24–27], DSR describes dissipative solitons that acquire theoretically infinite energy when the equation parameters approach a specific hyper-surface in the parameter space [21]. In practice, this implies that oscillators could be designed so that the pulse energy could increase linearly with the pumping power without suffering pulse break-up, within a narrow range of laser parameters. Pulses close to DSR region share common features, such as a clamped peak power and a finite spectral bandwidth, therefore, the boost in energy causes the duration of the chirped pulse to increase [28, 29].

The experimental demonstration of high energy mode-locked pulses directly from the laser cavity has been widely investigated. The variety of setups and experiments reported have extended length cavities with low repetition rates and relatively large value of net cavity dispersion. It has also been shown that the high nonlinearity plays an important role in widening the pulse [30]. In the DSR region, the generation of high energy square pulses has been demonstrated regardless the sign of the dispersion or the mode-locking mechanism. Thus, DSR square pulses have been documented in long cavities employing standard single mode amplifiers [30–37]. However, due to the limited gain of purely single-mode active fibers in these configurations, the output pulse energy is relatively low in the order of few to hundreds of nanojoules. Therefore, the obvious solution to increase energies of pulses generated in all-fiber lasers would be to use double-clad doped fibers, offering high gain and efficiency. The first demonstration of double-clad Er:Yb laser operating in DSR regime was reported in a figure-of-eight (F8L) fiber laser with a pulse energy of 2.12 μJ [38]. Later, highly energetic DSR pulses in fiber ring laser achieving 2.27 μJ [39] and in a F8L double amplifier configuration with a record pulse energy of 10 μJ energy [40] have been reported. Shortly after, a novel Figure-9 fiber laser setup was proposed [41].

In this chapter, we will use a numerical approach to verify the conditions of generation DSR pulses in a laser cavity, then we will focus on the demonstration of DSR square pulses and their dynamics in two main lasers configurations: the fiber ring laser and the nonlinear amplifying loop mirror (NALM). We will also demonstrate the possibility of pulse splitting in the DSR regime under certain circumstances.

4.1.1 Numerical Approach: Propagation in an Oscillator with a Saturable Absorber (SA)

In the framework of isotropic fibers that exhibit optical Kerr nonlinearity, let us use the modified scalar nonlinear Schrödinger equation to describe the evolution of the field in the fiber laser:

$$\frac{\partial A}{\partial z} + \frac{i}{2}\left(i\frac{g}{\Omega_g^2} + \beta_2\right)\frac{\partial^2 A}{\partial t^2} - \frac{1}{2}(g-\alpha)A = i\gamma|A|^2 A$$

where A is the slowly varying electric field envelope, z is the propagation distance, t is the pulse local time, γ is the fiber nonlinearity described as $\gamma = \frac{2\pi n_2}{\lambda A_{eff}}$ (n_2: the nonlinear refractive index, λ: central wavelength and A_{eff}: effective mode area), β_2 is the group velocity dispersion, α is the linear loss coefficient of the fiber and Ω_g is the bandwidth of the laser gain. The gain function of the active medium is expressed as:

$$g = \frac{g_0}{1 + \frac{E_p}{E_{sat}}}$$

where g_0 is the small signal gain, E_{sat} is the gain saturation energy which relates to the pumping strength and E_p is the pulse energy given by:

$$E_p = \int_{-T/2}^{T/2} |A|^2 dt$$

where T is the cavity roundtrip time.

The SA used in the model is considered as a lumped element. The total nonlinear transmission coefficient is expressed as:

$$T(I) = 1 - \frac{\alpha_0}{1 + I/I_{sat}} - \alpha_{ns}$$

where α_0 is the modulation depth, α_{ns} is the non-saturable absorption, I is the instantaneous pulse intensity and I_{sat} is the saturation intensity of the SA.

Starting with random noise as an initial condition, steady state is achieved after 50 roundtrips. By appropriately choosing the cavity parameters, self-started mode-locking can be achieved, and different pulse distribution can be obtained [42]. Figure 4.1 depicts the evolution of DSR characteristics as function of the pumping power, for $E_{sat} = 0.5$ nJ and g_0 varying from 0 to 3 m^{-1}. In Fig. 4.1a, the Gaussian-like pulse evolves into a square shaped pulse and its width gradually increases from 20 to 100 ps, whereas in Fig. 4.1b, E_p increases linearly from 0.2 to 6 nJ.

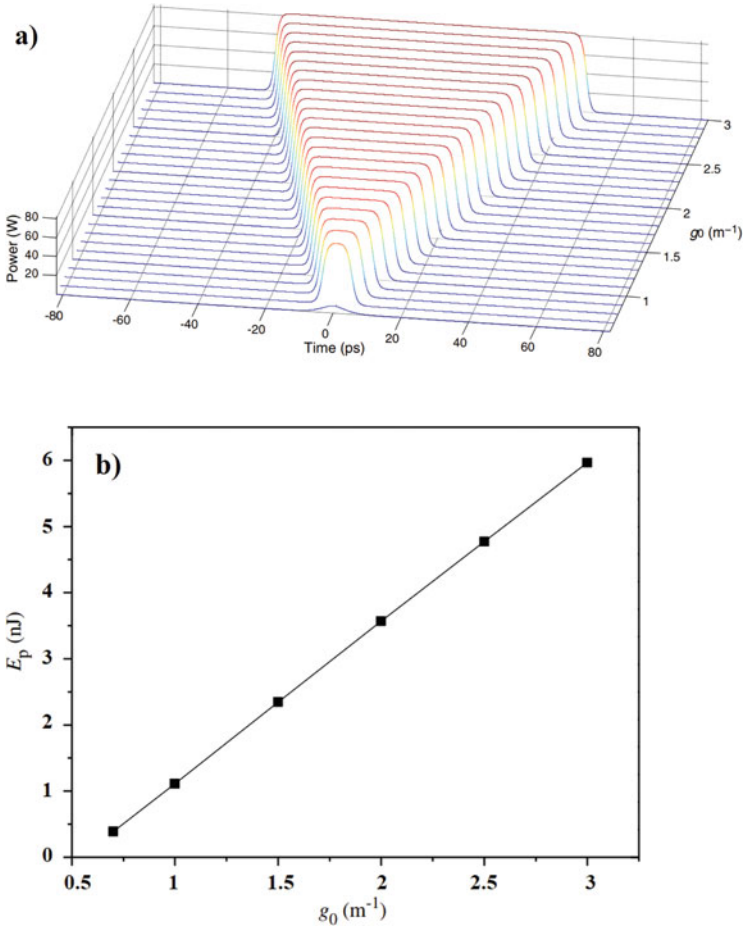

Fig. 4.1 DSR evolution with small signal gain. (**a**) Pulse evolution, and (**b**) pulse energy evolution

Basically, when the pump power is high enough, the transmission of the SA decreases as the peak power increases, which leads to larger losses encountered by the pulse in the SA. Subsequently, when the peak power reaches a certain level, the effective gain in the central region of the pulse becomes equivalent to the dynamical loss that it experiences, and at this point the pulse peak power is clamped. Therefore, further increase in the pump power leads to the increase of the pulse width rather than its peak power. Meanwhile, the chirp is moderately low in the central region of the pulse because of the small pulse power gradients variations near the center. So, most of the pulse energy is accumulated near the central wavelength of the pulse spectrum. Therefore, the spectral bandwidth of the pulse decreases as the small signal gain increases and it is smaller than the bandwidth of the spectral filter as exhibited in Fig. 4.2 [43, 44].

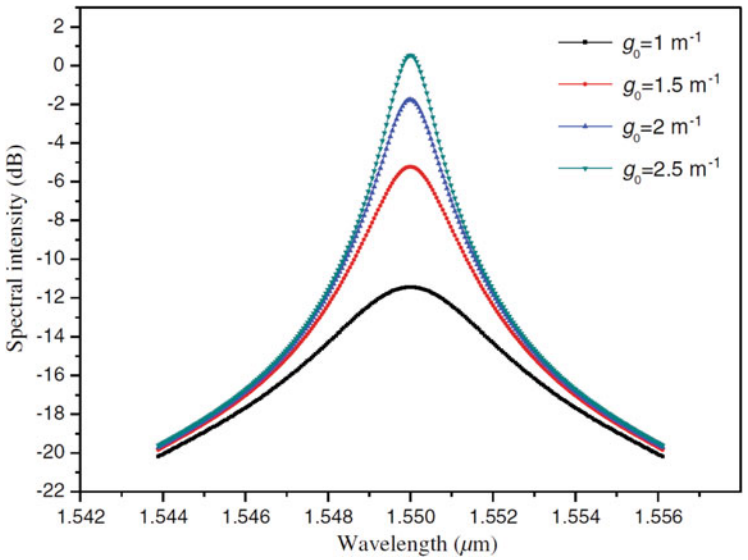

Fig. 4.2 Optical spectra of the square pulses under different small signal gains for $E_{sat} = 0.5$ nJ. (Figure reconstructed based on Ref. [42])

4.1.2 DSR Pulses in Passively Mode-Locked Fiber Lasers

The numerical simulations were realized with a real SA model, but it could also be done with nonlinear polarization evolution (NPE) or optical loops in order to obtain DSR pulses. The generation of these pulses does not depend on the mode-locking mechanism confirming their universality. Let us illustrate the observation of DSR pulses in fiber lasers and discover their singular features.

4.1.2.1 Experimental Features of DSR Pulses

Intrinsically, DSR pulses are square-shaped mode-locked pulses with a pulse width and energy scalable with the pump power whereas the peak power is clamped. Both theoretical and experimental investigations suggest that parameters of generated pulses should strongly rely on dispersion of the resonator and typically require large values.

Each oscillator has a lasing and mode-locking threshold. By carefully setting the adapted cavity parameters, the mode-locked square-wave pulses can be directly obtained. Let us take the case of an NPE setup illustrated in Fig. 4.3, as an example in this section for visualization purpose. If the polarization controllers are altered during the experiment, the established distribution remains stable most of the time till we have a pulse breaking and multiple square pulses appear. Figure 4.4 shows a stable square-wave pulse emission of the laser obtained with 4.7 W of pumping

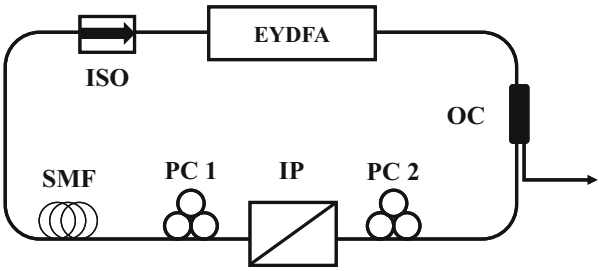

Fig. 4.3 Experimental setup of a fiber ring cavity. *EYDFA* Erbium-Ytterbium doped fiber amplifier, *OC* output coupler, *PC* polarization controller, *IP* inline polarizer, *ISO* isolator, *SMF* single mode fiber

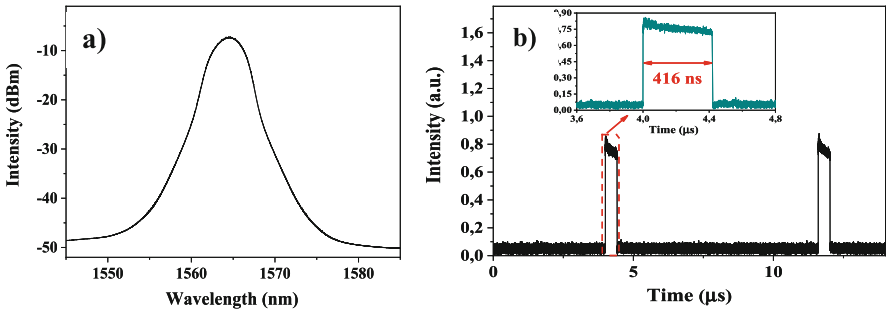

Fig. 4.4 Square-wave pulse emission of the laser at a fundamental frequency of 133 kHz and with 4.7 W of pumping power. (**a**) Pulse train of the temporal trace. (**b**) Temporal profile of single square-wave pulse

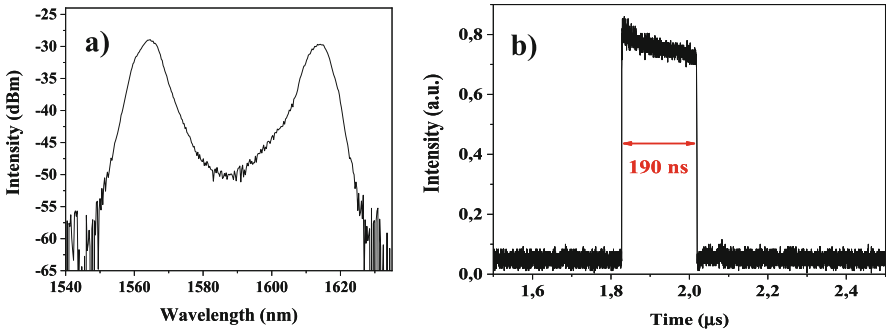

Fig. 4.5 Square-wave pulse emission of the laser. (**a**) Optical spectrum, and (**b**) Temporal profile of single square-wave pulse

power. It depicts a single wavelength emission centered around 1565 nm with a 3-dB bandwidth of 4 nm. The pulse train in Fig. 4.4b shows a relatively large single pulse per cavity roundtrip where the pulse width is about 416 ns [40].

There has also been reports on the generation of DSR pulses in fiber lasers with spectral doublet or dual-wavelength emission. Such two peaks spectrum has experimentally observed in DSR regime [45] and numerically demonstrated in fiber lasers [46]. In Fig. 4.5a, the first band is centered on 1566 nm with 8.5 nm of spectral

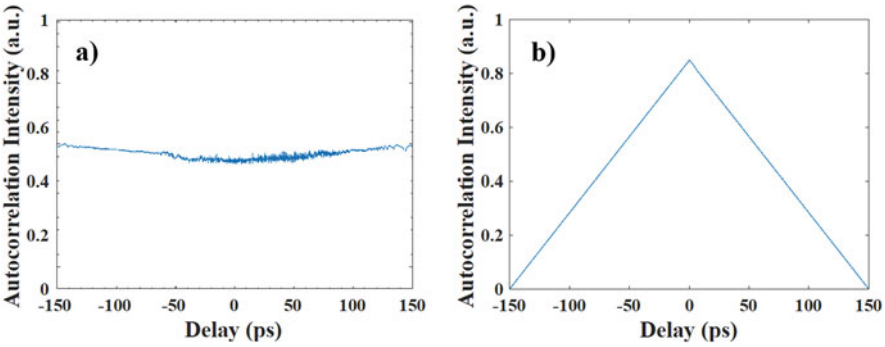

Fig. 4.6 Autocorrelation trace of the generated square-wave pulses: (**a**) large DSR pulse autocorrelation trace. (Figure reconstructed based on the results in Ref. [49]), and (**b**) autocorrelation trace of a ps range DSR pulse. (Figure reconstructed based on the results in Ref. [48])

bandwidth at −3 dB while the second band is centered on 1618 nm with 7 nm of spectral bandwidth at −3 dB. The spectral distance between the spectral peaks is 45 nm. The output pulse is square shaped and has a width of around 190 ns as in Fig. 4.5b.

When the pulses are very large, the low scanning range of the autocorrelator compared to the pulse width exhibits a constant level trace as in Fig. 4.6a. It shows there is not a coherent peak nor fine structures confirming that we are not in the presence of noise-like square-wave pulses [47]. Whereas, when the pulse width is in the picosecond range, the autocorrelator can produce a quasi-triangular profile corresponding to a square pulse as in Fig. 4.6b [48].

Another intrinsic feature of DSR pulses is their stability and radiofrequency profile. The signal to noise ratio is usually around 60 dB confirming that DSR pulses are very stable in the cavity, whereas the RF profile is a cardinal-sine envelope exhibiting characteristics modulation with periods corresponding to the width of the generated pulses as in Fig. 4.7.

In contrast with conventional solitons and short pulses, square shaped DSR pulses react differently to the increase of pump power in the cavity. Free from the soliton area theorem, their energy and width increase linearly with the pump power. Experimentally, most of the parameters should be fixed and only the power is kept variable. This results in increasing the pulse width while the peak is being clamped as in Fig. 4.8. The width of the pulse is related to the cavity roundtrip time, so the longer the cavity the bigger the possibility of obtaining larger pulse width [50]. In Fig. 4.8, pulse width is tuned from few nanoseconds to around 200 ns. The energy of the pulse is related to the average power $\mathbf{P_{average}}$ and the free spectral range **f** through the relation $E = \frac{P_{average}}{f}$, so the longer the cavity, the higher the energy of the pulses.

These results confirm the theoretical prediction in [51] where it was reported that when the peak power reaches the clamping region, the pulse width increases with the pump power. This behavior is depicted in Fig. 4.9.

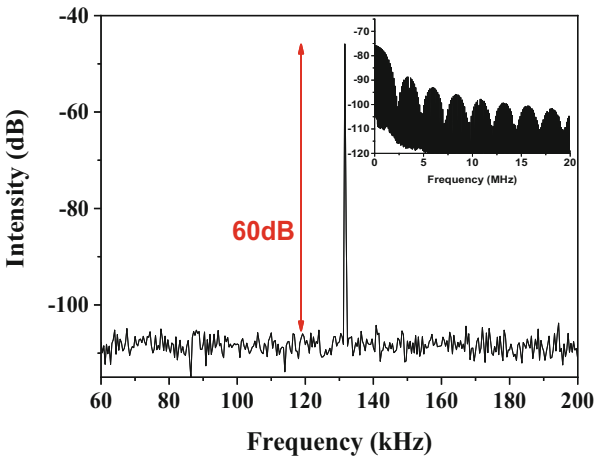

Fig. 4.7 Radiofrequency profile of a typical DSR pulse

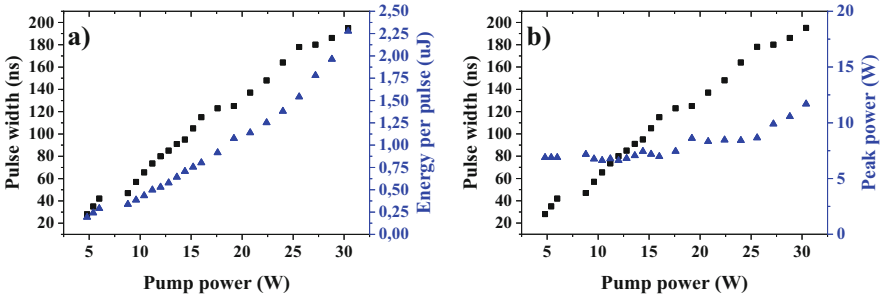

Fig. 4.8 Evolution of the pulse characteristics versus pump power: (**a**) Pulse width and energy, (**b**) Pulse width and peak power

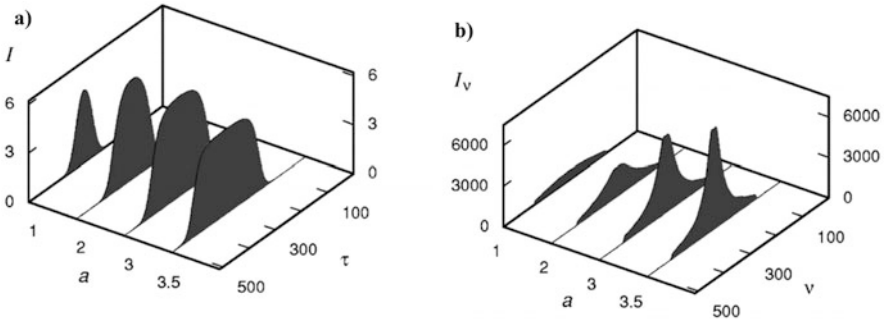

Fig. 4.9 Figure reconstructed based on data appeared originally in [51]. (**a**) Temporal evolution of the pulse vs. pump power. (**b**) Spectral evolution of pulse profile vs. pump power

4.1.2.2 Control of Pulse Characteristics in Dual-Amplifier Configuration

Since the DSR operational mode does not depend on the mode-locking mechanism nor the dispersion sign, experimental verification of this distinctive pulsed mode has been provided for several configurations. In the NALM configuration, it was demonstrated that the peak power clamping in the dissipative soliton regime can be explained by investigating the NALM transmission as a function of peak pulse power [34]. Conventionally in the DSR region, pulse width and energy can be tuned in certain range whereas the peak power remains at a stable level. By adjusting the gain in both loops, it was reported that the DSR pulse's characteristics can be controlled independently: the gain in the UR affects only the peak power by keeping the pulse width unchanged, whereas the gain in the NALM allows the tuning of the pulse width without altering the level of the peak power. In this section, the experiment in [34] is reexamined by introducing double-clad amplifiers instead of the standard amplifiers in both loops, and the results are compared to the previous ones in [34].

The experimental setup sketched in Fig. 4.10 is based on an all-fiber figure-of-eight laser cavity. It consists of a main unidirectional ring cavity (UR) connected to a nonlinear amplifying loop mirror NALM by a 70/30 fused fiber coupler to have an asymmetric light distribution in both paths of the NALM. The main cavity is composed of a C-band double-clad co-doped Er:Yb 30 dBm fiber amplifier (EYDFA1). The wideband polarization insensitive isolator (ISO) is inserted between the amplifier and the output coupler to block the counter-clockwise wave. A 1 km SMF coil (SMF1) is inserted after the output coupler to increase the nonlinearities and the round-trip time of the cavity. The mode-locking is achieved thanks to the intensity-dependent transmission of the NALM. The latter is composed of another 30 dBm C-band double-clad co-doped Er:Yb fiber amplifier (EYDFA2). A 500 m SMF coil (SMF2) is inserted after the amplifier to increase the asymmetric nonlinear phase shift between the clockwise and counterclockwise propagating light in the NALM. The total cavity length is about 1536 m and the net cavity dispersion is about -33.23 ps^2. The round-trip time is 7.65 µs corresponding to a free spectral range of

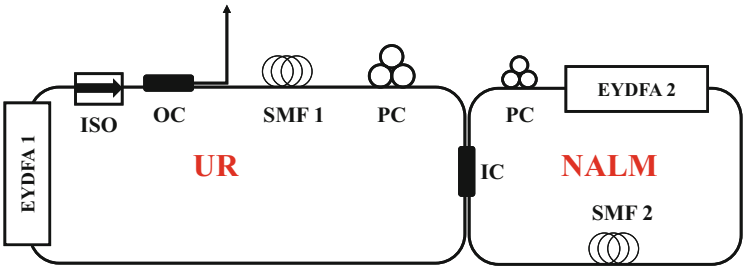

Fig. 4.10 Experimental setup of a figure-of-eight laser setup. EYDFA: Erbium-Ytterbium doped fiber amplifier, OC: output coupler, PC: polarization controller, IC: intracavity coupler, ISO: isolator, SMF: single mode fiber

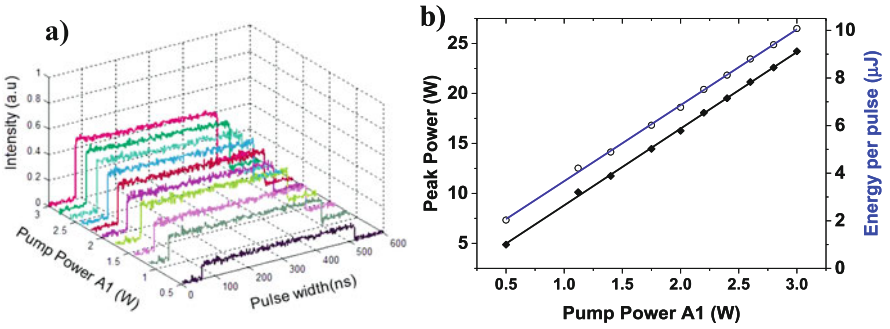

Fig. 4.11 Evolution of pulse characteristics EYDFA1: (**a**) temporal trace of the DSR pulse, and (**b**) pulse energy and peak power scaling

133 kHz. The choice of cavity length and internal coupler is based on different experiments to get a good compromise between the stability of the desired square-wave distribution and the maximal energy per pulse [52].

The cavity parameters are fixed when the square wave pulse state is achieved and only one pumping power is varied at a time in order to analyze the dependence of the peak power and pulse width versus the pump power of both amplifiers. While EYDFA2 is fixed to 1.7 W, amplifier EYDFA1 is tuned from 500 mW to its maximum of 3 W. Experimental results given in Fig. 4.11 shows the dependence of the pulse waveform versus EYDFA1. When the pump power is increased, the output pulse width remains constant at about 416 ns, whereas the peak power increases linearly. The output power of the laser increases from 250 mW to 1.333 W. Considering the output power, the laser's repeating frequency and the pulse width, the peak power of the square-wave pulse changes from 5 to around 24 W. EYDFA1 controls the pulse energy and peak power as shown in Fig. 4.11a, b. By increasing the gain in the UR, the peak power of the pulses increases while the pulse width remains constant in agreement with theoretical [42] and experimental results [34].

To verify the effect of EYDFA2, the pump power of EYDFA1 is set to 3 W and EYDFA2 is tuned from 150 mW to 1.7 W. With the increase of pump power, the square-wave pulse width and energy per pulse start increasing linearly as presented in Fig. 4.12. Note that, according to Fig. 4.12b, the peak power undergoes a slight modification caused by the variation of the ratio of pulse energy to pulse width.

If EYDFA1 is turned off, pulse characteristics can be controlled independently and the results are similar to [34], where the peak power remains nearly constant while the pulse duration linearly increases with EYDFA2. This behavior has been theoretically investigated in [42] where it was shown that the effect of the amplifiers was independent even when EYDFA1 was operating. However, this result was established by a specific set of parameters. Preliminary results of recent simulations seem to demonstrate that for other sets of parameters the effects of the amplifiers are not independent.

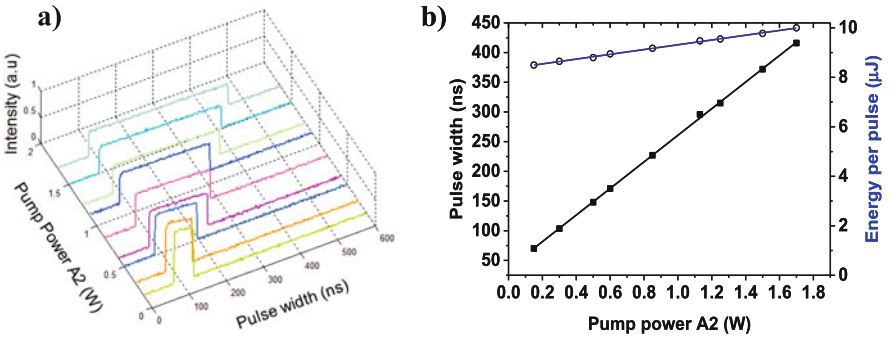

Fig. 4.12 Evolution of pulse characteristics EYDFA2: (**a**) Temporal trace of the DSR pulse, and (**b**) pulse energy and width scaling

4.2 Multi-pulsing Instabilities in DSR Regime

Although in the DSR regime pulses theoretically resist to perturbations, hence the term wave-breaking free pulses, multipulse operation is still possible. Komarov et al. have numerically demonstrated that an initial multipulse field with different amplitudes can evolve into a steady-state multipulse operation in DSR regime, where the number of pulses depends on the initial conditions [6]. In 2016, Armas-Rivera et al. have observed that a single DSR pulse can be transformed to multiple trapezoid-shaped pulses per roundtrip at high pump power [53]. In 2017, harmonic DSR pulses in anomalous dispersion Er-doped fiber ring lasers were experimentally and numerically investigated [49, 54, 55]. Similarly, DSR pulse splitting in normal dispersion fiber lasers were observed and the dynamics were numerically investigated [56, 57]. The entire splitting process from one single pulse to multiple DSR pulses and its mechanism has been recently numerically demonstrated in Yb-doped fiber laser [58].

The schematic of the proposed fiber ring laser based on NPE mode-locking mechanism is the same used in previous experiments as shown in Fig. 4.3. The total cavity length is 300 m, the net cavity dispersion is about -6.6 ps^2. The round-trip time of the cavity is 1.488 µs corresponding to a free spectral range of 672 kHz. The laser can operate in different regimes by carefully adjusting the polarization controllers through the variation of both the linear and nonlinear losses of the cavity. Stable mode-locking in the square pulse DSR regime was achieved with proper adjustment of the polarization controllers at 400 mW pump power. The pulse width was tunable from 95 ns to 270 ns, the pulse energy from 140 nJ to 409 nJ by increasing the pump power at fixed PC orientation while the peak power remains clamped. The pulse duration and the pulse energy can be quasi-linearly increased

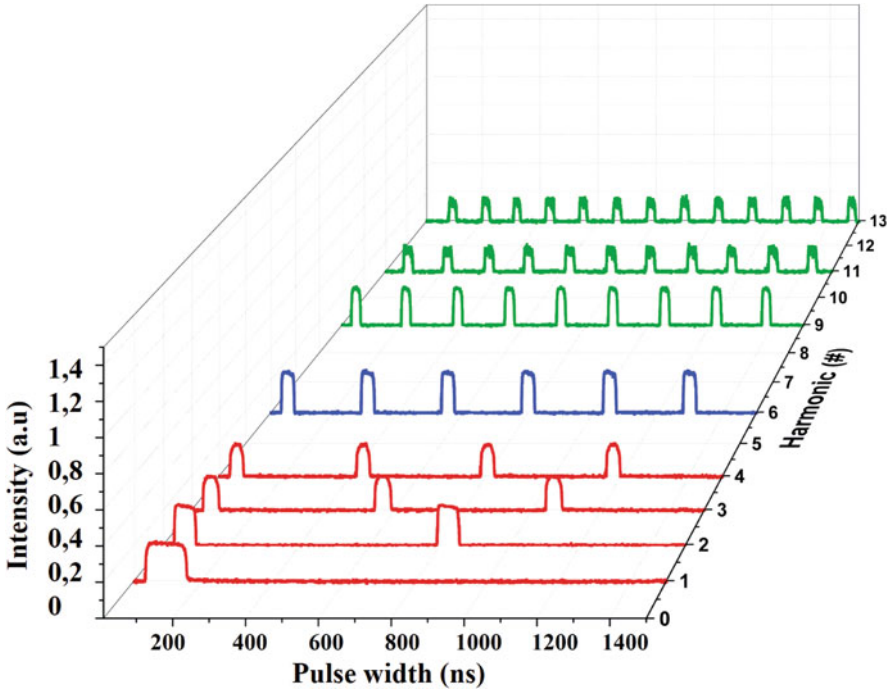

Fig. 4.13 Harmonic mode locked DSR square pulses train of different orders achieved by adjusting the PC. Each color is assigned to different pumping power (red for 1.18 W, blue for 1.6 W and green for 2.2 W). (Figure reconstructed based on data appeared in Ref. [49])

with the pumping power without significantly affecting the peak power. Under specific rotation of polarization controllers' paddles, the single square pulse packet can split into two or more pulses having the same shape as the original square pulse but with a smaller extent. Consequently, the laser evolves into a higher harmonic DSR mode-locking as in Fig. 4.13.

When the pump power is increased from 1.18 W to 2.2 W while carefully controlling the polarization state inside the cavity, a harmonic distribution of square pulses is generated and the order increases from 2nd to 13th. Above 2.2 W, no increase in the harmonic order has been detected. The square pulse width ranged from 102 ns at the fundamental frequency to 18 ns at the 13th harmonic order. The characteristics of the harmonic distribution are in agreement with the DSR pulse profile as shown in Fig. 4.14. The output energy per pulse at a fixed pump power of 1.18 W, follows a scaling law of 1/n where the pulse energy is inversely proportional to the harmonic order. This is mainly since the average output power remains nearly unchanged.

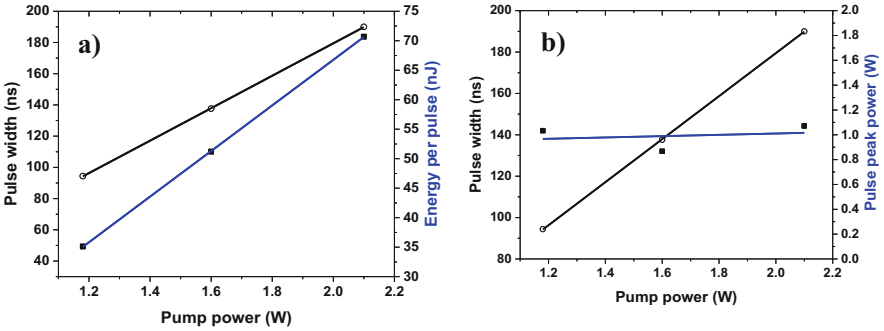

Fig. 4.14 Evolution of the 4th order harmonic mode-locked square pulse's characteristics: pulse width, energy, and peak power versus pump power

4.3 Chapter Summary

We have discussed the generation of square pulses operating in the dissipative soliton resonance regime in passively mode-locked fiber lasers. Different methods of mode-locking have been considered which proves the universality of this emission. From a numerical perspective, we demonstrated the possibility of obtaining square shaped DSR pulses in a laser cavity, and we presented the dynamics of such pulses. We also reported experimentally the features of DSR pulses, and the possibility of controlling the characteristics of the DSR square pulses by means of dual amplification in a figure-of-eight. Apart from the emission of DSR pulses, we demonstrated that even in the DSR regime, there exists instabilities depending on the parameters of the laser cavity, which lead to a harmonic distribution of the square pulses. The obtained results are records in energy scaling in a single fiber oscillator thus demonstrating the keen interest of DSR regime in energy scaling process.

References

1. N. Akhmediev and A. Ankiewicz, eds., *Dissipative Solitons*, Lecture Notes in Physics (Springer-Verlag, 2005).
2. P. Grelu and N. Akhmediev, "Dissipative solitons for mode-locked lasers," Nat. Photon. **6**, 84–92 (2012).
3. F. Sanchez, Ph. Grelu, H. Leblond, A. Komarov, K. Komarov, M. Salhi, A. Niang, F. Amrani, C. Lecaplain, and S. Chouli, "Manipulating dissipative soliton ensembles in passively mode-locked fiber lasers," Opt. Fiber Techn. **20**, 562–574 (2014).
4. F. Amrani, M. Salhi, P. Grelu, H. Leblond, and F. Sanchez, "Universal soliton pattern formations in passively mode-locked fiber lasers," Opt. Lett. **36**, 1545 (2011).
5. F. Amrani, A. Haboucha, M. Salhi, H. Leblond, A. Komarov, and F. Sanchez, "Dissipative solitons compounds in a fiber laser. Analogy with the states of the matter," Appl. Phys. B **99**, 107–114 (2009).

6. A. Komarov, F. Amrani, A. Dmitriev, K. Komarov, and F. Sanchez, "Competition and coexistence of ultrashort pulses in passive mode-locked lasers under dissipative-soliton-resonance conditions," Phys. Rev. A **87**, (2013).
7. A. Komarov, K. Komarov, A. Niang, and F. Sanchez, "Nature of soliton interaction in fiber lasers with continuous external optical injection," Phys. Rev. A **89**, 013833 (2014).
8. A. Komarov and F. Sanchez, "Structural dissipative solitons in passive mode-locked fiber lasers," Phys. Rev. E **77**, 066201 (2008).
9. M. L. Stock and G. Mourou, "Chirped pulse amplification in an erbium-doped fiber oscillator/erbium-doped fiber amplifier system," Opt. Comm. **106**, 249–252 (1994).
10. A. Galvanauskas, M. E. Fermann, P. Blixt, J. A. Tellefsen, and D. Harter, "Hybrid diode-laser fiber-amplifier source of high-energy ultrashort pulses," Opt. Lett. **19**, 1043–1045 (1994).
11. W. H. Renninger, A. Chong, and F. W. Wise, "Giant-chirp oscillators for short-pulse fiber amplifiers," Opt. Lett. **33**, 3025–3027 (2008).
12. B. G. Bale, S. Boscolo, and S. K. Turitsyn, "Dissipative dispersion-managed solitons in mode-locked lasers," Opt. Lett. **34**, 3286–3288 (2009).
13. F. O. Ilday, J. R. Buckley, F. W. Wise, and W. G. Clark, "Self-Similar Evolution of Parabolic Pulses in a Laser," Phys. Rev. Lett. **92**, (2004).
14. J. An, D. Kim, J. W. Dawson, M. J. Messerly, and C. P. J. Barty, "Grating-less, fiber-based oscillator that generates 25 nJ pulses at 80 MHz, compressible to 150 fs," Opt. Lett. **32**, 2010–2012 (2007).
15. A. Chong, W. H. Renninger, and F. W. Wise, "All-normal-dispersion femtosecond fiber laser with pulse energy above 20nJ," Opt. Lett. **32**, 2408–2410 (2007).
16. A. Hideur, T. Chartier, M. Brunel, S. Louis, C. Özkul, and F. Sanchez, "Generation of high energy femtosecond pulses from a side-pumped Yb-doped double-clad fiber laser," Appl. Phys. Lett. **79**, 3389–3391 (2001).
17. B. Ortaç, M. Baumgartl, J. Limpert, and A. Tünnermann, "Approaching microjoule-level pulse energy with mode-locked femtosecond fiber lasers," Opt. Lett. **34**, 1585–1587 (2009).
18. V. L. Kalashnikov, E. Podivilov, A. Chernykh, and A. Apolonski, "Chirped-pulse oscillators: theory and experiment," Appl. Phys. B **83**, 503 (2006).
19. E. J. R. Kelleher, J. C. Travers, E. P. Ippen, Z. Sun, A. C. Ferrari, S. V. Popov, and J. R. Taylor, "Generation and direct measurement of giant chirp in a passively mode-locked laser," Opt. Lett. **34**, 3526–3528 (2009).
20. W. Chang, A. Ankiewicz, J. M. Soto-Crespo, and N. Akhmediev, "Dissipative soliton resonances," Phys. Rev. A **78**, 023830 (2008).
21. P. Grelu, W. Chang, A. Ankiewicz, J. M. Soto-Crespo, and N. Akhmediev, "Dissipative soliton resonance as a guideline for high-energy pulse laser oscillators," Journal of the Optical Society of America B **27**, 2336 (2010).
22. E. Ding, P. Grelu, and J. N. Kutz, "Dissipative soliton resonance in a passively mode-locked fiber laser," Opt. Lett. **36**, 1146–1148 (2011).
23. A. Komarov, A. Dmitriev, K. Komarov, D. Meshcheriakov, G. Semaan, and F. Sanchez, "Theory of passively-mode-locked fiber lasers with phase-modulated square pulses," Phys. Rev. A **96**, 033820 (2017).
24. K. P. Komarov, "On the theory of transient evolution of the passive mode-locking," Opt. Comm. **54**, 233–235 (1985).
25. K. P. Komarov, A. S. Kuch'yanov, and V. D. Ugozhayev, "Generation of stationary ultra-short pulses by a passive mode-locking solid-state laser," Opt. Comm. **57**, 279–284 (1986).
26. K. P. Komarov, "Theory of stationary ultarshort pulses in solid-state laserswith passive mode locking," Opt. Spectrosc. (Engl. Transl.); (United States) **60:2**, (1986).
27. K. P. Komarov, "Transient evolution and steady-state emission from passively mode-locked lasers," Sov. J. Quantum Electron. **16**, 105 (1986).
28. V. L. Kalashnikov, "Chirped dissipative solitons of the complex cubic-quintic nonlinear Ginzburg-Landau equation," Phys. Rev. E **80**, (2009).

29. V. L. Kalashnikov and A. Apolonski, "Energy scalability of mode-locked oscillators: a completely analytical approach to analysis," Opt. Express **18**, 25757–25770 (2010).
30. X. Zhang, C. Gu, G. Chen, B. Sun, L. Xu, A. Wang, and H. Ming, "Square-wave pulse with ultra-wide tuning range in a passively mode-locked fiber laser," Opt. Lett. **37**, 1334 (2012).
31. L. Duan, X. Liu, D. Mao, L. Wang, and G. Wang, "Experimental observation of dissipative soliton resonance in an anomalous-dispersion fiber laser," Opt. Express **20**, 265 (2012).
32. Z.-C. Luo, W.-J. Cao, Z.-B. Lin, Z.-R. Cai, A.-P. Luo, and W.-C. Xu, "Pulse dynamics of dissipative soliton resonance with large duration-tuning range in a fiber ring laser," Opt. Lett. **37**, 4777 (2012).
33. T. Liu, D. Jia, Y. Liu, Z. Wang, and T. Yang, "Generation of microseconds-duration square pulses in a passively mode-locked fiber laser," Opt. Comm. **356**, 416–420 (2015).
34. L. Mei, G. Chen, L. Xu, X. Zhang, C. Gu, B. Sun, and A. Wang, "Width and amplitude tunable square-wave pulse in dual-pump passively mode-locked fiber laser," Opt. Lett. **39**, 3235 (2014).
35. X. Wu, D. Y. Tang, H. Zhang, and L. M. Zhao, "Dissipative soliton resonance in an all-normaldispersion erbium-doped fiber laser," Opt. Express **17**, 5580 (2009).
36. J. H Yang, C. Y Guo, S. C Ruan, D. Q Ouyang, H. Q Lin, Y. M Wu, and R. H Wen, "Observation of Dissipative Soliton Resonance in a Net-Normal Dispersion Figure-of-Eight Fiber Laser," IEEE Photonics Journal **5**, 1500806–1500806 (2013).
37. S.-K. Wang, Q.-Y. Ning, A.-P. Luo, Z.-B. Lin, Z.-C. Luo, and W.-C. Xu, "Dissipative soliton resonance in a passively mode-locked figure-eight fiber laser," Opt. Express **21**, 2402–2407 (2013).
38. K. Krzempek, "Dissipative soliton resonances in all-fiber Er-Yb double clad figure-8 laser," Opt. Express **23**, 30651 (2015).
39. G. Semaan, F. Ben Braham, M. Salhi, Y. Meng, F. Bahloul, and F. Sanchez, "Generation of high energy square-wave pulses in all anomalous dispersion Er:Yb passive mode locked fiber ring laser," Opt. Express **24**, 8399 (2016).
40. G. Semaan, F. B. Braham, J. Fourmont, M. Salhi, F. Bahloul, and F. Sanchez, "10 μJ dissipative soliton resonance square pulse in a dual amplifier figure-of-eight double-clad Er:Yb mode-locked fiber laser," Opt. Lett. **41**, 4767–4770 (2016).
41. K. Krzempek, J. Sotor, and K. Abramski, "Compact all-fiber figure-9 dissipative soliton resonance mode-locked double-clad Er:Yb laser," Opt. Lett. **41**, 4995–4998 (2016).
42. F. Bahloul, K. Guesmi, M. Salhi, F. Sanchez, and R. Attia, "Control of the square pulse properties in figure-of-eight microstructured fiber laser," Opt. Eng. **55**, 026102 (2016).
43. D. Li, D. Tang, L. Zhao, and D. Shen, "Mechanism of Dissipative-Soliton-Resonance Generation in Passively Mode-Locked All-Normal-Dispersion Fiber Lasers," J. Lightwave Tech. **33**, 3781–3787 (2015).
44. W. Du, H. Li, J. Li, P. Wang, S. Zhang, and Y. Liu, "Mechanism of dissipative-soliton-resonance generation in fiber laser mode-locked by real saturable absorber," Opt. Express **26**, 21314–21323 (2018).
45. N. Zhao, M. Liu, H. Liu, X.-W. Zheng, Q.-Y. Ning, A.-P. Luo, Z.-C. Luo, and W.-C. Xu, "Dual-wavelength rectangular pulse Yb-doped fiber laser using a microfiber-based graphene saturable absorber," Opt. Express **22**, 10906 (2014).
46. A. Komarov, A. Dmitriev, K. Komarov, D. Meshcheriakov, and F. Sanchez, "Spectral-doublet rectangular pulses in passive mode-locked fiber lasers with anomalous dispersion," Phys. Rev. A **94**, 043827 (2016).
47. J. Liu, Y. Chen, P. Tang, C. Xu, C. Zhao, H. Zhang, and S. Wen, "Generation and evolution of mode-locked noise-like square-wave pulses in a large-anomalous-dispersion Er-doped ring fiber laser," Opt. Express **23**, 6418–6427 (2015).
48. T. Du, Z. Luo, R. Yang, Y. Huang, Q. Ruan, Z. Cai, and H. Xu, "1.2-W average-power, 700-W peak-power, 100-ps dissipative soliton resonance in a compact Er:Yb co-doped double-clad fiber laser," Opt. Lett. **42**, 462–465 (2017).

49. G. Semaan, A. Niang, M. Salhi, and F. Sanchez, "Harmonic dissipative soliton resonance square pulses in an anomalous dispersion passively mode-locked fiber ring laser," Laser Phys. Lett. **14**, 055401 (2017).
50. A. V. Avdokhin, S. V. Popov, and J. R. Taylor, "Totally fiber integrated, figure-of-eight, femtosecond source at 1065 nm," Opt. Express **11**, 265–269 (2003).
51. A. Komarov, H. Leblond, and F. Sanchez, "Multistability and hysteresis phenomena in passively mode-locked fiber lasers," Phys. Rev. A **71**, 053809 (2005).
52. F. Ben Braham, G. Semaan, F. Bahloul, M. Salhi, and F. Sanchez, "Experimental optimization of dissipative soliton resonance square pulses in all anomalous passively mode-locked fiber laser," Journal of Optics (2017).
53. I. Armas-Rivera, C. Cuadrado-Laborde, A. Carrascosa, E. A. Kuzin, G. Beltrán-Pérez, A. Díez, and M. V. Andrés, "Dissipative soliton resonance in a full polarization-maintaining fiber ring laser at different values of dispersion," Opt. Express **24**, 9966–9974 (2016).
54. Y. Lyu, X. Zou, H. Shi, C. Liu, C. Wei, J. Li, H. Li, and Y. Liu, "Multipulse dynamics under dissipative soliton resonance conditions," Opt. Express **25**, 13286–13295 (2017).
55. Y. Lyu, H. Shi, C. Wei, H. Li, J. Li, and Y. Liu, "Harmonic dissipative soliton resonance pulses in a fiber ring laser at different values of anomalous dispersion," Photon. Res., PRJ **5**, 612–616 (2017).
56. S. D. Chowdhury, A. Pal, S. Chatterjee, R. Sen, and M. Pal, "Multipulse Dynamics of Dissipative Soliton Resonance in an All-Normal Dispersion Mode-Locked Fiber Laser," J. Lightwave Technol., JLT **36**, 5773–5779 (2018).
57. Y. Wang, L. Li, J. Zhao, S. Wang, C. Shu, L. Su, D. Tang, D. Shen, and L. Zhao, "Unusual Evolutions of Dissipative-Soliton-Resonance Pulses in an All-Normal Dispersion Fiber Laser," IEEE Photonics Journal **11**, 1–9 (2019).
58. Y. Lyu, C. Wei, W. Du, H. Li, and Y. Liu, "Splitting and Motions of Dissipative Soliton Resonance Pulses in Mode-Locked Fiber Lasers," Front. Phys. **7**, (2019).

Chapter 5
Ultra-Short High-Amplitude Dissipative Solitons

Sofia C. Latas, Margarida V. Facão, and Mário F. S. Ferreira

Abstract Starting from a singularity found by Akhmediev and co-workers, very high-amplitude (VHA) solitons of the cubic-quintic complex Ginzburg-Landau equation are predicted by the soliton perturbation theory. The propagation and the main characteristics of such VHA solitons are investigated numerically and using the method of moments both in the normal and anomalous dispersion regimes. The region of existence of these pulses is found numerically in the plane defined by the dispersion and the nonlinear gain saturation parameters. In general, numerical computations are in good agreement with the predictions based on the method of moments when a quartic trial function is assumed. High-energy ultrashort pulses are found mainly in the normal dispersion region, which agrees with the experimental observations reported by other authors. The impact on VHA solitons of some of higher order effects, namely, the intra-pulse Raman scattering (IRS) and the third-order dispersion (TOD) has been studied. We have found that the singularity giving origin to VHA pulses is no longer present if the intra-pulse Raman scattering effect is considered and zero velocity pulses may be achieved in the presence of both IRS and TOD.

Keywords Optical solitons · Dissipative solitons · High-energy solitons · Complex Ginzburg-Landau equation · Soliton perturbation theory · Method of moments · Higher-order effects · Intrapulse Raman scattering · Third-order dispersion

5.1 Introduction

High-energy ultra-short optical pulses can be generated by passively mode-locked fiber lasers and they are of great importance for a variety of applications [1–5]. In particular, they can be used to develop broadband supercontinuum light sources [2] that play a

S. C. Latas (✉) · M. V. Facão · M. F. S. Ferreira
I3N-Institute of Nanostructures, Nanomodelling and Nanofabrication, Department of Physics, University of Aveiro, Aveiro, Portugal
e-mail: sofia.latas@ua.pt; mfacao@ua.pt; mfernando@ua.pt

M. F. S. Ferreira (ed.), *Dissipative Optical Solitons*, Springer Series in Optical Sciences 238, https://doi.org/10.1007/978-3-030-97493-0_5

very important role in several biomedical and medical applications [4–8]. They can also be used, for example, in the acceleration of charged particles [9], in molecular finger printing [10], fabrication of optical couplers [11] optical communications [12], and optical microscopy [13].

A common approach to describe passively mode-locked lasers is an average model in which the effects of discrete laser components in the cavity are averaged over one round trip [14–17]. The resulting master equation is the cubic-quintic complex Ginzburg Landau equation (CGLE) or a generalized version of it.

The study of pulsed dynamics in the framework of the CGLE has provided an adequate explanation of several unusual single and multiple-pulse phenomena that have been observed in mode-locked lasers, such as self-pulsations [18], explosions [19], and the formation of multi-soliton complexes [20]. Such studies have been also of fundamental importance in the development of the concept of dissipative solitons (DSs) [21, 22]. Generally, a DS implies a composite balance between dispersion, nonlinearity, gain and loss [23, 24]. In addition to typical DS, the concept of dissipative soliton resonance (DSR) has also been proposed to achieve high-energy wave-breaking-free pulses [25–30]. With the increase of pump power, the energy of a DSR pulse increases mainly due to the increase of the pulse width, while keeping the amplitude at a constant level. In order to obtain high-energy ultrashort pulses, a linear pulse compression technique has to be used outside the laser cavity.

In this Chapter we discuss a different kind of high-energy ultrashort pulses, which correspond to the very high amplitude (VHA) soliton solutions of the CGLE [31, 32]. These VHA solutions occur due to a singularity first predicted both numerically and using the soliton perturbation theory in Refs. [33, 34], namely, as the nonlinear gain saturation effect tends to vanish. The increase in energy of these pulses is mainly due to the increase of the pulse amplitude, whereas the pulse width becomes narrower. Using this approach, high-energy ultrashort pulses can be obtained without using any additional pulse compression technique. High energy pulses are found mainly in the normal dispersion region, which is in agreement with the experimental observations. Indeed, the majority of observations of high energy pulses from passively mode- locked lasers, both fiber and solid-state ones, are in the normal dispersion regime of operation, [21, 22, 24].

This Chapter is organized as follows: In Sect. 5.2 we present the governing equation, which corresponds to the cubic-quintic complex Ginzburg-Landau equation. In Sects. 5.3 and 5.4 we present the soliton perturbation theory and the method of moments, respectively. In Sect. 5.5 we describe the very high amplitude (VHA) solutions of the CGLE, whereas in Sect. 5.6 we analyze the effects of dispersion on such pulses. Section 5.7 discusses the impact of some higher-order effects, namely the intrapulse Raman scattering and the third-order dispersion, on VHA solitons. Finally, Sect. 5.8 summarizes the main results.

5.2 The Cubic-Quintic Complex Ginzburg-Landau Equation

The cubic-quintic complex Ginzburg Landau equation can be written in the form [35–37]:

$$i\frac{\partial q}{\partial Z}+\frac{D}{2}\frac{\partial^2 q}{\partial T^2}+|q|^2 q=i\delta q+i\beta\frac{\partial^2 q}{\partial T^2}+i\varepsilon|q|^2 q+i\mu|q|^4 q, \tag{5.1}$$

where Z is the normalized propagation distance, T is the retarded time, q is the normalized envelope of the electric field respect β stands for spectral filtering ($\beta > 0$), δ is the linear gain or loss coefficient, ε accounts for nonlinear gain-absorption processes (for example, two-photon absorption), and μ represents a higher-order correction to the nonlinear gain-absorption. On the left-hand side, D represents the cavity group velocity dispersion, with $D > 0$ in the anomalous regime and $D < 0$ in the normal regime.

Equation (4.1) has been used to model the propagation of optical pulses in soliton transmission systems [35–37]. It has been also used as a master equation to describe the behavior of solid-state lasers [38] and mode-locked fiber lasers [39–41]. The relations between the physical parameters describing a ring fiber laser mode locking through nonlinear polarization rotation and the coefficients of CGLE have been derived in [42].

Equation (5.1) becomes the standard nonlinear Schrödinger equation (NLSE) when the right-hand side is set to zero. When this does not happen, Eq. (5.1) is non-integrable, and only particular solutions can be obtained. The soliton perturbation theory can be used in the anomalous dispersion regime (D > 0) for small values of the parameters [37]. In the case of the cubic CGLE ($\mu = 0$), exact solutions can be obtained using a special ansatz [43], Hirota bilinear method [44] or reduction to systems of linear PDEs [45]. Concerning the quintic CGLE, the existence of soliton-like solutions in the case $\varepsilon > 0$, as well as sources, sinks and fronts with fixed velocity have been demonstrated both analytically and numerically [36, 46]. Analytical solutions can be presented explicitly only for certain relations between the parameters of the equation. Furthermore, so far, only stationary solutions of the CGLE are known in analytical form. Actually, several types of localized pulsating solutions of the CGLE have been also found numerically [47–53]. Approximate expressions for some of these localized solutions can be derived for arbitrary values of the CGLE parameters by reducing this equation to finite-dimensional dynamical models. The reduced models can be obtained by applying the method of moments [54], or Lagrangian techniques [55–59].

5.3 Soliton Perturbation Theory

If all the coefficients in the right-hand side of Eq. (5.1) are small, the CGLE can be considered as a perturbed NLSE of the form

$$i\frac{\partial q}{\partial Z}+\frac{D}{2}\frac{\partial^2 q}{\partial T^2}+|q|^2 q=iP(q) \tag{5.2}$$

where $P(q)$ represents the various perturbations. Considering the case D = +1 (anomalous dispersion regime), the soliton solution has the same form as the fundamental bright soliton of the NLSE but with parameters evolving in Z, namely

$$q(T,Z)=\eta\,\mathrm{sech}[\eta(T+\kappa Z-T_0)]\exp\left(-i\kappa T+\frac{i}{2}\left(\eta^2-\kappa^2\right)Z+i\sigma\right). \tag{5.3}$$

This soliton solution is characterized by four parameters: the amplitude η (also the pulse width), the frequency κ (also the pulse speed), the time position T_0 and the phase σ. The soliton amplitude and width are coupled in Eq. (5.3), such that there is an inverse relationship between these two quantities.

The evolution of the four soliton parameters can be described using the soliton perturbation theory (PT), which provides the following equations [37].

$$\frac{d\eta}{dZ}=\mathrm{Re}\int_{-\infty}^{\infty}P(q)q^*dT \tag{5.4}$$

$$\frac{d\kappa}{dZ}=-\mathrm{Im}\int_{-\infty}^{\infty}P(q)\tanh\left(\eta(T-T_0)q^*dT\right. \tag{5.5}$$

$$\frac{dT_0}{dZ}=-\kappa+\frac{1}{\eta^2}\mathrm{Re}\int_{-\infty}^{\infty}P(q)(T-T_0)q^*dT \tag{5.6}$$

$$\frac{d\sigma}{dZ}=\frac{1}{2}\left(\eta^2-\kappa^2\right)+T_0\frac{d\kappa}{dZ}+\frac{1}{\eta}\mathrm{Im}\int_{-\infty}^{\infty}P(q)(1-\eta(T-T_0)\tanh\left[\eta(T-T_0)\right]q^*dT \tag{5.7}$$

where Re and Im stand for the real and imaginary parts, respectively. Equations (5.4), (5.5), (5.6) and (5.7) are used extensively in the theory of soliton communication systems [60–62].

In the case of Eq. (5.1), we have

$$P(q)=\delta q+\beta\frac{\partial^2 q}{\partial T^2}+\varepsilon|q|^2 q+\mu|q|^4 q \tag{5.8}$$

Substituting Eq. (5.8) in Eqs. (5.4), (5.5), (5.6) and (5.7), we obtain the following evolution equations for the soliton parameters:

$$\frac{\partial \eta}{\partial Z} = 2\delta\eta - 2\beta\eta\left(\frac{1}{3}\eta^2 + \kappa^2\right) + \frac{4}{3}\varepsilon\eta^3 + \frac{16}{15}\mu\eta^5 \tag{5.9}$$

$$\frac{d\kappa}{dZ} = -\frac{4}{3}\beta\eta^2\kappa \tag{5.10}$$

$$\frac{dT_0}{dZ} = -\kappa \tag{5.11}$$

$$\frac{d\sigma}{dZ} = \frac{1}{2}\left(\eta^2 - \kappa^2\right) + T_0\frac{d\kappa}{dZ} \tag{5.12}$$

As can be seen from Eq. (5.10), the soliton frequency approaches asymptotically to $\kappa = 0$ (stable fixed point) if $\eta \neq 0$. Considering the case of cubic CGLE ($\mu = 0$), a stationary soliton amplitude $\eta_s = 1$ is achieved when the following relation is verified:

$$3\delta + 2\varepsilon - \beta = 0 \tag{5.13}$$

The substitution of (5.13) into (5.9) leads to the following equation for the soliton amplitude in the vicinity of the stationary point ($\kappa = 0$):

$$\frac{d\eta}{dZ} = 2\delta\eta\left(1 - \eta^2\right) \tag{5.14}$$

We can verify that the soliton amplitude is stable to small perturbations for $\delta > 0$, though the system returns to the steady-state more slowly when δ decreases. However, the background is not stable when $\delta > 0$, since the linear waves are also amplified by the excess gain, leading to a destructive interference with the soliton [37]. On the other hand, the pulse amplitude $\eta = 1$ is no more a stable state when $\delta < 0$, since any perturbation would lead to the collapse or to the decayment of the soliton. The final conclusion is that either the pulse or the background is unstable in the case of a cubic CGLE.

In general, the stable fixed points for the soliton amplitude can be found by looking for the minimums of the potential function ϕ defined by:

$$\frac{d\eta}{dZ} = -\frac{d\phi}{d\eta} \tag{5.15}$$

Considering the Eq. (5.9), we have the following expression for the potential function:

$$\varphi(\eta) = -\delta\eta^2 + \frac{1}{6}(\beta - 2\varepsilon)\eta^4 - \frac{8}{45}\mu\eta^6 \tag{5.16}$$

For the zero-amplitude state to be stable, the potential function must have a minimum at $\eta = 0$, in addition to a minimum at $\eta = \eta_s \neq 0$. These objectives can be achieved if the following conditions are verified [37, 63]:

$$\delta < 0, \quad \mu < 0, \quad \varepsilon > \beta/2, \quad 15\delta > 8\mu\eta_s^4 \tag{5.17}$$

We can verify from the above conditions that the inclusion of the quintic term in Eq. (5.1) is necessary to have the double minimum potential.

The stationary value for the soliton amplitude can be obtained from Eq. (5.9) and is given by:

$$\eta_s^2 = \frac{-5(\varepsilon - \beta/2) \pm 5\sqrt{(\varepsilon - \beta/2)^2 - 24\delta\mu/5}}{8\mu} \tag{5.18}$$

From Eq. (5.18) it can be seen that, for $\varepsilon > \beta/2$, there are two real solutions for the stationary amplitude. Moreover, we observe that the higher amplitude solution grows to infinity when the nonlinear gain saturation parameter tends to zero. This corresponds a singularity first reported in Refs. [33, 34], which provides the possibility of observing the very high amplitude pulses discussed in this chapter.

Equation (5.18) shows that a stationary amplitude $\eta_s = 1$ occurs when the coefficients satisfy the relation:

$$15\delta + 5(2\varepsilon - \beta) + 8\mu = 0 \tag{5.19}$$

The discriminant in Eq. (5.18) must be greater than or equal to zero for the solution to exist. For given values of β, μ, and ε, the allowed values of δ to guarantee a stable pulse propagation must satisfy the condition $\delta_{\min} \leq \delta \leq 0$, where

$$\delta_{\min} \frac{5(\varepsilon - \varepsilon_s)^2}{24\mu} \tag{5.20}$$

where $\varepsilon_s = \beta/2$. When $\delta = 0$, the peak amplitude is found to achieve a maximum value:

$$\eta_{\max} = \sqrt{-\frac{5}{4}\frac{(\varepsilon - \varepsilon_s)}{\mu}} \tag{5.21}$$

For $\mu = 0$ and $\varepsilon - \varepsilon_s$ the peak amplitude becomes arbitrary.

On the other hand, for given values of β, μ, and δ, the minimum value of allowed ε becomes

$$\varepsilon_{\min} = \varepsilon_s + \sqrt{24\delta\mu/5} \tag{5.22}$$

5.4 Method of Moments

Approximate stationary solutions of Eq. (5.1) for arbitrary values of the parameter can also be obtained using the method of moments (MM), [23, 26, 54, 64]. This method provides a reduction of the complete evolution problem with an infinite number of degrees of freedom to the evolution of a finite set of pulse characteristics [23]. For a localized solution with a single maximum, these characteristics include the peak-amplitude, pulse width, center-of-mass position, and phase parameters. A full description of this method can be found in Refs [23, 26, 54] and references therein.

The method of moments makes use of the integrals for the energy and the momentum M, as given by

$$Q = \int_{-\infty}^{\infty} |q|^2 dT \tag{5.23}$$

$$M = \frac{1}{2} \int_{-\infty}^{\infty} \left(q \frac{\partial q^*}{\partial T} - q^* \frac{\partial q}{\partial T} \right) dT. \tag{5.24}$$

as well as of the higher-order generalized moments:

$$I_1 = \int_{-\infty}^{+\infty} T|q|^2 dT \tag{5.25}$$

$$I_2 = \int_{-\infty}^{+\infty} (T - T_0)^2 |q|^2 dT \tag{5.26}$$

$$I_3 = \int_{-\infty}^{+\infty} (T - T_0)\left(q^* q_T - q q_T^* dT\right. \tag{5.27}$$

where $T_0 = I_1/Q$.

The energy and the momentum, as well as the above three higher-order moments, are conserved quantities of the nonlinear Schrödinger equation. For Eq. (5.1), they are not conserved but satisfy the following truncated set of first-order ordinary differential equations [23, 26, 54]:

$$\frac{dQ}{dZ} = i \int_{-\infty}^{+\infty} (qR^* - q^* R) dT \tag{5.28}$$

$$\frac{dM}{dZ} = -i \int_{-\infty}^{+\infty} \left(q_T R^* + q_T^* R\right) dT \tag{5.29}$$

$$\frac{dI_1}{dZ} = iDM + i \int_{-\infty}^{+\infty} T(qR^* - q^* R) dT \tag{5.30}$$

$$\frac{dI_2}{dZ} = -iDI_3 + i \int_{-\infty}^{+\infty} (T - T_0)^2 (qR^* - q^* R) dT \tag{5.31}$$

$$\frac{dI_3}{dZ} = 2M \frac{dT_0}{dz} + i \int_{-\infty}^{+\infty} \left(2D|q_T|^2 - |q|^4\right) dT + 2i \int_{-\infty}^{+\infty} (T - T_0) \times \left(q_T R^* + q_T^* R\right) dT + i \int_{-\infty}^{+\infty} (qR^* + q^* R) dT \tag{5.32}$$

where q_T represents the derivative of q relative to T, q^* is the complex conjugate of q and

$$R = i\delta q + i\beta \frac{\partial^2 q}{\partial T^2} + i\varepsilon |q|^2 q + i\mu |q|^4 q \tag{5.33}$$

Let us consider the following commonly used higher-order Gaussian trial function [23]:

$$q(T, Z) = A \exp\left(-\frac{T^2}{w^2} - \frac{T^4}{w^4}\right) \exp\left(iCT^2\right) \tag{5.34}$$

where A is the soliton amplitude, w is the soliton width, and C is the soliton chirp. Since the solutions we are looking for are symmetric, with zero (transverse) velocity, some of the moments are identically zero, and the nonzero moments obtained for the above trial function are:

$$Q = 1.051A^2 w, \quad I_2 = 0.145Qw^2, \quad I_3 = 4iCI_2 \tag{5.35}$$

A second trial function is related to the previous one but it involves only a quartic term, which is considered more appropriate for pulses with extremely values of high energy [26]:

$$q(T, Z) = A \exp\left(-\frac{T^4}{w^4}\right) \exp\left(iCT^2\right) \tag{5.36}$$

The nonzero moments obtained for the above trial function are:

$$Q = 1.524A^2 w, \;\; I_2 = 0.239Qw^2, \;\; I_3 = 4iCI_2 \tag{5.37}$$

Inserting (5.34) into the equations of the method of moments [23, 26], we obtain the following evolution equations for the soliton parameters [26]:

$$\frac{dQ}{dZ} = Q\left(2\delta - \frac{2.738\beta}{w^2} - 1.158C^2w^2\beta + \frac{1.433Q\varepsilon}{w} + \frac{1.146Q^2\mu}{w^2}\right) \tag{5.38a}$$

$$\frac{dw}{dZ} = w\left(2CD + \frac{2.142\beta}{w^2} - 0.874C^2w^2\beta - \frac{0.290Q\varepsilon}{w} - \frac{0.325Q^2\mu}{w^2}\right) \tag{5.38b}$$

$$\frac{dC}{dZ} = \frac{1}{w^2}\left(-2C^2w^2D + \frac{6.453D}{w^2} - \frac{1.237Q}{w} - 19.624C\beta\right) \tag{5.38c}$$

Considering the trial function given by Eq. (5.36), we obtain the following evolution equations [32]:

$$\frac{dQ}{dZ} = Q\left(2\delta - \frac{2.868\beta}{w^2} - 1.912C^2w^2\beta + \frac{1.103Q\varepsilon}{w} + \frac{0.654Q^2\mu}{w^2}\right) \tag{5.39a}$$

$$\frac{dw}{dZ} = w\left(2CD + \frac{0.388\beta}{w^2} - 1.136C^2w^2\beta - \frac{0.162Q\varepsilon}{w} - \frac{0.138Q^2\mu}{w^2}\right) \tag{5.39b}$$

$$\frac{dC}{dZ} = \frac{1}{w^2}\left(-2C^2w^2D + \frac{3D}{w^2} - \frac{0.577Q}{w} - 16.74C\beta\right) \tag{5.39c}$$

It can be seen that both systems given by Eqs. (5.38) and (5.39) are structurally similar, differing only in the values of the coefficients of each term.

5.5 Very-High Amplitude CGLE Solitons

Figure 5.1 shows the stationary amplitudes, η_S, given by Eq. (5.18), against the nonlinear gain saturation parameter, μ, for $\delta = -0.1$, $\varepsilon = 0.35$, and four different values of the filter strength: $\beta = 0.05$, 0.1, 0.2, and 0.5. For each set of parameter values, two different solutions are obtained: small amplitude (SA) solutions, i.e., $\eta_S \lesssim 1$, and very high amplitude (VHA) solutions, i.e., $\eta_S \gg 1$. As $\mu \to 0^-$ the SA solution remains almost unchanged, whereas the amplitude of the VHA solution tends to infinity, i.e., shows a singularity. In general, the amplitude of the VHA solution is higher for a lower value of the filter strength.

Figure 5.2 shows the stationary amplitude against the nonlinear gain parameter, ε, for two different values of nonlinear gain saturation, μ. In each case, four different values of the filter strength, β, are considered.

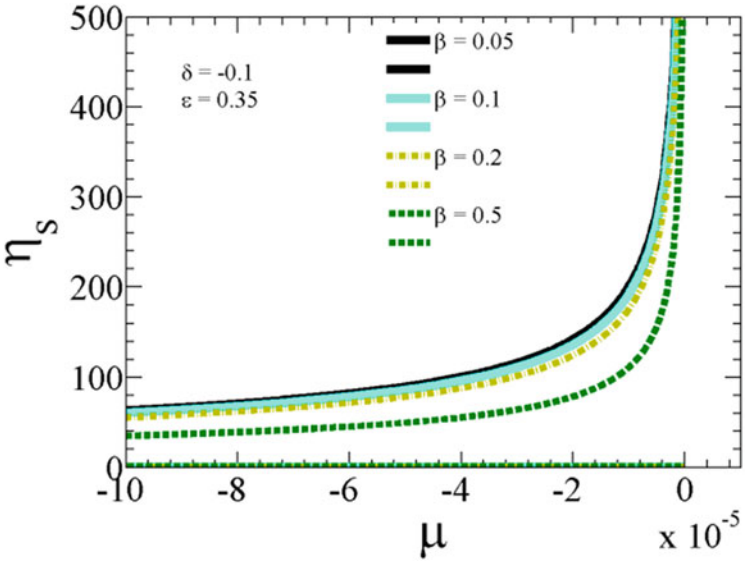

Fig. 5.1 Stationary amplitude, η_S, against the nonlinear gain saturation parameter, μ, for different values of the filter strength: $\beta = 0.05$ (thin solid curve), $\beta = 0.1$ (thick solid curve), $\beta = 0.2$ (dashed-dotted curve) and $\beta =$ with per0.5 (dashed curve). The other parameter values are $\delta = -0.1$ and $\varepsilon = 0.35$. (Reprinted with permission from [31] © The Optical Society)

It follows from Fig. 5.2 that, for each value of the spectral filtering parameter, β, there is a minimum value of the nonlinear gain, $\varepsilon_{0,}$ below which there are no solutions ($\varepsilon_0 \approx \beta/2$). For values of ε above this threshold, a bifurcation occurs and both SA and VHA solutions exist. As in the case of Fig. 5.1, the VHA solution exhibits higher amplitude for weak spectral filtering. The amplitude of the VHA solutions grows with ε, assuming higher values when the magnitude of μ is reduced.

The numerical simulation of pulse propagation is illustrated in Fig. 5.3 considering (a) $\mu = -0.00001$) and (b) $\mu = -0.0001$. Figure 5.3c, d show the temporal and the spectral density final profiles, respectively, for the cases presented in (a) (solid curves) and (b) (dashed curves). When the magnitude of μ is lower the pulse amplitude is higher and its width is smaller, which means the possibility to achieve an effective pulse compression. As predicted by the perturbation theory, the simulations also reveal that there is no limit for the pulse amplitude.

5.6 Effects of Dispersion

In this section we consider the effects of dispersion on the propagation of the very high-amplitude solitons. Since the soliton perturbation theory is only valid in the anomalous dispersion regime, an approach based on the method of moments will be used for this purpose.

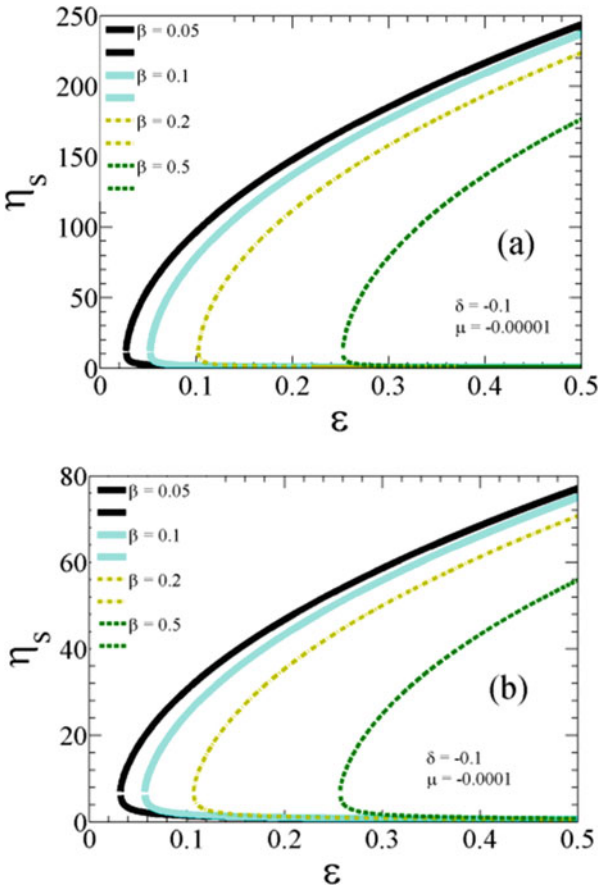

Fig. 5.2 Equilibrium amplitudes, η_S, versus nonlinear gain parameter, ε, for two different values of the nonlinear gain saturation: (**a**) $\mu = -0.00001$ and (**b**) $\mu = -0.0001$. A linear gain $\delta = -0.1$ and four different values of the spectral filtering parameter were considered, namely, $\beta = 0.05$ (thin solid curve), $\beta = 0.1$ (thick solid curve), $\beta = 0.2$ (dashed-dotted curve) and $\beta = 0.5$ (dashed curve), respectively. (Reprinted with permission from [31] © The Optical Society)

Figure 5.4 shows the stationary amplitudes against the nonlinear gain saturation parameter, μ, considering six different values of dispersion parameter D. These results were obtained by solving numerically the system of Eq. (5.39), but similar results are provided by the system of Eq. (5.38). The remaining parameter values are the same as in previous section, namely: $\delta = -0.1$, $\beta = 0.2$, and $\varepsilon = 0.35$. We observe from Fig. 5.4 that, as $\mu \to 0-$, the pulse amplitude tends to infinity, i.e., a singularity is found, for all the values of D considered. However, pulse decay is observed for $D = 0$.

Figure 5.5 shows (a) the stationary pulse amplitude and (b) the energy against the dispersion parameter, D, considering four different values of nonlinear gain saturation parameter, μ. The results were obtained using the dynamical system given by Eq. (5.38).

From Fig. 5.5a it can be seen that the pulses equilibrium amplitude evolve with D in a similar fashion for all the different values of μ considered. In general, as the magnitude of D decreases, the amplitude also decreases and a minimum is found

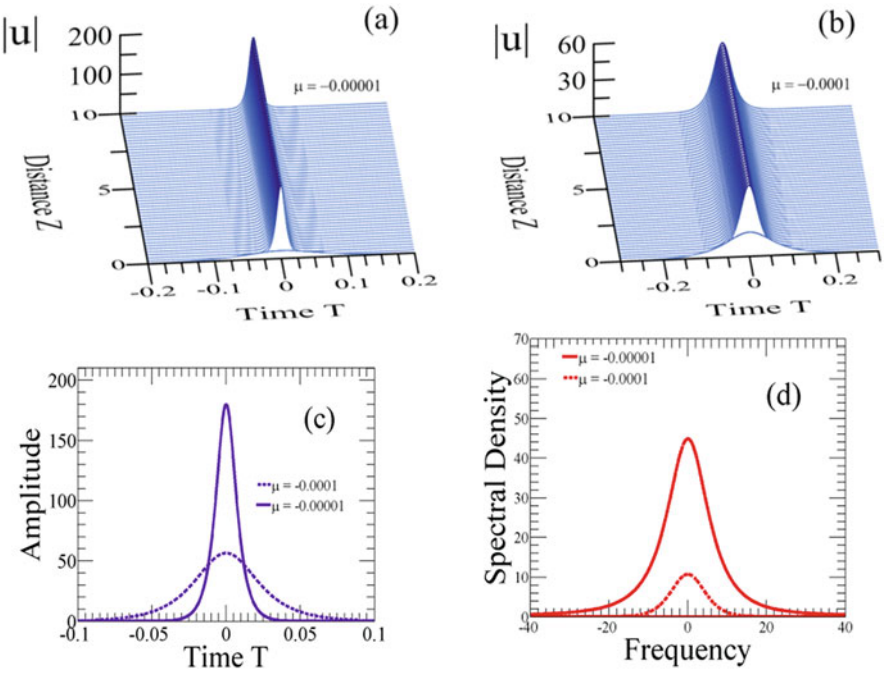

Fig. 5.3 Pulse evolution for two different values of the nonlinear gain saturation parameter: (**a**) $\mu = -0.00001$ and (**b**) $\mu = -0.0001$. Temporal (**c**) and spectral density (**d**) profiles for the cases presented in (**a**) (solid curves) and in (**b**) (dashed curves). The other parameter values are: $\delta = -0.1$, $\beta = 0.2$, and $\varepsilon = 0.35$. (Reprinted with permission from [31] © The Optical Society)

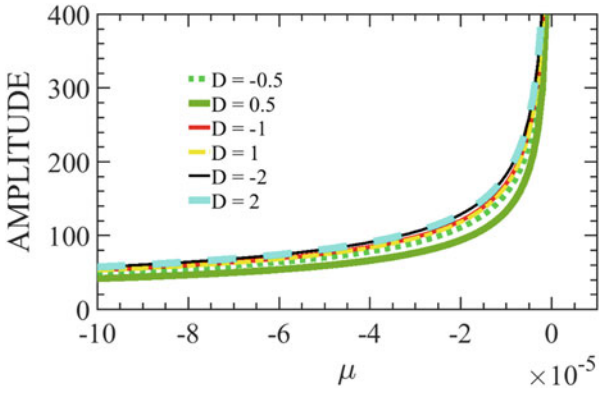

Fig. 5.4 Stationary pulse amplitude against the nonlinear gain saturation parameter, μ, for six different values of dispersion parameter: D = 0.5 (thick solid curve), D = −0.5 (dotted curve), D = 1 (dashed-dotted curve), D = −1 (medium solid curve), D = −2 (thin solid curve) and D = 2 (dashed curve). The other parameter values are: $\delta = -0.1$, $\beta = 0.2$, and $\varepsilon = 0.35$. (Reprinted with permission from [32] © The Optical Society)

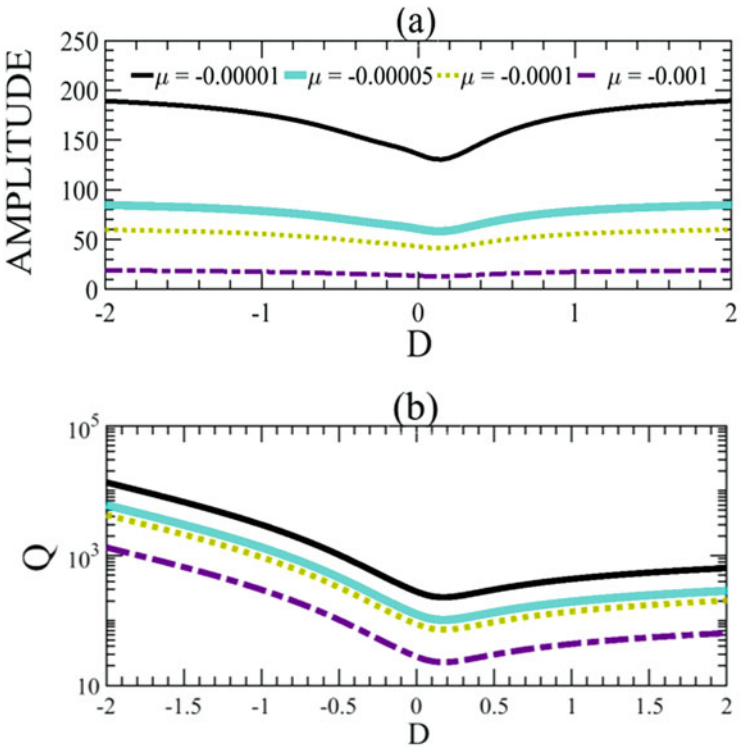

Fig. 5.5 Pulse stationary amplitude, (**a**) and energy (**b**), versus dispersion parameter, D, for different values of the nonlinear gain saturation: $\mu = -0.00001$ (thin solid curve), $\mu = -0.00005$ (thick solid curve), $\mu = -0.0001$ (dotted curve), and $\mu = -0.001$ (dashed-dotted curve). The other parameter values are: $\delta = -0.1$, $\beta = 0.2$, and $\varepsilon = 0.35$. These results were obtained using the dynamical system (5.38). (Reprinted with permission from [32] © The Optical Society)

nearby $D \approx +0.1$. Each curve looks almost symmetric relatively to this minimmum, such that for symmetric values of D the amplitude looks nearly the same.

Concerning the pulse energy, Fig. 5.5b shows that it decreases with the magnitude of D, until a minimum is reached nearby $D \approx +0.1$. However, the energy is not symmetric around this minimum, since it reaches much higher values in the normal than in the anomalous dispersion regimes. For example, the pulse energy for $D = -2$ is higher by one order of magnitude than for $D = +2$.

Figure 5.6 shows (a) the stationary pulse amplitude and (b) the energy against the dispersion parameter, D, for the same cases considered in Fig. 5.5, but using the system of Eq. (5.9). We observe that, in general, the amplitude and the energy depends on D in a similar fashion. However, a main difference occurs in the range $-0.1 < D < 0.4$, where no stationary solutions are found in Fig. 5.6.

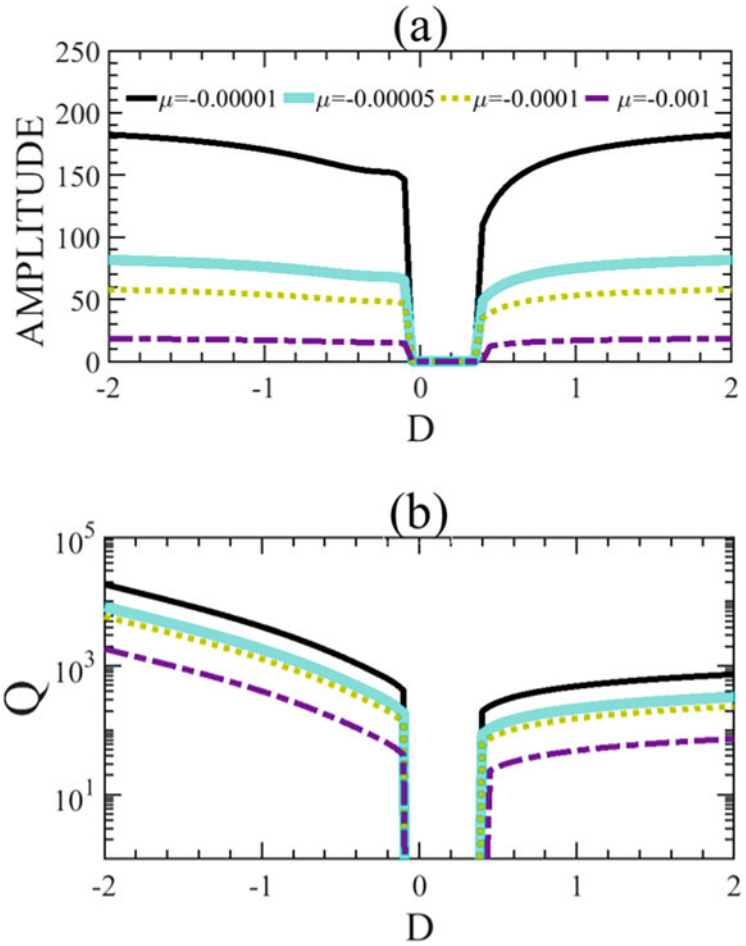

Fig. 5.6 Pulse stationary amplitude, (**a**) and energy (**b**), versus dispersion parameter, D, for different values of the nonlinear gain saturation: $\mu = -0.00001$ (thin solid curve), $\mu = -0.00005$ (thick solid curve), $\mu = -0.0001$ (dotted curve), and $\mu = -0.001$ (dashed-dotted curve). The other parameter values are: $\delta = -0.1$, $\beta = 0.2$, and $\varepsilon = 0.35$. These results were obtained using the dynamical system (5.39). (Reprinted with permission from [32] © The Optical Society)

In order to clarify which of dynamical systems (5.38) or (5.39) are more accurate, Eq. (5.1) was numerically solved. The region of existence of stationary pulses (SPs) of the CGLE in the plane (μ, D) is illustrated in Fig. 5.7.

The region of existence of SPs shown in Fig. 5.7 is not as large as that predicted by the method of moments in Fig. 5.6. In the normal dispersion regime, front's expansion was observed for $D < -1.65$. On the other hand, on the upper right corner (anomalous dispersion regime), instability was found. Furthermore, for the assumed values of μ, stationary pulses were not found for D between -0.5 and 0.1. This result

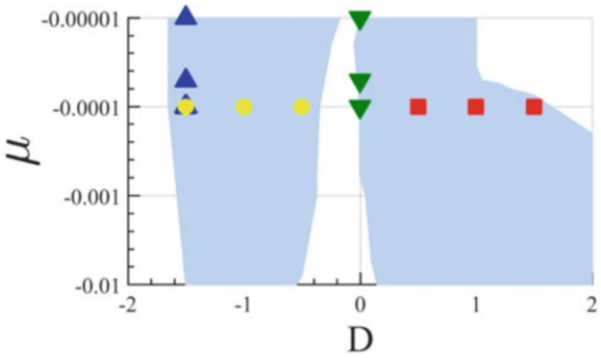

Fig. 5.7 Region of existence of stationary pulses (SPs) of the CGLE in the plane (μ, D). The other parameters are $\delta = -0.1$, $\beta = 0.2$, and $\varepsilon = 0.35$. The circles and squares correspond to SPs profiles represented in Fig. 5.8a, c. The triangles (down and up) correspond to SPs profiles represented in Fig. 5.9a, c, respectively. (Reprinted with permission from [32] © The Optical Society)

is in good qualitative agreement with the predictions of the method of moments, as given by the system of Eq. (5.39). However, comparing with Fig. 5.6, we observe that the region of nonexistence of SPs in Fig. 5.7 is slightly shifted to the normal dispersion regime.

Figures 5.8 and 5.9 illustrate some of the VHA stationary solutions found numerically in the plane (μ, D). In Fig. 5.8 several values of D were considered, and the nonlinear gain saturation parameter was kept constant, with a value $\mu = -0.0001$. The other parameter values are $\delta = -0.1$, $\beta = 0.2$, and $\varepsilon = 0.35$.

Figure 5.8a, c illustrate the pulse profiles in the normal ($D < 0$) and anomalous ($D > 0$) dispersion regimes, respectively, for $D = \pm 1.5, \pm 1, \pm 0.5$. The pulse width changes significantly with D in the normal dispersion regime, whereas it remains almost unchanged in the anomalous dispersion regime. In general, pulses are wider in the first case when compared with second one. The pulse power spectral density is represented in Fig. 5.8b, d, for $D < 0$ and $D > 0$, respectively. One main feature is that the spectral range is almost the same for all cases in both regimes. On the other hand, the spectra peak power achieves higher values when increasing the magnitude of D, which corresponds to higher values of the pulse energy.

Figure 5.9 presents several pulse amplitude profiles and the respective power spectral density, for different values of the nonlinear gain saturation parameter and for two values of the dispersion parameter: $D = 0$ and $D = -1.5$. The other parameter values are similar to those in Fig. 5.8.

Figure 5.9a, b show that the peak amplitude increases and the pulse becomes narrower as $\mu \to 0-$, which is more evident in the case $D = -1.5$ (normal dispersion regime). The pulses power spectra are represented in Fig. 5.9b, d for $D = 0$ and $D = -1.5$, respectively. We observe that both the peak values and the spectral range of such pulses increase as $\mu \to 0-$. Once more, the spectral range seems to be almost independent of D and strongly dependent of the nonlinear gain saturation parameter, μ. Decreasing the magnitude of this parameter allows the pulses in the normal

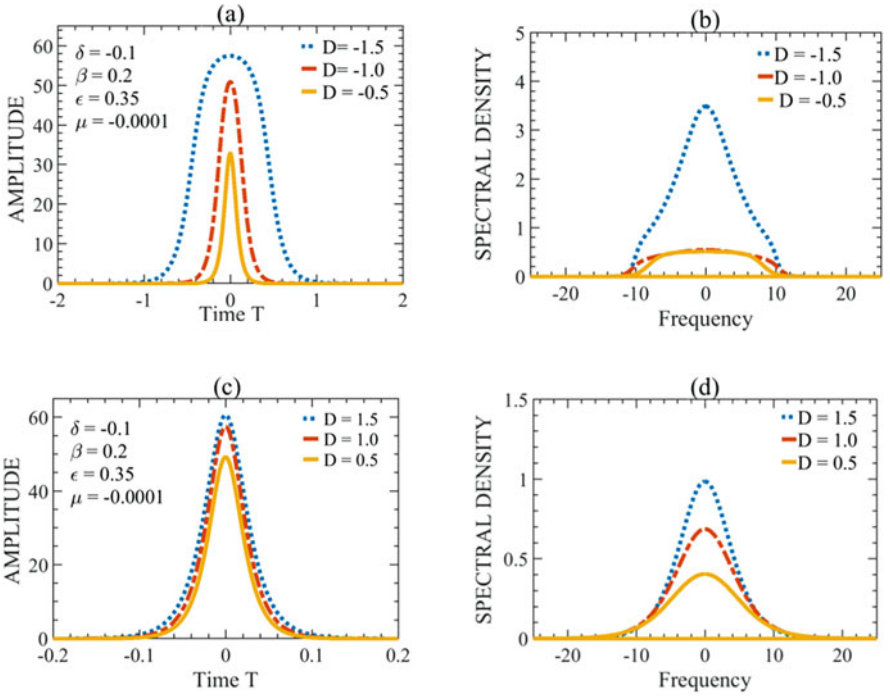

Fig. 5.8 Amplitude profiles, (**a** and **c**), and power spectral density, (**b** and **d**), in the normal (D < 0) and anomalous (D > 0) dispersion regimes, respectively, for D = ±1.5 (dashed curves), D = ±1 (dashed-dot curves) and D = ±0.5 (solid curves). The other parameter values are: $\delta = -0.1$, $\beta = 0.2$, and $\varepsilon = 0.35$. (Reprinted with permission from [32] © The Optical Society)

dispersion regime to reach very high energies. For instance, in the case D = −1.5 the pulse energies are $Q = 2487$, 3469, and 7870, for $\mu = -0.0001$, −0.00005, and −0.00001, respectively.

It is important to recognize a significant difference between the VHA pulses discussed in this chapter and the high energy pulses found numerically in Ref. [25]. Actually, it has been found numerically that the energy of a dissipative soliton solution of the CGLE increases indefinitely when the equation parameters converge to a given region of the parameter space. Such set of parameters was called a dissipative soliton resonance (DSR) [26]. Found in the normal dispersion regime, it initially required a positive quintic reactive nonlinearity to appear [25, 26], but then DSR was also revealed in the chromatic dispersion-free (D = 0) regime, along with negative quintic reactive nonlinearity [27]. The concept of dissipative soliton resonance has soon been proposed to achieve high-energy wave-breaking-free pulses [25–30].

The energy of a DSR pulse increases mainly due to the increase of the pulse width, while keeping the amplitude at a constant level [25, 26]. Nevertheless, as the DSR pulse is highly chirped, this can be used to compress the pulse [65] and hence

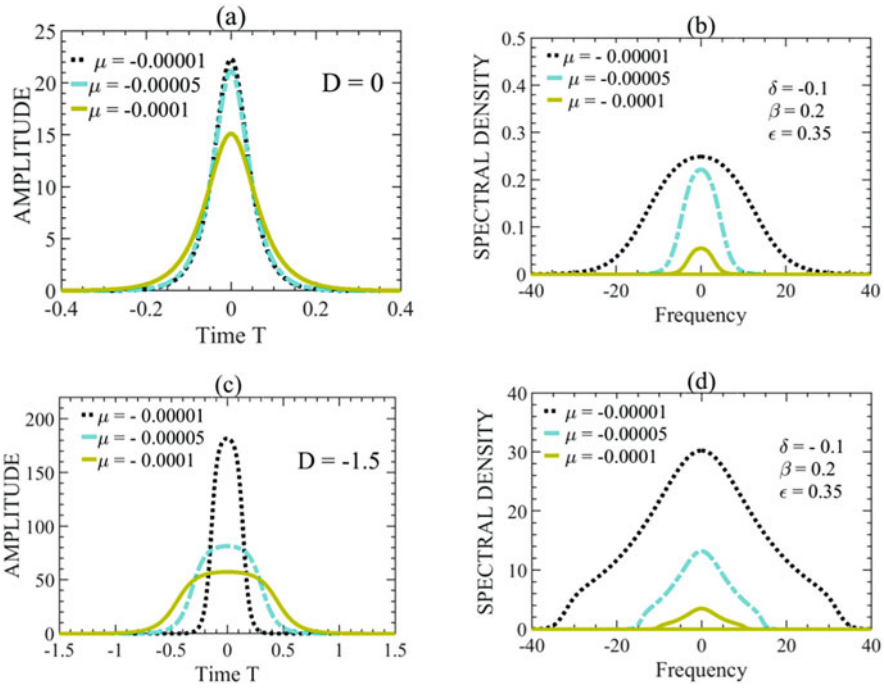

Fig. 5.9 Amplitude profiles, (**a** and **c**), and power spectral density, (**b** and **d**), for D = 0 and D = −1.5, respectively. The nonlinear gain saturation parameter assumes the values: $\mu = -0.00001$ (dashed curves), $\mu = -0.00005$ (dashed-dot curves) and $\mu = -0.0001$ (solid curves). The other parameter values are: $\delta = -0.1$, $\beta = 0.2$, and $\varepsilon = 0.35$. (Reprinted with permission from [31] © The Optical Society)

obtain high energy ultrashort pulses. Experimental demonstrations for the existence of the DSR phenomenon have been reported [66–71].

In contrast with the DSR pulse, the increase in energy of the pulses discussed in this chapter, which occurs when the absolute value of μ decreases, is mainly due to the increase of the pulse amplitude, whereas the pulse width becomes narrower. Clearly, high-energy ultrashort pulses can be obtained in this case without using any additional linear pulse compression technique. It might be noted, from Fig. 5.1, that there is no limit for the pulse amplitude. However, a limitation could be imposed by some higher-order effects, as seen in the next section.

5.7 Impact of Higher-Order Effects

The propagation of ultrashort optical pulses in fibers must take into account several higher-order effects, namely the intra-pulse Raman scattering (IRS) and the third-order dispersion (TOD). Considering these effects, the propagation equation is given

by a generalized version of the cubic-quintic CGLE given by Eq. (5.1), which assumes then the following form [37]:

$$i\frac{\partial q}{\partial Z}+\frac{D}{2}\frac{\partial^2 q}{\partial T^2}+|q|^2 q=i\delta q+i\beta\frac{\partial^2 q}{\partial T^2}+i\varepsilon|q|^2 q+i\mu|q|^4 q+i\beta_3\frac{\partial^3 q}{\partial T^3}+\tau_R q\frac{\partial|q|^2}{T} \tag{5.40}$$

where the parameters β_3 and τ_R, govern, respectively, the effects of TOD and IRS, respectively.

5.7.1 Results of the Soliton Perturbation Theory

Assuming that all the coefficients on the right-hand side of Eq. (5.40) are small and considering the anomalous dispersion regime (D = +1), we can use the adiabatic soliton perturbation theory to get the following set of ordinary differential equations:

$$\frac{d\eta}{dZ}=2\delta\eta-2\beta\eta\left(\frac{1}{3}\eta^2+\kappa^2\right)+\frac{4}{3}\varepsilon\eta^3+\frac{16}{15}\mu\eta^5 \tag{5.41}$$

$$\frac{d\kappa}{dZ}=-\frac{4}{3}\beta\eta^2\kappa-\frac{8}{15}\tau_R\eta^4 \tag{5.42}$$

$$\frac{dT_0}{dZ}=-\kappa+\beta_3\left(\eta^2+3\kappa^2\right) \tag{5.43}$$

$$\frac{d\sigma}{dZ}=\frac{1}{2}\left(\eta^2-\kappa^2\right)+T_0\frac{d\kappa}{dZ}+\beta_3\kappa\left(3\eta^2+\kappa^2\right) \tag{5.44}$$

The steady-state solutions, η_s and κ_s, of Eqs. (5.41) and (5.42) are obtained considering $\frac{d\eta}{dZ}=\frac{d\kappa}{dZ}=0$ and satisfy the conditions:

$$\delta-\beta\kappa_s^2+\frac{1}{3}(2\varepsilon-\beta)\eta_s^2+\frac{8}{15}\mu\eta_s^4=0 \tag{5.45}$$

$$\beta\kappa_s+\frac{2}{5}\tau_R\eta_s^2=0 \tag{5.46}$$

Substituting Eq. (5.46) in Eq. (5.45) we find that the stationary pulse amplitude is given by:

$$\eta_s=\left[A\pm\left[A^2-B\right]^{1/2}\right]^{1/2} \tag{5.47}$$

where

$$A = \frac{\beta - 2\varepsilon}{2W} \tag{5.48}$$

$$B = \frac{3\delta}{W} \tag{5.49}$$

$$W = \frac{8}{5}\mu - \frac{12}{25}\frac{\tau_R^2}{\beta} \tag{5.50}$$

The steady-steady value of the amplitude must be real and positive. This is the case only for $\varepsilon \geq \varepsilon_0$, where ε_0 is a threshold value of nonlinear gain, given by:

$$\varepsilon_0 = \frac{\beta}{2} + \sqrt{\frac{3\delta}{5}\left(8\mu - \frac{12}{5}\frac{\tau_R^2}{\beta}\right)} \tag{5.51}$$

We find from Eq. (5.47) that there are two steady-state solutions in the case:

$$\text{(i)} \quad A > \sqrt{B} > 0. \tag{5.52}$$

On the other hand, there is only one steady-state solution in the following cases:

$$\text{(ii)} \quad B < 0 \tag{5.53}$$

$$\text{(iii)} \quad A = \sqrt{B} > 0 \tag{5.54}$$

$$\text{(iv)} \quad B = 0 \text{ and } A > 0 \tag{5.55}$$

In the absence of nonlinear gain ($\varepsilon = \mu = 0$) there is one steady-state solution corresponding to case ii). Considering that $\beta > 0$, the linear gain δ must be positive in this case, which will lead to instability of the background. On the other hand, in the presence of nonlinear gain proportional to the square of the amplitude of such that ($\mu = 0$), there is one steady-state solution if $\delta > 0$ (case ii)) and eventually two solutions if $\delta > 0$, corresponding to case i).

5.7.2 *Linear Stability Analysis*

Linearizing Eqs. (5.41) and (5.42) around the steady-state solution, we can write the system of equations describing the evolution of the small deviations $\Delta\eta$ and $\Delta\kappa$ in the following matrix for

$$\begin{bmatrix} \frac{d\Delta\eta}{dZ} \\ \frac{d\Delta\kappa}{dZ} \end{bmatrix} = \begin{bmatrix} a_{11} & a_{12} \\ a_{21} & a_{22} \end{bmatrix} \begin{bmatrix} \Delta\eta \\ \Delta\kappa \end{bmatrix} \tag{5.56}$$

where

$$a_{11} = 2\delta - 2\beta\kappa_s^2 + (4\varepsilon - 2\beta)\eta_s^2 + \frac{16}{3}\mu\eta_s^4 \tag{5.57}$$

$$a_{12} = -4\beta\kappa_s\eta_s \tag{5.58}$$

$$a_{21} = -\frac{8}{3}\beta\kappa_s\eta_s - \frac{32}{15}\tau_R\eta_s^3 \tag{5.59}$$

$$a_{22} = -\frac{4}{3}\beta\eta_s^2 \tag{5.60}$$

The two eigenvalues (λ_1, λ_2) of the matrix $\begin{bmatrix} a_{11} & a_{12} \\ a_{21} & a_{22} \end{bmatrix}$ satisfy the characteristic equation:

$$\lambda^2 - \frac{8}{15}\eta_s^2\left[5(2\varepsilon - \beta) + 8\mu\eta_s^2\right]\lambda - \frac{16}{9}\beta\eta_s^4\left[2\varepsilon - \beta + \left(\frac{16}{5}\mu + \frac{24}{25}\frac{\tau_R^2}{\beta}\right)\eta_s^2\right] = 0 \tag{5.61}$$

The steady-state solution (η_s, κ_s) is linearly stable if the real parts of the two eigenvalues are negative. This is the case if the following conditions are verified:

$$8\mu\eta_s^2 + 5(\varepsilon - \beta) < 0 \tag{5.62}$$

$$2\varepsilon - \beta + \left(\frac{16}{5}\mu - \frac{24}{25}\frac{\tau_R^2}{\beta}\right)\eta_s^2 < 0 \tag{5.63}$$

Inserting the equilibrium solutions, η_s and κ_s, into Eq. (5.43) we obtain:

$$\frac{dT_0}{dZ} = \frac{2}{5}\frac{\tau_R}{\beta}\eta_s^2 + \beta_3\left[\eta_s^2 + \left(\frac{2\sqrt{3}}{5}\frac{\tau_R}{\beta}\right)^2\eta_s^4\right] \tag{5.64}$$

whose direct integration gives:

$$T_0(Z) = T_0(0) + \left\{\frac{2}{5}\frac{\tau_R}{\beta}\eta_s^2 + \beta_3\left[\eta_s^2 + \left(\frac{2\sqrt{3}}{5}\frac{\tau_R}{\beta}\right)^2\eta_s^4\right]\right\}Z \tag{5.65}$$

or

$$T_0(Z) = T_0(0) + vZ \tag{5.66}$$

where v is a constant velocity defined by the equation parameter values. As a consequence, $T_0(Z)$ varies linearly with Z. From Eq. (5.65) we observe that negative TOD can compensate the effects of IRS, allowing us to obtain a solution with reduced or even zero velocity.

The above results obtained using the perturbation theory should be a good approximation of the actual solution for small values of the parameters. Nevertheless, they are in general a good starting point to predict solutions and their stability even for parameters that are not as small.

5.7.3 Numerical Results

Figure 5.10 illustrates the equilibrium amplitude, η_S, as a function of the nonlinear gain saturation parameter, μ, in the presence of IRS ($\tau_R = 0.01$), as obtained from Eq. (5.47). Four different values of the spectral filtering were considered: $\beta = 0.05$ (thin solid curve), $\beta = 0.1$ (thick solid curve), $\beta = 0.2$ (dashed-dotted curve), and $\beta = 0.5$ (dashed curve), while the other parameter values were the following: $\delta = -0.1$, $\varepsilon = 0.35$, and $\beta_3 = 0$ (absence of TOD). Similarly to the results obtained in Sect. 5.5, both SA and VHA solutions are obtained. Moreover, we observe that the amplitude of the VHA solutions increases when $\mu \to 0^-$, which is more significant for stronger spectral filtering. However, such increase is limited, which means that the singularity is no longer observed in the presence of IRS.

Figure 5.11 shows the numerical results for (a) the amplitude evolution and (b) the stationary profile of a VHA pulse in the presence of IRS ($\tau_R = 0.01$), considering the following parameter values: $\delta = -0.1$, $\beta = 0.2$, $\varepsilon = 0.35$, $\mu = -0.0001$, and $\beta_3 = 0$ (absence of TOD). The numerical result for the peak

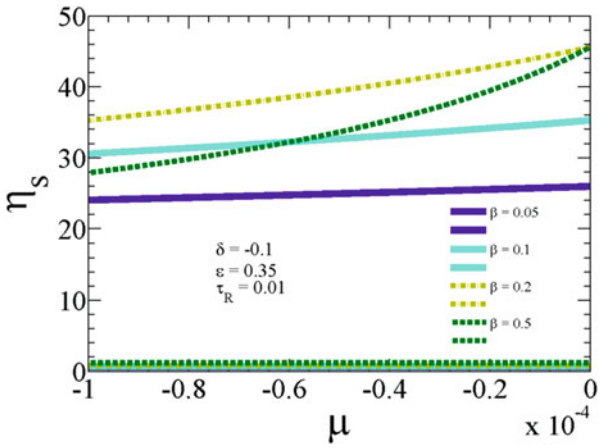

Fig. 5.10 Equilibrium amplitude, η_S, versus nonlinear gain saturation parameter, μ, in the presence of IRS ($\tau_R = 0.01$), as obtained from Eq. (5.47). Four different values of the spectral filtering were considered: $\beta = 0.05$ (thin solid curve), $\beta = 0.1$ (thick solid curve), $\beta = 0.2$ (dashed-dotted curve), and $\beta = 0.5$ (dashed curve), while the other parameter values were the following: $\delta = -0.1$, $\varepsilon = 0.35$, and $\beta_3 = 0$ (absence of TOD). (Reprinted with permission from [31] © The Optical Society)

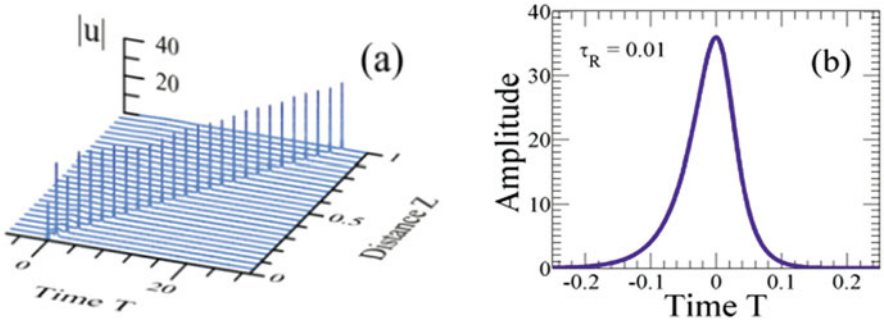

Fig. 5.11 Numerical results for (**a**) the amplitude evolution and (**b**) the stationary profile of a VHA pulse in the presence of IRS ($\tau_R = 0.01$), considering the following parameter values: $\delta = -0.1$, $\beta = 0.2$, $\varepsilon = 0.35$, $\mu = -0.0001$, and $\beta_3 = 0$ (absence of TOD). (Reprinted with permission from [31] © The Optical Society)

amplitude for the VHA solution is 35.95, whereas the perturbation theory predicts 35.35 (a difference <2%). Comparing with Figs. 5.3 and 5.11 shows that IRS determines both a reduction of the pulse amplitude and a deceleration of the pulse.

From Eq. (5.63), we have $T_0\,(Z = 1) \simeq 25$, a value that agrees with the position of the pulse after propagation up to $Z = 1$, as can be seen from Fig. 5.11a. The eigenvalues obtained from the linear stability analysis applied to this stationary solution are λ_1, $\lambda_2 = -8.31 \times 10^{-1} \pm i7.6 \times 10^2$. Since the real part of both eigenvalues is negative, the stationary solution is stable and the pulse propagates steadily.

Considering that the nonlinear gain saturation parameter is $\mu = -0.00001$ and keeping the remaining parameter values, the perturbation theory predicts a VHA solution with an amplitude peak of 44.2 and λ_1, $\lambda_2 = 3.1 \times 10^2 \pm i\,7.6 \times 10^2$. Since the real part of both eigenvalues is positive, the solution is unstable is such case.

Figure 5.12 shows the (a) amplitude evolution and (b) the stationary amplitude profile for a VHA pulse in the presence of negative TOD ($\beta_3 = -0.005$), considering the following values for the remaining parameter: $\delta = -0.1$, $\beta = 0.2$, $\varepsilon = 0.35$, $\mu = -0.0001$, and $\tau_R = 0$ (absence of IRS). In Fig. 5.12b we observe a pulse distortion, which occurs mainly on the leading edge of the pulse. On the other hand, the pulse peak amplitude is slightly higher than that observed in Fig. 5.3b. This result is good agreement with the prediction of the perturbation theory, since Eqs. (5.41) and (5.42) do not depend on β_3, and $\tau_R = 0$ was assumed.

Figure 5.13 shows the propagation of VHA pulses in the presence of both IRS ($\tau_R = 0.01$) and TOD: (a) $\beta_3 = -0.0041$ and (b) $\beta_3 = -0.005375$. The other parameter values are: $\delta = -0.1$, $\beta = 0.2$, $\varepsilon = 0.35$, and (a) $\mu = -0.00001$ and (b) $\mu = -0.0001$, respectively. The values of β_3 have been chosen in order to provide a reduced pulse velocity. Figure 5.13a demonstrates the stable propagation of the VHA pulse in the case $\mu = -0.0001$ and $\tau_R = 0.01$, which is only possible if TOD is also considered. Figure 5.13c, d show the pulse amplitude profiles and their spectral densities for both values of μ and β_3. Once more, the pulse peak amplitudes of both

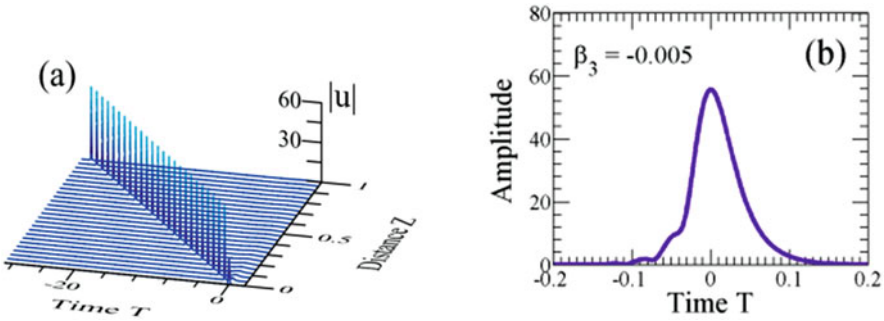

Fig. 5.12 (**a**) Amplitude evolution and (**b**) the stationary amplitude profile for a VHA pulse in the presence of negative TOD ($\beta_3 = -0.005$). The remaining parameter are: $\delta = -0.1$, $\beta = 0.2$, $\varepsilon = 0.35$, $\mu = -0.0001$, and $\tau_R = 0$ (absence of IRS). (Reprinted with permission from [31] © The Optical Society)

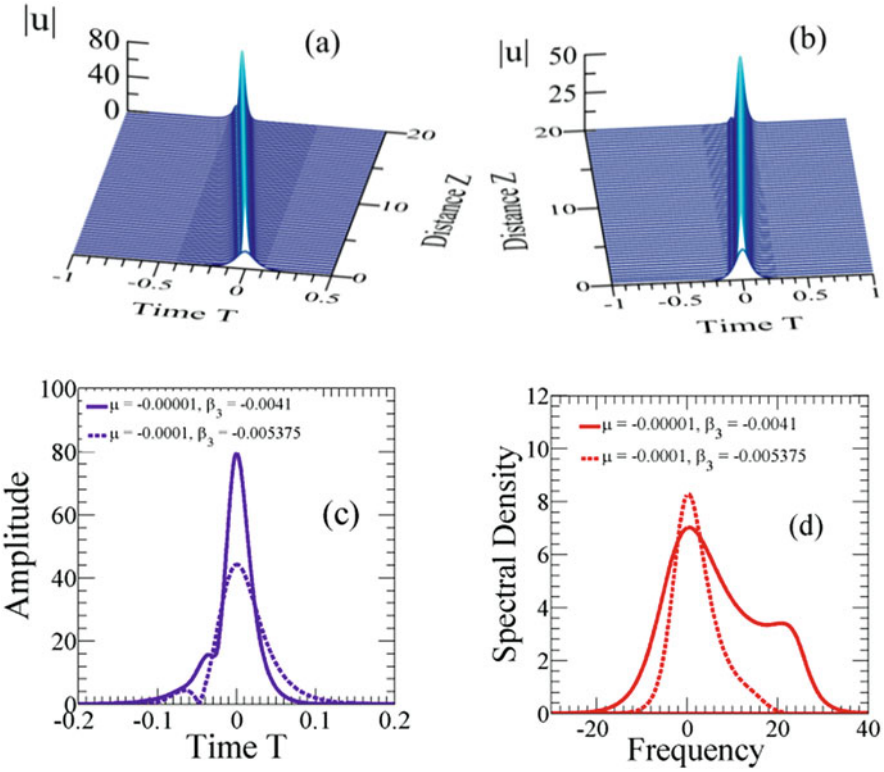

Fig. 5.13 Propagation of VHA pulses in the presence of both IRS ($\tau_R = 0.01$) and TOD: (**a**) $\beta_3 = -0.0041$ and (**b**) $\beta_3 = -0.005375$. The other parameter values are: $\delta = -0.1$, $\beta = 0.2$, $\varepsilon = 0.35$, and (**a**) $\mu = -0.00001$ and (**b**) $\mu = -0.0001$. (**c** and **d**) show the amplitude and spectral density profiles for the pulses presented in (**a**) (solid curves) and in (**b**) (dashed curves), respectively. (Reprinted with permission from [31] © The Optical Society)

pulses are smaller than those in Fig. 5.3, which is mainly due to the IRS effect. The amplitude profiles are asymmetric, with a major distortion occurring on the pulses leading edge. The spectral profile also becomes asymmetric as a consequence of both higher-order effects. The spectral range of the higher amplitude pulse is $\Delta f \approx 50$, whereas for the smaller amplitude pulse is $\Delta f \approx 30$.

5.8 Conclusions

In this chapter, very high amplitude (VHA) pulses of the CGLE are presented, due to a singularity predicted by the soliton perturbation theory when the nonlinear gain saturation parameter (μ) tends to zero. Their existence is also predicted by the method of moments and confirmed numerically. They are pulses with zero (transverse) velocity, with symmetric temporal and spectral profiles.

A region of existence of these VHA pulses was found numerically in the plane defined by the nonlinear gain saturation parameter and the dispersion parameter, D. A good agreement was found between the numerical simulations and the method of moments predictions, considering a trial function with a quartic term only. For a fixed value of the nonlinear gain saturation parameter, the pulse amplitude decreases almost symmetrically as $|D| \to 0$, for $|D| > 0.5$. However, the pulses have higher energies in the normal dispersion regime than in the anomalous dispersion regime. The pulse width decreases significantly as D increases, for $D < 0$, and increase slightly with D, for $D > 0$.

The increase in energy of the pulses discussed in this work, found in the normal dispersion regime when the magnitude of μ decreases, is mainly due to the increase of amplitude, whereas the pulse width becomes narrower. This is a different mechanism of the one observed in DSR, were the growth of energy is mainly due to the increase of the pulse width, while pulse amplitude and spectral range remain constant.

The singularity giving origin to the VHA pulses is no longer present if the intrapulse Raman scattering (IRS) effect is considered, as predicted by the soliton perturbation theory. In this case, the pulses exhibit asymmetric temporal and spectral profiles, have nonzero velocities, and their amplitudes are still high but finite for $\mu = 0$. In the presence of third-order dispersion (TOD) only, the amplitude remains almost unaffected, as predicted by the perturbation theory. Even so, the pulse velocities and their temporal profiles are strongly affected. The combined effect of IRS and negative TOD allows us to find pulses with almost zero velocity, for a proper choice of the parameter values.

Aknowledgment We aknowledge FCT - Fundação para a Ciência e a Tecnologia (Project UID/CTM/50025/2020).

References

1. I. P. Christov, M. M. Murnane, and H. C. Kapteyn, Phys. Rev. Lett. **78**, 1251 (1997).
2. G. Genty, S. Coen, and J. M. Dudley, J. Opt. Soc. Am. B **24**, 1771, (2007).
3. I. Maxwell, S. Chung, and E. Mazur, Med. Laser Appl. **20**, 193 (2005).
4. T.P. Horikis, and M. J. Ablowitz, J. Opt. Soc. Am. B, **31**, 2748, (2014).
5. W. Fu, L. G. Wright, P. Sidorenko, S. Backus, and F. W. Wise, Opt. Exp., **26**, 9432, (2018).
6. H. Kawagoe, S. Ishida, M. Aramaki, Y. Sakakibara, E. Omoda, H. Kataura, and N. Nishizawa, Biomed. Opt. Express **5**, 932 (2014).
7. K. Lindfors, T. Kalkbrenner, P. Stoller, and V. Sandoghdar, Phys. Rev. Lett. **93**, 037401 (2004).
8. A. Labruyère, A. Tonello, V. Couderc, G. Huss, and P. Leproux, Opt. Fiber Technol. 18, 375 (2012).
9. M. Kando et al., Jpn. J. Appl. Phys., **38**, L967 (1999).
10. S. A. Diddams, L. Hollberg, and V. Mbele, Nature **445**, 627 (2007).
11. K. Suzuki, V. Sharma, J. G. Fujimoto, E. P. Ippen, and Y. Nasu, Opt. Express **14**, 2335 2006.
12. J. Kang, C. Kong, P. Feng, X. Wei, Z. C. Luo, E. Y. Lam, and K. K. Y. Wong, IEEE Photonics Technol. Lett. **30**, 311 (2018).
13. S. Hu, J. Yao, M. Liu, A. P. Luo, Z. C. Luo, and W. C. Xu, Opt. Express **24**, 10786 (2016).
14. S. Wang, A. Docherty, B. S. Marks, and C. R. Menyuk, J. Opt. Soc. Am. B **30**, 3064 (2013).
15. S. Wang, B. S. Marks, and C. R. Menyuk, Opt. Express **24**, 20228 (2016).
16. S. Wang, S. Droste, L. C. Sinclair, I. Coddington, N. R. Newbury, T. F. Carruthers, and C. R. Menyuk, Opt. Lett. **42**, 2362 (2017).
17. R. Liao, Y. Song, L. Chai, and M. Hu, Opt Express, 27, 14705 (2019).
18. J. M. Soto-Crespo, M. Grapinet, Ph. Grelu, and N. Akhmediev, Phys. Rev. E **70**, 066612 (2004)
19. S. Cundiff, J. M. Soto-Crespo, and N. Akhmediev, Phys. Rev. Lett. **88**, 073903 (2002).
20. N. Akhmediev, J. M. Soto-Crespo, M. Grapinet, and Ph. Grelu, Opt. Fiber Technol. **11**, 209 (2005).
21. A. Chong, W. H. Renninger, and F. W. Wise, Opt. Lett. **32**, 2408 (2007).
22. L. M. Zhao, D. Y. Tang, and J. Wu, Opt. Lett. **31**, 1788 (2006).
23. N. Akhmediev, and A. Ankiewicz, Dissipative Solitons: '*From Optics to Biology and Medicine*', Lecture notes in Physics (Springer 2008).
24. P. Grelu and N. Akhmediev, Nat. Photonics **6**, 84 (2012).
25. N. Akhmediev, J.-M. Soto-Crespo, and P. Grelu, Phys.Lett. A, **372**, 3124 (2008).
26. W. Chang, A. Ankiewicz, J.-M. Soto-Crespo, and N. N. Akhmediev, Phys. Rev. A **78**, 023830 (2008).
27. W. Chang, J. Soto-Crespo, A. Ankiewicz, and N. Akhmediev, Phys.Rev.A, **79**, 033840, (2009).
28. P. Grelu, W. Chang, A. Ankiewicz, J. Soto-Crespo, and N. Akhmediev, J. Opt. Soc. Am. B **27**, 2336 (2010).
29. A. Komarov, F. Amrani, A. Dmitriev, K. Komarov, and F. Sanchez, Phys. Rev. A **87**, 023838 (2013).
30. W. Du, H. Li, J. Li, Z. Wang, P. Wang, Z. Zhang, and Y. Liu, Opt Express, **27**, 8059 (2019).
31. S. C. Latas, M. F. Ferreira, and M. Facão, J. Opt. Soc. Am. B **35**, 1033 (2017).
32. S. C. Latas and M. F. Ferreira, *J. Opt. Soc. of Am. B*, **36**, 3016 (2019)
33. J. M. Soto-Crespo, N. N. Akhmediev, V. V. Afanasjev, and S. Wabnitz, Phys. Rev. E, **55**, 4783 (1997).
34. V. V. Afanasjev, Opt. Lett. **20**, 704 (1995).
35. M. Matsumoto, H. Ikeda, T. Uda, and Hasegawa, J. Lightwave Technol. **13**, 658 (1995).
36. N. Akhmediev and A. Ankiewicz, *Solitons: Nonlinear Pulses and Beams,* Chapman and Hall, London (1997).
37. M. F. Ferreira, *Nonlinear Effects in Optical Fibers*, John Wiley & Sons, Hoboken, New Jersey (2011).
38. H. A. Haus, J. G. Fujimoto, and E. P. Ippen, J. Opt. Soc. Am. B **8**, 2068 (1991).

39. L. E. Nelson, D. J. Jones, K. Tamura, H. A. Haus, and E. P. Ippen, Appl. Phys. B **65**, 277 (1997).
40. F. W. Wise, A. Chong, and W. H. Renninger, Laser Phot. Rev. **2**, 58 (2008).
41. W. H. Renninger, A. Chong, and F. W. Wise, Opt. Express **19**, 22496 (2011).
42. A. Komarov, H. Leblond, and F. Sanchez, Phys. Rev. E **72**, 025604(R) (2005).
43. N. Pereira and L. Stenflo, *Phys. Fluids* **20**, 1733 (1977).
44. K. Nozaki and N. Bekki, *Phys. Soc. Japan* **53**, 1581 (1984).
45. R. Conte and M. Musette, *Physica D* **69**, 1 (1993).
46. N. Akhmediev, V. Afanasjev, and J. Soto-Crespo, *Phys. Rev. E* **53**, 1190 (1996).
47. O. Thual and S. Fauvre, *J. Phys*. **49**, 1829 (1988).
48. J. Soto-Crespo, N. Akhmediev, and A. Ankiewicz, *Phys. Rev. Lett*. **85**, 2937, (2000).
49. N. Akhmediev, J. Soto-Crespo, and G. Town, *Phys. Rev. E*. **63**, 056602 (2001).
50. N. Akhmediev, and J. Soto-Crespo, *Phys. Lett A*. **317**, 287 (2003).
51. N. Akhmediev, J. Soto-Crespo, *Phys. Rev. E*., **70**, 036613 (2004).
52. J. Soto-Crespo, and N. Akhmediev, *Phys. Rev. Lett*. **95**, 024101 (2005).
53. J. Soto-Crespo, N. Akhmediev, *Math. Comp. Simulation* **69**, 526 (2005).
54. E. Tsoy, A. Ankiewicz, and N. Akhmediev, *Phys. Rev. E*. **73**, 036621-1-10 (2006).
55. A. Ankiewicz, N. Akhmediev, and N. Devine, *Optical Fib. Technol*. **13**, 91 (2007).
56. M. Manousakis, P. Papagiannis, N. Moshonas, and K. Hizanidis, *Opt. Commun*. **198**, 351 (2001).
57. S. Mancas and S. Choudhury, *Theor. Math. Phys*. **152**,1160 (2007).
58. S. Mancas and S. Choudhury, *Chaos, Solitons & Fractals*, **40**, 9 (2009).
59. M. F. Ferreira, IET Optoelectron., **12**, 122, 2018.
60. A. Hasegawa, Pure Appl. Opt. **4**, 265 (1995).
61. A. Hasegawa and Y. Kodama, *Solitons in Optical Communications*. (Oxford University Press, Oxford, UK, 1995).
62. M. F. Ferreira, M. V. Facão, S. V. Latas, and M. H. Sousa, Fiber Integrated Opt., 24, 287 (2005).
63. M. F. Ferreira, M. V. Facão, and S. V. Latas, Fiber Integrat. Opt. **19**, 31 (2000).
64. I. M. Uzunov, T. N. Arabadzhiev, Z. D. Georgiev, Opt. Fib. Tech., **24**, 15 (2015).
65. D. Grischkowsky and A. C. Balant, *Appl. Phys. Lett*. **41**, 1 (1982).
66. X. Wu, Tang, D. Y., Zhang, H. & Zhao, L. M. *Opt. Express* **17**, 5580 (2009).
67. X. Liu, *Phys. Rev. A* **81**, 053819 (2010).
68. D. Li, L. Li, J. Zhou, L. Zhao, D. Tang, and D. Shen, *Scientific Rep.* **6**, 23631 (2016)
69. K. Krzempek, *Opt. Express*, **23**, 30651 (2015)
70. A. Rivera, C. Laborde, A. Carrascosa, E. Kuzin, G. Beltrán-Perez, A. Díez, and M. Andrés, *Opt. Express*, **24**, 9966 (2016)
71. K. Krzempek, D. Tomaszewska, and K. Abramski, *Opt. Express*, **25**, 24853 (2017

Chapter 6
Vector Dissipative Solitons

Luming Zhao

Abstract Dissipative solitons (DSs) as localized waves outgrow their remarkable theory and applications in passively mode-locked fiber lasers. Composite balance of nonlinearity, dispersion, laser gain and loss jointly spread profound framework for unveiling the pulse dynamics in presence of continuous energy flows between environment and soliton structures. Birefringence of optical fiber reminisces the polarization nature of light. Thereby the physical models of oscillators are intrinsically vectorial, serving as an optimal platform for gaining insight into vector dissipative solitons (VDSs) composing of two orthogonally polarized components. This chapter focuses on the following three subjects: DS trapping in fiber lasers, various forms of VDSs, and their real-time dynamics. The outcomes of soliton trapping in birefringent fibers facilitate the investigation on the polarization evolution of DSs in passively mode-locked fiber lasers. Various forms of VDSs highlight the universality in fiber lasers. By using the dispersive Fourier transform (DFT) technique, real-time polarization evolution and pulsation of VDSs are observed. All these findings highlight the potential application scenarios of increasing the data-carrying capacity beyond traditional binary coding of the scalar counterparts in optics communication systems.

Keywords Ultrafast fiber lasers · Mode-locking · Polarization resolved measurement · Dispersive Fourier transform · Dissipative solitons · Soliton dynamics · Vector solitons · High-order vector solitons · Dark-bright vector solitons · Noise-like pulses · Soliton pulsation

L. Zhao (✉)
Jiangsu Key Laboratory of Advanced Laser Materials and Devices, School of Physics and Electronic Engineering, Jiangsu Normal University, Xuzhou, Jiangsu, China
e-mail: zhaoluming@jsnu.edu.cn

M. F. S. Ferreira (ed.), *Dissipative Optical Solitons*, Springer Series in Optical Sciences 238, https://doi.org/10.1007/978-3-030-97493-0_6

6.1 Introduction

The term 'soliton' was introduced in 1965 [1], referring to the localized solutions in varieties of nonlinear systems such as fluids, plasma physics, Bose-Einstein condensates, and optics. Particularly, optical fibers serve as a classical system for optical conservative solitons. Ultrashort pulses can propagate without distortion due to presence of the balance between fiber nonlinearity and dispersion [2]. The conservative solitons are natural bit units and can carry binary coding optical information, which is set for the application scenarios of optical soliton communications. Beyond the simple balance between nonlinearity and dispersion/diffraction in integrable systems, additional nonlinear gain and loss can be also involved in a composite balance for an extended theory of DSs [3, 4]. Passively mode-locked fiber lasers are extremely attractive for the application prospect of ultrashort pulse emission. As a dissipative system, they have been also serving as an optimal platform for unveiling dynamics of DSs.

When the freedom of vectorial nature of light is released, the framework of vector solitons is founded beyond their scalar counterparts. Governed by the coupled Ginzburg-Landau Equation (GLE), the VDS is essentially a multi-pulse complex at polarization directions [5]. The two orthogonally polarized components can trap each other and propagate as a non-dispersive unit in the laser cavity by oppositely shifting their central frequencies with respect to the net birefringence [6–8]. The VDSs not only possess much more plentiful behaviors and richer dynamics than their scalar counterparts, but also pave a promising way for numerous applications from nano-optics to high-capacity fiber optic communications. Since the first report on vector solitons in 1997 [9], varieties of vector solitons with vivid polarization dynamics such as polarization locked vector solitons [10–12], polarization rotating solitons [12, 13], high-order vector solitons [14] and dark-bright VDSs [15], have been observed in polarization non-discriminated mode-locked fiber lasers. Besides, group-velocity locked vector solitons (GVLVSs) were demonstrated by L. M. Zhao in 2008 [16]. Two sets of Kelly sidebands are interpreted as the distinct spectral feature for this kind of vector solitons. Accompanying with the development of dispersion management and the goal of ultrashort pulses with high energy, scientific interest of mode-locking operation is gradually shifted into normal-dispersion regime, where spectral filtering gets involved in the composite balance [17–20]. DSs formed in normal-dispersion regime are distinctly characterized by steep spectral edges and large frequency chirp, as well as possessing much larger pulse energy and broader spectral bandwidth [21–24]. Therefore, the investigations on VDSs in normal-dispersion regime is twofold motivated by both the novel dynamics from conventional solitons and the improved performance for practical applications.

Indeed, the vectorial nature of DSs is universal with respect to different self-assembled forms of pulses. In particular, the emergence of soliton molecules and vectorial nature of light spreads a new concept of vector soliton molecules that inspires us to reveal more interesting behaviors and underlying dynamics of these compound multi-soliton complexes formed at both time domain and polarization

directions. Apart from the operation regime of regular pulses, passively mode-locked fiber lasers can also deliver the so-called noise-like pulse (NLP), which is essentially a pulse envelope consisting of a bunch of randomly evolving femtosecond ultrashort pulses [25, 26]. It is of great interest to shed new light on the dynamics of NLPs beyond the scalar model.

More recently, time-stretch dispersive Fourier transform (TS-DFT) technique [27] has been developed to trace the buildup of mode-locking in ultrafast lasers [28–30]. Therefrom, single-shot spectral views bring about profound insights into the transient dynamics of ultrafast pulses through mapping the spectral information into the time domain. In particular, exotic dynamics of soliton explosion was studied and an abrupt collapse of soliton structure was recorded by virtue of the shot-to-shot spectra [31, 32]. Dynamically evolving soliton molecules are also experimentally resolved to feature the vivid scenarios of pulse interactions, including the formation of soliton molecules [33, 34] and their internal dynamics [35–39]. The shot-to-shot spectral views can also enable the insights into the transient polarization dynamics of vector solitons. Both polarization locking and polarization rotation of these two orthogonally polarized components have been experimentally verified.

In this chapter, we present the vectorial nature of DSs in passively mode-locked fiber lasers. In Sect. 6.2, DS trapping is introduced, which manifests the polarization evolution from the scalar model to the vectorial one. In Sect. 6.3, various forms of VDSs such as high-order VDSs, dark-bright VDSs, vector soliton molecules and vector noise-like pulses are presented to highlight the universality of vectorial nature in fiber lasers. In Sect. 6.4, dispersive Fourier transform (DFT) technique is utilized to reveal the real-time polarization evolution and pulsation of VDSs. All these findings can facilitate the understanding towards the framework of DS dynamics.

6.2 DS Trapping in Fiber Lasers

Solitons could be nonlinear pulses that propagate without dispersing in the anomalous dispersion regime of single-mode optical fibers. However, single-mode fibers are really bimodal because of the existence of birefringence, which may lead to a substantial splitting of the two orthogonally polarized components. It is found that the effect can be eliminated by the Kerr nonlinearity. It refers to the phenomenon of soliton trapping that two solitons formed along each of the two orthogonal polarization directions of a weakly linear birefringent fiber can trap each other and co-propagate as a non-dispersive unit despite of their intrinsic group velocity difference. Soliton trapping in optical fibers was first theoretically predicted by Curtis Menyuk et al. [6]. To analyze the mechanism, coupled nonlinear Schrodinger equation is introduced. If u and v are the electric fields along the two polarized axes of the fiber, then the equations normalized in soliton units can be expressed as:

$$-\mathrm{i}\left(\frac{\partial u}{\partial z}+\delta\frac{\partial u}{\partial t}\right)=\frac{1}{2}\frac{\partial^2 u}{\partial t^2}+|u|^2u+\frac{2}{3}|v|^2v$$

$$-\mathrm{i}\left(\frac{\partial v}{\partial z}-\delta\frac{\partial v}{\partial t}\right)=\frac{1}{2}\frac{\partial^2 v}{\partial t^2}+|v|^2v+\frac{2}{3}|u|^2u$$

where t is the local time on the pulse and z is the normalized distance along the fiber. The terms on the right-hand side correspond to group-velocity dispersion, self-phase modulation, and cross-phase modulation, respectively. The pulses create an attractive potential well along the orthogonal axis through cross-phase modulation, and this coupling mechanism is independent of the phase between the two pulses. Birefringence is included through the term with δ, where D is the dispersion parameter and δn is the index difference between the two orthogonally polarized components.

When we shift to the optical solitary waves formed in fiber lasers, additional laser gain and loss jointly play roles in the soliton formation, which is dissipative in nature. Except the polarization maintaining fiber being used, the cavity of a fiber laser is weakly birefringent. Therefore, the DS generation and propagation in a fiber laser cavity are always subjected to the influence of the cavity birefringence. For fiber lasers mode-locked by the nonlinear polarization rotation technique, because a polarizer is inserted in the cavity for achieving the artificial saturable absorption effect, it defines the soliton polarization at the position. The situation is changed when using a real saturable absorber such as the semiconductor saturable absorber mirror (SESAM), Graphene and carbon nanotube etc. for achieving mode locking. In particular, the mechanism of VDSs is governed by the coupled GLE as expressed as follow:

$$\frac{\partial u}{\partial z}-i\beta u+\delta\frac{\partial u}{\partial t}+\frac{ik''}{2}\frac{\partial^2 u}{\partial t^2}-\frac{ik'''}{6}\frac{\partial^3 u}{\partial t^3}=i\gamma\left(|u|^2+\frac{2}{3}|v|^2\right)u+\frac{i\gamma}{3}v^2u^*+\frac{g}{2}u+\frac{g}{2\Omega_g^2}\frac{\partial^2 u}{\partial t^2}$$

$$\frac{\partial v}{\partial z}+i\beta v-\delta\frac{\partial v}{\partial t}+\frac{ik''}{2}\frac{\partial^2 v}{\partial t^2}-\frac{ik'''}{6}\frac{\partial^3 v}{\partial t^3}=i\gamma\left(|v|^2+\frac{2}{3}|u|^2\right)v+\frac{i\gamma}{3}u^2v^*+\frac{g}{2}v+\frac{g}{2\Omega_g^2}\frac{\partial^2 v}{\partial t^2}$$

where u and v are the normalized envelopes of the optical pulses along the two orthogonal polarizations. $2\beta = 2\pi\Delta n/\lambda$ is the wave-number difference between the two modes. $2\delta = 2\beta\lambda/2\pi c$ is the inverse group velocity difference. k'' and k''' are the second and third order dispersion coefficients, respectively. γ is the fiber nonlinear coefficient. g and Ω_g represent the gain coefficient and gain bandwidth of the active fiber.

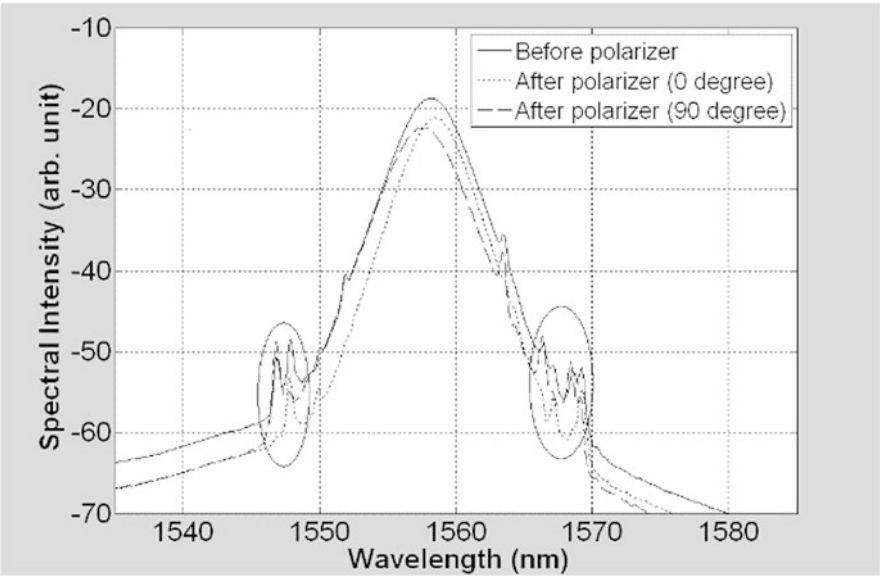

Fig. 6.1 Optical spectrum of the GVLVS with soliton trapping [16]

Group-velocity-locked vector solitons (GVLVS) and the phase locked vector solitons (PLVS) could be formed in a linear cavity fiber laser. In particular, the PLVS could maintain its polarization during propagation in the cavity, while the GVLVS is characterized by its polarization rotation during the propagation. Figure 6.1 shows the optical spectrum of a GVLVS [16]. On its optical spectrum apart from the polarization sidebands, two sets of soliton sidebands were observed. Slightly changing the orientations of the paddles of the polarization controller shifted the separation between the two sets of sidebands as well as the central wavelength of the soliton spectrum. Polarization resolved measurement is used to verify the formation mechanism of the extra set of spectral sidebands. The measurement procedure was as the following: the output of the laser pass through an external linear polarizer, through orienting the polarizer the direction of maximum pulse intensity transmission is first determined, and the optical spectrum is recorded along the polarization direction. Then rotating the polarizer by 90°, the soliton spectrum along the orthogonal polarization direction is recorded. After the polarization resolved measurement of the soliton spectrum, it turned out that the soliton components along each of the two orthogonal directions have much different central frequencies. Solitons along one polarization direction form one set of soliton sidebands. As shown in Fig. 6.1, one set of sidebands disappeared in the polarization resolved spectra, and the separation between the two sets of sidebands is exactly the soliton central frequency shift.

Numerically simulation also elucidates the influence of birefringence on the formation of the GVLVS. Figure 6.2 shows the optical spectrum of the stable pulses when the cavity beat length was selected as (a) $L_b = L/2$, (b) $L_b = L/20$, and

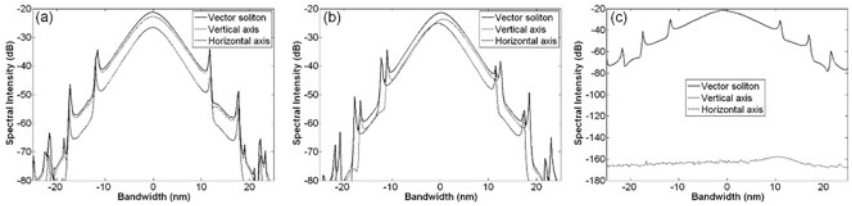

Fig. 6.2 The optical spectrum of the numerically obtained vector soliton with same parameters except that (**a**) $L_b = L/2$; (**b**) $L_b = L/20$; (**c**) $L_b = L/200$ [16]

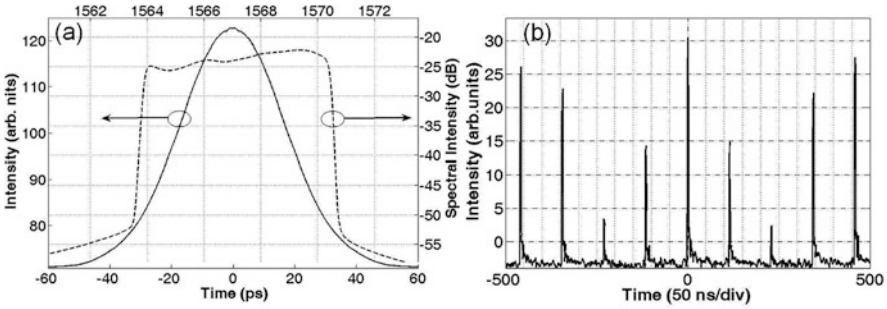

Fig. 6.3 (**a**) Spectrum and corresponding autocorrelation trace of a polarization rotating DVS emission state of the laser; (**b**) Oscilloscope trace of (**a**) after passing through a polarizer [40]

(c) $L_b = L/200$, respectively. When the cavity birefringence is small, for example L b = L/2, the solitons formed along the two orthogonal polarization directions have only slight central wavelength shift. Consequently, no double sets of soliton sidebands could be observed. While as the cavity birefringence becomes large, e.g. $L_b = L/20$, the central wavelength shift between the orthogonally polarized solitons is obvious. The solitons along each of the polarization directions generates its own sidebands, therefore, resulting in double sets of sidebands on the spectrum. When the birefringence of the cavity is too strong, the stable solitons formed are linearly polarized along one polarization direction.

Formation of VDS has also been demonstrated in normal dispersion regime [40]. By managing the net cavity dispersion, the fiber lasers can emit the DSs with rectangle spectral shape and large chirp. Figure 6.3a shows a typical optical spectrum and autocorrelation trace of the DSs at a large net normal dispersion regime. Different from the DSs formed in the fiber lasers mode-locked with the NPR technique, the soliton consists of two orthogonal polarization components. To highlight the vectorial nature of the soliton, a rotatable external cavity polarizer is utilized to compared the features of the pulse train before and after passing through the polarizer, either with a high-speed oscilloscope or a RF spectrum analyzer. It is found that the VDS shown in Fig. 6.3a was a polarization rotating one. Polarization rotation of the soliton could be easily identified by the oscilloscope trace measurement. Without passing through the external polarizer, the soliton pulse had identical

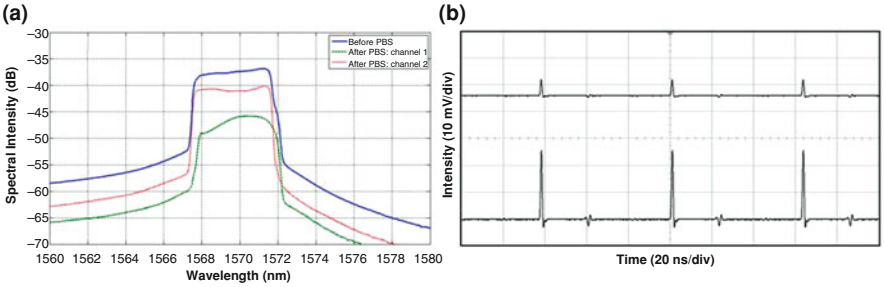

Fig. 6.4 (**a**) Optical spectrum and (**b**) oscilloscope traces of pulse train of the GVLVDS [41]

pulse intensity on the oscilloscope trace for each cavity roundtrip, while after passing through the polarizer it became varying with the cavity roundtrips as shown in Fig. 6.3b. It indicates that the polarization of the soliton rotated along the cavity.

The net cavity birefringence has played a crucial role on the coupling of the two polarization components and the property of the formed stable DSs. When the cavity birefringence is weak, coherent coupling between the polarization components occurs; consequently, either the polarization-rotating or polarization-locked vector DSs could be formed. At moderate cavity birefringence, the formed DSs along each of the cavity principal polarization directions have large central wavelength difference, incoherent coupling between them occurs, and eventually the group-velocity-locked vector DS (GVLVDS) is formed, as presented in Fig. 6.4 [41]. It reminisces the mechanism of DS trapping in net normal dispersion regime. Whereas when the cavity birefringence is too large, no group velocity locking is possible, and DSs along different polarization axes propagate independently.

Indeed, scalar model is just an approximation. Solitons generated in fiber lasers are vector pulses and exhibit periodic parameter change including polarization evolution even when there is a polarizer inside the cavity [42]. Figure 6.5 presents the period doubling eigenstates of polarization components of the soliton solitons generated in a NPR fiber laser. From the numerical simulations results, it is found that each polarization component of the soliton could show independent behavior of period doubling while there exists interaction between the two orthogonal polarization components and the polarization was normalized every time when the soliton periodically passes the polarizer. Depending on the detailed parameters, either synchronous evolution or asynchronous development between the two polarization components of the generated soliton under period doubling appearance can be achieved. Specifically, period doubling of one polarization component while the other polarization component maintaining period-one can as-well be achieved. The discovery above great enriches our understanding on soliton dynamics in fiber lasers and highlights the vectorial eigenstates of DSs formed in ultrafast fiber lasers with or without a polarization discrimination component.

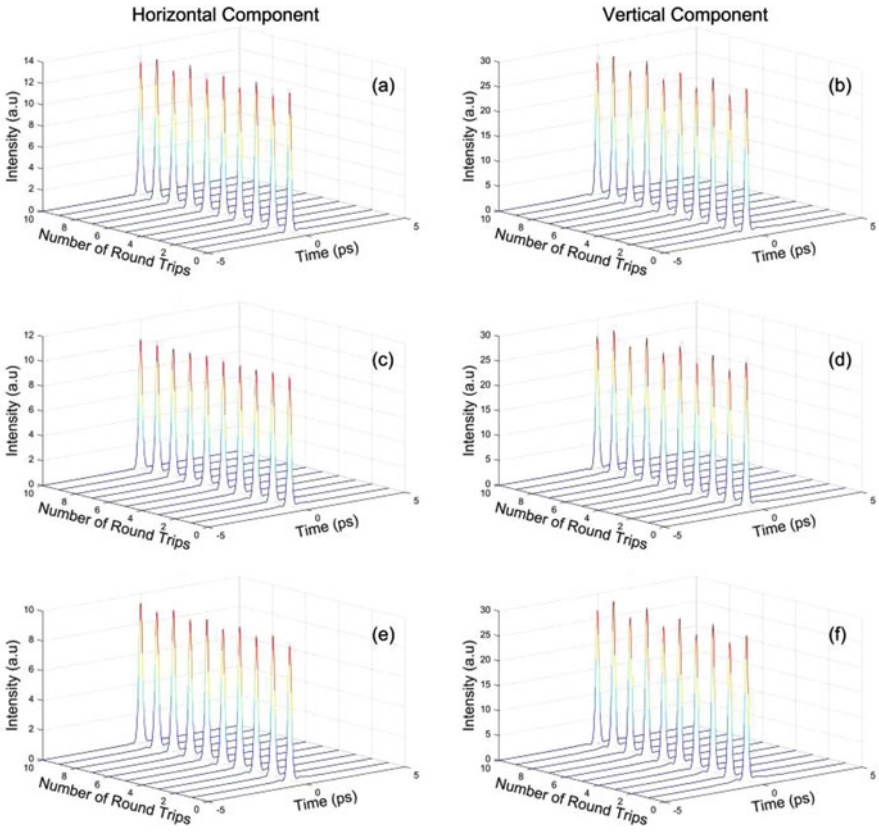

Fig. 6.5 Detailed period doubling eigenstates of period doubling solitons. (**a** and **b**) synchronous; (**c** and **d**) the horizontal component is period one while the vertical component is period doubling; (**e** and **f**) asynchronous [42]

6.3 Various Forms of VDSs

Vectorial nature is universal for DSs formed in fiber lasers without polarization discrimination. In this section, we will introduce four different forms of VDSs or the deformable unities from both the experimental and numerical points of view.

6.3.1 High-Order VDSs

Back in 1988, Christodoulides and Joseph first theoretically predicted a form of phase-locked vector soliton in birefringent dispersive media [43], which is now known as a high-order phase-locked vector soliton in SMFs. The fundamental form of the phase-locked vector solitons was recently experimentally observed

[44]. Numerical studies have shown that the high-order phase-locked vector solitons are unstable in SMFs [45]. However, stable phase-locked high-order VDS in a mode-locked fiber laser were experimentally observed. Multiple high-order VDSs with identical soliton parameters coexisting in a laser cavity and harmonic mode locking of the high-order VDSs were also observed. Moreover, based on a coupled Ginzburg-Landau equation model, phase-locked high-order VDSs are stable in mode-locked fiber lasers.

Through splicing a fiber-pigtailed optical isolator between the output port and the external cavity measurement apparatus, which serves to suppress the influence of back reflections on the operation of the laser, the high-order phase-locked VDSs could be indeed obtained. Figure 6.6 shows, for example, the optical spectra and autocorrelation traces of the DS observed. Polarization locking of the DS is identified by measuring the polarization evolution frequency (PEF) of the DS pulse train [46]. No PEF could be detected. As the VDS has a stationary elliptic polarization, one could use an external polarizer to separate its two orthogonal polarization components. The optical spectra of the components are shown in Fig. 6.6a. The spectra have the same central wavelength and about 10 dB peak intensity difference. Both spectra display Kelly sidebands. In contrast to the polarization resolved spectra of the fundamental phase-locked VDSs, there is a strong spectral dip at the center of the spectrum of the weaker component. No such dip appears in the spectrum of the stronger component. To identify the cause of the spectral dip, the autocorrelation traces of each of the DS components were further measured. It turned out that the weak component of the VDS had a double-humped intensity profile as shown in Fig. 6.6b. The pulse width of the humps is about 719 fs if a sech^2 profile is assumed, and the separation between the humps is about 1.5 ps. The strong component of the VDS is a single-hump soliton. It has a pulse width of about 1088 fs if a sech^2 profile is assumed. The components of the VDS have pulse intensity profiles exactly like those predicted by Akhmediev et al. [48] and Christodoulides [43] for a high-order phase-locked vector soliton. Based on the autocorrelation traces, obviously the spectral dip is formed due to the spectral interference between the two humps, and the strong dip at the center of the spectrum indicates that the two humps have 180° phase difference, which is also in agreement with the theoretical prediction.

To confirm the experimental observations, the coupled Ginzburg-Landau equations were used to describe the pulse propagation in the weakly birefringent fibers in the cavity and numerically simulate the operation of the laser. The standard split-step Fourier technique was employed to solve the equations and a so-called pulse tracing method to model the effects of laser oscillation [47]. the simulations were always started with an arbitrary weak light input. Figure 6.7 shows one of the typical results obtained. With a cavity linear birefringence of $L_b = 3$ L, a stable high-order phase-locked VDS state was obtained. The weak polarization component of the VDS consists of two bound solitons with pulse separation of ~1 ps, while the strong polarization component of the VDS is a single-hump soliton. It is found that the pulse of the strong component is only temporally overlapped with one of the two pulses of the weak component. Because of the strong cross-phase coupling between the temporally overlapped pulses, the two pulses of the weak components have

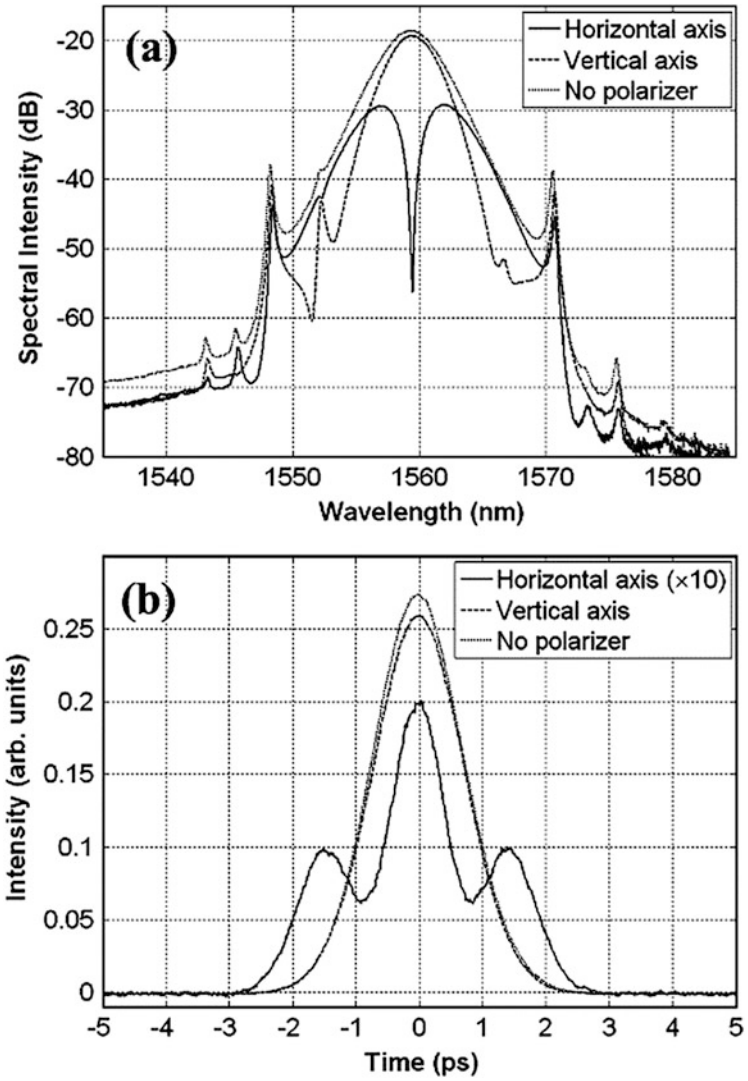

Fig. 6.6 Polarization resolved soliton spectra and autocorrelation traces of the VDS observed. (**a**) Soliton spectra. (**b**) Autocorrelation traces [14]

different pulse widths and intensities. Propagating within the cavity, obvious coherent energy exchange between the two temporally overlapped DSs is visible. Figure 6.7b further gives the calculated spectra of the VDS components, which also show that the phase difference between the two bound solitons of the weak component is 180°.

Depending on the laser parameters selected, other high-order phase-locked VDSs, such as the one with both soliton components having a double-humped structure, can be numerically obtained. Noted that similar high-order vector solitons

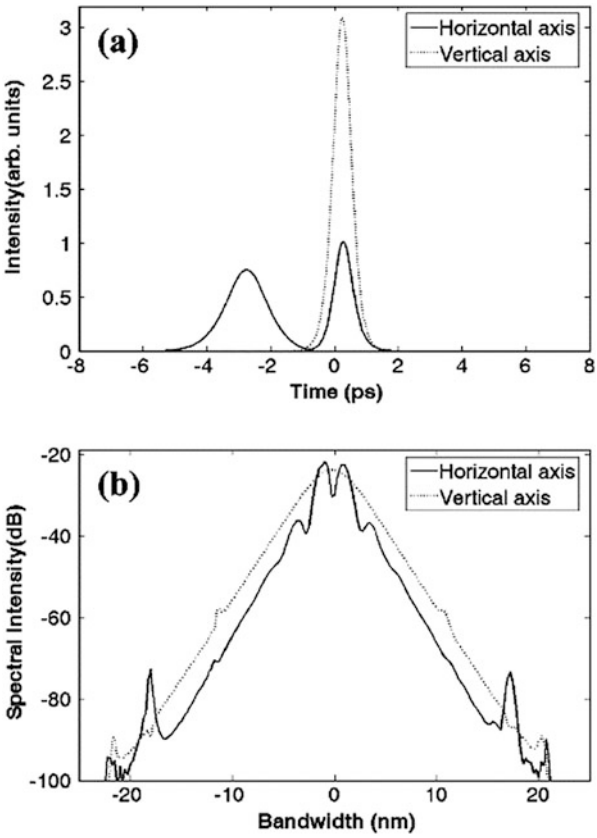

Fig. 6.7 A stable high-order phase-locked VDS state numerically calculated. (**a**) Soliton intensity profiles of the two orthogonally polarized components. (**b**) The corresponding optical spectra of (**a**) [14]

were also predicted for pulse propagation in weakly birefringent fibers, but they are unstable. However, it is found that all the high-order phase-locked VDSs obtained numerically were stable in the laser. The differences in stability of the high-order phase-locked vector solitons between fiber and fiber lasers could be traced back to their different soliton natures. While the soliton formed in a SMF is essentially a Hamiltonian soliton, the one formed in a fiber laser is a DS, which is in fact an attractor of the laser system.

6.3.2 Dark-Bright VDSs

Two types of vector solitons have been predicted from the coupled GLEs [15]. The first type has a close relation to their scalar counterparts, namely bright vector solitons. It is just the aforementioned VDSs. In this subsection, another type of VDSs will be discussed. Different from the VDSs with the characteristic that each of their polarization components can exist as a scalar soliton even when there is no

coupling, the second type of vector solitons has no scalar, one-component counterparts. Examples of these solitons are the polarization-domain wall solitons [48] and the dark-bright vector solitons [49]. Formation of these vector solitons is purely a result of cross-polarization coupling. They therefore constitute a fundamentally new type of optical solitons. Previously, S. Pitois et al. have reported the experimental observation of the polarization domain wall solitons by mixing two intense counter-propagation laser beams in a spun fiber [50]. Polarization-domain wall solitons in a single mode fiber laser was also shown in a previous study [51].

However, the experimental demonstration of this type of vector solitons is challenging. Considering the standard single mode fiber to generate these vector solitons at 1.55 μm, to form a soliton with 1 ps pulse width, the fiber birefringence would need to be as small as $\sim 3 \times 10^{-9}$, and the CW beam power at least ~20 W to support the dark soliton [15]. In practice, it is difficult to find fibers with such small birefringence over long lengths. An innovative approach is introduced to solve this problem. Instead of traversing light over a long fiber length, light can be circulated in an active fiber ring cavity. It can be theoretically shown that under suitable conditions the average dynamics of light circulating in an active fiber ring cavity is equivalent to light propagation along an endless fiber [52]. Moreover, the approach has the advantage that the average dynamics of the light is governed by the averaged cavity dispersion and birefringence. By using cavity dispersion and birefringence management, one can fine-tuning the effective cavity dispersion and birefringence and even make them close to zero. Using this technique, phase locked and polarization rotation bright vector solitons were successfully demonstrated experimentally, whose formations also require coherent cross-polarization coupling of light in weakly birefringent fibers [13, 14].

The fiber ring laser is constructed as shown in Fig. 6.8 for the experiment. Briefly, it comprises 3.0 m erbium-doped fiber with a group velocity dispersion (GVD) coefficient of 63.6 ps^2/km, a 13.4 m long standard single mode fiber (SMF28) with a GVD coefficient of -23.8 ps^2/km, and 12.9 m of dispersion-shifted fiber (DSF) with a GVD coefficient of 5.3 ps^2/km. A fiber pigtailed polarization insensitive isolator was used to force the unidirectional operation of the fiber ring. A polarization controller (PC) was used in the cavity to finely adjust the cavity net birefringence. The output was obtained through a 10% fiber output coupler. A fiber pigtailed polarization beam splitter was used to separate the two polarizations of the laser emission.

The fiber laser cavity had very small net birefringence, as reflected by the fact that the laser emission along the two orthogonal polarization directions of the cavity had a very small wavelength difference of less than 1 nm. Consequently, incoherent cross-polarization coupling always occurred with the laser emission alternating between the two orthogonal polarization modes [52]. Starting from such an initial laser operational state, the pump power was fixed, and the net cavity birefringence was then carefully reduced through appropriately setting the intra cavity PC. Phase locking between the two orthogonal polarization-modes was eventually achieved, which switched the mode coupling to the coherent regime.

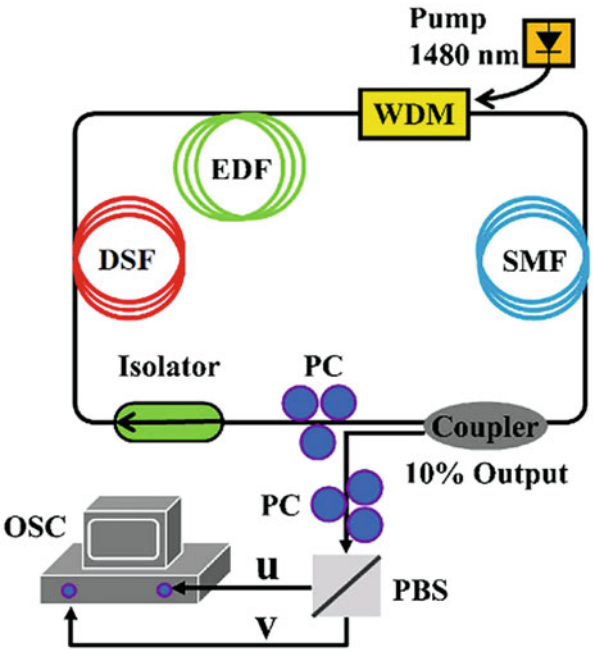

Fig. 6.8 Schematic of the fiber laser setup. *EDF* erbium-doped fiber, *DSF* dispersion shifted fiber, *SMF* single mode fiber, *PC* polarization controller, *PBS* polarization beam splitter, *OSC* oscilloscope [15]

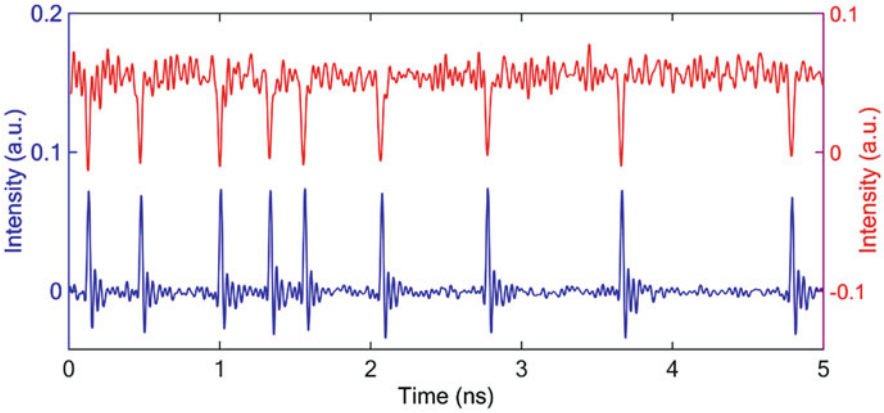

Fig. 6.9 Coupled dark-bright pulse pair emission of the fiber laser measured at an estimated net cavity birefringence of $\Delta n < 10^{-10}$. The intra cavity beam power: ~700 mW [15]

Experimentally, a number of interesting laser operation states were obtained under coherent polarization coupling. Figure 6.9 shows one of such states observed with a cavity that had an averaged dispersion coefficient of ~2.1 ps^2/km and close to zero net birefringence [15]. The two traces shown are the polarization resolved laser emissions. It clearly demonstrates that while along one polarization direction the laser emitted bright soliton pulses, along the orthogonal polarization direction it

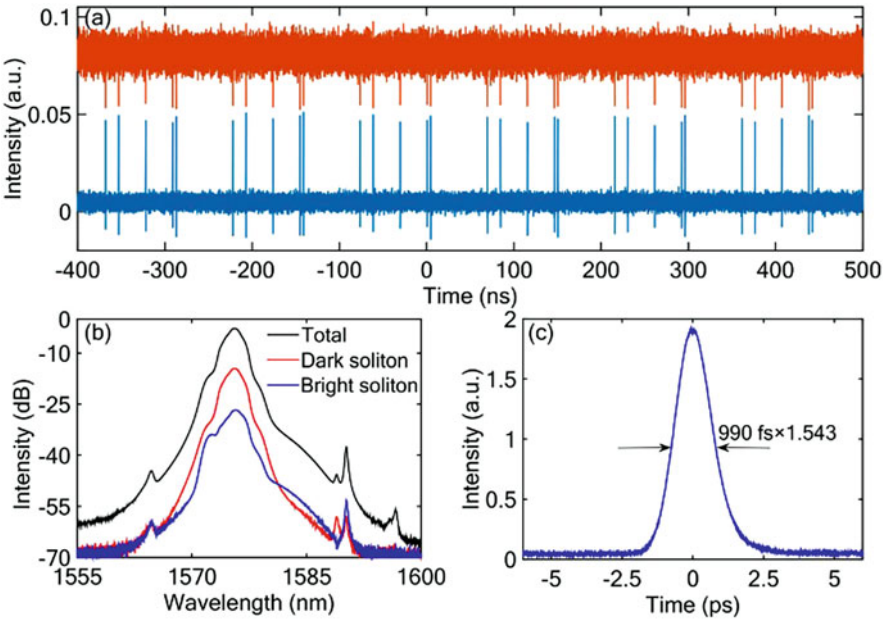

Fig. 6.10 Dark-bright pulse pair emission of the fiber laser measured at a relatively larger net cavity birefringence than the state shown in Fig. 6.7; (**a**) Polarization resolved laser emissions; (**b**) Optical spectra; (**c**) Autocorrelation trace of the bright solitons; The intra cavity beam power: ~700 mW [15]

emitted simultaneously a dark soliton pulse. Many coupled dark-bright pulse pairs were formed in the cavity, and in particular, all the pairs had almost identical pulse parameters.

The features of the dark-bright pulse pairs were experimentally characterized at relatively large net cavity birefringence where the pulse width is insensitive to small net cavity birefringence change. Figure 6.10a shows again the polarization resolved emissions of the laser. Five pairs of the dark-bright pulses coexisted in the cavity, and they repeated with the cavity roundtrip time. Figure 6.10b is the corresponding optical spectra. Both the Kelly sidebands and the coherent energy exchange spectral sidebands are obviously observable in the spectra, which clearly shows that both the bright and dark pulses are solitons. The FWHM of the autocorrelation of the bright pulses was 1.53 ps with the assumption of a sech^2 profile, and its width was estimated to be 990 fs, as shown in Fig. 6.10c. Due to the low repetition rate of the pulses, the width of the dark solitons could not be measured with the autocorrelation method. However, the Kelly sidebands of the dark solitons had the same positions as those of the bright solitons, indicating that they should have the same pulse width.

6.3.3 *Vector Soliton Molecules*

The emergence of soliton molecules and vectorial nature of light spreads a new concept of VDS molecules formed at both time domain and polarization directions in a unique testbed [53–55]. It is found that VDSs as a non-dispersive unit can also attract or repel each other to form the VDS molecules, which provide a possibility for twofold increasing the optical communication capacity.

In the presented study [56], by carefully manipulating the intra-cavity polarization state, the separate particle-like solitons can be bound together to form DS molecules due to internal interaction, which are interpreted as another type of multi-soliton complexes formed in time domain. As shown in Fig. 6.11a, the distinct indicator of GVLVSs, namely two sets of Kelly sidebands, is also observed from the optical spectrum of the formed DS molecules. It implies that these DS molecules stem from the interaction of two GVLVSs, and still have the vector features. The unique feature of the DS molecules is expressed by the strongly modulated spectral fringes. And the 3.5-nm modulation period manifests that the two GVLVSs are closely spaced. Moreover, the DS molecules can be further verified by the double-humped intensity profile, as shown in Fig. 6.11b. The pulse width of the individual

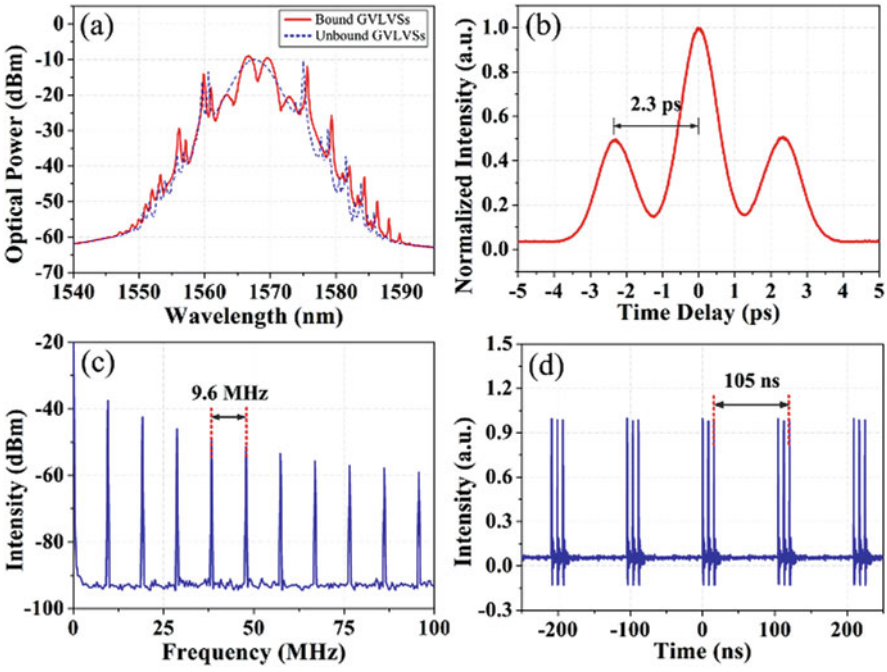

Fig. 6.11 Group-velocity-locked VDS molecules. (**a**) Optical spectra of the GVLVSs and GVLVS molecules (dashed blue line and solid red line, respectively); (**b**) autocorrelation trace and (**c**) RF spectrum of the GVLVS molecules; (**d**) oscilloscope trace of the triple-pulse state [56]

DS is about 0.81 ps if a $sech^2$ pulse shape is assumed; the soliton separation is estimated to be 2.3 ps, exactly matching the modulation period of the spectral fringes. The soliton separation is approximately 2.8 times of the pulse width, and the height ratio of the three peaks of the autocorrelation trace is around 1:2:1. Thus it can be seen that two GVLVSs of identical intensity are tightly bound together to form the GVLVS molecule. Figure 6.11c presents the corresponding RF spectrum. The fundamental repetition rate maintains at 9.6 MHz. Apart from the fundamental mode-locking state of GVLVS molecules, these compound multi-soliton complexes as a unit can also rearrange themselves in a high-pump regime. In particular, triple-pulse state is confirmed by the oscilloscope trace as shown in Fig. 6.11d, where three GVLVS molecules, essentially six GVLVSs coexist in the fiber laser.

Furthermore, polarization-resolved measurement is adopted to get insight of the vectorial nature of these GVLVS molecules. Figure 6.12a shows the polarization-resolved spectra. 'Total' refers to the direct output of the fiber laser; 'Horizontal axis' and 'Vertical axis' refer to the polarization-resolved output after the PBS, respectively. The polarization-resolved spectra are all strongly modulated with the same period of 3.5 nm. Each of the components along the two orthogonally polarized axes respectively corresponds to an individual set of Kelly sidebands, which is in

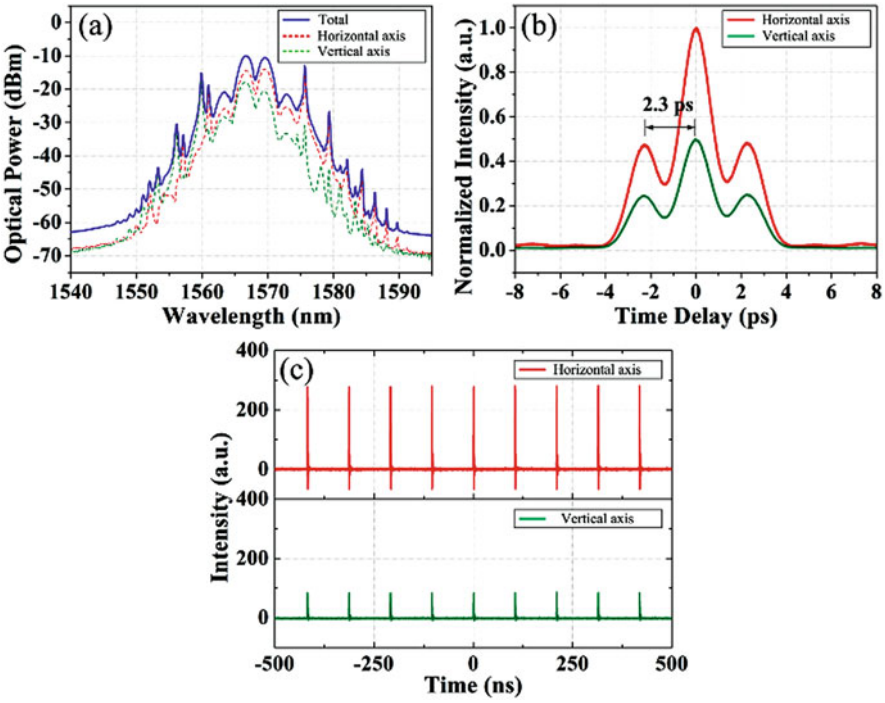

Fig. 6.12 Polarization-resolved measurement of GVLVS molecules. (**a**) Polarization-resolved spectra of the GVLVS molecules; (**b**) autocorrelation traces and (**c**) oscilloscope traces of the two orthogonally polarized components of the GVLVS molecules [58]

accordance with the GVLVSs. The slight residual of the sidebands from the other polarization direction results from the low polarization extinction ratio of the PBS. Figure 6.12b depicts the autocorrelation traces of the polarization-resolved components of the GVLVS molecule. The double-humped intensity profiles suggest that the two orthogonally polarized components could be both considered as DS molecules. They possess almost the same pulse width of 1.08 ps with the assumption of a $sech^2$ pulse shape, and soliton separation of 2.3 ps. Compared to the pulse width of the individual DS presented in Fig. 6.12b, the pulse width of the corresponding polarization-resolved component is broadened from 0.81 ps to 1.08 ps. It is most likely ascribed to the extra dispersion introduced by the pigtails of the PBS. Figure 6.12c presents the polarization-resolved oscilloscope traces of fundamental GVLVS molecules. The pulse intensity of each orthogonally polarized component is identical.

6.3.4 *Vector Noise-Like Pulses*

As one of the special soliton states, the noise-like pulses could be frequently observed in fiber lasers. The noise-like pulse is found to be a localized wave packet that consists of many chaotic pulses with high peak powers [57]. Moreover, the noise-like pulses possess broadband and smooth mode-locked spectrum. Therefore, considering the unique characteristics of noise-like pulse both in time and spectral domains, it would be interesting to investigate the vectorial nature of noise-like pulses in fiber lasers.

Figure 6.13a shows the spectral components of the two orthogonal polarization states [58]. Notably, it can be seen that the two orthogonal polarization components located at different wavelengths (1564.9 nm and 1568 nm) with a separation of 3.1 nm, which is much larger than that of conventional soliton trapping. The corresponding pulse-trains of the two orthogonal polarization states are shown in Fig. 6.13b. Apart from the intensity difference of the two pulse-trains, they are similar to each other. The autocorrelation traces of the polarization resolved components are presented in Fig. 6.13c, indicating that both of them operated in noise-

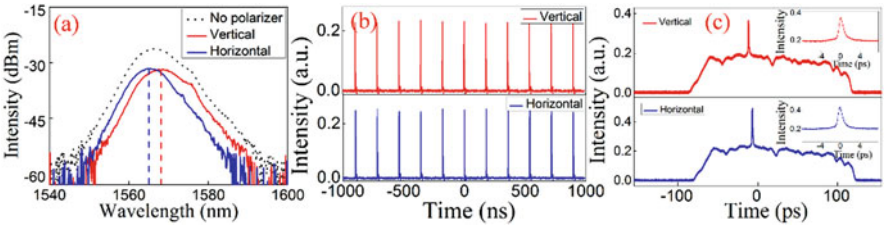

Fig. 6.13 Noise-like pulse trapping. (**a**) Polarization-resolved spectra; (**b**) Corresponding pulse trains; (**c**) Corresponding autocorrelation traces [58]

like mode-locking states. The comparative experiments demonstrated that although the fiber laser was constructed by SMF with moderate cavity birefringence, the two polarization components of the noise-like pulse still could trap each other, which is similar to the case of conventional solitons. It should be also noted that if the cavity birefringence is too large to be compensated, the soliton trapping would not occur [59].

It is well known that the wavelength separation of soliton trapping could be influenced by the cavity birefringence due to the compensation of the birefringence-induced polarization dispersion [59]. To investigate this issue, the PCs were further adjusted to purposely change the cavity birefringence. It was found that the wavelength shift of noise-like pulse is sensitive to the cavity birefringence. Meanwhile, the wavelength shift of noise-like pulse trapping is much larger than that of a conventional soliton trapping. It has been shown that the tiny pulses inside the noise-like pulse packet possess high peak power, which could be used for supercontinuum generation in optical fiber laser [60]. In this case, the nonlinear birefringence induced by the noise-like pulse could be larger than that induced by the conventional solitons. Therefore, in the case of noise-like operation regime in the fiber laser, the frequency shift of the two polarized components needs to be large enough to compensate the fiber birefringence-induced polarization dispersion. Then, they could trap each other as a group velocity locked vector soliton. Because of the high peak power of the noise-like wave packet, it is expected that the wavelength shift would be sensitive to the cavity birefringence, which was also verified by our experimental results. However, note that the individual pulse inside the noise-like wave packet could not be resolved by the autocorrelator. Therefore, the precise peak powers of the noise-like pulses could not be calculated. Moreover, in order to better quantifiably relate the cavity birefringence to the wavelength shift of pulse trapping, the adjustment of cavity birefringence by coiling the fiber sections could be introduced in the laser cavity to control the cavity birefringence. It was demonstrated that the spectral bandwidth of noise-like pulse is related to the average cavity birefringence. Thus, it is expected that larger spectral bandwidth of noise-like pulse as well as the larger wavelength shift could be observed by properly optimizing the cavity birefringence [61].

6.4 Real-Time Dynamics of VDSs

In recent years, the dispersive Fourier transform (DFT) technique opens a promising opportunity for unfolding the transient dynamics of ultrafast lasers. In this section, we will present the real-time polarization dynamics and pulsation of VDSs by using the DFT technique.

6.4.1 Dispersive Fourier Transform Based Polarization Resolved Analysis

DFT technique is an emerging measurement that overcomes the speed limitations of traditional optical instruments and enables fast continuous single-shot measurements in optical sensing, spectroscopy and imaging. Using chromatic dispersion, dispersive Fourier transformation maps the spectrum of an optical pulse to a temporal waveform whose intensity mimics the spectrum, thus allowing a single photodetector to capture the spectrum at a scan rate significantly beyond what is possible with conventional space-domain spectrometers [62].

Polarization-resolved measurement is always adopted to explore the vectorial nature of the VDSs. In particular, to get insight into the two orthogonally polarized components, a polarization beam splitter (PBS) is connected to the output port of the output coupler (OC). The incoming branch of the PBS is made of SMF, while its two outgoing branches are made of PMF. To avoid influence of the fiber birefringence introduced by the fiber segments between the OC and the measurement devices, a fiber-based PC is employed to compensate the extra birefringence. Combining the DFT technique and polarization-resolved measurement, we can get insight into the transient polarization dynamics of the VDSs. The schematic of DFT based polarization resolved measurement is illustrated in Fig. 6.14.

6.4.2 Real-Time Polarization Dynamics of VDSs

In this sub-section, we present the real-time polarization dynamics of the GVLVSs formed in the anomalous-dispersion regime [63]. Figure 6.15a depicts the corresponding linear optical spectrum of the GVLVSs. The 2D contour plots of the shot-to-shot spectra with 860 roundtrips is provided in Fig. 6.15b. It is found that

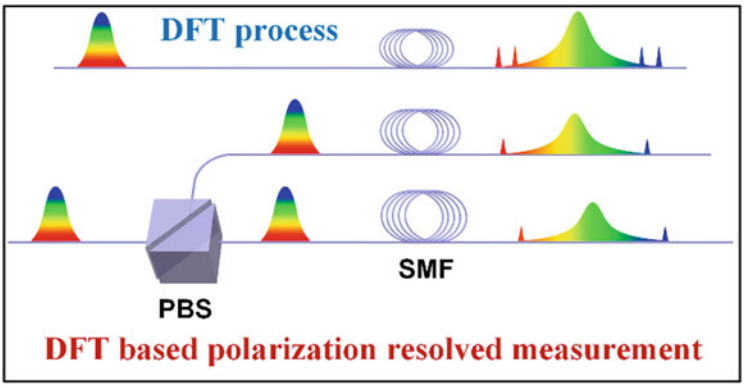

Fig. 6.14 Schematic of the DFT based polarization resolved measurement

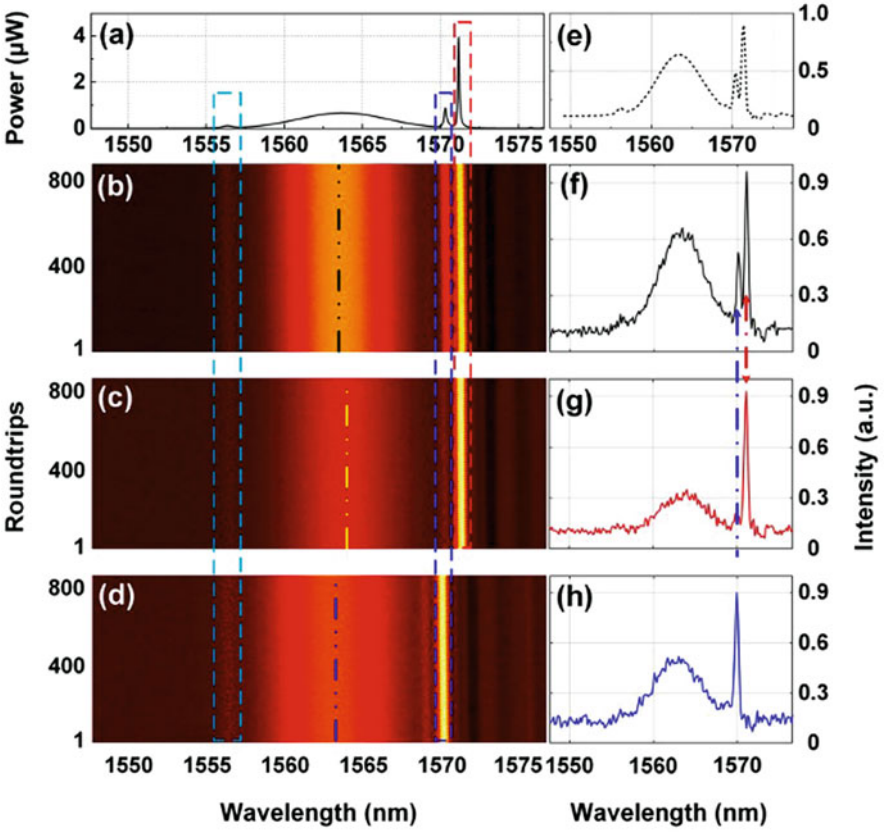

Fig. 6.15 (**a**) Linear optical spectrum measured by OSA before PBS; (**b**) 2D contour plots of the shot-to-shot spectra before PBS and (**c**) horizontal axis and (**d**) vertical axis after PBS; (**e**) averaged spectrum over all roundtrips; (**f–h**) single-shot spectra of the first roundtrip respectively correspond to (**b–d**) [63]

the two sets of Kelly sidebands agree well with the time-averaged linear spectrum. Figure 6.15c, d respectively present the 2D contour plots of the shot-to-shot spectra along the two orthogonally polarized axes. Each component corresponds to one set of the Kelly sidebands of the total spectra. The two bright fringes remaining unchanged indicate that the two orthogonally polarized components are of stationary relations. Moreover, it can be seen that the central wavelength of these two components are different. They oppositely shift their central wavelengths to compensate the polarization dispersion, further stabilizing the conventional soliton trapping state. The averaged spectrum over all roundtrips of the GVLVSs is depicted in Fig. 6.15e, which agrees well with the time-averaged spectrum in Fig. 6.15a. Meanwhile, the single-shot spectra of the GVLVSs and their two polarized components are respectively presented in Fig. 6.15f–h. It is found that the transient spectrum of only one roundtrip also show the same polarization dynamics of the GVLVSs as the time-

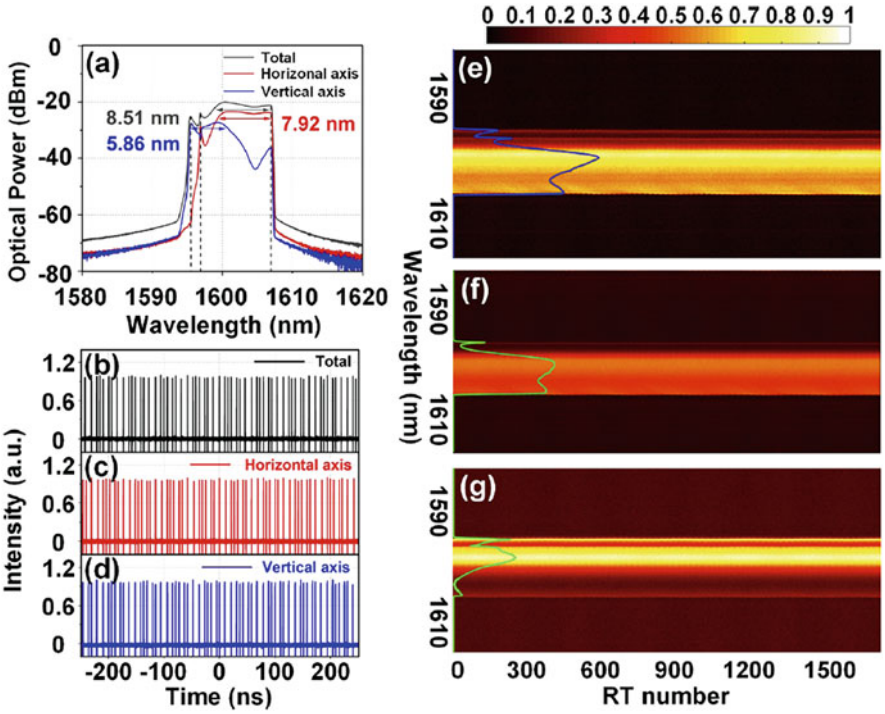

Fig. 6.16 Stationary GVLVDSs: (**a**) Polarization resolved time-averaged optical spectra; (**b**–**d**) total and polarization resolved pulse trains; (**e**–**g**) 2D contour plots of the total and the polarization resolved shot-to-shot spectra, insets show the corresponding single-shot spectra of the first roundtrip [65]

averaged measurement. For the first time, the DFT based polarization resolved measurement was employed to get insight into the vectorial nature of GVLVSs in real time.

Apart from the soliton trapping in the anomalous-dispersion regime, DS trapping [41] has also been demonstrated in the normal-dispersion regime in previous sections. In contrast to the GVLVSs with two sets of Kelly sidebands, gradient edges of the rectangle spectrum are interpreted as the indicator of the group-velocity-locked VDSs (GVLVDSs) [64]. The typical polarization resolved spectra are shown in Fig. 6.16a. In particular, the two orthogonally polarized components possess different central wavelengths and spectral shapes. Their spectra are not entirely overlapped. The 3-dB bandwidths of the vertical and horizontal spectra are 5.86 nm and 7.92 nm, respectively. The total spectrum is the superposition of these two spectra, thus inducing the gradient spectral edges or the aforementioned spectral spikes. Accordingly, the corresponding pulse trains are of uniform pulse intensity as depicted in Figs. 6.16b and 6.3d and the two orthogonally polarized components own the different output power of 1.80 mW and 5.20 mW. To gain insight into the real-time spectral information, DFT based polarization resolved

measurement is also utilized for the GVLVDSs. Figures 6.16e and 6.3g present the 2D contour plots of the shot-to-shot spectra before and after the polarization resolved measurements with 1735 consecutive roundtrips. The corresponding single-shot spectra of the first roundtrip are illustrated as the insets in Fig. 6.16e–g, which are highly in accordance with the polarization resolved time-averaged spectra, as depicted in Fig. 6.16a. It is found that no obvious variations of the spectral profiles are observed for the total and the polarization resolved shot-to-shot spectra; the intensities are uniform along roundtrips. Hence, the two orthogonally polarized components are stably trapped together to form GVLVDSs with polarization locking state. Meanwhile, the formed vectorial complexes are stationary GVLVDSs without pulsating manners in terms of the mainly invariable spectral profile.

6.4.3 Pulsation of VDSs

As a complex nonlinear phenomenon, soliton pulsation is generally verified by the periodic evolution of the spectral profile and pulse energy with respect to nanoseconds even microseconds timescales. The time-stretch dispersive Fourier transform (TS-DFT) technique also provides an optimal method to capture the transient evolution of the pulsating manners. Consecutive recordings of the shot-to-shot spectra enable insight into the periodic spectral breathing. Indeed, the emergence of pulsating manners and vectorial nature will shed a new light on the transient ultrafast dynamics of multi-soliton complexes in polarization directions.

As presented in [65], Fig. 6.17a presents the time-averaged spectra before and after the polarization resolved measurement. The total spectrum and the polarization resolved spectra are all characterized by the similar features to the stationary ones. Obvious central wavelength shift of the two orthogonally polarized components manifests the generation of GVLVDSs. By using the polarization resolved measurement, two orthogonally polarized components are obtained. The corresponding output powers are measured as 1.3 mW and 4.2 mW. Furthermore, the DFT process is introduced to illustrate the real-time pulsating manners. It is noted that, in these multiple-pulse states, all pulses are of similar pulsating manners and one pulse was chosen as a representative to illustrate the soliton dynamics. Accordingly, the 2D contour plots of the shot-to-shot total spectra with 1735 consecutive roundtrips are respectively displayed in Fig. 6.17b–d. It is found that the spectra of the GVLVDSs pulsate periodically evolved along roundtrips. The energy and bandwidth variations versus to roundtrips of the total spectra are extracted in Fig. 6.17e, f. Both the spectral profile and pulse energy oscillate with a period of 280 roundtrips, corresponding to 16.15 μs. The oscillations are almost harmonic with small changing amounts. This pulsating manner is regarded as a quasi-stationary state considering that the pulse can recover its original spectrum after specific roundtrips. Particularly, the recurrent broadening of the spectral profile principally derives from the enhanced self-phase modulation (SPM) induced by the increasing pulse energy. Inversely, the

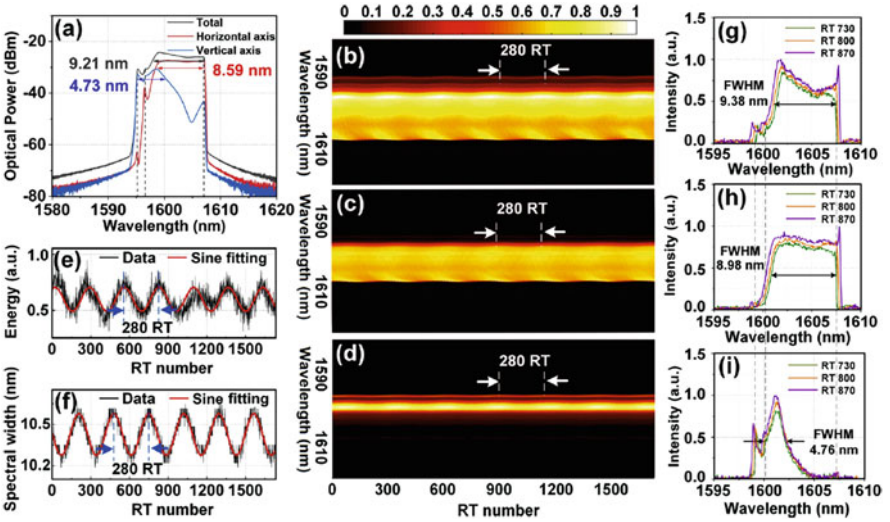

Fig. 6.17 Pulsating GVLVDSs: (**a**) Polarization resolved time-averaged optical spectra; (**b–d**) 2D contour plots of the total and the polarization resolved shot-to-shot spectra; (**e–f**) energy and bandwidth variations versus to roundtrips of the total spectrum; (**g–i**) single-shot spectra of the GVLVDSs and two polarized components at roundtrip 730, 800, and 870 [65]

intra-cavity filtering effect will clamp the spectral profile to the minimal bandwidth. Figure 6.17g–i respectively present the single-shot spectra of the GVLVDSs and two polarized components at roundtrip 730, 800 and 870. The spectral oscillations are restricted in a small range. This slightly pulsation state is just nearby the bifurcation point. By finely adjusting the settings, the pulsating GVLVDSs may approach into the stationary states or other severer pulsating states with large diverging values of the energy and spectral profile. Additionally, the 2D contour plots of the polarization resolved shot-to-shot spectra indicate that the two orthogonally polarized components synchronously inherit the pulsating manners. They are characterized by both oscillating energy and breathing spectral profile with the identical period of 280 roundtrips.

Previous works demonstrated that pulsating manners of DSs can transform the steep spectral edges into gradient ones, which is interpreted as a distinct indicator of the pulsating DSs [64]. However, it seems inconspicuous for the observations depicted in Fig. 6.17. The time-averaged spectrum of the pulsating GVLVDSs still possesses steep edges. It is deemed that this phenomenon should be ascribed to the small oscillating amount of the spectral profiles. The slight spectral differences of the pulsating pulses will not notably reshape the edges in the time-averaged spectra. Furthermore, recurrent oscillation in the shot-to-shot spectra becomes more complicated for the two orthogonally polarized components. In our case, polarization locking state of the GVLVDSs excludes the polarization evolution induced spectral oscillation of these two components. Especially, polarization rotation of the

GVLVDSs can also bring about similar shot-to-shot spectral evolution with respect to the pulsating manners. The observed spectral oscillation may be the superposition of both the pulsating manners and the polarization rotation. Moreover, the synchronization of the pulsating manners is related to the soliton trapping and formation mechanisms. XPM can balance the polarization-mode dispersion.

6.5 Conclusions

In conclusion, we have discussed the VDSs composing of two orthogonally polarized components in ultrafast fiber lasers. DS trapping is numerically predicted and experimentally demonstrated, which highlights the vectorial eigenstates beyond the approximate scalar model. Particularly, various forms of VDSs such as high-order VDSs, dark-bright VDSs, vector soliton molecules and vector noise-like pulses are presented to manifest the universality of the vectorial eigenstates in fiber lasers. By using the DFT based polarization resolved measurement, both real-time polarization evolution and pulsation of VDSs are revealed. All these findings can facilitate the understanding towards the framework of DS dynamics, as well as highlight the potential application scenarios of increasing the data-carrying capacity beyond traditional binary coding of the scalar counterparts in optics communication systems.

References

1. N. J. Zabusky and M. D. Kruskal, Phys. Rev. Lett. **15**, 6 (1965).
2. L. F. Mollenauer, R. H. Stolen, and J. P. Gordon, Phys. Rev. Lett. **45**, 13 (1980).
3. P. Grelu and N. Akhmediev, Nat. Photonics **6**, 2 (2012).
4. N. Akhmediev and A. Ankiewicz, Dissipative solitons: From optics to biology and medicine (Springer, Berlin, Heidelberg, 2008).
5. M. N. Islam, C. D. Poole, and J. P. Gordon, Opt. Lett. **14**, 18 (1989).
6. C. R. Menyuk, Opt. Lett. **12**, 8 (1987).
7. C. R. Menyuk, J. Opt. Soc. Am. B **5**, 2 (1988).
8. N. Akhmediev, A. Buryak, and J. M. Soto-Crespo, Opt. Commun. **112**, 5–6 (1994).
9. S. T. Cundiff, B. C. Collings, and W. H. Knox, Opt. Express **1**, 1 (1997).
10. S. T. Cundiff, B. C. Collings, N. N. Akhmediev, J. M. Soto-Crespo, K. Bergman, and W. H. Knox, Phys. Rev. Lett. **82**, 20 (1999).
11. C. Mou, S. Sergeyev, A. Rozhin, and S. Turistyn, Opt. Lett. **36**, 19 (2011).
12. L. Zhao, D. Tang, H. Zhang, and X. Wu, Opt. Express **16**, 14 (2008).
13. L. Zhao, D. Tang, X. Wu, H. Zhang, and H. Y. Tam, Opt. Lett. **34**, 20 (2009).
14. D. Tang, H. Zhang, L. Zhao, and X. Wu, Phys. Rev. Lett. **101**, 15 (2008).
15. J. Ma, G. Shao, Y. Song, L. Zhao, Y. Xiang, D. Shen, M. Richardson, and D. Tang, Opt Lett. **44**, 9 (2019).
16. L. Zhao, D. Tang, H. Zhang, X. Wu, and N. Xiang, Opt. Express **16**, 13, (2008).
17. L. Zhao, D. Tang, and J. Wu, Opt. Lett. **31**, 12 (2006).
18. L. Zhao, D. Tang, T. Cheng, and C. Lu, Opt. Lett. **31**, 20 (2006).
19. A. Chong, J. Buckley, W. Renninger, and F. Wise, Opt. Express **14**, 21 (2006).

20. F. W. Wise, A. Chong, and W. H. Renninger, Laser Photonics Rev. **2**, 1–2 (2008).
21. V. L. Kalashnikov and A. Chernykh, Phys. Rev. A **75**, 3 (2007).
22. A. Chong, W. H. Renninger, and F. W. Wise, Opt. Lett. **32**, 16 (2007).
23. K. Kieu, W. H. Renninger, A. Chong, and F. W. Wise, Opt. Lett. **34**, 5 (2009).
24. X. Liu, Opt. Express **17**, 25 (2009).
25. M. Horowitz, Y. Barad, and Y. Silberberg, Opt. Lett. **22**, 11, (1997).
26. Y. Jeong, L. A. Vazquez-Zuniga, S. Lee, and Y. Kwon, Opt. Fiber Technol. **20**, 6 (2014).
27. A. Mahjoubfar, D. V. Churkin, S. Barland, N. Broderick, S. K. Turitsyn, and B. Jalali, Nat. Photonics **11**, 6 (2017).
28. G. Herink, B. Jalali, C. Ropers, and D. R. Solli, Nat. Photonics **10**, 5 (2016).
29. X. Liu and Y. Cui, Adv. Photon. **1**, 1 (2019).
30. X. Liu, D. Popa, and N. Akhmediev, Phys. Rev. Lett. **123**, 9 (2019).
31. A. F. J. Runge, N. G. R. Broderick, and M. Erkintalo, Optica **2**, 1 (2015).
32. Y. Yu, Z. Luo, J. Kang, and K. K. Y. Wong, Opt. Lett. **43**, 17 (2018).
33. X. Liu, X. Yao, and Y. Cui, Phys. Rev. Lett. **121**, 2 (2018).
34. J. Peng and H. Zeng, Laser Photon. Rev. **12**, 8 (2018).
35. G. Herink, F. Kurtz, B. Jalali, D. R. Solli, and C. Ropers, Science **356**, 6333 (2017).
36. Z. Wang, K. Nithyanandan, A. Coillet, P. Tchofo-Dinda, and P. Grelu, Nat. Commun. **10**, 1 (2019).
37. Y. Luo, R. Xia, P. P. Shum, W. Ni, Y. Liu, H. Q. Lam, Q. Sun, X. Tang, and L. Zhao, Photon. Res. **8**, 6 (2020).
38. R. Xia, Y. Luo, P. P. Shum, W. Ni, Y. Liu, H. Q. Lam, Q. Sun, X. Tang, and L. Zhao, Opt. Lett. **45**, 6 (2020).
39. Y. Luo, Y. Xiang, T. Liu, B. Liu, R. Xia, Z. Yan, X. Tang, D. Liu, Q. Sun, and P. P. Shum, Opt. Lett. **44**, 17 (2019).
40. H. Zhang, D. Tang, L. Zhao, X. Wu, and H. Y. Tam, Opt. Express **17**, 2 (2009).
41. L. Zhao, D. Tang, X. Wu, and H. Zhang, Opt. Lett. **35**, 11 (2010).
42. X. Yao, L. Li, A. Komarov, M. Klimczak, D. Tang, D. Shen, L. Su, and L. Zhao, Opt. Express **28**, 7 (2020).
43. D. N. Christodoulides and R. I. Joseph, Opt. Lett. **13**, 1 (1988).
44. B. C. Collings, S. T. Cundiff, N. N. Akhmediev, J. M. SotoCrespo, K. Bergman, and W. H. Knox, J. Opt. Soc. Am. B **17**, 3 (2000).
45. K. J. Blow, N. J. Doran, and D. Wood, Opt. Lett. **12**, 3 (1987).
46. N. N. Akhmediev, A. V. Buryak, J. M. Soto-Crespo, and D. R. Andersen, J. Opt. Soc. Am. B **12**, 3 (1995).
47. D. Tang, L. Zhao, B. Zhao, A. Liu, Phys. Rev. A **72**, 4 (2005).
48. M. Haelterman and A. P. Sheppard, Opt. Lett. **19**, 2 (1994).
49. D. N. Christodoulides, Phys. Lett. A **132**, 8–9 (1988).
50. S. Pitois, G. Millot, and S. Wabnitz, Phys. Rev. Lett. **81**, 7 (1998).
51. H. Zhang, D. Tang, L. Zhao, and X. Wu, Phys. Rev. B **80**, 5 (2009).
52. D. Tang, J. Guo, Y. Song, G. Shao, L. Zhao, and D. Shen, J. Opt. Soc. Am. B **31**, 12 (2014).
53. C. Mou, S. V. Sergeyev, A. G. Rozhin, and S. K. Turitsyn, Opt. Express **21**, 22 (2013)
54. V. Tsatourian, S. V. Sergeyev, C. Mou, A. Rozhin, V. Mikhailov, B. Rabin, P. S. Westbrook, and S. K. Turitsyn, Sci. Rep. **3**, 1 (2013).
55. L. Zhao, D. Tang, H. Zhang, and X. Wu, IEEE Photon. J. **7**, 6 (2015).
56. Y. Luo, J. Cheng, B. Liu, Q. Sun, L. Li, S. Fu, D. Tang, L. Zhao, and D. Liu, Sci. Rep. **7**, 2369 (2017).
57. S. Kobtsev, S. Kukarin, S. Smirnov, S. Turitsyn, and A. Latkin, Opt. Express **17**, 23 (2009).
58. A. Luo, Z. Luo, H. Liu, X. Zheng, Q. Ning, N. Zhao, W. Chen, and W. Xu, Opt. Express **23**, 8 (2015).
59. Y. Wang, S. Wang, J. Luo, Y. Ge, L. Li, D. Tang, D. Shen, S. Zhang, F. Wise, and L. Zhao, IEEE Photon. Technol. Lett. **26**, 8 (2014).

60. A. Zaytsev, C. H. Lin, Y. J. You, C. C. Chung, C. L. Wang, and C. L. Pan, Opt. Express **21**, 13 (2013).
61. D. Lei, H. Yang, H. Dong, S. Wen, H. Xu, and J. Zhang, J. Mod. Opt. **56**, 4 (2009).
62. K. Goda and B. Jalali, Nat. Photonics **7**, 2 (2013).
63. R. Xia, Y. Luo, P. P. Shum, Y. Xiang, W. Ni, Y. Liu, H. Q. Lam, D. Tang, and X. Tang, IEEE Photon. J. **12**, 2 (2020).
64. Y. Du, Z. Xu, and X. Shu, Opt. Lett. **43**, 15 (2018).
65. Y. Luo, Y. Xiang, P. P. Shum, Y. Liu, R. Xia, W. Ni, H. Q. Lam, Q. Sun, and X. Tang, Opt. Express **28**, 3 (2020).

Chapter 7
Dynamics of Pulsating Dissipative Solitons

Xiaoqing Wang, Jiangyong He, Baiwei Mao, Zhi Wang, and Yan-ge Liu

Abstract Pulsating soliton is an important local structure of dissipative nonlinear system and a transition state of multi-pulse operation, which is characterized by periodic oscillation of pulse parameters, including the spectrum, temporal profile, pulse energy, etc. Based on the numerical and semi-analytical analysis of the Ginzberg Landau equation, the essence of the pulsation corresponds to the Hopf bifurcation of the system in the parameter space. In recent experiments, various kinds of pulsation dynamics are observed at higher resolution due to the real-time detection technique, including single-period or double-period pulsation soliton, pulsation soliton molecule, synchronous and asynchronous pulsation soliton in multi-soliton pulsation state. Especially, the periodic soliton explosion phenomenon is observed, which is related to the extreme soliton pulsation. As a result, to further researching the multi-soliton dynamic, it's of great significance to regard pulsating solitons as fundamental interaction elements. In this chapter, a summary of pulsating soliton dynamics is provided, mainly introducing the corresponding theories and recent observations about pulsating soliton interaction.

Keywords Dissipative soliton · Pulsation soliton · Cubic-quintic Ginzburg Landau equation · Moment method · Variational method · Mode-locked fiber laser · Dispersive Fourier transform · Synchronous pulsation · Asynchronous pulsation · Soliton molecule

7.1 Introduction

Passively mode-locked fiber lasers have long been the focus of basic scientific explorations and diversified applications. For one thing, they offer a unique opportunity to implement optically a Poincaré mapping in the phase space of a variety of

X. Wang · J. He · B. Mao · Z. Wang · Y.-g. Liu (✉)
Institute of Modern Optics, Tianjin Key Laboratory of Micro-scale Optical Information Science and Technology, Nankai University, Tianjin, China
e-mail: wxqing@mail.nankai.edu.cn; 1120190097@mail.nankai.edu.cn; maobaiwei@mail.nankia.edu.cn; zhiwang@nankai.edu.cn; ygliu@nankai.edu.cn

M. F. S. Ferreira (ed.), *Dissipative Optical Solitons*, Springer Series in Optical Sciences 238, https://doi.org/10.1007/978-3-030-97493-0_7

complex dissipative dynamical systems operating far from the equilibrium [1]. For another, as a simple and economic ultra-short pulse source, mode-locked fiber laser has various applications ranging from spectroscopy and medicine to metrology and telecom. Understanding of such complex optical dynamical systems revealing, for instance, ultrafast dynamics of the dissipative solitons (DSs) and more complex regimes is important for advancing specification and performance of the mode-locked lasers used in a vast number of applications.

As a part of the localized structures in nonlinear systems, pulsating solitons show fascinating periodicity [2], and play an important role in the dynamics of the laser multi-pulse transition (N pulses to N + 1 pulses) [3–6].This metastable state is no less important than the stable soliton in the self-organization of laser energy. Based on the theoretical analyses and numerical simulations, various complicated pulsating behaviors of solitons and their corresponding existence regions in the parameter space have been found [7–10]. Benefit from the advantages of real-time detection technology, diverse pulsation phenomena of dissipative solitons have also been observed experimentally [11–15]. Unlike the constant pulse in stable regime, it is demonstrated that the spectrum, temporal profile, pulse energy and group velocity of the pulsating soliton may evolve periodically along with the cavity round trips. Continuous adjustment of one or more parameters continuously and crossing the borders of different regions may result in the transitions between different pulsation solutions or even the three major classes of solutions (stationary, pulsating, and chaotic solutions).

In this chapter, the pulsating dynamics will be introduced firstly in the view of numerical method based on cubic-quintic Ginzburg Landau equation (CQGLE). It's easy to obtain the evolution of solitons under given parameters. Nevertheless, the solution to this problem usually requires massive numerical simulations with different sets of parameters and initial conditions. For finding simplified models, several analytical methods with proper approximation are proposed, like moment method and variational method, which will be introduced soon. Then, several pulsating soliton results unveiled by virtue of the dispersive Fourier transform (DFT) technique [16] on the experimental platform of an L-band normal-dispersion mode-locked fiber laser will be discussed.

7.2 Theory of Pulsating Dissipative Solitons

In general, the average dynamic process in the laser can be described by the CQGLE [17–19]:

$$i\frac{\partial \mathrm{U}}{\partial \mathrm{z}}+\frac{D}{2}\frac{\partial^2 U}{\partial t^2}+|U|^2U=i\delta U+i\beta\frac{\partial^2 U}{\partial t^2}+i\varepsilon|U|^2U-\nu|U|^4U+i\mu|U|^4U+HOE$$

$$\mathrm{HOE} = \mathrm{i}\beta_3 \frac{\partial^3 U}{\partial\, t^3} - is\frac{\partial}{\partial t}\left(|U|^2 U\right) + \gamma\, U\frac{\partial}{\partial t}\left(|U|^2\right) \tag{7.1}$$

Here, U is the electric field envelope, D is the group velocity dispersion coefficient, where D > 0 represents the abnormal dispersion regime and D < 0 represents the normal dispersion regime; δ is the linear gain/loss coefficient, and β is the spectral filter coefficient, ε is the nonlinear gain or absorption coefficient (the nonlinear gain comes from saturation absorption), μ is generally negative, indicating the saturation of the nonlinear gain; similarly, the negative value of ν corresponds to the saturation of the nonlinear refractive index. HOE is other higher-order linear and nonlinear effects, mainly including higher-order dispersion, self-steep effect and Raman effect. More complex models need to consider the gain dynamics, the most important of which is the gain saturation effect. At this time, the linear gain coefficient δ will be rewritten as [20]:

$$\delta = \frac{g_0}{1 + \frac{\left\langle |U|^2 \right\rangle}{I_s}} - r \tag{7.2}$$

Here, the parameters are linear gain coefficient g_0, linear losses r, saturation intensity I_s, and average intensity $\left\langle |U|^2 \right\rangle = \frac{1}{T}\int_{-\infty}^{+\infty} |U|^2 dt$, where T is the round-trip time.

CQGLE provides a clear physical picture for understanding the influence of laser parameters on pulse dynamics, providing convenience in both numerical analysis and analytical analysis. Based on the analysis of CQGLE, dynamic processes such as soliton molecule [21, 22], soliton rain [23, 24] and soliton pulsation [2, 25] have been explained.

7.2.1 Numerical Analysis of Pulsation Dynamics

Numerical analysis is the main way to understand most of the dynamics in a laser. In fact, the existence of the pulsation solution can be found in the parameter space of different numerical models. The pulsation structure is an energy effect, embodied as the energy of the pulse changing periodically, in sync with the pulsation. Therefore, the properties of pulsation are strongly related to the parameter of the CQGLE equation.

N. Akhmediev and J. M. Soto-Crespo have done a lot of key work on the numerical analysis of pulsating soliton [2, 8, 9, 25, 26]. They accurately divided the parameter regions of the stable soliton and the soliton of different pulsating states, and gave the path of the soliton from the stable state to the chaos through the period-doubling bifurcation of energy under the specific CQGLE parameters. Figures 7.1a–c show the numerical results, consisting of temporal, spectral and energy evolutionary process, of a pulsation in CQGLE under the parameter (D, ν,

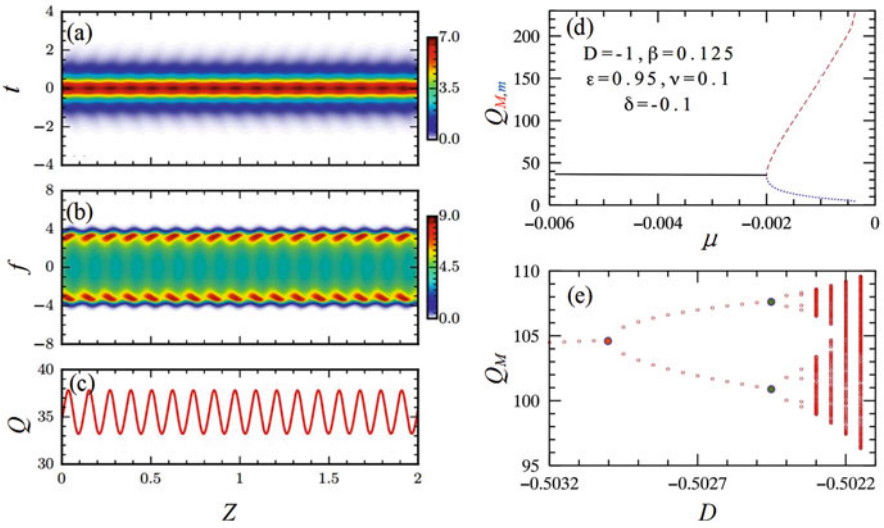

Fig. 7.1 Numerical analysis of pulsation. (**a**) Temporal evolution of pulsation; (**b**) Spectral evolution of pulsation; (**c**) Energy evolution of pulsation. (**d**) Bifurcation diagram vs μ. The minimal Q_m (dotted blue curve) and maximal Q_M (dashed red curve) values of Q quickly diverge with the increase of μ. (**e**) Bifurcation diagram vs D. Only the maxima of the energy Q_M are plotted in this diagram. (Reprinted with permission from Ref. [9] © American Physical Society)

$\varepsilon, \mu, \delta, \beta) = (-1, 0.1, 0.95, -0.002, 0.1, 0.125)$. From Fig. 7.1c, it can be found that the pulse energy Q oscillates in a single period during transmission, for which reason this pulsation structure is called single-period pulsation. Corresponding to this energy oscillation, both the temporal structure and the spectral structure of the pulse exhibit the property like breath, which is attributed to the self-phase modulation and spectral filter effect. The generation of the pulsation structure can be characterized by the energy bifurcation path in Fig. 7.1d. By fixing the other parameters of the equation, with the increase of μ, the pulse energy will take bifurcation near $\mu = -0.002$. Behind the bifurcation point, the pulse energy may be located at either of two possible positions Q_M and Q_m. Thus, the soliton becomes unstable, leading to the generation of a pulsating soliton. Moreover, the interval of these two possible positions are further enlarged along with the value of μ, embodied as a more violent pulsation soliton. Under specific parameter conditions, there can be some extreme cases [9, 27]: pulsation possesses extremely high energy ratios, which is related to the periodic soliton explosion. Besides the change of μ, the generation of pulsating structure can also be triggered by the change of any other parameter in Eq. (7.1) [25, 26, 28, 29]. Figure 7.1e shows the energy bifurcation path produced by changing the dispersion parameter D (Here, the change in the maximum value of energy is used as the investigation of the pulsating structure change). When D = -0.5032, the pulse has a single-period pulsation, which corresponds to a single energy maximum value. When D increases to -0.5030, the energy takes period

doubling bifurcation and two energy maxima are produced, so the pulsation changes to a double-period pulsation. Further, the energy continues to undergo period-doubling bifurcation with the increase of D, resulting in multiperiod pulsations and eventually turning into chaos. This path from period-doubling bifurcation to chaos is the Feigenbaum path [30].

The formation and characteristic of pulsation can be better understood by describing the evolution of pulse parameters. Before introducing that, a concept named attractor is introduced first. Attractor is a structure that any initial point in the phase plane tends to converge as the evolution, divided into fixed point (FP) and limit cycle (LC), etc. A stable soliton corresponds to a stable FP in the phase plane. As a result, for any initial pulse (corresponding to a specific point in the phase plane), it will eventually converge to a FP on the phase plane as the pulse evolves. As comparison, a pulsating structure corresponds to LC in the phase plane [31]. As shown in Fig. 7.2b, there is just a closed loop in the LC structure (the blue solid loop) for a single-period pulsation. When the pulse takes $(\sigma_F, Q) = (0.36, 4)$ as the initial value (point A), where σ_F is the pulse spectral width and Q is the pulse energy. As evolution, the initial point gradually converges to the LC structure. Similarly, with point B as the initial value, the evolutionary trajectory will eventually converge to the LC along a different path. Once falling to the LC, the point will always cycle on that if there is no enough turbulence. The corresponding temporal evolution is depicted in Fig. 7.2a, which is a single-period pulsation of single soliton. Different from a single-period pulsation, a double-period or multiperiod pulsation means that the LC structure contains more closed loops. For example, Fig. 7.2d depict a two-dimensional phase plane composed of pulse spectral width σ_F and pulse energy Q. Further, Fig. 7.2c show the temporal evolution of Fig. 7.2d, which is also a pulsation soliton, but with two periods. It should be pointed out that in some parameter areas, the system has a multi-stable solution [10, 25]. At this time, the attractor structure is local, that is, the final steady state is related to the initial value. In a word, the essence of pulsation is stable LC. In Figs. 7.1d, e, as the system parameters change, the energy bifurcation actually corresponds to the change of the attractor structure caused by the system parameter changes. For a nonlinear system, when the attractor structure changes from a stable FP to a stable LC, it means that the system has experienced Hopf bifurcation, so the transformation from a stationary soliton to a pulsating soliton is the result of Hopf bifurcation.

In fact, in addition to the pulsating behavior of single soliton, the pulsating structure of multi-soliton also has different forms under different system parameters, which are mainly divided into synchronous pulsation and asynchronous pulsation. Figures 7.3a, b show respectively the temporal evolution and energy evolution of two synchronous pulsating solitons, which corresponds to the system parameters $(D, \nu, \varepsilon, \mu, \delta, \beta) = (1, -0.1, 0.7, -0.12, -0.1, 0.01)$. These two solitons breathe synchronously and periodically. Figures 7.3c, d correspond to the temporal and energy evolutions of two asynchronous pulsating solitons, under the system parameters $(D, \nu, \varepsilon, \mu, \delta, \beta) = (1, -0.1, 0.76, -0.12, -0.1, 0.125)$ respectively. Figure 7.3d

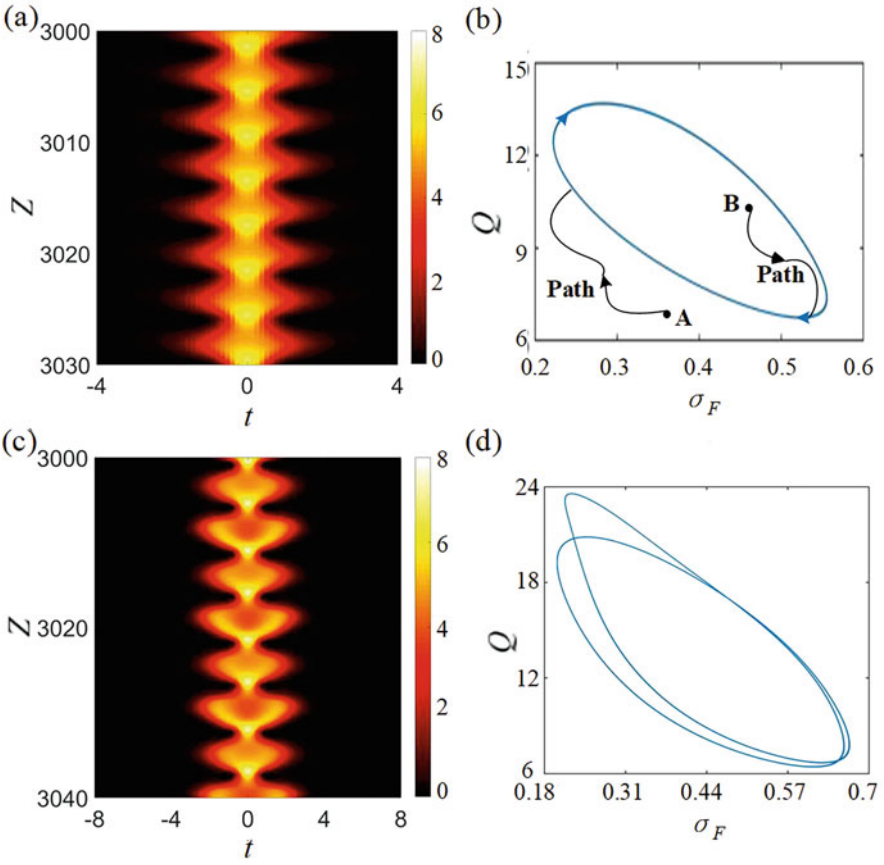

Fig. 7.2 Pulsation evolution and the corresponding phase diagrams. Temporal evolution of stable (**a**) single-period and (**c**) double-period pulsation; (**b**) Evolution trajectory in (σ_F, Q) space. A and B are the different initial point. The blue solid loop is the stable LC of pulsation. (**d**) Evolution trajectory for stable double-period pulsation. (Reprinted with permission from Ref. [10] © The Optical society)

shows that the asynchronous pulsating solitons undergone periodic evolution, but the energy of each soliton does not reach the highest or lowest at the same time. The asynchronous pulsation can also be described by the LC structure. Asynchronous pulsating solitons with the same energy oscillation curve are due to the same LC but different initial value. Various soliton solutions can coexist in certain parameter areas [25]. The LC structure of different soliton solutions caused by parameter changes is different, the coexistence of these different forms of pulsation structures will result more complex forms of asynchronous pulsation.

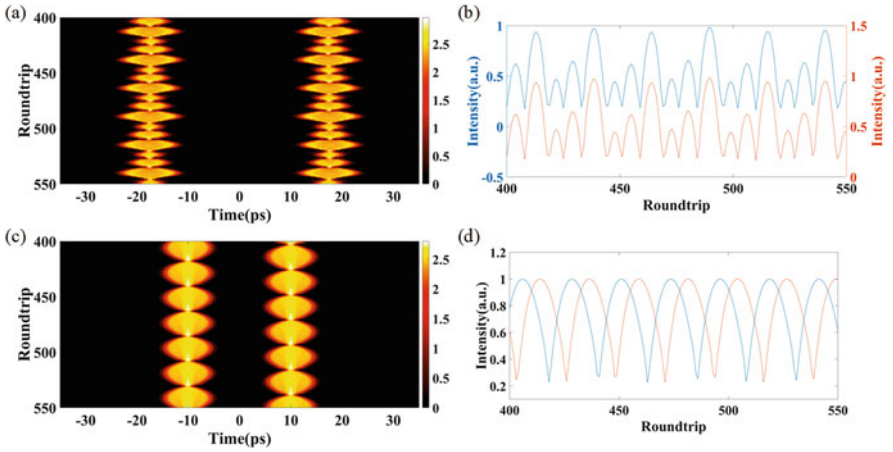

Fig. 7.3 Evolution of multi-soliton pulsation. Temporal evolution of (**a**) synchronous and (**c**) asynchronous pulsating soliton; energy evolution of (**b**) synchronous and (**d**) asynchronous pulsating soliton (the blue curve for the left soliton, the red curve for the right soliton)

7.2.2 *Semi-Analytical Analysis of Pulsation Dynamics*

Unlike the integrable nonlinear Schrodinger equation (NLSE), CQGLE does not exist an accurate soliton solution by inverse scattering method, so when dealing with CQGLE, it is necessary to assume a proper form of solution or additional approximate conditions. The moment method [32–35] and the variation method [36, 37] are two common analytical methods. The main idea of these two methods is to transform the problem of infinite dimensions into finite dimensions by designing the form of pulse solutions in advance. Through these two methods, the stability of the pulse can be analytically related to the system parameters, thus providing a simple model for understanding the pulsation.

The moment method was applied to the field of nonlinear optics as early as 1971. Five moments are generally introduced in the moment method [32]:

$$\begin{aligned} Q &= \int_{-\infty}^{+\infty} |U|^2 dt \\ P &= \frac{1}{2}\int_{-\infty}^{+\infty} (UU_t^* - U^* U_t) dt \\ I_1 &= \int_{-\infty}^{+\infty} t|U|^2 dt \\ I_2 &= \int_{-\infty}^{+\infty} (t - t_0)^2 |U|^2 dt \end{aligned} \tag{7.3}$$

$$I_3 = \int_{-\infty}^{+\infty} (t - t_0)(UU_t^* - U^* U_t)dt$$

Here $t_0 = I_1/Q$ is the position of the centroid of the pulse. The integrals Q and P indicate the energy and momentum of soliton, I_1, I_2 and I_3 are the other three higher-order distribution moments related to the properties of soliton. When high-order effects are not considered, CQGLE can be expressed as:

$$i\frac{\partial U}{\partial z} + \frac{D}{2}\frac{\partial^2 U}{\partial t^2} + |U|^2 U = i\delta U + i\beta\frac{\partial^2 U}{\partial t^2} + i\varepsilon|U|^2 U - \nu|U|^4 U + i\mu|U|^4 U = R[U] \tag{7.4}$$

Here, $R[U]$ is the perturbation of NLSE, which is the left side of Eq. (7.4). Combining Eqs. (7.3) and (7.4), the evolution equation of moments can be obtained:

$$\begin{aligned}
\frac{dQ}{dz} &= i\int_{-\infty}^{+\infty} UR^* - U^* R dt \\
\frac{dP}{dz} &= -i\int_{-\infty}^{+\infty} U_t R^* + U_t{}^* R dt \\
\frac{dI_1}{dz} &= iDP + i\int_{-\infty}^{+\infty} t(UR^* - U^* R)dt \\
\frac{dI_2}{dz} &= -iDI_3 + i\int_{-\infty}^{+\infty} (t - t_0)^2 (UR^* - U^* R)dt \\
\frac{dI_3}{dz} &= 2P\frac{dt_0}{dz} + i\int_{-\infty}^{+\infty} \left(2D|U_t|^2 - |U|^4\right)dt + 2i\int_{-\infty}^{+\infty} (t - t_0)(U_t R^* + U_t{}^* R)dt \\
&\quad + i\int_{-\infty}^{+\infty} UR^* + U^* R dt
\end{aligned} \tag{7.5}$$

The evolution of the pulse parameters is obtained by combining the proposed pulse solution and Eq. (7.5). Generally, there will be different forms of the pulse solution in different dispersion regions, but in order to simplify the problem, the Gaussian solution or the hyperbolic secant solution is used. For matching with Eq. (7.5), the hyperbolic secant pulse should be:

$$U(t, z) = A\text{sech}\left(\frac{t - t_0}{w}\right)\exp\left\{i\left[\phi + b(t - t_0) + c(t - t_0)^2\right]\right\} \tag{7.6}$$

where $A(z)$, $w(z)$, $\phi(z)$ and $t_0(z)$ are the amplitude, width, phase and position of the pulse, respectively, $b(z)$ is the angular frequency of the pulse, and $c(z)$ is the chirp parameter. Substituting Eq. (7.6) into Eq. (7.3) and Eq. (7.5) respectively, the evolution equations about the pulse parameters are obtained [33, 34]:

$$\frac{dQ}{dz} = F_1 = 2Q\left[\delta - \beta b^2 + \frac{\varepsilon}{3}\frac{Q}{w} + \frac{2\mu Q^2 - 5\beta}{15w^2} - \frac{\pi^2}{3}\beta c^2 w^2\right]$$

$$\frac{dw}{dz} = F_2 = -\frac{2\varepsilon}{\pi^2}Q + \frac{8\beta - \mu Q^2}{\pi^2 w} + 2Dcw - \frac{16}{15}\pi^2\beta c^2 w^3$$

$$\frac{dc}{dz} = F_3 = -2Dc^2 - \frac{1}{\pi^2 w^2}\left[4\left(\frac{\pi^2}{3} + 1\right)\beta c + \frac{Q}{w} + \frac{8\nu Q^2 - 30D}{15w^2}\right] \tag{7.7}$$

$$\frac{dt_0}{dz} = F_4 = b\left(D - \frac{2\pi^2}{3}\beta c w^2\right)$$

$$\frac{db}{dz} = F_5 = -\frac{4}{3}\beta\left(\frac{1}{w^2} + \pi^2 c^2 w^2\right)b$$

The parameter space is defined by five parameters, that is Q, w, c, t_0 and b. FPs of the dynamical system can be found from the set of algebraic equations $F_j = 0$ ($j = 1 - 5$). The stability of these FPs is determined by the eigenvalue λ_j of the Jacobian matrix $M_{ij} = \frac{\partial F_i}{\partial p_j}$, where $p_j = (Q, w, c, t_0, b)$. When the real part of arbitrary λ_j is positive, the FP is unstable. Figure 7.4a obtained by Eq. (7.7) shows the characteristic of FPs in (ν, ε) plane, where $(D, \delta, \beta, \mu) = (1, -0.1, 0.08, -0.1)$ are constants. When the value of the gain ε is small, there are no stable or unstable FPs (no stationary solitons) in the system because of the threshold for FP existence. Curve 1 in Fig. 7.4a is the bifurcation boundary (threshold) where the stable FP turns into an unstable one. Below Curve 1, the eigenvalues λ_j meet

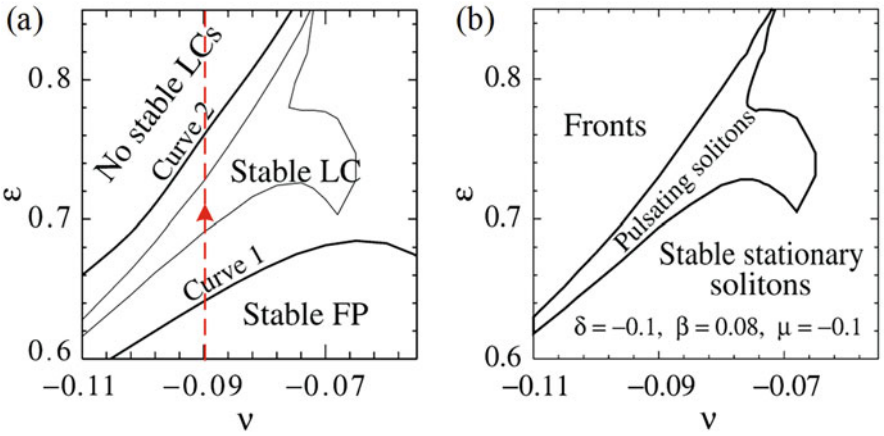

Fig. 7.4 Phase plane derived from different theoretical methods. The region of FP and limit cycles in the parameter space (ν, ε) derived from (**a**) the moment method and (**b**) the numerical method based on CQGLE. (Reprinted with permission from Ref. [33] © Elsevier BV)

$$\mathrm{Re}[\lambda_{1,2,3}] < 0 \tag{7.8}$$

Thus, this area corresponds to a stable FP, indicating a stable soliton. For the region above Curve 1, the eigenvalues λ_j meet:

$$\mathrm{Re}[\lambda_{1,2}] < 0, \mathrm{Re}[\lambda_3] > 0 \tag{7.9}$$

It means that a stable FP is transformed into an unstable FP, and the topology of attractor are transformed from a FP to a LC. Further, there is no stable LC above Curve 2, the soliton energy Q and width w increase monotonically with evolution in this area. When the value of ν is fixed at -0.09 (the Red dotted line), as ε gradually increases, the solitons are stable at first. When ε reaches the value on Curve 1, the Hopf bifurcation occurs, resulting in pulsating soliton. For exhibiting the corresponding relationship, the numerical simulation of CQGLE under the same parameter plane (ν, ε) can obtain the interval of different soliton state as shown in Fig. 7.4b. The pulsating soliton region based on the numerical simulation directly from CQGLE is enclosed by Curve 1 and Curve 2. Figures 7.4a, b are obtained in moment method and numerical method respectively but show a dramatic consistence. It proves the reliability of the dynamic model established by Eq. (7.7).

Fig. 7.5 provides two examples of stable LC in (Q, w, c)-space based on the calculation of Eq. (7.7), which reveals the characteristic of the pulsating structure changes along with the parameters. By comparing the LC structure in Figs. 7.5a, b, it can be found that when keep other parameters unchanged and increases the nonlinear gain ε from 0.66 to 0.72, the oscillation interval of Q also increases, which means the intensity of the pulsation increased.

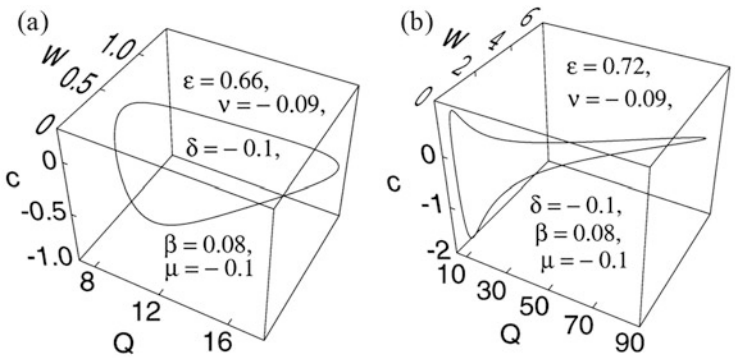

Fig. 7.5 Two examples of stable limit cycle in (Q, w, c)-space. (**a**) Stable limit cycle structure under parameter $\varepsilon = 0.66$ and (**b**) $\varepsilon = 0.72$ when $(\nu, \delta, \beta, \mu) = (-0.09, -0.1, 0.08, -0.1)$. (Reprinted with permission from Ref. [33] © Elsevier BV)

In addition to the moment method, the analysis of pulsation dynamics using the variational method has also been studied [38, 39] In general, both the moment method and the variation method are based on the assumption that dissipative perturbation does not affect the pulse shape function, so the evolution of pulse parameters can be characterized by a set of nonlinear differential equations and directly related to the system parameters (such as linear gain/loss δ or nonlinear gain ε).

In summary, through the evolution dynamic equations of the pulse parameters, the pulsation can be qualitatively defined as: under specific laser parameters, due to the Hopf bifurcation, the unstable FP of the dynamic equation lead to the generation of stable LC. It means the periodic evolution of the pulse, indicating a pulsating structure.

7.3 Transient Behaviors of Pulsating Dissipative Solitons

In recent years, significant advances have been made in the real-time measurement of fleeting transient dynamics [40, 41]. The most widespread is the DFT technique, by which the spectral information is mapped in time domain by using group velocity dispersion [16]. This relatively simple but powerful technique has been extensively used in revealing the sophisticated dynamics in ultrafast lasers, such as soliton rain [24], soliton molecules [42–45], soliton pulsations [11, 14, 46–48], soliton explosions [49–51], etc. In experiment, the changes of pump power and polarization settings correspond to the adjustments of the coefficients in theoretical simulations to some extent. However, not all pulsating dynamics predicted theoretically can be easily observed in experiment for the experimental parameters cannot be flexibly adjusted. In this section, several types of typical pulsating dynamics, which are unveiled by virtue of DFT technique on the experimental platform of an L-band normal-dispersion mode-locked fiber laser, will be discussed.

The schematic diagram of the L-band dissipative soliton fiber laser is shown in Fig. 7.6. It has a ring cavity configuration. As gain medium and dispersion management component, a segment of 9.5 m long normal-dispersion erbium-doped fiber [EDF, Fibercore, I-25(980/125)] is forward pumped by a 976 nm laser diode (LD) through a 980/1550 nm wavelength division multiplexer (WDM). Nonlinear polarization rotation technology with a polarization dependent isolator (PD-ISO) sandwiched by two polarization controllers (PCs) produces an artificial saturable absorber effect for laser mode locking. In addition, the PCs are employed to adjust the polarization states of light for mode-locking optimization and the PD-ISO is employed to ensure unidirectional operation. An output coupler (OC) is utilized to extract 79% of the intracavity pulse energy. The dispersions of device pigtails (single-mode fiber, ~9 m in total) and EDF are -23 and 40 ps^2/km at 1550 nm, respectively. The net cavity dispersion is estimated to be 0.19 ps^2. The total cavity length of ~18.5 m entails the single roundtrip (RT) time of ~89.2 ns. As shown in Fig. 7.6, the laser output is split into three branches for synchronously monitoring of

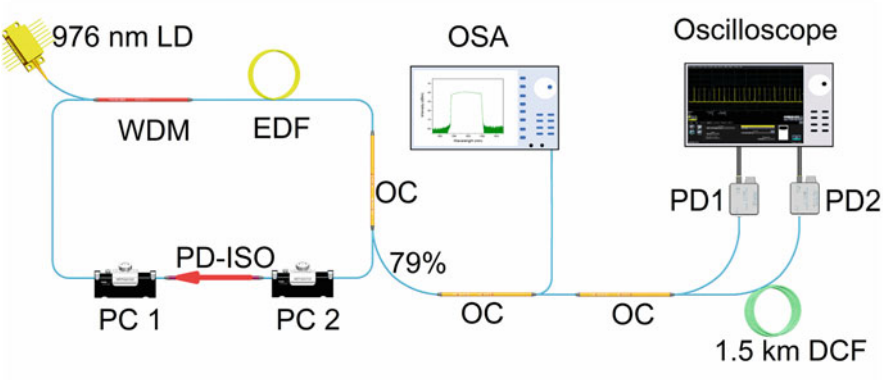

Fig. 7.6 Schematic of the L-band normal-dispersion mode-locked fiber laser and its detection system. (Reprinted with permission from Ref. [52] © The Optical society)

average spectra, temporal and spectral evolutions. An optical spectrum analyzer (OSA, Yokogawa, AQ6370D), a high-speed real-time oscilloscope (33-GHz bandwidth, 100 Gsamples/s, Tektronix, DPO75902SX) and two photodetectors (PD1, 45-GHz bandwidth, DiscoverySemi, DSC10H; PD2, 50-GHz bandwidth, Finisar, XPDV2320R) are employed. The temporal evolution is obtained when the signal is directly captured (undispersed) by a photodetector and sent to a real-time oscilloscope. The real-time spectra of the laser pulse are measured by the DFT technology, where the signal is fed into a 1.5 km long dispersive compensation fiber (DCF, YOFC DM1010-D, −131.34 ps/(nm·km) @ 1545 nm) to stretch the pulses and then detected via a photodetector and a real-time oscilloscope, thus yield the spectral evolution. As a result, the real-time spectral resolution is estimated to be 0.152 nm. The time series recorded by the oscilloscope are segmented according to the single roundtrip (RT) time, and then the transient dynamics of solitons can be depicted by the single RT time and the RT number.

7.3.1 Stationary Soliton

The stationary soliton state could be easily achieved in properly parameter space by adjusting the pump power and the PCs of the L-band laser. For a pump power of 178.8 mW, the steady-state output characteristics are presented by the OSA-measured spectrum (black curve) and the average of 7006 consecutive real-time spectra (red curve) concurrently. As shown in Fig. 7.7a, the mode locked spectra with the central wavelength of 1598.3 nm and a 3 dB bandwidth of 41.0 nm possess extremely steep edges and relatively flat tops, which is the typical output of the L-band normal-dispersion regime laser [53]. The corresponding pulse

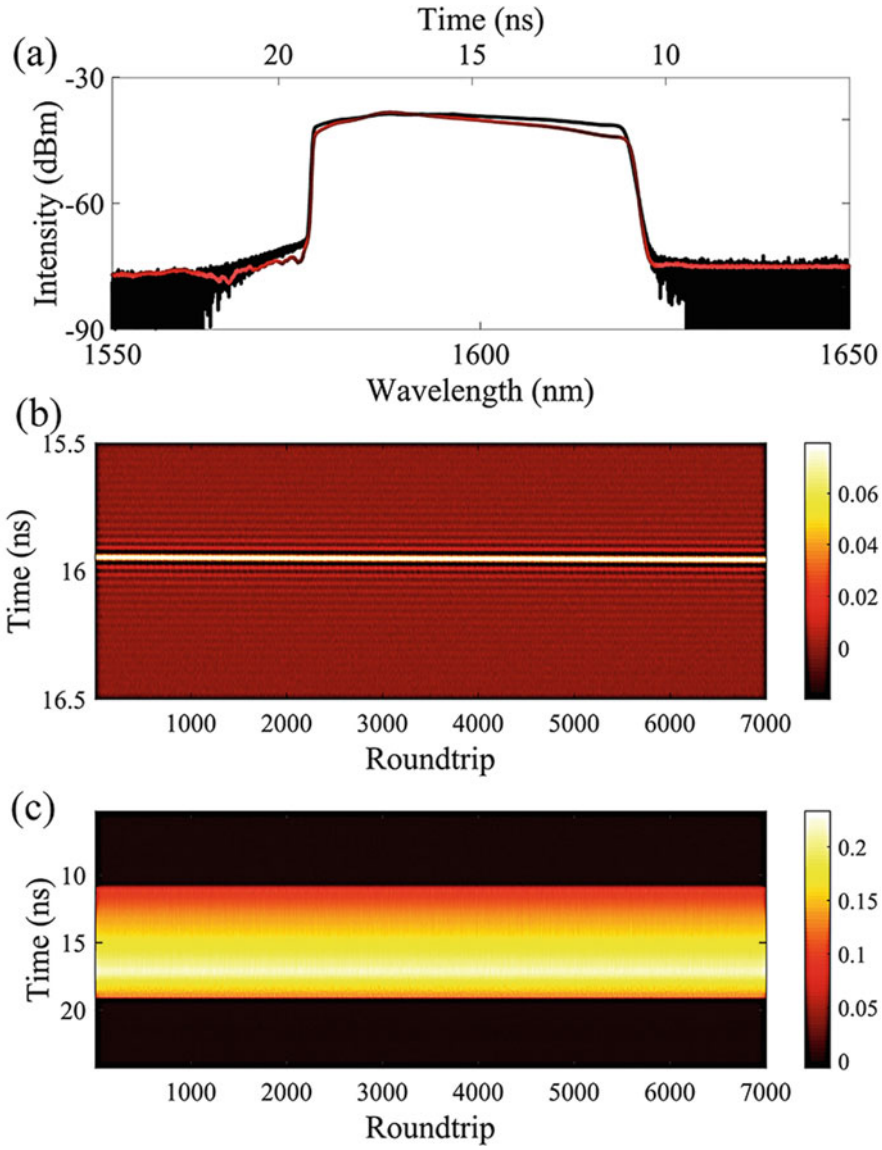

Fig. 7.7 Characteristics of stationary soliton state. (**a**) Optical spectrum directly recorded by the OSA (black curve) and the average of 7006 consecutive single-shot spectra (red curve). (**b**) Spatio-temporal dynamics. (**c**) Spatio-spectral dynamics

train with uniform intensity is illustrated in Fig. 7.7b and the real-time spectra over 7006 consecutive RTs are presented in Fig. 7.7c, indicating that the fiber laser is operating in a stable, time-invariant mode-locking state.

7.3.2 *Single-Period Pulsating Soliton*

In general, the constant pulse energy may bifurcate under certain parameter conditions, and the working state of the laser will change from steady state to pulsating state [8, 9]. Figure 7.8 shows an example of a pulsating soliton found experimentally, which embodies energy bifurcation and periodic behavior. The spectrum directly recorded by the OSA and the one by averaging the DFT data are compared and plotted in Fig. 7.8a. Different from the extremely steep spectral edges for stationary solitons, the spectra of pulsating solitons show arcuate edges. The radio-frequency (RF) spectrum is shown in Fig. 7.8b, the frequency difference between the first-order satellite peak caused by pulsation and the main peak representing the fundamental frequency is 138.8 kHz, which is equivalent to ~808 RTs when converted to time. The spatio-temporal and spatio-spectral dynamics of 7006 consecutive RTs are recorded by the real-time oscilloscope, as shown in Figs. 7.8c, d, respectively. Figure 7.8e provides the pulse energy evolution by summing the intensity of all sampling points of a roundtrip. For the pulse evolution in the time domain, the amplitude fluctuates periodically. In addition, the pulse oscillates back and forth relative to its average position, demonstrating a periodical temporal shift. The spectral evolution exhibits an interesting breathing characteristic: repeated broadening and contraction, which echoes the arcuate edges of the average spectra. Note that the periodic temporal shifts are attributed to the periodic changes in group velocity caused by spectral breath and the drifts of the central wavelength [10]. The growth (decline) of the pulse energy is in sync with the expansion (contraction) of the spectrum. In a word, the pulse varies in adjacent roundtrip but it recovers its exact initial shape periodically after multiple roundtrips, indicating that the fiber laser is operating in pulsating regime. The pulsating period is ~808 RTs, consistent well with the frequency difference in the RF spectrum.

To further illustrate the pulse evolution, Fig. 7.9 shows eight typical spectra within a pulsating period. Due to the incomplete balance among the dispersion, nonlinearity, gain and loss within one roundtrip, spectral breath and amplitude pulsation can be observed. As shown in Figs. 7.9a–e, modulation peaks arise at the edges of the spectra, then increase and enhance during the spectrum widening interval, and finally decay rapidly before the bandwidth reaches the wide extreme point, showing almost the same process as the dissipative soliton buildup dynamics in the normal-dispersion fiber laser. Subsequently, as shown in Figs. 7.9e–h, the spectrum gradually shrinks. Herein, the spectral broadening effect is attributed to the increase of the self-phase modulation effect with the pulse energy increasing, while the spectral contraction can be explained that the high energy pulse is susceptible to dissipative effects such as spectral filtering. It is worth mentioning that, owing to the pulse shaping mechanism in the normal dispersion regime, the spectrum of high energy pulses will gradually evolve to the M-shape when the mode-locked fiber lasers operate at high nonlinearity. C. Lecaplain et al. proposed a generic explanation for the formation of these M-shaped spectra that the large fringes appearing at the edges of the spectrum are caused by discontinuities in the spectral phase [54]. Generally, spectral phase jumps appear as soon as the gain saturation becomes large enough.

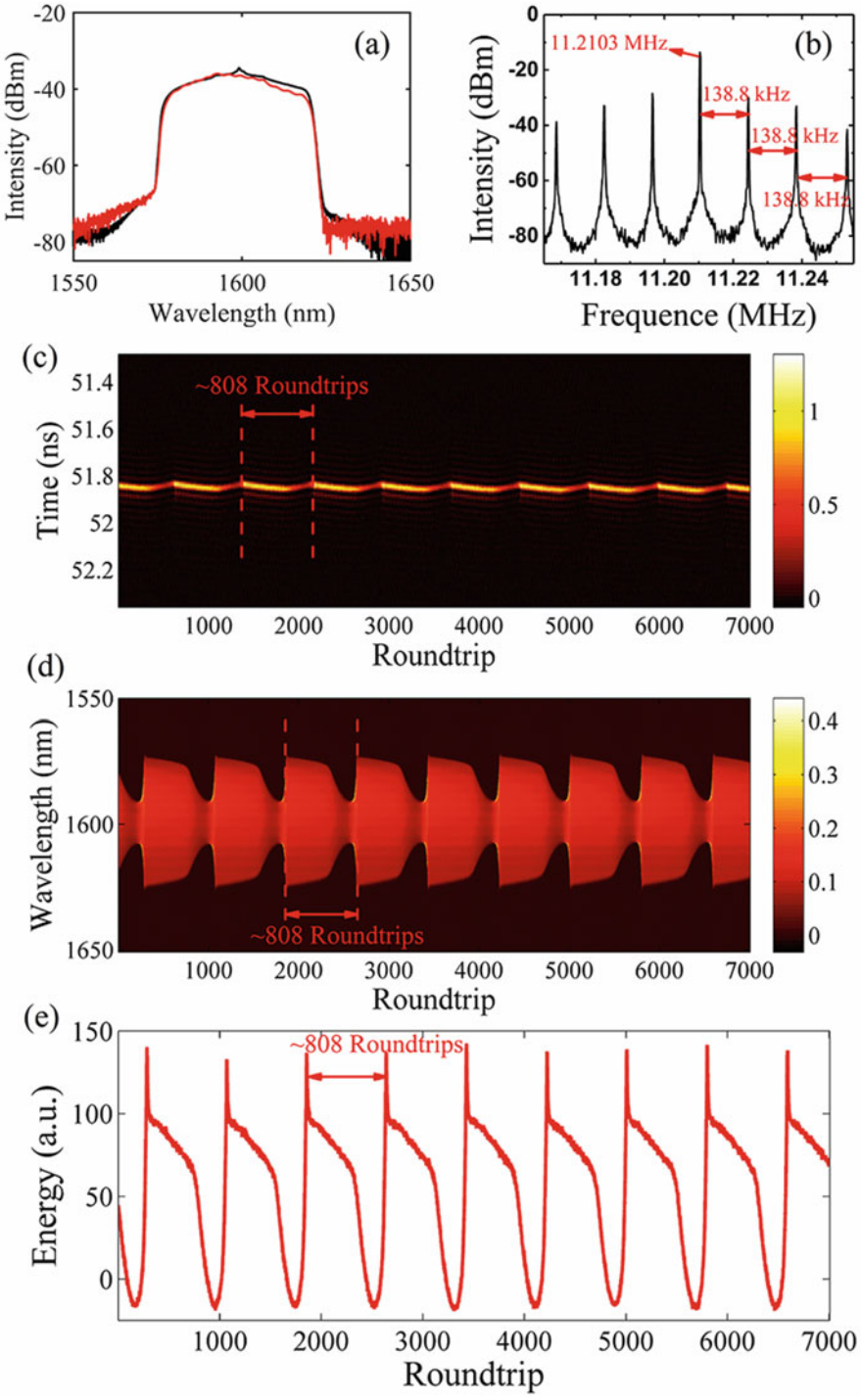

Fig. 7.8 The pulsating soliton with single period (pumping power: 174.9 mW). (**a**) Optical spectrum directly recorded by the OSA (black curve) and the average of 7006 consecutive single-shot spectra (red curve). (**b**) RF spectrum. (**c**) Spatio-temporal dynamics. (**d**) Spatio-spectral dynamics. (**e**) Pulse energy evolution. (Reprinted with permission from Ref. [14] © The Optical society)

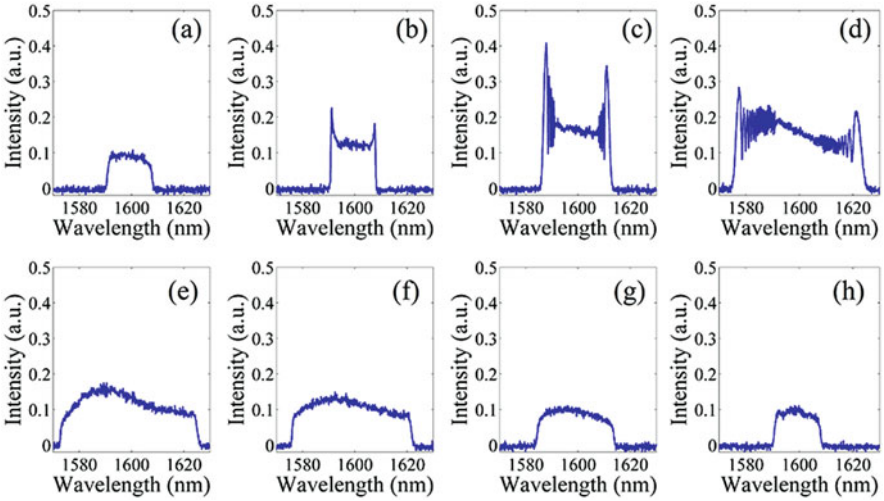

Fig. 7.9 Typical spectra within a pulsating period. (**a**) 190th RT. (**b**) 230th RT. (**c**) 270th RT. (**d**) 285th RT. (**e**) 300th RT. (**f**) 600th RT. (**g**) 800th RT. (**h**) 980th RT. (Reprinted with permission from Ref. [14] © The Optical society)

It has been demonstrated theoretically that pulsating solitons do exist whether the net dispersion in the cavity is normal or anomalous [2, 9]. Furthermore, experimental examples of pulsating solitons in the region of anormal-dispersion have also been presented successively. In 2017, the real-time evolutions of soliton self-organization and pulsation were observed in an anomalous-dispersion mode-locked fiber laser [11]. The authors demonstrated that the periodic radiation dispersion waves are in sync with the pulsation. Soon after, Wei et al. provided an experimental observation of the pulsating soliton with chaotic behavior [46]. Later, a novel type of soliton pulsation in an anormal-dispersion ultrafast laser is unveiled. The pulsating behavior features that the soliton experiences periodic peak power variation but with almost invariable pulse energy [48].

7.3.3 Double-Period Pulsating Soliton

It is found that the appearance of the soliton pulsation is sensitive to the pump power level [14, 48]. Mode-locked lasers generally present an important hysteresis with respect to the pumping power [55], which was applied in the experiment of generating double-periodic pulsations. On the basis of single-periodic pulsation shown in Fig. 7.8, the pump power was attenuated slowly and the PCs was fine-tuned to get further bifurcation of pulse energy. Meanwhile, the spectral evolution was monitored through DFT technology. Finally, a pulsation dynamic phenomenon corresponding to the energy evolution of the pulse form two loops connected in numerical analysis

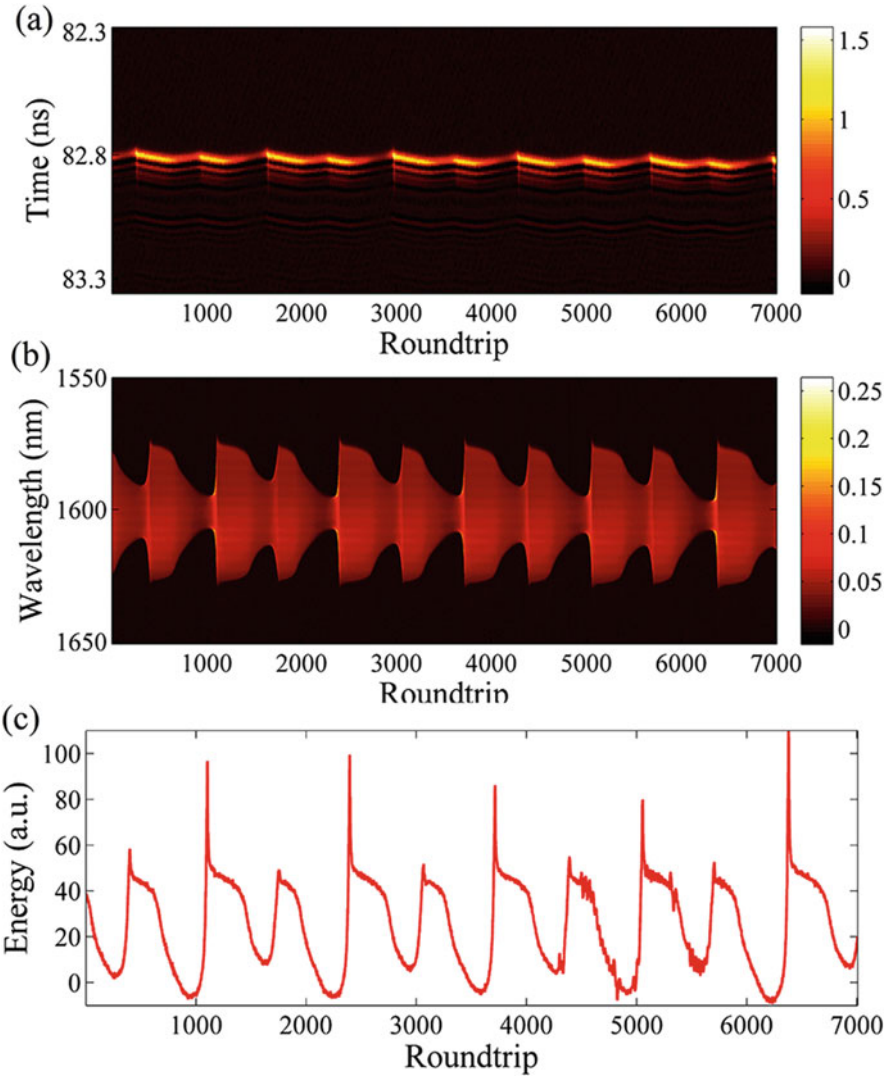

Fig. 7.10 The pulsating soliton with double period. (**a**) Spatio-temporal dynamics. (**b**) Spatio-spectral dynamics. (**c**) Pulse energy evolution. (Reprinted with permission from Ref. [14] © The Optical society)

[8], namely the double-period pulsation soliton, was captured at the pump power of 173.3 mW. The corresponding output performances are shown in Fig. 7.10. Figures 7.10a–c show the temporal evolution, the spectral evolution and the corresponding energy evolution within 7006 RTs, respectively. It can be observed that the double-periodic pulsation has almost all the features of the single-periodic pulsation described above, such as energy oscillation, spectral breath, temporal shift, etc. The difference is that the pulse repeats itself every two oscillation intervals. The

adjacent oscillations with unequal period exhibit different extrema of both energy and spectral bandwidth, and the larger energy (spectral) modulation corresponds to the longer oscillation period.

Essentially, the double-period pulsation is caused by the doubled bifurcation of energy based on the single-period pulsation, that is, the period doubling phenomenon. Numerical results demonstrated that the form of the bifurcation diagram depends on the path in the parameter space for the simulations and any imaginable combination of periods in the dynamics can be realized with a proper choice of the system parameters. Furthermore, higher-order bifurcations may generate infinite periods and the fiber laser steps to chaotic operation regime, which is exactly Feigenbaum type route to chaos [8, 56]. Surely, the above example with two periods in pulsations is only the first step in this direction, which cannot represent the whole complexity of possible bifurcation dynamics. As a matter of fact, other forms of bifurcation phenomena or periodic combinations have also been reported. In 2004, the first experimental observation of the laser output pulses combining period doubling and long period ($\approx$33) pulsations was demonstrated based on temporal pulse sequence measured by oscilloscope [8]. In 2020, similar phenomena were observed in real-time, where the DFT data demonstrated that the spectra of odd RTs and even RTs have their own periodicity [48, 57].

7.3.4 Periodic Soliton Explosion

Another class of pulsating solitons which suffers erupting instabilities can be called as periodic "exploding" or "erupting" solitons [2]. Due to the energy oscillation, the intracavity nonlinear effect oscillates near the boundary between the stationary and chaotic regimes, resulting in "exploding' at a periodic manner. In other words, the periodic soliton explosion is a transition state between the pure pulsation and the chaos. Figure 7.11 summarizes the performances of the periodic soliton explosion at the pump power of 168.2 mW. Figure 7.11a demonstrates the spatio-temporal dynamics within 6800 roundtrips. The corresponding spectral evolution and energy evolution are reflected in Figs. 7.11b, c, respectively. "Exploding" soliton evolution starts from a relatively stationary localized solution that has a perfect spectral profile [25]. After a while, the spectrum experiences a sharp shrink followed by a dramatic expansion, and very soon, cracks into pieces like an explosion. These completely chaotic, but well-localized spectral structures restore the original relatively stable mode-locked profile after about 160 RTs, presenting analogies with the "cooling process" in real explosions. For temporal evolution, there are shifts and fractures. The former is attributed to the group velocity disturbances caused by the changes of spectral range. The latter is due to the extremely low pulse energy and the insufficient detection dynamic range. Because of the limited memory of the oscilloscope, less than three explosions could be recorded at a time without sacrificing resolution. Actually, the periodic explosion may last quite a while, although the duration and interval of "eruptions" fluctuate slightly.

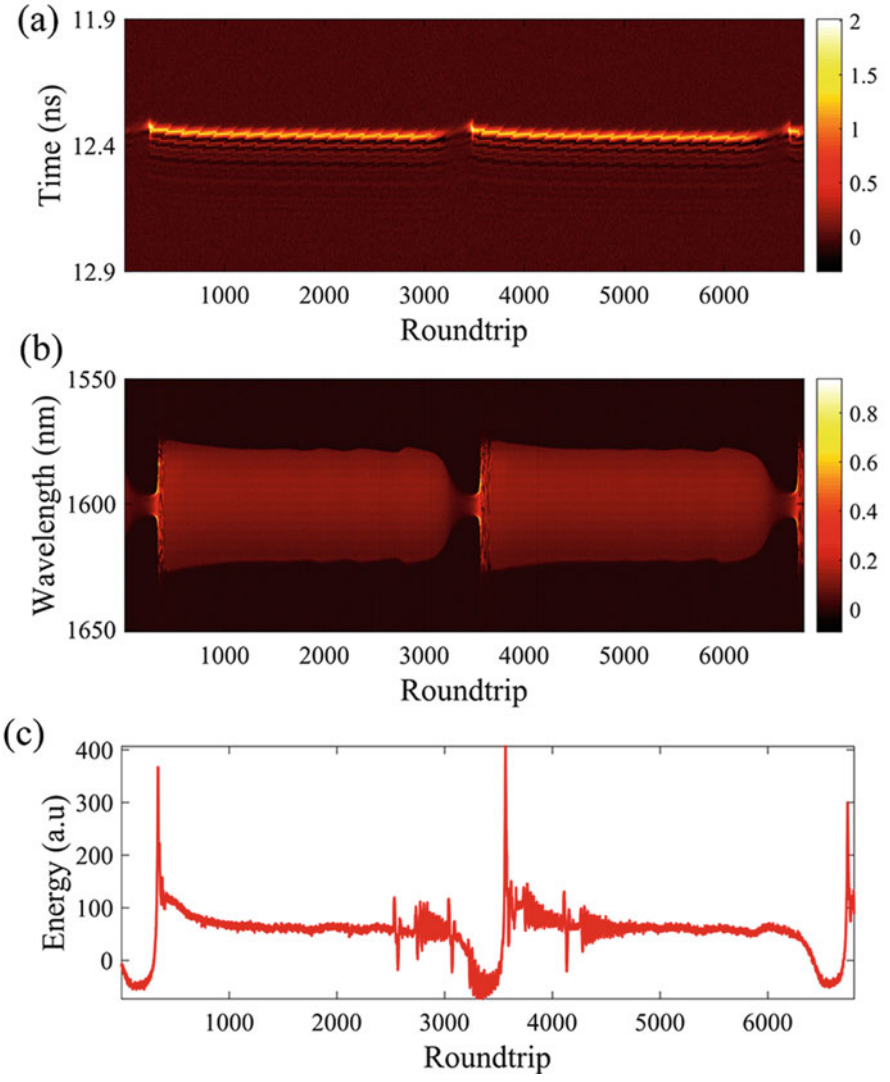

Fig. 7.11 The periodic soliton explosion. (**a**) Spatio-temporal dynamics. (**b**) Spatio-spectral dynamics. (**c**) Pulse energy evolution. (Reprinted with permission from Ref. [14] © The Optical society)

To illustrate the explosion behavior of the pulses in more detail, the typical spectra over an explosion period are presented in Fig. 7.12. As can been seen, the exploding evolution is approximate to the pure pulsating process. However, the amplitude of the pulse energy oscillation is much larger than that of pure pulsation. Correspondingly, the spectral modulation peaks caused by spectral phase disturbance are stronger. In the later stage of energy growth, as shown in Fig. 7.12e, the

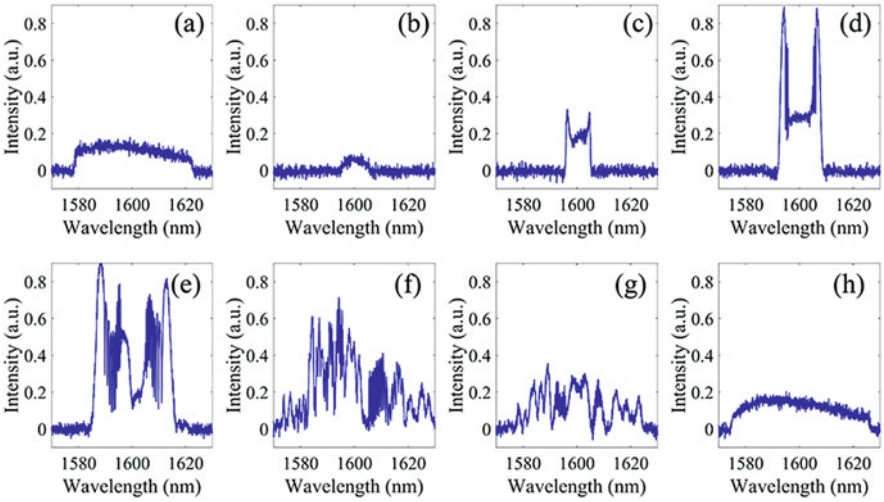

Fig. 7.12 Typical spectra over an explosion period. (**a**) 3000th RT. (**b**) 3400th RT. (**c**) 3520th RT. (**d**) 3550th RT. (**e**) 3560th RT. (**f**) 3570th RT. (**g**) 3600th RT. (**h**) 3700th RT. (Reprinted with permission from Ref. [14] © The Optical society)

overdriven nonlinear effect leads to an abrupt spectral collapse. Eventually, the spectral fragments of the burst gradually return to a smooth profile with the dissipation of energy, approaching its pre-explosion state. Even though the exploding behavior seems to be similar to chaos, it shows periodic characteristic, which falls in the criterion of the soliton pulsation. In this sense, this periodic soliton explosion can be called as soliton pulsations. In 2018, similar spectral periodicity of soliton explosions was unveiled in a broadband mode-locked Yb fiber laser by using time-stretch spectroscopy [58]. However, not all periodic soliton explosions are associated with pulsation. In 2020, M. Liu et al. report the periodic soliton explosions induced by intracavity soliton collisions in a dual-wavelength mode-locked Yb-doped fiber laser [51].

7.3.5 Multi-Soliton Synchronous Pulsation

Among diverse dynamics, multi-pulse operation has long been a hotspot on both theory and experiment [59–61]. With the increase of the laser pumping power, multiple pulses can be generated routinely due to the accumulation of excessive nonlinear phase during a cavity round trip [62]. Furthermore, the intertwined physical effects promote a variety of unusual self-organized structures, from stable pulse patterns to pulsating or chaotic distributions [11, 24]. An important characteristic of the stable multi-soliton patterns is that the solitons all have exactly same pulse properties when they are far apart, namely, soliton energy quantization effect

[63]. However, in nonstationary regime, the enhancement or attenuation of any signal will affect all other signals, multi-soliton follows various fascinating internal dynamics, such as soliton rain [24], mutually ignited soliton explosions [49]. dual--color-soliton collision [64], etc. This section reveals the simplest case of the multi-soliton pulsating dynamics: the multiple solitons execute periodic evolution synchronously and constitute merely a periodic solution.

Figures 7.13a, b show the spectral evolution and the corresponding energy evolution of triple-soliton pulsation at the pumping power of 261.8 mW, respectively. There are three dissipative solitons arranged from 1 to 3 according to their temporal positions in the cavity, whose spectra evolve like breathing, indicating that the laser operates in pulsating state. An enlarged energy evolution is plotted in Fig. 7.8c, the insets show two representative real-time spectra at the 763th and 800th RTs. Obviously, the evolutions of the three solitons in the process of energy

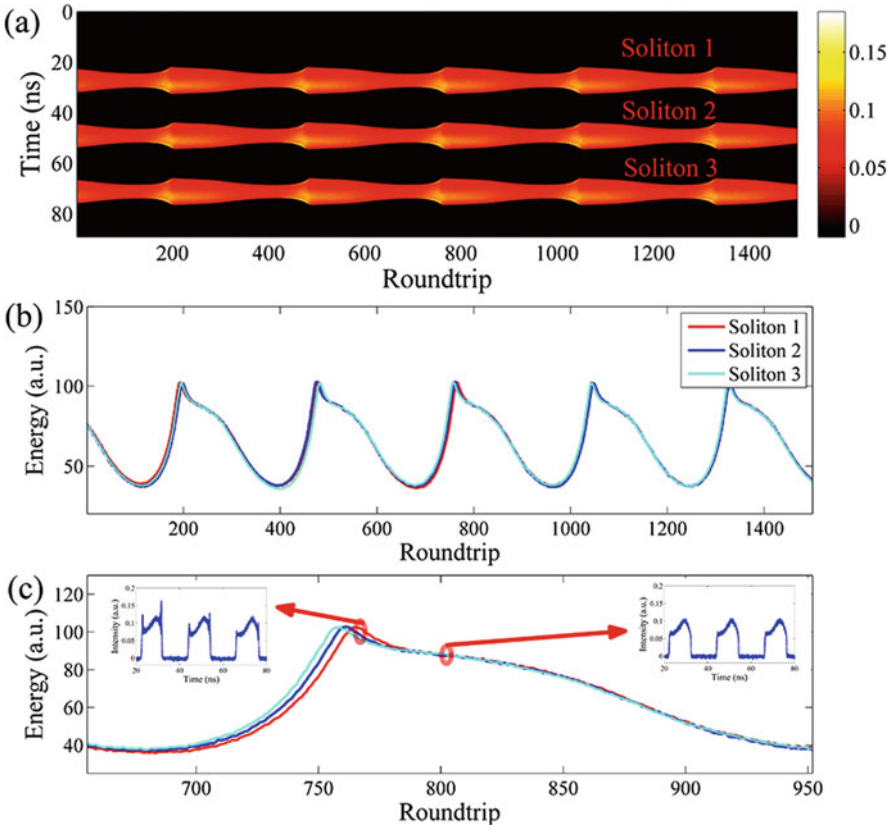

Fig. 7.13 The pulsating soliton in the triple-soliton regime. (**a**) Spatio-spectral dynamics. (**b**) Pulse energy evolutions. (**c**) Pulse energy evolutions with higher resolution. The insets are spectra at 763th and 800th roundtrips, respectively. (Reprinted with permission from Ref. [14] © The Optical society)

rise are out of sync while the paces of energy decline are almost the same. At higher power levels, solitons pulsation with more pulses can be observed.

In addition, the period-doubling phenomena for multi-soliton are also observed at higher power levels taking advantage of the pumping power hysteresis. One of these cases is shown in Fig. 7.14, the mode-locked fiber laser operates in double-soliton double-periodic pulsation regime when the pump power is 210.7 mW. As can be seen, it has all the characteristics of the single soliton double-periodic pulsation, including spectral breath, time domain shift and energy bifurcation.

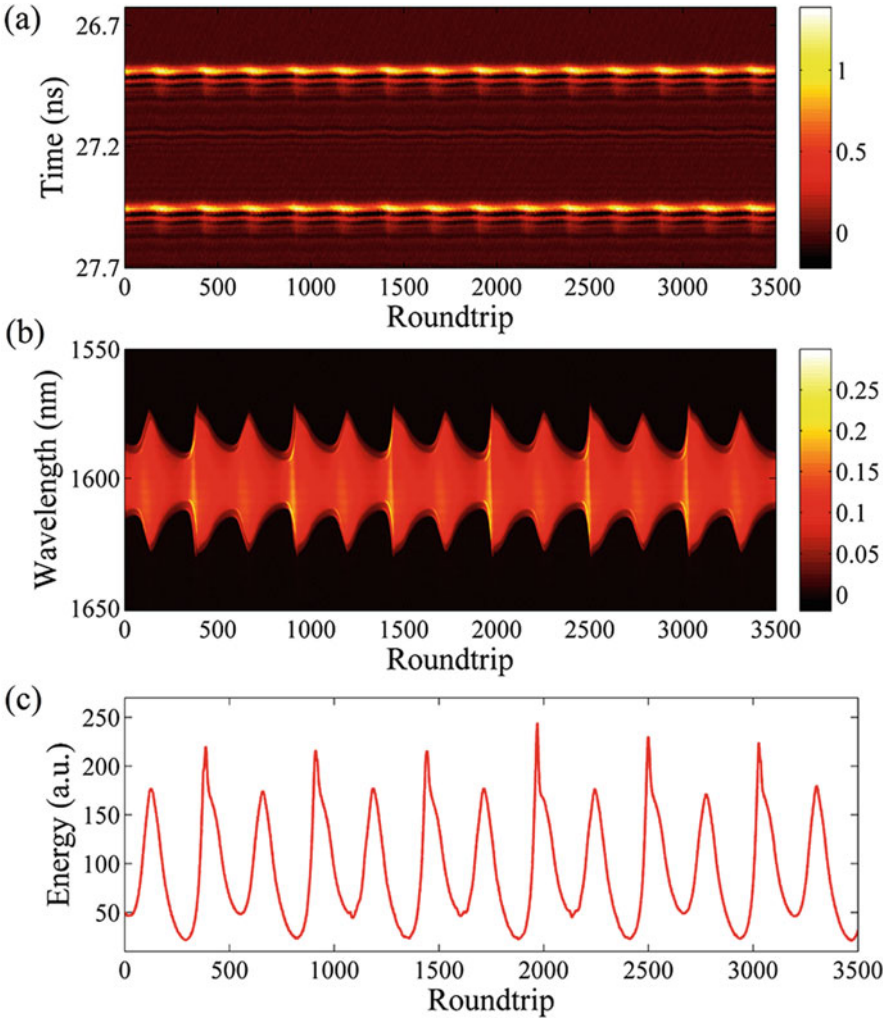

Fig. 7.14 The double-soliton pulsation with double period. (**a**) Spatio-temporal dynamics. (**b**) Spatio-spectral dynamics. (**c**) Pulse energy evolution. (Reprinted with permission from Ref. [14] © The Optical society)

However, no matter how the PCs and the laser pumping power are adjusted, the multi-soliton synchronous explosion similar to above pure pulsation cannot be implemented in the L-band dissipative soliton fiber laser. Generally, the fluctuation of pulse energy in pure pulsation is relatively moderate, whereas the soliton explosion means violent oscillation of energy. In the multi-pulse state, the violent fluctuation of the energy of a certain pulse is bound to cause a chain reaction of other pulses. Therefore, the synchronous explosion of multiple solitons is difficult to achieve. Nevertheless, the possibility of this dynamics cannot be ruled out without sufficient evidence.

7.3.6 *Pulsating Soliton Molecule*

In synchronous pulsating pattern, the interactions between solitons separated by a couple or dozens of pulse widths typically result in bound states, that is, pulsating soliton, whose spectrum has breathing characteristics and interference fringes [52]. For an appropriate setting of PCs, soliton bunch state with more than 5 pulsating solitons was obtained at a high pump power above 400 mW. Subsequently, solitons could be annihilated one by one by decreasing the pump power and pulse self-assembly took place during this process. Meanwhile, the spectral and temporal evolution of pulse were monitored by real-time oscilloscope in order to capture pulsating soliton molecules in time. Figures 7.15a–g summarize the performances of pulsating soliton molecules at the pump power of 362.2 mW. The real-time spectra of 2000 consecutive RTs are mapped in Fig. 7.10a, showing bandwidth pulsating property with a period of ~200 RTs. Correspondingly, the energy and temporal evolutions are presented in Figs. 7.15b, c. For pulsating solitons, the changes in group velocity induced by the variety of spectral composition generally lead to

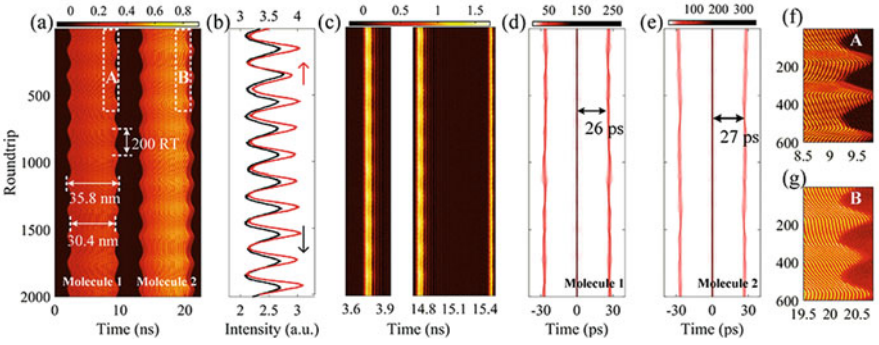

Fig. 7.15 Characteristics of pulsating soliton molecules. (**a**) Spatio-spectral dynamics. (**b**) Energy evolutions of Molecules 1 (black curve) and 2 (red curve), respectively. (**c**) Spatio-temporal dynamics. (**d**) and (**e**) Autocorrelation traces calculated from the real-time spectra of Molecules 1 and 2, respectively. (**f**) and (**g**) Close-ups of the data from the A and B regions of Fig. 7.10a, respectively. (Reprinted with permission from Ref. [52] © The Optical society)

periodical temporal shifts, which are invisible in this case due to the insufficient detection resolution. Combining Figs. 7.15a–c, there are 5 synchronous pulsating solitons self-assembling into two soliton molecules, where the trailing molecule is accompanied by an unbound soliton. The leading molecule is defined as Molecule 1 and the trailing one is defined as Molecule 2. Figures 7.15d, e show autocorrelation traces obtained by performing the fast Fourier transformations of the real-time spectra of Molecules 1 and 2, respectively. The distance between the central peak and the satellite peaks in the autocorrelation trace refers to the temporal separation inside a molecule. As can be seen, the separations inside both the two molecules jitter over time, slightly, chaotically and asynchronously. For better displaying the spectral fringes arising from interference between bound pulsating solitons, the spectra close-ups are drawn in Figs. 7.15f and 7.15g, respectively for Molecules 1 and 2. The irregular fringes indicate that the temporal separations and phase differences between the molecule constituents irregularly evolve with RT time. In addition, it is procurable to induce pulsating bound triplet states by identical pump power adjustment manner.

As shown in Fig. 7.16a, the average spectrum measured by the OSA presents arcuate edges, which is typical for pulsating solitons. Note that no interference pattern can be observed on the average spectrum due to the chaotic evolutions of both temporal separations and phase differences inside the two molecules. For better characterizing the pulsating soliton molecules, Figs. 7.16b, c illustrate the real-time spectra corresponding to the extrema of the oscillations of Molecules 1 and 2, respectively. The spectral fringes corresponding to the interference inside molecules are clearly visible. The spectral modulation period of both molecules is close to 0.304 nm, well consistent with the temporal separations in autocorrelation traces (shown in Figs. 7.15d, e.

7.3.7 Multi-Soliton Asynchronous Pulsation

As a matter of fact, soliton pulsation is essentially a metastable state with likelihood of asynchronous evolution in multi-pulse situation. From this perspective, different types of pulsating solutions can coexist in laser cavity, this is, each soliton may evolve periodically in different ways under certain parametric conditions. Here, three types of multi-soliton asynchronous pulsation phenomena are revealed in the L-band dissipative soliton fiber laser.

At the pump power of 364.5 mW, the first type of pulsating dynamics was captured, as shown in Figs. 7.17a–d. The real-time spectra of 7006 consecutive RTs and corresponding temporal evolutions are mapped in Figs. 7.17a, b. There are four dissipative solitons arranged from 1 to 4 according to their temporal positions in the cavity, whose spectra evolve like breathing, indicating that the laser operates in pulsating state. The ratio of the widest to the narrowest spectral bandwidth within a pulsating period is defined as spectral breathing ratio. Note that the time intervals among the leading three solitons are less than 1 ns, resulting in heavily overlapped

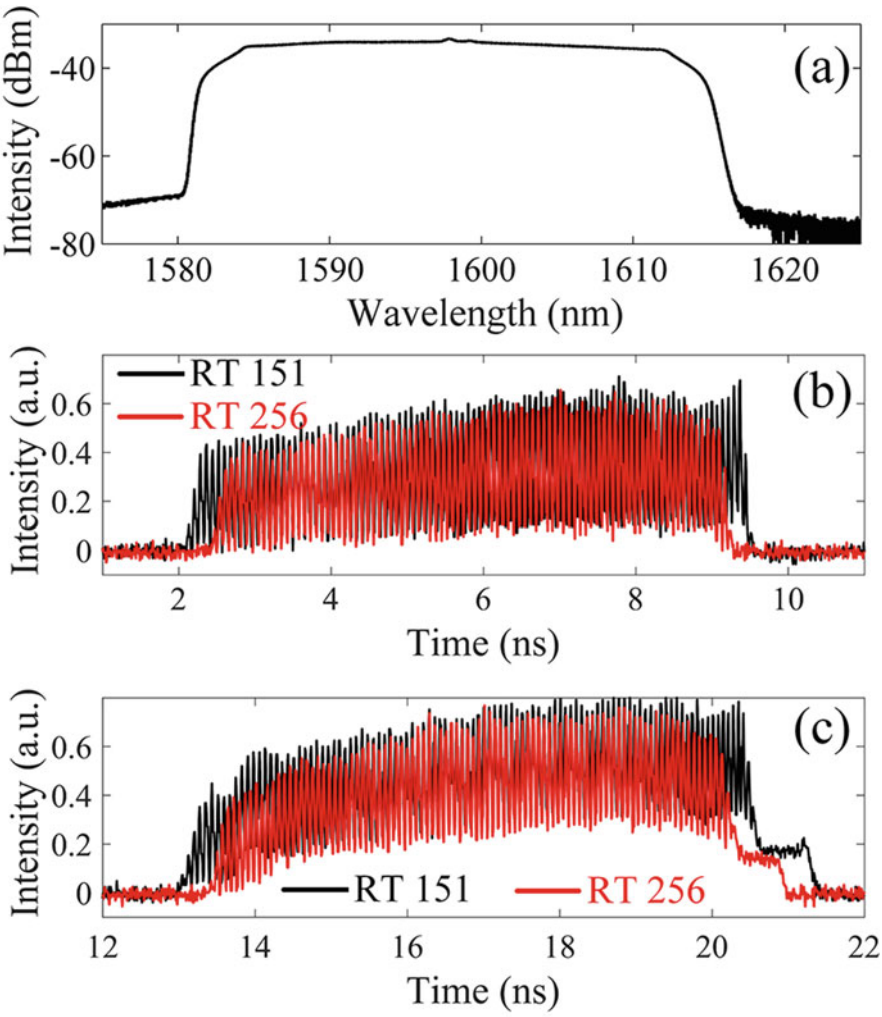

Fig. 7.16 Spectral characteristics of pulsating soliton molecules. (**a**) Optical spectrum directly recorded by the OSA. (**b**) and (**c**) Real-time spectra of Molecules 1 and 2, respectively; corresponding to the cross sections at the RT 151 (black curve) and 256 (red curve) of Fig. 7.10a. (Reprinted with permission from Ref. [52] © The Optical society)

real-time spectra. Further, the evolutions of the Solitons 1, 2 and 3 follow the same periodic solution with comparatively small spectral breathing ratio. For Soliton 4, the evolution abides by another periodic solution and the spectral breathing ratio reaches up to 6. Notably, the above two evolutionary paths have the same period of ~1280 RTs. The evolution of the pulse temporal profile, especially the peak intensity, is also periodic, with the highest (lowest) peak intensity naturally occurring in the vicinity of the position where the spectrum reaches the largest (narrowest)

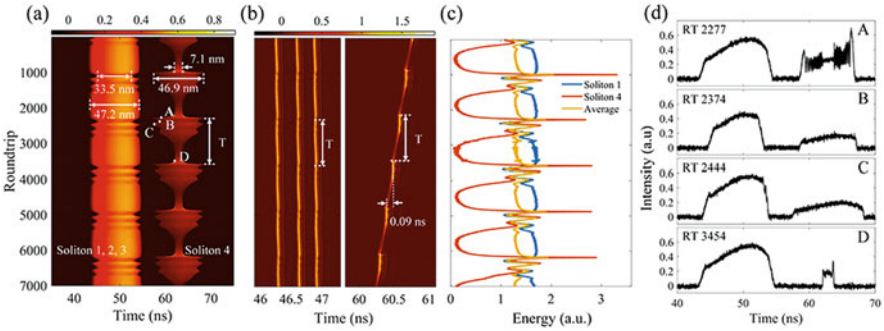

Fig. 7.17 Characteristics of simultaneous but unsynchronized pulsation of multi-soliton. (**a**) Spatio-spectral dynamics. (**b**) Spatio-temporal dynamics. (**c**) Energy evolutions. (**d**) Real-time spectra corresponding to the roundtrip of points A, B, C and D in Fig. 7.12a. (Reprinted with permission from Ref. [65] © The Optical society)

width. Moreover, the changes in group velocity induced by spectral variations lead to periodical temporal shifts, and the shift degree corresponds to the ratio of spectral breath. By piecewise integration of the spectral power density, the energy evolutions of pulsating solitons are calculated and plotted in Fig. 7.17c. The growth (decline) of the pulse energy is in sync with the expansion (contraction) of the spectrum. Correspondingly, the amplitude of the energy oscillation echoes the spectral breathing ratio. Note that the energy oscillations of the two pulsating solutions are complementary, thus mitigating the fluctuations of the total energy in cavity. For further characterizing the above asynchronous pulsation phenomenon, Figs. 7.17d illustrate four representative real-time spectra corresponding to the roundtrip of points A, B, C and D in Fig. 7.17a, respectively. Obviously, the spectral breathing ratio of Soliton 4 is much larger than those of the leading three. In addition, due to the discontinuity of the spectral phase at high nonlinearity [33], modulation peaks arise gradually at the spectral edges of Soliton 4 as its energy increases. While the other solitons do not have this feature. In a word, there are four dissipative solitons in the cavity, which follow two pulsating solutions with the same period, exhibiting simultaneous but unsynchronized pulsation of multi-soliton.

By finely tuning the PCs, another multi-soliton asynchronous pulsation phenomenon was observed at the same pump power. Figure 7.18a shows the spectral evolution of this fascinating transient dynamics. Corresponding temporal evolution is presented in Fig. 7.18b. It is a pity that the energy evolution of individual soliton cannot be plotted precisely because of the spectral overlaps. However, the spectral and temporal evolutions suffice to summarize most dynamic characteristics. Similar to the asynchronous pulsation phenomenon in Figs. 7.17a, b, there are still four dissipative solitons evolving along two periodic solutions. But here, the evolutions of the leading two solitons follow the same periodic solution with smaller spectral breathing ratio, whose period is ~1090 RTs; whereas Solitons 3 and 4 evolve along the other periodic solution with larger spectral breathing ratio, whose period, ~2180 RTs, is exactly twice of the former's. For further illustrating the dynamics of the

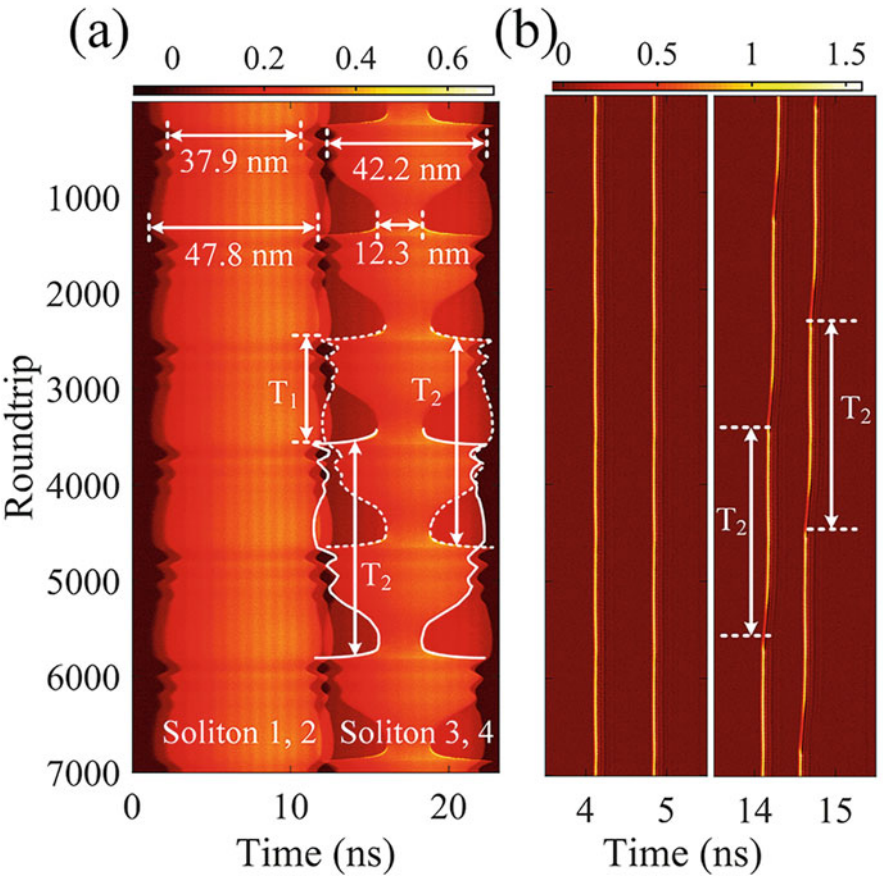

Fig. 7.18 Characteristics of multi-soliton asynchronous pulsation with energy rising (falling) alternately. (**a**) Spatio-spectral dynamics. (**b**) Spatio-temporal dynamics. (Reprinted with permission from Ref. [65] © The Optical society)

latter two solitons, the spectral evolution contours of Solitons 3 and 4 over a period with full line and dotted lines is outlined respectively in Fig. 7.18a. Combining Figs. 7.18a, b, the drastic spectral contraction of Soliton 3 or 4 is complementary with the expansions of all the others (ignoring slight, synchronous energy fluctuations). In other words, although following the same periodic solution, Solitons 3 and 4 evolve asynchronously with energy rising (falling) alternately, which alleviates the fluctuations of the total energy in cavity. Further, the leading two solitons undergo two periods synchronously during each sharp energy oscillation of soliton 3 or 4.

The nonlinear phenomenon of soliton explosion accompanied by violent energy oscillations is not peculiar in ultrafast fiber laser. Here, the experimental observation of the multi-soliton asynchronous pulsation containing periodic soliton explosions are demonstrated. Figures. 7.19a, b illustrate the real-time spectra and corresponding temporal evolution of this pulsating dynamics at the pump power of 245.8 mW,

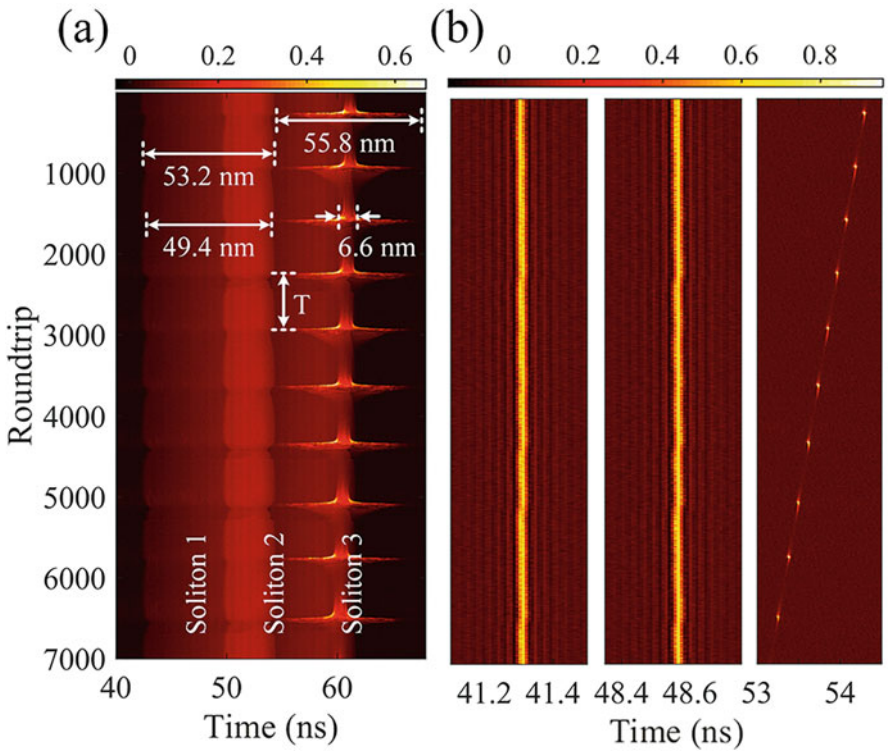

Fig. 7.19 Characteristics of multi-soliton asynchronous pulsation containing periodic soliton explosions. (**a**) Spatio-spectral dynamics. (**b**) Spatio-temporal dynamics. (Reprinted with permission from Ref. [65] © The Optical society)

respectively. As can be seen, three dissipative solitons evolve simultaneously but asynchronously in the cavity, following two different periodic solutions (including a periodic explosion solution) and exhibiting the same period of ~660 RTs. The evolutions of Solitons 1 and 2 follow a pure pulsation solution. Their spectral breaths are so weak that the temporal profile variations and periodic temporal shifts are invisible. When it comes to Soliton 3, the evolution conforms to the criterion of periodic soliton explosion. The erupting evolution starts from a metastable state with narrow spectral bandwidth. After a while, the spectrum experiences a violent expansion, and very soon, bursts to pieces like an explosion. Then these completely chaotic but well-localized spectral structures gradually recover to a smooth profile after ~50 RTs, concurrently, the spectral width decreases sharply. Eventually, the spectrum shrinks to its pre-explosion state. It's worth mentioning that the spectral breathing ratio of Soliton 3 is up to 8. For temporal evolution, there are shifts and fractures. The former is attributed to the group velocity disturbances caused by the changes of spectral range. The latter is due to the extremely low pulse energy and the insufficient detection dynamic range.

The above experimental results reveal the diversity of soliton pulsation dynamics in dissipative systems. Although far from covering the numerous and complicated pulsation dynamics, it is helpful for a more comprehensive understanding of the soliton pulsation phenomenon and to promote further theoretical and experimental research.

References

1. Y. Q. Du, et al., *Alternation of the Mode Synchronization and Desynchronization in Ultrafast Fiber Laser.* Laser & Photonics Reviews, 2020. **14**(3): p. 1900219.
2. J. M. Soto-Crespo, N. Akhmediev, and A. Ankiewicz, *Pulsating, creeping, and erupting solitons in dissipative systems.* Physical Review Letters, 2000. **85**(14): p. 2937-2940.
3. B. G. Bale, et al., *Transition dynamics for multi-pulsing in mode-locked lasers.* Optics Express, 2009. **17**(25): p. 23137-23146.
4. J. Zeng and M. Y. Sander, *Real-time transition dynamics between multi-pulsing states in a mode-locked fiber laser.* Optics Letters, 2020. **45**(1): p. 5-8.
5. J. Huang, et al., *Route from single-pulse to multi-pulse states in a mid-infrared soliton fiber laser.* Optics Express, 2019. **27**(19): p. 26392-26404.
6. F. Li, P. K. A. Wai, and J. N. Kutz, *Geometrical description of the onset of multi-pulsing in mode-locked laser cavities.* Journal of the Optical Society of America B-Optical Physics, 2010. **27**(10): p. 2068-2077.
7. R. J. Deissler and H. R. Brand, *Periodic, quasiperiodic, and chaotic localized solutions of the quintic complex Ginzburg-Landau equation.* Physical Review Letters, 1994. **72**(4): p. 478-481.
8. J. M. Soto-Crespo, et al., *Bifurcations and multiple-period soliton pulsations in a passively mode-locked fiber laser.* Physical Review E, 2004. **70**(6): p. 066612.
9. W. Chang, et al., *Extreme soliton pulsations in dissipative systems.* Physical Review E, 2015. **92**(2).
10. R. J. He, et al., *Dynamic evolution of pulsating solitons in a dissipative system with the gain saturation effect.* Optics Express, 2018. **26**(25): p. 33116-33128.
11. Z. H. Wang, et al., *Self-organized compound pattern and pulsation of dissipative solitons in a passively mode-locked fiber laser.* Optics Letters, 2018. **43**(3): p. 478-481.
12. J. Peng, et al., *Breathing dissipative solitons in mode-locked fiber lasers.* Science Advances 2019. **5**(11): p. eaax1110.
13. H. J. Chen, et al., *Dynamical diversity of pulsating solitons in a fiber laser.* Optics Express, 2019. **27**(20): p. 28507-28522.
14. X. Q. Wang, et al., *Transient behaviors of pure soliton pulsations and soliton explosion in an L-band normal-dispersion mode-locked fiber laser.* Optics Express, 2019. **27**(13): p. 17729-17742.
15. Z. H. Wang, et al., *Generation and pulsating behaviors of loosely bound solitons in a passively mode-locked fiber laser.* Physical Review A, 2020. **101**(1): p. 013825.
16. K. Goda and B. Jalali, *Dispersive Fourier transformation for fast continuous single-shot measurements.* Nature Photonics, 2013. **7**(2): p. 102-112.
17. A. Komarov, H. Leblond and F. Sanchez, *Quintic complex Ginzburg-Landau model for ring fiber lasers.* Physical Review E, 2005. **72**(2): p. 025604.
18. E. Ding and J. N. Kutz, *Operating regimes, split-step modeling, and the Haus master mode-locking model.* Journal of the Optical Society of America B-Optical Physics, 2009. **26**(12): p. 2290-2300.
19. S. C. V. Latas and M. F. S. Ferreira, *Emerging fixed-shape solutions from a pulsating chaotic soliton.* Optics Letters, 2012. **37**(18): p. 3897-3899.

20. A. Niang, et al., *Influence of gain dynamics on dissipative soliton interaction in the presence of a continuous wave.* Physical Review A, 2015. **92**(3): p. 03831.
21. J. M Soto-Crespo, et al., *Soliton complexes in dissipative systems: Vibrating, shaking, and mixed soliton pairs.* Physical Review E, 2007. **75**(1): p. 016613.
22. N. N. Akhmediev, A. Ankiewicz and J. M. Soto-Crespo, *Stable soliton pairs in optical transmission lines and fiber lasers.* Journal of the Optical Society of America B-Optical Physics, 1998. **15**(2): p. 515-523.
23. R. Weill, et al., *Noise-mediated Casimir-like pulse interaction mechanism in lasers.* Optica, 2016. **3**(2): p. 189-192.
24. K. Sulimany, et al., *Bidirectional Soliton Rain Dynamics Induced by Casimir-Like Interactions in a Graphene Mode-Locked Fiber Laser.* Physical Review Letters, 2018. **121**(13): p. 133902.
25. N. Akhmediev, J. M. Soto-Crespo and G. Town, *Pulsating solitons, chaotic solitons, period doubling, and pulse coexistence in mode-locked lasers: Complex Ginzburg-Landau equation approach.* Physical Review E, 2001. **63**(5): p. 056602.
26. J. M. Soto-Crespo, N. Devine and N. Akhmediev, *Dissipative solitons with extreme spikes: bifurcation diagrams in the anomalous dispersion regime.* Journal of the Optical Society of America B-Optical Physics, 2017. **34**(7): p. 1542-1549.
27. C. Cartes and O. Descalzi, *Periodic exploding dissipative solitons.* Physical Review A, 2016. **93**(3): p. 031801.
28. S. C. V. Latas, M. F. S. Ferreira and M. V. Facao, *Characteristics of fixed-shape pulses emerging from pulsating, erupting, and creeping solitons.* Applied Physics B-Lasers and Optics, 2014. **116**(2): p. 279-286.
29. S. C. V. Latas, M. F. S. Ferreira and M.V. Facao, *Impact of higher-order effects on pulsating, erupting and creeping solitons.* Applied Physics B-Lasers and Optics, 2011. **104**(1): p. 131-137.
30. M. J. Feigenbaum, *Quantitative universality for a class of nonlinear Transformations.* Journal of Statistical Physics 1978. **19**(1): p. 25-52.
31. P. Grelu and N. Akhmediev, *Dissipative solitons for mode-locked lasers.* Nature Photonics, 2012. **6**(2): p. 84-92.
32. A. I. Maimistov, *Evolution of solitary waves which are approximately solitons of a nonlinear Schrödinger equation.* Soviet Journal of Experimental & Theoretical Physics, 1993. **77**: p. 727-731.
33. E. N. Tsoy and N. Akhmediev, *Bifurcations from stationary to pulsating solitons in the cubic–quintic complex Ginzburg–Landau equation.* Physics Letters A, 2005. **343**(6): p. 417-422.
34. E. N. Tsoy, A. Ankiewicz and N. Akhmediev, *Dynamical models for dissipative localized waves of the complex Ginzburg-Landau equation.* Physical Review E, 2006. **73**(3): p. 036621.
35. I. M. Uzunov, Z. Georgiev and T. Arabadzhiev, *Influence of intrapulse Raman scattering on stationary pulses in the presence of linear and nonlinear gain as well as spectral filtering.* Physical Review E, 2014. **90**(4): p. 042906.
36. D. Anderson, *Variational Approach to Nonlinear Pulse Propagation in Optical Fibers.* Journal of Optical Communications, 2015. **27**(3): p. 3135-45.
37. D. Anderson, M. Lisak and T. Reichel, *Approximate analytical approaches to nonlinear pulse propagation in optical fibers: A comparison.* Physical Review A, 1988. **38**(3): p. 1618-1620.
38. I. M. Uzunov, Z. D. Georgiev, and T. N. Arabadzhiev, *Transitions of stationary to pulsating solutions in the complex cubic-quintic Ginzburg-Landau equation under the influence of nonlinear gain and higher-order effects.* Physical Review E, 2018. **97**(5): p. 052215.
39. S. C. Mancas and S. R. Choudhury, *Spatiotemporal structure of pulsating solitons in the cubic–quintic Ginzburg–Landau equation: A novel variational formulation.* Chaos Solitons Fractals, 2009. **40**(1): p. 91-105.
40. P. Ryczkowski, et al., *Real-time full-field characterization of transient dissipative soliton dynamics in a mode-locked laser.* Nature Photonics, 2018. **12**(4): p. 221–227.
41. A. Tikan, et al., *Single-shot measurement of phase and amplitude by using a heterodyne time-lens system and ultrafast digital time-holography.* Nature Photonics, 2018.

42. J. S .Peng and H. P. Zeng, *Dynamics of soliton molecules in a normal-dispersion fiber laser.* Optics Letters, 2019. **44**(11): p. 2899-2902.
43. J. S. Peng and H. P. Zeng, *Build-Up of Dissipative Optical Soliton Molecules via Diverse Soliton Interactions.* Laser & Photonics Reviews, 2018. **12**(8).
44. X. M. Liu, X. K. Yao, and Y. D. Cui, *Real-Time Observation of the Buildup of Soliton Molecules.* Physical Review Letters, 2018. **121**(2): p. 023905.
45. K. Krupa, et al., *Real-Time Observation of Internal Motion within Ultrafast Dissipative Optical Soliton Molecules.* Physical Review Letters, 2017. **118**(24): p. 243901.
46. Z. W. Wei, et al., *Pulsating soliton with chaotic behavior in a fiber laser.* Optics Letters, 2018. **43**(24): p. 5965-5968.
47. Y. Q. Du, Z. W. Xu and X. W. Shu, *Spatio-spectral dynamics of the pulsating dissipative solitons in a normal-dispersion fiber laser.* Optics Letters, 2018. **43**(15): p. 3602-3605.
48. M. Liu, et al., *Visualizing the "Invisible" Soliton Pulsation in an Ultrafast Laser.* Laser & Photonics Reviews, 2020. **14**(4): p. 1900317.
49. Y. Yu, et al., *Mutually ignited soliton explosions in a fiber laser.* Optics Letters, 2018. **43**(17): p. 4132-4135.
50. A. F. J. Runge, N. G. R. Broderick and M. Erkintalo, *Observation of soliton explosions in a passively mode-locked fiber laser.* Optica, 2015. **2**(1): p. 36-39.
51. M. Liu, et al., *"Periodic" soliton explosions in a dual-wavelength mode-locked Yb-doped fiber laser.* Photonics Research, 2020. **8**(3): p. 246-251.
52. X. Q. Wang, et al., *Real-time observation of dissociation dynamics within a pulsating soliton molecule.* Optics Letters, 2019. **27**(20): p. 28214.
53. X. Q. Wang, et al., *L-Band Efficient Dissipative Soliton Erbium-Doped Fiber Laser With a Pulse Energy of 6.15 nJ and 3 dB Bandwidth of 47.8 nm.* Journal of Lightwave Technology, 2019. **37**(4): p. 1168-1173.
54. C. Lecaplain, et al., *Dissipative shock waves in all-normal-dispersion mode-locked fiber lasers.* Optics Letters, 2014. **39**(2): p. 263-266.
55. X. M. Liu, et al., *Multistability evolution and hysteresis phenomena of dissipative solitons in a passively mode-locked fiber laser with large normal cavity dispersion.* Optics Express, 2009. **17**(10): p. 8506-8512.
56. D. Y. Tang, et al., *Observation of bound states of solitons in a passively mode-locked fiber laser.* Physical Review A, 2001. **64**(3): p. 033814.
57. J. Chen, et al., *Generation and observation of ultrafast spectro-temporal dynamics of different pulsating solitons from a fiber laser.* Optics Express, 2020. **28**(9): p. 14127-14133.
58. M. Suzuki, et al., *Spectral periodicity in soliton explosions on a broadband mode-locked Yb fiber laser using time-stretch spectroscopy.* Optics Letters, 2018. **43**(8): p. 1862-1865.
59. N. Akhmediev, A. Ankiewicz and J. Soto-Crespo, *Multisoliton Solutions of the Complex Ginzburg-Landau Equation.* Physical Review Letters, 1997. **79**(21): p. 4047-4051.
60. Y. Yu, et al., *Spectral-temporal dynamics of multipulse mode-locking.* Applied Physics Letters, 2017. **110**(20): p. 875-882.
61. M. Pang, et al., *All-optical bit storage in a fibre laser by optomechanically bound states of solitons.* Nature Photonics, 2016. **10**(7): p. 454-458.
62. C. K. Lee, J. J. Kang and G. R. Lin, *Competition of Rational Harmonic Mode-Locking and Continuous-Wave Lasing in Semiconductor Optical Amplifier Fiber Laser Under Optical Pulse Injection.* Journal of Lightwave Technology, 2009. **27**(7): p. 851-856.
63. D. Y. Tang, et al., *Mechanism of multisoliton formation and soliton energy quantization in passively mode-locked fiber lasers.* Physical Review A, 2005. **72**(4): p. 043816.
64. Y. Wei, et al., *Ultrafast spectral dynamics of dual-color-soliton intracavity collision in a mode-locked fiber laser.* Applied Physics Letters, 2018. **112**(8): p. 081104.1-081104.5.65
65. X. Q. Wang, et al., Real-time observation of multi-soliton asynchronous pulsations in an L-band dissipative soliton fiber laser, Optics Letters, 2020, to be published.

Chapter 8
Raman Dissipative Solitons

Denis S. Kharenko, Anastasia E. Bednyakova, Innokentiy Zhdanov, Vlad D. Efremov, Evgeniy V. Podivilov, Mikhail P. Fedoruk, and Sergey A. Babin

Abstract In this chapter, we give an overview of high-energy dissipative solitons generation via Raman gain. Such pulses have been proven to be a new kind of solitons—Raman dissipative soliton (RDS). Two basic configurations of the laser cavity with intra- and extra-cavity formation of the RDS are presented and the properties specific to each of them are discussed. Intra-cavity configuration provides a mutual coherence between the Raman and pump pulses generated in common cavity. Their mixing in a highly-nonlinear fiber results in cascaded generation of clones of the input DSs, forming a comb of highly chirped pulses in the spectral domain. Extra-cavity configuration gives more freedom in Raman cavity design, as net cavity dispersion together with the external pump pulse energy, duration and spectral width can be adjusted independently. As a result, it becomes possible to generate intensive laser radiation beyond the emission spectrum of typical active media, namely around 1.3 μm region, by using phosphosilicate fibers with the large Stokes shift. Thus, RDSs generation undoubtedly reveals new possibilities for numerous applications.

Keywords Fiber lasers · Femtosecond lasers · Ultrashort pulses · Highly-chirped pulses · Raman dissipative soliton · Stimulated Raman scattering · Synchronous pump · Spectral comb · Pulse propagation

D. S. Kharenko (✉) · I. Zhdanov · V. D. Efremov · E. V. Podivilov · S. A. Babin
Institute of Automation and Electrometry SB RAS, Novosibirsk, Russia

Novosibirsk State University, Novosibirsk, Russia
e-mail: kharenko@iae.nsk.su

A. E. Bednyakova · M. P. Fedoruk
Novosibirsk State University, Novosibirsk, Russia

Institute of Computational Technologies SB RAS, Novosibirsk, Russia

M. F. S. Ferreira (ed.), *Dissipative Optical Solitons*, Springer Series in Optical Sciences 238, https://doi.org/10.1007/978-3-030-97493-0_8

8.1 Introduction

Dissipative soliton (DS) generation is a powerful technique for producing high-energy femtosecond pulses in fiber lasers [1, 2]. However, it has been explored mainly for lasers with rare-earth-doped gain media, such as Yb-doped fiber (YDF) and Er-doped fiber (EDF) with optical gain near 1 μm [3, 4] and 1.55 μm [5, 6] correspondingly. An alternative approach is based on pump-induced Raman gain in passive fibers offering operation at almost any wavelength. Previously reported techniques of mode-locking in Raman fiber lasers exhibit low efficiency and/or rather long pulses. This is the main reason why pulsed Raman lasers keep great attention over decades. Starting from the single-mode optical fibers placed into the synchronously-pumped external linear cavity [7], Raman lasers were gradually evolving with the development of fiber optics technologies [8–11]. The interest was also sparked by great success of the continuum wave (CW) Raman fiber lasers [12–15] that encourages researchers to apply similar principles for the pulsed lasers.

A novel approach to the generation of high-energy ultrashort pulses by stimulated Raman scattering (SRS) was demonstrated recently in different laser schemes [16–19]. The pulse at a Stokes-shifted wavelength generated by SRS process was proved to be a new kind of solitons—Raman dissipative soliton (RDS) [16, 20]. Relatively high (up to 20 nJ) RDS energy could be achieved at different wavelengths, as far as pump and Raman lasers can be optimized independently and different passive fibers could be used to produce Raman shift [18]. Besides single-pulse RDS generation, cascaded generation of the first- and second-order RDS in the common cavity of an ytterbium fiber laser oscillator was obtained [21]. All the generated pulses (DS, first- and second-order RDS) are coherent, linearly chirped (instantaneous frequency linearly changes in time), and can be externally compressed to 200–300 fs durations. As the result of combining technology of synchronously pumped Raman fiber lasers [22] with the new concept of Raman dissipative solitons [16, 23], 18 nJ RDS has been demonstrated in a passive fiber cavity synchronously pumped by an external pulsed laser [17].

In this chapter, we give an overview of our results on high-energy dissipative solitons generation via Raman gain. We describe main principles of RDS generation in two basic configurations of the laser cavity. The first one is an intra-cavity scheme when Raman pulse formation is reached by a small feedback and additional delay line at the Stokes wavelength to compensate the group velocity difference. The second one is an extra-cavity configuration in which the Raman pulse forms in an independent fiber cavity and only exact matching between the repetition rate of pump pulses and the roundtrip frequency is necessary. We demonstrate, that the Raman and conventional dissipative solitons, generating in the common cavity, are mutually coherent [23], which results in formation of soliton complexes with high energy, broad spectrum, and short duration [24]. Extra-cavity configuration gives more freedom in cavity design, as net cavity dispersion together with the pump pulse energy, duration and spectral width can be adjusted independently. It made possible to generate RDS in the region of 1.3 mkm using phosphosilicate fibre, attractive for biomedical applications [18].

8.2 Principle of Generation

Energy of highly chirped DS ($\Delta t\,\Delta\nu \gg 1$) generated in fiber lasers may exceed a threshold of SRS, leading to formation of a noisy Raman pulse (RP). As it was demonstrated recently, a feedback realized by re-injection of the RP into the laser cavity could yield formation of RDS with characteristics similar to DS both in the intra- and extra-cavity configurations [16, 17]. The process of the RDS formation (as well as its amplification) can be described in a following way (Fig. 8.1). Initial wavelength-shifted pulse starts from the noise and amplifies due to SRS gain, while DS pulse serves as a pump. Pulses have a limited length of interaction because of the temporal walk-off effect, but the energy conversion can be efficient at high peak powers. So, in a case of the adjusted repetition rates the pump pulse and the signal pulse become synchronized and the stable generation regime can be achieved. The spectral width of the signal pulse, on the one hand, is limited by the pump bandwidth and by the Raman gain bandwidth of the used propagation media. But on the other hand, it could be broadened significantly by self-phase modulation effect. In fact there is dynamic balance between spectral filtering on one side, and nonlinearity, dispersion and gain on the other side, that leads to the formation of highly-chirped dissipative solitons in all-normal-dispersion fibre lasers [1, 2].

Figure 8.2 shows the conceptual difference between the intra- (left dashed block) and extra-cavity (right dashed block) schemes, realized around a ring fiber Raman cavity. In the first one the Raman cavity is a part of DS fiber laser, where a small feedback is introduced at the Stokes wavelength. A precise time delay is provided by the delay line (DL) to compensate the group velocity difference between the Stokes and pump pulses. The DS, amplified in the YDFA, serves as a pump for the RDS, and both pulses circulate inside a common laser cavity. The RDS spectrum acquires characteristic soliton shape with steep edges at the cavity feedback $\leq$1% (Fig. 8.3a). Under optimal conditions, the DS (1030 nm) and RDS (1070 nm) have similar parameters: ~10 nJ energy, ~40 ps duration dechirped to 200–300 fs by a grating compressor. Additionally, the pulses can be combined coherently, thus resulting in interference pattern with ~75 fs period [23].

In the second scheme the fiber Raman cavity is an external passive cavity pumped synchronously by a high-energy picosecond laser. In this case only exact matching between the repetition rate of pump pulses and the roundtrip frequency in the external Raman cavity is necessary for successful RDS generation. In combination with the optimal output coupling (85%) such laser generates RDS with energy up to 18 nJ [17] and compressible down to 150 fs (in accordance with a broad RDS optical

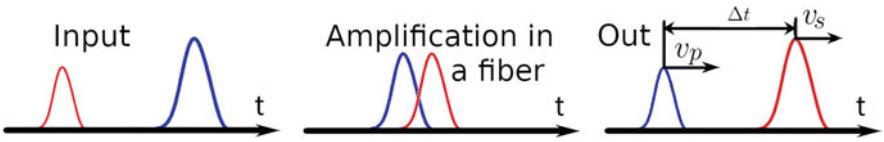

Fig. 8.1 Mechanism of the SRS amplification and pulse formation

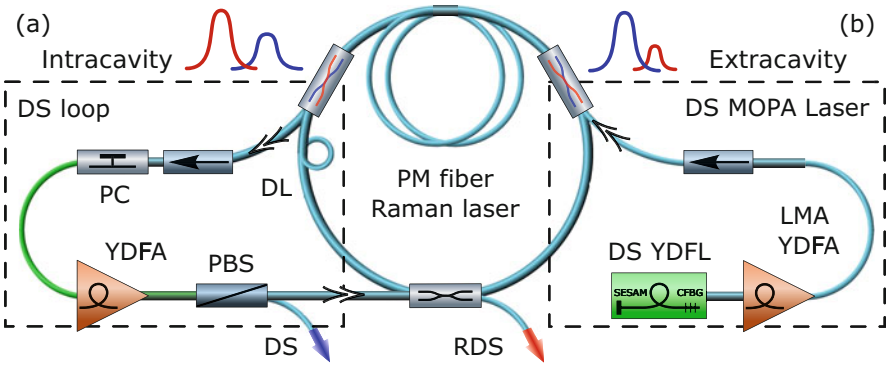

Fig. 8.2 PM-fiber Raman laser in two configurations: (**a**) synchronous generation of dissipative soliton and Raman dissipative soliton in a common cavity with DS loop involving YDF amplifier, polarization controller (PC) and beam splitter (PBS); (**b**) external pumping by MOPA laser consisting of YDF laser and amplifier

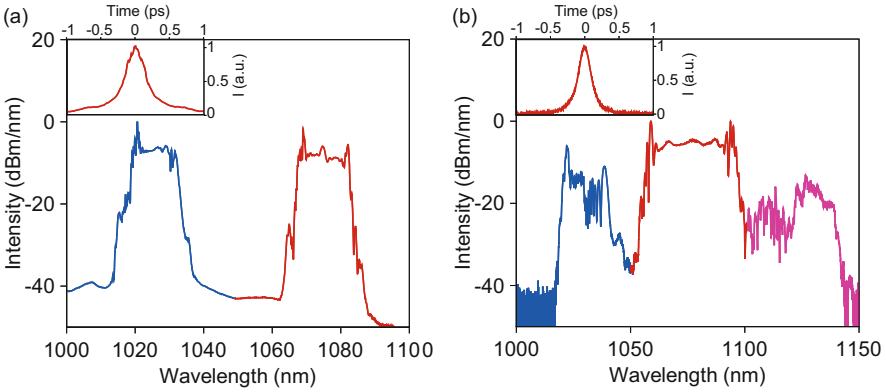

Fig. 8.3 Measured spectra for intra- (**a**) [16] and extra-cavity (**b**) [17] generation schemes with the ACF of the compressed RDS in the corresponding insets

spectrum depicted in Fig. 8.3b). The additional benefit is that net cavity dispersion together with the pump pulse energy, duration and spectral width could be adjusted independently. This makes it possible to generate RDS near 1.3 μm [18] by using a new type of P_2O_5 polarization maintaining (PM) fiber (FORC, Moscow) [25]. Thus, the second scheme offers shorter duration and higher pulse energy (with 88% efficiency with respect to pump radiation in the case of GeO_2 silica fiber), whereas the first scheme keeps nearly equal parameters of DS and RDS, demonstrating mutual coherence.

In both cases the level of feedback plays a crucial role in RDS formation. A standard GeO_2 fiber has a high Raman gain that results in rapid energy conversion. In the intracavity scheme it could lead to destabilization of the mode-locking regime.

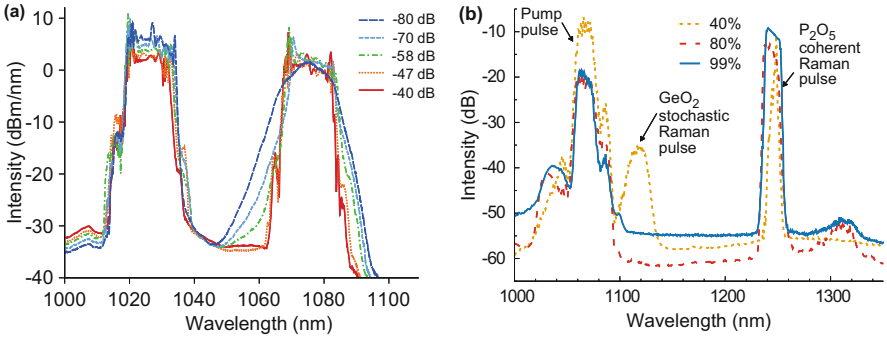

Fig. 8.4 The optical spectra measured at the output of fiber oscillators with the common GeO_2 cavity (**a**) and external P_2O_5 cavity (**b**) at different feedback ratio

Thus, a very small feedback of only 0.01% is enough to provide RDS generation with comparable energy and to preserve pump pulse for the next roundtrip (Fig. 8.4a). In the case of external cavity the pump pulse can be depleted completely and the value of feedback could be as high as 10%, keeping the output coupling ratio high enough. The situation is changing for P_2O_5-doped fiber, where competition between germanium and phosphorous amplification peaks takes place. In this case 40% feedback is not strong enough to support RDS recirculation inside the external cavity. The reason is that the phosphorous gain is lower and a stochastic Raman pulse appears at the germanium-shifted wavelength (see Fig. 8.4b). Only if the feedback is greater than 80%, it becomes possible to generate pulses with the steep edges in the optical spectrum, typical for highly-chirped dissipative soliton operation.

As the generated Raman pulses are highly-chirped dissipative solitons it can be used as a pump for second-order RDS. So the generation can be iterative. Such possibility was demonstrated both experimentally and numerically for the first time in [21]. The main DS centered at 1020 nm transfers its energy to the first Raman DS at 1065 nm and the second Raman DS at 1115 nm. Numerical results show that hard filtering holds the promise for extending the spectral range to 1200 nm and further. Two 10 nJ Raman DSs can be coherently combined with DS, increasing thus threefold the energy of the cascade.

Summarizing the above, the proposed approaches enable femtosecond Raman lasing at new wavelengths, which are not available from the rare-earth-doped fiber lasers. Mutual coherence of DS and RDS results in formation of multi-color soliton complexes with higher energy, broader spectrum and shorter duration. At the same time, RDS generation in the external cavity allows to use nonstandard fibers to produce large frequency shift. Numerous applications can benefit from this approach, including frequency comb spectroscopy, transmission lines, parametric amplifiers, CARS or multi-photon fluorescence microscopy.

8.3 Simulation

Next we provide details about numerical simulations of RDS generation inside fiber cavities, based on GeO_2 and P_2O_5-doped fibers, exhibiting different Stokes shifts. The laser scheme used in numerical simulations coincides well with the experimental one presented in Fig. 8.2. We have taken a discreet approach based on the Nonlinear Schrödinger equation (NLSE) to observe the RDS formation inside the cavity. The optical field consequently propagates through the elements inside the cavity, the key of which is a Raman gain fiber. The discrete elements, such as optical filter and polarization beam splitter, are described by their transmission functions (see details in [16]. The signal propagation along the fibers is described by the generalized NLSE.

Raman Gain Fiber

SRS leads to generation of the Stokes wave whose frequency is determined by the peak of the Raman gain. In the case of GeO_2-doped fiber, Raman gain reaches its maximum for the frequency component that is downshifted from the pump frequency by about 13.2 THz. The Raman gain of P_2O_5-doped fiber can be expressed as the linear superposition of the Raman gain due to SiO_2 and the Raman gain due to P_2O_5, corresponding to large 39 THz Stokes shift (see Fig. 8.5a).

To model pulse propagation in the Raman gain fibers we used generalized Nonlinear Schrödinger equation:

$$\frac{\partial A}{\partial z} = -i\frac{\beta_2}{2}\frac{\partial^2 A}{\partial t^2} + \frac{\beta_3}{6}\frac{\partial^3 A}{\partial t^3} + i\gamma\left(1 + \frac{i}{\omega_0}\frac{\partial}{\partial t}\right)\left(A(z,t)\int_0^\infty R(t')|A(z,t-t')|^2 dt'\right), \tag{8.1}$$

where $A(z, t)$ is the electric field envelope, β_2 and β_3 are the second- and third-order dispersion coefficients at the central frequency ω_0, $\gamma = n_2\omega_0/(cA_{\text{eff}})$ is the Kerr nonlinearity coefficient with the nonlinear refractive index n_2 and effective fibre

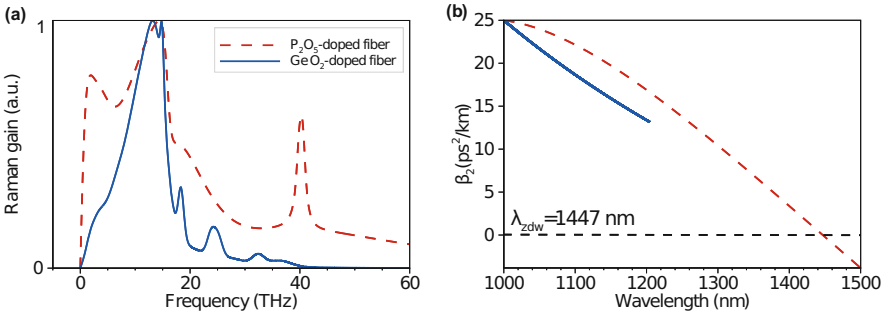

Fig. 8.5 Calculated Raman gain spectrum (**a**) and dispersion curves (**b**) of P_2O_5 and GeO_2 fibers used in different schemes

cross-section area A_{eff} for the fundamental mode. We neglect such effects as self-steepening and optical shock formation. The response function $R(t)(1-f_R)\delta(t) + f_R h_R(t)$ includes both instantaneous electronic and delayed Raman contributions, where f_R represents the fractional contribution of the delayed Raman response to the instantaneous nonlinear polarization.

Special attention should be paid to calculation of the Raman response function $h_R(t)$, which defines the Raman gain spectrum given by $g_R(\Delta\omega) = 2\gamma f_R Im[h_R(\Delta\omega)]$. To model signal propagation inside conventional GeO_2-doped fiber, we use the multiple-vibrational-mode model for the Raman response, described in [26]. This model provides a simple analytical expression for the Raman response function using convolutions of Lorentzians with Gaussians, the parameters in which were chosen in such way that the model's Raman gain spectrum and Raman response function both fit well with experiment.

In the case of the P_2O_5-doped fiber the Raman response function was derived from the Raman gain spectrum through a sine Fourier transform [27]:

$$f(s) \sim \frac{2}{\pi}\int_0^\infty d\Omega N_2''(\Omega)\sin(\Omega s)\ , \tag{8.2}$$

where $s = t - t'$—time delay, Ω—frequency, $N_2''(\Omega)$—imaginary part of third-order susceptibility, which is proportional to the Raman gain. Note, the Raman response function of phosphosilicate fiber can be also approximated by a superposition of six phase-shifted under-damped functions [28]. Parameters for the fitting functions of phosphosilicate fiber are given in the paper for 9.1 mol% of P_2O_5.

The Raman gain spectrum of phosphosilicate-doped fiber, used in numerical simulations, is shown in Fig. 8.5a (red dashed line) and agrees well with the typical experimentally measured gain spectrum of the P_2O_5 fiber [25]. Blue solid line in the same figure shows the Raman gain spectrum of standard Germanium-doped fiber.

Dispersion Curve

The considered in simulations spectral window should be relatively high to take into account the influence of high-order Stokes waves. For the cavity comprised of standard GeO_2 fiber the shortest wavelength was about 860 nm and the longest one was 1260 nm. Such a wide spectral range requires appropriate dispersion curve, so the third order dispersion term was introduced in the equation (blue solid line on Fig. 8.5b). However, the Stokes shift for P_2O_5 fiber is much larger and requires to extend the considered spectral window proportionately: from 700 nm to 2000 nm. The corresponding dispersion curve has been obtained by fitting the experimentally measured points near 1, 1.3 and 1.55 μm (red dashed line on Fig. 8.5b). All this allowed us not only to achieve agreement between the existing experimental data and simulation results, but also to make predictions about attainable absolute maximum ratings of the generated pulses. It should be noted that a novel efficient numerical model which uses a pair of meshes (for pump and Stokes waves) can be used to improve a calculation speed and memory consumption at the expense of about 10% inaccuracy [29].

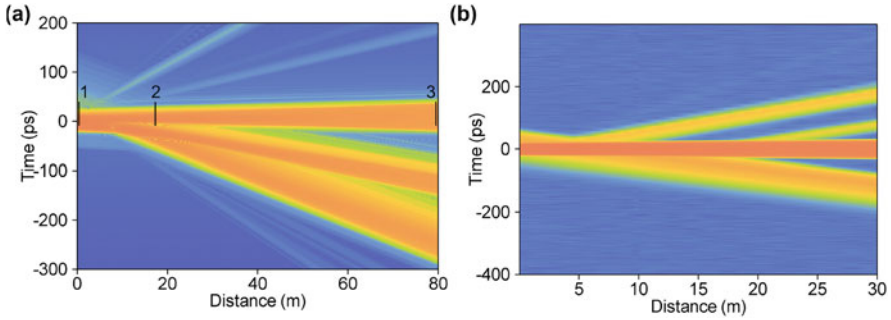

Fig. 8.6 Intracavity dynamics for the cascaded RDS generation in GeO_2 fiber cavity (**a**) and far-detuned first-order RDS generation in P_2O_5 fiber cavity (**b**)

Pump and Raman Pulse Temporal Synchronization

The difference in the group velocities of DS and RDS generated in a common cavity can be compensated by the delay line for the Raman pulse. If RDS generation takes place in the external cavity, exact matching between the repetition rate of pump pulses and the roundtrip frequency is required. In simulation temporal delay of the pump pulse in the both considered configurations can be compensated by multiplication of the optical field, corresponding to the Raman pulse, on the term $\exp(id_{\text{shift}}\omega)$ in Fourier domain, where d_{shift} is the temporal mismatch between the pulses, acquired after one round-trip.

The equation (8.1) was solved by using the symmetrized split-step Fourier-transform method. The simulations are run until the pulse field reaches the steady state after a certain number of cavity roundtrips, taking into consideration the contributions of the point-action intracavity devices. it is noteworthy, that once an agreement with the experiment has been reached in terms of spectral shape, pulse duration and power, we can take a look inside the laser cavity. For example, evolution of the temporal shape reveals typical interaction lengths between the pump and Raman pulses (Fig. 8.6). Here points '1' and '2' show the propagation length with intensive energy exchange between the DS and RDS, while along the fiber confined by the points '2' and '3' they propagate independently.

8.4 Brief Theory

Why is the Raman pulse a dissipative soliton? In fact, it is not easy to describe RDS evolution analytically to show relationships and properties inherent to dissipative solitons. The nonlinear Raman gain is the main issue. If the pump pulse is coherent and chirped, it serves not only as an amplification profile but also as a self-amplitude modulation (SAM) mechanism. The resulted Raman pulse is chirped, which means an internal re-distribution of its energy as the consequence of the energy interchange with the environment. The main manifestation of high chirp for the Raman pulse in

the experiment is its typical M-shaped ("Batman"-type) spectrum just like for DS [1, 30]. Experimental demonstration of dechirping was also shown clearly [16, 17]. So, the generated pulse looks exactly like a highly-chirped dissipative soliton, solution of the complex Ginzburg-Landau equation (CGLE) that includes both spectral filtration (β) and SAM (ϵ, μ) terms [1, 31]:

$$i\psi_x + D\psi_{tt}/2 + |\psi|^2\psi = i\delta\psi + i\beta\psi_{tt} + i\epsilon|\psi|^2\psi + i\mu|\psi|^4\psi, \tag{8.3}$$

where ψ is the normalized optical field envelope, t is the retarded time in the frame moving with the pulse, $x = z/L$—the propagation distance normalized on the cavity length L. It should be noted that Raman cavity does not contain spectral filtering and SAM elements, which have to be exist according to equation (8.3). So, its action can be attributed to coherence of the pump pulses together with the Raman gain. This point is also supported by recent investigation in which noise-like pulses (so-called double-scaled or incoherent) can produce coherent pulses only if spectral filtering and SAM elements exist in the Raman laser cavity [32].

For a more rigorous proof we can compare solutions of equations (8.3) and (8.1), which is actually used in numerical simulations. As the CGLE incorporates the main physical ingredients in a distributed way instead of considering point-action components used in a real laser system, we have to relate, albeit in an approximate way, all its coefficients to the physical parameters of the laser. We assume that RDS evolution consists of a long distributed part (nonlinearity and dispersion terms) and short point-action part (all other terms). So, split the roundtrip into two parts and define the fields between them as A_2 and A_3 (according to Fig. 8.6a). In this way the distributed evolution results in field transformation from the point A_2 to A_3, and the point-action return it back to the initial state. The nonlinearity Γ and dispersion D considered in their cumulative values over the distributed part $\Gamma = \gamma L$ and $D = -\beta_2 L$ where L is the cavity length. We neglect the third and further dispersion orders terms and consider that the Raman response function $h_R(t)$ can be attributed to point-action terms, since the interaction of DS and RDS takes place only in a relatively short part of the cavity. The point-action terms include also the effects of spectral filtering, gain, loss and SAM. The last one results in reshaping and shortening of the pulse. In phenomenological way it could be written as $\Delta A_3\sqrt{\Gamma} = (\epsilon|\psi|^2 + \mu|\psi|^4 + \delta)\psi$, where coefficients ϵ and μ can be related to the critical power P_{cr}. Amplification (with the net Raman gain coefficient G) is $A_2 = GA_1$, where $G \cdot R \simeq 1$ means loss compensation during the roundtrip. Filtering is $\Delta A_2\sqrt{\Gamma} = \beta\partial_t^2\psi$. The RDS spectrum in the point A_2 has the parabolic profile ($\beta\omega^2$) is defined by the Gaussian gain profile near the gain maximum ($Ge^{-\beta\omega^2}$, see supplementary in [16]).

After making such distribution of the point-action terms, we solved the CGLE using numerical methods for simulation of chirped DS [31]. Then we compared the CGLE solutions with the local solutions of the NLSE at points A_2 and A_3 and made the arithmetic mean of them supposing that the solution of the CGLE based on average coefficients should be close to the mean solution of the NLSE covering most

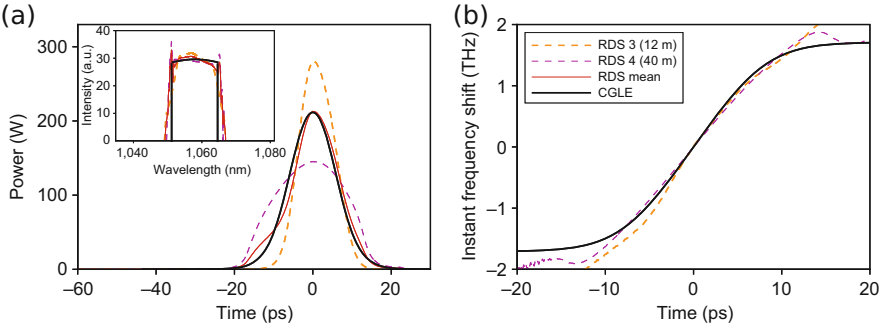

Fig. 8.7 Comparison of the NLSE and CGLE solutions. The solutions of CGLE are solid black curves. The pulse parameters are shown for RDS at the start A_1 and the end A_2 of distributed part of the cavity (yellow and pink dashed lines, correspondingly) and the arithmetic mean of them (solid red). (**a**) The pulse power, $P = |A|^2 = |\Psi|^2 / \Gamma$, with the corresponding spectra shown in the inset; and (**b**) the corresponding instant frequency shift $(2\pi)^{-1} d\phi / dt$ versus time t

of the pulse evolution in the cavity. The results of comparison are summarized in Fig. 8.7. The parameters of point-action therms were extracted by fitting resulted pulse duration and spectra. As a result, the averaged pulse optical spectrum, temporal shape and chirp are in agreement with the solution of CGLE that allows us to attribute the generated Raman pulses to a pure DSs. For more details you could see the supplementary materials in [16].

8.5 Applications

Demonstrated way to generate stable chirped Raman dissipative solitons in the fiber cavity undoubtedly reveals new possibilities for numerous applications. There are two key properties of RDS. The first one is the mutual coherence between the generated Raman and pump pulses. So, a wide range of nonlinear conversion processes is possible in all fiber schemes including parametric four-wave mixing [33] or spectral comb of highly chirped pulses generation [24]. The second one is the shift of a carrier frequency of ultrashort pulses. The frequency shift is not so high in standard GeO_2 fiber but in case of P_2O_5 fibers it becomes possible to generate intensive laser radiation beyond the emission spectrum of typical active media [18]. In this section we discuss the most exciting examples in both cases.

Mixing of two frequency-shifted dissipative solitons in a highly-nonlinear fiber with dispersion close to zero results in generation of chirped pulses at new wavelengths. This process can be described as cascaded generation of clones of the input DSs, forming a comb of highly chirped pulses in the spectral domain. The FWM plays here a key role and a simple analytical model could be developed for a nonlinear non-dispersive medium [24]. For a single pulse with a high peak power, propagating in a highly-nonlinear fiber, significant spectral broadening is observed.

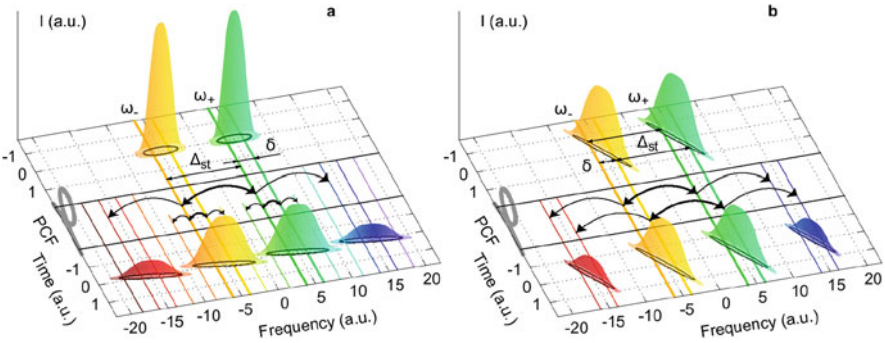

Fig. 8.8 Nonlinear mixing in a PCF of two solitons (**a**) and two equally chirped dissipative solitons (**b**) with frequency separation Δ_{st}, each of which consisting of laser modes with separation δ

It can be interpreted as FWM between internal frequency components (laser modes) with spacing δ between them, resulting in generation of new components separated by δ. The corresponding qualitative picture in the time-frequency plane is shown in Fig. 8.8a. When we mix two mutually coherent solitons, overlapped in time, which carrier frequencies are separated by Δ_{st}, additional components separated by Δ_{st} appear after propagation through PCF. The processes of new components generation ($\sim \Delta_{st}$) and pulse broadening ($\sim\delta$) occur simultaneously, finally leading to formation of a continuously broadened frequency comb. In the case of chirped dissipative solitons with the same spectral width Δ, the picture is principally different. If the pulses are similarly chirped, they overlap in time by different spectral components: low-frequency parts at the leading edges and high-frequency parts at the trailing edges (Fig. 8.8b). In terms of the FWM process, it means that the mixing between intra-pulse components (δ) is suppressed, because they do not overlap in time, whereas corresponding Stokes-shifted (Δ_{st}) parts of the pulses are effectively mixed.

Figure 8.9a shows the results of numerical simulation of the frequency-shifted DSs propagation in a nonlinear medium, gradually taking into account the effects of Raman scattering and dispersion. The full dispersion curve is shown by the Y-axis on the right side. One can see that dispersion could significantly decrease the number of spectral satellites (clones), generated during DS-RDS propagation in a nonlinear fiber, while the influence of Raman effect is not so strong. In the experiment, we use the DS/RDS generator producing highly-chirped pulses centered at 1025 nm and 1070 nm. New spectral components appear at >1100 nm and <1000 nm, the most eminent from which are the first Stokes and anti-Stokes pulses at 1110 and 980 nm with 1.6 and 1.7 nJ energies, respectively. We observe up to eight equidistant components in the >300-nm interval in total (Fig. 8.9b). Their coherence was proved by the FROG and interferometric ACF measurements together with dechirping by diffraction grating compressor. The results are shown in Fig. 8.10a, b for the first anti-Stokes ($\sim$990 nm) and Stokes ($\sim$1110 nm) satellites, demonstrating nearly a linear chirp within its spectral width of 10–15 nm for a duration of 10–15 ps compressible to 300–800 fs. The parameters are similar to the input pulses: linewidth

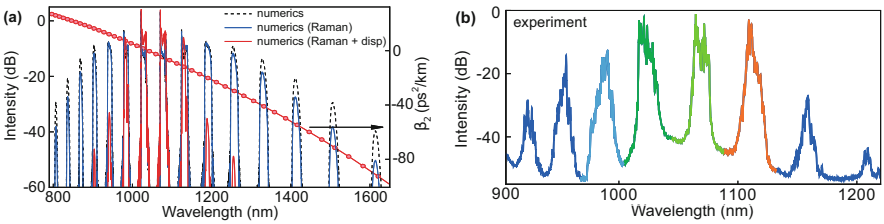

Fig. 8.9 (**a**) Output spectra calculated numerically with neglected dispersion and Raman effects (dashed line) and with account for Raman and dispersion effects (blue and red lines correspondingly). Coefficient β_2 is shown by circles. (**b**) Experimentally measured output spectrum

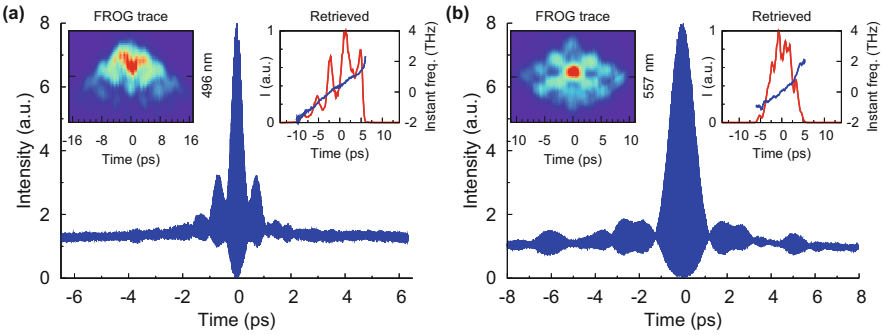

Fig. 8.10 Temporal characteristics of the generated anti-Stokes (**a**) and Stokes (**b**) pulses: Interferometric ACF for a compressed pulse, FROG trace (left inset) and retrieved pulse amplitude and instantaneous frequency (right inset)

of ∼15 nm and duration of ∼20 ps dechirped to 230–400 fs. In spite of some difference in values, the satellites can be treated as clones of the input dissipative solitons having nearly the same chirp, whereas their number is limited by dispersion.

Note that the mixing of chirped pulses in a long PCF with high integral dispersion is defined by the phase matching condition enabling generation of only one narrow (∼1 nm) Stokes component tunable within a ∼20-nm range by varying the delay between the input pulses [33]. A short PCF placed in a cavity of optical parametric amplifier or oscillator also generates only one component (Stokes or anti-Stokes), see e.g. ref. [34] and citation therein. Further increase of input pulse energies and/or using a PCF with a broader low-dispersion window may result in an octave-spanning comb of equidistant chirped pulses. The comb period may be adjusted by means of the frequency difference variation between the DS and RDS or doubling it in the second-order RDS scheme [21]. This approach can be also transferred to other spectral regions by using other types of fiber lasers for generation of DS/RDS pump pulses, e.g. Er (1.55 μm) or Tm, Ho (2 μm) [35], as well as to microresonators, which also exhibit different Raman effects such as Raman self-frequency shift of Kerr solitons [36], Raman frequency comb formation [37], and synchronous Stokes soliton generation in presence of the main soliton [38].

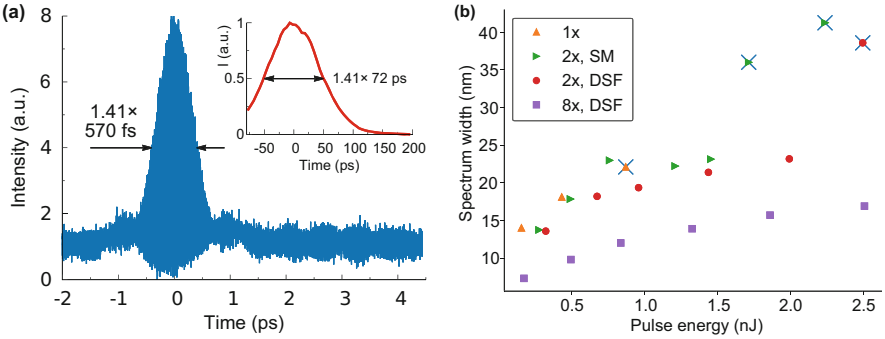

Fig. 8.11 (**a**) Experimentally measured interferometric and intensity (inset) auto-correlation traces of dechirped and chirped pulses near 1.3 μm, respectively. (**b**) Optical spectrum width (at a level −10 dB) of the generated pulse vs. pulse energy. The crosses mark the points of transition to the regime of noise-like pulses

Another area of practical interest for RDS applications is related to a large frequency shift. It can be highly demanded for biomedical applications such as multiphoton fluorescence microscopy. This is because one of so-called water transparency windows exists around 1.3 μm and effective attenuation length in biomedical tissue is quite long [34]. So, significantly greater penetration depth can be reached without damaging of an object. The soliton self-frequency shift is one of the widely used methods for obtaining femtosecond pulses at new wavelengths. It requires fibers with an anomalous dispersion, which is possible at 1.3 μm only for special fibers supporting high-order modes, and huge power pump lasers [39]. The cost of such device is too high for practical applications. Alternatively, phosphosilicate (P_2O_5) fiber gives a great advantage to a far-detuned Raman generation due to the large Stokes frequency shift of 39 THz. In particular, it is possible to obtain generation of highly-chirped dissipative solitons near 1.3 μm, compressible down to 570 fs (see Fig. 8.11a) in one cascade by using well-developed pulsed Ytterbium-doped fiber sources near 1.1 μm as a pump.

The significant benefit of RDS generation technique is the all-fiber design providing stability and high beam quality [18, 19, 40]. The limitation of this technique consists in the relatively low output pulse energy. In the first experiments the energy reached 1.6 nJ [18] and was increased further up to 2.5 nJ by managing the length and dispersion of the external cavity (Fig. 8.11b) [40]. Higher energies (more than 9 nJ) can be obtained by incorporating the last stage of the pump amplifier into the external Raman cavity [19]. However, it is still far from 30–50 nJ energies required for practical applications. What's interesting is that the numerical simulations did not show a possibility to obtain pulses with sufficiently high energy from the RDS oscillator [41]. The energy grows with the pump power increase but is limited by the next order SRS threshold, which is related to germanium amplification peak and lower in the long cavity (Fig. 8.12a). So much higher energy (up to 6 nJ) can be obtained from the 5-m long cavity (Fig. 8.12b). At the same time, the spectrum width reaches 50 nm which corresponds to ∼100 fs duration

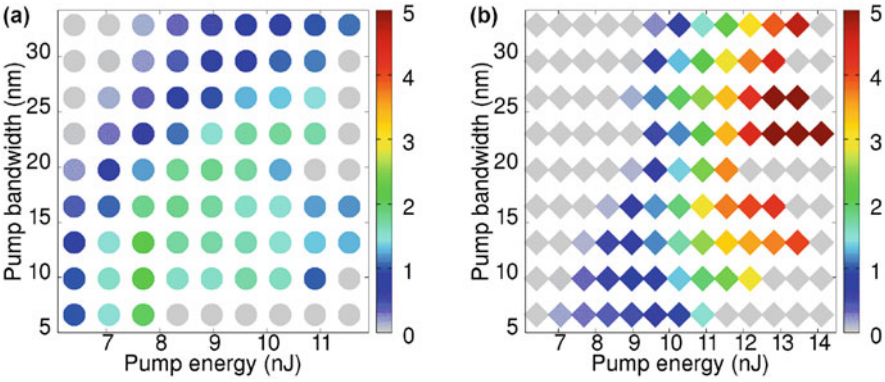

Fig. 8.12 Calculated areas of stable RDS generation in the 30-m long cavity comprised of 10-m P_2O_5 fiber and standard fiber with the same dispersion curve (**a**) and 5-m long P_2O_5 cavity (**b**). Color shows the RDS energy

of the transform limited pulse. Such duration is comparable to the best one obtained to date [42].

Finally, the one way to make RDS more suitable for further applications is an amplification. One of the native ideas was to separate pump and signal pulses after every roundtrip of the external cavity and then mix them again in the phosphosilicate fiber at the output of the laser. The first attempts have shown only ~3 dB increase [43]. Another idea is to use continuous wave pump at the P_2O_5 or GeO_2 Raman peak or use special bismuth-doped phosphosilicate fiber [44]. Further investigation will reveal an optimal scheme, new properties and possibilities of RDS generation.

Conclusion

We believe, that the observed new kind of soliton, namely Raman Dissipative Soliton, offers wide possibilities for numerous applications. So far, the first- and second-order RDS generation inside the intra- and extra-cavity configurations have been demonstrated both numerically and experimentally. Numerical simulations based on the nonlinear Schrödinger equation with the Raman gain is a powerful tool not only for reproducing the experimental results, but also for predicting new lasing regimes and complex optimization of the experimental schemes.

Together with the contribution to fundamental science, the proposed approach to generation of ultrashort pulses at Stokes-shifted wavelengths opens up new possibilities for practical applications. A proper phase correction and coherent combination of the comb components may be used for generation of high-energy few-cycle pulses and/or for arbitrary waveform synthesis, in a similar manner to conventional continuous frequency comb (coherent supercontinuum) or several synchronized mode-locked lasers operating in

(continued)

different spectral ranges. In comparison with the use of independent sources, the method of the coherent chirped-pulses comb generation is intrinsically stable and much simpler in realization. Such a comb, centered at 1.55 μm, can be implemented in ultra-broadband transmission lines with new coherent modulation/demodulation formats. Other applications can also benefit from this approach, including frequency comb spectroscopy, mid-IR and THz generation. At the same time a far-detuning in the phosphosilicate fiber can be used to build low-cost and stable sources of ultrashort pulses at specific wavelengths (e.g. 1.3 μm) for applications in nonlinear optical bioimaging—multiplex coherent anti-Stokes Raman scattering microscopy, multiphoton fluorescence microscopy, and optical coherence tomography.

References

1. Ph. Grelu and N. N. Akhmediev. Dissipative solitons for mode-locked lasers. *Nat. Photonics*, 6(2):84–92, 2012.
2. W. H. Renninger and F. W. Wise. Dissipative soliton fiber laser. In O. G. Okhotnikov, editor, *Fiber Lasers*, pages 97–134. Wiley, 2012.
3. S. Lefrançois, T. S. Sosnowski, C.-H. Liu, A. Galvanauskas, and F. W. Wise. Energy scaling of mode-locked fiber lasers with chirally-coupled core fiber. *Opt. Express*, 19(4): 3464–3470, 2011.
4. D. S. Kharenko, V. A. Gonta, and S. A. Babin. 50 nJ 250 fs all-fibre Raman-free dissipative soliton oscillator. *Laser Phys. Lett.*, 13(2):025107, 2016.
5. M Tang, H Wang, R Becheker, J.-L. Oudar, D. A. Gaponov, T. Godin, and A Hideur. High-energy dissipative solitons generation from a large normal dispersion Er-fiber laser. *Opt. Lett.*, 40(7):1414–1417, 2015.
6. D. S. Kharenko, I. S. Zhdanov, A. E. Bednyakova, E. V. Podivilov, M. P. Fedoruk, A. Apolonski, S. K. Turitsyn, and S. A. Babin. All-fiber highly chirped dissipative soliton generation in the telecom range. *Opt. Lett.*, 42(16):3221–3224, 2017.
7. K. Smith, P. N. Kean, D. W. Crust, and W. Sibbett. An experimental study of a synchronously pumped fibre raman oscillator. *J. Mod. Opt.*, 34(9):1227–1233, 1987.
8. P. N. Kean, B. D. Sinclair, K. Smith, W. Sibbett, C. J. Rowe, and D. C. Reid. Experimental evaluation of a fibre raman oscillator having fibre grating reflectors. *J. Mod. Opt.*, 35(3): 397–406, 1988.
9. A. S. Kurkov, V. V. Dvoyrin, V. M. Paramonov, O. I. Medvedkov, and E. M. Dianov. All-fiber pulsed Raman source based on Yb:Bi fiber laser. *Laser Phys. Lett.*, 4(6):449–451, 2007.
10. Dejiao Lin, Shaif-ul Alam, Peh Siong Teh, Kang Kang Chen, and David J Richardson. Tunable synchronously-pumped fiber Raman laser in the visible and near-infrared exploiting MOPA-generated rectangular pump pulses. *Opt. Lett.*, 36(11):2050–2, 2011.
11. He Chen, Sheng-Ping Chen, Zong-Fu Jiang, Ke Yin, and Jing Hou. All-fiberized synchronously pumped 1120 nm picosecond Raman laser with flexible output dynamics. *Opt. Express*, 23(18): 24088, 2015.
12. Evgeny M. Dianov and Alexander M. Prokhorov. Medium-power CW Raman fiber lasers. *IEEE J. Sel. Top. Quantum Electron.*, 6(6):1022–1028, 2000.
13. Yan Feng, Luke R. Taylor, and Domenico Bonaccini Calia. 150 W highly-efficient Raman fiber laser. *Opt. Express*, 17(26):23678, 2009.

14. S. K. Turitsyn, S. A. Babin, A. E. El-Taher, P. Harper, D. V. Churkin, S. I. Kablukov, Juan Diego Ania-Castañón, V. Karalekas, and E. V. Podivilov. Random distributed feedback fibre laser. *Nat. Photonics*, 4(4):231–235, 2010.
15. E. A. Zlobina, S. I. Kablukov, A. A. Wolf, A. V. Dostovalov, and S. A. Babin. Nearly single-mode Raman lasing at 954 nm in a graded-index fiber directly pumped by a multimode laser diode. *Opt. Lett.*, 42(1):9, 2017.
16. S. A. Babin, E. V. Podivilov, D. S. Kharenko, A. E. Bednyakova, M. P. Fedoruk, V. L. Kalashnikov, and A. A. Apolonski. Multicolour nonlinearly bound chirped dissipative solitons. *Nat. Commun.*, 5:4653, 2014.
17. D. Churin, J. Olson, R. A. Norwood, N. Peyghambarian, and K. Kieu. High-power synchronously pumped femtosecond Raman fiber laser. *Opt. Lett.*, 40(11):2529, 2015.
18. Denis S. Kharenko, Vlad D. Efremov, Ekaterina A. Evmenova, and Sergey A. Babin. Generation of Raman dissipative solitons near 1.3 microns in a phosphosilicate-fiber cavity. *Opt. Express*, 26(12):15084, 2018.
19. Orkhongua Batjargal, Yi-Hsin Ou, Kelli Keikens, Jennifer K. Barton, and Khanh Kieu. All-Fiber Dissipative Soliton Raman Laser Based on Phosphosilicate Fiber. *IEEE Photonics Technol. Lett.*, 30(21):1846–1849, 2018.
20. Claude Aguergaray, David Méchin, Vladimir Kruglov, and John D Harvey. Experimental realization of a mode-locked parabolic Raman fiber oscillator. *Opt. Express*, 18(8): 8680–8687, 2010.
21. Denis S. Kharenko, Anastasia E. Bednyakova, Evgeniy V. Podivilov, Mikhail P. Fedoruk, Alexander Apolonski, and Sergey A. Babin. Cascaded generation of coherent Raman dissipative solitons. *Opt. Lett.*, 41(1):175, 2016.
22. C. J. S. de Matos, S. V. Popov, and J. R. Taylor. Short-pulse, all-fiber, Raman laser with dispersion compensation in a holey fiber. *Opt. Lett.*, 28(20):1891–1893, 2003.
23. Denis S. Kharenko, Anastasia E. Bednyakova, Evgeniy V. Podivilov, Mikhail P. Fedoruk, Alexander Apolonski, and Sergey A. Babin. Feedback-controlled Raman dissipative solitons in a fiber laser. *Opt. Express*, 23(2):1857, 2015.
24. Evgeniy V. Podivilov, Denis S. Kharenko, Anastasia E. Bednyakova, Mikhail P. Fedoruk, and Sergey A. Babin. Spectral comb of highly chirped pulses generated via cascaded FWM of two frequency-shifted dissipative solitons. *Sci. Rep.*, 7(1):2905, 2017.
25. FORC-Photonics. Phosphorus doped fiber PDF-5/125. http://www.forc-photonics.ru/en/fibers_and_cables/P_doped_fibers/1/114
26. Dawn Hollenbeck and Cyrus D. Cantrell. Multiple-vibrational-mode model for fiber-optic Raman gain spectrum and response function. *J. Opt. Soc. Am. B*, 19(12):2886–2892, 2002.
27. R. H. Stolen, J. P. Gordon, W. J. Tomlinson, and H. A. Haus. Raman response function of silica-core fibers. *J. Opt. Soc. Am. B*, 6(6):1159–1166, 1989.
28. Guillermo Salceda-Delgado, Alejandro Martinez-Rios, Boaz Ilan, and David Monzon-Hernandez. Raman response function and Raman fraction of phosphosilicate fibers. *Opt. Quantum Electron.*, 44(14):657–671, 2012.
29. Sergey Smirnov. Efficient numerical model of stimulated Raman scattering in optical fibers. *J. Opt. Soc. Am. B*, 37(4):1219, 2020.
30. A. Chong, W. H. Renninger, and F. W. Wise. Properties of normal-dispersion femtosecond fiber lasers. *J. Opt. Soc. Am. B*, 25(2):140–148, 2008.
31. D. S. Kharenko, O. V. Shtyrina, I. A. Yarutkina, E. V. Podivilov, M. P. Fedoruk, and S. A. Babin. Highly chirped dissipative solitons as a one-parameter family of stable solutions of the cubic-quintic Ginzburg-Landau equation. *J. Opt. Soc. Am. B*, 28(10):2314–2319, 2011.
32. A. Kokhanovskiy, S. Smirnov, and S. Kobtsev. Raman converter of noisy double-scale pulses into coherent pulses. *J. Opt. Soc. Am. B*, 37(8):2523, 2020.
33. Ekaterina A. Zlobina, Denis S. Kharenko, Sergey I. Kablukov, and Sergey A. Babin. Four wave mixing of conventional and Raman dissipative solitons from single fiber laser. *Opt. Express*, 23(13):16589, 2015.

34. C. Xu and F. W. Wise. Recent advances in fiber lasers for nonlinear microscopy. *Nat. Photonics*, 7(11):875–882, 2013.
35. Stuart D. Jackson. Towards high-power mid-infrared emission from a fibre laser. *Nat. Photonics*, 6(7):423–431, 2012.
36. Maxim Karpov, Hairun Guo, Arne Kordts, Victor Brasch, Martin H. P. Pfeiffer, Michail Zervas, Michael Geiselmann, and Tobias J. Kippenberg. Raman Self-Frequency Shift of Dissipative Kerr Solitons in an Optical Microresonator. *Phys. Rev. Lett.*, 116(10):103902, 2016.
37. Tobias Hansson, Daniele Modotto, and S. Wabnitz. Mid-infrared soliton and Raman frequency comb generation in silicon microrings. *Opt. Lett.*, 39(23):6747, 2014.
38. Qi-Fan Yang, Xu Yi, Ki Youl Yang, and Kerry Vahala. Stokes solitons in optical microcavities. *Nat. Phys.*, 1(September):1–6, 2016.
39. Lars Rishoj, Gautam Prabhakar, Jeffrey Demas, and Siddharth Ramachandran. 30 nJ, ˜50 fs All-Fiber Source at 1300 nm Using Soliton Shifting in LMA HOM Fiber. In *Conf. Lasers Electro-Optics*, number c, page STh3O.3, Washington, D.C., 2016. OSA.
40. D. S. Kharenko, V. D. Efremov, and S. A. Babin. Study on harmonic generation regimes of Raman dissipative solitons in an external fibre cavity in a spectral region of 1.3 μm. *Quantum Electron.*, 49(7):657–660, 2019.
41. A. E. Bednyakova, D. S. Kharenko, Innokentiy Zhdanov, E. V. Podivilov, M. P. Fedoruk, and S. A. Babin. Raman dissipative solitons generator near 1.3 mkm: limiting factors and further perspectives. *Opt. Express*, 28(15):22179, 2020.
42. L. Rishøj, B. Tai, P. Kristensen, and S. Ramachandran. Soliton self-mode conversion: revisiting Raman scattering of ultrashort pulses. *Optica*, 6(3):304, 2019.
43. I. Zhdanov, D. S. Kharenko, A. E. Bednyakova, M. P. Fedoruk, and S. A. Babin. All-fiber pulsed laser source based on Raman dissipative soliton generation for biological tissue analysis. In *Ultrafast Nonlinear Imaging Spectrosc. VIII*, volume 11497, page 1149717. SPIE, 2020.
44. A M Khegai, F V Afanas'ev, K E Riumkin, S V Firstov, V F Khopin, D V Myasnikov, M A Mel'kumov, and E M Dianov. Picosecond 1.3-μm bismuth fibre laser mode-locked by a nonlinear loop mirror. *Quantum Electron.*, 46(12):1077–1081, 2016.

Chapter 9
L-Band Wavelength Tunable Dissipative Soliton Fiber Laser

Qianqian Huang, Zinan Huang, Lilong Dai, Mohammed AlAraimi, Zhijun Yan, Junjie Jiang, Aleksey Rozhin, and Chengbo Mou

Abstract We have compared the wavelength tuning capability of filter-controlled fiber laser with cavity loss-controlled fiber laser when they emit dissipative soliton in L band. Two types of typical tunable filters (birefringence filter and fiber taper filter) and variable attenuators (a taper-type attenuator and commercial mechanical attenuator) are selected and incorporated in a fiber laser, respectively. It is observed that tunable filter control is preferred to dissipative soliton wavelength tuning operation, exhibiting wider continuous spectral tunability, more wavelength switchable potential, no forbidden region, less pulse variation and easier implementation. As long as the tunable filter is controlled suitably, the wavelength tuning can be achieved without variation of other cavity parameters, namely, pump power. Also, it is pivotal to choose a suitable tunable filter. Filter with broad operating wavelength range, large free spectral range, high extinction ratio as well as favorable controllability is more desirable in wavelength tunable dissipative soliton fiber laser. Our work may open the door to extend the tuning range of dissipative soliton in fiber laser.

Q. Huang · Z. Huang · L. Dai · J. Jiang · C. Mou (✉)
The Key Lab of Specialty Fiber Optics and Optical Access Network, Shanghai University, Shanghai Institute of Communication and Advanced Data Science, Joint International Laboratory of Specialty Fiber Optics and Advanced Communication, Shanghai, China
e-mail: huangqq@shu.edu.cn; mouc1@shu.edu.cn

M. AlAraimi
Higher College of Technology, Al-Khuwair, Sultanate of Oman
e-mail: mohammed.alaraimi@hct.edu.om

Z. Yan
School of Optical and Electronic Information, Huazhong University of Science and Technology, Wuhan, China
e-mail: yanzhijun@hust.edu.cn

A. Rozhin
Aston Institute of Photonic Technologies (AIPT), Aston University, Birmingham, UK
e-mail: a.rozhin@aston.ac.uk

M. F. S. Ferreira (ed.), *Dissipative Optical Solitons*, Springer Series in Optical Sciences 238, https://doi.org/10.1007/978-3-030-97493-0_9

9.1 Introduction

Recently, the advent of widely wavelength tunable fiber laser has unlocked diverse applications ranging from fiber sensing [1], biomedical research [2], optical signal processing [3], and high capacity optical transmission system [4]. Therefore, intensive researches have been attracted to explore the wavelength tunable fiber laser.

Conventionally, the wavelength tuning operation can be achieved by controlling the effective gain profile. As shown in Fig. 9.1, in a filter-less fiber laser, the foremost factor influencing the effective gain profile is certainly the intrinsic gain spectrum. The broad gain bandwidth creates a basis for wide wavelength tunability. The intrinsic gain spectrum in fiber laser is not immutable, which shows great dependence on gain fiber length [5–7], rare earth doping concentration [8], cavity loss [9–11] as well as pumping scheme [12, 13]. These cavity parameter changes lead to the variation of population inversion level in the gain fiber, which directly connects with the profile of gain spectrum. Early in 2001, A. Bellemare *et al* and S. Yamashita *et al* declared that the gain bandwidth was largely conditional on the length of gain fiber [5, 6]. It was shown that short Er-doped fiber (EDF) length leaded to the reduction of long wavelength emission while long EDF length introduced the limitation of short wavelength emission, thus placing restrictions on wavelength tuning range. By proper selection of EDF length, they realized continuous wave (CW) wavelength tuning operation from 1520 to 1600 nm and from 1480 to 1620 nm, respectively. When the gain fiber is selected, cavity loss change becomes one of the most efficient and easiest ways to modify the intrinsic gain profile. The cavity loss control can be obtained by inserting a variable optical attenuator (VOA) or tunable-ratio output coupler (OC). In 1994, P. Franco *et al* theoretically and experimentally provided the first investigation of cavity loss impact on the wavelength selection by embedding a VOA in laser [9]. Hereafter substantial wavelength tuning operations were realized by adjusting VOA [11, 14–16].

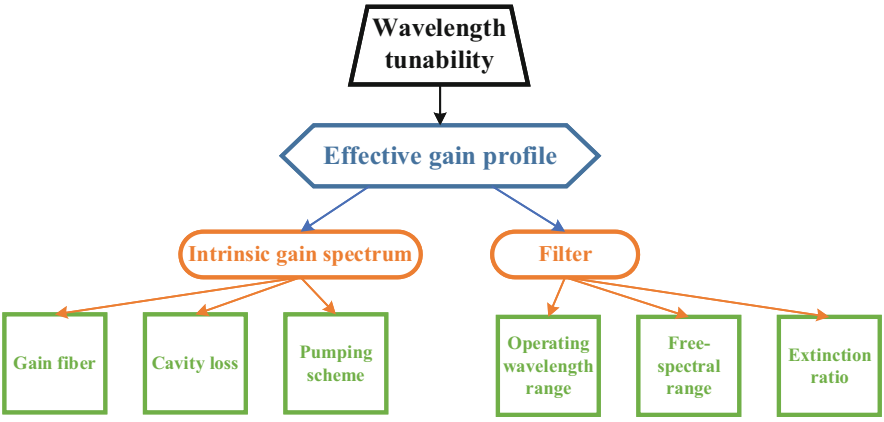

Fig. 9.1 Influences of wavelength tunability in fiber laser

However, taking advantage of tunable-ratio OC to realize wavelength tuning is comparatively rare and firstly achieved in 2006 [17]. This report provided the experimental demonstration of CW wavelength tuning operation from 1567 to 1625 nm and pointed out that the upper limit of tuning range can be extended if the cavity loss greatly reduced, indicating wavelength tuning range extension. One year later, the pulse wavelength tuning operation between 1567 and 1625 nm was obtained in the similar laser scheme where additional Mach-Zehnder modulator was applied [18]. Furthermore, the systematic study about the influence of pump power on wavelength tunability in cavity loss-controlled fiber laser was bought out [12]. It was displayed that the higher pump power could decline the lower limit of wavelength tuning range, permitting wider wavelength tunability. Also, S. Lin *et al* confirmed that different pumping scheme including pump configuration and pump power could give rise to different population inversion distribution, thus resulting in different wavelength emission [13].

When there is an optical tunable filter in the fiber laser, the effective gain profile eventually hinges on the optical tunable filter. Conventionally, optical tunable filter exploited in wavelength tunable fiber laser is mainly divided into bulky-type tunable filter and fiber-type tunable filter. Bulky-type tunable filter contains Mach-Zehnder interferometer [19], Fabry-Perot interferometer [20] and commercial mechanical tunable filter [16]. Despite the fact that bulky-type tunable filter is operational ease, the incorporation will inevitably introduce large insertion loss and break the all-fiber laser construction, leading to integration problem. As an alternative, the fiber format tunable filter is more desirable considering its inherent merits such as simple manufacture, low cost, low insertion loss, miniature dimension as well as good fiber compatibility. The classic examples of fiber-type tunable filters are chirped fiber Bragg grating [21], W-shaped long period grating (LPG) [22], few-mode fiber filter [23], fiber taper [24], birefringence filter [25], *etc*. Worthy of mentioning, the wavelength tuning range and generated pulse performance are susceptible to the features of tunable filter including operating wavelength range, free spectral range (FSR) and extinction ratio. Therefore, great attention must be devoted to choose a reasonable optical tunable filter. Up to now, all previously reported wavelength tuning operations have been achieved by controlling effective gain profile via regulating some specific cavity parameters (gain fiber properties, cavity loss and pumping scheme) or adjusting the well-suited intracavity optical tunable filter.

When wavelength tuning range covers L band, some potential applications of wavelength tunable fiber laser can be extended such as spectroscopy [26], biomedical diagnosis [27], most importantly, enlarging the optical communication capacity further [28]. Consequently, it is of great practical interest to explore L-band wavelength tunable fiber laser. In principle, L-band laser emission can be achieved if the gain spectrum locates at L-band region. In practice, one could employ long EDF length [29] or cascading different type EDFs [30] or reduce the cavity loss to some extent [14] to enable the occurrence of intra-band absorption in EDF, which contributes to the red shift of gain spectrum. As a result, L-band emission can be realized. In order to achieve the combined operation of L-band emission and

wavelength tunability, some attempts have been made in last few years. J. Luo *et al* successfully realized wavelength tuning operation from 1575 to 1603 nm by incorporating long EDF and an intrinsic nonlinear polarization rotation (NPR) related birefringence filter in fiber laser [31]. One year later, the achievement of widely spectral tuning range covering conventional band and L band was reported, where the NPR-related birefringence filter together with cavity loss control were introduced in the laser [15]. At the same year, another effective approach employing W-shape LPG as a tunable band-pass filter was adopted in the realization of wavelength tuning [22]. The center wavelength of the generated pulse could be shifted from 1553 to 1597 nm. Recently, the continuous tuning within the range of 1524–1602 nm has been obtained by rotating a diffraction grating in fiber laser [32].

Nevertheless, the above-mentioned reports center upon the conventional soliton (CS). And multiple CSs could appear sometimes during the wavelength tunable process due to the limited pulse energy, challenging the practical use of these wavelength tunable fiber lasers [15, 31]. On the contrary, dissipative soliton (DS) is more resistant to pulse breaking thanks to relatively high pulse energy and giant pulse chirp, making it useful for some applications that require high energy pulse [33]. DS has been known as the result of fine balance among gain, loss, dispersion and nonlinear effect [34]. Despite these appreciable DS characteristics and potential applications, to date there are only few researches investigating the DS L-band wavelength tunable fiber laser. The first demonstration of DS L-band wavelength tunable fiber laser was proposed by H. Zhang *et al*, where graphene was exploited as a whole band saturable absorber (SA) [35]. Then, DS fiber lasers with wavelength tuning range from 1566 to 1594 nm and from 1581 to 1602 nm were demonstrated by D. Han *et al* [36] and D. Yan *et al* [29], respectively. Very recently, by optimizing the applied EDF length, our group demonstrated a DS widely wavelength tunable fiber laser in which center wavelength could be tuned from 1567 to 1606 nm [37]. It is the widest tuning range obtained in L-band DS fiber laser. However, all of the wavelength tuning operations are realized by using an artificial birefringence fiber. As mentioned above, cavity loss control is also one of the most efficient ways to realize wavelength tuning operation. However, it has not yet been applied in the achievement of DS wavelength tuning. Since DS exhibits some specific characteristics compared with CS, one may wonder whether it have an effect on the effectiveness of this wavelength tuning method. And will different types of VOA affect wavelength tunability? Furthermore, there is no systemic comparison about the influence of different wavelength tuning methods, *i.e.* tunable filter control and cavity loss control, on the wavelength tuning capability and the generated DS performance, which needs in-depth investigation.

In this chapter, we make a comparison between the effects of different wavelength tuning methods, including tunable filter control and cavity loss control, on the wavelength tunability and pulse performance in L-band DS wavelength tunable fiber laser. Two different optical tunable filters including birefringence filter and taper-type filter and two different VOAs including commercial mechanical VOA and taper-type VOA are applied in a laser cavity, respectively. It is turned out that the relatively wider continuous wavelength tuning operation can be obtained by merely

controlling the tunable filter appropriately while simultaneously suitable adjustments of VOA and pump power lead to narrower continuous wavelength tuning range. Therefore, it is identified that for DS wavelength tunability, the tunable filter control is more favorable if a suitable tunable filter is selected. First of all, this wavelength tunable pattern is simple to operate, which need no additional adjustment of other cavity parameters. Especially, it provides greater possibility for the extension of continuous wavelength tuning range due to the absence of forbidden region. Furthermore, it shows less variation of DS performance versus operating wavelength. Moreover, since characteristics of tunable filter have great implications on wavelength tunability and the generated pulse performance, it is important to choose a reasonable filter with broad operating wavelength range, large FSR, high extinction ratio, particularly operation handiness. Our investigation offers a great reference for the construction of DS wavelength tunable fiber laser not just operating in L-band region.

9.2 Laser Design

The proposed laser employs conventional ring cavity format, as illustrated schematically in Fig. 9.2a. It is organized by a commercial wavelength-division multiplexer (WDM), an isolator (ISO), a 30:70 OC, a SA provided by single walled carbon nanotubes (SWCNTs) film, 2.86 m EDF (OFS EDF 80), a section of single mode fiber (SMF), and most importantly, the key component of wavelength tunability. The net cavity dispersion is always managed to be positive to allow the generation of DS. It is noteworthy that the EDF length has been optimized to ensure wide gain spectrum covering L band, creating a basis of widely L-band wavelength tunability. The corresponding amplified spontaneous emission (ASE) spectra in log scale and linear scale under 70 mW pump power are shown in Fig. 9.2b. It is seen that they cover the whole L-band region with a peak of 1574 nm, which is attributed to intraband absorption occurrence when EDF length is long [31]. Figure 9.2c displays the nonlinear transmission of SWCNTs-SA with a home-made L-band fiber laser, indicating the modulation depth of 3.15%, saturation fluence of 1.34 μJ/cm^2 and

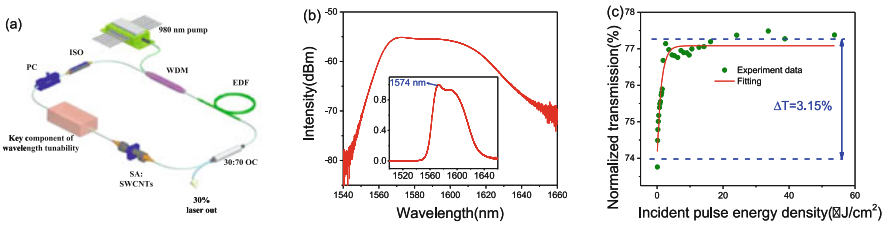

Fig. 9.2 (**a**) The schematic configuration of L-band wavelength tunable fiber laser. (**b**) The ASE spectra in log scale and in linear scale (inset) under 70 mW pump power. (**c**) The measured nonlinear transmission of SWCNTs-SA

nonsaturable loss of 23.85%. It manifests that the SWCNTs-SA is capable of mode locking in L band. In general, the cavity loss is supposed to be reduced so as to increase the long wavelength extremity of tuning range [17]. In this sense, OC with small output ratio is more favorable. However, given that the small saturation fluence of SWCNTs-SA is conducive to pulse splitting [38], the OC with appropriate output ratio (30:70) is carefully chosen. Besides, in our experiment, we only replace different key components of wavelength tunability while maintaining similar cavity structure.

9.3 Methods of Wavelength Tuning

9.3.1 Wavelength Tuning Based on Spectral Birefringence Filter with 45°Tilted Fiber Grating

9.3.1.1 Laser Setup and Device Characteristics

The spectral birefringence filter generally involves a pair of polarizers and a section of birefringence fiber [39]. Only one polarizer is required thanks to the ring cavity configuration, where the applied fibers can be deemed as birefringence medium. Apart from its structural simplicity, it possesses other appealing virtues such as low expense, low loss, good fiber compatibility, wide operating wavelength range, great robustness and high flexibility. In our experiment, a 45 degree tilted fiber grating (45°TFG) utilized as a desired fiber-type polarizer [40] is introduced in the ring fiber laser, as depicted in Fig. 9.3a. Typical characteristics of the 45°TFG are shown in Fig. 9.3b, where the peak of polarization dependent loss (PDL) value is up to 48 dB locating at 1593 nm. We should stress that such 45°TFG is designed specifically to make the PDL response spread over the whole L band. Also, it can be seen that a

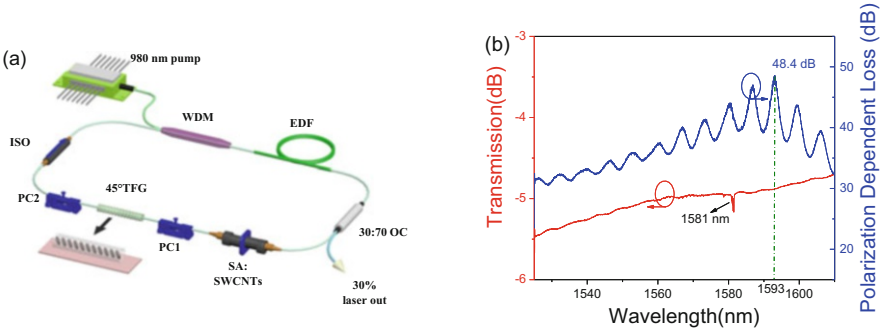

Fig. 9.3 (**a**) The L-band wavelength tunable fiber laser configuration based on birefringence filter. (**b**) The transmission curve and PDL response of 45°TFG

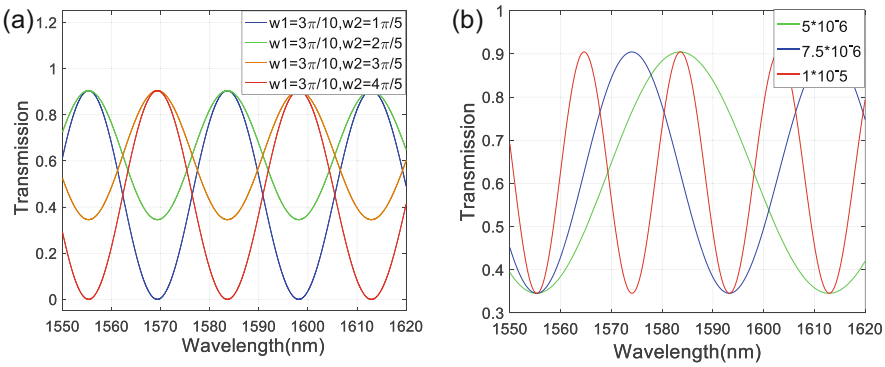

Fig. 9.4 The simulation transmission curves with (**a**) different ω_1 and ω_2 and (**b**) different birefringence strengths

clear dip lies at 1581 nm attributed to the existence of second order Bragg resonance. The cavity length is designed to 8.71 m and net dispersion is calculated to +0.06 ps^2/km.

The transmission curve of the spectral birefringence filter can be stimulated easily if the cavity parameters are plugged into the transmission function of this type filter, which has been described detailly in Ref. [41]. Transmission curves with different angles of polarizer and analyzer with respect to the fast axis of fiber (ω_1 and ω_2) and with different birefringence strengths are plotted in Fig. 9.4, respectively. It is clear that different ω_1 and ω_2 result in the variations of peak location and extinction ratio while the change of birefringence strength is able to alter the FSR value. In practice, adjusting PC can cause the alternation involving ω_1, ω_2 and birefringence strength, which has a great effect on gain distribution. As a result, wavelength selection can be realized.

9.3.1.2 Experimental Results and Discussions

When pump power is set at 55 mW, single pulse oscillation is obtainable immediately. The wavelength tunability within the range of 1570.81–1602.03 nm is achieved under pump power of 57 mW by merely manipulating the intracavity PCs, as presented in Fig. 9.5a. The operating wavelength locates in L band, benefiting from the effective optimization of EDF as well as the suitable properties of the birefringence fiber. The pulse spectra sustain rectangular-like profiles over the whole tuning range, taken as an indication of DS generation. The corresponding pulse bandwidth and duration at different center wavelength are shown in Fig. 9.5b. The 3 dB bandwidth varies from 5.2 to 12.2 nm while the pulse duration varies from 8 to 25 ps. Clearly, DS within range of 1575–1593 nm exhibits wider pulse duration and narrower pulse bandwidth. The variation of pulse performance under different operating wavelength is attributed to different pulse shaping effect, which is greatly dependent on intracavity polarization state, gain intensity and cavity dispersion.

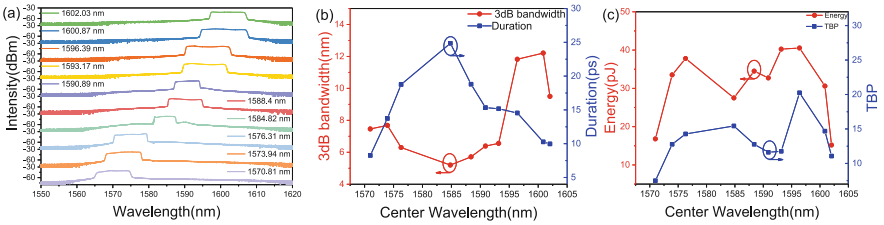

Fig. 9.5 (**a**) Optical spectra over the entire wavelength tuning range from 1602.03 to 1570.81 nm. (**b**) 3 dB bandwidth and pulse duration at different center wavelength. (**c**) Pulse energy and TBP as a function of center wavelength

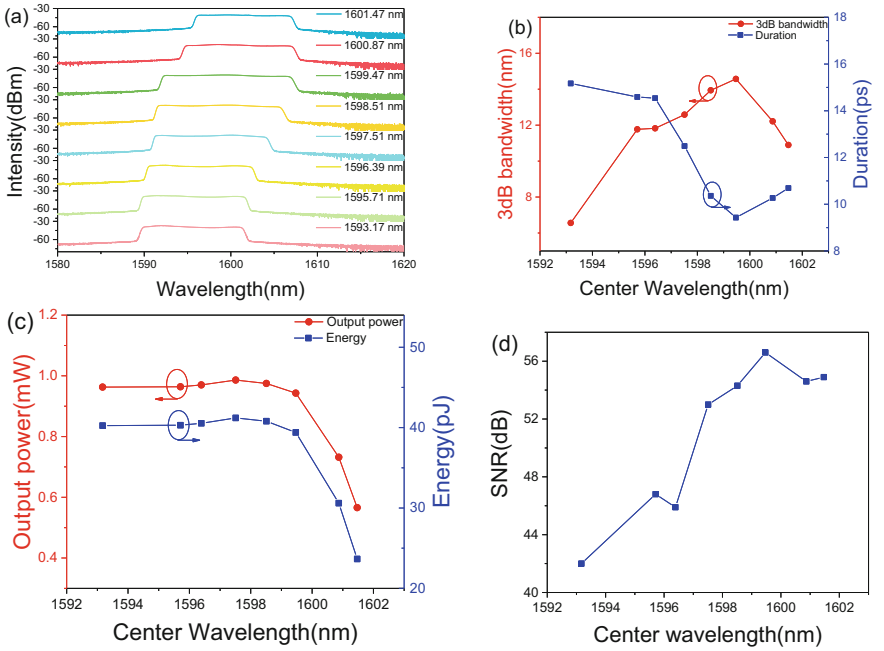

Fig. 9.6 The evolutions of DS performances with continuous wavelength tuning of 1601.47–1593.17 nm: (**a**) Output spectra, (**b**) 3 dB bandwidth, pulse duration, (**c**) output power, pulse energy, (**d**) and SNR at different center wavelength

Figure 9.5c displays pulse energy and time bandwidth product (TBP) versus center wavelength, suggesting little variations except for the points on both sides of the wavelength tuning range.

It should be noted that the continuous wavelength tuning only occurs at the range of 1593–1601 nm by rotating a PC in a single direction, as described in Fig. 9.6a. Considered that DS is a result of delicate balance among gain, loss, dispersion and nonlinearity, it is easy to upset the balance when adjusting intracavity PC, resulting in disappearance of mode locking or transformation to noise-like pulse. As a result, the continuous tuning range is narrower compared to wavelength tunability of

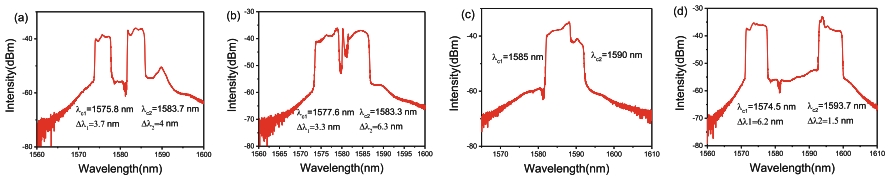

Fig. 9.7 The dual-wavelength spectra with different wavelength spacings under different PCs settings

CS. The pulse performances within the continuous wavelength range are illustrated in Fig. 9.6b–e. As shown in Fig. 9.6b, the DS with broader bandwidth shows narrower pulse duration. And the shortest pulse is 9.43 ps under the status of 1599.47 nm center wavelength. The 3 dB bandwidth varies from 6.5 to 14.5 nm, and the pulse duration changes from 9.34 to 15.2 ps. The changes of output power and pulse energy are displayed in Fig. 9.6c. From it, we can see that both of them are relatively lower at the long wavelength end of wavelength tuning range (1600 nm and 1601 nm) due to the smaller gain intensity, while pulses within the range of 1593–1599 nm show relatively stable output power and pulse energy. The notable pulse stability is verified by the facts that all of the signal-to-noise ratios (SNRs) are better than 42 dB and the mode locking under different center wavelength can maintain for a few hours in good working order.

In addition, the wavelength switchable and dual-wavelength operations appear frequently provided that the PCs are set at appreciate states, reflecting excellent wavelength switchable potential of the birefringence filter-based laser. The dual wavelength spectra with different wavelength spacings are depicted in Fig. 9.7, where there is always a dip at 1581 nm resulting from the existence of second order Bragg resonance.

As mentioned above, the achievement of wavelength tunability stems from the alternative of the birefringence filter transmission by adjustment of intracavity PCs. Proceeding from our experiment, the tunable filter-controlled method of wavelength tuning based on birefringence filter offers the merits including simple operation, convenient installation, low expense and excellent wavelength switchable potential. However, filter features including FSR, peak location and extinction ratio are related to PCs settings, which results in the difficulty of precise wavelength control, relatively narrow continuous wavelength tuning range, poor reversibility as well as repeatability. In our experiment, the restraint of wavelength tuning range is imposed by the low delivered pump power. On the one hand, the applied SWCNTs-SA featuring low saturation fluence is advantageous to pulse breaking. To avoid this, the pump power must be reduced. On the other hand, NPR exists not only as a mere birefringence filter but also as a mode-locking element if high pump power is launched. It gives rise to DS generation with broad bandwidth, making implementation of wavelength tuning complex. Therefore, if the SWCNTs-SA is removed and the cavity dispersion is managed to be more positive simultaneously, the wavelength tuning range is expected to be extend dramatically with high pump power, similar to Ref. [37]. But the continuous wavelength tuning range will be reduced instead.

9.3.2 *Wavelength Tuning Based on Tunable Filter with Fiber Taper*

9.3.2.1 Laser Setup and Device Characteristics

Fiber taper has been a sought-after device in many applications such as fiber sensing [42], supercontinuum generation [43], and fiber coupler fabrication [44]. Interestingly, it is also found that fiber taper can function as an effective tunable filter applied in wavelength tunable fiber laser [24]. Conventionally, fiber taper is fabricated by heating and stretching SMF, where the coating is peeled off. When the fiber diameter is reduced to some extent, the single mode light is allowed to couple into different modes, which interfere mutually in the waist zone, leading to periodic oscillation in the transmission curve. As expected, stretching fiber taper without heating causes the change of interaction length, subsequently blue-shifting the spectral response [24]. The phenomenon reflects the key property of tunable filter. The taper-type filter shows conspicuous advantages including low insertion loss, simple manufacture, ease of integration and high miniaturization.

In our experiment, a fiber taper is connected after SWCNTs-SA, as shown in Fig. 9.8a. It is mounted between two precision 3-axis micro-positioning stages (Max312D, Thorlabs), where both pigtails are fixed by a pair of fiber fixtures. The rotation of micrometers with minimum precision of 1 μm attached to the micro-positioning stages enables fiber taper stretched or unstretched. The stretch displacement can be obtained from the micrometer reading. Benefiting from the precious micrometers, the taper-type filter features convenient operation, strong controllability with good accuracy. Figure 9.8b displays the spectral responses with different tensile strength, indicating sinusoidal oscillations with FSR of 24.5 nm and extinction ratio of 1 dB. Notably, the obvious beating behavior is blue-shifted along with the increasing of stretch displacement. The waist zone of applied fiber taper with 7.54 μm taper diameter and about 3 mm taper length is detected by a microscope, as shown in Fig. 9.8c. The cavity length is managed to be 7.62 m and net dispersion is +0.085 ps^2/km. Emphasis should be given that the cavity length is shorter than that of birefringence filter-based laser due to the higher nonlinearity imposed by the fiber taper, which is favorable to single pulse operation.

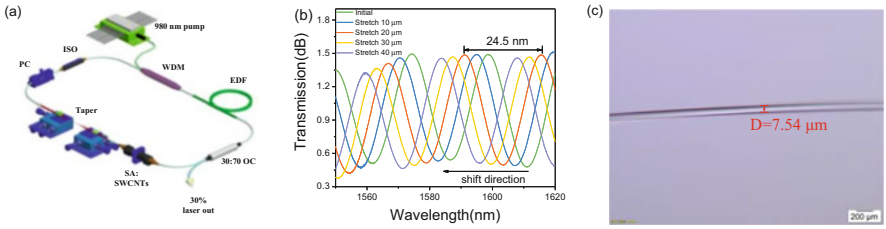

Fig. 9.8 **(a)** The schematic of L-band wavelength tunable fiber laser with a taper-type filter. (**b**) Spectral responses of the taper-type filter with different tensile strength. (**c**) The microscope image of the applied taper

9.3.2.2 Experimental Results and Discussions

Under the initial status of fiber taper, the self-started mode locking with stable DS operating at 1606.25 nm is obtained easily under the pump power of 44 mW. The center wavelength can be tuned continuously by stretching fiber taper while maintaining PC and pump power invariable. Figure 9.9a shows the spectral evolution over the entire wavelength tuning range. From it, we can see that the generated DS with different operating wavelength has similar spectral profile, reflecting a fascinating aspect of admirable wavelength tunable fiber laser. Figure 9.9b summarizes the operating wavelength of DS versus stretch displacement of fiber taper. The center wavelength is shifted from 1606.25 to 1590.65 nm continuously while the corresponding stretch displacement increases from 0 to 60 μm monotonously. Obviously, the relationship between them possesses perfectly linear, reflecting fascinating controllability. If the stretch displacement is enlarged further, the operating wavelength jumps from 1590 to 1606 nm and the wavelength tuning is obtained in a recurrent mode. The reason is attributed to cyclical oscillation in the transmission curve of the used fiber taper. The changes of corresponding pulse characteristics are plotted in Fig. 9.9c–e. The 3 dB bandwidth ranges from 4.6 to 7.5 nm and pulse width changes from 11.8 to 19.5 ps. At the short wavelengths of the tuning range, it exhibits wider pulse duration. And the output power and pulse energy vary from 0.3 to 0.78 mW and from 10.7 to 28.4 pJ, respectively. The operation stability is proved by high SNRs (>45 dB). Also, it should be noted that the presented laser can run sustainably for several hours regardless of the operating wavelength.

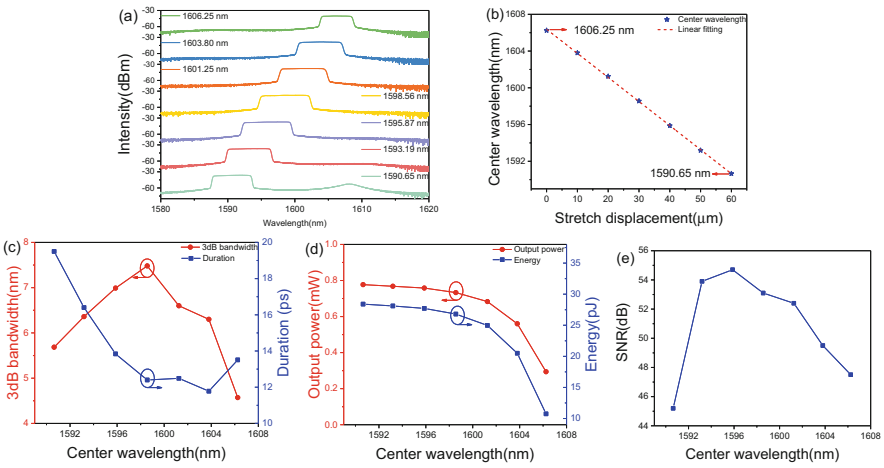

Fig. 9.9 (**a**) Continuously tunable spectra with range of 1606.25–1590.65 nm by stretching fiber taper. (**b**) The operating wavelength of DS versus stretch displacement of fiber taper. Variations of pulse characteristics within the continuous wavelength tuning range: (**c**) 3 dB bandwidth and pulse duration, (**d**) output power and pulse energy, (**e**) SNR

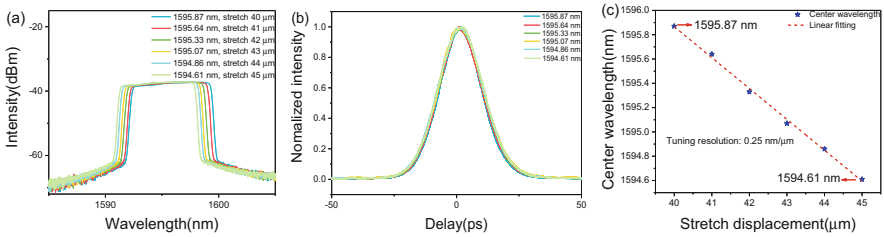

Fig. 9.10 (**a**) Output spectra of the precise wavelength tuning process over the range of 1595.87–1594.61 nm with 1 μm stretching interval. (**b**) The corresponding autocorrelation traces. (**c**) The dependence of operating wavelength on relative stretch length within the range

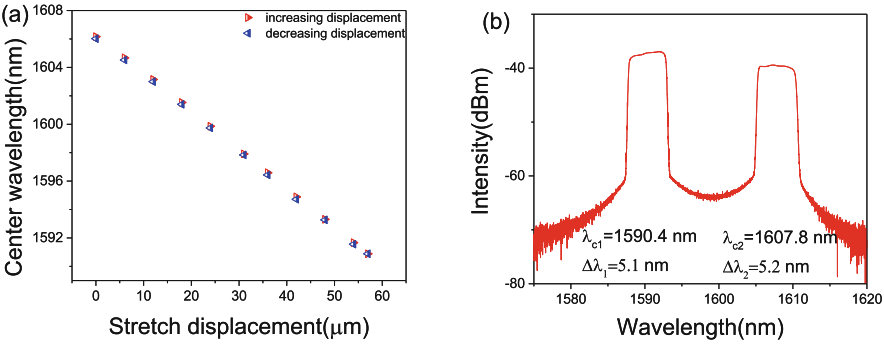

Fig. 9.11 (**a**) Variations of center wavelength when increasing and decreasing displacement of fiber taper. (**b**) The dual-wavelength spectrum

Specifically, benefitting from high stretching sensitivity of fiber taper and high precision of micrometers, the operating wavelength can be tuned with great accuracy. Figure 9.10a visualizes the precise wavelength tuning process over the range of 1595.87–1594.61 nm with 1 μm stretch interval. It is found that accompanying with center wavelength changed, the pulse performances including spectral profile, spectral bandwidth and pulse duration remain almost constant, having positive effect on use of the proposed wavelength tunable fiber laser. The linear dependence of operating wavelength on stretch displacement is manifested in Fig. 9.10c, where the estimate of tuning resolution is 0.25 nm/μm. Remarkably, the fiber taper shows a certain degree of flexibility and elasticity, thus leading to potential reversibility of wavelength tuning. The reversibility is examined in Fig. 9.11a. It is seen that the operating wavelengths almost coincide under the same stretch displacement of fiber taper. Furthermore, the laser permits the generations of wavelength switching and dual-wavelength operation. The dual-wavelength spectrum is shown in Fig. 9.11b. The wavelength spacing is un-adjustable, which determined by FSR of taper-type filter.

As discussed above, taking advantages of fiber taper with intermodal interference, the continuous wavelength tuning is implemented with stretching fiber taper. Considering that the transmission just blue-shifts with invariable FSR and extinction ratio when stretching fiber taper, it will not break conditions of DS generation easily, consequently resulting in long continuous wavelength tuning range. Apart from that, the tunable filter-controlled method based on fiber taper provides favorable properties of simple operation, high precision, good controllability and reversibility. However, one pronounced shortcoming is the easy brittleness of fiber taper, which restricts its practicability. In our experiment, the continuous wavelength range is constrained to FSR and extinction ratio of fiber taper. It is expected that the continuous wavelength tuning range can be scaled up if fiber taper is further optimized [45]. Besides, another effective solution may be to cascade several fiber tapers.

9.3.3 Wavelength Tuning Based on Cavity Loss Control with Commercial Mechanical VOA

9.3.3.1 Laser Setup and Device Characteristics

As we know, mechanical VOA has been a mature product long time ago, where a blocking component is plugged between two collimators generally to cause optical attenuation. It possesses some appealing merits such as small volume, light heft, robust structure, good portability, reliable stabilization and convenient use. In our experiment, a commercial rotary VOA (MVOA Series, AFR) is exploited in laser to control the cavity loss, as shown in Fig. 9.12a. The picture in Fig. 9.12b displays its outward appearance. The insertion loss is also measured over the range of 1520–1620 nm under the initial state of VOA, which is illustrated in Fig. 9.12c. It implies the VOA features fairly wide and flat working band as well as low initial insertion loss of 0.41 dB. The proposed laser with 8.76 m cavity length and net dispersion of +0.059 ps^2/km is similar to that described in Sect. 9.3.3.1.

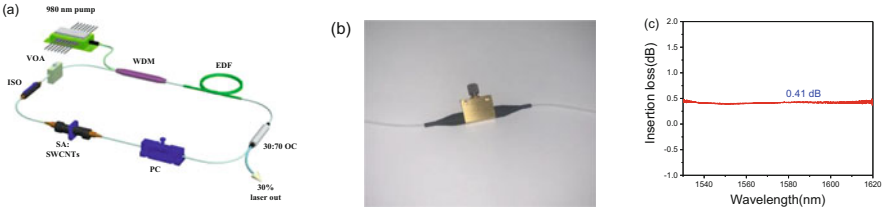

Fig. 9.12 (**a**) Experimental setup of L-band wavelength tunable fiber laser with a commercial mechanical VOA. (**b**) The outward appearance of the applied commercial mechanical VOA. (**c**) The measured insertion loss

9.3.3.2 Experimental Results and Discussions

Initializing mode locking with stable DS operation easily under pump power of 44.7 mW when no additional loss is induced by VOA. When merely adjusting VOA to add cavity loss gradually, the DS spectrum evolves with progressive decreasing of 3 dB bandwidth but nearly constant center wavelength firstly, then transforms into CW or ASE spectrum. The wavelength tuning is achieved by adjusting VOA and pump power simultaneously. The wavelength tuning process ranging from 1600.26 to 1570.43 nm is vividly displayed in Fig. 9.13a. It is clearly seen that under precondition of growing intracavity loss, increasing pump power from 50 to 96.1 mW simultaneously leads to continuous operating wavelength tuning from 1600.26 to 1593.27 nm, while decreasing pump power from 66 to 53 mW simultaneously leads to continuous operating wavelength tuning from 1574.72 to 1570.43 nm. The different variation trends of pump power are attributed to different maximum energy that a single DS can withstand under different operating wavelength. It is noteworthy that when DS works at 1593 nm, the center wavelength switches to 1574 nm directly with occurrence of pulse splitting if the cavity loss is enlarged further. That is to say, there is always a forbidden region where the operating wavelength can't be selected whatever the settings of PC and pump power. It is postulated that the present of large cavity loss results in complete population inversion of EDF, which makes the gain profile similar to ASE spectrum described in Fig. 9.2b [9]. The gain peak is shifted from 1593 to 1574 nm directly, which is consistent with the fact that DS is switched from 1593 to 1574 nm. Figure 9.13b, c display the pulse performances within the entire wavelength tuning range. The pulse duration and TBP at 1570.43 nm can't be obtained due to the low pulse energy and sensitivity limitation of autocorrelator. DS working in the range of 1600.26–1593.27 nm exhibits wider spectral bandwidth and narrower pulse duration overall than those working in the range of 1574.72–1570.43 nm. Figure 9.13c shows that the varying tendency of pulse energy is similar to that of TBP, implying potential connection between pulse energy and pulse chirp [46]. Obviously, the pulse energy increases from 52.4 to 110.6 pJ with center wavelength tuning from

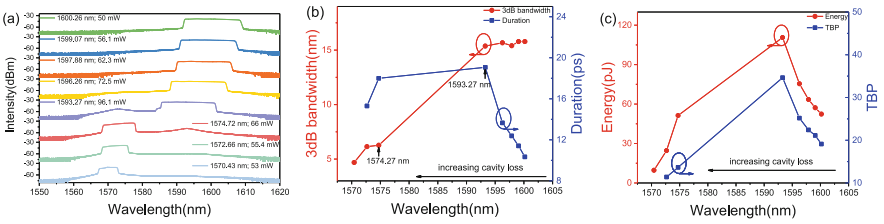

Fig. 9.13 The wavelength tuning process ranging from 1600.26 to 1570.43 nm: (**a**) the output spectra and inserted numbers showing the center wavelength and corresponding pump power. (**b**) 3 dB bandwidth and pulse duration versus center wavelength. (**c**) Pulse energy and TBP versus center wavelength

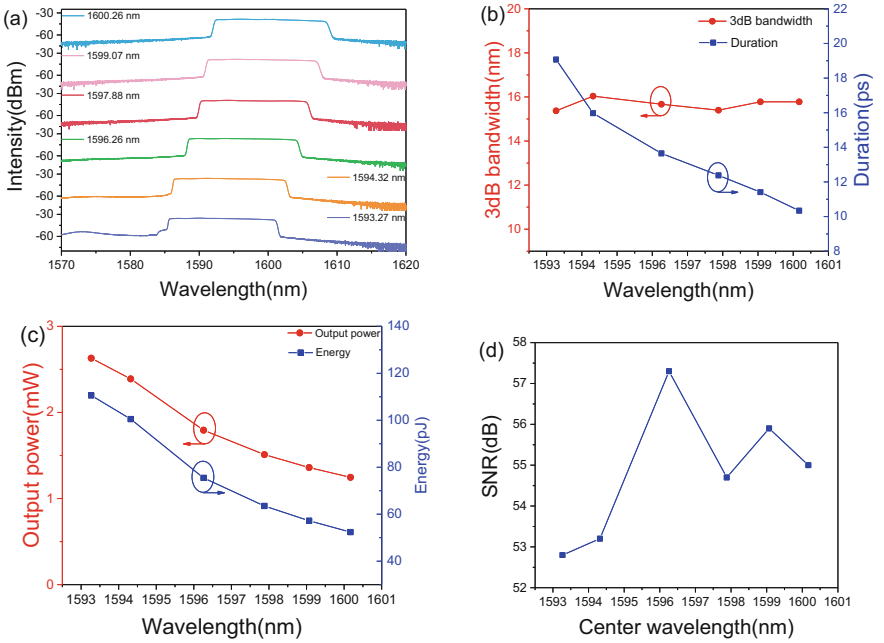

Fig. 9.14 The evolutions of DS performances with continuous wavelength tuning of 1600.26–1593.27 nm: (**a**) Output spectra, (**b**) 3 dB bandwidth, pulse duration, (**c**) output power, pulse energy, (**d**) and SNR at different center wavelength

1600.26 to 1593.27 nm while it decreases from 51.3 to 9.7 pJ with center wavelength tuning from 1574.72 to 1570.43 nm, which is in accordance with the change of pump power.

The DS evolution with continuous wavelength tuning of 1600.26–1593.27 nm is described detailly in Fig. 9.14. It is found that DS at different operating wavelength shows similar spectral profile. Considering the phenomenon that DS spectrum exhibits variable bandwidth and almost constant center wavelength along with the change of cavity energy, the effective control of pulse spectral bandwidth at each operating wavelength can be realized to some extent by managing pump power and cavity loss. In our experiment, the spectral bandwidth is controlled within the range of 15.3–16 nm while the corresponding pulse duration increases monotonously from 10.3 to 19 ps as the decreasing of operating wavelength. Furthermore, the variations of output power, pulse energy resemble the trend of pulse duration variation. The noteworthy pulse stability is verified by high SNR values (>52.5 dB) and the laser is able to work uninterruptedly for several hours, providing a solid evidence of long-term stability. Moreover, the realizations of wavelength switching and dual-wavelength operation with fixed wavelength spacing are demonstrated by careful adjustment of VOA. The dual-wavelength spectra are illustrated in Fig. 9.15. It is

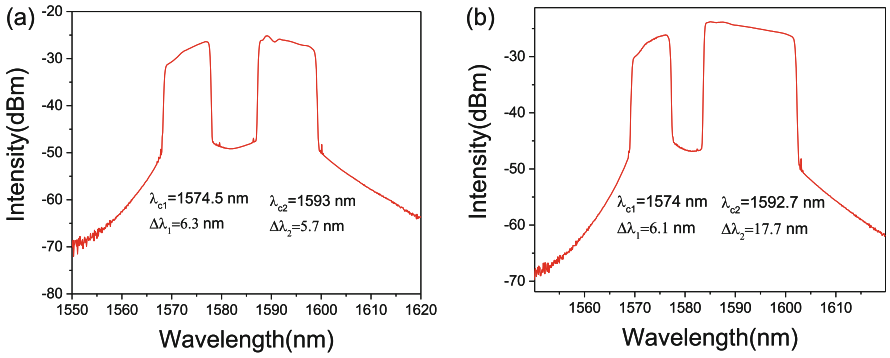

Fig. 9.15 Dual-wavelength spectra with fixed wavelength spacing and different energy distribution

plain to see that some small spikes appear in the spectra, making an indication of instability state. Worthy of mentioning, the energy distribution between two pulses at different center wavelength can be regulated by manipulating VOA carefully.

It is well known that manipulating cavity loss can cause the change of population inversion level, resulting in the modification of intrinsic gain profile and consequently tuning the operating wavelength [9, 12, 14, 15]. It has been checked in many CS wavelength tunable fiber lasers [14, 15]. Hence, in the first instance, we expect to realize DS wavelength tunability easily by merely adjusting VOA. However, in practice, increasing cavity loss enables DS to narrow spectral bandwidth but maintain constant center wavelength, subsequently making DS turn into CW or ASE spectrum. On the one hand, the phenomenon is associated with an intrinsic feature of DS, namely, the increasing of cavity energy causing no pulse splitting but wider spectral bandwidth and invariable center wavelength [47]. It is speculated that due to the distinct DS property, the spectrum possesses narrower bandwidth and constant center wavelength inversely when decreasing cavity loss by adding cavity loss through VOA. On the other hand, further decline of cavity energy can't provide enough energy to generate DS, thus turning into CW or ASE spectrum. Therefore, only the combined operation of adjusting VOA and pump power can tune DS center wavelength, accompanying with control of DS spectral bandwidth. However, the combined operation is complicated. And most importantly, there is always a forbidden region in which operating wavelength can't be selected, imposing conspicuous limitation of laser use. Furthermore, the additional cavity loss is unknown and can't be controlled precisely, because the applied VOA is mechanical rotation, making the wavelength tuning process lack of reproducibility. In addition, the VOA with spatial structure breaks all-fiber structure of laser. In this experiment, the wavelength tunability is constrained by relatively large original cavity loss and low pump power. As mentioned in Sect. 9.3.2, SWCNTs-SA with small saturation fluence is the main restraint. As a consequence, one solution is to choose a suitable SA and reduce output ratio.

9.3.4 *Wavelength Tuning Based on Cavity Loss Control with Taper-Type VOA*

9.3.4.1 Laser Setup and Device Property

Fiber taper, found to be particularly susceptible to bend, has been a great candidate for a fiber-type VOA [16, 48, 49]. It is preferred to conventional commercial VOA mentioned in Sect. 9.3.3 since it features low insertion loss, all-fiber format, simple manufacture, low cost, reading availability, accurate controllability and easy operation. The proposed laser structure is same as that of Sect. 9.3.2, as shown in Fig. 9.16a, where fiber taper is bent by controlling micrometers attached to the micro-positioning stages. The difference is the characteristics of applied fiber taper. It is seen from Fig. 9.16b that the insertion loss increases along with the curvature increased. When there is no bending of fiber taper, the original insertion loss is 0.74 dB at 1601 nm. Figure 9.16c displays the microscope image of taper waist zone, suggesting taper waist diameter of 30.66 μm and taper waist length of 0.7 mm. The laser length and net dispersion are designed identically with those described in Sect. 9.3.3.

9.3.4.2 Experimental Results and Discussions

Under the original state of fiber taper, the mode locking with stable DS operation is achieved automatically by inputting pump power above 41 mW. The low threshold is mainly attributed to additional nonlinearity introduced by fiber taper. The experimental phenomena are quite close to those described in Sect. 9.3.3. including DS evolutions with just controlling additional cavity loss and with controlling cavity loss and pump power at the same time. Likewise, the combined operation of adjusting cavity loss and pump power is carried out to realize DS wavelength tunability. The spectral evolution and the changes of DS characteristic over the entire wavelength tuning range are plotted in Fig. 9.17. The center wavelength is shifted continuously from 1601.07 to 1593.7 nm with pump power increased from

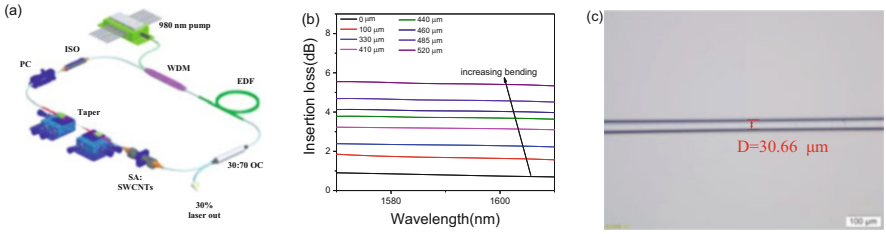

Fig. 9.16 (**a**) The schematic diagram of L-band wavelength tunable fiber laser with a taper-type VOA. (**b**) The insertion loss responses along with the increasing of curvature. (**c**) The microscope image of the applied taper

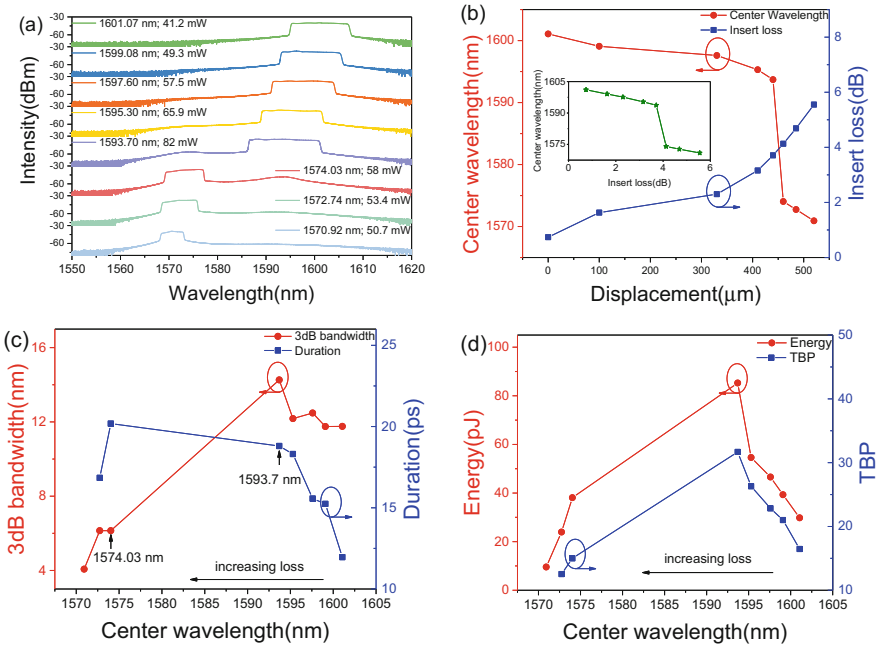

Fig. 9.17 The wavelength tuning process ranging from 1601.07 to 1570.92 nm: (**a**) the output spectra and inserted numbers showing the center wavelength and corresponding pump power. (**b**) Center wavelength and insertion loss of fiber taper along with the increasing displacement. Inset: center wavelength as a function of insertion loss of fiber taper. (**c**) 3 dB bandwidth and pulse duration versus center wavelength. (**d**) Pulse energy and TBP versus center wavelength

41.2 to 82 mW and additional loss increased from 0.74 to 3.71 dB while when center wavelength is tuned from 1574.03 to 1570.92 nm with increasing additional loss from 4.13 to 5.55 dB, the corresponding pump power is decreased from 58 to 50.7 mW. Notably, the operating wavelength undergoes a jump from 1593.7 to 1574.03 nm with pulse splitting when additional loss is only enlarged from 3.71 to 4.13 dB, meaning the existence of a forbidden region. Apart from the wavelength switching from 1593.7 to 1574.03 nm, the relation between center wavelength with insertion loss of taper exhibits approximately linear slope, as depicted in the inset of Fig. 9.17b. Worthy of mentioning, the insert taper loss is enlarged exponentially with respect to increasing bend displacement of fiber taper [16]. The 3 dB bandwidth and pulse duration vary from 4 to 14.3 nm and from 12 to 20.2 ps, respectively. The variation trends of energy and TBP are alike, showing the inherent link between them. The pulse energy changes from 10 to 85 pJ while the TBP changes from 12.5 to 32.

The continuous wavelength tuning ranges from 1601.07 to 1593.7 nm plotted in Fig. 9.18. Due to the fact that taper-type VOA features readable additional loss and accurate loss controlling, the center wavelength can be tuned more delicately. The center wavelength is shifted almost linearly with insertion loss of taper and pump

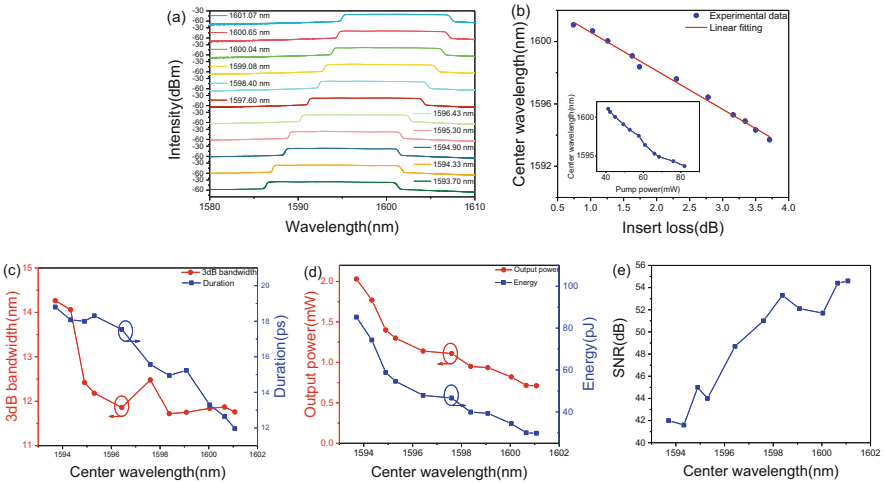

Fig. 9.18 (**a**) Continuously tunable spectra with range of 1601.07–1593.7 nm by bending fiber taper and increasing pump power simultaneously. (**b**) The operating wavelength of DS versus insertion loss of fiber taper. Insert: the operating wavelength versus pump power. Some pulse performances within the continuous wavelength tuning range: (**c**) 3 dB bandwidth, pulse duration, (**d**) output power, pulse energy, (**e**) and SNR at different center wavelength

power. The 3 dB bandwidth varies from 11.7 to 14.3 nm and the corresponding pulse duration increases monotonously along with the decreasing of center wavelength. Similarity, the spectral bandwidth can be controlled to some extent benefiting from the distinct DS spectrum changing versus the change of cavity energy. The variations of output power and pulse energy show monotonous increasing trends with decreasing of center wavelength. The measured SNR values are over 42 dB regardless of operating wavelength, reflecting outstanding stability. And the long-term stability is also tested by a few hours continuous work of the proposed fiber laser. Furthermore, the wavelength switching and dual-wavelength operation are similar to those described in Sect. 9.3.3. The dual-wavelength spectrum is illustrated in Fig. 9.19, where there is no spike implying relatively stable state.

Regarding the fact that increasing curvature of taper results in enlargement of taper insertion loss, the fiber taper employed as VOA can be used to tune operating wavelength. It not only maintains all-fiber laser structure, but also leads to more precise wavelength tunability with good repeatability. It mainly benefits from some instinctive features of taper-type VOA including all-fiber format, readable additional loss, accurate loss controlling and easy manipulation. Taking full advantages of the distinct DS spectrum changing versus the change of cavity energy, DS operation with a degree of spectral bandwidth controllability can be realized. However, this DS property also leads to necessity of simultaneous control of pump power and cavity loss for the purpose of wavelength tuning, which increases operation complexity. Besides, the obtained wavelength tunability still remains the inherent shortcoming of cavity loss-controlled method, namely, the existence of forbidden region.

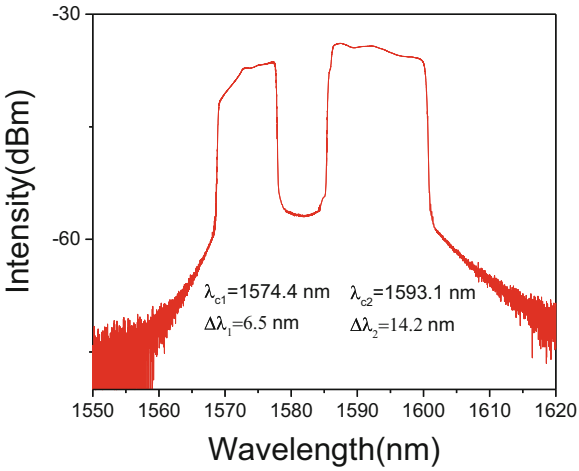

Fig. 9.19 Dual-wavelength spectrum with fixed wavelength spacing

Additionally, the fiber taper is inherently fragile, making it easy to be broken. Similar to the discussion in Sect. 9.3.3, it is believed that the wavelength tuning range is limited by the initial cavity loss and limited pump power. Besides the improvements mentioned in Sect. 9.3.3, another solution is to choose better fiber taper which possesses lower initial insertion loss and higher bending sensitivity.

9.3.5 Comparison with Different Wavelength Tuning Methods

Table 9.1 summarizes the properties of the four L-band DS wavelength tunable fiber lasers mentioned above. For comparison of different filters influence on wavelength tunability, the first two lines show the wavelength tunability and pulse performance in a birefringence filter-based laser and a taper-type filter-based laser, respectively. The high nonlinearity provided by taper-type filter has a contribution to lower the pump threshold. Clearly, the birefringence filter-based laser features wider wavelength tuning range but narrower continuous wavelength tuning range. It means that the wavelength tunability is closely interrelated with filter selection. On the one hand, in our experiment, the birefringence filter presents larger and more flexible FSR than taper-type filter, thereby leading to wider wavelength tuning range. On the other hand, the adjustment of PC in birefringence filter-based laser can introduce many filter parameter changes including FSR, extinction ratio and peak location, which impairs the delicate balance among dispersion, nonlinearity, gain and loss, resulting in disappearance of DS. Alternatively, the taper-type filter can sidestep this drawback, whose transmission curve shifts without changing FSR and extinction ratio via stretching the fiber taper, thus possessing wider continuous wavelength tuning range. Furthermore, this unique property allows smaller range of pulse performances changes, which is favorable to practical applications. Furthermore,

Table 9.1 Properties of L-band DS wavelength tunable fiber lasers

Key component in laser	Pump threshold (mW)	Tuning range (nm)	Continuous tuning range (nm)	Forbidden region (nm)	Pulse performances when center wavelength locates at the range of 1593–1601 nm				
					Pump power (mW)	3 dB bandwidth (nm)	Pulse width (ps)	Energy (pJ)	TBP
Birefringence filter	55	1570–1602	1593–1601	NO	57.1	6.5–10	9.5–15	23–40	13–20.2
Taper-type filter	44.6	1590–1606	1590–1606	NO	44	6–7.5	12–16	25–28	8.5–12.5
Commercial VOA	44.7	1570–1600	1593–1600	1574–1593	50–96	15–16	10–19	52–111	19–35
Taper-type VOA	41	1570–1601	1593–1601	1574–1593	41–82	11.7–14.3	12–19	30–86	16–32

the taper-type filter possesses inherent advantage of good controllability with high accuracy, making the wavelength tuning become precisely controllable, reversible and repeatable. Also, it is pointed out that the DS generated from taper-type filter-based laser shows narrower spectral bandwidth, wider pulse duration, lower pulse energy and smaller pulse chirp. It primarily results from lower pump power and larger positive dispersion rather than different properties of the chosen filters since FSRs of two filters are too large to limit the DS spectral bandwidth. Therefore, a filter having combined advantages from the two filters, viz. broad operating wavelength range, large FSR, high extinction ratio as well as favorable controllability, is an optimal choose to realize wide wavelength tuning.

In order to compare the effect of different VOAs on wavelength tunability, the last two lines show the wavelength tunability and pulse performance in a commercial mechanical VOA-based laser and a taper-type VOA-based laser, respectively. Likewise, the laser with a fiber taper has lower pump threshold due to the induced additional nonlinearity. It comes to our attention that there is no obvious difference in wavelength tuning range, continuous wavelength tuning range as well as pulse performances variation. It suggests that the VOA properties have little effect on wavelength tunability and pulse performance variation. In particular, considering the instinctive merits of taper-type VOA such as all-fiber format, readable additional loss, accurate loss controlling and easy manipulation, the wavelength tuning process exhibits better controllability, accuracy and reproducibility. In addition, it is seen that the obtained DS in the taper-type VOA-based laser with narrower spectral bandwidth, wider pulse duration, lower pulse energy and smaller pulse chirp is mainly because of the lower pump power (the cavity dispersions are same).

Comparatively, Table 9.1 gives the impression that tunable filter control is superior to cavity loss control in terms of DS wavelength tunability. Firstly, regarding the remarkable phenomenon that DS spectrum shows decreasing spectral bandwidth but invariable center wavelength when only increasing cavity loss, the collaborative adjustment of pump power and cavity loss is supposed to be carried out in cavity loss-controlled fiber laser. Fortunately, in tunable filter-controlled fiber laser, it is only necessary to control the applied filter, verifying the effectiveness and manipulability of this method. Moreover, there is no forbidden region in which center wavelength can't be selected in tunable filter-controlled fiber laser, providing more possibility for the realization of wider continuous wavelength tuning. The reason is that the effective gain profile is decided by intrinsic gain spectrum together with the filter property. Benefitting from it, the wavelength switchable operations with different wavelength spacings are possible to be realized. Particularly, the variations of pulse performance in tunable filter-controlled laser are seemed to be smaller than those of cavity loss-controlled laser. On the one hand, only filter is needed to be adjusted without changing pump power. On the other hand, the existence of filter can reduce the sensitivity of pulse performances from cavity parameter change to some extent, such as dispersion, gain intensity [9]. However, as for the cavity loss control, the only virtue is a degree of DS spectral bandwidth controllability. Therefore, the tunable filter control is more favorable to realized DS wavelength tunability in fiber laser.

9.4 Conclusion

We have evaluated the usability of tunable filter control and cavity loss control on DS wavelength tunability in L-band fiber laser. Two typical filters—birefringence filter and taper-type filter, and two typical VOAs—commercial mechanical VOA and taper-type VOA, are served as key components incorporated in laser, respectively. Through symmetric comparison and analysis, it is identified that the tunable filter control outperforms cavity loss control in terms of DS wavelength tuning. First of all, wavelength tuning requires only adjustment of the applied filter, highlighting operation simplicity. More importantly, the obtained wavelength tuning operation features wider continuous tuning range, more wavelength switchable potential, no forbidden region, less pulse variation. Furthermore, it is found that the wavelength tunability is closely bound up with filter property. If the applied filter features broad operating wavelength range, large FSR, high extinction ratio, and outstanding controllability with good accuracy, the wavelength tuning operation is able to possess wide wavelength tuning range, high tunable resolution, great reversibility as well as repeatability. In this regard, exploration of fiber-type tunable filter with miniaturization, highly-integration and high performance is forecasted to be one of the most potential future trends. Reciprocally, the development of fiber-type filter can accelerate the advance of wavelength tunable laser sources. Our research not only enables deeper understanding of wavelength tunable mechanism, but also provides guidelines to construct DS wavelength tunable fiber laser, not just working in L band. From the applied perspective, wavelength tunable fiber laser with attractive characteristics such as wide wavelength tuning range, high tunable resolution, great reversibility and repeatability is advantageous to expand application scope.

Acknowledgments We would like to express our gratitude to the National Natural Science Foundation of China (NSFC) (61975107,61605107) and Natural Science Foundation of Shanghai (20ZR1471500). RAEng and the Leverhulme Trust Senior Research Fellowships (LTSRF1617/13/57).

References

1. X. Hao, Z. Tong, W. Zhang, and Y. Cao, Opt. Commun. **335**, 78-81 (2015)
2. S. Huang, Y. Wang, P. Yan, J. Zhao, H. Li, and R. Lin, Opt. Express **22**, 11417-11426 (2014)
3. X. Liu, L. Zhan, S. Luo, Y. Wang, and Q. Shen, J. Lightwave Technol. **29**, 3319-3326 (2011)
4. T. Miyazaki, N. Edagawa, S. Yamamoto, and S. Akiba, IEEE Photonics Technol. Lett. **9**, 910-912 (1997)
5. A. Bellemare *et al.*, IEEE J. Sel. Top. Quantum Electron. **7**, 22-29 (2001)
6. S. Yamashita, IEEE J. Sel. Top. Quantum Electron. **7**, 41-43 (2001)
7. X. Dong, P. Shum, N. Ngo, H.-Y. Tam, and X. Dong, J. Lightwave Technol. **23**, 1334 (2005)
8. J. Wagener, P. Wysocki, M. Digonnet, H. Shaw, and D. DiGiovanni, Opt. Lett. **18**, 2014-2016 (1993)

9. P. Franco, M. Midrio, A. Tozzato, M. Romagnoli, and F. Fontana, JOSA B **11**, 1090-1097 (1994)
10. X. Zhao *et al.*, Opt. Express **19**, 1168-1173 (2011)
11. B. Dong, J. Hu, C.-Y. Liaw, J. Hao, and C. Yu, Appl. Opt. **50**, 1442-1445 (2011)
12. V. Deepa and R. Vijaya, Appl. Phys. B **89**, 329-332 (2007)
13. S.-F. Lin and G.-R. Lin, Opt. Express **22**, 22121-22132 (2014)
14. K. Guesmi *et al.*, Opt. Lett. **39**, 6383-6386 (2014)
15. Y. Meng, M. Salhi, A. Niang, K. Guesmi, G. Semaan, and F. Sanchez, Opt. Lett. **40**, 1153-1156 (2015)
16. M. Melo, O. Frazao, A. Teixeira, L. Gomes, J. F. Da Rocha, and H. Salgado, Appl. Phys. B **77**, 139-142 (2003)
17. G.-R. Lin, J.-Y. Chang, Y.-S. Liao, and H.-H. Lu, Opt. Express **14**, 9743-9749 (2006)
18. G.-R. Lin and J.-Y. Chang, Opt. Express **15**, 97-103 (2007)
19. J. Zhang *et al.*, J. Opt. **14**, 015402 (2011)
20. J. S. Milne, J. M. Dell, A. J. Keating, and L. Faraone, J. Microelectromech. Syst. **18**, 905-913 (2009)
21. J. Wang, Y. Yan, A. P. Zhang, B. Wu, Y. Shen, and H.-y. Tam, Opt. Express **24**, 22387-22394 (2016)
22. J. Wang, A. P. Zhang, Y. H. Shen, H.-y. Tam, and P. Wai, Opt. Lett. **40**, 4329-4332 (2015)
23. Y. Qi *et al.*, Opt. Laser Technol. **81**, 26-32 (2016)
24. K. Kieu and M. Mansuripur, Opt. Lett. **31**, 2435-2437 (2006)
25. Z. Zhang, Z. Xu, and L. Zhang, Opt. Express **20**, 26736-26742 (2012)
26. J. Marshall, G. Stewart, and G. Whitenett, Meas. Sci. Technol. **17**, 1023 (2006)
27. O. Okhotnikov, A. Grudinin, and M. Pessa, New J. Phys. **6**, 177 (2004)
28. A. Srivastava *et al.*, IEEE Photonics Technol. Lett. **12**, 1570-1572 (2000)
29. D. Yan, X. Li, S. Zhang, M. Han, H. Han, and Z. Yang, Opt. Express **24**, 739-748 (2016)
30. Z. Wang, L. Zhan, X. Fang, C. Gao, and K. Qian, J. Lightwave Technol. **34**, 4128-4134 (2016)
31. J. L. Luo *et al.*, IEEE Photonics Technol. Lett. **26**, 2438-2441 (2014)
32. B. Nyushkov, S. Kobtsev, A. Antropov, D. Kolker, and V. Pivtsov, J. Lightwave Technol. **37**, 1359-1363 (2019)
33. Z. Wang, K. Qian, X. Fang, C. Gao, H. Luo, and L. Zhan, Opt. Express **24**, 10841-10846 (2016)
34. P. Grelu and N. Akhmediev, Nat. Photonics **6**, 84-92 (2012)
35. H. Zhang, D. Tang, R. J. Knize, L. Zhao, Q. Bao, and K. P. Loh, Appl. Phys. Lett. **96**, 111112 (2010)
36. D. Han, Appl. Opt. **53**, 7629-7633 (2014)
37. Q. Huang *et al.*, Opt. Express **27**, 20028-20036 (2019)
38. J. Bogusławski, G. Soboń, R. Zybała, and J. Sotor, Photonics Res. **7**, 1094-1100 (2019)
39. Z. Yan *et al.*, Opt. Lett. **37**, 353-355 (2012)
40. K. Zhou, G. Simpson, X. Chen, L. Zhang, and I. Bennion, Opt. Lett. **30**, 1285-1287 (2005)
41. D. Tang, L.-M. Zhao, B. Zhao, and A. Liu, Phys. Rev. A **72**, 043816 (2005)
42. F. J. Arregui, I. R. Matías, and M. López-Amo, Sens. Actuators, A **79**, 90-96 (2000)
43. T. Birks, W. Wadsworth, and P. S. J. Russell, Opt. Lett. **25**, 1415-1417 (2000)
44. J. C. Knight, G. Cheung, F. Jacques, and T. Birks, Opt. Lett. **22**, 1129-1131 (1997)
45. Q. Fang, K. Kieu, and N. Peyghambarian, IEEE Photonics Technol. Lett. **22**, 1656-1658 (2010)
46. W. H. Renninger, A. Chong, and F. W. Wise, JOSA B **27**, 1978-1982 (2010)
47. J. Peng *et al.*, I IEEE Photonics Technol. Lett. **24**, 98-100 (2011)
48. 戴礼龙 *et al.*, 中国激光 **46**, 0508026 (2019)
49. Y. Feng, X. Li, S. Zhang, M. Han, J. Liu, and Z. Yang, IEEE Photonics Technol. Lett. **29**, 2175-2178 (2017)

Chapter 10
Multiplexed Dissipative Soliton Fiber Lasers

Tianye Huang, Pan Huang, Bingye Zhan, Dazhong Zhang, and Zhichao Wu

Abstract In this chapter, the multiplexed dissipative soliton fiber lasers including bidirectional multiplexing, wavelength multiplexing, polarization multiplexing are discussed. In bidirectional multiplexed soliton lasers, the features of various saturable absorbers are introduced. For wavelength multiplexed ones, balancing the gain competition by filter, attenuation or other methods is essential. Additionally, the polarization multiplexed ones are often used as the light sources for dual-comb spectroscopy. Finally, we discussed the emerging multiplexed methods such as mode multiplexing and orbital angular momentum multiplexing.

Keywords Bidirectional multiplexing · Wavelength multiplexing · Polarization multiplexing · Mode multiplexing · Orbital angular momentum multiplexing · Dual-comb · Fiber laser · Nonlinear polarization rotation · Graphene · Carbon nanotube

10.1 Introduction

Since first experimentally observed in single mode fibers (SMFs) by Mollenauer in 1980, solitons as stable localized nonlinear waves, have been investigated in various physical systems, especially in fiber lasers. Apart from dispersion and Kerr nonlinear effect during propagation in SMFs that form the laser cavity, a pulse propagating in a

T. Huang (✉)
School of Mechanical Engineering and Electronic Information, China University of Geosciences (Wuhan), Wuhan, China

Wuhan National Laboratory Optoelectronics, Wuhan, China
e-mail: huangty@cug.edu.cn

P. Huang · B. Zhan · D. Zhang · Z. Wu (✉)
School of Mechanical Engineering and Electronic Information, China University of Geosciences (Wuhan), Wuhan, China
e-mail: wuzhichao@cug.edu.cn

M. F. S. Ferreira (ed.), *Dissipative Optical Solitons*, Springer Series in Optical Sciences 238, https://doi.org/10.1007/978-3-030-97493-0_10

fiber laser is also subject to actions of the laser gain and loss of cavity components, which makes the laser cavity a dissipative system so that Ginzburg-Landau (GL) equation is often used to describe the soliton evolution and dynamics. Since the optical soliton formed in fiber lasers is a result of mutual interaction among the cavity dispersion, fiber nonlinearity, laser gain saturation and gain bandwidth filtering and so on, it is desirable to introduce various multiplexed mechanisms to realize multi-soliton co-existence inside one single mode-locked fiber laser, which can further extend its potential applications.

Firstly, if there is no unidirectional component such as isolator inside laser cavity, it would be a bidirectional oscillation that gives rise to a new dimension of multiplexing. In this type of fiber lasers, the pulses can circulate along either the clockwise or counterclockwise direction as long as the laser gain on the two directions are both efficient. Also, the recovery time of the used mode-locker needs to be quite short in order to support mode-locked operation on both directions. Therefore, artificial mode-lockers based on Kerr nonlinearity are normally used to realize bidirectional mode-locking. Recently, together with relatively long cavity structure, real mode-locked materials such as saturable absorber mirror (SESAM), graphene, carbon nanotube(CNT) also contribute to the direction-multiplexed soliton generation.

Secondly, by utilizing wavelength selection mechanisms and components, such as Mach-Zehnder (MZ) interferometer, chirped fiber Bragg grating (CFBG), Sagnac fiber filter, nonlinear polarization rotation (NPR) filter and so on, dual- or triple-wavelength solitons can be generated in the laser cavity. Compared to those solitons that operate at single wavelength, these wavelength-multiplexed fiber lasers can simultaneously emit pulse-trains at different central wavelengths. Such type of fiber lasers has attracted much interest as ultrafast laser technologies develop rapidly, and they can be used wavelength division multiplexing (WDM) transmission, optical signal processing and precision spectroscopy.

Thirdly, without polarization restriction mechanism, the laser cavity can support two orthogonal polarization modes owing to the fiber birefringence. Vector soliton is a typical form of polarization-multiplexed output which refers to solitons that have mutually coupled polarized components. Consider that vector solitons have been investigated in detail in previous chapters, here we mainly focus on group velocity unlocked polarization-multiplexed fiber lasers. Different from vector solitons that are normally generated in weakly birefringent SMFs, these polarization-multiplexed solitons need manipulation of the optical path along two orthogonal polarized axes to generate two pulses with different repetition rate and less interaction.

In the following sections, we will separately introduce the above three multiplexing methods of generating multi-solitons in dissipative laser cavities.

10.2 Bidirectional Multiplexed Dissipative Soliton Fiber Lasers

For most conventional fiber ring lasers, normally there is an isolator inside the cavity to ensure the unidirectional operation of the laser, thereby reducing the spurious cavity reflection and decreasing the mode-locked threshold. However, the isolator in a ring cavity results in a less compact laser structure and only unidirectional operation of the pulse trains. There have been revived interests in the bidirectional oscillation in fiber-based lasers without an intracavity optical isolator to realize another dimension of multiplexing, i.e. the directional multiplexing. In the bidirectional mode-locked fiber laser, pulses can circulate in either the clockwise (CW) or counterclockwise (CCW) direction, and the CW and CCW pulse trains can be emitted and separated by using a 2 × 2 output coupler (OC). With more complex cavity designs that enable different optical paths for the CW and CCW pulses, the characteristics of the two output pulses can be different and adjustable.

In 1967, the first bidirectional mode-locked laser was demonstrated by Buholz and Chodorow as a gyroscopic sensor [1]. Later, various gyroscopes based on mode-locked lasers were reported. In 2008, Kieu and Mansuripur designed the first stable all-fiber bidirectional passively mode-locked ring laser [2]. Since then, different types of nonlinear elements have been proposed to achieve passive mode-locking, such as the SESAM, NPR, nonlinear optical loop mirrors (NOLM), CNT and graphene. The mode-locked elements of bidirectional mode-locked fiber lasers mainly include CNT, SESAM, NPR, graphene and hybrid elements as shown in Fig. 10.1. Here, hybrid elements refer to more than one mode-locked mechanism in a laser cavity.

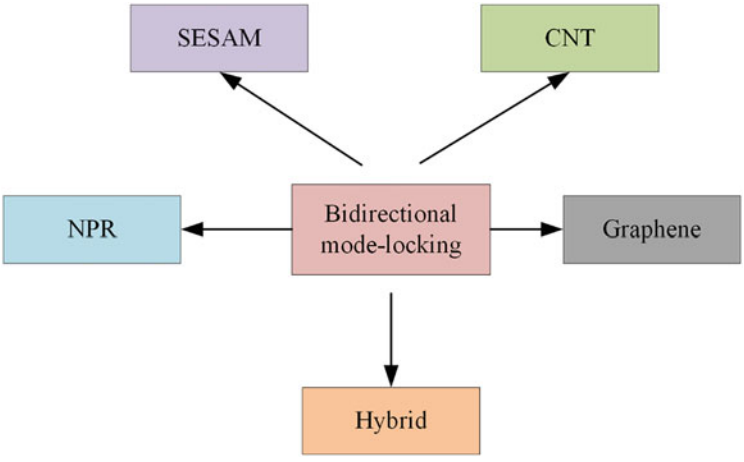

Fig. 10.1 Types of bidirectional mode-locking according to different mode-locked elements

10.2.1 SESAM

Among these mode lockers, SESAM has been widely used for passive mode locking over the past decades. An all-fiber bidirectional passively mode-locked soliton laser with a four-port circulator and two different SESAMs were inserted into the laser cavity to enable bidirectional mode locking as shown in Fig. 10.2a [3]. Two independent countercirculating pulse trains with repetition rates of 21.3 and 15.2 MHz were obtained simultaneously, which also could be adjusted by varying the SESAM pigtail length. The output pulse profiles in the time and frequency domains are illustrated in Fig. 10.2b. Output pulse in the CW direction has a 3-dB bandwidth of 4.1 nm centered at 1558.3 nm, while the pulse in the opposite direction has a 3 dB bandwidth of 2.4 nm centered at 1559.8 nm. Their corresponding pulse durations are 378 and 681 fs, respectively. These different characteristics for the CW and CCW pulses can be explained by the asymmetry of the cavity, which mainly derives from the unidirectional pumping configuration, different cavity lengths and dynamics of the countercirculating pulses. It is worth mentioned that by controlling the intracavity loss imposed on these two pulse trains, either one of the two pulse trains can be independently switched on or off. In Ref. [5], W. Zhou et al. reported on a novel polarization switching laser from a bidirectional passively mode-locked thulium-doped fiber oscillator for the first time. Different from the conventional ring-shaped and linear lasers, the laser was constructed by folding two "overlapped" linear lasers, which simultaneously generated lasers with two directions of CW and CCW. The switching laser was created by combing two orthogonally stable vector solitons, which were found to be wave-breaking-free pulses in the all-anomalous-

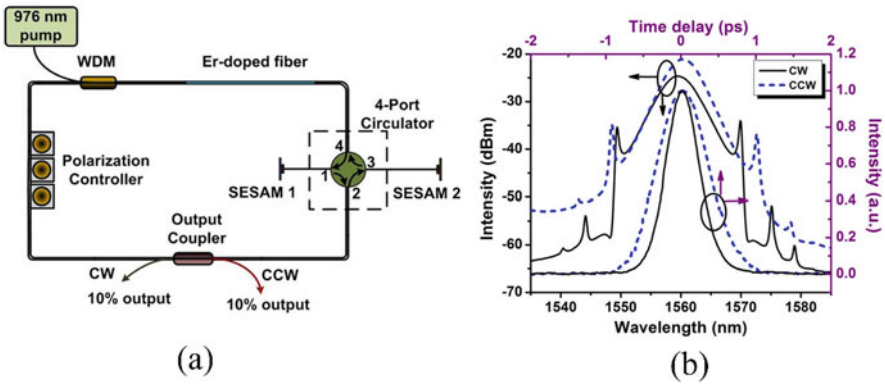

Fig. 10.2 Bidirectional mode-locked fiber laser based on SESAM. (**a**) Experimental setup of the all-fiber bidirectional passively mode-locked soliton laser with a four-port circulator and incorporated two different SESAMs into the laser cavity, (**b**) output optical spectra and the corresponding autocorrelation traces of the mode-locked pulses in the CW and CCW directions. (Figures (**a**) and (**b**) reprinted with permission from The Optical Society.: C. Ouyang et al., Opt. Letter 36, 2089–2091 (2011) [3])

dispersion regime. The measured repetition rates of switching laser and the corresponding vector solitons were 49.596 MHz, 24.798 MHz, and 24.798 MHz. By controlling wave plates, either of the polarized pulse trains can be switched on or off. The spectra of I_x, I_y and I_{total} nearly share the same central wavelength of ~2002 nm and the 3-dB bandwidth of ~0.9 nm. And the relatively smooth peaks of the spectrum indicated a stable mode-locked operation.

10.2.2 CNT

SESAM always has distinct drawbacks of small tuning range and cost-ineffectiveness. Currently, single-wall carbon nanotubes (SWNTs) have been widely investigated for mode locking due to their advantages of the ultrafast recovery time, wide operation ranges and polarization insensitivity. In the first stable all-fiber bidirectional passively mode-locked ring laser, a short segment of a fiber taper embedded in carbon nanotubes/polymer composite, acting as a saturable absorber, was used to enable bidirectional mode locking [2]. It must be noticed that most of the CNT-based bidirectional mode-locked ring lasers have similar structure as the fiber cavity Kieu and Mansuripur proposed [4]. A bidirectional soliton laser based on a SWNT-PVA mode-locker consists of erbium-doped fiber (EDF) for gain amplification, a polarization controller (PC) for optimizing the mode-locking conditions and other basic elements including SMF, 2 × 2 OC, WDM and pump [4]. Two stable pulse trains with different central wavelengths, pulse durations and repetition rates in opposite directions are delivered simultaneously from the ring cavity. Changing the pump power and adjusting the PC state can achieve the adjustment for the central wavelength of the two pulses. Moreover, by appropriately adjusting the PC and designing the cavity length, the pulses in opposite directions have the same central wavelength at 1559.7 nm, which illustrates that the nonidentical central wavelengths contribute to different repetition rates of two pulses. The unique features of the bidirectional pulses mainly result from the cavity asymmetry and fiber birefringence. There are many reports on ring bidirectional mode-locked fiber lasers like this [4–7], and most of them have demonstrated the potential of application in dual-comb spectroscopy [8–10]. Unlike common ring cavity, a nanotube-mode-locked dispersion-managed Er-fiber laser with an ultra-simple linear cavity was reported in Ref. [11]. The all-fiber linear cavity is constructed by a pair of homemade fiber end-facet mirrors (M1 and M2). What's important is that this is the first demonstration of such compact bidirectional soliton fiber laser with the sub-200 fs pulses. Interestingly, the bidirectional operations can show the different bound states, i.e. the forward bound solitons with phase difference of + π/2, and the backward ones with phase difference of -π/2.

10.2.3 Graphene

Recently, graphene, a two-dimensional atomic layer of carbon atoms, has been proved to be a novel saturable absorber (SA) for the development of ultrafast lasers. The gapless linear dispersion of Dirac electrons allows broadband saturable absorption in graphene. Additionally, graphene has the intrinsic advantages of an ultrafast recovery time, higher damage threshold, lower saturation intensity and the ability to operate in transmission, reflection, and bidirectional modes. All of these factors make graphene an ideal SA for mode-locked lasers over an ultra-wide spectral range from the visible to the far-infrared. Graphene-based SAs are preferred over SESAMs and CNTs as they do not require band-gap design and diameter control to improve their performance. The first all-fiber bidirectional passively mode-locked soliton laser with a graphene-based saturable absorber is shown in Fig. 10.3a [12]. This cavity design includes a four-port circulator to introduce different sections of cavity for the two counter-propagating pulses, so they have distinct output characteristics. The two sub-paths consist of a PC and a graphene based SA which is mated to a highly reflective fiber mirror. The combination of a graphene-based SA and fiber mirror serves as a reflective SA, which here is called the combination a Graphene Saturable Absorber Mirror (GSAM). Simultaneous bidirectional operation is achieved by appropriately adjusting the net cavity birefringence and loss. As shown in Fig. 10.3b, in the CW direction, the laser emits ~750 fs pulses at

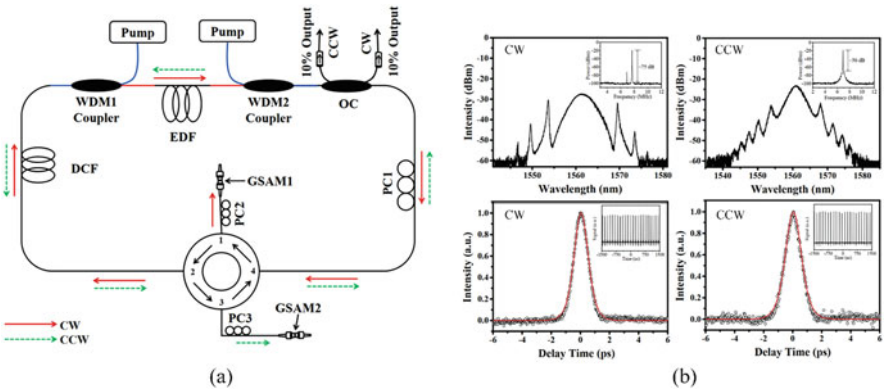

Fig. 10.3 Bidirectional mode-locked fiber laser based on graphene. (**a**) The experimental setup of the graphene-based passively mode-locked bidirectional fiber laser, GSAM: combination of graphene-based SA with fiber mirror; (**b**) The upper row: output optical spectrum of the CW pulses and the CCW pulses under the condition of unidirectional pumping, insets are the corresponding RF spectra, the bottom row: autocorrelation traces of the CW pulses and the CCW pulses under the condition of unidirectional pumping, insets are the oscilloscope traces. (Figures (**a**) and (**b**) reprinted with permission from The Optical Society.: V. Mamidala et al., Opt. Express 22, 4539–4546 (2014) [12])

1561.6 nm, with a repetition rate of 7.68 MHz. In the CCW direction, the central wavelength, pulse width, and repetition rate are 1561.0 nm, ~850 fs, and 6.90 MHz, respectively. GSAM in Fig. 10.3a is a liquid-phase exfoliation prepared graphene-based SA with a pump threshold of 150 mW. However, in order to obtain high-efficiency operation of a fibre laser, it is necessary to ensure a low laser threshold where a high-performance SA becomes essential. A passively mode-locked femtosecond erbium-doped bidirectional fiber laser with low pump threshold using chemical vapour deposition grown graphene SAs was also demonstrated [13]. This fiber laser can simultaneously produce two synchronised stable output soliton pulse trains with a similar fundamental repetition rate of ~10.38 MHz at a pump power as low as 56 mW from a single-pump laser diode.

10.2.4 NPR

Apart from the above real materials, artificial mode lockers also receive lots of attentions due to their easy configuration and high damage threshold. A bidirectional fiber laser scheme for validating the possibility of a multiplexed laser system, which is passively mode-locked by NPR technique, configured by a polarizer and three PCs respectively inserted in the main cavity and two branches with different dispersion distributions was reported in Ref. [14]. Thus, different formation mechanisms are introduced into the lasing oscillator. By this means, stable conventional solitons (CSs) and dissipative solitons (DSs) are respectively formed in the CW and CCW directions of the same lasing oscillator. Moreover, attributing to the strong birefringence filtering effect, the wavelength selection mechanism is induced. Through the proper management of intra-cavity birefringence, wideband wavelength tuning and switchable multi-wavelength operations can be observed. The central wavelength of CS can be continuously tuned from 1560 nm to 1602 nm. Benefiting from the multiplexed laser scheme, bidirectional lasing oscillation, multi-state soliton emission, wavelength tuning and multi-wavelength operations are synchronously realized in a single laser cavity. Also based on the NPR mold-locking technology, a θ-shape auxiliary cavity based on chirped fiber Bragg grating (CFBG) is proposed to simultaneously introduce large anomalous and normal dispersion into the lasing oscillator [15]. Thus, CSs and DSs also can be emitted from the counter-propagation directions. Recent discovery on scalar-vector features of ultrashort pulses sheds new light on the polarization dynamics of ultrafast fiber lasers. A NPR-based bidirectional mode-locked fibre laser emitting scalar and vector solitons from the counter-propagation directions is proposed [16]. Through introducing different polarization evolving mechanisms into the counter-propagation branches, the fiber laser respectively approaches the scalar-soliton regime and vector-soliton regime in the CW and CCW directions.

10.2.5 Hybrid

The introduction of hybrid mode-locked mechanism brings more possibilities for the regulation of bidirectional mode-locked fiber lasers. The Erbium-doped fibre ring laser hybrid mode-locked with SWNT and nonlinear polarization evolution (NPE) realized by polarizing optical fiber and a pair of PCs without an optical isolator is presented in Ref. [17]. The SWNT-PVA, refereed in this case as to comparatively slow SA (relaxation time is 300–700 fs), is used for mode locking initiation. The NPE features relaxation time in order of 10 fs and therefore, ensures efficient pulse narrowing and stabilization. The switching between regimes with different generation directions can be achieved by adjusting the intracavity birefringence. In the bidirectional operation regime, a laser pumped with 75 mW power at 980 nm generates almost identical 790 and 570 fs soliton pulses with an average power of 1.17 and 1.11 mW. It is also mentioned that based on a laser cavity configuration similar to that in Ref. [17], depending on the total intracavity dispersion value, the laser emits conservative solitons, transform-limited Gaussian pulses, or highly chirped stretched pulses with almost 20 nm wide parabolic spectrum in both CW and CCW directions of the ring [18]. And a study on the gyroscopic effect in the bidirectional ultra-short pulse erbium-doped all-fiber ring soliton laser is also reported [19]. Such as, a thulium-doped bidirectional fiber laser mode-locked by a combination of SESAM and nonlinear NPR, which is another popular hybrid mode locker [20]. The laser outputs from two directions have significant spectral overlap, the FWHM spectral bandwidths of CW and CCW signals are 3.2 nm and 1.8 nm, respectively. The difference in spectral profiles is caused by the different polarization events experienced in each path as well as the amount of gain and losses each path experiences. For autocorrelation traces, pedestals extending over the entire autocorrelation window indicate that the laser operates in a multiple-pulse regime. It is should be stressed that output wavelengths are tunable by 35 nm around a central wavelength of 1.917 μm and the repetition rate difference can be arbitrarily adjusted using a tunable optical delay line placed on one of the cavity paths. What makes sense is that a bidirectional mode-locked Er-fiber laser based on two saturable absorber mirrors (SAMs) and NPR was proposed to generate high-coherence ultra-broadband frequency combs by nonlinear spectral broadening [21].

10.3 Wavelength Multiplexed Dissipative Soliton Fiber Lasers

Wavelength multiplexing is another dimension for laser multiplexing, which is manifested in fiber lasers that can output multi-wavelength soliton. Until now, different methods have been reported, such as adjusting the intensity loss of the cavity or changing the birefringence intensity of the cavity as summarized in Fig. 10.4.

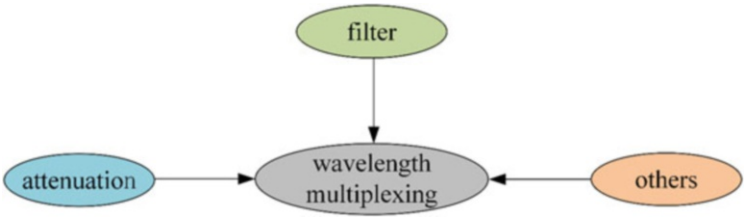

Fig. 10.4 Methods of wavelength multiplexing

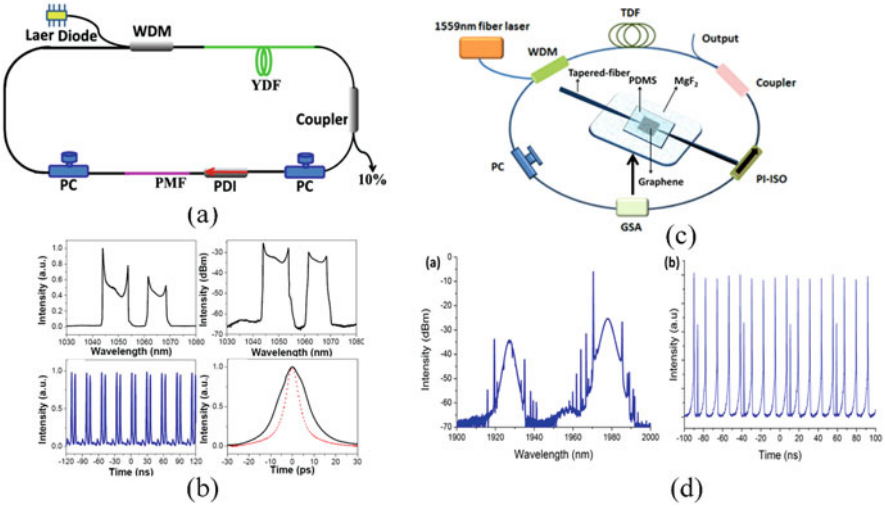

Fig. 10.5 (**a**) Structure of all-normal dispersion multi-wavelength ytterbium-doped fiber laser with periodic birefringence fiber filter. (**b**) Dual-wavelength dissipative soliton output of the laser in (**a**). (**c**) The generation of dual-wavelength ultrafast Tm3 + −doped fiber laser at 2 μm region based on GSA, insert is an image of GSA structure based on microfiber. (**d**) The dual-wavelength solitons output spectrum and pulse trains of the laser in (**c**). Figures (**a**) and (**b**) reprinted with permission from The Optical Society.: Z. X. Zhang et al., Opt. Express 20, 26736–26742 (2012) [23]. (Figures (**c**) and (**d**) reprinted from Optics & Laser Technology, 105, G. Yang et al., 76–79., Copyright (2018), with permission from Elsevier [26])

Adjusting the birefringence of the cavity is a common method to realize wavelength-multiplexing. The generation of multi-wavelength DS in an all-normal dispersion mode-locked fiber laser based on SESAM was reported in Ref. [22]. Although no polarizing components were used in the cavity, the slight residual polarization asymmetry of the components used, such as the SESAM and the circulator, could still cause the formation of a linear artificial birefringent filter in the cavity. Single/dual/triple-wavelength spectra obtained through rotating PC. Similarly, an all-normal-dispersion multi-wavelength DS Ytterbium-doped fiber (YDF) laser with a periodic birefringence fiber filter was reported as shown in Fig. 10.5a [23]. The mode-locked operation with NPR can effectively induce the

intensity and wavelength-dependent loss, so as to reduce the mode competition caused by uniform gain broadening. By adding a length of polarization-maintaining fiber (PMF) into the cavity, the birefringent fiber filter is formed, which can play the role of wavelength selection. The tunable dual-wavelength DS output is realized by adjusting the PC as shown in Fig. 10.5b. And the filter bandwidth can be changed by PMF length. In addition, the triple-wavelength DSs output can be realized by this structure as well [24]. There is also an all-normal-dispersion mode-locked ytterbium-doped fiber laser based on graphene oxide saturable absorber (GOSA) [25]. The induced cavity birefringence through over bending the single-mode fibers is responsible for the multi-wavelength filtering. Tunable and switchable single-, dual-, and triple-wavelength DSs can be output. The dual-wavelength ultrafast Tm^{3+}-doped fiber laser at 2 μm region based on graphene saturable absorber is shown in Fig. 10.5c [26]. A section of graphene film is transferred on a microfiber, which allows light-graphene interaction via the evanescent field. The graphene interacting with optical evanescent light can generate a polarizing effect as a weak polarizer. The graphene-induced polarizing effect combined with the cavity birefringence constructs an artificial birefringent filter, and the filter together with the thulium-doped fiber determines the effective laser gain. By tuning the pump power and the PC, the transmission of the artificial birefringent filter can be effectively changed, and the multi-wavelength mode-locking can be realized as shown in Fig. 10.5d.

Among these techniques for dual-wavelength or multi-wavelength mode-locking, Lyot-filter (birefringence-induced spectral filter) is a common approach because of its compact structure and broadband operation property [27, 28]. A typical dual-wavelength mode-locked fiber laser based on Lyot-filter was reported as shown in Fig. 10.6a [29]. By bending the single-mode fiber, dual-wavelength mode-locking

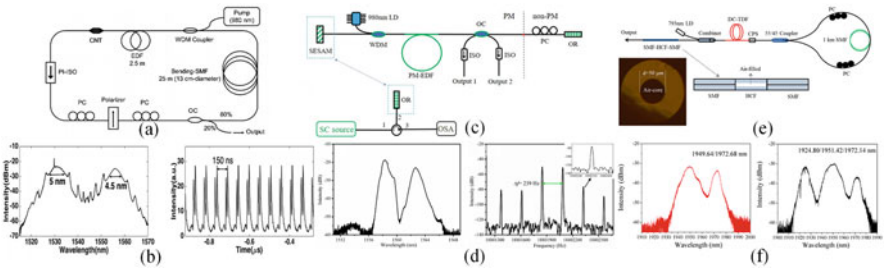

Fig. 10.6 (**a**) Configuration of dual-wavelength mode locked fiber laser based on Lyot-filter. (**b**) The dual-wavelength output spectrum and time waveform of the laser in (**a**) are obtained by adjusting PC. (**c**) Configuration of the all-fiber linear cavity mode-locked laser based on SESAM. The components on the left of the broken line are polarization-maintaining and those on the right are non-polarization-maintaining. (**d**) the spectrum of dual-wavelength mode-locking at 1557.7 nm and 1562.7 nm, and corresponding RF spectrum around the first harmonic and (inset) local view of a subsidiary peak. (**e**) Schematic configuration of the multi-wavelength mode-locked TDFL, insert is an image of cross-section of the hollow-core fiber (HCF). (**f**) The output spectrum of dual/triple-wavelength mode-locking of the laser in (**e**) by changing the PC. (Figures (**e**) and (**f**) reprinted with permission from IOP Publishing © Astro Ltd.: M. Wang et al., Laser Physics Letters 15, 085110 (2018) [31])

can be achieved, as shown in Fig. 10.6b. Figure 10.6c is also a mode-locked laser based on the Lyot-filter [30]. Periodic Lyot-filtering effect appears because of the polarization-dependent loss of the PM WDM combined with the PM fibers in the laser cavity. By properly setting the state of the polarization, stable dual-wavelength synchronized mode-locked pulse trains with the repetition rate difference of hundreds of Hertz can be achieved, as shown in Fig. 10.6d. In addition, the filter based on the mode interference mechanism can also realize wavelength multiplexing. In Fig. 10.6e, an all-fiberized multi-wavelength mode-locked thulium-doped fiber laser (TDFL) based on fiber-optic Fabry–Perot interferometer (FPI) and NOLM was reported [31]. The fiber-optic FPI played the roles of wavelength selective filter and output mirror, which constructs by a single mode-hollow core-single mode fiber structure (SMF-HCF-SMF). A NOLM with wavelength-dependent cavity loss was employed to alleviate the mode competition in thulium-doped fiber and enabled the multi-wavelength mode-locking. With proper manipulation of the PC and the pump power, besides the single-wavelength fundamental, switchable dual-wavelength and stable triple-wavelength mode-locked operations are obtained as shown in Fig. 10.6f.

Using fiber grating as a spectral filter in the laser cavity, wavelength-multiplexing can be realized. A switchable dual-wavelength and passively mode-locked ytterbium-doped fiber laser in the all-normal-dispersion regime was reported in Ref. [32]. Using a phase-shifted long-period fiber grating (PS-LPFG) as an all-fiber format spectral filter in the laser cavity, a stable and switchable dual-wavelength mode-locked operation is achieved by NPE. The wavelength position of the dual-wavelength output is determined by the passbands of the PS-LPFG filter. The mode-locked dual-wavelength laser can further be switched by adjusting the polarization states of the waveplates in the cavity. The output wavelength of the mode-locked pulse is very consistent with the passband wavelength of PS-LPFG. Moreover, the tunable dual-wavelength and triple-wavelength mode-locked pulse output can be realized based on PS-LPFG [33]. A nanotube-mode-locked all-fiber ultrafast oscillator emitting triple-wavelengths at the central wavelengths of about 1540, 1550, and 1560 nm, which are tunable by stretching fiber Bragg gratings were reported in Ref. [34]. Three chirped fiber Bragg gratings (CFBG) in the cavity are used as wavelength selectors to select the mode-locked wavelength, and the laser output wavelength is separated by the other three CFBGs to represent a single wavelength. Thus, the triple-wavelengths output of the laser can be realized. Moreover, based on the cascade of CFBGs, the laser system with more than triple-wavelengths (e.g. four and five wavelengths) can be achieved in principle.

By adjusting the intracavity loss, the gain profile of the homogeneous-doped fiber laser is effectively controlled, wavelength multiplexing can then be realized. The operating status and the output wavelength of the laser can be controlled by adjusting an attenuator in the fiber ring in Ref. [35]. By adjusting the cavity loss and pump power, the output spectrum is changing from single-wavelength mode-locking to dual-wavelength mode-locking. In Fig. 10.7a, a nanotube/microfiber-mode-locked fiber laser where the operation wavelength depends on the intracavity loss was reported [36]. With the appropriate pump power and intracavity loss, dual-

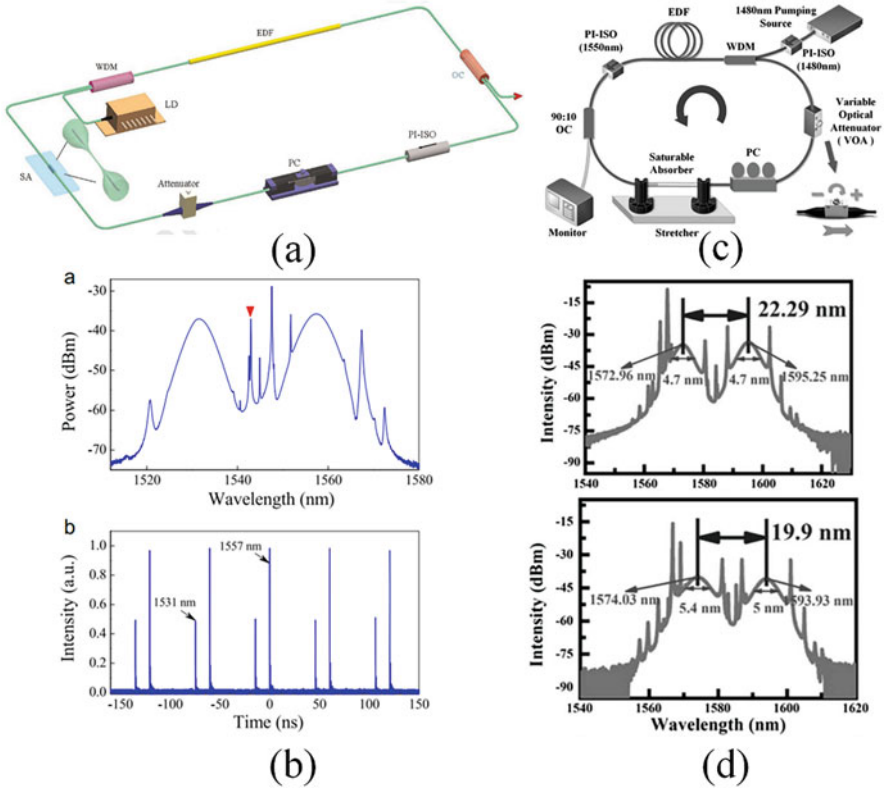

Fig. 10.7 (**a**) Configuration of a nanotube/microfiber-mode-locked fiber laser. (**b**) By adjusting the intracavity attenuator, the dual-wavelength mode-locked spectrum of the laser in (**a**) obtained. (**c**) Configuration of dual-wavelength mode locked laser. Using a hybrid no-core fiber graded-index multi-mode fiber as the saturable absorber. (**d**) By adjusting the attenuator in the cavity, the tunable dual-wavelength mode-locked spectrum of the laser output in (**c**) is obtained. Figures (**a**) and (**b**) reprinted from Optics Communications, 347, C. Zeng et al., 44–49., Copyright (2015), with permission from Elsevier [36]. (Figures (**c**) and (**d**) reprinted with permission from CLP Publishing.: T. Zhu et al., Photonics Research 7, 853 (2019) [37])

wavelength solitons are achieved simultaneously as shown in Fig. 10.7b. The center wavelengths of mode-locked are 1531 nm and 1557 nm. In addition, a wavelength-tunable and coherent dual-wavelength mode-locked operation are realized in an all-fiber EDF laser using a hybrid NCF-GIMF structure-based SA as shown in Fig. 10.7c [37]. The switching of single wavelength or dual-wavelength mode-locked can be realized by changing the cavity loss, and the tunable dual-wavelength mode-locking can also be realized as shown in Fig. 10.7d.

The dual-wavelength soliton pulse can be realized by placing a special SA in the cavity. An Er-doped fiber laser with single and dual-wavelength mode-locked output based on WS_2 was reported in Ref. [38]. Few-layer WS_2, as a novel two-dimensional (2D) material, has been discovered to possess both the saturable absorption effect

and the huge nonlinear refractive index. The single- and dual-wavelength soliton pulses by properly adjusting the pump strength and the polarization state. That WS_2-based fiber taper can be operated as both a promising SA for ultrafast pulse generation and a promising high nonlinear photonic material for generation multi-wavelength. In Fig. 10.8a, A dual-wavelength soliton fiber laser based on the use of tin disulfide (SnS_2) as SA was reported [39]. A dual-wavelength soliton was obtained at a relatively low threshold pump power of 75 mW. The two peaks of the dual-wavelength soliton are located at 1536.7 nm and 1562.6 nm with a pulse width of 5.3 ps as shown in Fig. 10.8b. Other materials were used to achieve multi-

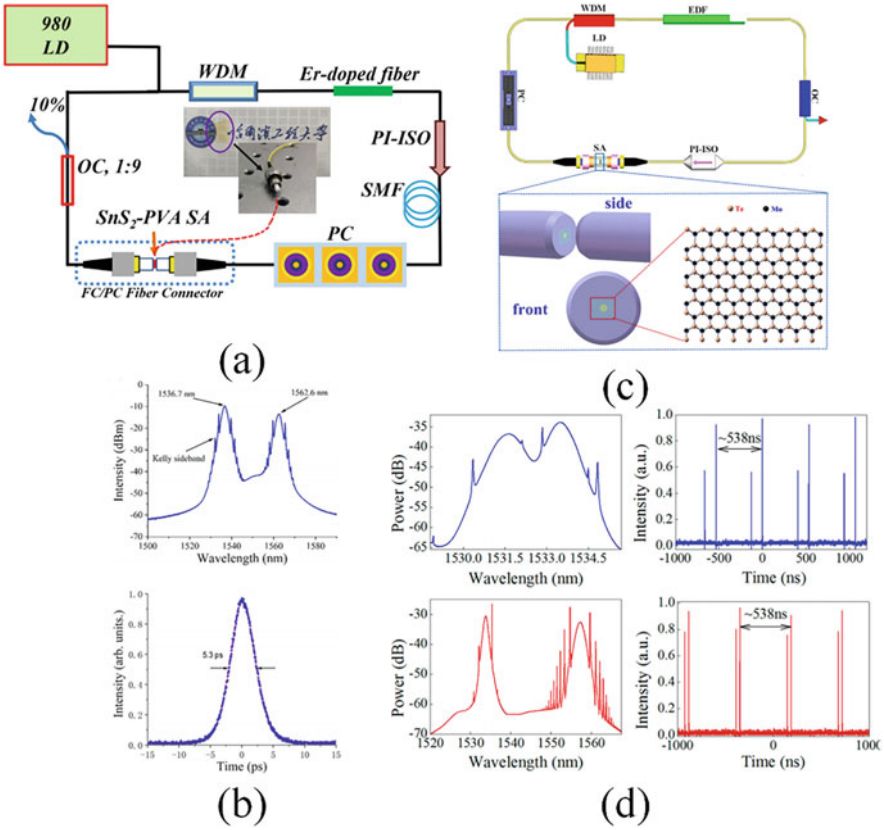

Fig. 10.8 (**a**) Configuration of dual-wavelength mode-locked erbium-doped fiber laser based on tin disulfide thin film as SA. Inset: schematic diagram of SA in laser. (**b**) The dual-wavelength soliton spectrum and autocorrelation trace of the laser in (**a**). (**c**) Configuration of the monolayer-MoTe2-film-based mode-locked fiber laser. Insert: Side and front schematics of fiber connector with monolayer MoTe2 film coating on the pinhole of the pigtail. (**d**) The tunable dual-wavelength mode-locked spectrum and oscilloscope trace of the laser in (**c**). Figures (**a**) and (**b**) reprinted with permission from AIP Publishing.: S. Li et al., Journal of Applied Physics 125, 243,104 (2019) [39]. (Figures (**c**) and (**d**) reprinted with permission from Taylor & Francis Ltd., http://www.tandfonline.com.: A. Yasim, Journal of Modern Optics 67, 367–373 (2020) [40])

wavelength mode-locked. As shown in Fig. 10.8c, the erbium-doped fiber laser based on $MoTe_2$ achieved dual-wavelength soliton output [40]. By tuning the state of PC, another single-wavelength mode-locking state can be obtained in the fiber laser, as shown in Fig. 10.8d.

10.4 Polarization Multiplexed Dissipative Soliton Fiber Lasers

In this section, we will focus on the polarization-multiplexed dissipative soliton fiber lasers. Polarization-multiplexed solitons means that when the solitons propagate in the birefringent fiber, they are decomposed into two solitons with orthogonal polarization states, so that the two polarization states can be used independently because of their weakly interference. Vector soliton is a typical form of polarization-multiplexed soliton. Because it has been introduced in detail in the previous chapter, here, group velocity unlocked polarization-multiplexed solitons will be discussed.

The mode-locked elements of polarization-multiplexed mode-locked fiber lasers mainly include nonlinear amplifying loop mirror (NALM) [44, 47], SWNT [41, 43, 48], graphene-based saturable absorber (GSA) [45], nonlinear multimode interference (NL-MMI) [45] and others [42].

In order to easily adjust the repetition frequency, Y. Nakajima et al. introduced a spatial light structure. They developed an all-PM, polarization-multiplexed, dual-solitons fiber laser with a NALM mode-locked mechanism [44]. Owing to the use of the slow and fast axes of PMF, the dual-solitons with slightly different repetition rates from the single-laser cavity are generated at the same center wavelength without extra-cavity nonlinear spectral broadening. The narrow relative beat note between the two frequency combs is obtained with a full-width-at-half-maximum of ~1 kHz in the optical frequency domain. The repetition rate ($f$rep) for both the outputs was 21.2 MHz, and Δfrep was 8.9 kHz. Both the $f$rep values could be varied independently by the position of each collimator in the free-space section of linear arm. In Fig. 10.9 the dual-solitons generation from an all PM dual-color ytterbium (Yb) fiber laser was reported, in which spectral overlap of the two pulse trains is achieved outside the laser cavity by amplifying the 1030-nm pulses and broadening them in a nonlinear fiber [47]. Two pulse trains with center wavelengths at 1030 nm and 1060 nm respectively are generated within the same laser cavity with a repetition rate around 77 MHz.

Z. Zheng et al. proposed and demonstrated that polarization-multiplexed single-cavity dual-comb source (SCDCS) by a mode-locked fiber laser with non-negligible birefringence [43]. The repetition rates are 44.102951 and 44.103377 MHz respectively. Furthermore, it is observed that the repetition rate difference Δfrep can be varied by tuning the intracavity PC. Under different dispersion regimes, dual-solitons sharing the same spectral window could be generated with different optical bandwidths and pulse widths. It could be possible to further explore direct

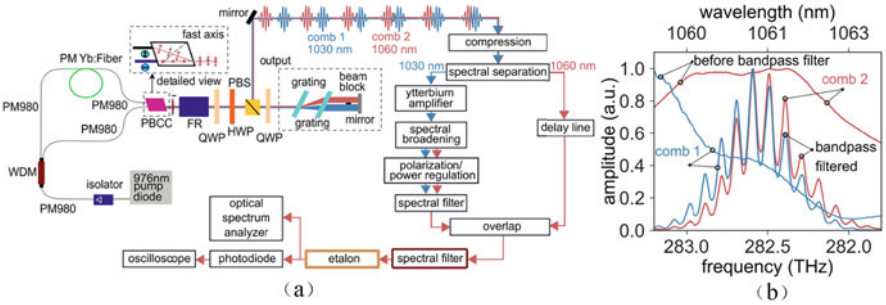

Fig. 10.9 (**a**) Overview of the all-PM NALM mode-locked single-cavity dual-comb setup. Due to the mechanical spectral fliter, the laser oscillator emits two pulse trains with different repetition around 77 MHz and center wavelengths around 1030 nm and 1060 nm, respectively. The output of the dual-color laser is spectrally separated using a dichroic filter: The pulse centered around 1030 nm is amplified and nonlinearly broadened. The pulse centered around 1060 nm is delayed using a passive fiber. Subsequently, spatial overlapping in a 50:50 fiber splitter/combiner leads to the generation of a dual-comb interferogram. Bandpass filtering of the light is applied to avoid spectral aliasing. The feasibility of spectral measurement is demonstrated by measuring the transmission of different etalons. The light is detected by a simple photodiode and measured with an oscilloscope (**b**) Output spectrum of the dual-comb laser before spectral separation and spectrum of the broadened 1030-nm pulse recorded with an optical spectrum analyzer. (**b**) Spatially overlapped dual-comb output after amplification and spectral broadening after filtering the light using 3-nm bandpass filter. The modulations on the spectrum are caused by the bandpass filter

generation of dual-solitons with further increased bandwidths through intracavity dispersion design. In Ref. [48], the multi-solitons generation which could be realized by tapping into the multidimensional joint parameter space was reported. Up to four wavelength/polarization multiplexed, asynchronous ultra-short pulse sequences can be generated with good stability from an all-fiber, mode-locked ring-cavity laser. A. Sterczewski et al. further simplified the structure of the laser cavity and they showed for the first time that by employing polarization multiplexing in an all-fiber single-cavity dual-solitons laser composed of just a few basic fiber components [45]. One can perform high-resolution broadband molecular spectroscopy with tooth-resolved RF lines using a completely free-running system characterized by low power consumption and compact size.

In Fig. 10.10a simple and low-cost approach to generate dual-solitons from a single fiber-ring cavity based on nonlinear multimode interference was reported [46]. A single-mode fiber-graded-index multimode-single-mode fiber structure serves as an all-fiber saturable absorber for mode-locking. A pair of solitons with different repetition rate are generated by dual-wavelength and polarization-multiplexed mechanisms. The two pulse trains exhibit repetition frequencies of 24.83345 MHz and 24.834083 MHz, respectively.

Figure 10.11a shows a robust fiber laser in the eye-safe thulium wavelength regime which did not use a mode-locked device like CNT or SWNT. A polarization soliton operation in a frequency-halved state with orthogonally polarized interlaced pulses is demonstrated without requiring any free-space alignment [42].

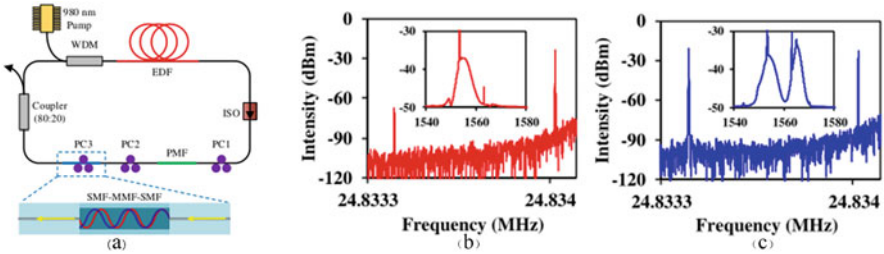

Fig. 10.10 (**a**) Schematic of the mode-locked fiber laser (right) Polarization-resolved measurement; (**b**) RF spectrum of the horizontal axis output (inset, optical spectrum); (**c**) RF spectrum of the vertical axis output (inset, optical spectrum). (Figures (**a**) and (**b**) reprinted with permission from The Optical Society.: K. Zhao et al., Opt. Letters, 44(17), 4323–4326 (2019) [46])

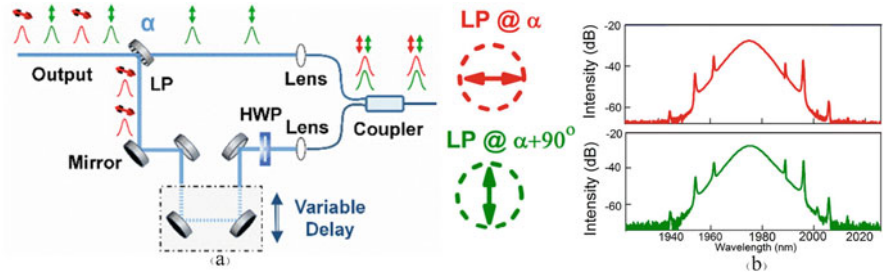

Fig. 10.11 (**a**) Schematic of set-up for optical interference of the individual pulse trains. (**b**) Schematic of set-up for optical interference of the individual pulse trains. (**b**) The optical spectrum of LP at the angle of α and LP at the angle of α + 90°. (Figures (**a**) and (**b**) reprinted with permission from The Optical Society.: E. Akosman et al., Opt. Express 25, 18592–18602 (2017) [42])

10.5 Conclusion and Outlook

In this chapter, we have discussed various approaches for multiplexed dissipative fiber laser. These schemes are highly related to the degree of freedom of the lightwave such as propagation direction, wavelength, and polarization. Recently, due to the strong demand on the transmission capacity, mode demultiplexing which employs various higher-order modes (HOMs) for information distribution has attracted wide attention. These HOMs are orthogonal in nature and can be a potential dimension for multiplexed fiber laser. Currently, mode-locked fiber lasers which can emit HOMs such as LP11 based on mode selective coupler was reported [49]. Transverse-mode-selected mode-locked fiber lasers can also be realized by using few-mode fiber Bragg grating (FBG). By properly inscribing Bragg grating in few-mode fibers, different Bragg reflection peaks will selectively generate different modes which satisfy phase-matching conditions [50]. Based on this principle, mode-locked fiber lasers are able to produce transverse-mode-selected pulses [50, 51]. Orbital angular momentum (OAM) is another representation for the transverse mode. Benefiting from the helix wavefront of the OAM mode, it is

regarded as a useful tool to manipulate nano- and micro-particles and offers a new approach to boost the communication capacity. Like the HOMs in optical fiber, the OAM modes are orthogonal as well. Normally, the OAM modes can be formed by the combination of special HOMs with π/2 phase shift. Therefore, femtosecond pulses carrying OAM mode can be produced by the transverse-mode-selected fiber laser [51–54]. It should be noted that although these lasers can emit various HOMs and OAMs, they cannot be named as multiplexed fiber lasers. This is because the light oscillating in the laser cavity is still in the fundamental mode state except at the mode-selective devices such as mode coupler and FBG. To achieve the real HOM- or OAM-multiplexed fiber laser, the special fibers which can carry and amplify these modes are essential. With the rapid development of these devices, HOM and OAM will be promising degree of freedoms for future multiplexed dissipative fiber laser.

References

1. N. Buholz, and M. Chodorow, "Acoustic wave amplitude modulation of a multimode ring laser," IEEE Journal of Quantum Electronics 3, 454-459 (1967).
2. K. Kieu, and M. Mansuripur, "All-fiber bidirectional passively mode-locked ring laser", Optics Letters 33, 64-66 (2008).
3. C. Ouyang, P. Shum, K. Wu, J. Wong, H. Lam, and S. Aditya, "Bidirectional passively mode-locked soliton fiber laser with a four-port circulator," Optics Letter 36, 2089-2091 (2011).
4. C. Zeng, X. M. Liu, and L. Yun, "Bidirectional fiber soliton laser mode-locked by single-wall carbon nanotubes," Optics Express 21, 18937-18942 (2013).
5. X. K. Yao, "Generation of bidirectional stretched pulses in a nanotube-mode-locked fiber laser," Applied Optics 53, 27-31 (2014).
6. H. B. Jiang, Y. Wang, S. Y. Set, and S. J. Yamashita, "Bidirectional mode-locked soliton fiber laser in 2μm using CNT saturable absorber," Laser Congress 2017 (ASSL, LAC), OSA Technical Digest (online) (Optical Society of America, 2017), paper JM5A.21.
7. H. Afkhamiardakani, and J. C. Diels, "Controlling group and phase velocities in bidirectional mode-locked fiber lasers," Optics Letters 44, 2903-2906 (2019).
8. Mehravar, R. A. Norwood, N. Peyghambarian, and K. Kieu, "Real-time dual-comb spectroscopy with a free-running bidirectionally mode-locked fiber laser," Applied physics Letters 108, 231104 (2016).
9. J. Olson, Y. H. Ou, A. Azarm, and K. Kieu, "Bi-directional mode-locked thulium fiber laser as a single-cavity dual-comb source," IEEE Photonics Technology Letters 30, 1772-1775 (2018).
10. R. D. Baker, N. T. Yardimci, Y. H. Ou, K. Kieu and M. Jarrahi, "Self-triggered asynchronous optical sampling terahertz spectroscopy using a bidirectional mode-locked fiber Laser," Scientific Reports 8, 14802 (2018).
11. L. Li, Q. J. Ruan, R. H. Yang, L. M. Zhao, and Z. Q. Luo, "Bidirectional operation of 100 fs bound solitons in an ultra-compact mode-locked fiber laser," Optics Express 24, 21020-21026 (2016).
12. V. Mamidala, R. I. Woodward, Y. Yang, H. H. Liu, and K. K. Chow, "Graphene-based passively mode-locked bidirectional fiber ring laser", Optics Express 22, 4539-4546 (2014).
13. K. K. Chow, "CVD graphene based low pump threshold bidirectional mode-locked fibre laser," Electronics Letters 53, 1127-1128 (2017).
14. B. W. Liu, Y. Y. Lu, Y. Xiang, X. P. Xiao, Q. Z. Sun, D. M. Liu, and P. P. Shum, "Multiplexed ultrafast fiber laser emitting multi-state solitons," Optics Express 26, 27461-27471 (2018).

15. B. W. Liu, Y. Y. Luo, Y. Xiang, W. Zhou, P. P. Shum, "CFBG-based bidirectional mode-locked fiber laser emitting conventional and dissipative solitons," IEEE Photonics Technology Letter 31, 1737-1740 (2019).
16. Y. Xiang, Y. Y. Luo, B. W. Liu, R. Xia, P. P. Shum, X. H. Tan, D. M. Liu, and Q. Z. Su, "Scalar and vector solitons in a bidirectional mode-locked fibre laser," Journal of Lightwave Technology 37, 5108-5114 (2019).
17. M. Chernysheva, M A. Araimi, H. Kbashi, R. Arif, S. V Sergeyev, and A. Rozhin, "Isolator-free switchable uni- and bidirectional hybrid mode-locked erbium-doped fiber laser," Optics Express 24, 15721-15729 (2016).
18. A. A. Krylov, D. S. Chernykh, N. R. Arutyunyan, V. V. Grebenyukov, A. S. Pozharov, and E. D. Obraztsova, "Generation regimes of bidirectional hybridly mode-locked ultrashort pulse erbium-doped all-fiber ring laser with a distributed polarizer," Applied Optics 55, 420-4209 (2016).
19. A. A. Krylov, D. S. Chernykh, and E.D. Obraztsova, "Colliding-pulse hybridly mode-locked erbium-doped all-fiber soliton gyrolaser," Laser Physics 28, 015103 (2018).
20. N. Abdukerim, M. I. Kayes, A. Rekik, and M. Rochette, "Bidirectional mode-locked thulium-doped fiber laser," Applied Optics 57, 7198-7202 (2018).
21. Y. Nakajima, Y. Hata, and K. Minoshima, "High-coherence ultra-broadband bidirectional dual-comb fiber laser," Optics Express 27, 5931-5944 (2019).
22. H. Zhang, D. Y. Tang, X. Wu, and L. M. Zhao, "Multi-wavelength dissipative soliton operation of an erbium-doped fiber laser," Optics Express 17, 12692-12697 (2009).
23. Z. X. Zhang, Z. W. Xu, and L. Zhang, "Tunable and switchable dual-wavelength dissipative soliton generation in an all-normal-dispersion Yb-doped fiber laser with birefringence fiber filter," Optics Express 20, 26736-26742 (2012).
24. Z. W. Xu, and Z. X. Zhang, "All-normal-dispersion multi-wavelength dissipative soliton Yb-doped fiber laser," Laser Physics Letters 10, 085105 (2013).
25. S. Huang, Y. Wang, P. Yan, J. Zhao, H. Li, and R. Lin, "Tunable and switchable multi-wavelength dissipative soliton generation in a graphene oxide mode-locked Yb-doped fiber laser," Optics express 22, 11417-11426 (2014).
26. G. Yang, Y. Liu, Z. Wang, G. Wang, Z. Wang, and X. Wang, "Dual-wavelength mode-locked Tm3+-doped fiber laser at 2 μm region with controllable soliton pulse number by employing graphene on microfiber," Optics & Laser Technology 105, 76-79 (2018).
27. C. S. Kim and J. U. Kang, "Multiwavelength switching of Raman fiber ring laser incorporating composite polarization-maintaining fiber Lyot-Sagnac filter," Applied Optics 43, 3151–3157 (2004).
28. S. Sugavanam, Z. Yan, V. Kamynin, A. S. Kurkov, L. Zhang, and D. V. Churkin, "Multiwavelength generation in a random distributed feedback fiber laser using an all fiber Lyot filter," Optics Express 22, 2839–2844 (2014).
29. Y. Zhu, F. Xiang, L. Jin, S. Y. Set, and S. Yamashita, "All-fiber dual-wavelength mode-locked laser using a bend-induced-birefringence Lyot-Filter as gain-tilt equalizer," IEEE Photonics Journal 11, 1-7 (2019).
30. X. Luo, T. H. Tuan, T. S. Saini, H. P. T. Nguyen, T. Suzuki, and Y. Ohishi, "Tunable and switchable all-fiber dual-wavelength mode locked laser based on Lyot filtering effect," Optics Express 27, 14635-14647 (2019).
31. M. Wang, Y. J. Huang, J. W. Yang, Y. Zhang, and S. C. Ruan, "Multi-wavelength mode-locked thulium-doped fiber laser based on a fiber-optic Fabry-Perot interferometer and a nonlinear optical loop mirror," Laser Physics Letters 15, 085110 (2018).
32. X. Zhu, C. Wang, S. Liu, D. Hu, J. Wang, C. Zhu, "Switchable dual-wavelength and passively mode-locked all-normal-dispersion Yb-doped fiber lasers," IEEE Photonics Technology Letters 23, 956-958 (2011).
33. X. Zhu, C. Wang, G. Zhang, and R. Xu, "Tunable dual- and triple-wavelength mode-locked all-normal-dispersion Yb-doped fiber laser," Applied Physics B 118, 69-73 (2014).
34. X. Liu, D. Han, Z. Sun, C. Zeng, H. Lu, D. Mao, Y. Cui, and F. Wang, "Versatile multi-wavelength ultrafast fiber laser mode-locked by carbon nanotubes," Scientific reports 3, 2718 (2013).

35. X. Zhao, Z. Zheng, L. Liu, Y. Liu, Y. Jiang, X. Yang, and J. Zhu, "Switchable, dual-wavelength passively mode-locked ultrafast fiber laser based on a single-wall carbon nanotube mode-locker and intracavity loss tuning," Optics Express 19, 1168-1173 (2011).
36. C. Zeng, Y. D. Cui, and J. Guo, "Observation of dual-wavelength solitons and bound states in a nanotube/microfiber mode-locking fiber laser," Optics Communications 347, 44-49 (2015).
37. T. Zhu, Z. Wang, D. N. Wang, F. Yang, and L. Li, "Generation of wavelength-tunable and coherent dual-wavelength solitons in the C + L band by controlling the intracavity loss," Photonics Research **7**, 853 (2019).
38. B. Guo, Y. Yao, P. Yan, K. Xu, J. Liu, S. Wang, and Y. Li, "Dual-wavelength soliton mode-locked fiber laser with a ws2-based fiber taper," IEEE Photonics Technology Letters 28, 323-326 (2016).
39. S. Li, Y. Yin, G. Ran, Q. Ouyang, Y. Chen, M. Tokurakawa, E. Lewis, S. W. Harun, and P. Wang, "Dual-wavelength mode-locked erbium-doped fiber laser based on tin disulfide thin film as saturable absorber," Journal of Applied Physics 125, 243104 (2019).
40. A. Yasim, "Switchable and dual-wavelength ultrafast fibre lasers with a $MoTe_2$-based saturable absorber," Journal of Modern Optics 67, 367-373 (2020).
41. K. Zhao, C. Gao, X.Xiao, and C. Yang, "Buildup dynamics of asynchronous vector solitons in a polarization-multiplexed dual-comb fiber laser," Opt. Lett. 45, 4040-4043 (2020)
42. E. Akosman and M. Y. Sander, "Dual comb generation from a mode-locked fiber laser with orthogonally polarized interlaced pulses," Optics Express 25, 18592-18602 (2017).
43. X. Zhao, T. Li, Y. Liu, Q. Li, and Z. Zheng, "Polarization-multiplexed, dual-comb all-fiber mode-locked laser," Photon. Res. 6(9), 853-857 (2018).
44. Y. Nakajima, Y. Hata, and K. Minoshima, "All-polarization-maintaining, polarization-multiplexed, dual-comb fiber laser with a nonlinear amplifying loop mirror," Optics Express 27(10), 14648-14656 (2019).
45. A. Sterczewski, A. Przewłoka, and W. Kaszub, "Computational Doppler-limited dual-comb spectroscopy with a free-running all-fiber laser," https://arxiv.org/abs/1905.04647 (2019).
46. K. Zhao, H. Jia, P. Wang, J. Guo, and C. Yang, "Free-running dual-comb fiber laser mode-locked by nonlinear multimode interference," Optics Letters, 44(17), 4323-4326 (2019).
47. J. Fellinger, A. S. Mayer, G. Winkler, W. Grosinger, G. W. Truong, and S. Droste, et al. "Tunable dual-comb from an all-polarization-maintaining single-cavity dual-color Yb:fiber laser," Optics Express 27(20), 28062-28074 (2019).
48. T. Li, X. Zhao, J. Chen, Q. Li, S. Xie, and Z. Zheng. "Tri-comb and quad-comb generation based on a multi-dimensional multiplexed mode-locked laser," IEEE Journal of Lightwave Technology 37(20), 5178-5184 (2019).
49. F. Shi, P. Cheng, Y. Huang, H. Yao, T. Wang, F. Pang, and X. Zeng, "Mode-locked all-fiber laser emitting two-color high-order transverse mode," IEEE Photonics Technology Letters, 31(7), 497-500, 2019.
50. T. Huang, S. Fu, C. Ke, P. P. Shum, and D. Liu, "Characterization of fiber Bragg grating inscribed in few-mode silica-germanate fiber," IEEE Photonics Technology Letters, 26(19), 1908-2001, 2014.
51. J. Dong, and K. Chiang, "Mode-locked fiber laser with transverse-mode selection based on a two-mode FBG," IEEE Photonics Technology Letters, 26(19), 1908-2001, 2014.
52. T. Liu, S. Chen, and J. Hou, "Selective transverse mode operation of an all-fiber laser with a mode-selective fiber Bragg grating pair," Optics Letters, 41(24), 5692-5695, 2016
53. T. Wang, F. Wang, F. Shi, F. Pang, S. Huang, T. Wang, X. Zeng, "Generation of femtosecond optical vortex beams in all-fiber mode-locked fiber laser using mode selective coupler," IEEE Journal of Lightwave Technology, 35(11), 2161-2166, 2017
54. Z. Zhang, Y. Cai, J. Wang, H. Wan, and L. Zhang, "Switchable dual-wavelength cylindrical vector beam generation from a passively mode-locked fiber laser based on carbon nanotubes," IEEE IEEE Journal of Selected Topics in Quantum Electronics, 24(3), 1100906, 2018.

Chapter 11
Multi-soliton Complex in Nonlinear Cavities

Chengying Bao and Xiaosheng Xiao

Abstract Dissipative nonlinear cavities can accommodate multiple solitons. When there are more than one soliton in the cavity, these multiple solitons could inter-act with other solitons, leading to various new phenomena. In this chapter, we will discuss the multi-soliton complex in dissipative Kerr cavities mainly including mode-locked fiber lasers and high-Q microcavities. Dissipative solitons in these systems can interact via tails of the solitons, dispersive waves or active gain dynamics in the system. Multi-soliton complex such as soliton molecules, soliton crystals, vibrating solitons, rogue waves have been observed in dissipative cavities. Multi-soliton complex has also been used in applications such as optical buffers and frequency comb generation. These phenomena highlight the particle-like features of solitons and greatly enrich the soliton dynamics.

Keywords Soliton · Mode-locked fiber lasers · Microresonators · Kerr nonlinearity · Soliton trapping · Microcavity solitons · Dispersive wave · Soliton interactions · Multi-soliton complex · Soliton molecules · Soliton crystals · Spatio-temporal mode-locking

11.1 Introduction

Solitons are particle like wavepackets that can interact. When there are multiple solitons in a dissipative cavity with gain either from active gain or parametric gain, these solitons can interact via various mechanisms. For example, for shortrange interaction, the solitons can interact via their overlapping waveform tails [1]. For

C. Bao (✉)
State Key Laboratory of Precision Measurement Technology and Instruments, Department of Precision Instruments, Tsinghua University, Beijing, China
e-mail: cbao@tsinghua.edu.cn

X. Xiao
State Key Laboratory of Information Photonics and Optical Communications, School of Electronic Engineering, Beijing University of Posts and Telecommunications, Beijing, China
e-mail: xsxiao@bupt.edu.cn

M. F. S. Ferreira (ed.), *Dissipative Optical Solitons*, Springer Series in Optical Sciences 238, https://doi.org/10.1007/978-3-030-97493-0_11

long range interaction, the solitons can interact via acoustic-optical effects [2], gain medium dynamics [3], dispersive waves [4] etc. These interactions contribute to different nonlinear attractors and various multi-soliton complex. Besides co-propagating multi-soliton complex in the cavity, counter-propagating multi-soliton complex can also exist in dissipative cavities, adding a new dimension to host multi-soliton [5, 6]. Furthermore, novel measurement techniques such as dispersive Fourier transform (DFT) [7] has been used to measure the real time dynamics of the multi-soliton complexes, which gives new insights into the dissipative soliton dynamics. In addition to mode-locked lasers, multi-soliton state in high-Q microcavities also offers a way to generate coherent microcavity based frequency combs (microcombs) with high output power [8, 9] and enables new applications. In the following, we discuss the recent advances of the multi-soliton complex studies in mode-locked lasers and microcavities.

11.2 Multi-soliton Complex in Mode-Locked Fiber Lasers

Considering its compactness, mode-locked fiber lasers have become an attractive method to generate ultrashort pulses and dissipative solitons. Due to the confinement of light with high peak power in the fibers with small area, the nonlinearity is prominent in mode-locked fiber lasers, which also makes them an ideal platforms to investigate dissipative soliton dynamics [10]. Among these various nonlinear dynamics, multi-soliton complex is one of the most commonly observed phenomena. Herein, recent progress of the investigation of multi-soliton complex in mode-locked fiber lasers are introduced. The discussion includes the latest observations related to multi-soliton states, rapid measurements of multi-soliton dynamics, and the phenomena of multi-soliton in an emerging type of fiber lasers, i.e., the spatio-temporal mode-locked multi-mode fiber lasers [11].

11.2.1 Multi-soliton States in Mode-Locked Lasers and Their Interaction

The general architecture of passively mode-locked fiber lasers is shown in Fig. 11.1a. The gain medium is an active fiber, whose operation wavelength (typical wavelength of 1, 1.5, 2 μm) is determined by the doped ion in the gain fiber. There may be passive fibers which are used for dispersion/nonlinearity management or control of the repetition rate of output pulse train. The net dispersion of the cavity could be negative, positive, or near-zero. A saturable absorber (SA) is used for initiating and stabilizing the mode-locking. It could be material-based real SA (e.g., graphene [12]) or artificial SA based on nonlinear effects (e.g., nonlinear polarization rotation technique [13], nonlinear loop mirror [14]).

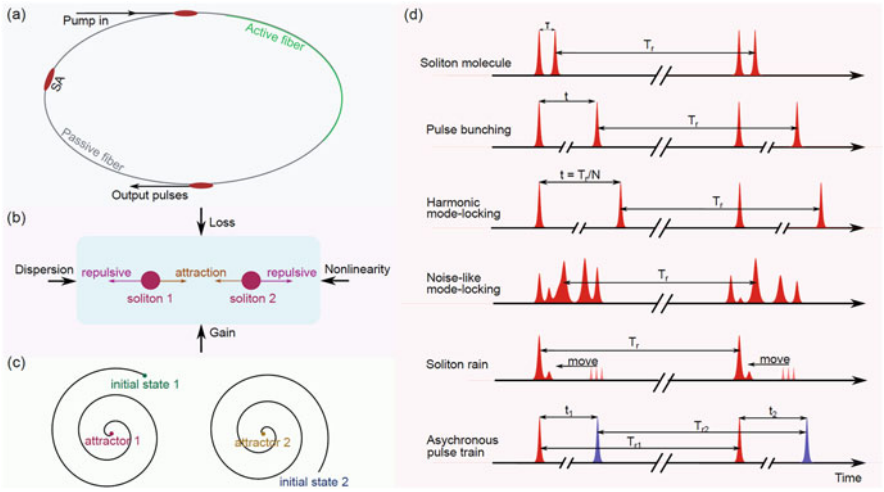

Fig. 11.1 Multi-soliton in passively mode-locked fiber lasers. (**a**) General scheme of passively mode-locked fiber lasers. SA: saturable absorber. (**b**) Generation of multi-soliton (e.g., soliton molecule) in fiber lasers through various interactions mediated by different mechanism. For example, two solitons with a same phase, their overlapping part will induce an attractive force between them, while two out-of-phase solitons will experience repulsive force. (**c**) Approaching different attractors with different initial states. (**d**) Examples of different patterns of multi-soliton in temporal domain

There are several explanations for the generation of multi-soliton in mode-locked fiber lasers [15–22]. In general, the amount of nonlinear phase shift which the cavity pulse could tolerate is limited [23]. When the nonlinear phase shift experienced by the pulse is too large, wave-breaking will occur and multi-soliton appear [15]. This is also referred to as the area theorem, which was not only proposed in anomalous dispersion regime [16] but also in normal dispersion regime [17]. Peak-power-limiting effect has also been proposed to explain the multi-soliton generation in lasers mode-locked by nonlinear polarization rotation [18]. Spectral filtering resulting from the birefringence of the cavity components or from the limited gain bandwidth could also cause multi-soliton [19].

As shown in Fig. 11.1b, the laser cavity is a dissipative system, and the generation of multi-soliton is determined by the cavity structure and parameters [24], including the dispersion, nonlinearity (e.g., the optical Kerr and Raman effects in the fibers, the nonlinear loss of SA and the nonlinear gain of active fiber), gain, and loss (including the loss induced by optical filters). The final output multi-soliton is a balanced state mediated by various interactions among the solitons [24], including short-range (order of pulse duration) interactions and long-range (much larger than pulse duration) interactions. The former could result from the fiber nonlinearity (e.g., cross-phase modulation, Raman scattering) [25], time-dependent loss of SA [24], and the latter could be mediated by continuous-wave (e.g., dispersive wave) [26], photoacoustic effect [27], dynamics of the gain medium [3].

There are numerous parameters and interactions in the fiber cavity, leading to the rich dissipative soliton dynamics. Depending on the spatial distributions of multi-solitons in the cavity, we can roughly classify the multi-soliton into soliton molecule, pulse bunching, and harmonic mode-locking [28], as shown in Fig. 11.1d. In the case of soliton molecules (also termed as bound state of solitons), the distance of multi-soliton is usually small and comparable to the pulse duration so that the short-range interaction among them can be important [10]. For the state with longer distance among the solitons [29], we call it as pulse bunching. Especially, if all the pulses within a single round-trip are equally separated, it is called harmonic mode-locking and the pulse repetition rate is multiple of the fundamental repetition rate [30]. For the latter two states, the long-range interactions among the pulses dominate the formation of the multi-soliton complex.

An interesting phenomenon usually observed in these multi-soliton states is the quantization of the output parameters. For instance, the energies of the multiple pulses are identical [17–19, 29]. Another interesting phenomenon of multi-soliton is that the final output states of a fixed cavity may be different when shutting down and then turning on the laser again, since the steady state of multi-soliton depends on the initial state of the laser [20, 24]. This also suggests that there may be several attractors in a mode-locked fiber laser [20], as shown in Fig. 11.1c. Depending on the initial condition, the final attractors, as well as the evolution paths, can be different. Aside from the steady attractors, there are attractors with periodically vitiation, or even unstable attractor, and the corresponding multi-soliton could periodically evolve (e.g., soliton rain [31]) or be unstable (noise-like pulses/rouge wave), as shown in Fig. 11.1d. In mode-locked lasers, pulses with different wavelength/polarization/propagation directions, can exist in a single cavity simultaneously [32–34]. The propagation velocity of these pulse trains could be different due to different group velocity [34, 35], or they are locked by internal interactions and propagate with the same velocity [36, 37]. We will discuss these phenomena in details in the following.

11.2.1.1 Soliton Molecule

Soliton molecule is a common multi-soliton phenomenon in mode-locked fiber lasers, exhibiting strong short-range interaction and specific phase relation among the sub-pulses (a sub-pulse is an individual soliton within a soliton molecule). In 1991, soliton molecule was theoretically predicted to exist in nonlinear systems described by Schrödinger-Ginzburg-Landau equation [38]. In 2001, soliton molecule was experimentally observed in a passively mode-locked fiber laser [39]. Since then the soliton molecule has been extensively investigated, which could refer to the review papers [24, 40]. Soliton molecule has been observed in cavities with different dispersion distribution, including anomalous dispersion regime, normal dispersion regime, and nearly zero net-cavity dispersion regime, with different operation wavelength including 1, 1.5 and 2 μm, with different laser types including traditional

soliton, stretched-pulse, all-normal-dispersion, self-similar fiber lasers, and with different mode-locking techniques including various real SAs and effective SAs [24]. These results show that soliton molecule is an intrinsic state in mode-locked fiber lasers.

Sub-pulses usually have identical pulse energies, and the phase difference and temporal separation between the sub-pulses within the soliton molecule are quantized [24, 41–45]. For example, the phase difference is usually equal to multiple $\pi/2$ for typical solitons [24, 45–47]. However, the phase relationship may change when considering other perturbations to the soliton. For example, when the net group velocity dispersion of the cavity is near zero and the third-order dispersion results in asymmetric Kelly sidebands, the phase difference of the sub-pulses could differ from a multiple of $\pi/2$ [24, 26]. The Kelly sidebands also leads to quantized separations between the sub-pulses [44, 45]. Other types of soliton molecules like vibrating soliton pair will have time-varying pulse separation, phase difference [48–50]; soliton molecule with flipping phase also exists [51].

Moreover, the number of sub-pulses in soliton molecule could be two or more [43], and soliton molecular complex composed of several soliton-pair molecules has also been observed [43, 52]. Recently, vortex soliton molecule was generated by use of a mode selective coupler [53]. The relative timing jitter and phase jitter between the sub-pulses of soliton molecule have been measured [54, 55]. Since the pulses in soliton molecule are deformable, a theoretical study revealed the dynamics of distorted and undistorted soliton molecules [56]. Sub-pulses are usually closely spaced in a soliton molecule, but widely spaced soliton molecule with separation ($\sim$60 ps) up to 100 times of pulse duration has also been reported [57].

11.2.1.2 Pulse Bunching and Harmonic Mode-Locking

Pulse bunching and harmonic mode-locking are states with multi-soliton well separated; hence, the short-range interaction can be negligible in these states. The long-range interaction (see the beginning of Sect. 11.2.1) determines the multi-soliton state and usually results in an identical energy and relative separation for pulses. Several mechanisms of harmonic mode-locking have been proposed, including the photoacoustic effect [27], gain depletion and recovery [3]. It was pointed that, for different cavities, the interaction of harmonic mode-locking maybe different [58]. Recently, harmonic mode-locking in fiber lasers with novel SAs were investigated. For instance, harmonic mode-locking with pulse repetition rate up to several giga-hertz using topological insulator-based SA has been reported [59, 60]. Associated with the dissipative Faraday instability, harmonic mode-locking (with repetition rate up to $\sim$100 GHz) in thulium-doped Mamyshev fiber lasers was numerically predicted [61].

11.2.1.3 Other States

Aside from the multi-soliton states mentioned above, there are numerous other multi-soliton patterns in mode-locked fiber lasers. Herein some examples are listed, and part of them are illustrated in Fig. 11.1d. For example, soliton rains have been observed in both anomalous and normal dispersion regimes [31, 62, 63]. In this state, multi-soliton includes main pulse (condensed phase) and drifting solitons, which will continuously move towards the main pulse. In addition, noise-like mode-locking comprising lots of incoherent sub-pulses [64–66] can also exists in mode-locked fiber lasers, and rogue wave was found to originate from the state of noise-like mode-locking [67]. Mixed states with multi-soliton were also observed, e.g., harmonic mode-locking of soliton molecule [68], bidirectional operation of bound solitons [69], asynchronized dual-wavelength mode-locking with harmonic mode-locking [34].

A special and interesting multi-soliton state is that pulse trains with different repetition rates exist in a single cavity simultaneously. A bidirectional mode-locked fiber laser without intracavity isolator was proposed, and counter-propagating pulse trains with different repetition rates were achieved due to the asymmetry of the two directions in the cavity [70]. Birefringence induced asynchronous pulse trains with different polarization states were also proposed. Pulse trains with orthogonal polarizations was achieved in a unidirectional fiber laser, where the repetition rate difference is induced by a segment of polarization-maintaining fiber [71]. In fiber lasers, the group velocities of pulses at different wavelength are different due to the cavity dispersion, thus the pulse trains can be asynchronous. By adjustment of intracavity loss and controlling the gain peaks, a dual-wavelength mode-locked fiber laser was demonstrated [33]. Based on a Sagnac loop filter, an all-polarization-maintaining dual-wavelength mode-locked fiber laser was demonstrated [72]. This state of multiple pulse train with different repetition rates can be used as a promising dual-comb source, without complex frequency stabilization systems [35, 73, 74]. Sharing the same cavity, the two pulses are inherently coherent which preserves the repetition rate difference between them passively.

11.2.2 Rapid Measurements of Multi-soliton Dynamics in Mode-Locked Fiber Lasers

The pulses in a mode-locked fiber laser usually has a sub-picosecond duration, which are too short for direct photodetection. In recent years, with the emerging techniques such as DFT (also called as time-stretch method) [7], and time lens [75–77], the fast evolution and internal motions of the pulses could be observed in real time. For the DFT technique, the output pulse from mode-locked lasers propagates through an optical element (e.g., a spool of fiber of tens kilometers long) with very large accumulated dispersion. Neglecting the nonlinearity, higher-order dispersion

of the dispersive element, the pulse output from the element will be significantly broadened (e.g., the duration in the order of nanosecond). Thus, the temporal details could be detected by fast photodetector and oscilloscope. This propagation process could be analogue with the Fourier transform, and the temporal profile of the broadened pulse reflects the single-shot spectrum of the pulse. The formation and dynamics of multi-soliton, including the internal motion among the sub-pulses, have been revealed in recent years using this technique.

The internal dynamics of various soliton molecule, including vibrating soliton pairs, have been experimentally observed by the DFT technique [78, 79]. The build-up processes of soliton molecules in different laser systems through diverse soliton inter-actions were also reported [80–82]. Molecular complex with two soliton molecules has been real-time observed and the difference between intra- and inter-molecular bonds was discussed [52]. The DFT technique has also been applied to the 2 μm band to resolve the transient soliton molecule dynamics in a thulium-doped fiber laser [83]. Dynamics of soliton molecules in the normal-dispersion regime was investigated, and a periodical evolutions of the sub-pulses in a soliton molecule was observed [84]. The dynamics of breathing soliton molecules and breathing pulse bunching were observed [85]. Multi-soliton (including two-molecule complex) in pulsating regime was reported, and the dissociation dynamics within these solitons were observed [86]. Shaking soliton molecules was also observed, where multiple oscillatory motions are jointly involved in the internal dynamics [87]. Full-field (both amplitude and phase) characterization of the build-up and internal collision of multi-soliton was achieved by combining DFT and time lens [75]. The detailed build-up dynamics of harmonic mode-locking was also observed by DFT technique [58, 88].

DFT technique has also been used to reveal other complicated multi-soliton dynamics. The transition dynamics between consecutive multi-pulsing states (e.g., a two-pulse and a three-pulse states) was recorded [89]. Asynchronous build-up of multi-soliton in an all-polarization-maintaining fiber laser was observed [90]. The dynamics of various assembling forms of multi-soliton, including the combination of soliton singlets and molecules, were traced and characterized [91–93]. Soliton explosion is a striking nonlinear phenomenon, where the pulse intermittently explodes but return to its original state [94]. The entire process of soliton interaction or collision induced soliton explosion was observed [95, 96]. Generation of optical rogue waves during random multi-soliton build-up was revealed [97].

The decaying evolution dynamics of multi-soliton was also observed [98]. It has been discovered that, during the birth of stable single pulse from noise or other state, multiple pulses will be generated then decay, and eventually only one pulse survives [99, 100]. For the cavity hosting two asynchronous pulse trains simultaneously, the build-up dynamics and the intracavity collision of the asynchronous pulses were also been investigated [101, 102]. These new observed real time dynamics could improve our understanding of multi-soliton complex to another level.

11.2.2.1 Multi-soliton in Spatiotemporal Mode-Locked Fiber Lasers

The multi-soliton complex discussed above is all investigated in fiber lasers comprising a single transverse (spatial) mode. There is great significance in studying nonlinear spatiotemporal dynamics in ultrafast lasers. And spatiotemporal mode-locking (or multimode mode-locking), in which both the longitudinal and transverse modes were locked simultaneously, was proposed and demonstrated in lasers com-posed of multimode fibers recently [11]. By use of graded-index multimode fibers with small modal dispersion, the walk-off of different transverse modes can be balanced by intracavity spatial filter. The mechanism of spatiotemporal mode-locking was analyzed, and several distinct forms of spatiotemporal dynamics which have no analogues in single-mode lasers were predicted [103].

Multi-soliton states were also observed in spatiotemporal mode-locked (STML) lasers. In a typical STML fiber laser, double-cladding gain fiber (with 10 μm core, core and cladding NA of 0.08 and > 0.48, respectively) and passive multimode fiber with 50 μm core were used to build the laser cavity [104]. Nonlinear polarization rotation was used for mode-locking [13]. The injection of signal light into gain fiber with smaller core size would cause loss of some transverse modes, which serves as aspatial filter. In conjunction with an intracavity spectral filter, spatiotemporal mode-locking can be initialized. Soliton molecule [104], harmonic mode-locking and pulse bunching [28] were reported, some of which are shown in Fig. 11.2. Figure 11.2a gives the results about three states of soliton molecule with different separations, which can be controlled by tuning intracavity waveplates used for nonlinear polarization rotation. The distributions of transverse modes for these soliton molecules are different, with the beam profiles shown in the inset of Fig. 11.2a. Figures 11.2b–d give typical outputs of pulse bunching and harmonic mode-locking in a STML laser, respectively. For the harmonic mode-locking state, the interval of output pulses is 8.2 ns, half of the cavity round-trip time. In order to investigate the spatial characteristics of this state, the output is spatially-sampled at different positions, illustrated by the black circles in the inset of Fig. 11.2d. The average powers sampled at different positions are presented in Fig. 11.2d, reflecting the intensity distribution of the beam. Moreover, the pulse intervals of the pulse trains sampled by the moving sampler stays the same as shown in Fig. 11.2d. The results of spatial sampling measurement show that the multiple pulses are multimodal. Furthermore, various dual-soliton states, including the pulsating dual-soliton, were observed in STML fiber lasers [105]. Single- and multi-soliton states with switchable central wavelengths were observed in an all-fiber STML laser [106]. Replacing the quasi-single-mode active fiber with multimode step-index active fiber, it was found that spatiotemporal mode-locking could also be supported in these lasers [107], where multi-soliton states were observed recently. The investigations of nonlinear spatiotemporal dynamics in STML multimode fiber lasers are still in the early age, and we expect that more nonlinear dynamics of multi-soliton will be revealed.

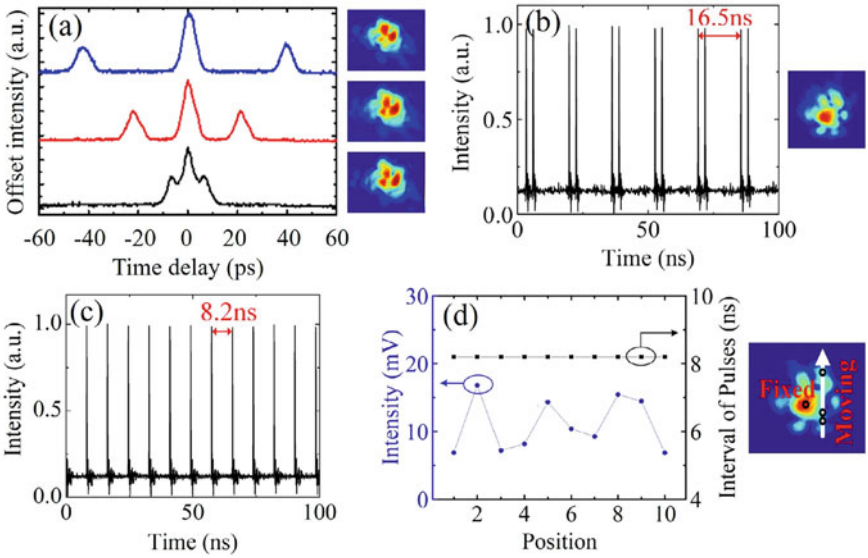

Fig. 11.2 Multi-soliton states observed in spatiotemporal mode-locked multimode fiber lasers. (**a**) Soliton pairs with different separations. The measured autocorrelation traces are given. Inset of (**a**): beam profiles corresponding to soliton pair states depicted with blue, red and black lines, respectively. (**b**) Pulse bunching state. Pulse train measured by oscilloscope is given. Inset of (**b**): the corresponding beam profile. (**c–d**) Harmonic mode-locking state. (**c**) Pulse train measured by oscilloscope; (**d**) Pulse intensities and pulse intervals of the pulse trains sampled at different position. Inset of (**d**): beam profile of the whole output, with black circles represented the spatial sampling positions (one sampler fixed at the center, and another sampler moving along the direction of arrow). Panel (**a**) is adapted from ref. [104], OSA; Panels (**b–d**) are adapted from ref. [28], OSA

11.3 Mutli-soliton Complex in Microcavities

Temporal soliton generation in coherently pumped Kerr resonators has provided a new way to obtain dissipative optical solitons in cavities [9, 108–110]. These solitons are a train of pulses sitting atop a coherent background that provides parametric gain via the Kerr effect. Such coherently pumped temporal solitons were first investigated and demonstrated in passive fiber cavities (unlike fiber lasers, there is no active gain fiber in the cavity) [108, 111]. Then its demonstration in microcavities have fueled the progress of microcavity based frequency combs (microcombs) [9]. Microcombs are an array of equidistantly spaced optical frequencies generated in microcavities that can be linked to microwave frequencies; each frequency can be written as $\nu_N = Nf_r + f_0$ where f_r is repetition rate of the solitons and f_0 is the carrier-envelope offset frequency [9, 112]. When the pumping field is a continuous wave laser, the soliton number generated in a coherently pumped cavity is usually random and larger than one [109]. This feature makes coherently pumped cavities a new platform to study multi-soliton complex. Since there is no active gain

medium in the cavity, soliton interaction via gain saturation dynamics will not occur incoherently pumped cavities. However, perturbations such as spatial-mode-interaction is more prominent in microcavities, which adds new freedoms to control the soliton interaction dynamics in microcavities. In this section, we discuss the multi-soliton complex in coherently pumped Kerr resonators and their applications to frequency microcombs.

11.3.1 Basic Principle of Coherently Pumped Solitons

The coherently pumped cavity solitons are governed by the Lugiato-Lefever equation (LLE) [113–115]. The equation can be written as

$$\frac{\partial A}{\partial T} = -\left(\frac{\kappa}{2} + i\delta\omega\right)A - i\frac{\beta_2 L}{2T_R}\frac{\partial^2 A}{\partial t^2} + \frac{i\gamma L}{T_R}|A|^2 A + \sqrt{\frac{\kappa_e P_{\text{in}}}{T_R}} \tag{11.1}$$

where A is the envelope of the intracavity field, T is the slow time, t is the fast co-moving time frame for the solitons, β_2 is the group velocity dispersion, γ is the nonlinear coefficient of the cavity, L is the cavity length and T_R is the round-trip time, $\delta\omega$ is the frequency detuning between pump and cavity resonance, P_{in} is the pump power, κ and κ_e are the total and coupling loss rate, respectively. This equation was firstly introduced to model spatial cavity solitons [113, 116–118] and it works equally well for temporal cavity solitons. This equation includes the basic soliton dynamics impacted by the group velocity dispersion and the Kerr nonlinearity as well as gain and loss. As a dissipative soliton, stable propagation of the soliton in a cavity requires the double balance between dispersion and nonlinearity as well as gain and loss. For the requirement of dispersion and nonlinearity balance, the soliton pulse will have a sech-like shape and peak power and duration needs to satisfy the following relationship, $\gamma P_s = |\beta_2|/\tau_s^2$ where P_s is the peak power of the soliton and τ_s is the pulse-width of the soliton [15]. For temporal cavity solitons, the coherent pumping nature results in the following relationship between P_s and $\delta\omega$ [109, 111, 119, 120],

$$\gamma P_s L \approx 2\delta\omega T_R \tag{11.2}$$

Thus, the properties of a dissipative soliton in a coherently pumped cavity can be accurately controlled by the pump-resonator frequency detuning $\delta\omega$.

Equation 11.1 can be used to simulate the intracavity soliton dynamics in coherently pumped systems using the split-Fourier algorithm [15]. And it has been revealed that the intracavity field can operate at different regimes depending on $\delta\omega/\kappa$ [109, 121–123]. We show a typical intracavity dynamics numerically simulated using the LLE in Fig. 11.3. The simulation starts from noise, and intracavity

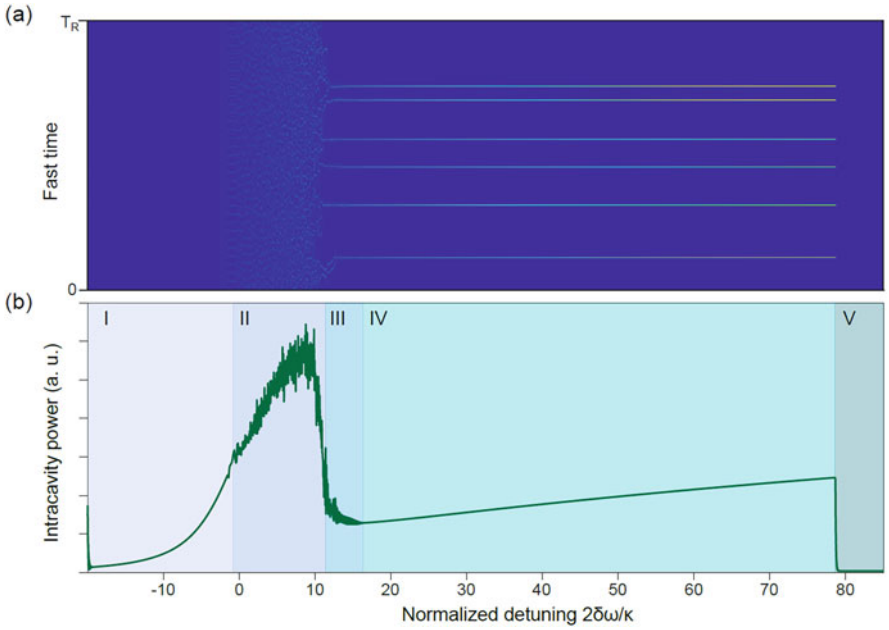

Fig. 11.3 Intracavity soliton dynamics when scanning the pump-resonator frequency detuning simulated using the LLE. (**a**) Intracavity field dynamics when scanning $\delta\omega$ from blue-detuned to red-detuned. Multiple solitons are generated at a larger detuning. (**b**) Change of the intracavity power when $\delta\omega$ is scanned. The operation regimes of the microcomb generation can be categorized into 5 regimes, I stable modulation instability, II chaotic state, III breather soliton, IV stable soliton, V out of resonance

power increases when scanning the pump-resonance detuning $\delta\omega$ from blue-detuned to red-detuned. With the increase of the intracavity power, stable modulation instability [15] is initiated (regime I). When further tuning the laser to the red side, the intracavity field becomes chaotic (regime II). Then there is a drop of the intracavity power and pulses emerges from the chaotic state. Pulses in this state are unstable and exhibit periodic change of the duration and peak power, which are referred to as breather solitons (regime III) [124]. Stable solitons can be generated when further increasing $\delta\omega$ (regime IV). The simulated soliton stream comprises 6 solitons in one round-trip as shown in Fig. 11.3a. Solitons only exists in a limited range of detuning and will annihilate when the detuning is too large (regime V). From Fig. 11.3, we can see that the detuning $\delta\omega$ usually needs to be much larger than the cavity linewidth κ to obtain a well developed soliton. Furthermore, the simulated intracavity dynamics for microcavity solitons have also been experimentally measured [125]. Equation 11.1 can also be easily extended to include the effects of high-order dispersion, stimulated Raman scattering, Kerr shock [126], which can be critical for modeling ultrashort solitons.

11.3.2 Multi-soliton States and Their Interactions in Microcavities

Since the pumping background is uniform, usually multiple solitons are supported (see also Fig. 11.3). Typically, the solitons generated in coherently pumped macroscopic fiber cavities hosts many solitons, which can be written from external triggers and used as optical buffer [108]. Since the temporal solitons in fiber cavities are usually widely spaced, their interaction is usually weak when there is no resonant emission in the system. However, these solitons can also interact weakly via the acoustic effects in the fibers [2], similar to solitons in mode-locked fiber lasers. When moving from fiber cavities to microcavities whose round-trip time is usually only hundreds picosecond to picoseconds, the soliton separation between the soliton decreases substantially. The multi-soliton state can be interact stronger and exhibit new phenomena, especially when considering dispersive wave emission in microcavities [127, 128].

11.3.2.1 Dispersive Wave Emission in Microcavities

Dispersive wave emission (also known as Cherenkov radiation) was first investigated for ultrashort pulses propagation under the perturbation of third-order dispersion in optical fibers [127, 128]. When the phase-matching is satisfied (e.g., $\beta_2\omega^2/2 + \beta_3\omega^3/6 \approx 0$), powers around the corresponding frequency band will be enhanced and known as dispersive wave emission (see the green line in Fig. 11.4a). For microcavity solitons, the emission was first observed in soliton generation in silicon nitride cavities [129]. This high-order dispersion (not limited to third order dispersion) enabled dispersive wave emission has been used to extend the microcomb bandwidth to octave spanning that can be used self-referencing [112, 130, 131]. For multi-spatial-mode microcavities, another type of dispersive wave emission can arise from spatial mode-interaction [132–136]. Spatial mode-interaction can modify the local dispersion and shift the resonances of two interacting mode families [132, 133] (see the blue line in Fig. 11.4a). This local dispersion change can lead to enhancement of the comb line powers which can be interpreted as dispersive wave emission [134], see Fig. 11.4b for an example. Such an emission is used to be thought to be detrimental for soliton generation in microcavities [132]. However, it also facilitates interaction of the multi-soliton and the emergence of multi-soliton complex.

If the pumping background is homogeneous, multiple solitons will be randomly spaced in the microcavity. In the presence of dispersive waves, the background is no longer uniform, since the emission manifests as an oscillating tails for microcavity solitons (see Fig. 11.4c). The nonuniform background can act as a refractive index trapping potential that traps the solitons, a phenomenon known as soliton trapping [137]. It has been shown theoretically and experimentally (first in fiber cavities) [4, 138] that resonant emissions can stabilize the relative spacing of coherently

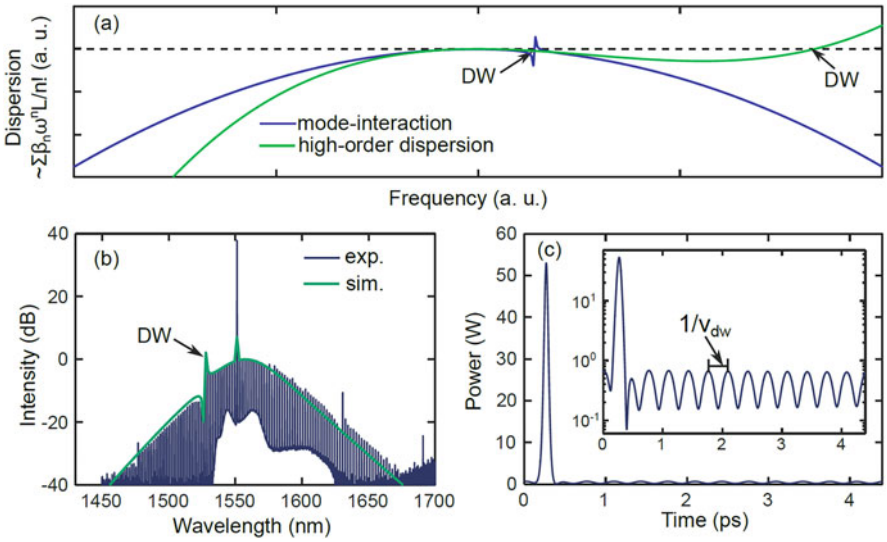

Fig. 11.4 Dispersive wave emission in microcavities. (**a**) An illustration of group delay dispersion and dispersive wave emission enabled by mode-interaction and high-order dispersion. (**b**) An example of the experimentally measured and numerically simulated optical spectrum of a soliton microcomb comprising dispersive wave emission. (**c**) The temporal waveform of the simulated soliton which has an oscillating tail from the dispersive wave emission. Panels (**b**), (**c**) are adapted from ref. [136], OSA

pumped cavity solitons (similar to the quantized spacing in soliton molecules in mode-locked lasers [44, 45]). For example, if there is a dispersive wave emission at the frequency of ν_{dw} from the pump, the solitons will be spaced by $m/|\nu_{\mathrm{dw}}|$ where m is an integer number. Therefore, multi-soliton states in microcavities tend to have a regular spacing in microcavities. Moreover, unlike dispersive wave induced by high-order dispersion or Kelly sidebands in mode-locked fiber lasers, the spatial mode-interaction induced dispersive wave emission may only include a small number of cavity modes. The oscillating tail and the refractive potential can be sine-like and not decaying (see Figs. 11.4a, b). Thus, dispersive wave mediated interaction can last from a long range temporal separation.

The soliton interaction and regular spacing can also provide a passive mechanism to induce deterministic single soliton generation in microcavities [136]. Due to the regular spacing, dispersive wave power can be enhanced when the soliton number increases. The optical spectrum of a multi-soliton complex can be written as,

$$S_n(\omega) = \mathcal{F}\left\{\sum\nolimits_{j=1}^{j=n} A_1(\tau - \tau_j)\right\} = S_1(\omega)e^{i\omega\tau_1}\sum\nolimits_{j=1}^{j=n} e^{i\omega(\tau_j - \tau_1)} \tag{11.3}$$

where $\mathcal{F}$ denotes Fourier transform, ω is the frequency relative to the pump, A_1 is the envelope of a single soliton with S_1 being its spectrum, and τ_j is the location for the j th soliton. In deriving Eq. 11.3, we use the property that multiple solitons have the

same phase because they share a same phase offset with respect to the pump [136]. Since the solitons are spaced by $m/|\nu_{dw}|$, the power of the dispersive wave will be $S_n(\nu_{dw}) = n^2 S_1(\nu_{dw})$ for a soliton stream consisting n solitons in the cavity (the actual dispersive wave power can be lower than this considering the spectral recoiling effect [128]).Since dispersive wave emission can be considered as a nonlinear loss for a soliton [128], n-soliton-state will experience a larger nonlinear loss than a single-soliton state. Therefore, to sustain the multi-solitons with a strong dispersive wave emission, a higher pump power is needed. It has been shown theoretically that dispersive wave emission can set an upper limit soliton number for a given pump power [136]. When the upper limit number is 1, deterministic single solitons can be possible via the interaction between the solitons via the dispersive wave emission. The smooth spectrum for a single-soliton state can be desired for many applications.

11.3.2.2 From Soliton Molecules to Soliton Crystals in Microcavities

As the simplest multi-soliton state, two-soliton state or soliton molecules widely exist in microcavities. Reliable generation of the two-soliton state can be achieved by controlling the comb power via feedback [139] or backward tuning of the pump (from low frequency to high frequency) after solitons with a larger number is generated [140]. This two-soliton state is stabilized by dispersive waves and can also be compared to soliton molecules similar to mode-locked lasers. The relative separation between the two solitons can only be some discrete values as discussed above. Such two-soliton microcombs have also been used for microwave filtering [141]. The microwave frequency passband can be tuned by controlling the relative separation between the two solitons [141].

Other soliton number can also be possible. Indeed, a large soliton number can be useful to mitigate the thermal instability for soliton generation [140, 142]. Moreover, multi-soliton states can be a way to increase to increase the output comb power and the pump-to-comb conversion efficiency [143]. However, it should be noted that the multi-soliton states will result in a structured microcomb spectrum, and some lines may be quite weak (see Eq. 11.3). Moreover, the structure is not deterministic but depends on the relative separation of the solitons which is randomly determined (despite being discrete) when the solitons are triggered. Hence, it can be difficult to reproduce the spectrum. These features can make multi-soliton state undesirable for some applications.

A special case of the regular spacing is that multiple solitons in a microcavity can form the soliton crystal state [144–148] (see Fig. 11.5). A soliton crystal state in a microcavity comprises multiple solitons that are equidistantly spaced (Fig. 11.5a). Dispersive waves have been known to be responsible for this regular spacing [145]. The soliton crystal state can have some defects (with some solitons missing from the crystal); for example there can be X solitons spaced by $T_R/(X + X_0)$ in the cavity (X_0 is the number of defects or missing solitons) [145, 146] (Fig. 11.5c). In the

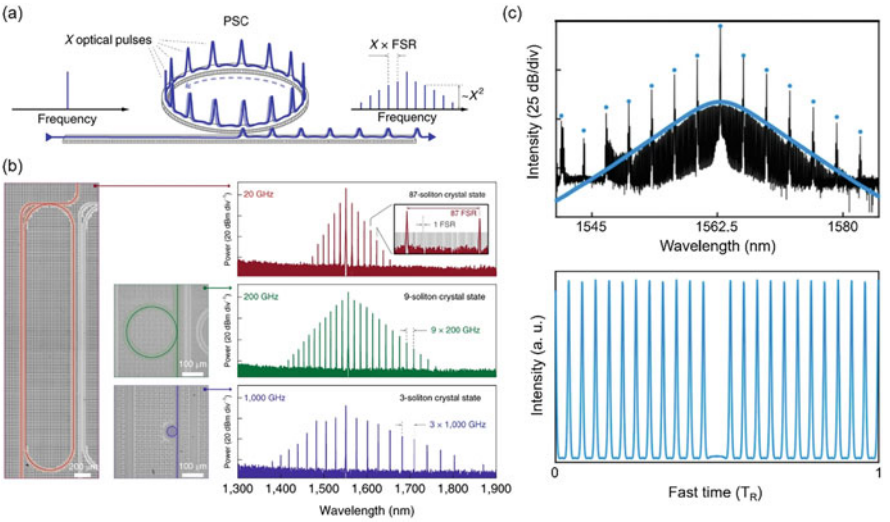

Fig. 11.5 Soliton crystals in microcavities. (**a**) When pumping a microcavity with a single frequency laser, *X*-soliton equidistantly spaced can be generated in the microcavity and a comb with a large line spacing of *X*-FSR can be obtained. (**b**) Picture of the microcavites and the generated perfect soliton crystal spectra. (**c**) Optical spectrum and temporal waveform of a soliton crystal with one defect (one missing soliton). Due to the defect, the spectrum has a line spacing of a FSR. Panels (**a**), (**b**) are adapted from ref. [144], NPG; panel (**c**) is adapted from ref. [145], NPG

frequency domain, the comb lines will be spaced by a free-spectral-range (FSR) of the cavity due to the defects. However, comb lines spaced by $X\cdot$ FSR from the pump will be much stronger than other lines. Perfect soliton crystals without defects can also be formed that is a state with X solitons spaced by T_R/X in the cavity [144, 147]. The corresponding microcomb has comb lines spaced by $X\cdot$ FSR of the cavity and there are no other lines in the spectrum. It has also been revealed that there is a threshold pump power below which perfect soliton crystal can be generated [144]. Such perfect soliton crystal can be used to generate soliton streams with ultrahigh repetition rates (more than THz) from microcavities. The soliton crystal can be used for microwave-to-THz-wave links. Soliton crystal microcombs have also been used for microwave photonics enabling application including (but not limited to) RF channelizer [148] and Hilbert transformer [149]. Furthermore, soliton crystals have also been demonstrated in a silicon nitride cavity around 780 nm [150]. Also, the perfect soliton crystal generation dynamics is deterministic without the chaotic regime [144]. This soliton generation route was also theoretically investigated [151]. Similar to soliton crystals, cnoidal waves or Turing rolls consisting of multiple equidistantly spaced pulses can also be generated in microcavities [152].

11.3.2.3 Multi-soliton State Using Advanced Pumping Schemes

The multi-soliton states in the above section only corresponds to one microcomb in the frequency domain. In other words, the solitons cannot be controlled independently. In addition to pumping the microcavity by a single laser, multi-soliton can also be generated using advanced pumping schemes (see Fig. 11.6). For example, when counter-pumping a cavity in two directions, counter-propagating solitons can be generated from the cavity [6, 153]. The counter-pumps can be derived by splitting a single pumps and using two acoustic-optical modulators (AOMs) to control their relative frequencies [6]. Therefore, the pump conditions in two directions can be controlled independently. As a result, the offset frequencies and the repetition rates of the soliton microcombs can be controlled to be different, i.e., two combs can be generated from a single cavity. Multi-soliton generated from a single cavity can enjoy the common noise suppression. Hence, such comb sources can be useful for applications like dual-comb spectroscopy [73], as the counter-propagating pulses in mode-locked lasers [5, 70] introduced in the above section.

Two counter-propagating solitons generated in this way can interact via the Rayleigh backscattering of the cavity. When the two counter-pumps are frequency detuned by $\Delta\nu_P$ (e.g., several MHz for silica microcavities) and the two soliton streams have a repetition rate difference of Δf_r, there can be a pair of lines in two directions whose comb line number with respect to the pump is M that are close in comb frequency or $\Delta\nu_P - M\Delta f_r \sim 0$. The comb line pair can be locked via backscattering and injection locking [6]. This interaction can stabilize the repetition rate difference of two counter-propagating soliton streams $\Delta f_r = \Delta\nu_P/M$. In this way, two mutually coherent soliton microcombs can be obtained (two line pairs are correlated, i.e., the pump pair and the injection locked pair). Indeed, counter-propagating soliton microcombs in this configuration have been used for range measurements [155] and Vernier spectrometer [156].

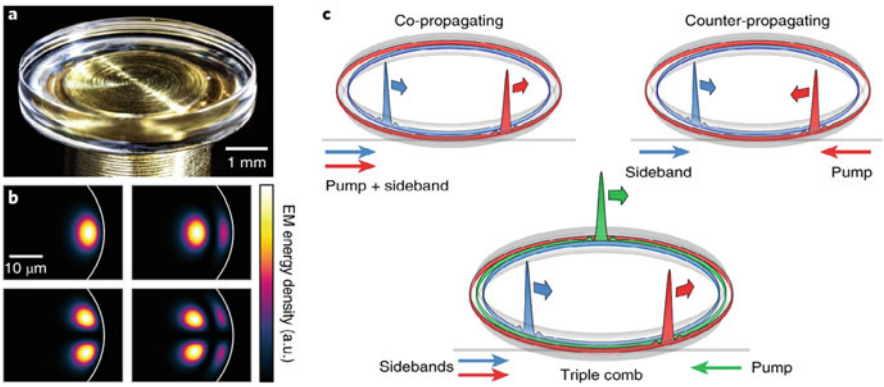

Fig. 11.6 Generation of solitons using multiple pumps. (**a**) Picture of a MgF_2 microcavity. (**b**) Simulated intensity profile of different spatial modes. (**c**) Different pumping schemes. Figure adapted from ref. [154], NPG

When the two pumps are only slightly detuned (e.g., less than hundreds of kHz for silica microcavities), the two counter-propagating soliton will mutually trap each other via the Kerr-mediated soliton trapping [137]. In a typical trapping case, two interacting solitons will have an identical group velocity and fixed relative delay. However, the presence of coherent pumping for microcavities will periodically modulate the spectral center frequencies of the counter-propagating solitons. Therefore, the group velocities and their relative position (after coupling out from the cavity) of the counter-propagating solitons will experience oscillatory modulation in this case [157]. Note that different from the above interaction that stabilizes Δf_r via a single line, this interaction involves two soliton wavepackets as entities. This interaction highlights the importance of coherent pumping to microcavity solitons dynamics.

Multiple solitons can also be generated in a microcavity when pumping different spatial modes in one direction [154]. In this case, the two pumps can be obtained by modulating a single laser via single-sideband modulation (the residual seed and the modulated sideband acts as two pumps). Since different mode families have different FSRs, the corresponding combs differ in the repetition rate and can also be used for dual-comb spectroscopy. In this scheme, up to 3 soliton microcombs (2 co-propagating and 1 counter-propagating) can be generated from a single microcavity [154]. Different from pumping multiple spatial modes in one direction, a two-soliton state can also be generated by pumping one cavity mode with two slightly frequency detuned pumps (frequency detuning on the cavity linewidth scale) in one direction [158]. In this case, soliton interaction and trapping can lock their group velocities to a same value, forming a soliton molecule. Since the pumping source is different, this type of soliton molecule is referred to as heteronuclear soliton molecules [158]. Different from the soliton molecules formed by dispersive waves, the hetronuclear soliton molecule is usually closely separated (a separation comparable to the soliton duration) and can interact directly via the Kerr cross-phase-modulation. Two solitons' peak power and duration can be quite different for a heteronuclear soliton molecules. Co-propagating pumping two different resonances of a single mode family by two lasers can also form multi-soliton complex [159]. When the two pumps are only detuned by a small number of FSR and $\delta\omega$ for two resonances are close, the generated multiple solitons can be locked and form soliton molecules. When the pumps are far detuned or $\delta\omega$ differs significantly, the generated solitons can have different traveling group velocities and collide in the cavity [159]. In such a way, it also provides a method to study the soliton collision dynamics experimentally.

11.4 Summary and Discussions

The multi-soliton complex in nonlinear cavities including mode-locked fiber lasers and coherently pumped microcavities have been discussed. In addition to dispersion and the Kerr effect, other effects including active gain, SA dynamics and spectral/

spatial filtering (for lasers) and coherent pumping, spatial mode-interaction (for microcavities) lead to a wide range of soliton phenomena. These solitons can interact via short range and long range effects. Both stable multi-soliton complex and unstable multi-soliton complex exist in these nonlinear resonators. Although the balance between dispersion and nonlinearity in these two systems is quite similar, the gain-loss balance in the two systems is quite different (mode-locked pulses are regenerated via amplification from the gain medium while microcavity solitons are regenerated via the parametric gain). Such differences also help to reveal the dissipative nature of multi-soliton states, and results in the different phenomena discussed above. In addition to multiple soliton travelling with a same group velocity, multi-soliton with different group velocities can also be generated in a single cavity. The inherent coherence between these asynchronous pulses makes them appropriate for dual-comb applications. Advanced pulse characterization techniques are being developed. We anticipate that more powerful tools can be used to investigate the multi-soliton dynamics in the near future. With these new tools and observations, we can improve the understanding of the multi-soliton complex and harness them for applications.

References

1. Gordon, J. Interaction forces among solitons in optical fibers. Opt. Lett. 8, 596–598 (1983).
2. Jang, J. K., Erkintalo, M., Murdoch, S. G. & Coen, S. Ultraweak long-range interactions of solitons observed over astronomical distances. Nature Photonics 7, 657–663 (2013).
3. Kutz, J. N., Collings, B., Bergman, K. & Knox, W. Stabilized pulse spacing in soliton lasers due to gain depletion and recovery. IEEE J. Quantum Electron. 34, 1749–1757 (1998).
4. Wang, Y.et al. Universal mechanism for the binding of temporal cavity solitons. Optica 4, 855–863 (2017).
5. Ideguchi, T., Nakamura, T., Kobayashi, Y. & Goda, K. Kerr-lens mode-locked bidirectional dual-comb ring laser for broadband dual-comb spectroscopy. Optica 3, 748–753 (2016).
6. Yang, Q.-F., Yi, X., Yang, K. Y. & Vahala, K. Counter-propagating solitons in microresonators. Nature Photonics 11, 560–564 (2017).
7. Goda, K. & Jalali, B. Dispersive fourier transformation for fast continuous single-shot measurements. Nature Photonics 7, 102–112 (2013).
8. Vahala, K. J. Optical microcavities. Nature 424, 839–846 (2003).
9. Kippenberg, T. J., Gaeta, A. L., Lipson, M. & Gorodetsky, M. L. Dissipative Kerr solitons in optical microresonators. Science 361, eaan8083 (2018).
10. Grelu, P. & Akhmediev, N. Dissipative solitons for mode-locked lasers. Nature photonics 6, 84–92 (2012).
11. Wright, L. G., Christodoulides, D. N. & Wise, F. W. Spatiotemporal mode-locking in multimode fiber lasers. Science 358, 94–97 (2017).
12. Zhang, H., Tang, D., Zhao, L., Bao, Q. & Loh, K. Large energy mode locking of an erbium-doped fiber laser with atomic layer graphene. Optics Express 17, 17630–17635 (2009).
13. Matsas, V., Newson, T., Richardson, D. & Payne, D. N. Self-starting, passively mode-locked fibre ring soliton laser exploiting non-linear polarisation rotation. Electronics Letters 28, 1391–1393 (1992).
14. Doran, N. & Wood, D. Nonlinear-optical loop mirror. Opt. Lett. 13, 56–58 (1988).
15. Agrawal, G. P. Nonlinear fiber optics (Academid Press, 2006).

16. Nelson, L., Jones, D., Tamura, K., Haus, H. & Ippen, E. Ultrashort-pulse fiber ring lasers. Appl. Phys. B65 (1997).
17. Renninger, W. H., Chong, A. & Wise, F. W. Area theorem and energy quantization for dissipative optical solitons. J. Opt. Soc. Am. B27, 1978–1982 (2010).
18. Tang, D., Zhao, L.-M., Zhao, B. & Liu, A. Mechanism of multisoliton formation and soliton energy quantization in passively mode-locked fiber lasers. Phys. Rev. A72, 043816 (2005).
19. Haboucha, A., Komarov, A., Leblond, H., Sanchez, F. & Martel, G. Mechanism of multiple pulse formation in the normal dispersion regime of passively mode-locked fiber ring lasers. Optical Fiber Technology 14, 262–267 (2008).
20. Komarov, A., Leblond, H. & Sanchez, F. Multistability and hysteresis phenomena in passively mode-locked fiber lasers. Phys. Rev. A71, 053809 (2005).
21. Weill, R., Vodonos, B., Gordon, A., Gat, O. & Fischer, B. Publisher's note: Statistical light-mode dynamics of multipulse passive mode locking [phys. rev. e 76, 031112 (2007)]. Phys. Rev. E76, 059903 (2007).
22. Liu, X. Hysteresis phenomena and multipulse formation of a dissipative system in a passively mode-locked fiber laser. Phys. Rev. A81, 023811 (2010).
23. Wise, F. W., Chong, A. & Renninger, W. H. High-energy femtosecond fiber lasers based on pulse propagation at normal dispersion. Laser & Photonics Reviews 2, 58–73 (2008).
24. Gui, L.et al. Soliton molecules and multisoliton states in ultrafast fibre lasers: Intrinsic complexes in dissipative systems. Applied Sciences 8, 201 (2018).
25. Olivier, M., Roy, V. & Piché, M. Influence of the raman effect on bound states of dissipative solitons. Opt. Express 14, 9728–9742 (2006).
26. Olivier, M., Roy, V. & Piché, M. Third-order dispersion and bound states of pulses in a fiber laser. Opt. Lett. 31, 580–582 (2006).
27. Pilipetskii, A., Golovchenko, E. & Menyuk, C. Acoustic effect in passively mode-locked fiber ring lasers. Opt. Lett. 20, 907–909 (1995).
28. Ding, Y., Xiao, X., Wang, P. & Yang, C. Multiple-soliton in spatiotemporal mode-locked multimode fiber lasers. Opt. Express 27, 11435–11446 (2019).
29. Grudinin, A., Richardson, D. & Payne, D. Energy quantisation in figure eight fibre laser. Electronics Letters 28, 67–68 (1992).
30. Grudinin, A. & Gray, S. Passive harmonic mode locking in soliton fiber lasers. J. Opt. Soc.Am. B14, 144–154 (1997).
31. Chouli, S. & Grelu, P. Rains of solitons in a fiber laser. Opt. Express 17, 11776–11781 (2009).
32. Cundiff, S. T.et al. Observation of polarization-locked vector solitons in an optical fiber. Phys. Rev. Lett. 82, 3988 (1999).
33. Zhao, X.et al. Switchable, dual-wavelength passively mode-locked ultrafast fiber laser based on a single-wall carbon nanotube mode locker and intracavity loss tuning. Opt. Express 19, 1168–1173 (2011).
34. Huang, X. & Xiao, X. Harmonic mode-locking of asynchronous dual-wavelength pulses in mode-locked all-fiber lasers. Opt. Comm. 126079 (2020).
35. Zhao, K.et al. Free-running dual-comb fiber laser mode-locked by nonlinear multimode interference. Opt. Lett. 44, 4323–4326 (2019).
36. Zhang, Z., Xu, Z. & Zhang, L. Tunable and switchable dual-wavelength dissipative soliton generation in an all-normal-dispersion yb-doped fiber laser with birefringence fiber filter. Opt. Express 20, 26736–26742 (2012).
37. Tang, D., Zhang, H., Zhao, L. & Wu, X. Observation of high-order polarization-locked vector solitons in a fiber laser. Phys. Rev. Lett. 101, 153904 (2008).
38. Malomed, B. A. Bound solitons in the nonlinear schrödinger/ginzburg-landau equation. In Large Scale Structures in Nonlinear Physics, 288–294 (Springer, 1991).
39. Tang, D., Man, W., Tam, H. & Drummond, P. Observation of bound states of solitons in a passively mode-locked fiber laser. Phys. Rev. A64, 033814 (2001).
40. Li, L.et al. Various soliton molecules in fiber systems. Appl. Opt. 58, 2745–2753 (2019).

41. Komarov, A., Komarov, K. & Sanchez, F. Quantization of binding energy of structural solitons in passive mode-locked fiber lasers. Phys. Rev. A79, 033807 (2009).
42. Grelu, P., Belhache, F., Gutty, F. & Soto-Crespo, J.-M. Phase-locked soliton pairs in a stretched-pulse fiber laser. Opt. Lett. 27, 966–968 (2002).
43. Zhao, L., Tang, D., Wu, X., Lei, D. & Wen, S. Bound states of gain-guided solitons in a passively mode-locked fiber laser. Opt. Lett. 32, 3191–3193 (2007).
44. Wang, P., Xiao, X. & Yang, C. Quantized pulse separations of phase-locked soliton molecules in a dispersion-managed mode-locked tm fiber laser at 2μm. Opt. Lett. 42, 29–32 (2017).
45. Soto-Crespo, J. M., Akhmediev, N., Grelu, P. & Belhache, F. Quantized separations of phase-locked soliton pairs in fiber lasers. Opt. Lett. 28, 1757–1759 (2003).
46. Akhmediev, N., Ankiewicz, A. & Soto-Crespo, J. Stable soliton pairs in optical transmission lines and fiber lasers. J. Opt. Soc. Am. B15, 515–523 (1998).
47. Akhmediev, N., Ankiewicz, A. & Soto-Crespo, J. Multisoliton solutions of the complex ginzburg-landau equation. Phys. Rev. Lett. 79, 4047 (1997).
48. Grapinet, M. & Grelu, P. Vibrating soliton pairs in a mode-locked laser cavity. Opt. Lett. 31, 2115–2117 (2006).
49. Zaviyalov, A., Iliew, R., Egorov, O. & Lederer, F. Multi-soliton complexes in mode-locked fiber lasers. Appl. Phys. B104, 513 (2011).
50. Soto-Crespo, J. M., Grelu, P., Akhmediev, N. & Devine, N. Soliton complexes in dissipative systems: Vibrating, shaking, and mixed soliton pairs. Phys. Rev. E75, 016613 (2007).
51. Zavyalov, A., Iliew, R., Egorov, O. & Lederer, F. Dissipative soliton molecules with independently evolving or flipping phases in mode-locked fiber lasers. Phys. Rev. A80, 043829 (2009).
52. Wang, Z., Nithyanandan, K., Coillet, A., Tchofo-Dinda, P. & Grelu, P. Optical soliton molecular complexes in a passively mode-locked fibre laser. Nature communications 10, 1–11 (2019).
53. Wang, Y.-E.et al. Vortex soliton molecule in a fiber laser. Opt. Express 28, 9666–9676 (2020).
54. Shi, H., Song, Y., Wang, C., Zhao, L. & Hu, M. Observation of subfemtosecond fluctuations of the pulse separation in a soliton molecule. Opt. Lett. 43, 1623–1626 (2018).
55. Tian, H., Zou, O., Zhao, Y., Song, Y. & Hu, M. Power spectral density analysis of relative phase jitter in a twin-soliton molecule. In 2019 Conference on Lasers and Electro-Optics (CLEO), 1–2 (IEEE, 2019).
56. Igbonacho, J.et al. Dynamics of distorted and undistorted soliton molecules in a mode-locked fiber laser. Phys. Rev. A99, 063824 (2019).
57. Gui, L., Li, X., Xiao, X., Zhu, H. & Yang, C. Widely spaced bound states in a soliton fiber laser with graphene saturable absorber. IEEE Photonics Technology Letters 25, 1184–1187 (2013).
58. Wang, X., Peng, J., Huang, K., Yan, M. & Zeng, H. Experimental study on buildup dynamics of a harmonic mode-locking soliton fiber laser. Opt. Express 27, 28808–28815 (2019).
59. Luo, Z.-C.et al. 2 ghz passively harmonic mode-locked fiber laser by a microfiber-based topological insulator saturable absorber. Opt. Lett. 38, 5212–5215 (2013).
60. Jin, L.et al. 3 ghz passively harmonic mode-locked er-doped fiber laser by evanescent field-based nano-sheets topological insulator. Opt. Express 26, 31244–31252 (2018).
61. Wang, P., Yao, S., Grelu, P., Xiao, X. & Yang, C. Pattern formation in 2-μm tm mamyshev oscillators associated with the dissipative faraday instability. Photonics Research 7, 1287–1295 (2019).
62. Chouli, S. & Grelu, P. Soliton rains in a fiber laser: An experimental study. Phys. Rev. A81,063829 (2010).
63. Bao, C., Xiao, X. & Yang, C. Soliton rains in a normal dispersion fiber laser with dual-filter. Opt. Lett. 38, 1875–1877 (2013).
64. Horowitz, M., Barad, Y. & Silberberg, Y. Noiselike pulses with a broadband spectrum generated from an erbium-doped fiber laser. Opt. Lett. 22, 799–801 (1997).

65. Huang, Y.-Q., Qi, Y.-L., Luo, Z.-C., Luo, A.-P. & Xu, W.-C. Versatile patterns of multiplerectangular noise-like pulses in a fiber laser. Opt. Express 24, 7356–7363 (2016).
66. Zhou, R., Liu, X., Yu, D., Li, Q. & Fu, H. Versatile multi-soliton patterns of noise-like pulses in a passively mode-locked fiber laser. Opt. Express 28, 912–923 (2020).
67. Lecaplain, C. & Grelu, P. Rogue waves among noiselike-pulse laser emission: an experimental investigation. Phys. Rev. A90, 013805 (2014).
68. Wang, Y.et al. Harmonic mode locking of bound-state solitons fiber laser based on mos_2 saturable absorber. Opt. Express 23, 205–210 (2015).
69. Li, L., Ruan, Q., Yang, R., Zhao, L. & Luo, Z. Bidirectional operation of 100 fs bound solitons in an ultra-compact mode-locked fiber laser. Opt. Express 24, 21020–21026 (2016).
70. Kieu, K. & Mansuripur, M. All-fiber bidirectional passively mode-locked ring laser. Opt. Lett. 33, 64–66 (2008).
71. Zhao, X., Li, T., Liu, Y., Li, Q. & Zheng, Z. Polarization-multiplexed, dual-comb all-fiber mode-locked laser. Photonics Research 6, 853–857 (2018).
72. Li, R.et al. All-polarization-maintaining dual-wavelength mode-locked fiber laser based on sagnac loop filter. Opt. Express 26, 28302–28311 (2018).
73. Coddington, I., Newbury, N. & Swann, W. Dual-comb spectroscopy. Optica 3, 414–426 (2016).
74. Zhao, X.et al. Picometer-resolution dual-comb spectroscopy with a free-running fiber laser. Opt. Express 24, 21833–21845 (2016).
75. Ryczkowski, P.et al. Real-time full-field characterization of transient dissipative soliton dynamics in a mode-locked laser. Nature Photonics 12, 221–227 (2018).
76. Wei, X.et al. Unveiling multi-scale laser dynamics through time-stretch and time-lens spectroscopies. Opt. Express 25, 29098–29120 (2017).
77. Tikan, A., Bielawski, S., Szwaj, C., Randoux, S. & Suret, P. Single-shot measurement of phase and amplitude by using a heterodyne time-lens system and ultrafast digital time-holography. Nature Photonics 12, 228–234 (2018).
78. Herink, G., Kurtz, F., Jalali, B., Solli, D. R. & Ropers, C. Real-time spectral interferometry probes the internal dynamics of femtosecond soliton molecules. Science 356, 50–54 (2017).
79. Krupa, K., Nithyanandan, K., Andral, U., Tchofo-Dinda, P. & Grelu, P. Real-time observation of internal motion within ultrafast dissipative optical soliton molecules. Phys. Rev. Lett. 118, 243901 (2017).
80. Liu, X., Yao, X. & Cui, Y. Real-time observation of the buildup of soliton molecules. Phys. Rev. Lett. 121, 023905 (2018).
81. Peng, J. & Zeng, H. Build-up of dissipative optical soliton molecules via diverse soliton interactions. Laser & Photonics Reviews 12, 1800009 (2018).
82. Lapre, C.et al. Real-time characterization of spectral instabilities in a mode-locked fibre laser exhibiting soliton-similariton dynamics. Scientific reports 9, 1–12 (2019).
83. Hamdi, S., Coillet, A. & Grelu, P. Real-time characterization of optical soliton molecule dynamics in an ultrafast thulium fiber laser. Opt. Lett. 43, 4965–4968 (2018).
84. Peng, J. & Zeng, H. Dynamics of soliton molecules in a normal-dispersion fiber laser. Opt. Lett. 44, 2899–2902 (2019).
85. Peng, J., Boscolo, S., Zhao, Z. & Zeng, H. Breathing dissipative solitons in mode-locked fiber lasers. Science advances 5, eaax1110 (2019).
86. Wang, X.et al. Real-time observation of dissociation dynamics within a pulsating soliton molecule. Opt. Express 27, 28214–28222 (2019).
87. Xia, R.et al. Experimental observation of shaking soliton molecules in a dispersion-managed fiber laser. Opt. Lett. 45, 1551–1554 (2020).
88. Liu, X. & Pang, M. Revealing the buildup dynamics of harmonic mode-locking states in ultrafast lasers. Laser & Photonics Reviews 13, 1800333 (2019).
89. Zeng, J. & Sander, M. Y. Real-time transition dynamics between multi-pulsing states in a mode-locked fiber laser. Opt. Lett. 45, 5–8 (2020).

90. Liu, X., Han, X. & Zhang, Y. Observation of multi-soliton asynchronous buildup dynamics in all-pm mode-locked lasers. arXiv preprint arXiv: 1905.02333 (2019).
91. Luo, Y.et al. Real-time access to the coexistence of soliton singlets and molecules in an all-fiber laser. Opt. Lett. 44, 4263–4266 (2019).
92. Yu, Y.et al. Spectral-temporal dynamics of multipulse mode-locking. Appl. Phys. Lett. 110, 201107 (2017).
93. Lapre, C., Billet, C., Meng, F., Genty, G. & Dudley, J. M. Dispersive fourier transform characterization of multipulse dissipative soliton complexes in a mode-locked soliton-similariton laser. OSA Continuum 3, 275–285 (2020).
94. Cundiff, S. T., Soto-Crespo, J. M. & Akhmediev, N. Experimental evidence for soliton explosions. Phys. Rev. Lett. 88, 073903 (2002).
95. Yu, Y., Luo, Z.-C., Kang, J. & Wong, K. K. Mutually ignited soliton explosions in a fiber laser. Opt. Lett. 43, 4132–4135 (2018).
96. Peng, J. & Zeng, H. Soliton collision induced explosions in a mode-locked fibre laser. Communications Physics 2, 1–8 (2019).
97. Luo, Z.-C.et al. Optical rogue waves by random dissipative soliton buildup in a fiber laser. IEEE Photonics Technology Letters 30, 1803–1806 (2018).
98. Wang, G., Chen, G., Li, W., Zeng, C. & Yang, H. Decaying evolution dynamics of double-pulse mode-locking. Photonics Research 6, 825–829 (2018).
99. Liu, X., Popa, D. & Akhmediev, N. Revealing the transition dynamics from q switching to mode locking in a soliton laser. Phys. Rev. Lett. 123, 093901 (2019).
100. Pu, G.et al. Intelligent control of mode-locked femtosecond pulses by time-stretch-assisted real-time spectral analysis. Light: Science & Applications 9, 1–8 (2020).
101. Wei, Y., Li, B., Wei, X., Yu, Y. & Wong, K. K. Ultrafast spectral dynamics of dual-color-soliton intracavity collision in a mode-locked fiber laser. Appl. Phys. Lett. 112, 081104 (2018).
102. Zhao, K., Gao, C., Xiao, X. & Yang, C. Buildup dynamics of asynchronous vector solitons in a polarization-multiplexed dual-comb fiber laser. Opt. Lett. 45, 4040–4043 (2020).
103. Wright, L. G.et al. Mechanisms of spatiotemporal mode-locking. Nature Physics 16, 565–570 (2020).
104. Qin, H., Xiao, X., Wang, P. & Yang, C. Observation of soliton molecules in a spatiotemporal mode-locked multimode fiber laser. Opt. Lett. 43, 1982–1985 (2018).
105. Ding, Y., Xiao, X. & Yang, C. Spatiotemporal dynamics of dual-soliton states in a multimode fiber laser. InCLEO: QELS_Fundamental Science, JW2A–87 (Optical Society of America, 2019).
106. Wu, H.et al. Pulses with switchable wavelengths and hysteresis in an all-fiber spatio-temporal mode-locked laser. Appl. Phys. Express 13, 022008 (2020).
107. Ding, Y.et al. Spatiotemporal mode-locking in lasers with large modal dispersion. Phys. Rev. Lett. 126, 093901 (2021).
108. Leo, F.et al. Temporal cavity solitons in one-dimensional Kerr media as bits in an all-optical buffer. Nature Photonics 4, 471 (2010).
109. Herr, T.et al. Temporal solitons in optical microresonators. Nature Photonics 8, 145 (2014).
110. Wang, W., Wang, L. & Zhang, W. Advances in soliton microcomb generation. Advanced Photonics 2, 034001 (2020).
111. Wabnitz, S. Suppression of interactions in a phase-locked soliton optical memory. Opt. Lett. 18, 601–603 (1993).
112. Cundiff, S. T. & Ye, J. Colloquiu Femtosecond optical frequency combs. Rev. Mod. Phys. 75, 325 (2003).
113. Lugiato, L. A. & Lefever, R. Spatial dissipative structures in passive optical systems. Phys. Rev. Lett. 58, 2209 (1987).
114. Coen, S., Randle, H. G., Sylvestre, T. & Erkintalo, M. Modeling of octave-spanning Kerr frequency combs using a generalized mean-field Lugiato–Lefever model. Opt. Lett. 38, 37–39 (2013).

115. Chembo, Y. K. & Menyuk, C. R. Spatiotemporal lugiato-lefever formalism for kerr-comb generation in whispering-gallery-mode resonators. Phys. Rev. A87, 053852 (2013).
116. Barland, S.et al. Cavity solitons as pixels in semiconductor microcavities. Nature 419, 699–702 (2002).
117. Firth, W. & Scroggie, A. Optical bullet holes: robust controllable localized states of a nonlinear cavity. Phys. Rev. Lett. 76, 1623 (1996).
118. Ackemann, T., Firth, W. & Oppo, G.-L. Fundamentals and applications of spatial dissipative solitons in photonic devices. Advances in Atomic, Molecular, and Optical Physics 57, 323–421 (2009).
119. Coen, S. & Erkintalo, M. Universal scaling laws of kerr frequency combs. Opt. Lett. 38, 1790–1792 (2013).
120. Bao, C. & Yang, C. Carrier-envelope phase dynamics of cavity solitons: scaling law and soliton stability. Phys. Rev. A92, 053831 (2015).
121. Godey, C., Balakireva, I. V., Coillet, A. & Chembo, Y. K. Stability analysis of the spatiotemporal Lugiato-Lefever model for kerr optical frequency combs in the anomalous and normal dispersion regimes. Phys. Rev. A89, 063814 (2014).
122. Leo, F., Gelens, L., Emplit, P., Haelterman, M. & Coen, S. Dynamics of one-dimensional Kerr cavity solitons. Opt. Express 21, 9180–9191 (2013).
123. Lamont, M. R., Okawachi, Y. & Gaeta, A. L. Route to stabilized ultrabroadband microresonator-based frequency combs. Opt. Lett. 38, 3478–3481 (2013).
124. Bao, C.et al. Observation of Fermi-Pasta-Ulam recurrence induced by breather solitons in an optical microresonator. Phys. Rev. Lett. 117, 163901 (2016).
125. Yi, X., Yang, Q.-F., Yang, K. Y. & Vahala, K. Imaging soliton dynamics in optical microcavities. Nature Communications 9(2018).
126. Bao, C., Zhang, L., Kimerling, L. C., Michel, J. & Yang, C. Soliton breathing induced by stimulated raman scattering and self-steepening in octave-spanning Kerr frequency comb generation. Opt. Express 23, 18665–18670 (2015).
127. Wai, P., Menyuk, C. R., Lee, Y. & Chen, H. Nonlinear pulse propagation in the neighborhood of the zero-dispersion wavelength of monomode optical fibers. Opt. Lett. 11, 464–466 (1986).
128. Akhmediev, N. & Karlsson, M. Cherenkov radiation emitted by solitons in optical fibers. Phys. Rev. A51, 2602 (1995).
129. Brasch, V.et al. Photonic chip–based optical frequency comb using soliton Cherenkov radiation. Science 351, 357–360 (2016).
130. Li, Q.et al. Stably accessing octave-spanning microresonator frequency combs in the soliton regime. Optica 4, 193–203 (2017).
131. Pfeiffer, M. H.et al. Octave-spanning dissipative kerr soliton frequency combs in si 3 n 4microresonators. Optica 4, 684–691 (2017).
132. Herr, T.et al. Mode spectrum and temporal soliton formation in optical microresonators. Phys. Rev. Lett. 113, 123901 (2014).
133. Liu, Y.et al. Investigation of mode coupling in normal-dispersion silicon nitride microresonators for kerr frequency comb generation. Optica 1, 137–144 (2014).
134. Matsko, A. B., Liang, W., Savchenkov, A. A., Eliyahu, D. & Maleki, L. Optical Cherenkov radiation in overmoded microresonators. Opt. Lett. 41, 2907–2910 (2016).
135. Yang, Q.-F., Yi, X., Yang, K. Y. & Vahala, K. Spatial-mode-interaction-induced dispersive waves and their active tuning in microresonators. Optica 3, 1132–1135 (2016).
136. Bao, C.et al. Spatial mode-interaction induced single soliton generation in microresonators. Optica 4, 1011–1015 (2017).
137. Menyuk, C. R. Stability of solitons in birefringent optical fibers. I: equal propagation amplitudes. Opt. Lett. 12, 614–616 (1987).
138. Taheri, H., Matsko, A. B. & Maleki, L. Optical lattice trap for Kerr solitons. Eur. Phys. J. D71, 153 (2017).
139. Yi, X., Yang, Q.-F., Yang, K. Y. & Vahala, K. Active capture and stabilization of temporal solitons in microresonators. Opt. Lett. 41, 2037–2040 (2016).

140. Guo, H.et al. Universal dynamics and deterministic switching of dissipative Kerr solitons in optical microresonators. Nature Physics 13, 94–102 (2017).
141. Hu, J.et al. Reconfigurable radiofrequency filters based on versatile soliton microcombs. Nature Communications 11, 4377 (2020).
142. Bao, C.et al. Direct soliton generation in microresonators. Opt. Lett. 42, 2519–2522 (2017).
143. Yu, M., Okawachi, Y., Griffith, A. G., Lipson, M. & Gaeta, A. L. Mode-locked mid-infrared frequency combs in a silicon microresonator. Optica 3, 854–860 (2016).
144. Karpov, M.et al. Dynamics of soliton crystals in optical microresonators. Nature Physics 15, 1071–1077 (2019).
145. Cole, D. C., Lamb, E. S., Del'Haye, P., Diddams, S. A. & Papp, S. B. Soliton crystals in Kerr resonators. Nature Photonics 11, 671 (2017).
146. Wang, W.et al. Robust soliton crystals in a thermally controlled microresonator. Opt. Lett. 43, 2002–2005 (2018).
147. He, Y., Ling, J., Li, M. & Lin, Q. Perfect soliton crystals on demand. Laser & Photonics Reviews 14, 1900339 (2020).
148. Xu, X.et al. Photonic rf channelizer based on 49ghz soliton crystal microcombs. TechRxiv. Preprint (2020).
149. Tan, M.et al. Microwave photonic fractional hilbert transformer with an integrated optical soliton crystal micro-comb. arXiv preprint arXiv:1910.06282 (2019).
150. Zhao, Y.et al. Visible nonlinear photonics vi a high-order-mode dispersion engineering. Optica 7, 135–141 (2020).
151. Jaramillo-Villegas, J. A., Xue, X., Wang, P.-H., Leaird, D. E. & Weiner, A. M. Deterministic single soliton generation and compression in microring resonators avoiding the chaotic region. Opt. Express 23, 9618–9626 (2015).
152. Qi, Z.et al. Dissipative cnoidal waves (turing rolls) and the soliton limit in microring resonators. Optica 6, 1220–1232 (2019).
153. Joshi, C.et al. Counter-rotating cavity solitons in a silicon nitride microresonator. Opt. Lett. 43, 547–550 (2018).
154. Lucas, E.et al. Spatial multiplexing of soliton microcombs. Nature Photonics 12, 699–705 (2018).
155. Suh, M.-G. & Vahala, K. J. Soliton microcomb range measurement. Science 359, 884–887 (2018).
156. Yang, Q.-F.et al. Vernier spectrometer using counterpropagating soliton microcombs. Science 363, 965–968 (2019).
157. Bao, C.et al. Oscillatory motion of a counterpropagating Kerr soliton dimer. Phys. Rev. A103, L011501 (2021)
158. Weng, W.et al. Heteronuclear soliton molecules in optical microresonators. Nature Communications 11, 2402 (2020).
159. Weng, W., Bouchand, R. & Kippenberg, T. J. Formation and collision of multistability-enabled composite dissipative Kerr solitons. Phys. Rev. X10, 021017 (2020).

Chapter 12
Dissipative Solitons in Microresonators

Cristina Rimoldi, Bennet Fischer, Luigi Di Lauro, Mario Chemnitz, Alessia Pasquazi, David J. Moss, and Roberto Morandotti

Abstract In this Chapter we will illustrate the state-of-art in the generation of dissipative solitons in Kerr microresonator-based systems. After a brief introduction on the origin of this field of research, we will discuss the modeling of these microcavities using the generalized Lugiato-Lefever equation. Further, we will discuss the different techniques used for dispersion engineering in these systems. We will then focus on the description of the frequency combs generated by microring resonators in the Kerr soliton regime and illustrate different schemes that have been developed in this context to grant better control of the microcavity dynamics. Finally, we will review the large number of applications that these objects have originated in several fields of optics.

Keywords Dissipative solitons · Kerr media · Integrated photonics · Microring resonators · Comb generation · Soliton combs · Soliton crystals · Quantum combs · Radio-frequency microcombs · Soliton control · Self-injection locking · Dispersion engineering

12.1 Introduction

In the past 10 years, microresonators have revolutionized the field of optics with several applications in sensing [1–3], spectroscopy [4, 5], communication [6–9], astronomy [10, 11], and quantum optics [12–20]. These devices, generally featuring

C. Rimoldi · B. Fischer · L. Di Lauro · M. Chemnitz · R. Morandotti (✉)
INRS-EMT, Quebec, Canada
e-mail: morandotti@emt.inrs.ca

A. Pasquazi
Emergent Photonics (Epic) Laboratory, Department of Physics and Astronomy, University of Sussex, Brighton, UK

D. J. Moss
Centre for Microphotonics, Swinburne University of Technology, Hawthorn, VIC, Australia

M. F. S. Ferreira (ed.), *Dissipative Optical Solitons*, Springer Series in Optical Sciences 238, https://doi.org/10.1007/978-3-030-97493-0_12

a high quality (Q) factor, can be realized under many forms, such as micro-toroids [21], spheres [22, 23], disks [24], rods [25], and integrated ring resonators [26, 27]. Further, they have been studied in many different materials, such as calcium [28] and magnesium [29] fluorides (CaF_2, MgF_2, respectively), lithium niobate ($LiNbO_3$) [30], aluminum nitride (AIN) [31], tantalum pentoxide (Ta_2O_5) [32], silica glass [33], diamond [34], silicon [26, 35], silicon nitride (Si_3N_4) [36], oxynitrides (SiO_xN_x) [37], and high-index glass [38, 39], each offering specific advantages (and disadvantages) depending on the considered application. While these devices and materials have since been thoroughly investigated for the generation of frequency combs [40–42], the first direct demonstration of dissipative solitons in microresonators only dates back to 2014 [29], building upon the first experimental observation of Kerr solitons in a fiber cavity [43]. Kerr solitons arise from the mutual interplay of, on the one hand, dispersion and nonlinearity, and on the other hand, gain and losses. The resulting broadband frequency combs exhibit a high level of coherence, which is of fundamental importance for applications in spectroscopy, communications, and quantum measurements, as illustrated later in this Chapter.

Frequency combs, generated through cascaded four-wave mixing (FWM) in the microresonator blue-detuned regime, can exhibit either an aperiodic temporal waveform, due to arbitrary and constant phases of the comb lines, or coherent sidebands with a low repetition rate and reduced bandwidth [28, 44]. In contrast, soliton frequency comb lines display synchronized phases with higher repetition rates and bandwidths, thus resulting in an extremely narrow pulsed temporal shape [29, 45, 46]. Differently from solitons generated through mode-locked laser techniques exploiting incoherent pumping schemes, Kerr soliton frequency combs present the pump frequency within their spectrum and their generation does not make use of saturable absorbers for stabilization [47, 48]. The first experimental demonstration of dissipative Kerr solitons (DKSs) in microresonators [29] was performed in an MgF_2 crystal driven by a continuous wave (CW) pump laser. Here, solitons were observed when the optical system undergoes the transition between the effectively blue- and red-detuned regimes. In particular, while scanning for decreasing values of pump frequency, the system first displays primary sidebands in the frequency domain due to FWM, which are then followed by secondary lines. When the broadband radio-frequency (RF) signal transitions to a low-noise beatnote, a series of discrete steps in the transmission is observed and identified as a clear sign of the generation of Kerr solitons, which were then temporally characterized by the authors through frequency-resolved gating (i.e. FROG measurements). While for the general description of the microresonator system dynamics we refer the reader to [49], in the following we are going to discuss the details of the most used modeling approaches.

12.2 Modeling

The generation of dissipative Kerr solitons in microresonators can be described by means of the Lugiato-Lefever equation [50, 51] (LLE). This model was first developed for the description of pattern formation in the transverse plane (i.e., the plane orthogonal to the propagation direction) of a Kerr medium, contained in a high-finesse cavity [50]. It is derived from Maxwell's equations considering nonlinear contributions, under paraxial, slowly varying amplitude, and mean-field approximations in the low-transmission limit [52, 53].

Years after its original formulation, the model was then adapted towards its highly successful temporal/longitudinal version [51] by Haelterman et al., where the diffraction is replaced by the group velocity dispersion term and two independent temporal variables are introduced, the time t and the retarded time $t - z/v_g$, where v_g represents the group velocity and z is the propagation direction. Such a formulation describes a field that is uniform in the transverse plane while propagating along the cavity. A form equivalent to the temporal/longitudinal LLE, with quantities related to the parameters of a microring resonator (MRR), is the following

$$\frac{\partial E}{\partial t} = F - E - i\delta E + i|E|^2 E - i\frac{\beta}{2}\frac{\partial^2 E}{\partial \theta^2}$$

where E is the electric field and F is the optical injected field amplitude. The detuning term δ between the cavity frequency ω_0 and the closest input frequency ω_p is normalized to the cavity decay rate and β is proportional to the group velocity dispersion $\left(\partial v_g/\partial\omega\right)_{\omega=\omega_0}$, while the time variable t is normalized to the cavity decay time. The azimuthal angle is defined as $\theta = z/R$, where R is the MRR radius, and z is the propagation variable [54, 55]. Note that for any solution of the LLE in the above form with periodic boundary conditions in $-\pi < \theta < \pi$, θ will then need to be substituted by $\theta - (v_g/R)t$ [52].While most early descriptions of Kerr frequency comb generation have often employed coupled mode theory (CMT) for the description of FWM in the frequency domain, the LLE, which can also be derived from CMT [54, 56], was later used to give a picture of the mean field in the temporal domain [57]. Indeed, although CMT equations offer an easy control of frequency-dependent absorption and coupling terms, they do not give direct access to the information in the time domain, which is instead easily obtained through the LLE [56]. Further, the LLE, which can be easily described as a driven, detuned, and damped nonlinear Schrödinger equation, allows for the straightforward inclusion of additional terms for Raman scattering and higher-order dispersion, as we will discuss in more detail in the following sections. On the other hand, thermo-optic effects, which can represent a limitation for Kerr combs in MRRs [58], have been successfully modeled in some systems through coupled mode equations [59, 60] as well as using the LLE [29]. For the modeling of resonator dynamics through CMT, we refer the reader to [40, 61].

12.2.1 Higher-Order Dispersion

In some experimental cases, solitons with sufficiently short temporal duration exhibit a spectral bandwidth that extends towards the normal dispersion region. Such solitons cannot be properly described through the LLE in the above-mentioned form, which in fact needs to be adjusted (in its temporal version [40, 51]) through the addition of higher-order dispersion terms of the form [62]

$$D_n = i^{n+1} \frac{\beta_n}{n!} \frac{\partial^n E}{\partial \tau^n}$$

for $n > 2$, where β_n is the n-th order dispersion coefficient and τ is a time variable, proportional to the previously mentioned retarded time. These additional terms allow for the modeling of soliton bandwidth restrictions in realistic cavities as well as dispersive wave generation [55], where the soliton repels a fraction of its energy into a radiant mode, an effect that can be interpreted as the optical analog of Cherenkov radiation. Additionally, higher-order dispersion mediates the interplay between FWM and dispersive wave formation, in turn giving rise to a spectral recoil, where the soliton spectral peak shifts from the original pump frequency [62, 63]. Finally, we would like to point out that higher-order dispersion terms are often accompanied by a self-steepening effect, as described in [64].

12.2.2 Raman Effect

The Raman effect in microresonators has been demonstrated to be non-negligible in specific materials, such as Si_3N_4 and silica [65]. This effect is usually modeled in the LLE as a fraction of the cubic nonlinearity of the form [66]

$$f_R h_R \otimes |E|^2 \approx f_R |E|^2 - f_R \tau_R \frac{\partial |E|^2}{\partial \tau}$$

often approximated to first order [65], where f_R is the Raman fraction, h_R represents the Raman response function, and τ_R is the Raman shock time. In microresonators, the effect of Raman scattering implies the development of a self-frequency shift, where the soliton peak frequency is redshifted with respect to the CW pump laser frequency. The compensation of this shift through the spectral recoil generated by higher-order dispersion has been studied in [65]. Additionally, a new type of soliton, called Stokes soliton, has been demonstrated in the presence of Raman gain [67]. In terms of Kerr frequency comb generation, it is important to note that stimulated Raman scattering can ultimately limit the temporal and spectral width of dissipative Kerr solitons [68].

12.3 Dispersion Engineered Cavity Dynamics

One of the key advantages of waveguide-integrated MRRs is the large variety of wavelength dispersion properties determining the linear propagation characteristics of the optical modes. In contrast to the unilateral geometries of whispery-gallery mode and photonic belt resonators [69, 70], the bilateral optical mode confinement in MRR opens a large variety of possibilities to adjust the dispersion properties of the circumventing modes. These include (a) adjusting the dimensions of the waveguide cross-section [71–73] or geometry (e.g. split or "race-track" waveguide) [14, 74], as well as (b) altering the composition of the waveguide core (see e.g. the recent works about Kerr combs in $LiNO_3$ [75], SiO_xN_y [44, 76, 77], Si_3N_4 [78], Diamond, Si) or the coating/cladding materials [36, 72]. While a very detailed overview of emerging materials for integrated microcavities is given in the comprehensive reviews by Kovach et al. [79] and Kippenberg et al. [47], here we aim to summarize the essentials of dispersion engineering in waveguide-based MRRs and its advantages for altering the temporal dynamics of DKSs.

12.3.1 Capabilities of Dispersion Engineering

The key for dispersion engineering in optical waveguides is a careful balance between material- and mode-specific waveguide dispersion. The choice of appropriate core, cladding, and cover layer materials alters the modal dispersion, while defining the guidance and dispersion constraints given by the individual material refractive indices. However, the waveguide geometry (i.e., cross-section and dimensions) may significantly change the modal confinement, increase the field overlap to the surrounding material (i.e. cladding [36] or cover layer [72]), and thus vary the dispersive properties of the mode. Moreover, the lithographic fabrication of photonic on-chip waveguides allows for the incorporation of gaps or slot layers, which add even more free parameters towards tailoring both dispersion and nonlinearity [80, 81]. In general, an appropriate choice of the waveguide materials, geometry, and dimension enables a plethora of dispersion landscapes, ranging from flat normal (i.e. without zero-dispersion) to anomalous dispersion with one, two, or even more zero-dispersion wavelengths in the vicinity of the pump field [81–83]. Commercially available numerical finite-element solvers are required to find the eigenmodes of the Maxwell's equations in the boundary problem imposed by the rectangular waveguide cross-sections of the MRRs. However, limitations in the fabrication processes, such as material inhomogeneity, stress built-up, and lithographic mask imperfections, usually limit the range of accessible design parameters. On the positive side, recent years have seen a considerable improvement in the fabrication processes (e.g., hybrid material systems, stress release patterns, mask improvements) [47, 79] enabling ever more access to novel dispersion regimes.

12.3.2 Advanced Control of Dissipative Soliton Dynamics

Dispersion engineering allows waveguide-integrated optical MRR to unlock unprecedented application capabilities. Transferring operation concepts such as controlled dispersive wave emission [84–86], tailored higher-order mode coupling [87–89], and soliton molecule formation [90–93] from nonlinear fibers to MRR has enabled the observation and advanced control over the dynamics of many different cavity soliton states in recent years. In the following, we are going to highlight a few of these advances.

Beyond theoretical modeling, physical limitations in the microcavity design, such as higher-order dispersion or dispersive nonlinearity, severely impact the formation of solitons in terms of bandwidth, power, and mode order. Multiple numerical and experimental studies propose practical approaches in order to optimize Kerr comb properties. In silicon nitride systems, for example, changes as small as a few hundred nm in the waveguide dimension can lead to a significant extent of the anomalous dispersion region causing a fivefold spectral extension of the Kerr comb [94]. The same study also demonstrated the selection of a suitable pump wavelength as a practical tool to alter the Kerr comb spectral extent and power after device fabrication. If pump wavelength tuning remains inaccessible, fine detuning of the free spectral range (FSR), bandwidth, and number of DKS through controlled heating of the MRR can offer an attractive alternative [95]. Similar advantages at faster tuning rates might be offered in the near future by second-order nonlinear materials such as $LiNO_3$-based MRRs [75]. Another promising approach on the fabrication side are multi-layer (slot) waveguides [81, 96] and non-uniform MRRs [97] that allow for the accurate adjustment of the cavity net-dispersion and nonlinearity, ultimately granting precise control over higher-order dispersion terms.

Such terms (i.e. $\beta_n > \beta_2$) have been demonstrated to significantly boost the comb bandwidth through one-sided or two-sided dispersive wave generation [36, 81, 98]. Dispersive wave generation is a nonlinear optical conversion process that requires a soliton-like optical pump with a flat phase in order to fulfill the phase-matching condition [62, 99]

$$\Delta\beta = \beta - \beta_s - (\omega - \omega_s)\beta_{1,s} - \frac{1}{2}\gamma_0 P_s = 0.$$

The condition compares the flat phase of a soliton $\beta_s + \frac{1}{2}\gamma_0 P_s$ (with nonlinear parameter γ_0 and soliton peak power P_s) with the propagation constant of a linear wave $\beta(\omega)$ in the moving frame of the soliton $(\omega - \omega_s)\beta_{1,s}$ (with ω and ω_s angular frequencies of the linear wave and soliton respectively, and $\beta_{1,s}$ the group dispersion of the soliton), which accounts for the group velocity mismatch. The broadband spectra generated by the interplay of dispersive wave and soliton are of fundamental use for optical metrology [36, 100] as well as future spectroscopic applications similar to [4, 101, 102]. However, due to the nature of this radiation, the dispersive part of the spectrum does not contribute to the pulsed waveform of the Kerr soliton

and thus constitutes a considerable energy loss to the soliton. Moreover, it causes the soliton to spectrally shift in order to compensate for the momentum loss (known as the soliton recoil effect). Depending on the application of the comb system, these effects might be detrimental and worth being reduced through proper dispersion design.

Finally, we like to highlight an unprecedented consequence of dispersion engineering in microcavities, which is the reduction of thermal noise in so-called quiet soliton combs [103, 104]. A comprehensive study recently revealed that operating in a cavity-specific ideal dispersion domain can reduce the thermal instabilities of soliton states up to 60 dB (with 15 dB improvement experimentally shown), thus drastically stabilizing the comb repetition rate and long-term stability [104].

12.3.3 Novel Phenomena in Dispersion-Tailored Microring Resonators

Advanced access to waveguide properties also enables the observation of a few unique effects of which no real equivalent exists in optical fiber systems. One of these effects is dispersive wave generation induced by avoided mode-crossing. Avoided mode-crossings may occur in waveguides with relatively large dimensions, which support more than one (fundamental) transversal mode per polarization (i.e., usually TE_{00} and TM_{00}) within the bandwidth of the optical source. Here, the avoided intersections of two transversal modes cause a significant change of the individual mode dispersions (see Fig. 12.1a), which can be a few orders of magnitude stronger than any other waveguide-intrinsic dispersion change and perturb soliton formation. Similar effects were observed between two different polarization modes [105].

Since larger waveguide sizes are a necessity for anomalous dispersion and power scaling of DKSs [78], intermodal crossings are very likely to occur in MRRs. However, for the purpose of favorable power scaling of cavity solitons, energy leakage due to non-solitonic radiation is largely undesired. Efforts to decrease the impact of higher-order modes include the incorporation of tapered sections into the MRRs [78, 97] as well as higher-order mode isolation couplers [106].

On the contrary, it is noteworthy that mode-crossings, in turn, host the unique capability to steer dispersive-wave formation, since they provide a strong variation of the dispersion. Thus, such crossings eventually provide a set of well defined, very narrow wavelength regions of perfect phase-matching between a soliton pump (in the transversal mode 1) and a dispersive wave (in the transversal mode 2) [103, 107]. Hence, the involvement of avoided mode-crossings imposes advantages on (i) the tuneability of the overall comb bandwidth, (ii) the accurate spectral relocation of dispersive wave energy, as well as (iii) refining the temporal characteristics of the dispersive radiation. Most notably, tailored narrow-band mode-crossings were utilized for the highly efficient generation of dispersive radiation

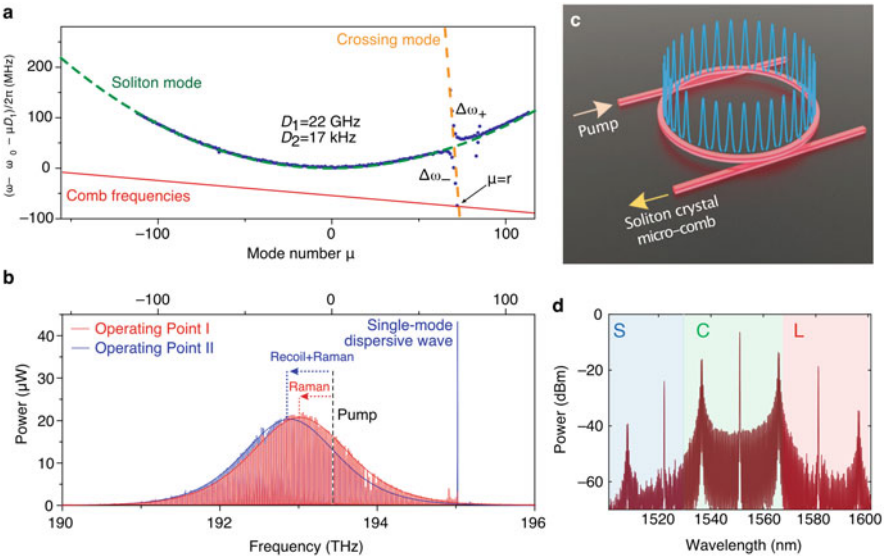

Fig. 12.1 (**a**) Dispersion of a cavity soliton with avoided mode-crossing. (**b**) Spectrum of soliton comb featuring a single-mode dispersive wave (blue). (**a**-**b**) adapted (labels, font size and line widths) from [103] under CC BY 4.0 license. (**c**) Illustration of a soliton crystal state and (**d**) respective measured spectrum. (c-d) adapted (font size) from [108] under CC BY 4.0 license

into a single resonator mode (see Fig. 12.1b) [103]. The study reports further on hysteresis-like interaction between this strong mode and the spectro-temporal behavior of the soliton as well as on the ability of repetition rate stabilization (so-called quiet states), which clearly hosts advantages for switching and long-term stable applications.

A further specialty of MRRs is the greater ability to reach stable control over the formation of multi-soliton states. Here, mastering of cavity stability through a balance of dispersion, nonlinearity, gain and loss, allows for the formation of multiple cavity solitons. In particular, the fine control over the dispersive properties of the cavity via thermal tuning as fast as 100 μs ultimately enables an on-demand increase of the soliton number and the controlled study of multi-soliton behavior [95]. These achievements resulted in the observation and active control of soliton crystals [33, 109]. Here, nonlinear nearest neighbor interactions allow phase-locked multi-photon states distributed over an equidistant temporal grid. The robustness of this highly ordered temporal alignment, in combination with the control over spacing and the existence of vacancies (i.e. Schottky defects) in the temporal grid, gives rise to the name *soliton crystals* in analogy to solid-state atomic crystals. The narrow spacing of the solitons in the MRR allows for a very practical indirect read-out through their spectra. For instance, through straight-forward Fourier transform rules, the number of solitons in the crystal can be read from the FSR of the most dominant cavity modes, while the number and positions of vacancies become apparent from the underlying modulation structure of the secondary modes (see Fig. 12.1c,d). The

manifold of crystal states and their robustness open up unique and unprecedented applications, among which we can mention background-free soliton lasers with GHz repetition rates [110], ultra-dense data transmission for telecommunications [111], as well as activation functionalities for photonic neural networks [108].

12.4 Soliton Comb Generation Schemes

Although Kerr frequency combs promise a powerful alternative to fiber-based frequency comb systems, they come with certain limitations that prevent their widespread use. Indeed, the generation of Kerr combs and their reliable long-term stabilization is currently one of the major bottlenecks that prevent a successful commercialization. In particular, DKSs (a subgroup of Kerr combs) are of high interest for a variety of applications due to their inherent GHz [112] to THz [113] repetition rates, short pulse durations, as well as their high phase stability between comb lines. In order to reach stable soliton operation, several different techniques have been developed in recent years and are briefly described below. For a more thorough review of soliton comb generation schemes, see for example refs. [16, 40, 47, 114].

In general, the majority of developed schemes rely on a tunable narrow linewidth CW laser source that is swept into the microcavity to reach the red-detuned soliton operation point. In 2013, Matsko et al. theoretically showed how to achieve DKSs through continuous scanning of the pump frequency, from blue-detuned to red-detuned values (i.e. from a higher optical frequency to a lower optical frequency with zero detuning from the center of the resonance) [115], as was also reported in later works [29, 64, 116]. When an MRR reaches a regime that allows for the propagation of stable DKSs, the intra-cavity energy experiences a sudden drop in intensity. The understanding of this behavior led to the demonstration of DKSs in microresonators in 2014 by Herr et al. [29]. These were previously observed in 2013 by Saha et al. under the form of femtosecond stable pulses in Si_3N_4 MRRs [117].

In 2009, Strekalov and Yu proposed a pumping scheme based on the use of a bi-chromatic source to produce frequency combs in MgF_2 MRRs, exploiting cascaded FWM rather than optical parametric generation [118, 119], leading to highly efficient DKS generation. Similarly, an electro-optic pumping scheme was exploited by Papp et al. [120, 121], which has experimentally shown the realization and control of extremely precise equidistant comb lines, essential for achieving ultra-stable solitons.

Additionally, techniques adapted from classical metrology such as the locking of the carrier-envelope-offset (CEO) frequency via self-referencing (i.e. *f*-2*f* interferometry [122]) of the generated comb have been investigated in order to obtain fully stabilized frequency combs in a compact footprint [123, 124]. Towards long-term stabilization, several techniques such as Pound-Drever-Hall feedback control systems [103], servo feedback loops [125], or sideband modulation [126, 127] have been explored.

12.4.1 Frequency Scanning

Initial schemes have utilized a simple, yet effective technique in order to overcome the issue of thermal cavity drifts [29, 115]: By shifting the CW laser source from the blue- to the red-detuned regime, an intracavity thermal equilibrium can be reached, allowing the stable generation of soliton combs. Here, the sweeping speed of the laser is crucial for the generation of the soliton combs and should match the microcavities photon and thermal lifetime, which can be difficult to achieve for some material platforms. As described earlier, the detuning of the pump starting from the blue side leads first to a primary frequency comb, formed through the intracavity power build-up, which in turn seeds FWM within the cavity. Further detuning of the pump laser results in to the generation of 'subcombs' and unstable combs formed by modulation instabilities (MI). The common feature of these combs in the blue-detuned regime is high noise in the RF-domain, due to multiple and broad RF beatnotes arising from MI. Once the red-detuned regime is reached, the intracavity power shows an abrupt decline in power and the so-called *soliton steps* can be observed, which show characteristic step sizes depending on the chosen material platform. Here, the generated solitons feature very narrow RF beatnotes as well as stable optical comb outputs. At the beginning of this regime, multi-soliton states are generated and, with increased detuning, they subsequently break down until a single soliton-state is reached. The goal of the frequency scanning method is, to stop the frequency detuning of the laser, once the single soliton state is obtained, which is easier achievable if the soliton step-sizes feature longer time durations (~ms for e.g. MgF_2 [29]).

12.4.2 Power Kicking

The power-kicking method [36, 128] is a widely used technique that allows for the generation of soliton combs in materials that feature a high thermo-optic coefficient. In these materials (such as Si_3N_4), the observed soliton steps exhibit very short time durations (~μs), which prevent the effective use of the frequency scanning method (i.e. to precisely stop the laser frequency on one of the soliton steps). Instead of using only a single tunable CW laser, two intensity modulators (acousto-optic and electro-optic modulators, AOM and EOM, respectively) are included before the microcavity. The use of the EOM is necessary to obtain the required speed, which cannot be provided by the AOM alone. Here, the AOM reduces the pump power of the source before tuning into the resonance, allowing to quickly reach the soliton steps. Subsequently, the AOM increases the pump power in order to stabilize the reached soliton step. After the AOM, an EOM helps diminishing thermal instabilities by effectively reducing the pump power right before the zero-detuning point (i.e. the resonance center), which also ensures a fast transition to the soliton steps. When the

settings (and timings) for the laser frequency sweeping and both modulations are correctly chosen, this method allows for the reliable generation of soliton combs in materials featuring higher thermo-optic coefficients.

12.4.3 Thermal Tuning

A more inexpensive method can be realized with on-chip resistive heaters on top of the microcavities [95, 129]. In this scheme, the tunable CW laser is replaced by a fixed frequency CW laser diode and the cavity resonance is thermally tuned by inducing a refractive index change caused by the thermo-optic effect. This can be realized through, for example, an electrode on top of the microcavity, which is current controlled. This allows for relatively fast speeds (given the small structure and thermal mass of the electrode) as well as for the fine tuning precision (determined by the bit-depth of the used digital-to-analog converter) required to directly obtain the short (~μs) soliton steps. Furthermore, although similar to the frequency scanning scheme, the thermal tuning technique offers advantages due to the use of single frequency lasers with lower RF noise as well as narrower linewidths (compared to tunable lasers), resulting in combs with lower noise. However, for use in more complex photonic integrated circuits (PICs), local heating of the chip might pose additional restrictions as other integrated elements would need to be shielded from any temperature gradients and effects (i.e. thermal crosstalk), thus potentially limiting the scope of this technique [130].

12.4.4 Self-Injection Locking and Laser-Based Configurations

The previously reported schemes rely on the use of CW lasers for pumping, which are far from being monochromatic sources (with linewidth shifts of tens of kHz), suffer from instabilities due to noise, and require extensive optical pump power (~ Watt level), as well as elaborate feedback control systems. Additionally, thermal instabilities can strongly affect the ability to generate and stabilize coherent states, since solutions may experience thermal drifting, hence, leading to the destruction of the coherent soliton regimes.

Thermo-optical nonlinearity, originating from the thermal capacitance of the microresonator material, modifies the steady-state solutions of the intra-cavity field, by creating a slow dependence of the refractive index from the temperature. This, in turn, induces an additional detuning with respect to the pump frequency, which competes with the ultra-fast Kerr red-shift, resulting in a variety of non-solitonic nonlinear regimes, such as self-pulsing and deterministic chaos [49, 60, 85, 115, 131–134].

In order to address stabilization issues, Yi et al. [125] proposed an active approach by employing a feedback loop for the self-adjustment of the output power. Such a configuration allowed to achieve coherent states that are robust against thermal instabilities over long times. This in turn led to the development of even more efficient schemes that allow for the generation of stable solitons through passive driving and control of the cavity parameters, known as passive self-injection locking. This technique was proposed in an initial work by Liang et al., to narrow the linewidth of a distributed feedback laser with an MRR [135].

Injection-locking schemes based on free-running diode lasers have gained increased interest for the use in simplified, small footprint turn-key soliton generators [136–139]. Here, instead of using a tunable CW laser for pumping (which needs to be optically isolated from the microcavity – a difficult task for monolithic integration), the microcavity is directly attached to a semiconductor laser diode (e.g. a distributed feedback laser, DFB), which is operated in a free-running mode. Small back-reflections inside the microcavity are being utilized to lock the free-running diode to the microcavity resonance, which subsequently allows for stable soliton generation.

In 2020, Shen et al. demonstrated a turn-key soliton comb generator based on a DFB laser coupled to a Si_3N_4 microresonator chip packaged inside a commercially available butterfly package [138]. The authors showed reliable soliton comb generation with an FSR of 40 GHz spanning 30 nm, requiring only 30 mW of optical pump power. Remarkably, the demonstrated system not only allows for reliable turn-key operation (meaning that repeated on and off switching results in the same comb output) but it also exhibits much lower noise figures than other monolithic integrated lasers and even off-the-shelf tunable external cavity lasers.

In 2019, Bao and coauthors used a nested cavity configuration scheme for producing Kerr solitons [110, 133, 140], based on a nested configuration where an MRR is embedded in an external fiber cavity, which allows for signal reinjection into the ring.

This setup, illustrated in Fig. 12.2, is inspired by a passive laser mode-locking setup, first demonstrated by Pasquazi, Peccianti et al. in 2012 [40, 141–146], which embeds an MRR in an active laser loop. The result is a mode-locking almost insensitive to thermally-induced fluctuations. Remarkably, Bao et al. recently demonstrated a new class of DKSs that can be generated upon a free-CW background, with a tunable repetition rate of megahertz, sustained by the gain of the lasing medium, with a mode efficiency of 75% at average powers that are one order of magnitude lower than the energy threshold for soliton generation predicted by the LLE [110].

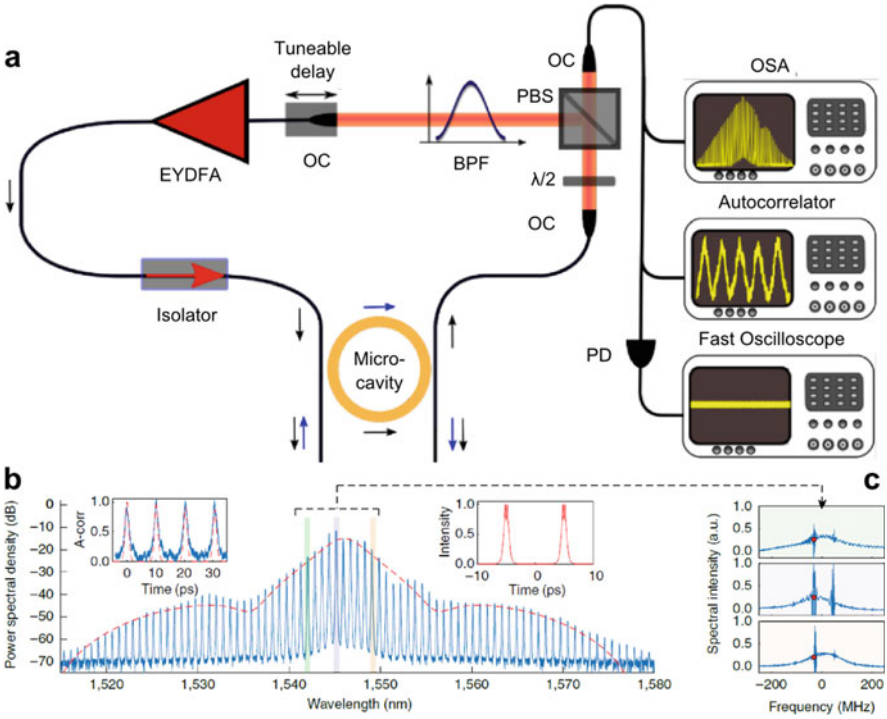

Fig. 12.2 Nested cavity setup for soliton generation. (**a**) The setup consists of a high-doped index silica glass (Hydex) MRR (Microcavity) nested in an external feedback fiber cavity, composed of a short-length erbium-ytterbium co-doped fiber amplifier (EYDFA), an optical isolator to ensure unidirectional propagation, a tunable optical bandpass filter (BPF), a tunable delay line, a polarizer (PBS), a waveplate (λ/2) for polarization control and three optical collimators (OCs). The external propagation cavity modes sustain the microcavity pulses, which are broadened by the Kerr nonlinearity over the gain bandwidth. This setup allows to reach stable soliton states with a variable repetition rate in the order of megahertz. (**b**) Soliton generation for two equidistant solitons per round-trip, with 150 mW output power from the amplifier and 30 mW output from the MRR. The experimental (blue) and theoretical (red) values of the spectrum measured with an optical spectrum analyzer (OSA) and autocorrelation trace are shown in the left and right insets, respectively. The temporal intensity output from the fiber cavity is monitored with a photodiode (PD) and a fast oscilloscope (**c**) Intracavity spectrum (blue), showing the mode lasing within each microcavity resonance. Adapted (cropped with modified font size and labels) with permission from figures (3, S6) in Bao et al. Nature Photonics 13: 384–389 [110]

12.5 Nonlinear Dynamics of DKS

Cavity solitons in MRRs can exhibit a rich variety of nonlinear dynamical regimes and intriguing nonlinear effects that have been exploited in a plethora of practical applications in spectroscopy, sensing, and telecommunications (see the following section for more details). Some examples of the available regimes are bright and dark

solitons states [147], soliton Cherenkov radiation [62], Stokes solitons [67], as well as soliton crystallization [109, 111, 148], switching [149], and breather states [150, 151].

Bright and dark solitons can coexist in Kerr media that undergo third-order dispersion in the normal regime, as studied by Parra-Rivas et al. [152]. Indeed, Xue and coauthors have shown that dark soliton states can be observed in the normal dispersion regime [153]. Moreover, as outlined earlier, Brasch et al., reported that higher-order dispersion terms in silicon nitride MRRs, while inducing a spectral broadening of the coherent states, can enable Cherenkov radiation associated to DKS propagation [36]. Stokes solitons have been also observed in MRRs, where their generation is mediated by the compensation process between Raman interaction and dispersion, which supports stable soliton propagation [47]. This is achieved through the exchange of energy with a primary DKS, formed via Kerr nonlinearity, and Stokes states, belonging to a distinct mode family.

Remarkably, in 2019, Karpov et al. demonstrated the generation of deterministic soliton crystal states in MRRs for a critical pump power value, corresponding to a stable defect-free lattice of optical pulses, sustained by the modulated driving field of a CW source [154]. The investigation of soliton crystals revealed the interesting dynamical features stemming from the switching of these states into transient chaos and the formation of breathers via a melting and recrystallization process.

12.6 Applications

Since their first introduction in 2007 [155], Kerr frequency combs (incl. soliton combs) have gained increased interest as a powerful, small-scale alternative to traditional frequency combs [122, 156], arising from their potentially low power consumption [113] as well as their cost-efficient, mass producible integration through the same CMOS-processes and infrastructure of the semiconductor industry [80]. Moreover, as outlined earlier, the generated Kerr frequency combs can eventually span, depending on the chosen material platform and dispersion engineering, the ultraviolet [157, 158], the visible [159], the mid-infrared [160], up to the THz regimes [161], offering great opportunities for many fields of application. Further, the capability of precisely adjusting the dispersion allows for the generation of combs that can intrinsically cover more than one octave (where a frequency and its double both exist within the generated spectrum, e.g. 150 THz (~2 μm) and 300 THz (~1 μm)), avoiding the need for further broadening in a preceding nonlinear device, which is important for comb stabilization [98, 124] and crucial for most of their intended applications. As a result of this versatility, Kerr soliton frequency combs have already revolutionized many applications, including classical frequency comb adaptions such as dual-comb spectroscopy [4]. Moreover, due to the small structures of microcavities, high FSRs (ranging from GHz to THz) can be achieved, which makes these platforms interesting for telecommunications applications. In fact, the FSRs of microcavities can be finely adjusted to match the WDM

(wavelength division multiplexing, 100 GHz) and DWDM (dense WDM, 50 GHz) telecom grids, thus allowing for massively parallel and high-bandwidth transmission schemes obtained by exclusively using a single optical source [9, 111]. Other novel concepts and demonstrations include optical clockworks/gears, which are able to coherently link different electromagnetic domains, e.g. from hundreds of THz to MHz. This in turn allows the optical frequency of an atomic reference (e.g. Rb) to be counted by standard electrics [162–164]. Besides, promising applications including optical frequency synthesizers [165], RF processing [166], ultra-fast and multicolor optical ranging (i.e. LIDAR, light detection and ranging) [167–169], the generation of THz radiation [161], as well as astrocombs [10, 11, 170] have been all demonstrated, to only name a few.

More recently, advanced 'hybrid' approaches such as the combination of microcavities with piezo-electric materials [169], opto-mechanical designs [171], and integrated MRRs in electro-optic materials [75] have been investigated, offering new possibilities and functionalities for these powerful microcavity platforms.

Finally, it is noteworthy that besides the aforementioned soliton applications, microcavities have attracted significant attention for utilization outside the soliton regime in applications such as biosensing [172, 173], narrow-linewidth lasers schemes [174], optical machine-learning [108, 175–178], and quantum technologies [13, 15, 17, 18, 179–184].

References

1. Vollmer F, Braun D, Libchaber A, et al (2002) Protein detection by optical shift of a resonant microcavity. Appl Phys Lett 80:4057–4059. https://doi.org/10.1063/1.1482797
2. Arnold S, Khoshsima M, Teraoka I, et al (2003) Shift of whispering-gallery modes in microspheres by protein adsorption. Opt Lett 28:272. https://doi.org/10.1364/OL.28.000272
3. Armani AM (2010) Single molecule detection using optical microcavities. In: Chremmos I, Schwelb O, Uzunoglu N (eds) Photonic Microresonator Research and Applications. Springer US, Boston, MA, pp. 253–273
4. Suh M-G, Yang Q-F, Yang KY, et al (2016) Microresonator soliton dual-comb spectroscopy. Science 354:600–603. https://doi.org/10.1126/science.aah6516
5. Yu M, Okawachi Y, Griffith AG, et al (2017) Microresonator-based high-resolution gas spectroscopy. Opt Lett 42:4442. https://doi.org/10.1364/OL.42.004442
6. Pfeifle J, Brasch V, Lauermann M, et al (2014) Coherent terabit communications with microresonator Kerr frequency combs. Nat Photonics 8:375–380. https://doi.org/10.1038/nphoton.2014.57
7. Liang W, Eliyahu D, Ilchenko VS, et al (2015) High spectral purity Kerr frequency comb radio frequency photonic oscillator. Nat Commun 6:7957. https://doi.org/10.1038/ncomms8957
8. Nguyen TG, Shoeiby M, Chu ST, et al (2015) Integrated frequency comb source based Hilbert transformer for wideband microwave photonic phase analysis. Opt Express 23:22087. https://doi.org/10.1364/OE.23.022087
9. Marin-Palomo P, Kemal JN, Karpov M, et al (2017) Microresonator-based solitons for massively parallel coherent optical communications. Nature 546:274–279. https://doi.org/10.1038/nature22387
10. Obrzud E, Rainer M, Harutyunyan A, et al (2019) A microphotonic astrocomb. Nat Photonics 13:31–35. https://doi.org/10.1038/s41566-018-0309-y

11. Suh M-G, Yi X, Lai Y-H, et al (2019) Searching for exoplanets using a microresonator astrocomb. Nat Photonics 13:25–30. https://doi.org/10.1038/s41566-018-0312-3
12. Lefèvre-Seguin V, Haroche S (1997) Towards cavity-QED experiments with silica microspheres. Mater Sci Eng B 48:53–58. https://doi.org/10.1016/S0921-5107(97)00080-9
13. Reimer C, Kues M, Roztocki P, et al (2016) Generation of multiphoton entangled quantum states by means of integrated frequency combs. Science 351:1176–1180. https://doi.org/10.1126/science.aad8532
14. Okawachi Y, Yu M, Luke K, et al (2016) Quantum random number generator using a microresonator-based Kerr oscillator. Opt Lett 41:4194. https://doi.org/10.1364/OL.41.004194
15. Kues M, Reimer C, Lukens JM, et al (2019) Quantum optical microcombs. Nat Photonics 13:170–179. https://doi.org/10.1038/s41566-019-0363-0
16. Wang F, Wang W, Niu R, et al (2020) Quantum key distribution with on-chip dissipative Kerr soliton. Laser Photon Rev 14:1900190. https://doi.org/10.1002/lpor.201900190
17. Reimer C, Zhang Y, Roztocki P, et al (2018) On-chip frequency combs and telecommunications signal processing meet quantum optics. Front Optoelectron 11:134–147. https://doi.org/10.1007/s12200-018-0814-0
18. Caspani L, Reimer C, Kues M, et al (2016) Multifrequency sources of quantum correlated photon pairs on-chip: a path toward integrated quantum frequency combs. Nanophotonics 5:351–362
19. Reimer C, Kues M, Caspani L, et al (2015) Cross-polarized photon-pair generation and bi-chromatically pumped optical parametric oscillation on a chip. Nat Commun 6:8236. https://doi.org/10.1038/ncomms9236
20. Sciara S, Roztocki P, Rimoldi C, et al (2019) Generation and processing of complex photon states with quantum frequency combs. IEEE Photonics Technol Lett 31:1862–1865. https://doi.org/10.1109/LPT.2019.2944564
21. Armani DK, Kippenberg TJ, Spillane SM, Vahala KJ (2003) Ultra-high-Q toroid microcavity on a chip. Nature 421:925–928. https://doi.org/10.1038/nature01371
22. Braginsky VB, Gorodetsky ML, Ilchenko VS (1989) Quality-factor and nonlinear properties of optical whispering-gallery modes. Phys Lett A 137:393–397. https://doi.org/10.1016/0375-9601(89)90912-2
23. Gorodetsky ML, Savchenkov AA, Ilchenko VS (1996) Ultimate Q of optical microsphere resonators. Opt Lett 21:453. https://doi.org/10.1364/OL.21.000453
24. Yi X, Yang Q-F, Yang KY, et al (2015) Soliton frequency comb at microwave rates in a high-Q silica microresonator. Optica 2:1078. https://doi.org/10.1364/OPTICA.2.001078
25. Zhang S, Silver JM, Del Bino L, et al (2019) Sub-milliwatt-level microresonator solitons with extended access range using an auxiliary laser. Optica 6:206. https://doi.org/10.1364/OPTICA.6.000206
26. Almeida VR, Barrios CA, Panepucci RR, Lipson M (2004) All-optical control of light on a silicon chip. Nature 431:1081–1084. https://doi.org/10.1038/nature02921
27. Duchesne D, Ferrera M, Razzari L, et al (2009) Efficient self-phase modulation in low loss, high index doped silica glass integrated waveguides. Opt Express 17:1865. https://doi.org/10.1364/OE.17.001865
28. Savchenkov AA, Matsko AB, Strekalov D, et al (2004) Low threshold optical oscillations in a whispering gallery mode CaF2 resonator. Phys Rev Lett 93:243905. https://doi.org/10.1103/PhysRevLett.93.243905
29. Herr T, Brasch V, Jost JD, et al (2014) Temporal solitons in optical microresonators. Nat Photonics 8:145–152. https://doi.org/10.1038/nphoton.2013.343
30. He Y, Yang Q-F, Ling J, et al (2019) Self-starting bi-chromatic LiNbO3 soliton microcomb. Optica 6:1138. https://doi.org/10.1364/OPTICA.6.001138
31. Gong Z, Bruch A, Shen M, et al (2018) High-fidelity cavity soliton generation in crystalline AlN micro-ring resonators. Opt Lett 43:4366. https://doi.org/10.1364/OL.43.004366

32. Wu C-L, Hung Y-J, Fan R, et al (2019) Tantalum pentoxide (Ta2O5) based athermal micro-ring resonator. OSA Contin 2:1198. https://doi.org/10.1364/OSAC.2.001198
33. Lu Z, Wang W, Zhang W, et al (2019) Deterministic generation and switching of dissipative Kerr soliton in a thermally controlled micro-resonator. AIP Adv 9:025314. https://doi.org/10.1063/1.5080128
34. Hausmann BJM, Bulu I, Venkataraman V, et al (2014) Diamond nonlinear photonics. Nat Photonics 8:369–374. https://doi.org/10.1038/nphoton.2014.72
35. Griffith AG, Lau RKW, Cardenas J, et al (2015) Silicon-chip mid-infrared frequency comb generation. Nat Commun 6:6299. https://doi.org/10.1038/ncomms7299
36. Brasch V, Geiselmann M, Herr T, et al (2016) Photonic chip-based optical frequency comb using soliton Cherenkov radiation. Science 351:357–360. https://doi.org/10.1126/science.aad4811
37. Chen D, Kovach A, Shen X, et al (2017) On-chip ultra-high-Q silicon oxynitride optical resonators. ACS Photonics 4:2376–2381. https://doi.org/10.1021/acsphotonics.7b00752
38. Moss DJ, Morandotti R, Gaeta AL, Lipson M (2013) New CMOS-compatible platforms based on silicon nitride and Hydex for nonlinear optics. Nat. Photonics 7:597–607
39. Ferrera M, Duchesne D, Razzari L, et al (2012) Advanced integrated photonics in doped silica glass. Springer Ser. Opt. Sci. 47–92
40. Pasquazi A, Peccianti M, Razzari L, et al (2018) Micro-combs: A novel generation of optical sources. Phys Rep 729:1–81. https://doi.org/10.1016/j.physrep.2017.08.004
41. Caspani L, Duchesne D, Dolgaleva K, et al (2011) Optical frequency conversion in integrated devices [Invited]. J Opt Soc Am B 28:A67. https://doi.org/10.1364/josab.28.000a67
42. Pasquazi A, Ahmad R, Rochette M, et al (2010) All-optical wavelength conversion in an integrated ring resonator. Opt Express 18:3858. https://doi.org/10.1364/oe.18.003858
43. Leo F, Coen S, Kockaert P, et al (2010) Temporal cavity solitons in one-dimensional Kerr media as bits in an all-optical buffer. Nat Photonics 4:471–476. https://doi.org/10.1038/nphoton.2010.120
44. Razzari L, Duchesne D, Ferrera M, et al (2010) CMOS-compatible integrated optical hyper-parametric oscillator. Nat Photonics 4:41–45. https://doi.org/10.1038/nphoton.2009.236
45. Herr T, Hartinger K, Riemensberger J, et al (2012) Universal formation dynamics and noise of Kerr-frequency combs in microresonators. Nat Photonics 6:480–487. https://doi.org/10.1038/nphoton.2012.127
46. Bao H, Cooper A, Chu ST, et al (2018) Type-II micro-comb generation in a filter-driven four wave mixing laser [Invited]. Photonics Res 6:B67. https://doi.org/10.1364/prj.6.000b67
47. Kippenberg TJ, Gaeta AL, Lipson M, Gorodetsky ML (2018) Dissipative Kerr solitons in optical microresonators. Science 361:eaan8083. https://doi.org/10.1126/science.aan8083
48. Caspani L, Reimer C, Pasquazi A, et al (2013) A novel integrated laser source without a laser. SPIE Newsroom. https://doi.org/10.1117/2.1201312.005240
49. Herr T, Gorodetsky ML, Kippenberg TJ (2015) Dissipative Kerr solitons in optical microresonators. In: Nonlinear Optical Cavity Dynamics. Wiley-VCH Verlag GmbH & Co. KGaA, Weinheim, Germany, pp. 129–162
50. Lugiato LA, Lefever R (1987) Spatial dissipative structures in passive optical systems. Phys Rev Lett 58:2209–2211. https://doi.org/10.1103/PhysRevLett.58.2209
51. Haelterman M, Trillo S, Wabnitz S (1992) Dissipative modulation instability in a nonlinear dispersive ring cavity. Opt Commun 91:401–407. https://doi.org/10.1016/0030-4018(92)90367-Z
52. Lugiato LA, Prati F, Gorodetsky ML, Kippenberg TJ (2018) From the Lugiato–Lefever equation to microresonator-based soliton Kerr frequency combs. Philos Trans R Soc A Math Phys Eng Sci 376:20180113. https://doi.org/10.1098/rsta.2018.0113
53. Lugiato L, Prati F, Brambilla M (2015) Nonlinear optical systems. Cambridge University Press, Cambridge

54. Chembo YK, Menyuk CR (2013) Spatiotemporal Lugiato-Lefever formalism for Kerr-comb generation in whispering-gallery-mode resonators. Phys Rev A 87:053852. https://doi.org/10.1103/PhysRevA.87.053852
55. Coen S, Randle HG, Sylvestre T, Erkintalo M (2013) Modeling of octave-spanning Kerr frequency combs using a generalized mean-field Lugiato–Lefever model. Opt Lett 38:37. https://doi.org/10.1364/OL.38.000037
56. Hansson T, Modotto D, Wabnitz S (2014) On the numerical simulation of Kerr frequency combs using coupled mode equations. Opt Commun 312:134–136. https://doi.org/10.1016/j.optcom.2013.09.017
57. Matsko AB, Savchenkov AA, Strekalov D, et al (2005) Optical hyperparametric oscillations in a whispering-gallery-mode resonator: Threshold and phase diffusion. Phys Rev A 71:033804. https://doi.org/10.1103/PhysRevA.71.033804
58. Drake TE, Stone JR, Briles TC, Papp SB (2019) Thermal decoherence and laser cooling of Kerr microresonator solitons. ArXiv 1903.00431
59. Ilchenko VS, Gorodetsky ML (1992) Thermal nonlinear effects in optical whispering gallery microresonators. Laser Phys 2:1004
60. Di Lauro L, Li J, Moss DJ, et al (2017) Parametric control of thermal self-pulsation in micro-cavities. Opt Lett 42:3407. https://doi.org/10.1364/OL.42.003407
61. Chembo YK, Strekalov D V., Yu N (2010) Spectrum and dynamics of optical frequency combs generated with monolithic whispering gallery mode resonators. Phys Rev Lett 104:103902. https://doi.org/10.1103/PhysRevLett.104.103902
62. Cherenkov A V., Lobanov VE, Gorodetsky ML (2017) Dissipative Kerr solitons and Cherenkov radiation in optical microresonators with third-order dispersion. Phys Rev A 95:033810. https://doi.org/10.1103/PhysRevA.95.033810
63. Erkintalo M, Xu YQ, Murdoch SG, et al (2012) Cascaded phase matching and nonlinear symmetry breaking in fiber frequency combs. Phys Rev Lett 109:223904. https://doi.org/10.1103/PhysRevLett.109.223904
64. Lamont MRE, Okawachi Y, Gaeta AL (2013) Route to stabilized ultrabroadband microresonator-based frequency combs. Opt Lett 38:3478. https://doi.org/10.1364/OL.38.003478
65. Karpov M, Guo H, Kordts A, et al (2016) Raman self-frequency shift of dissipative Kerr solitons in an optical microresonator. Phys Rev Lett 116:103902. https://doi.org/10.1103/PhysRevLett.116.103902
66. Blow KJ, Wood D (1989) Theoretical description of transient stimulated Raman scattering in optical fibers. IEEE J Quantum Electron 25:2665–2673. https://doi.org/10.1109/3.40655
67. Yang Q-F, Yi X, Yang KY, Vahala K (2017) Stokes solitons in optical microcavities. Nat Phys 13:53–57. https://doi.org/10.1038/nphys3875
68. Wang Y, Anderson M, Coen S, et al (2018) Stimulated Raman scattering imposes fundamental limits to the duration and bandwidth of temporal cavity solitons. Phys Rev Lett 120:053902. https://doi.org/10.1103/PhysRevLett.120.053902
69. Grudinin IS, Yu N (2015) Dispersion engineering of crystalline resonators via microstructuring. Optica 2:221. https://doi.org/10.1364/optica.2.000221
70. Yang KY, Beha K, Cole DC, et al (2016) Broadband dispersion-engineered microresonator on a chip. Nat Photonics 10:316–320. https://doi.org/10.1038/nphoton.2016.36
71. Foster MA, Turner AC, Sharping JE, et al (2006) Broad-band optical parametric gain on a silicon photonic chip. Nature 441:960–963. https://doi.org/10.1038/nature04932
72. Riemensberger J, Hartinger K, Herr T, et al (2012) Dispersion engineering of thick high-Q silicon nitride ring-resonators via atomic layer deposition. Opt Express 20:27661. https://doi.org/10.1364/OE.20.027661
73. Zhang L, Bao C, Singh V, et al (2013) Generation of two-cycle pulses and octave-spanning frequency combs in a dispersion-flattened micro-resonator. Opt Lett 38:5122. https://doi.org/10.1364/ol.38.005122

74. Kim S, Han K, Wang C, et al (2017) Dispersion engineering and frequency comb generation in thin silicon nitride concentric microresonators. Nat Commun 8. https://doi.org/10.1038/s41467-017-00491-x
75. Wang C, Zhang M, Yu M, et al (2019) Monolithic lithium niobate photonic circuits for Kerr frequency comb generation and modulation. Nat Commun 10:978. https://doi.org/10.1038/s41467-019-08969-6
76. Ferrera M, Duchesne D, Razzari L, et al (2009) Low power four wave mixing in an integrated, micro-ring resonator with Q = 12 million. Opt Express 17:14098. https://doi.org/10.1364/oe.17.014098
77. Ferrera M, Razzari L, Duchesne D, et al (2008) Low-power continuous-wave nonlinear optics in doped silica glass integrated waveguide structures. Nat Photonics 2:737–740. https://doi.org/10.1038/nphoton.2008.228
78. Kordts A, Pfeiffer MHP, Guo H, et al (2016) Higher order mode suppression in high-Q anomalous dispersion SiN microresonators for temporal dissipative Kerr soliton formation. 2016 Conf Lasers Electro-Optics, CLEO 2016 41:452–455. https://doi.org/10.1364/ol.41.000452
79. Kovach A, Chen D, He J, et al (2020) Emerging material systems for integrated optical Kerr frequency combs. Adv Opt Photonics 12:135. https://doi.org/10.1364/aop.376924
80. Leuthold J, Koos C, Freude W (2010) Nonlinear silicon photonics. Nat Photonics 4:535–544. https://doi.org/10.1038/nphoton.2010.185
81. Bao C, Taheri H, Zhang L, et al (2017) High-order dispersion in Kerr comb oscillators. J Opt Soc Am B 34:715. https://doi.org/10.1364/josab.34.000715
82. Turner AC, Manolatou C, Schmidt BS, et al (2006) Tailored anomalous group-velocity dispersion in silicon waveguides. Conf Lasers Electro-Optics 2006 Quantum Electron Laser Sci Conf CLEO/QELS 2006 14:4357–4362. https://doi.org/10.1109/CLEO.2006.4628293
83. Klenner A, Mayer AS, Johnson AR, et al (2016) Gigahertz frequency comb offset stabilization based on supercontinuum generation in silicon nitride waveguides. Opt Express 24:11043. https://doi.org/10.1364/oe.24.011043
84. Tartara L, Cristiani I, Degiorgio V (2003) Blue light and infrared continuum generation by soliton fission in a microstructured fiber. Appl Phys B Lasers Opt 77:307–311. https://doi.org/10.1007/s00340-003-1172-0
85. Chemnitz M, Scheibinger R, Gaida C, et al (2018) Thermodynamic control of soliton dynamics in liquid-core fibers. Optica 5:695. https://doi.org/10.1364/OPTICA.5.000695
86. Cristiani I, Tediosi R, Tartara L, Degiorgio V (2004) Dispersive wave generation by solitons in microstructured optical fibers. Opt Express 12:124–135. https://doi.org/10.1364/OPEX.12.000124
87. Demas J, Steinvurzel P, Tai B, et al (2015) Intermodal nonlinear mixing with Bessel beams in optical fiber. Optica 2:14. https://doi.org/10.1364/optica.2.000014
88. Wright LG, Christodoulides DN, Wise FW (2017) Spatiotemporal mode-locking in multimode fiber lasers. Science 358:94–97. https://doi.org/10.1126/science.aao0831
89. Wright LG, Christodoulides DN, Wise FW (2015) Controllable spatiotemporal nonlinear effects in multimode fibres. Nat Photonics 9:306–310. https://doi.org/10.1038/nphoton.2015.61
90. Haboucha A, Leblond H, Salhi M, et al (2008) Coherent soliton pattern formation in a fiber laser. Opt Lett 33:524. https://doi.org/10.1364/ol.33.000524
91. Amrani F, Salhi M, Grelu P, et al (2011) Universal soliton pattern formations in passively mode-locked fiber lasers. Opt Lett 36:1545. https://doi.org/10.1364/OL.36.001545
92. Grelu P, Akhmediev N (2012) Dissipative solitons for mode-locked lasers. Nat Photonics 6:84–92. https://doi.org/10.1038/nphoton.2011.345
93. Qin H, Xiao X, Wang P, Yang C (2018) Observation of soliton molecules in a spatiotemporal mode-locked multimode fiber laser. Opt Lett 43:1982. https://doi.org/10.1364/OL.43.001982

94. Okawachi Y, Lamont MRE, Luke K, et al (2014) Bandwidth shaping of microresonator-based frequency combs via dispersion engineering. Opt Lett 39:3535. https://doi.org/10.1364/OL.39.003535
95. Joshi C, Jang JK, Luke K, et al (2016) Thermally controlled comb generation and soliton modelocking in microresonators. Opt Lett 41:2565. https://doi.org/10.1364/OL.41.002565
96. Guo Y, Jafari Z, Agarwal AM, et al (2016) Bilayer dispersion-flattened waveguides with four zero-dispersion wavelengths. Opt Lett 41:4939. https://doi.org/10.1364/ol.41.004939
97. Huang SW, Liu H, Yang J, et al (2016) Smooth and flat phase-locked Kerr frequency comb generation by higher order mode suppression. Sci Rep 6:1–7. https://doi.org/10.1038/srep26255
98. Pfeiffer MHP, Herkommer C, Liu J, et al (2017) Octave-spanning dissipative Kerr soliton frequency combs in Si3N4 microresonators. Optica 4:684. https://doi.org/10.1364/OPTICA.4.000684
99. Husakou A V, Herrmann J (2001) Supercontinuum generation of higher-order solitons by fission in photonic crystal fibers. Phys Rev Lett 87:203901. https://doi.org/10.1103/PhysRevLett.87.203901
100. Newman ZL, Maurice V, Drake T, et al (2019) Architecture for the photonic integration of an optical atomic clock. Optica 6:680. https://doi.org/10.1364/optica.6.000680
101. Yu M, Okawachi Y, Joshi C, et al (2018) Gas-phase microresonator-based comb spectroscopy without an external pump laser. ACS Photonics 5:2780–2785. https://doi.org/10.1021/acsphotonics.8b00579
102. Yu M, Okawachi Y, Griffith AG, et al (2018) Silicon-chip-based mid-infrared dual-comb spectroscopy. Nat Commun 9:6–11. https://doi.org/10.1038/s41467-018-04350-1
103. Yi X, Yang Q-F, Zhang X, et al (2017) Single-mode dispersive waves and soliton microcomb dynamics. Nat Commun 8:14869. https://doi.org/10.1038/ncomms14869
104. Stone JR, Papp SB (2020) Harnessing dispersion in soliton microcombs to mitigate thermal noise. ArXiv 2006.10907v1
105. Ramelow S, Farsi A, Clemmen S, et al (2014) Strong polarization mode coupling in microresonators. Opt Lett 39:5134. https://doi.org/10.1364/ol.39.005134
106. Yu Z, Yuhang W, Xinxuan M, et al (2019) High-order mode suppressed microresonators based on multimode waveguides and a low-loss mode remover. Front Opt - Proc Front Opt + Laser Sci APS/DLS 1:3–4. https://doi.org/10.1364/FIO.2019.JTu4A.89
107. Yang Q-F, Yi X, Yang KY, Vahala K (2016) Spatial-mode-interaction-induced dispersive waves and their active tuning in microresonators. Optica 3:1132. https://doi.org/10.1364/optica.3.001132
108. Xu X, Tan M, Corcoran B, et al (2020) Photonic perceptron based on a Kerr microcomb for high-speed, scalable, optical neural networks. Laser Photon Rev 2000070. https://doi.org/10.1002/lpor.202000070
109. Cole DC, Lamb ES, Del'Haye P, et al (2017) Soliton crystals in Kerr resonators. Nat Photonics 11:671–676. https://doi.org/10.1038/s41566-017-0009-z
110. Bao H, Cooper A, Rowley M, et al (2019) Laser cavity-soliton microcombs. Nat Photonics 13:384–389. https://doi.org/10.1038/s41566-019-0379-5
111. Corcoran B, Tan M, Xu X, et al (2020) Ultra-dense optical data transmission over standard fibre with a single chip source. Nat Commun 11:2568. https://doi.org/10.1038/s41467-020-16265-x
112. Suh M-G, Vahala K (2018) Gigahertz-repetition-rate soliton microcombs. Optica 5:65. https://doi.org/10.1364/OPTICA.5.000065
113. Stern B, Ji X, Okawachi Y, et al (2018) Battery-operated integrated frequency comb generator. Nature 562:401–405. https://doi.org/10.1038/s41586-018-0598-9
114. Gaeta AL, Lipson M, Kippenberg TJ (2019) Photonic-chip-based frequency combs. Nat Photonics 13:158–169. https://doi.org/10.1038/s41566-019-0358-x

115. Matsko AB, Liang W, Savchenkov AA, Maleki L (2013) Chaotic dynamics of frequency combs generated with continuously pumped nonlinear microresonators. Opt Lett 38:525. https://doi.org/10.1364/ol.38.000525
116. Webb KE, Erkintalo M, Coen S, Murdoch SG (2016) Experimental observation of coherent cavity soliton frequency combs in silica microspheres. Opt Lett 41:4613. https://doi.org/10.1364/ol.41.004613
117. Saha K, Okawachi Y, Shim B, et al (2013) Modelocking and femtosecond pulse generation in chip-based frequency combs. Opt Express 21:1335. https://doi.org/10.1364/oe.21.001335
118. Strekalov DV, Yu N (2009) Generation of optical combs in a whispering gallery mode resonator from a bichromatic pump. Phys Rev A 79:. https://doi.org/10.1103/physreva.79.041805
119. Hansson T, Wabnitz S (2014) Bichromatically pumped microresonator frequency combs. Phys Rev A 90:013811. https://doi.org/10.1103/PhysRevA.90.013811
120. Papp SB, Del'Haye P, Diddams SA (2013) Parametric seeding of a microresonator optical frequency comb. Opt Express 21:17615. https://doi.org/10.1364/oe.21.017615
121. Papp SB, Beha K, Del'Haye P, et al (2014) Microresonator frequency comb optical clock. Optica 1:10. https://doi.org/10.1364/optica.1.000010
122. Udem T, Reichert J, Holzwarth R, Hänsch TW (1999) Absolute optical frequency measurement of the cesium D1 line with a mode-locked laser. Phys Rev Lett 82:3568–3571. https://doi.org/10.1103/PhysRevLett.82.3568
123. Jost JD, Herr T, Lecaplain C, et al (2015) Counting the cycles of light using a self-referenced optical microresonator. Optica 2:706. https://doi.org/10.1364/OPTICA.2.000706
124. Brasch V, Lucas E, Jost JD, et al (2017) Self-referenced photonic chip soliton Kerr frequency comb. Light Sci Appl 6:e16202–e16202. https://doi.org/10.1038/lsa.2016.202
125. Yi X, Yang Q-F, Youl Yang K, Vahala KJ (2016) Active capture and stabilization of temporal solitons in microresonators. Opt Lett 41:2037. https://doi.org/10.1364/OL.41.002037
126. Del'Haye P, Coillet A, Fortier T, et al (2015) Phase coherent link of an atomic clock to a self-referenced microresonator frequency comb. arXiv 1511.08103
127. Lamb ES, Carlson DR, Hickstein DD, et al (2018) Optical-frequency measurements with a Kerr microcomb and photonic-chip supercontinuum. Phys Rev Appl 9:024030. https://doi.org/10.1103/PhysRevApplied.9.024030
128. Brasch V, Geiselmann M, Pfeiffer MHP, Kippenberg TJ (2016) Bringing short-lived dissipative Kerr soliton states in microresonators into a steady state. Opt Express 24:29312. https://doi.org/10.1364/OE.24.029312
129. Wang W, Lu Z, Zhang W, et al (2018) Robust soliton crystals in a thermally controlled microresonator. Opt Lett 43:2002. https://doi.org/10.1364/OL.43.002002
130. Milanizadeh M, Aguiar D, Melloni A, Morichetti F (2019) Canceling thermal cross-talk effects in photonic integrated circuits. J Light Technol 37:1325–1332. https://doi.org/10.1109/JLT.2019.2892512
131. Jin L, Pasquazi A, Lauro L Di, et al (2016) Demonstration of bi- and multi-stability in a high order ring resonator. In: 2016 21st OptoElectronics and Communications Conference (OECC) held jointly with 2016 International Conference on Photonics in Switching (PS). pp 1–3
132. Jin L, Di Lauro L, Pasquazi A, et al (2020) Optical multi-stability in a nonlinear high-order microring resonator filter. APL Photonics 5:56106. https://doi.org/10.1063/5.0002941
133. Rowley M, Wetzel B, Di Lauro L, et al (2019) Thermo-optical pulsing in a microresonator filtered fiber-laser: a route towards all-optical control and synchronization. Opt Express 27:19242–19254
134. Hansson T, Modotto D, Wabnitz S (2013) Dynamics of the modulational instability in microresonator frequency combs. Phys Rev A 88. https://doi.org/10.1103/physreva.88.023819
135. Liang W, Ilchenko VS, Savchenkov AA, et al (2010) Whispering-gallery-mode-resonator-based ultranarrow linewidth external-cavity semiconductor laser. Opt Lett 35:2822. https://doi.org/10.1364/ol.35.002822

136. Kondratiev NM, Lobanov VE, Cherenkov A V., et al (2017) Self-injection locking of a laser diode to a high-Q WGM microresonator. Opt Express 25:28167. https://doi.org/10.1364/oe.25.028167
137. Pavlov NG, Koptyaev S, Lihachev G V., et al (2018) Narrow-linewidth lasing and soliton Kerr microcombs with ordinary laser diodes. Nat Photonics 12:694–698. https://doi.org/10.1038/s41566-018-0277-2
138. Shen B, Chang L, Liu J, et al (2020) Integrated turnkey soliton microcombs. Nature 582:365–369. https://doi.org/10.1038/s41586-020-2358-x
139. Liang W, Ilchenko VS, Eliyahu D, et al (2015) Ultralow noise miniature external cavity semiconductor laser. Nat Commun 6:7371. https://doi.org/10.1038/ncomms8371
140. Bao H, Olivieri L, Rowley M, et al (2020) Turing patterns in a fiber laser with a nested microresonator: Robust and controllable microcomb generation. Phys Rev Res 2. https://doi.org/10.1103/physrevresearch.2.023395
141. Pasquazi A, Caspani L, Peccianti M, et al (2013) Self-locked optical parametric oscillation in a CMOS compatible microring resonator: a route to robust optical frequency comb generation on a chip. Opt Express 21:13333. https://doi.org/10.1364/oe.21.013333
142. Pasquazi A, Peccianti M, Little BE, et al (2012) Stable, dual mode, high repetition rate mode-locked laser based on a microring resonator. Opt Express 20:27355. https://doi.org/10.1364/oe.20.027355
143. Bao H, Cooper A, Di Lauro L, et al (2017) Repetition rate controllable filter-driven four wave mixing laser. 2017 Conf. Lasers Electro-Optics Eur. Eur. Quantum Electron. Conf.
144. Pasquazi A, Peccianti M, Chu ST, et al (2016) Novel ultrafast sources on chip: filter driven four wave mixing lasers, from high repetition rate to burst mode operation. Laser Reson. Microresonators, Beam Control XVIII
145. Peccianti M, Pasquazi A, Park Y, et al (2012) Demonstration of a stable ultrafast laser based on a nonlinear microcavity. Nat Commun 3:765. https://doi.org/10.1038/ncomms1762
146. Pasquazi A, Peccianti M, Clerici M, et al (2014) Collapse arrest in instantaneous Kerr media via parametric interactions. Phys Rev Lett 113:. https://doi.org/10.1103/physrevlett.113.133901
147. Weiner AM, Heritage JP, Hawkins RJ, et al (1988) Experimental observation of the fundamental dark soliton in optical fibers. Phys Rev Lett 61:2445–2448. https://doi.org/10.1103/PhysRevLett.61.2445
148. Xu X, Tan M, Wu J, et al (2020) Broadband photonic RF channelizer with 92 channels based on a soliton crystal microcomb. J Light Technol 38:5116–5121. https://doi.org/10.1109/JLT.2020.2997699
149. Guo H, Karpov M, Lucas E, et al (2016) Universal dynamics and deterministic switching of dissipative Kerr solitons in optical microresonators. Nat Phys 13:94–102. https://doi.org/10.1038/nphys3893
150. Lucas E, Karpov M, Guo H, et al (2017) Breathing dissipative solitons in optical microresonators. Nat Commun 8:736. https://doi.org/10.1038/s41467-017-00719-w
151. Matsko AB, Savchenkov AA, Maleki L (2012) On excitation of breather solitons in an optical microresonator. Opt Lett 37:4856. https://doi.org/10.1364/ol.37.004856
152. Parra-Rivas P, Gomila D, Gelens L (2017) Coexistence of stable dark- and bright-soliton Kerr combs in normal-dispersion resonators. Phys Rev A 95:. https://doi.org/10.1103/physreva.95.053863
153. Xue X, Xuan Y, Liu Y, et al (2015) Mode-locked dark pulse Kerr combs in normal-dispersion microresonators. Nat Photonics 9:594–600. https://doi.org/10.1038/nphoton.2015.137
154. Karpov M, Guo H, Pfeiffer MHP, et al (2017) Dynamics of soliton crystals in optical Microresonators. 2017 Conf. Lasers Electro-Optics, CLEO 2017 - Proc. 2017-Janua:1–2
155. Del'Haye P, Schliesser A, Arcizet O, et al (2007) Optical frequency comb generation from a monolithic microresonator. Nature 450:1214–1217. https://doi.org/10.1038/nature06401

156. Glauber RJ, Hall JL, Hänsch TW (2005) Advanced information on the Nobel Prize in Physics 2005. Quantum-mechanical theory of optical coherence - Laser-based precision spectroscopy and optical frequency comb techniques. General introduction. 1–14
157. Liu X, Bruch AW, Gong Z, et al (2018) Ultra-high-Q UV microring resonators based on a single-crystalline AlN platform. Optica 5:1279. https://doi.org/10.1364/OPTICA.5.001279
158. Dorche AE, Timucin D, Thyagarajan K, et al (2020) Advanced dispersion engineering of a III-Nitride micro-resonator for a blue/UV frequency comb. arXiv 2006.07391
159. Lee SH, Oh DY, Yang Q-F, et al (2017) Towards visible soliton microcomb generation. Nat Commun 8:1295. https://doi.org/10.1038/s41467-017-01473-9
160. Hansson T, Modotto D, Wabnitz S (2014) Mid-infrared soliton and Raman frequency comb generation in silicon microrings. Opt Lett 39:6747. https://doi.org/10.1364/OL.39.006747
161. Zhang S, Silver JM, Shang X, et al (2019) Terahertz wave generation using a soliton microcomb. Opt Express 27:35257. https://doi.org/10.1364/OE.27.035257
162. Ye J, Hall JL, Diddams SA (2000) Precision phase control of an ultrawide-bandwidth femtosecond laser: a network of ultrastable frequency marks across the visible spectrum. Opt Lett 25:1675. https://doi.org/10.1364/OL.25.001675
163. Diddams SA, Udem T, Bergquist JC, et al (2001) An optical clock based on a single trapped 199Hg+ ion. Science 293:825–828. https://doi.org/10.1126/science.1061171
164. Diddams SA, Vahala K, Udem T (2020) Optical frequency combs: coherently uniting the electromagnetic spectrum. Science 369:eaay3676. https://doi.org/10.1126/science.aay3676
165. Spencer DT, Drake T, Briles TC, et al (2018) An optical-frequency synthesizer using integrated photonics. Nature 557:81–85. https://doi.org/10.1038/s41586-018-0065-7
166. Xu X, Tan M, Wu J, et al (2019) Microcomb-based photonic RF signal processing. IEEE Photonics Technol Lett 31:1854–1857. https://doi.org/10.1109/LPT.2019.2940497
167. Randel S, Kordts A, Freude W, et al (2018) Ultrafast optical ranging using microresonator soliton frequency combs. Science 359:887–891. https://doi.org/10.1126/science.aao3924
168. Suh M, Vahala K (2017) Soliton microcomb range measurement. 887:884–887. https://doi.org/10.1126/science.aao1968
169. Liu J, Tian H, Lucas E, et al (2020) Monolithic piezoelectric control of soliton microcombs. Nature 583:385–390. https://doi.org/10.1038/s41586-020-2465-8
170. Roztocki P, Morandotti R (2019) Astrocombs for extreme-precision spectroscopy. Nat Astron 3:135–136. https://doi.org/10.1038/s41550-019-0698-y
171. Liu L, Ye M, Yu Z (2020) Ultra-high peak rejection all-optical microwave filter based on the opto-mechanical rings. IEEE Photonics Technol Lett 1–1. https://doi.org/10.1109/LPT.2020.3013437
172. De Vos K, Bartolozzi I, Schacht E, et al (2007) Silicon-on-Insulator microring resonator for sensitive and label-free biosensing. Opt Express 15:7610. https://doi.org/10.1364/OE.15.007610
173. Tu X, Chen S-L, Song C, et al (2019) Ultrahigh Q polymer microring resonators for biosensing applications. IEEE Photonics J 11:1–10. https://doi.org/10.1109/JPHOT.2019.2899666
174. Kues M, Reimer C, Wetzel B, et al (2017) Passively mode-locked laser with an ultra-narrow spectral width. Nat Photonics 11:159–162. https://doi.org/10.1038/nphoton.2016.271
175. Tait AN, de Lima TF, Zhou E, et al (2017) Neuromorphic photonic networks using silicon photonic weight banks. Sci Rep 7:7430. https://doi.org/10.1038/s41598-017-07754-z
176. Feldmann J, Youngblood N, Wright CD, et al (2019) All-optical spiking neurosynaptic networks with self-learning capabilities. Nature 569:208–214. https://doi.org/10.1038/s41586-019-1157-8
177. Feldmann J, Youngblood N, Karpov M, et al (2020) Parallel convolution processing using an integrated photonic tensor core. 2002.00281v1
178. Miscuglio M, Sorger VJ (2020) Photonic tensor cores for machine learning. Appl Phys Rev 7:031404. https://doi.org/10.1063/5.0001942
179. Reimer C, Caspani L, Clerici M, et al (2014) Integrated frequency comb source of heralded single photons. Opt Express 22:6535. https://doi.org/10.1364/OE.22.006535

180. Roztocki P, Kues M, Reimer C, et al (2017) Practical system for the generation of pulsed quantum frequency combs. Opt Express 25:18940. https://doi.org/10.1364/OE.25.018940
181. Kues M, Reimer C, Roztocki P, et al (2017) On-chip generation of high-dimensional entangled quantum states and their coherent control. Nature 546:622–626. https://doi.org/10.1038/nature22986
182. Imany P, Jaramillo-Villegas JA, Odele OD, et al (2018) 50-GHz-spaced comb of high-dimensional frequency-bin entangled photons from an on-chip silicon nitride microresonator. Opt Express 26:1825. https://doi.org/10.1364/OE.26.001825
183. Reimer C, Sciara S, Roztocki P, et al (2019) High-dimensional one-way quantum processing implemented on d-level cluster states. Nat Phys 15:148–153. https://doi.org/10.1038/s41567-018-0347-x
184. Caspani L, Xiong C, Eggleton BJ, et al (2017) Integrated sources of photon quantum states based on nonlinear optics. Light Sci Appl 6:e17100–e17100. https://doi.org/10.1038/lsa.2017.100

Chapter 13
Vector Vortex Solitons and Soliton Control in Vertical-Cavity Surface-Emitting Lasers

T. Ackemann, T. Guillet, H. Pulham, and G. -L. Oppo

Abstract The properties of vector vortex beams in vertical-cavity-surface emitting lasers with frequency-selective feedback are investigated. They are interpreted as high-order vortex solitons with a spatially non-uniform, but locally linear polarization state. In contrast to most schemes to obtain vector vortex beams relying on imprinting the polarization structure, vector vortex solitons form spontaneously due to the near polarization degeneracy in vertical-cavity devices. We observe radially, hyperbolic and spiral polarization configurations depending on small residual anisotropies in the system and multi-stability between different states. In addition, we demonstrate flip-flop operation of laser solitons via in principle local electronic nonlinearities. Combining the two themes might open up a route for a simple device enabling fast switching between different vector vortex beams for applications. The investigations connect nicely the fields of nonlinear science, singular optics, structured light and semiconductor laser technology.

Keywords Vector vortex beams · Vector solitons · Vortex solitons · High-order spatial solitons · Cavity solitons · Dissipative optical solitons · Switching dynamics · Bistability · Multistability · Flip-flop operation of solitons · VCSEL · Vertical-cavity surface-emitting laser · Semiconductor laser solitons

13.1 Introduction

In this chapter, we will review and provide new results on *high-order spatial lasers solitons* which have the non-trivial polarization characteristics of *vector vortex beams*. They provide a fascinating bridge between nonlinear science and singular

T. Ackemann (✉) · H. Pulham · G. -L. Oppo
SUPA and Department of Physics, University of Strathclyde, Glasgow, Scotland, UK
e-mail: thorsten.ackemann@strath.ac.uk; g.l.oppo@strath.ac.uk; harry.pulham@strath.ac.uk

T. Guillet
Laboratoire Charles Coulomb (L2C), University Montpellier, CNRS, Montpellier, France
e-mail: Thierry.Guillet@umontpellier.fr

M. F. S. Ferreira (ed.), *Dissipative Optical Solitons*, Springer Series in Optical Sciences 238, https://doi.org/10.1007/978-3-030-97493-0_13

optics, both thriving research fields on their own. Solitons or solitary waves are shape-stable waves for which the dispersive or diffractive spreading typical of linear waves is counteracted by nonlinearities. The first observation of a shape-stable 'wave of translation' was done by the Scottish engineer Scott Russell in the Union Channel in 1834 [1]. In optical context, solitonic behaviour can occur in time (temporal soliton [2, 3]) or in space (spatial soliton [4, 5]), both in the simplest case described by a Nonlinear Schrödinger Equation (NLSE) [6]. In the spatial case, self-localization can be understood by the concept of a self-induced nonlinear waveguide. The beam induces a refractive index distribution in a nonlinear medium with an intensity dependent refractive index, which—for a medium in which the refractive index is increasing with intensity, i.e. a self-focusing medium—will counteracts the linear diffractive spreading. For the soliton solution, the beam writing the refractive index distribution is the fundamental mode of the induced waveguide in a self-consistent way. If the concept of a single-humped fundamental soliton is already intriguing, it is the more remarkably that more complex wave distributions can propagate as high order solitons. Nevertheless, high-order fibre solitons were observed already in the first experiments of Mollenauer [3]. For spatial solitons, the analogy with linear modes suggests that a suitably nonlinear adaption of the ring-shaped doughnut as the first-order Laguerre-Gauss mode might be a suitable candidate for a high-order soliton. However, it turns out that their propagation is unstable resulting in the break-up to two fundamental solitons as the ring-shaped intensity structure is subject to a modulational instability [7–9] in the same way as a plane wave is modulationally unstable in a self-focusing medium [6].

One way to stabilize this high-order soliton is by adding dissipation and driving. In optics, this is usually achieved by placing the medium into a cavity. The resulting states are an attractor of the dissipative dynamics and referred to as *dissipative solitons, cavity solitons or localized structures* [10–13]. Dissipative systems support a wider range of solitary waves or localized structures than the conservative NLSE. Examples are the stability of spatial solitons in two spatial dimensions in the Lugiato-Lefever equation [14] (the dissipative extension of the NLSE describing a coherently driven cavity with an intra-cavity Kerr medium [15]), the existence and stability of fundamental solitons in lasers [16–18] and coherently driven cavity systems [15] with absorptive media, and, relevant for this chapter, the stabilization of vortex solitons in lasers. These were predicted in lasers with saturable absorbers [19, 20] and observed in coupled *vertical-cavity surface-emitting lasers (VCSELs)*, one operated as a gain device, one as saturable absorber [21]. A VCSEL is a semiconductor laser in which the emission is in the direction of the epitaxial growth [22]. This allows for a large Fresnel number [23, 24] enabling self-organization and solitons independent from boundary conditions (see Sect. 13.3.2). Vortices in self-focusing Ginzburg-Landau models were predicted in [25, 26]. Refs. [27, 28] predicted stable vortex solitons with a saturable or cubic (i.e. Kerr-like) self-focusing nonlinearity coupled to an additional linear filter. This system provides a minimal model for a VCSEL with frequency-selective feedback [29–31]. The experimental observation of vortex solitons in such a system was reported in [32].

These vortex solitons were homogeneously linearly polarized and can be described in a quasi-scalar theory. However, light is in general a vector wave providing many additional degrees of freedom for soliton formation. It is not possible to give a full account of the literature but we refer to [33–35]. Typically, these vector solitons consists of localized patches of one polarization state embedded in another one with a polarization domain wall in between. Interestingly, to our knowledge the first observation of stable high-order dissipative solitons were vector solitons in this sense [36]. What we are investigating here are structures in which the polarization is *continuously spatially varying*. They are usually referred to as *'vector vortex beams (VVBs)'* [37, 38] and possess a circularly symmetric intensity structure combined with a spatially non-uniform polarization field and a polarization singularity. We will review their properties, generation and applications in Sect. 13.3.1. For the moment the important point to note is that there are usually created by a bespoke, potentially complex, setup imposing the polarization structure onto the beam (see Sect. 13.3.1 for examples). In contrast, VVBs form spontaneously in the VCSEL with frequency-selective feedback discussed here [39]. This is enabled by the high circular symmetry of a VCSEL in the transverse plane of the microcavity. This is known to allow a degeneracy or near-degeneracy of polarization states but investigations were focused on linearly polarized states and switching between them, see e.g. [40–44]. One paper predicted the possibility of VVBs in free-running VCSELs already in 1997 [45] and thus established an early link between singular optics and VCSEL technology, but, appearing before the great upsurge in interest in vector vortex states, did not obtain the attention due and was not backed up by experiments.

The main contribution of this chapter (Sect. 13.3) is to review the properties of VVBs and solitons in VCSELs with frequency-selective feedback, and to report on experimental progress and new insights compared to Ref. [39]. In particular, we will argue in Sect. 13.3.6 why these states have been observed now in the VCSEL with feedback but not in free-running VCSELs as predicted in Ref. [45]. As a disclaimer, we would like to caution that we are using here the phrase vector vortex solitons for the vector vortex structures observed and we will argue in Sect. 13.3.6 for this interpretation. However, to our knowledge, there is no detailed theory demonstrating their stability in VCSELs with frequency-selective feedback. We hope that this review might instigate theoretical investigations to this effect. A recent prediction of vector vortex solitons in a laser with saturable absorption was made in Ref. [46]. It is important to note that vector vortex solitons in single-pass propagation schemes are known to be unstable for self-focusing media [47], similar to the quasi-scalar case [7–9], although less unstable than their quasi-scalar counterparts [48]. Vector vortex solitons in single-pass propagation schemes are predicted to exist for self-defocusing nonlinear media [49], but to our knowledge there is no experimental observation.

The final subject we are going to cover in this chapter is the all-optical control of a laser soliton as a memory element [50–53]. This property is intrinsically linked to dissipative soliton representing localized states. They can be present or absent under the same conditions and are hence necessarily bistable (see Sect. 13.2). This makes

optical solitons attractive for all-optical processing and storage schemes and motivated some of the research in semiconductor lasers [52, 53]. One of the advantages of laser cavity solitons is that they do not need to be sustained by a coherent holding beam with high spatial and temporal coherence but can draw their energy from an incoherent optical or electrical input. However, for the prospects of soliton control, this also removes an obvious and easy source for the control beams. We will review aspects of laser cavity soliton switching in Sect. 13.4.1 in more detail, but although already the first experiments on VCSEL lasers solitons demonstrated bistability and some control [29, 54, 55], switch-on and switch-off of laser cavity solitons had been only obtained in situation involving thermal and/or non-local effects for one of the two directions of switching [29, 55, 56]. In Sect. 13.4, we will demonstrate flip-flop operation, i.e. the setting and re-setting of an optical memory element by external optical pulses directed directly on the memory element, using a two-colour control scheme exploiting only local electronic nonlinearities.

13.2 Mechanism of Bistability in Lasers with Frequency-Selective Feedback

The experiment relies on the interaction of VCSEL with a frequency-selective element. A VCSEL is a semiconductor laser based on a high-Finesse plano-planar microcavity, e.g. [22]. The technical details are presented in Sect. 13.3.2. The cavity is very short (on the order of 1.2 μm) and hence it runs in single longitudinal mode, but the transverse aperture can be very large (about 200 μm) [23, 24] so that it has a very high Fresnel number and can run in many transverse modes or, in the present context, form self-localized structures which are independent from each other. The basic observation is illustrated in Fig. 13.1a and an experimental example is given in the inset of Fig. 13.9. If the current is slowly increased from zero, first only low-amplitude spontaneous emission is observed until there is a an abrupt transition to a localized high-amplitude state, the soliton. The soliton stays for a certain range of current, if the current is increased further, but more importantly it also stays on if the current is decreased again below the switch-on point $\mu_{\uparrow}$. Switch-down takes place only at a lower current $\mu_{\downarrow}$ creating a hysteresis loop. Within this hysteresis loop the soliton can be manipulated by external control beams that will be the subject of Sect. 13.4.

Figure 13.1b indicates what is happening with the carrier density at the position of the soliton during the process. Increasing the current in the non-lasing situation increases the carrier density. At the switch-on threshold there is a sudden drop of carrier density due to the onset of stimulated emission. Beyond threshold, for the operating laser soliton, carrier density is clamped and will stay approximately constant over the existence range. At the switch-off point, the carrier density is abruptly switching back to the unsaturated value. A free-running laser, in contrast to coherently driven passive cavity or optical feedback systems [52, 57–59], amplifiers

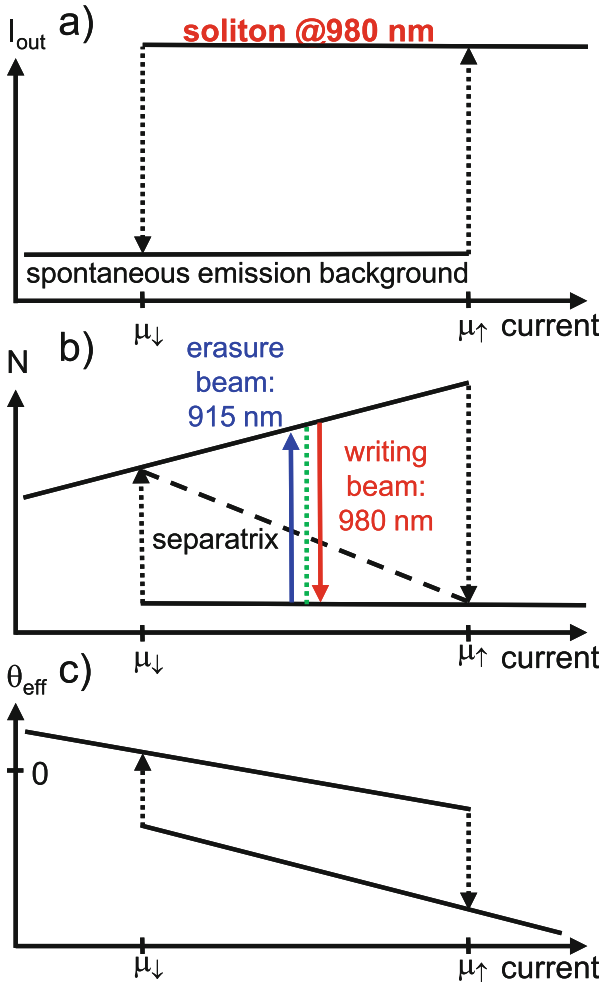

Fig. 13.1 Schematic drawings of hysteresis loops (solid black lines) for optical intensity (**a**), carrier density (**b**) and effective detuning Θ_{eff} (**c**) if the injection current is slowly increased and decreased. Panel (**b**) illustrates also the unstable branch (dashed black line) working as separatrix. Somewhere around the centre of the hysteresis loop there is the Maxwell point (dashed green line) at which the on- and off-states of the soliton have equal stability. Flip-flop operation in Sect. 13.4 is obtained around this point. Injected pulses around 980 nm (red line) will be amplified, decrease carrier density and hence work as writing beam. Injected pulses around 915 nm (blue line) increase carrier density via optical pumping and hence work as erasure beam. As the detuning varies (**c**), the carrier density is not totally constant even under lasing condition (as assumed in **b**), but this is a quantitative, not qualitative consideration

[53] or lasers with injection [60], does not require an external holding beam. On the one hand, this is a major advantage, on the other hand this implies that there is also no option to derive control beams from the holding beam and to implement coherent soliton control via the optical hysteresis loop. In contrast, soliton control takes place via the carrier density as will be discussed in detail in Sect. 13.4.

For an understanding of the origin of the hysteresis loop it is important to realize that the main effect of the current sweeping the hysteresis loop is not changing the gain but the detuning condition between the VCSEL cavity resonance ω_c and the VBG resonance ω_{VBG}, at least once sufficient gain is achieved to allow lasing for overlapped or close resonances. For consistency with the terminology used in [61, 62], we define

$$\Theta := \frac{\omega_c - \omega_{\mathrm{VBG}}}{\kappa} = \frac{\omega_c}{\kappa} = \Theta_0 - \zeta\mu, \tag{13.1}$$

where κ is the cavity linewidth (HWHM) for the field, $\omega_{\mathrm{VBG}} = 0$ is used as reference frequency, Θ_0 is the detuning for zero current and ζ is the proportionality factor between current and resonance shift due to Ohmic heating ($\zeta = 5.23$ in [62]). This is the 'cold' cavity resonance. In a semiconductor laser, the refractive index depends on carrier density N and in first approximation this phase-amplitude coupling is described by a simple proportionality constant, the so-called Henry's alpha-factor α [63]. Hence we define an effective detuning

$$\Theta_{\mathrm{eff}} := \Theta_0 - \zeta\mu + \alpha N, \tag{13.2}$$

which is depicted in Fig. 13.1c. For zero current, the cavity resonance is blue-detuned to the VBG resonance, $\Theta_{\mathrm{eff}} > 0$. Increasing the current red-shifts the cavity resonance via the heating and blue-shifts it via the carrier injection, but the former effect is prevailing ([62] assumed $\alpha = 5$ as a reasonable value for the alpha-factor) and the detuning is decreasing. If the detuning is sufficiently small, the reduced losses will favour an increase of (amplified) spontaneous emission, which in turn will decrease carrier density, increase refractive index and hence further decrease the detuning leading to a further decrease of losses and hence a tendency to higher intensity. At the spontaneous switch-on point, the non-lasing state becomes unstable to fluctuations due to this positive feedback and the system switches abruptly to an high amplitude state in which the resonances of VCSEL and VBG are (approximately) aligned. This high-amplitude state can be maintained to some extent (till the switch-off point) even if the cold cavity detuning is increased again via a reduction of current. This means that the laser with frequency-selective feedback works via a form of dispersive optical bistability [64]. The stability of the non-lasing state surrounding the soliton is achieved because it is off-resonant [28, 65] and not because it has higher losses as in lasers with saturable absorbers [16–18]. Laser solitons in semiconductor-based devices were realized first in [29] based on the dispersive effect. The counterpart relying on absorptive optical bistability can be

realized by coupling two VCSELs face-to-face [55], one more strongly pumped than the other, although dispersive components might be important in that configuration also.

The cold cavity resonance offset Θ_0 can be adjusted by adjusting the ambient temperature of the device. Hence a situation can be realized in which effective zero detuning is obtained for elevated temperature and low currents. In this situation, the first structure appearing at threshold is the fundamental soliton [31, 62]. This is the situation investigated in Sect. 13.4. Alternatively, at low ambient temperature a much higher Ohmic heating and hence current is needed to reach the effective zero detuning condition. In this situation, the spontaneous switch-on is to more complicated structures and in particular high-order solitons as vortices and vector vortices [39, 62]. As high threshold current implies high threshold gain, this tendency towards high-order structures is reasonable. This is the situation to be investigated in Sect. 13.3.

However, before turning to this subject, it should be mentioned as a final caveat that in an ideal, homogeneous system there would not be a spontaneous switch-on to a soliton but to a spatially extended modulated state, a spatial pattern, as the system would remain in the non-lasing or homogeneous state until the threshold for modulational instability (MI). Bistable solitons exist below the MI point down to the switch-off point. For experimental realizations using semiconductor microcavities this ideal situation cannot be realized in spite of these microcavities being marvels of vacuum-deposition technology as a growth error of a single monolayer is enough to change the detuning significantly due to the high cavity Finesse. Hence the solitons are pinned to certain positions in which the detuning conditions are favorable [53]. For the situation considered here these are the most red-shifted part of the cavity as investigated in detail in [66]. However, a huge body of experimental and numerical investigations indicate that within the hysteresis loop the solitons keep their important solitonic features except the mobility to move freely within the transverse aperture of the device and hence the community regards them as solitons [53, 67, 68].

13.3 Vector Vortex Solitons

13.3.1 What Are Vector Vortex Beams?

Vector vortex beams are a subset of beams with complex intensity, phase and polarization structure investigated in the field of 'structured light' [69–72]. In contrast to 'full Poincaré beams' utilizing the full Poincaré sphere [73], *'vector vortex beams'* (VVBs) [37, 38, 74] have a spatially non-uniform, but locally linear, polarization field. Although in general other configurations are possible, the beams investigated in practice possess a circular symmetric intensity structure in form of a doughnut. Figure 13.2 shows the states relevant for our considerations. For these first order VVBs four basis modes are needed. The first option is to construct them from

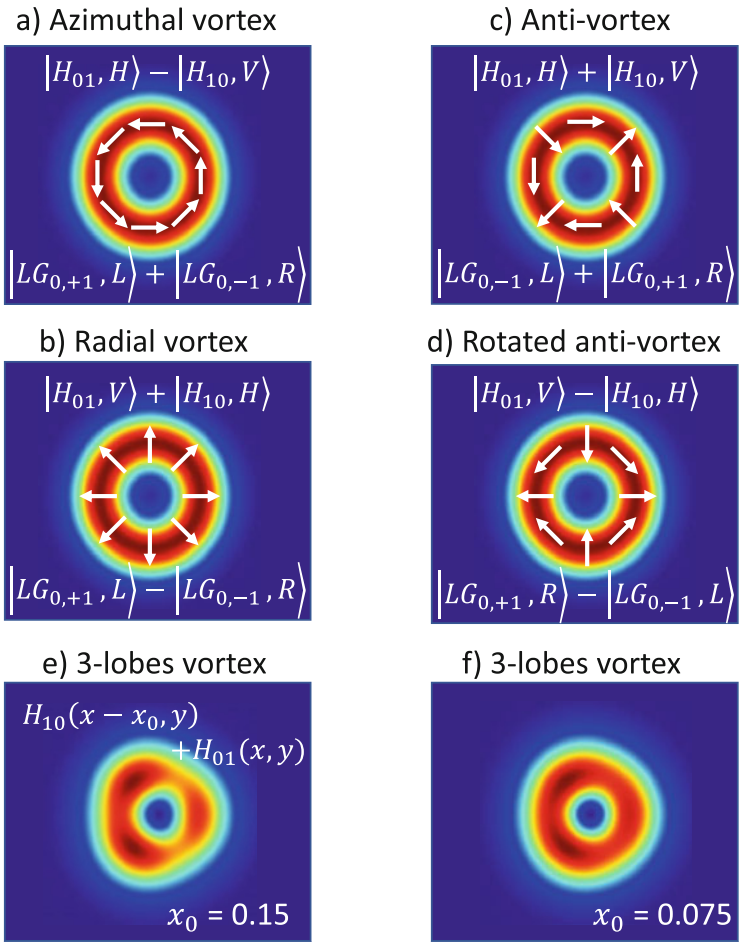

Fig. 13.2 (**a**–**d**) Illustration of different vector vortex beams as obtained from different superpositions of orthogonally polarized first order in a linearly polarized basis (or of circularly polarized Laguerre–Gaussian modes). Intensity in pseudocolour scale ranging dark blue (low intensity) to dark red (high intensity). (**e**, **f**) If the centre of the two orthogonal Hermite modes are slightly displaced by a fraction of x_0 of the beam waist of the fundamental mode, the ring is perturbed to a three spot structure. (**a**) Azimuthal vortex. (**b**) Radial vortex. (**c**) Anti-vortex. (**d**) Rotated anti-vortex. (**e**) 3-lobes vortex. (**f**) 3-lobes vortex

the two first-order Hermite-Gaussian modes (H_{10}, H_{01}) with horizontal (H) and vertical (V) polarization. Figure 13.2a, b show the azimuthally and radially polarized states, where the polarization structure possesses cylindrical symmetry ('cylindrical vector beams' [37, 75]). Beams with hyperbolic polarization structure are referred to as 'anti-vortices' [76] or 'π-vortices' [37]. They exist in two versions (Fig. 13.2c, d) with principal axes rotated by 45°. These beams do not have a phase singularity in the centre (an unique optical phase is ill defined with two polarization components

anyway) and hence do not carry orbital angular momentum, but they contain a singularity in the polarization field, respectively in the relative phase between the polarization components. Any projection onto a linearly polarized state yields a first-order Hermite-Gaussian modes with an orientation depending on the direction of the projection (see Sect. 13.3.3).

An alternative construction can be done in the Gaussian-Laguerre basis $LG_{0,\pm 1}$ and using the circular polarization basis (L, R). In this representation, it is apparent that VVBs contain orbital and spin angular momentum in a correlated manner. After projection on circular polarization basis, the resulting fields carry orbital angular momentum.

VVBs have intrinsic appeal and beauty, provide novel fundamental aspects in quantum optics and enable new applications or enhance existing ones in engineering and science. Examples are tight focusing [77], micro-machining [78], optical trapping [72, 79, 80], simultaneous spectroscopy of multiple polarization channels [81] and beam transformation in nanophotonics [82]. Particularly exciting is the realization that the correlation between spatial and polarization degrees of freedom resembles entanglement and might open up novel schemes for the use in quantum optics [83–85] and sensing [86].

Hence, considerable effort was spent on creating these unusual polarization states [70, 75, 87], relying on a substantial engineering effort based on specialized equipment as tailored laser resonators [88–91], meta-surfaces and spatially varying wave plates [92–94], Mach-Zehnder interferometers [80], modal control in few-mode fibers [95, 96], spatial light modulators [71, 72, 76], tailored Fresnel reflection from glass cones [97], and polariton microcavities [98–100]. In contrast, we demonstrate the spontaneous emergence of these structures in a conceptually simple system, a highly symmetrical vertical-cavity surface-emitting lasers (VCSEL) with frequency-selective feedback [39]. To our knowledge, this was the first experimental observation of the spontaneous formation of a vector vortex beam from spontaneous symmetry breaking. A more recent observation in a polariton laser is described in Ref. [101].

As a final remark before turning to the experiment, one can perturb the intensity distribution of VVB without destroying the polarization structure by providing a slight offset between the centres of the two orthogonal Hermite-Gaussian modes forming the VVB. In that case the intensity along doughnut ring becomes modulated (Fig. 13.2f) and becomes a '3-spot structure' at larger shifts (Fig. 13.2e).

13.3.2 Experimental Setup

The setup for the cavity soliton laser and the VCSEL devices used are described in detail in [23, 24, 31, 102] and reviewed in [103, 104]. The VCSELs used are broad-area electrically pumped devices. Three InGaAs quantum wells are serving as gain medium leading to emission in the 980 nm range. The quantum wells are surrounded by passive AlGaAs spacer layers with a total thickness of one wavelength. The cavity is closed by high reflectivity distributed Bragg reflectors (DBR) with 33 layers

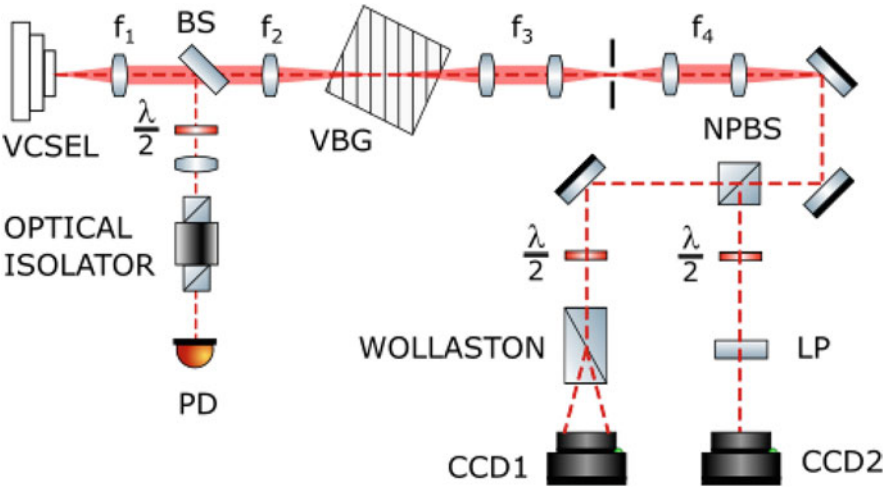

Fig. 13.3 Setup for measuring spatially resolved Stokes parameter in a VCSEL with frequency-selective feedback. f_i: lenses, VBG: volume Bragg grating (the inscribed grating is tilted by an angle $< 1^\circ$ with respect to the surface in reality), BS: beam sampler, NPBS: non-polarizing beam splitter, $\frac{\lambda}{2}$: half-wave plates, PD: amplified, slow photodiode (in reality there is a whole detection branch here but only the photodiode is used in these investigations), LP: linear polarizer, CCD: charge-coupled device cameras. The two folding mirror on the right are included for compactness of the drawing. The actual beam path is straight

AlGaAs/GaAs on the top side (p-contact) and 22 layers on the bottom side (n-contact). The laser has an emission wavelength around 975 nm at room temperature. The emission takes place through the n-doped Bragg reflector and through the transparent substrate. In this so-called bottom-emitting geometry a reasonable uniformity of carrier injection can be achieved over fairly large apertures. A 200 µm diameter circular oxide aperture provides optical and current guiding. This active diameter is much larger than the effective cavity length of about 1.2 µm. As a result, the VCSEL has a large Fresnel number allowing for the formation of many transverse cavity modes of fairly high order and of solitons which are independent of boundary conditions.

The optical setup is illustrated in Fig. 13.3. Frequency-selective feedback is provided by an external volume Bragg grating (VBG). The VBG has a reflection peak of about 95% at 978 nm and a bandwidth of slightly larger than 0.1 nm (FWHM). The VCSEL is collimated by $f_1 = 8$ mm focal length plano-convex aspheric lens. The second lens is a $f_2 = 50$ mm focal length plano-convex lens and is used to focus the light onto the VBG. The lenses are arranged as an afocal telescope giving a 6.25 : 1 magnification factor onto the VBG. This external cavity is self-imaging, i.e. every point of the VCSEL is imaged at the same spatial position after each round trip therefore maintaining the high Fresnel number of the VCSEL cavity and ensuring local feedback compatible with self-localization.

In the standard experimental scheme the output is monitored via the Fresnel reflection from a wedged intra-cavity beam sampler BS (front uncoated, back AR-coated). The cavity is isolated from the detection setup by an optical isolator. In this experiment, it is mainly used for monitoring the light-current (LI) characteristic by an amplified, slow photodetector. In addition, the output intensity distributions are monitored for alignment and analysis by charge-coupled device cameras (CCD) after suitable optics, in near field and far field (CCD1, CCD2 depicted in Fig. 13.9). The outcoupling is relying on Fresnel reflection and therefore is polarization dependent. The reflectivity is on the order of 10% for s-polarized light and 1% for p-polarized light and hence the polarization state of the intra-cavity is not adequately represented in this detector arm.

Hence, for the polarization resolved measurements presented here, we are analyzing the spatially resolved Stokes parameter in the field transmitted by the VBG. As the VBG is used at nearly normal incidence, the polarization state of the transmitted field is preserved. The image of the soliton on the VBG facet is relayed by a telescope ($f = 150$ mm for both lenses) to an intermediate image plane. In this plane, a part of the VCSEL aperture can be selected for analysis via a movable circular aperture. This plane is imaged by a further telescope (typically $f = 50$ mm for both lenses, but the second one can be adapted to serve different imaging needs) onto CCD cameras. The beam path is split by a non-polarizing beam splitter (Coherent, $T = 0.33$, $R = 0.67$). The transmitted arm is folded by a highly reflective mirror and traverses a half-wave plate (HWP) and Wollaston prism before creating an image on a CCD-camera. This allows for the simultaneous monitoring of the linear polarizations components at 0° and 90° to calculate the spatially resolved Stokes parameter S_1 or the linear polarizations components at $+45^\circ$ and -45° to calculate the Stokes parameter S_2. In the reflected arm, there is either an amplified, slow photodetector to monitor the polarization resolved total power or, more often, another CCD-camera monitoring the polarization at $+45^\circ$. In that case, both Stokes parameters S_1 and S_2 can be measured simultaneously, which is not only convenient but sometimes important, if structures change quite rapidly with changing current. As there is some jitter between different realizations of the experiment (see, e.g. Fig. 13.6), combining the measurements from different runs to calculate Stokes parameters introduces potentially some artifacts. If both arms in the VBG branch are used with CCD-cameras, the LI-curve of the system is monitored via the intra-cavity beam sampler (a rough correction can be done for the anisotropic Fresnel reflection). For the experiments reported in Fig. 13.5, a Mach-Zehnder interferometer is introduced into the beam path to confirm the phase properties of the vector vortex beams.

It should be noted that the intra-cavity beams sampler preserves the polarization state in transmission (0.99 vs. 0.9, ratio 1.1) much better than in reflection (0.1 vs. 0.01, ratio 10). Nevertheless, it will introduce a dichroism into the system, which breaks the (nominal) polarization degeneracy and is hence expected to influence the formation of vector vortex beams. Hence, in some experiments, the intra-cavity beam sampler is removed and detection takes place only via the VBG.

13.3.3 Principle Observations

Figure 13.4 gives an overview on the scenario for the formation of vector vortex solitons. We report on new and more complete results obtained without a beam sampler in the external cavity. However, the principal behaviour is identical to the situation with this beam sampler reported in Fig. 2 of [39]. Increasing the current, the output remains low, on spontaneous emission level, till there is a sudden switch-on to a high-amplitude lasing structure. This occurs at a quite large current of 641 mA since for the VCSEL submount temperature most of the thermal tuning to match VCSEL and VBG resonance comes from Ohmic heating (see discussion of Eq. (13.1)). Hence, the gain at threshold is quite large and fairly complex extended structures form which are not shown here but are reported in Fig. 8 of [62] and Fig. 2 of [39]. Reducing the current again, the output power reduces, mainly as the lasing

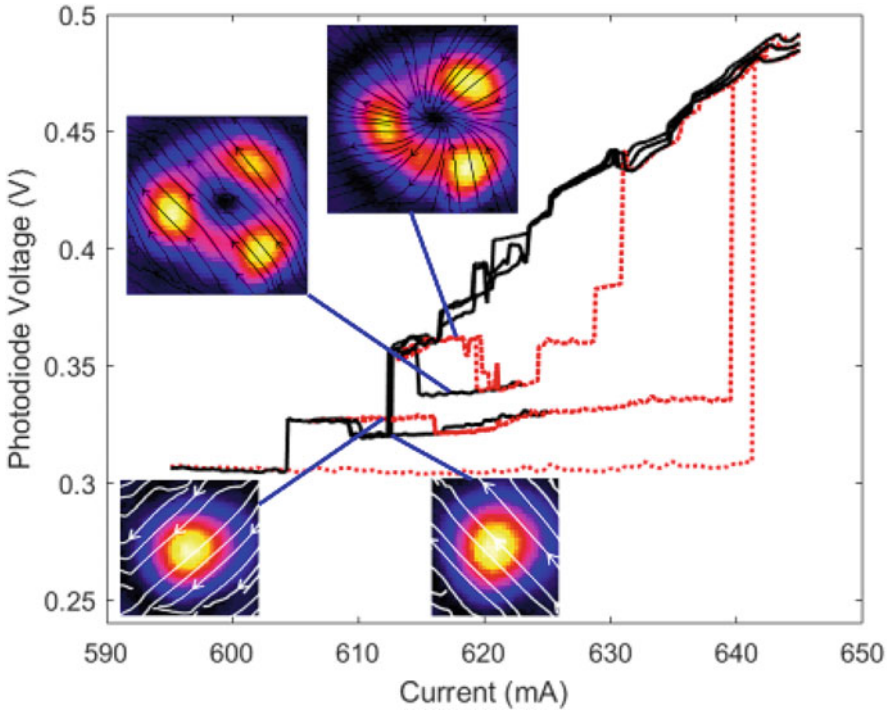

Fig. 13.4 LI-curve projected on a suitable, but arbitrary linear polarization state chosen to have good discrimination between structures. Up-scans of current are denoted by red dotted lines, down-scans by solid, black lines. We did not distinguish the down scans by different colours because we do not believe that the variations contain useful information but that the ensemble demonstrates robust behaviour. Insets show total intensity S_0 of structures in pseudo-colour (from low intensity black via blue and red to high intensity yellow-white) with polarization streamlines reconstructed from the polarization resolved Stokes parameters superimposed. Temperature of VCSEL submount: 17.5 °C

amplitude reduces, but partially also because the size of the lasing area reduces. However, typically a change of size and complexity of the lasing structures involves an abrupt sudden transition in modal shape and emitted total power. At a level of about 616 mA one reaches the vortex states. We will discuss these later.

Reducing the current further, the system switches at 613 mA to a single humped peak, the fundamental soliton, which is linearly polarized. The fundamental soliton shows a spontaneous switch to the orthogonal polarization at 609 mA (see also [105]). Polarization switching is a typical behaviour observed in VCSELs [40–44]. Further reducing the current, the fundamental soliton switches off at 604 mA. If the down-scan is stopped at 605 mA, and the current is increased again, one moves along the fundamental branch (with a polarization switch at 616 mA) until a switch to a very-high amplitude state occurs at 640 mA. If the scan is stopped before and reversed, the hysteresis loop of the polarization switch of the fundamental soliton can be explored.

If the original down-scan is stopped at 616 mA, the spatial structure of the total intensity, i.e. S_0 encountered has an approximate ring-shape with three dominant peaks along the ring. The polarization streamlines obtained from measuring the polarization resolved Stokes parameters are superimposed on the intensity image and show a radial polarization structure. This constitutes a radially polarized vector vortex beam where the deformation of the ring to three spots can be explained by spatial disorder in the VCSEL resonance (see discussion of Fig. 13.2). Increasing the current, there is an abrupt transition (at 619 mA) to a vortex structure with nearly the same intensity distribution but it is now linearly polarized. These structures were identified as vortex solitons in [32]. Reversing the current sweep, coexistence between the linearly and the radially polarized vortex is demonstrated. Increasing the current further, the system switches from vortex states to larger states at 629 mA and to even larger structures at 631 mA.

The final switch-up occurs to roughly the same branch for all situations, i.e. from the non-lasing state, the fundamental soliton branch, and, although typically via intermediaries, from the vortex branch. We kept all three realizations from the down-scan from these complex states in the figure to illustrate on the one hand robustness of the phenomena but also the importance of fluctuations. The main issues are thermal fluctuations and drifts leading to a variation of switch-on and switch-off points and a slight variations of amplitudes. Small spikes and jumps within one branch correspond usually to longitudinal mode hopes. We gave concrete numbers for the switching points in the discussion above in order to allow an easy identification of the points in the figure, but one should not put to much emphasis on the concrete numbers. However, we stress that the overall scenario is robust. In particular, there is an amazing amount of multi-stability in the system. For example, from 613–618 mA the off-state, the fundamental solitons, the vortex solitons and an even more complex state coexist, possibly even in several polarization configurations.

For the situation with the intra-cavity beam sampler placed within the cavity, the dominantly observed vector vortex is the anti-vortex with a hyperbolic polarization structure (see Fig. 13.5a). LI-curves and further details are reported in Ref. [39]. Its phase structure is analyzed further in Fig. 13.5. In subfigures (d–g) the VVB is

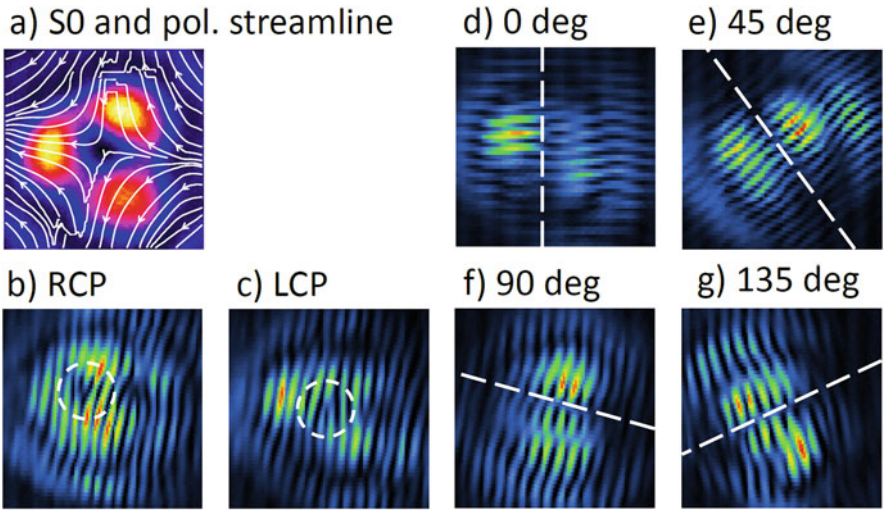

Fig. 13.5 Mach-Zehnder interferometry of an anti-vortex: (**a**) Total intensity S_0 (pseudo colours), and polarization streamline. (**b**, **c**) Polarization-resolved interferograms projected on circular polarization states (assignment of RCP and LCP arbitrary). Dashed circles indicate the forks evidencing the phase singularity. It should be noted that we are looking at the self-interference of two doughnut beams and not of one doughnut beam with a plane reference wave. Hence two forks indicate the presence of only one phase singularity. (**d**–**g**) Polarization-resolved interferograms projected on linear polarization states in 45° steps. Dashed lines indicate the nodal line evidencing the π phase shift. (**a**) S0 and pol. streamline. (**b**) RCP. (**c**) LCP. (**d**) 0 deg. (**e**) 45 deg. (**f**) 90 deg. (**g**) 135 deg

projected on linear polarization states and then interfered with itself in a Mach-Zehnder interferometer. After projection, the intensity structure is dominated by two elongated lobes. In between these lobes there is a nodal line with a π-phase jump across it as demonstrated by the staggered discontinuities of the interference fringes. This implies that the observed vector vortex beams are very close to the 'ideal' ones whose construction from first order Hermite-Gaussian modes is reported in Fig. 13.2. Obviously, there are differences from pure Hermite-Gaussian modes in the wings of the beams. Inspection of Fig. 13.5d and f yields that the vortex under study is a superposition of a horizontally polarized H_{10} and a vertically polarized H_{01}-mode. In order to obtain the hyperbolic polarization structure aligned (roughly) to the horizontal and vertical axes (see Fig. 13.2d) the relative phase between them needs to be π. Projection on polarization states at $\pm 45^\circ$ (Fig. 13.5e and g) yields first order Hermite modes with the nodal axis orthogonal to the polarization axis as expected for the anti-vortex. The supplementary material [106] of [39] contains a movie which shows this continuous counter-rotation of the spatial structure, if the angle of the polarizer analyzer is rotated, clearly.

After projection on a circular polarization state (Fig. 13.5b and c), the intensity structures are approximately circular and the phase structure contains now forks, i.e. evidence of phase singularities and not nodal lines. These are of opposite sign (opposite branching direction in the interferograms) for the two circular

polarizations. This reveals that the constituent modes are doughnuts themselves, i.e. carry orbital angular momentum, as expected if one calculates the corresponding transformations (e.g. [99]). VVBs carry spin and orbital momentum degrees of freedom in a correlated manner.

13.3.4 Complex Hysteresis Loops

After having established the principal observations in the previous section, we return to a more detail of the system without the intra-cavity beam sampler in Fig. 13.6. It shows the hysteresis loop between the radially polarized vortex and the linear polarized one, if the current is only swept up and down in a small vicinity of the transition. Repeated measurements done over a time scale of a few minutes show a robust coexistence on the one hand and some jitter of switching points and slight changes of amplitude. These are partially due to technical noise as current fluctuations and mirror vibrations, but mainly due to thermal fluctuations influencing the detuning between VCSEL and VBG being the most important and sensitive control

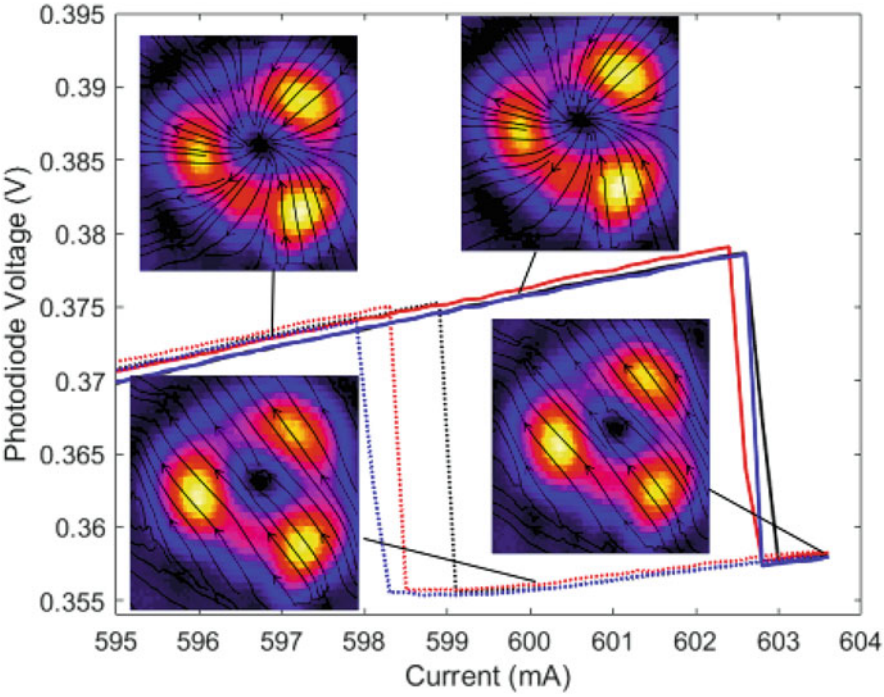

Fig. 13.6 LI-curves and inset illustrating bistability between the radially and uniformingly linearly polarized vortex. The four realizations shown give an indication of the stability of the system on the time scale of several minutes. Temperature of VCSEL submount: 19.5 °C

parameter (see the discussion on Fig. 13.1c). In particular, the switching point will be influenced by where the comb of the external cavity modes is with respect to the VBG and VCSEL resonances as this will render the spectrum of favourable soliton states discontinuous. Thermal drifts are limiting the long term stability.

Figure 13.7 provides an example of the complex switching behaviour possible, now again for the system containing the intra-cavity beam sampler. Figure 13.7a is a large scale view. Switch-on from the off-state occurs here directly to the vector vortex states. This behaviour is observed frequently, although the more typical behaviour is the switch-on to larger states at even higher currents (Fig. 13.4 and Fig. 2 of [39]). This behaviour might be related to minute misalignments of the retro-reflection angle of the VBG. Reducing the current, one obtains a two-lobe structure. The fact that the laser does not seem to find a doughnut (or three-spot) shaped locked state, but remains spatially symmetry broken might support the assumption of a small misalignment. This structure then switches to the fundamental soliton which in turn undergoes polarization switching. Interestingly, the two-lobe structure exists also in two polarization configurations. It can be linearly polarized (at about 621 mA) or consists of four domains of which the two adjacent have approximately orthogonal polarization and the opposing ones the same polarization (at 624 mA). The polarization principle axes of these domains are very similar to the ones of the two fundamental soliton ones with orthogonal polarization. This is not a vector vortex state as the polarization direction is not varying gradually over the beam. Instead, it seems to be related to the well-known polarization bistability of VCSELs along their principal axis but here realized in a spatially varying manner. It should be noted that also the approximately doughnut shaped three-spot structure can exist with such a polarization structure (Fig. 3 of [39, 106] and inset of Fig. 13.8a below). It is also interesting to note that the transition between the vector vortex beams and this structure can be gradual in the resolution of the experiment, whereas all transitions between vector vortex beams and from vector vortex to homogeneously linearly polarized ones are abrupt.

Figure 13.7b concentrates on the smaller range of currents above 626 mA. Between 626 mA and 630.5 mA the dominant structure is the anti-vortex. At 630.5 mA there is an abrupt transition to the linearly polarized vortex. In this case the hysteresis width is smaller than the jitter. For higher currents, the dominant structure is the linearly polarized vortex switching between different longitudinal modes and slightly different polarization directions. In the lower part, on the backward scan, a further novel structure is encountered, a vortex with a spiral polarization structure. It can be thought of as a superposition of radially and azimuthally polarized vortices or of all four Hermite-Gaussian basis modes (Fig. 13.2a, b). It exists only in a very small range and not necessarily in all scans (e.g. it is in the green, but not the red-dashed down-scan in Fig. 13.7b). The difference between the two realizations here is the scan speed. The spiral vortex occurs only for small enough current steps and can be easily missed. It is typically embedded in the existence range of the anti-vortex (see green curve in Fig. 13.7b).

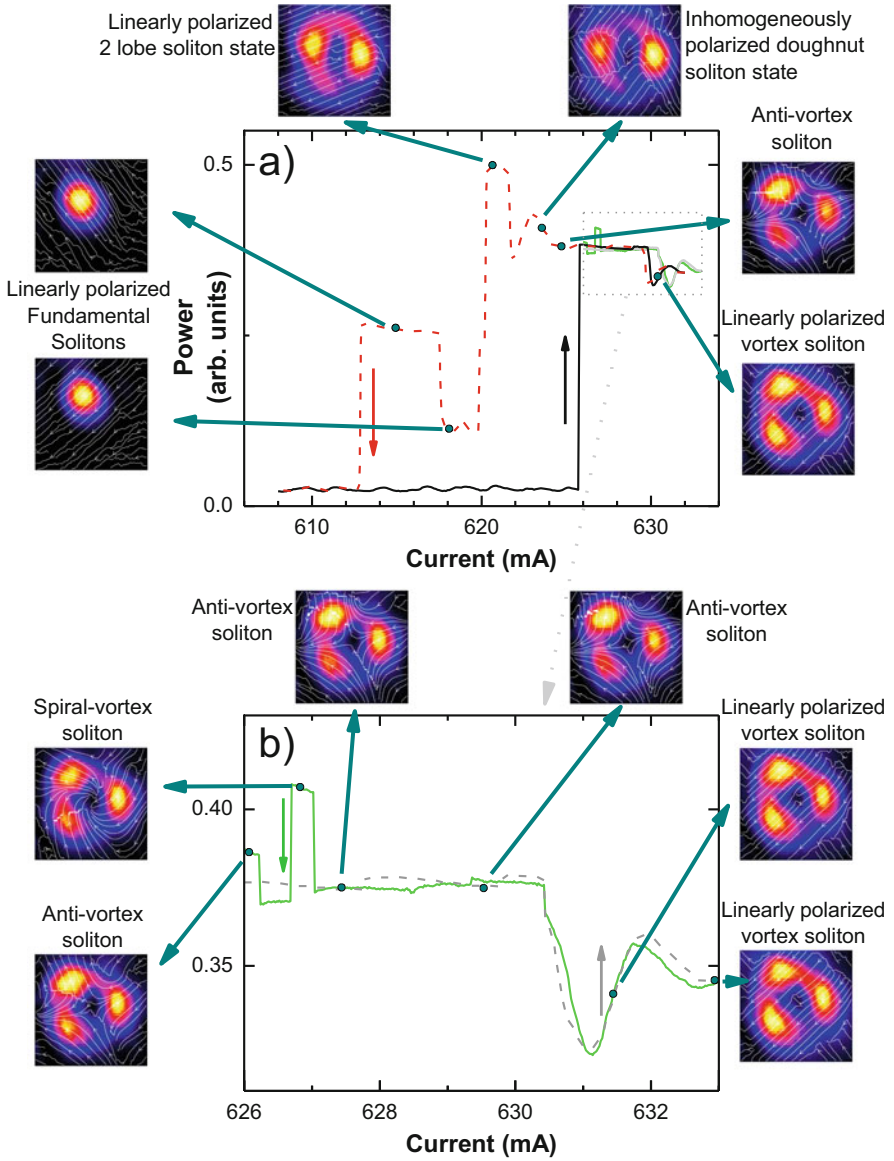

Fig. 13.7 (**a**) LI-characteristic of system with intra-cavity beam sampler with typical structures observed. Black line: up-scan, red dashed line: down scan at 0.1 mA per step and a waiting time of 500 ms waiting time per step. The dashed grey line and green solid are another realization of an up-scan and down-scan covering only the high current area at 0.02 mA per step and 500 ms waiting time per step. (**b**) Blow-up of region beyond 626 mA. Temperature of VCSEL submount: 19.6 °C

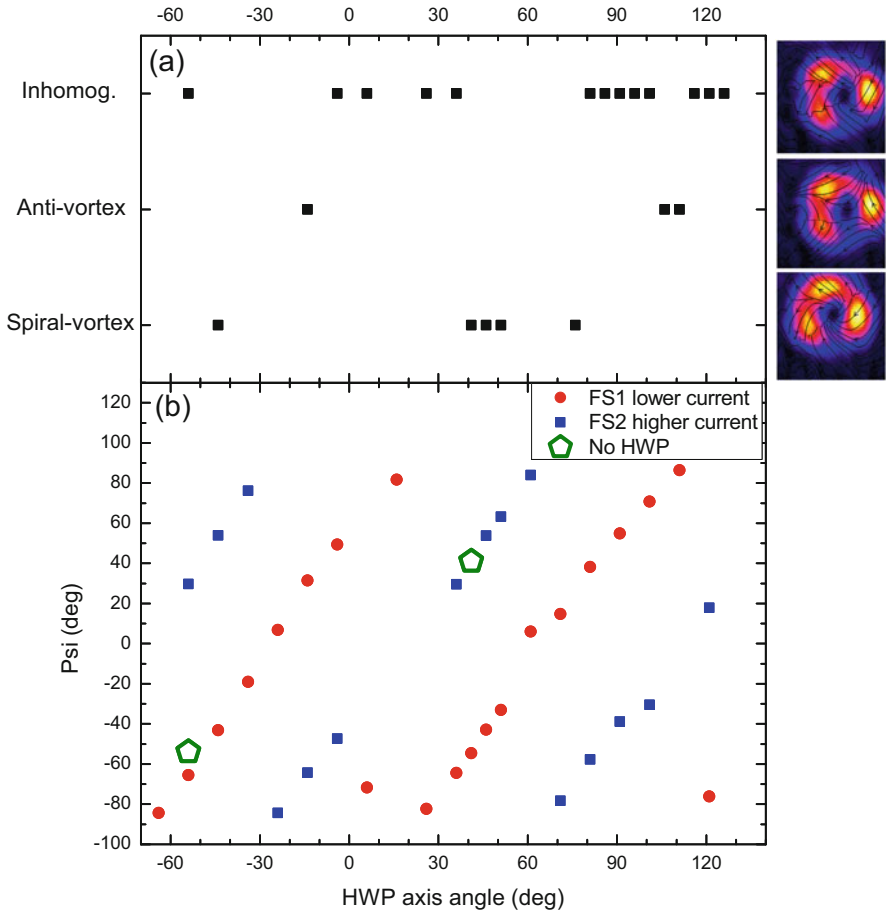

Fig. 13.8 Influence of an intra-cavity HWP on polarization direction of fundamental solitons ψ (**b**) and selection of VVB or domain structures (**a**). The reference axis for the angles is vertical. (**a**) Indication of which type of VVB is observed, insets show S_0 and polarization streamlines. We report the VVB obtained in the current range before switch-down to the fundamental soliton occurs, but checks were carried out via additional, smaller LI-curve, whether other VVBs might be accessible from other initial conditions (**b**) Red dots denote the main polarization direction of the fundamental soliton occurred at lower currents, blue of the one at higher current. The green rhombus indicates the selected polarization without HWP. The slope of polarization angle vs. HWP angle is 2 as a HWP turns the polarization by two times the deviation from its principal axis. The BS is present in the cavity

Minute adjustments, i.e. much smaller ones that the angular width of the vector vortex beams, influence whether the spiral vortex—and on a more relaxed level the other vortices—can be obtained. This indicates that the vector vortices are degenerate in a perfectly symmetric system but that small anisotropies and/or fluctuations select between them.

13.3.5 Influencing Polarization Selection by Intra-Cavity Waveplates

Although desirable, it is not straightforward to include means for controlling weak anisotropies in our setup, but we can introduce a strong anisotropy via a half-wave plate (HWP). This is introduced into the external cavity between the telescope lenses. First, we investigated the influence on the polarization properties of the fundamental solitons (Fig. 13.8b). It is obvious that the direction of polarization of the fundamental solitons is rotated in the same way as the HWP is rotated, which can be expected for such a large phase anisotropy like the HWP. Over most of the range both polarization states can be obtained with the exception of a region centred around a polarization angle $\psi \approx -10^{\circ}$, which is interestingly roughly in between the two polarization state of the two fundamental solitons without the introduction of the HWP. This seems to be the least favourable orientation with only the intrinsic anisotropies, and hence only the favoured polarization state might survive.

Figure 13.8a summarizes the observations at what angle of the HWP which type of VVB or domain structure is observed. In addition, linearly polarized vortex beams have been observed along some point of the hysteresis loop at most angles of the HWP. It is hard to recognize a pattern behind the selection but it is interesting to note that only a single type of VVB was found for each angle. The second observation is that the spiral vortex is a robust feature at the appropriate anisotropy, whereas it had been very difficult to obtain in the experiments discussed before. At the angles where no VVB or domain structure is reported, the linearly polarized vortex has a vertical polarization i.e. orthogonal to the horizontal one for which only one fundamental soliton exists. This reenforces the impression that vertical/horizontal polarization corresponds to some maximum polarization anisotropy. Apart from these observations, the figure mainly supports the notion that all or at least many kind of VVB exist in the system and the anisotropies decide whether are stable and accessible via LI-curves. We will discuss ideas how to develop these investigations in Sect. 13.5.

13.3.6 Interpretation

From the observation reported, it appears that small anisotropies in the system decide which VVB is stable and can be observed. This is in line with the theoretical analysis in [45] for a free running VCSEL predicting the existence and stability of the three types of VVB that we observe (anti-vortex, spiral vortex and radially polarized vortex). Perfect cylindrical symmetry is best for a large existence range, but they survive modest anisotropies. No detailed analysis of their stability against linear polarized vortices or between different kind of vector vortex beams is however given in Ref. [45]. It might be even possible that a VVB we did not observe is stable but cannot be accessed by conventional LI-curves.

The VVB states share many properties with high-order dissipative solitons as the localization to a small region in a broadly pumped plano-planar cavity, their coexistence with the non-lasing zero background and the abrupt emergence. The induced waveguide should be similar to the linearly polarized ones investigated in [32] as it depends on total intensity S_0. For these, theoretical investigations support the soliton interpretation [27, 28]. This supports the notion that the solitonic behaviour comes from quasi-scalar guiding (S_0) and the polarization structure forms spontaneously under the conditions of polarization degeneracy or near-degeneracy. The deformation of the doughnut rings to 3-spots is no counter-argument against solitonic character, although poorly understood. Corresponding generalized vortex solitons were predicted [107] and indications observed [108] in single-pass conservative systems and termed azimuthons. Theoretical predictions exists also for dissipative systems [19, 109] including a simplified model for a VCSEL with frequency-selective feedback [110]. A detailed theoretical treatment is currently beyond our resources but we hope that this contributions triggers theoretical efforts to this effect.

Coming back to why VVB as predicted by [45] were not observed in free-running VCSELs, it is important to realize that in all real VCSEL the polarization degeneracy will be lifted to some extend by the electro-optical effect in electrical pumped devices [111] and elasto-optical effects introduced via uncontrolled strain in the growth process [112]. This leads to birefringence and possibly dichroism. In addition, even monolayer fluctuations will influence detuning conditions. Typically these fluctuations will not have rotational symmetry, thus lifting the degeneracy between H_{10}- and H_{01}-modes (or better to say between nonlinear counterparts for the soliton states). Thus it might be that locking to a VVB is not possible. However, even minute tilts of the VBG will influence the feedback phase significantly and in a slightly different way across an extended structure like a doughnut. We demonstrated frequency tuning of fundamental solitons and differential frequency detuning between spatially separated solitons before [103, 113]. Hence, we conclude that minute alignment changes of the VBG, which are much smaller than the angular width of the soliton, can provide the necessary frequency fine tuning to allow the compensation of small intrinsic anisotropies and the formation of VVB. Tilting the VBG away from the condition used will destroy these states and favour linearly polarized ones or irregular domain structures. On the other hand, we stress that the observation of VVB is robust. Otherwise, we would not have discovered them as the observation reported in [39] was not anticipated.

13.4 Flip-Flop Operation of Laser Cavity Solitons

13.4.1 Soliton Control in Systems with and Without Holding Beams

As indicated in the introduction, a major advantage of a cavity soliton laser is that it does not need a broad coherent driving (or holding beam, HB) but can draw all its energy out of incoherent pumping. However, for soliton manipulation, the holding

beam provides actually the nice feature that a beam can be split off easily forming a focused addressing beam (AB) which can be used to switch solitons up and down in a conceptually simple way [50, 52, 53]. By controlling the phase between HB and AB and thus locally the driving intensity, the system can be switched from one of the bistable states to the other, up for constructive and down for destructive interference. In contrast, there is no beam before a cavity soliton switches on, but switch-on can be initiated by an external beam in the vicinity of the soliton frequency (ignition beam, IB). This has been achieved in various VCSEL laser systems relying on dispersive [29, 54, 114] or absorptive nonlinearities [55, 56, 115] or possibly a combination of them [55]. Inspection of Fig. 13.1b yields that the switch-on is related to a drop in carrier density which then shifts the detuning via phase-amplitude coupling. Similarly, in the system based on saturable absorption [55], reduction of carrier density caused by the IB leads to an increase in cavity finesse and hence soliton switch-on. For both systems, an erasure would demand adding carriers which cannot be achieved with optical injection close to the laser frequency but demands optical pumping at higher energies at which the semiconductor is absorptive. Such an experiment has not been performed for solitons in electrically pumped VCSELs, yet, but the switch-off of solitons has been obtained in [29, 31, 55] with an erasure beam (EB) aimed at the side of the solitons. This method utilizes that the detuning conditions vary over the cross-section of the wafer and hence of the broad-area laser. The EB drags the solitons out of their preferred positions in the centre of the traps providing the best detuning condition. They do not recover, if the EB is switched off. However, a two-colour flip-flop operation scheme has been demonstrated before for bistable states in edge-emitting semiconductor amplifiers [116]. Interesting experiments have been also performed using a mode-locked TiSa-laser in the absorptive regime of VCSEL amplifiers [117, 118] and VCSEL with integrated saturable absorber [56] demonstrating flip-flop operation with a single colour providing optical pumping. Here the switch-down can be understood via the mechanism discussed above but the up-switch is not fitting the expectation. The up-switch involves substantial delays and it is argued in [56, 117, 118] that the possibility of up-switching is due to a combination of thermal and non-local effects. Flip-flop operation relies on hitting a sweet spot in parameter space. Hence we are addressing below the question of robust two-colour flip-flop operation of laser cavity solitons.

13.4.2 Experimental Setup

The optical setup is illustrated in Fig. 13.9. A laser at 980 nm is used for the IB beam and a laser at 915 nm for the EB. Acousto-optical modulators (AOM) allow for a fast pulsing of the beams (minimal pulse duration about 25 ns for the IB, 200 ns (100 ns with a strong reduction of efficiency) for the EB). The beams are launched into single-mode fibres and combined in a 2×2 fibre-coupler with a nominal coupling rate of 50%. The output of one arms is monitored by a DC-coupled photodetector with 50 MHz bandwidth. The beam from the other output is collimated and then focused onto the VBG, size-matched to the soliton image at the VBG and hence to

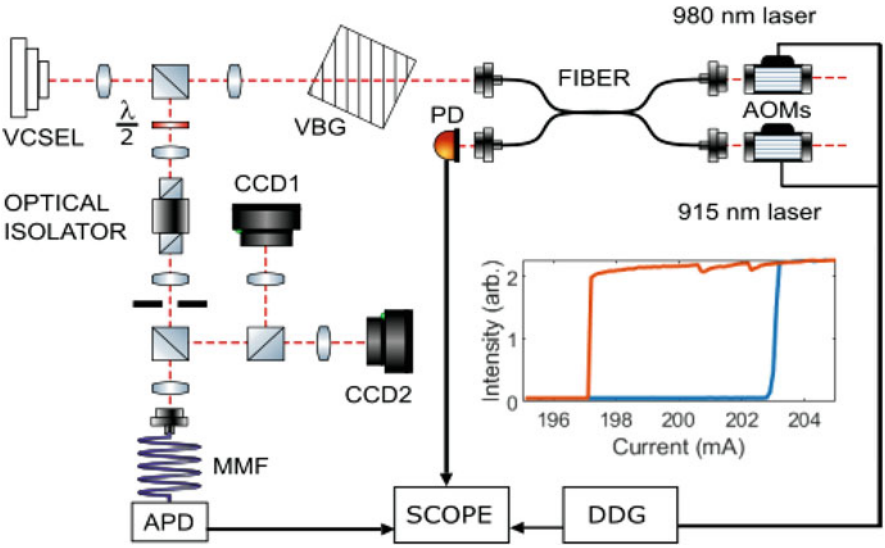

Fig. 13.9 Setup for flip-flop operation of laser cavity solitons. AOM: Acousto-optical modulator, MMF: multi-mode fibre, DDG: digital delay generator, APD: avalanche photodiode, CCD1(2): charge-coupled device cameras monitoring near and far field of the VCSEL. VBG: volume Bragg grating. The inset shows a LI-curve obtained at a VCSEL temperature of 47 °C for the fundamental soliton

the soliton in the VCSEL. The beam is then aligned to be on axis and hitting the soliton via the cameras monitoring near and far field. The output of the VCSEL is monitored by an AC-coupled avalanche photodiode (APD) operated in the linear regime with a bandwidth of 1.7 GHz. For some measurements, it was replaced by a DC-coupled photodetector with 50 MHz bandwidth. A delayed switching sequence of the AOMs was coordinated via a digital delay generator. Peak powers after the fibre are 2 mW for the 980 nm laser and 14 mW for the 915 nm laser.

The submount temperature of the VCSEL was put to 40–47 °C. As a result, the detuning position for soliton switching (Fig. 13.1c) is met at considerably lower currents than discussed in the previous sections and the first structure appearing is a fundamental soliton [62]. Its hysteresis loop is depicted in the inset of Fig. 13.9.

13.4.3 Experimental Results

In a first experiment, the laser is biased within the hysteresis loop, but close ('detuning' 1 mA) to the spontaneous switch-on point. Figure 13.10 demonstrates successful switch-on for pulse lengths of 100, 200 and 500 ns. The initial peak signal is from the IB itself. After a delay between 80 ns and 200 ns, there is a very fast and abrupt switch-on of the soliton. This stays on after the IB is switched off. The delay increases with increasing detuning from the spontaneous switch-on point and longer

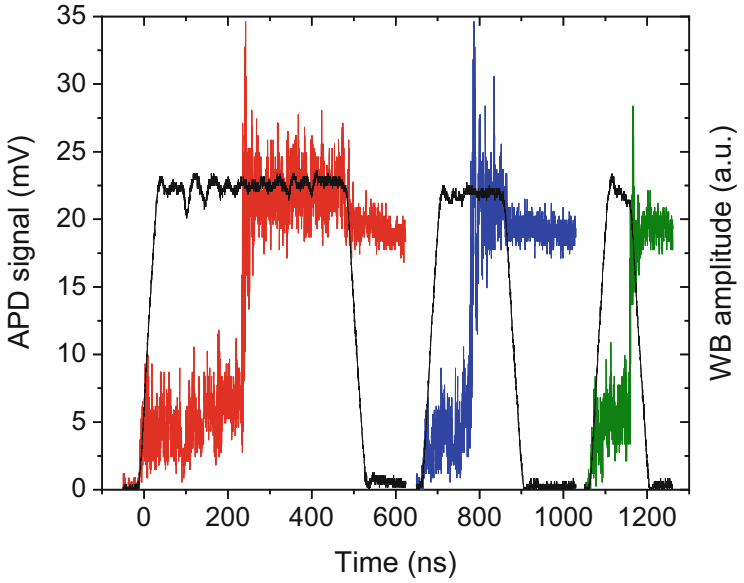

Fig. 13.10 Three independently performed switch-on events (offset on time axis for clarity), with pulse widths of 500, 200, and 100 ns from left to right. The right-axis gives the WB amplitude (black lines) of the three pulses detected in the 50 MHz bandwidth photodiode. The left axis is the signal from the APD (coloured lines). Temperature of VCSEL submount: 40 °C

pulses are required (at constant amplitude, e.g. ≈500 ns at ≈2 mA, tens of microseconds at ≈3 mA detuning). The jitter of the delay is related to fluctuations. These results match the observations and their numerical reproduction discussed in [114] and can be interpreted by the necessity to pass the separatrix indicated in Fig. 13.1b in Sect. 13.2. The separatrix represents the unstable soliton solution separating the basins of attraction of the two stable states.

Switch-off events close to the spontaneous switch-off point are documented in Fig. 13.11. For this, the current is increased until spontaneous switch-on occurs, and then reduced close to the point of spontaneous switch-off. The initial increase in the detector signal is due to the detection of the EB. The fast reduction of signal is then due to the switch-off of the soliton, which occurs within the duration of the EB. The final tail is the decay of the EB. As for the switch-on, the minimum pulse width needed to induce switching at constant amplitude increases with increasing detuning to the microsecond range (at ≈3 mA).

The scheme in Fig. 13.1b indicates that somewhere typically close to the centre of the hysteresis curve, upper and lower state have an equal stability and roughly equal distance to the separatrix. This so-called Maxwell point is hence the point to aim for flip-flop operation. As time scales are then in the tens of microseconds range the AC-coupled APD is not working well for monitoring the signal. The DC monitor provides evidence of flip-flop operation but due to its low bandwidth demands millisecond pulses. Hence a DC coupled detector with 50 MHz bandwidth but

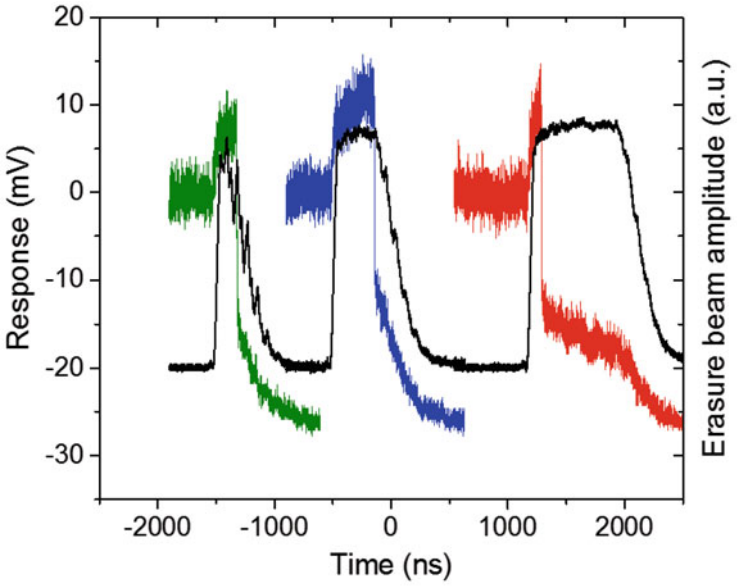

Fig. 13.11 Three independently observed switch-off events, with pulse widths of 200, 500, 1000 ns from left to right (see Fig. 13.10 for explanations). Note that, as the APD is AC-coupled, initially the soliton is on even if the signal is zero, which can be confirmed from examining the bias monitor output

much lower amplification is used. Figure 13.1b shows a realisation of a flip-flop event with input pulses of 50 μs width. The soliton switches on with the arrival of the 980 nm IB (it is unclear why the IB did not register in the detector in these experiments) and stays on until it is hit by the 915 nm EB. Further experiments indicate that the minimum pulse duration needed at the switching amplitudes available can be 10 μs, but switching is no longer robust.

A simulation demonstrating flip-flop operation of fundamental VCSEL solitons was performed using the model presented in [62] (a simplified version, without the external-cavity delay, of the model [61] used to reproduce the switch-on events in [114]) and is displayed in Fig. 13.13. No detailed investigation or matching of parameters is intended at this point, just a qualitative demonstration. Similar to Fig. 13.12, the sequence is initiated by an optical pulse close to the soliton frequency at $t = 0$ (Fig. 13.13). This causes a strong burst in the intra-cavity field, followed by a sudden drop as the end of the IB. Then the system approaches the steady-state in an oscillatory fashion. This kind of transient is typical of relaxation oscillations in semiconductor lasers but is not resolved in the current experiment as it takes only a few nanoseconds in the simulations. It should be noted that the actual switch-on transients observed experimentally and reproduced numerically in Ref. [114] are even more complex than this due to the external-cavity dynamics. However, these complex transients still die out within tens of nanoseconds. At the end (at $t = 1800$), a pulse is added to the current parameter to simulate the incoherent optical pumping. This is followed by a rapid switch-down of the soliton.

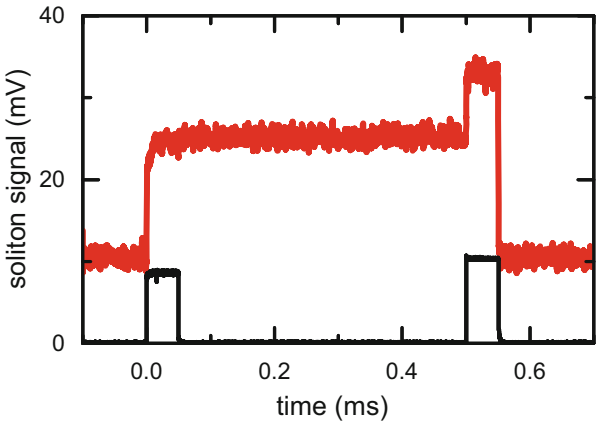

Fig. 13.12 Successful flip-flop event. The black trace shows the two input pulses (not to scale), the red trace the response. The red trace has been smoothed over 1 μs to remove high frequency noise. The offset of 10 mV is an electronic bias. Temperature of VCSEL submount: 47 °C

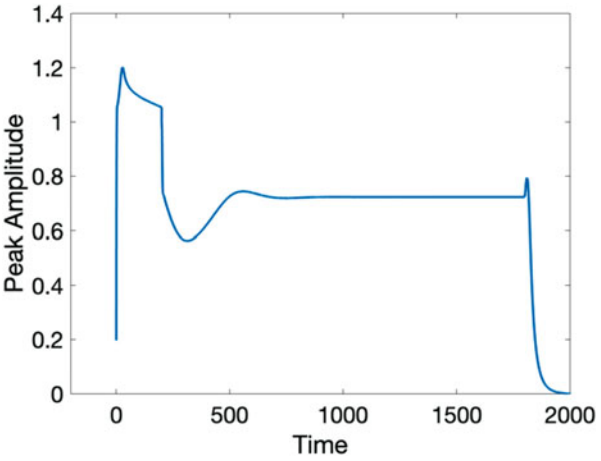

Fig. 13.13 Amplitude at centre of soliton during a numerically simulated flip-flop sequence. Optical injection takes place from $t = 0$ to $t = 200$ (amplitude 0.3), current injection from $t = 1800$ to $t = 2000$ (amplitude 0.7). Parameters (see [62]): $\Theta = -2.3$, $\alpha = 5$, $\gamma = 0.01$, $\lambda = 0.0271$, $\sigma = 0.6$ and $\mu = 0.55$. Time unit is the inverse of the cavity lifetime, about 10 ps

Obviously, more work is needed to explore and to optimize parameters but the results presented here are a proof-of-principle of flip-flop operation of laser cavity solitons via the carriers and not via parasitic thermal or non-local effects in both experiment and theory.

13.5 Conclusions and Outlook

We demonstrated in this contribution vector vortex solitons with spatially inhomogeneous polarization forming spontaneously from symmetry breaking. The current experiment uses the full vector properties of light except helicity yielding a beautiful connection between nonlinear science and singular optics (or structured light).

Another motivation to investigate optical solitons, in particular dissipative solitons, is their use in all-optical processing and memory applications. We reported on the flip-flop operation of laser cavity solitons via an in principle all-electronic process. Although it seems that applications of spatial solitons for parallel information storage are limited due to the sensitivity to detuning fluctuations, using a VCSEL (or, for power scaling, an optically pumped semiconductor disk laser) to create VVB might be a simple and cost-effective option. In particular, such a system might be able to switch between different VVB on time scales of hundreds of nanoseconds in response to internal parameter changes or external stimulus, whereas spatial light modulators have typically responses on the millisecond time scale. We note that not only the time scale for flip-flop operation of fundamental solitons can be improved by parameter optimization, but that switching between different vortex states might be faster as it does not involve a significant change of S_0 and hence carrier number in the semiconductor. This adaptability might be useful in polarization modulated spectroscopy, quantum optics or sensing applications. Obviously, some work is needed to achieve robustness in addition to flexibility.

Apart from potential applications, it is fascinating to think about the options of using external stimuli for switching between VVB for fundamental investigations. We floated the idea before that maybe VVB states we do not observe in an experimental situation might be still stable, but not accessible via the conventional LI-curves. This could be investigated by the injection of 'structured light'. By coupling the cavity to a spatial light modulator [91] it would be also possible to change the anisotropies in a controlled way and thus to understand the selection between different VVB. Another option is to use controlled strain to change the intrinsic anisotropies of the VCSEL [119–121], although the bending methods used in [120, 121] are probably not directly suitable for broad-area VCSELs. As the information on the polarization direction is not expected to be stored directly in the semiconductor electron-hole plasma, memory and hysteresis effects are likely to be related to differences in detuning conditions for nearly degenerate VVB. It will be interesting to include the spin degrees of freedom in the consideration as some memory of them is stored in the semiconductor and found not only to be important to understand some aspects of polarization switching in VCSELs [41–44] but also enabling novel spintronic applications [121]. There are indications that the helicity becomes nonzero and spatially varying in the VCSEL with frequency-selective feedback [39] but systematic investigations are lacking.

In summary, the results arguably support the notion of nonlinear optics being an excellent workhorse for investigations on conservative as well as dissipative solitons. Optical systems are not only highly controllable in parameters and have reasonably fast time scales to allow repeated experiments, but also—via the polarization degrees of freedom—many degrees of freedom to play with, provide an easy interface for outside control via beams and the options to tailor settings via feedback, coupled cavities, spatial light modulators and polarization changing elements.

Acknowledgements We are grateful to Jesus Jimenez-Garcia and Pedro Rodriguez for the collaboration in the earlier stages of the investigation of the vector vortex beams [39]. We note in particular that it was Jesus Jimenez-Garcia who realized that some of the states he observed had very peculiar polarization properties and worked out a first connection to VVB. The sabbatical of T. Guillet at Strathclyde was supported by the CNRS.

References

1. J.S. Russel, Brit. Assoc. Adv. Sci. pp. 311–392 (1844). Report on 14th meeting. Marray, London.
2. A. Hasegawa, F. Tappert, Appl. Phys. Lett. **23**, 142 (1973)
3. L.F. Mollenauer, R.H. Stolen, J.P. Gordon, Phys. Rev. Lett. **45**, 1095 (1980)
4. R.Y. Chiao, E. Garmire, C.H. Townes, Phys. Rev. Lett. **13**, 479 (1964)
5. J.E. Bjorkholm, A. Ashkin, Phys. Rev. Lett. **32**, 129 (1974)
6. L. Bergé, Phys. Rep. **303**, 259 (1998)
7. N.N. Rosanov, V.A. Smirnov, N.V. Vyssotina, Chaos, Solitons & Fractals **4**, 1767 (1994)
8. V. Tikhonenko, J. Christou, B. Luther-Daves, J. Opt. Soc. Am. B **12**, 2046 (1995)
9. W.J. Firth, D.V. Skryabin, Phys. Rev. Lett. **79**, 2450 (1997)
10. N. Akhmediev, A. Ankiewicz, *Dissipative solitons*, *Lecture Notes in Physics*, vol. 661 (Springer, Berlin, 2005)
11. N.N. Akhmediev, J.M. Soto-Crespo, P. Grelu, Chaos **17**, 037112 (2007)
12. M. Tlidi, P. Mandel, R. Lefever, Phys. Rev. Lett. **73**, 640 (1994)
13. W.J. Firth, A. Lord, J. Nonlinear Optical Physics & Materials **7**, 255 (1998)
14. L.A. Lugiato, R. Lefever, Phys. Rev. Lett. **58**, 2209 (1987)
15. W.J. Firth, A. Lord, J. Mod. Opt. **43**, 1071 (1996)
16. S.V. Fedorov, G.V. Khodova, N.N. Rosanov, Proc. SPIE **1840**, 208 (1991)
17. N.N. Rosanov, S.V. Fedorov, Opt. Spectr. **72**, 782 (1992)
18. V.Y. Bazhenov, V.B. Taranenko, M.V. Vasnetsov, Proc. SPIE **1840**, 183 (1991)
19. S.V. Fedorov, N.N. Rosanov, A.N. Shatsev, N.A. Veretenov, A.G. Vladimirov, IEEE J. Quantum Electron. **39**, 197 (2003)
20. N.N. Rosanov, S.V. Fedorov, A.N. Shatsev, Phys. Rev. Lett. **95**, 053903 (2005)
21. P. Genevet, S. Barland, M. Giudici, J.R. Tredicce, Phys. Rev. Lett. **104**, 223902 (2010)
22. K. Iga, IEEE J. Selec. Top. Quantum Electron. **6**(6), 1201 (2000)
23. M. Grabherr, R. Jäger, M. Miller, C. Thalmaier, J. Herlein, K.J. Ebeling, IEEE Photon. Technol. Lett. **10**, 1061 (1998)
24. M. Grabherr, M. Miller, R. Jäger, R. Michalzik, U. Martin, H.J. Unold, K.J. Ebeling, IEEE J. Sel. Top. Quantum Electron. **5**, 495 (1999)
25. L.C. Crasovan, B.A. Malomed, D. Mihalache, Phys. Rev. E **63**, 016605 (2000)
26. D. Mihalache, D. Mazilu, F. Lederer, H. Leblond, B.A. Malomed, Phys. Rev. A **77**, 033817 (2008)
27. P.V. Paulau, D. Gomila, P. Colet, N.A. Loiko, N.N. Rosanov, T. Ackemann, W.J. Firth, Opt. Exp. **18**, 8859 (2010)
28. P.V. Paulau, D. Gomila, P. Colet, B.A. Malomed, W.J. Firth, Phys. Rev. E **84**, 036213 (2011)
29. Y. Tanguy, T. Ackemann, W.J. Firth, R. Jäger, Phys. Rev. Lett. **100**, 013907 (2008)
30. Y. Tanguy, N. Radwell, T. Ackemann, R. Jäger, Phys. Rev. A **78**, 023810 (2008). https://doi.org/10.1103/PhysRevA.78.023810
31. N. Radwell, T. Ackemann, IEEE J. Quantum Electron. **45**, 1388 (2009)
32. J. Jimenez, Y. Noblet, P.V. Paulau, D. Gomila, T. Ackemann, J. Opt. **15**, 044011 (2013)
33. M. Haelterman, A.P. Sheppard, Opt. Lett. **19**, 96 (1994)

34. G.L. Oppo, A.J. Scroggie, W.J. Firth, J. Opt. B: Quantum Semiclass. Opt. **1**, 133 (1999)
35. M. Gilles, P.Y. Bony, J. Garnier, A. Picozzi, M. Guasoni, J. Fatome, Nature Phot. **11**, 102 (2017)
36. M. Pesch, E. Große Westhoff, T. Ackemann, W. Lange, Phys. Rev. Lett. **95**, 143906 (2005)
37. G. Milione, H.I. Sztul, D.A. Nolan, R.R. Alfano, Phys. Rev. Lett. **107**, 053601 (2011)
38. C.E.R. Souza, J.A.O. Huguenin, A.Z. Khoury, J. Opt. Soc. Am. A **31**, 1007 (2014)
39. J. Jimenez, P. Rodriguez, T. Guillet, T. Ackemann, Phys. Rev. Lett. **119**, 113902 (2017). https://doi.org/10.1103/PhysRevLett.119.113902
40. K.D. Choquette, D.A. Richie, R.E. Leibenguth, Appl. Phys. Lett. **64**, 2062 (1994)
41. M. San Miguel, Q. Feng, J.V. Moloney, Phys. Rev. A **52**, 1728 (1995)
42. M.P.v. Exter, M.B. Willemsen, J.P. Woerdman, Phys. Rev. A **58**, 4191 (1998)
43. M. San Miguel, S. Balle, J. Mulet, C. Mirasso, E. Tolkachova, J.R. Tredicce, Proc. SPIE **3944**, 242 (2000)
44. T. Ackemann, M. Sondermann, *Polarization dynamics in vertical-cavity surface emitting lasers.* (Research Signpost, Keralia, 2005), pp. 82–110
45. F. Prati, G. Tissoni, M.S. Miguel, N.B. Abraham, Opt. Commun. **143**, 133 (1997)
46. T. Mayteevarunyoo, B.A. Malomed, D.V. Skryabin, New J. Phys. **20**, 113019 (2018)
47. A.A. Ishaaya, L.T. Vuong, T.D. Grow, A.L. Gaeta, Opt. Lett. **33**, 13 (2008)
48. F. Bouchard, H. Larocque, A.M. Yao, C. Travis, I. De Leon, A. Rubano, E. Karimi, G.L. Oppo, R.W. Boyd, Phys. Rev. Lett. **117**, 233903 (2016)
49. A. Ciattoni, B. Crosignani, P. Di Porto, A. Yariv, Phys. Rev. Lett. **94**, 073902 (2005)
50. W.J. Firth, A.J. Scroggie, Phys. Rev. Lett. **76**, 1623 (1996)
51. M. Brambilla, L.A. Lugiato, M. Stefani, Europhys. Lett. **34**, 109 (1996)
52. L. Spinelli, G. Tissoni, M. Brambilla, F. Prati, L.A. Lugiato, Phys. Rev. A **58**, 2542 (1998)
53. S. Barland, J.R. Tredicce, M. Brambilla, L.A. Lugiato, S. Balle, M. Giudici, T. Maggipinto, L. Spinelli, G. Tissoni, T. Knödel, M. Miller, R. Jäger, Nature **419**, 699 (2002)
54. Y. Tanguy, T. Ackemann, R. Jäger, Opt. Exp. **15**, 16773 (2007)
55. P. Genevet, S. Barland, M. Giudici, J.R. Tredicce, Phys. Rev. Lett. **101**, 123905 (2008)
56. T. Elsass, K. Gauthron, G. Beaudoin, I. Sagnes, R. Kuszelewicz, S. Barbay, Appl. Phys. B **98**, 327 (2010)
57. M. Kreuzer, W. Balzer, T. Tschudi, Appl. Opt. **29**, 579 (1990)
58. M. Kreuzer, A. Schreiber, B. Thüring, Mol. Cryst. Liq. Cryst. **282**, 91 (1996)
59. B. Schäpers, T. Ackemann, J.P. Seipenbusch, W. Lange, J. Opt. B: Quantum Semiclass. Opt. **1**, 58 (1999)
60. X. Hachair, S. Barland, L. Furfaro, M. Giudici, S. Balle, J. Tredicce, M. Brambilla, T. Maggipinto, I.M. Perrini, G. Tissoni, L. Lugiato, Phys. Rev. A **69**, 043817 (2004)
61. A.J. Scroggie, W.J. Firth, G.L. Oppo, Phys. Rev. A **80**, 013829 (2009)
62. J. Jimenez, G.L. Oppo, T. Ackemann, J. Phys. D **49**, 095110 (2016)
63. C.H. Henry, IEEE J. Quantum Electron. **18**, 259 (1982)
64. L.A. Lugiato, Progress in Optics XXI pp. 69–216 (1984)
65. W.J. Firth, P.V. Paulau, Eur. Phys. J. D **59**, 13 (2010)
66. T. Ackemann, N. Radwell, Y. Noblet, R. Jäger, Opt. Lett. **37**, 1079 (2012)
67. T. Ackemann, G.L. Oppo, W.J. Firth, Adv. Atom. Mol. Opt. Phys. **57**, 323 (2009)
68. S. Barbay, R. Kuszelewicz, J.R. Tredicce, Adv. Opt. Tech. **2011**, 628761 (2011)
69. H. Rubinsztein-Dunlop, A. Forbes, M.V. Berry, M.R.D.D.L. Andrews, M. Mansuripur, C. Denz, C. Alpmann, P. Banzer, T. Bauer, E. Karimi, L. Marrucci, M. Padgett, M. Ritsch-Marte, N.M. Litchinitser, N.P. Bigelow, C. Rosales-Guzmán, A. Belmonte, J.P. Torres, T.W. Neely, M. Baker, R. Gordon, A.B. Stilgoe, J. Romero, A.G. White, R. Fickler, A.E. Willner, G. Xie, B. McMorran, A.M. Weiner, J. Opt. B **19**, 013001 (2017)
70. C. Rosales-Guzmán, B. Ndagano, A. Forbes, J. Opt. **20**, 123001 (2018)
71. A. Forbes, Laser Photonics Rev. **13**, 1900140 (2019)
72. E. Otte, C. Denz, Appl. Phys. Rev. **7**, 041308 (2020)

73. A.M. Beckley, T.G. Brown, M.A. Alonso, Opt. Exp. **18**, 10777 (2010)
74. A. Forbes, A. Dudley, M. McLaren, Adv. Opt. Phot. **8**, 200 (2016). https://doi.org/10.1364/AOP.8.000200
75. Q. Zhan, Adv. Opt. Phot. **1**, 1 (2009). https://doi.org/10.1364/AOP.1.000001
76. C. Maurer, A. Jesacher, S. Fürhapter, S. Bernet, M. Ritsch-Marte, New J. Phys. **9**, 78 (2007)
77. R. Dorn, S. Quabis, G. Leuchs, Phys. Rev. Lett. **91**, 233901 (2003)
78. O.J. Allegre, W. Perrie, S.P. Edwardson, G. Dearden, K.G. Watkins, J. Opt. **14**, 085601 (2012)
79. Y. Kozawa, S. Sato, Opt. Exp. **18**, 10828 (2010)
80. B.J. Roxworthy, K.C. Toussaint Jr, New J. Phys. **12**, 073012 (2010)
81. F.K. Fatemi, Opt. Exp. **19**, 25143 (2011)
82. N. Tischler, I. Fernandez-Corbaton, X. Zambrana-Puyalto, A. Minovich, X. Vidal, M.L. Juan, G. Molina-Terriza, Light: Science & Applications **3** (2014). https://doi.org/10.1038/lsa.2014.64
83. X.F. Qian, J.H. Eberly, Opt Lett. **36**, 4110 (2011). https://doi.org/10.1364/OL.36.004110
84. B. Ndagano, B. Perez-Garcia, F.S. Roux, M. McLaren, C. Rosales-Guzman, Y. Zhang, O. Mouane, R.I. Hernandez-Aranda, T. Konrad, A. Forbes, Nature Phys. **13**, 397 (2017)
85. X.F. Qian, A.N. Vamivakas, J.H. Eberly, Opt. Photon. News **17**(10), 34 (2017)
86. S. Berg-Johansen, F. Töppel, B. Stiller, P. Banzer, M. Ornigotti, E. Giacobino, G. Leuchs, A. Aiello, C. Marquardt, Optica **2**, 864 (2015)
87. J. Wang, F. Castellucci, S. Franke-Arnold, AVS Quantum Sci. **2** (2020)
88. M. Fridman, G. Machavariani, N. Davidson, A.A. Friesem, Appl. Phys. Lett. **93**, 191104 (2008)
89. Y. Senatsky, J.F. Bisson, J. Li, A. Shirakawa, M. Thirugnanasambandam, K.i. Ueda, Opt. Rev. **19**, 201 (2012)
90. S. Ngcobo, I. Litvin, L. Burger, A. Andrew Forbes, Nat. Commun. **4**, 2289 (2013)
91. D. Naidoo, F.S. Roux, A. Dudley, I. Litvin, B. Piccirillo, L. Marrucci, A. Forbes, Nat. Photon. **10**, 327 (2016). https://doi.org/10.1038/nphoton.2016.37.
92. G. Machavariani, Y. Lumer, I. Moshe, A. Meir, S. Jackel, Opt. Lett. **32**, 1468 (2007)
93. Y. Liu, X. Ling, X. Yi, X. Zhou, H. Luo, S. Wen, Appl. Phys. Lett. **104**, 191110 (2014)
94. T. Bauer, P. Banzer, E. Karimi, S. Orlov, A. Rubano, L. Marrucci, E. Santamato, R.W. Boyd, G. Leuchs, Science **347**, 964 (2015)
95. S. Ramachandran, P. Kristensen, Nanophotonics **2**, 455 (2013)
96. B. Ndagano, R. Brüning, M. McLaren, M. Duparré, A. Forbes, Opt. Exp. **23**, 17330 (2015)
97. N. Radwell, R. Hawley, J. Götte, S. Franke-Arnold, Nat. Commun. **7**, 10564 (2016). https://doi.org/10.1038/ncomms10564
98. K.G. Lagoudakis, T. Ostatnický, A.V. Kavokin, Y.G. Rubo, Y.G. André, B. Deveaud-Plédran, Science **326**, 974 (2009)
99. F. Manni, Y. Leéger, Y.G. Rubo, R. André, B. Deveaud, Nat. Commun. **4**, 2590 (2013)
100. V.G. Sala, D.D. Solnyshkov, I. Carusotto, T. Jacqmin, A. Lemaître, H. Tercas, A. Nalitov, M. Abbarchi, E. Galopin, I. Sagnes, J. Bloch, G. Malpuech, A. Amo, Phys. Rev. X **5**, 011034 (2015)
101. J. Hu, S. Kim, C. Schneider, S. Höfling, H. Deng, Phys. Rev. Appl. **14**, 044001 (2020)
102. M. Schulz-Ruhtenberg, Y. Tanguy, K.F. Huang, R. Jäger, T. Ackemann, J. Phys. D: Appl Phys. **42**, 055101 (2009)
103. T. Ackemann, G.L. Oppo, P.V. Paulau, C. McIntyre, Y. Noblet, P. Colet, W.J. Firth, *Frequency- and phase locking of laser cavity solitons* (Springer, New York, 2013), pp. 49–87. Progress in Optical Science and Photonics
104. T. Ackemann, J. Jimenez, Y. Noblet, N. Radwell, G. Ren, P. Paulau, C. McIntyre, G.L. Oppo, J.P. Toomey, D.M. Kane, *Dynamics and Interaction of Laser Cavity Solitons in Broad-Area Semiconductor Lasers* (Wiley, 2016), book section 3, pp. 41–76
105. P. Rodriguez, J. Jimenez, T. Guillet, T. Ackemann, Appl. Sci. **7**, 442 (2017). https://doi.org/10.3390/app7050442

106. J. Jimenez, P. Rodriguez, T. Guillet, T. Ackemann, Phys. Rev. Lett. (2017)
107. A.S. Desyatnikov, A.A. Sukhorukov, Y.S. Kivshar, Phys. Rev. Lett. **95**, 203904 (2005)
108. A. Minovich, D.N. Neshev, A.S. Desyatnikov, W. Krolikowski, Y.S. Kivshar, Opt. Exp. **17**, 23610 (2009)
109. J.M. Soto-Crespo, N. Akhmediev, C. Mejîa-Cortés, N. Devine, Opt. Exp. **17**, 4236 (2009)
110. P.V. Paulau (2015). Personal communication.
111. M.P.v. Exter, A.K.J.v. Doorn, J.P. Woerdman, Phys. Rev. A **56**, 845 (1997)
112. A.K.v. Doorn, M.P.v. Exter, J.P. Woerdman, Appl. Phys. Lett. **69**, 3635 (1996)
113. P.V. Paulau, C. McIntyre, Y. Noblet, N. Radwell, W.J. Firth, P. Colet, T. Ackemann, G.L. Oppo, Phys. Rev. Lett. **108**, 213904 (2012)
114. N. Radwell, C. McIntyre, A.J. Scroggie, G.L. Oppo, W.J. Firth, T. Ackemann, Eur. Phys. J. D **59**, 121 (2010)
115. M. Bache, F. Prati, G. Tissoni, R. Kheradmand, L.A. Lugiato, I. Protsenko, M. Brambilla, Appl. Phys. B **81**, 913 (2005)
116. D.N. Maywar, G.P. Agrawal, Y. Nakano, Opt. Express **6**, 75 (2000)
117. S. Barbay, Y. Ménesguen, X. Hachair, L. Leroy, I. Sagnes, R. Kuszelewicz, Opt. Lett. **31**, 1504 (2006)
118. S. Barbay, R. Kuszelewicz, Opt. Exp. **15**, 12457 (2007)
119. A.K. van Doorn, M.P. van Exter, J.P. Woerdman, IEEE J. Quantum Electron. **34**, 700 (1998)
120. K. Panajotov, B. Nagler, G. Verschaffelt, A. Georgievski, H. Thienpont, J. Danckaert, I. Veretennicoff, Appl. Phys. Lett. **77**(11), 1590 (2000)
121. M. Lindemann, G. Xu, T. Pusch, R. Michalzik, M.R. Hofmann, I. Zutic, N.C. Gerhardt, Nature **562**, 212 (2019)

Chapter 14
Discrete Solitons of the Ginzburg-Landau Equation

Mario Salerno and Fatkhulla Kh. Abdullaev

Abstract In this chapter we review recent results concerning localized and extended dissipative solutions of the discrete complex Ginzburg-Landau equation. In particular, we discuss discrete diffraction effects arising both from linear and nonlinear properties, the existence of self-localized dissipative solitons in the presence of cubic-quintic terms and modulational instability induced by saturable nonlinearities. Dynamical stability properties of localized and extended dissipative discrete solitons are also discussed.

Keywords Discrete Ginzburg-Landau equation · Nonlinear waveguides arrays · Bose-Einstein condensates · Complex band structure · Dissipative solitons · Cubic-Quintic nonlinearity · Modulational instability · Plane waves · Saturable nonlinearity · Nonlinear periodic waves

14.1 Introduction

The complex Ginzburg-Landau equation (GLE) is a fundamental equation of physics which appears in many different contexts, including phase transitions, superconductivity, nonlinear optics, non-equilibrium fluid dynamics, Bose-Einstein condensates, etc. [1–5]. Being intrinsically nonlinear the GLE displays a very reach dynamical range of behaviors ranging from chaotic motion to regular structures as vortex and dissipative solitons.

Properties of dissipative solitons of the continuous GLE equation have been largely investigated in the past decades [6]. They were predicted by Pereira-Stenflo in [7] (see also [8]), where the exact soliton solution of the one-dimensional cubic

M. Salerno (✉)
Dipartimento di Fisica "E.R. Caianiello", and INFN, Gruppo Collegato di Salerno, Università di Salerno, Salerno, Italy
e-mail: salerno@sa.infn.it

F. K. Abdullaev
Physical-Technical Institute, Uzbek Academy of Sciences, Tashkent, Uzbekistan

M. F. S. Ferreira (ed.), *Dissipative Optical Solitons*, Springer Series in Optical Sciences 238, https://doi.org/10.1007/978-3-030-97493-0_14

Ginzburg-Landau equation with filter was obtained for the first time. In contrast with solitons of Hamiltonian systems that usually appear as one-parameter families of solutions and whose existence relies on the balance between nonlinearity and dispersion, the existence of dissipative solitons of GLE requires two conditions to be simultaneously satisfied e.g. the equilibrium between nonlinearity and dispersion and the equilibrium between dissipation and amplification. Moreover, dissipative solitons do not appear in families but exist just for specific values of the parameters appearing in the equation. Dissipative solitons and breathers can also appear in the nonlinear Schrödinger equation in the presence of different types of complex periodic potentials [9].

Quite recently a great deal of attention has been devoted also to the study of nonlinear discrete optical systems modeled by a discrete version of the GLE (DGLE) [10–18], which is similar to the discrete nonlinear Schrödinger equation (DNLSE) but with dissipative and amplification effects included. The DGLE has been used to describe a number of physical systems, including arrays of waveguides with amplification and damping, arrays of semiconductor lasers [19], arrays of exciton-polariton condensates [20], frustrated vortices in hydrodynamics [21], dissipative discrete nonlinear electrical lattices with nearest-neighbor interaction [22], etc. In particular, in optics the DGLE appears in problems of beam propagation in the array of the nonlinear optical waveguides with Kerr and resonance nonlinearities [23–25]. The Kerr medium is assumed active and with intrinsic, saturable gain and damping. The existence of a variety of nonlinear localized modes in these systems, including moving discrete dissipative breather-solitons [23] and vortex dissipative solitons [26], was demonstrated.

Similarly to the continuous case, discrete solitons require the balance both of dispersion and nonlinearity and of dissipation and amplification. In this context discrete dissipative solitons have been investigated for power law [13] and saturable [18] nonlinearities, for complex extensions of the Ablowitz-Ladik equation [14, 27], for DNLS-type equations with cubic-quintic nonlinearities [28–31].

In the case of saturable nonlinearities, the study of solitons has been restricted mainly to the conservative case. In particular, discrete solitons of DNLSE with saturable nonlinearity were investigated in Refs. [32, 33] and discrete breathers for the same type of equation in Ref. [34]. In spite of the relevance of this type of nonlinearity for optics, existence and stability of dissipative solitons in the presence of a saturable nonlinearity are poorly investigated. In the continuum case saturable nonlinearities have been considered in the one-dimensional complex Ginzburg-Landau equation both for scalar and vectorial cases [35]. Modulational instability and stopping of Kerr self-focusing induced by nonconservative effects have also been investigated in the multidimensional continuous complex GL type equation with nonlinear saturation [36, 37].

In this chapter we review some recent results on localized and extended dissipative solutions of the discrete complex Ginzburg-Landau equation. In particular, we discuss discrete diffraction effects arising both from linear and nonlinear properties, the existence of self-localized dissipative solitons in the presence of cubic-quintic terms and the existence and stability of dissipative solitons of the DGLE with

saturable nonlinearity. In this last case we consider the problem of the instability of nonlinear plane waves solution under weak modulations, i.e. the modulational instability (MI) problem, which allows to define the region of parameters where solitons and train of solitons can be formed. For this we also construct discrete dissipative solitons and nonlinear periodic waves of DGLE with saturable nonlinearity. In particular, we provide explicit analytic expressions for periodic dissipative solitons solutions in the form of elliptic functions both on a zero and on a finite background. Stability properties of these solutions are investigated both by means of MI analysis and by direct numerical simulations of their propagation under the DGLE. As a result, we show that while discrete periodic waves and solitons on a zero background are stable, they become modulationally unstable on a finite background. The effect of a linear ramp potential on the dynamics of stable localized dissipative solitons is also considered.

14.2 The Model and Linear Dispersion Relation

The cubic-quintic DGLE can be obtained from a corresponding space-periodic continuous model in the tight binding approximation [38], and in normalized units can be written in full generality as [39].

$$i\frac{d\psi_n}{dz} = -\Gamma(\psi_{n+1} + \psi_{n-1}) + i\gamma_1\psi_n + (\gamma_3 + \gamma_5|\psi_n|^2)|\psi_n|^2\psi_n \tag{14.1}$$

with γ_1 real and $\Gamma = \Gamma_R + i\Gamma_I$, $\gamma_3 = \gamma_{3R} + i\gamma_{3I}$, $\gamma_5 = \gamma_{5R} + i\gamma_{5I}$ complex parameters. In the optical context Eq. (14.1) arises in connection with semiconductor laser arrays and optical amplifiers [39, 40] but it can be also used to model mean field properties of open Bose-Einstein condensates (BEC) trapped in deep optical lattices [41, 42]. In the optical context (resp. in the BEC context) z denotes the propagation length (resp. the time), ψ_n the amplitude of the electromagnetic wave on site n (resp. the condensate wavefunction at site n), Parameters Γ_R and Γ_I are the real and imaginary parts of the complex discrete diffraction in the paraxial approximation (resp. inter-well tunneling constant in BEC), γ_{3R}, γ_{5R} denote the strengths of the cubic and quintic nonlinearity (two and three body interaction terms in BEC) while γ_1, γ_{3I}, γ_{5I} are real coefficients related to the gain/loss mechanisms present in the optical system (resp. in open BEC). In the following we adopt the notation appropriate for the optical context.To investigate nonlinear property of this equation it is convenient to start with the band structure of the underlying linear system, this being important, at least for not too large nonlinearities, to understand the types of localized dissipative structures one can have in the system. For this we set $\gamma_3 = \gamma_5 = 0$ in Eq. (14.1) and look for plane wave solutions of the type $\psi_n = \exp i(kn - \Omega z)$ with $k \in R$ denoting the lattice quasi-momentum and Ω complex, i.e. $\Omega \equiv \Omega_R + i\Omega_I$, denoting the propagation wave number (in nonlinear Schrödinger lattices z plays the role of

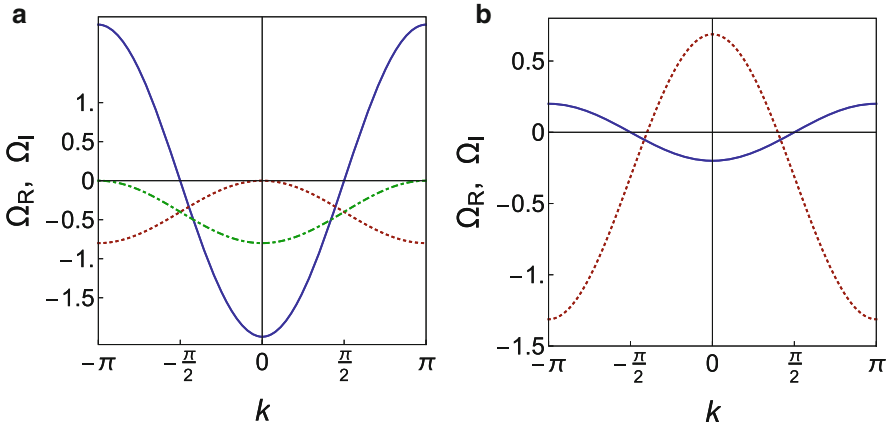

Fig. 14.1 Typical real (continuous blue curves) and imaginary (dotted red curves) linear bands in Eq. (14.2). Parameter values are fixed as $\Gamma_R = 1.0, \Gamma_I = -0.2, \gamma_1 = -0.4$, in the left panel and as $\Gamma_R = 0.1, \Gamma_I = -0.5, \gamma_1 = -0.3123246628$ in the right panel. The dot-dashed green curve in the left panel refers to the imaginary band obtained for $\Gamma_I = 0.2$, with real band and all other parameters unchanged

time and Ω corresponds to the complex energy, in $\hbar$ units). Direct substitution of the above wave in Eq. (14.1) leads to the following dispersion relations:

$$\Omega_R = 2\Gamma_R \cos(k), \Omega_I = \gamma_1 - 2\Gamma_I \cos(k), \tag{14.2}$$

and the periodicity of the lattice (lattice constant being fixed to 1) permits to restrict the resulting real and imaginary bands to the first BZ, e.g. $k \in [-\pi, \pi]$. In Fig. 14.1 are shown typical linear bands for different γ_1, Γ parameters.

While the real band has a direct correspondence in closed nonlinear lattices, the imaginary band is typical of open (i.e. dissipative) systems, playing an important role for stability of the stationary solutions in the system. Thus, for example, from Eq. (14.2) it follows that any zero amplitude solution in the Brillouin zone (BZ) can be stable if $\Omega_I(k) < 0$ for k, this implying that $\gamma_1 \leq 2\Gamma_I$. On the other hand stationary Bloch states of a given k can be stable under z-propagation only if the corresponding $\Omega_I(k)$ is exactly zero. As example, in the left panel of Fig. 14.1 we shown band structures for the cases in which Ω_I becomes zero at $k = 0$ (red dotted curve) or at the edges of the BZ $k = \pm\pi$ (green dot-dashed curve) corresponding to the cases $\Gamma_I = -0.2$ and $\Gamma_I = 0.2$, respectively. Note that the other parameters are fixed the same way so that the Ω_R band of the two

Thus, the ground state of the Ω_R band (i.e. the Bloch state at $k = 0$) is stable in the first case (e.g. $\Gamma_I = -0.2$) but not for second case (e.g. $\Gamma_I = 0.2$), as one can see from Fig. 14.2 where the z-propagation for the uniform ground state $|\psi_n| = 0.185695$, is reported for both cases. As it is evident from the left panel of Fig. 14.1, the opposite will be true for the highest excited Bloch state at the edge $k = \pi$

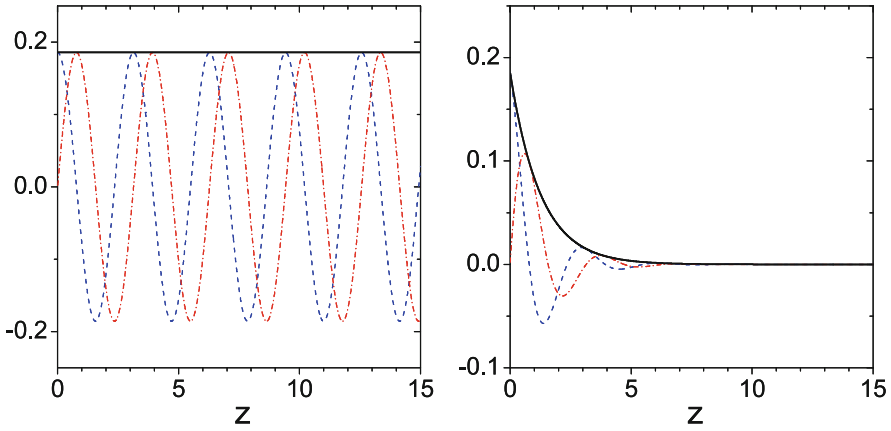

Fig. 14.2 Numerical z-evolution of the uniform Bloch state of the band structure depicted in the left panel of Fig. 14.1 at $k = 0$, for parameters values $\Gamma_I = -0.2$ (left panel) and $\Gamma_I = 0.2$ (right panel). Other parameters are fixed as in the left panel of Fig. 14.1. In the figures are depicted the modulo $|\psi_n|$ (black continuous curve), the real (dashed blue curve) and imaginary (red dot-dashed curve) parts of ψ_n at a generic site n of the lattice

of the BZ (not shown for brevity). All other k-Bloch states in the bands depicted in Fig. 14.1 will either grow, if their $\Omega_I(k) > 0$, or decay into the zero amplitude background if their $\Omega_I(k) < 0$. From this it is clear that the balance between dissipation and gain is very crucial for the existence of stable solutions.

14.3 Dissipative Solitons of the DGLE

In analogy with the usual nonlinear Schrödinger lattices one can expect that dissipative localized states occur from instabilities of the Bloch states either at the center or at the edges of the BZ, depending on the signs of the nonlinearities. For the NLS equation with periodic potentials (optical lattices) this was indeed proved in the small amplitude limit, starting from exact stable Bloch states of the underlying linear problem and using perturbation theory. The mechanism for the creation of nonlinear excitations in the band gaps was then ascribed to the MI of Bloch states [43]. In the complex case this is more complicated due to the further requirement of the gain/loss balance needed for stationarity, but conceptually the mechanism is the same. This means that nonlinear localised modes can fork from the extremes of the real band and move into the band-gaps as the nonlinearity is increased. In the small amplitude limit they can be viewed as superpositions of Bloch states with k values centered around either $k = 0$ or $k = \pm \pi$, depending on the signs of γ_{3R}, γ_{5R}, with corresponding imaginary band values $\Omega_I(k)$ appropriate for stability. The MI will be discussed in more detail in the next section for the case of a saturable nonlinearity.

Although it is possible to obtain for some specific case exact solutions of the DGLE, in general one must recourse to numerical methods. This can be done by substitution the stationary ansatz $\psi_n(z) = (u_n + iv_n) \exp(-i\Omega z)$ into Eq. (14.1) and solving the resulting algebraic system for u_n, v_n either by Newton iterations or by self-consistent diagonalizations of the non-hermitian and nonlinear eigenvalue problem [44]. Typical examples of dissipative discrete solitons obtained numerically are depicted in Figs. 14.3 and 14.4. Notice that the band structure of the underlying linear problem corresponding to the unstable inter-site symmetric dissipative soliton reported in the right panels of Fig. 14.4 is depicted in the right panel of Fig. 14.1 from which we see that the soliton instability under the z-propagation correlates with the existence of a wide k-interval around $k = 0$ for which $\Omega_I(k) > 0$ and the corresponding linear Bloch states are unstable.

14.4 Saturable Nonlinearity and MI Analysis

As is well known, the MI is a fundamental dynamical phenomenon responsible for soliton and pattern generation in nonlinear systems [45]. In comparison to the continuous (non periodic) case, the MI in the discrete case displays novel properties since the discrete diffraction makes possible to have MI also for defocusing (e.g. repulsive) nonlinearity. Since the parameter region where plane waves become modulationally unstable coincides with the existence region of solitons, one has that nonlinear lattices can support solitons also for defocusing interactions. This fact is true also in the continuous case, if a periodic potential is present [43]. Different discretizations of the same continuous nonlinearity can have different effects on the MI and, correspondingly, can lead to different conditions for the existence of soliton solutions [46]. We also remark that in the DNLSE for small wavenumbers of the nonlinear plane wave, all modulations become unstable if the power excess a threshold value [34]. For DNLSE with a saturable nonlinearity the gain and critical frequency are decreased in comparison with the Kerr nonlinearity model [29]. Experimentally discrete MI has been observed in the array of nonlinear optical waveguides [47] and in photovoltaic crystals [48].

In this and in the next section we study MI and exact solutions of DGLE with saturable nonlinearity and saturable gain/loss which appear when one considers the propagation of beams in the array of nonlinear optical waveguides with active Kerr medium and resonant interaction. The general form of the model for this was introduced in Refs. [23, 24] as

$$i\frac{d\psi_n}{dz} + \Gamma(\psi_{n+1} + \psi_{n-1}) - [|\psi_n|^2 - if_d(|\psi_n|^2)]\psi_n + Qf_{is}(|\psi_n|) = 0 \qquad (14.3)$$

where $f_d(x)$, $x \equiv |\psi_n|^2$, is a real function that describes the amplification and absorbtion of each waveguide of the array of the form [24, 25, 49].

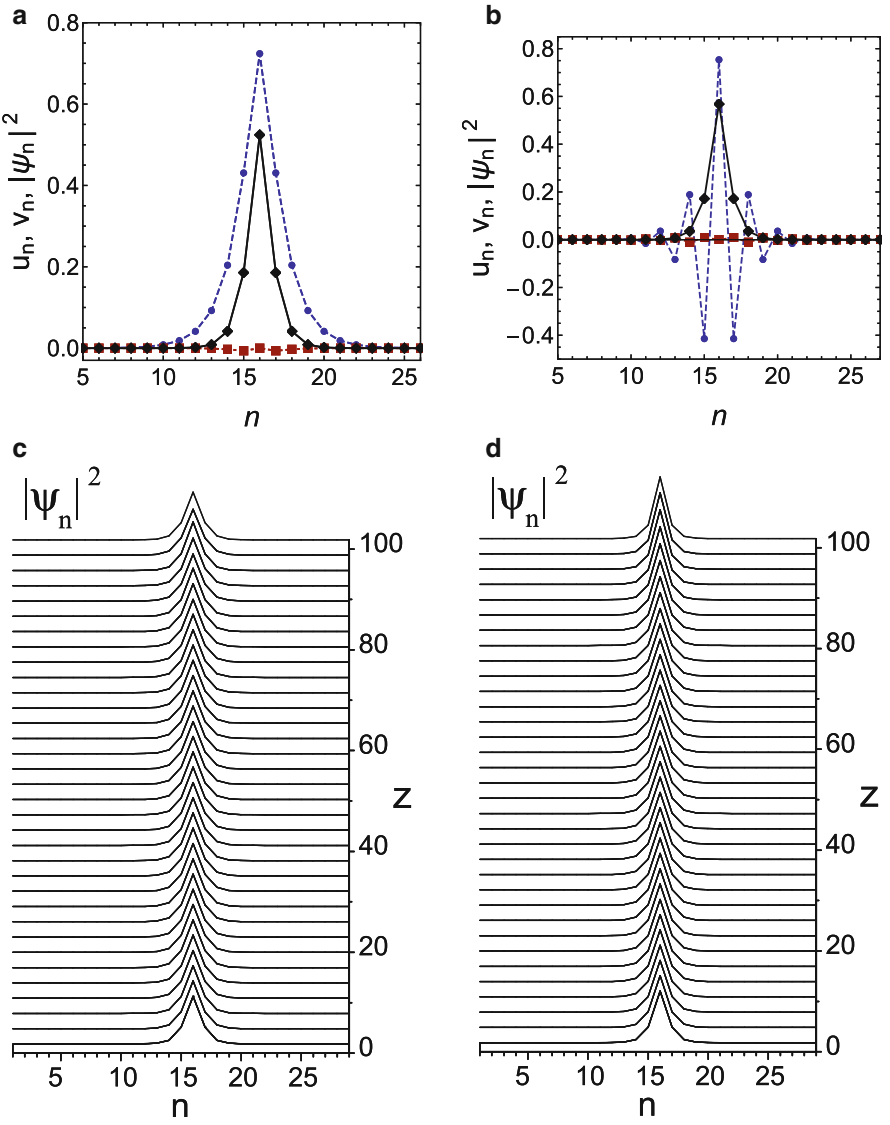

Fig. 14.3 Typical onsite-symmetric dissipative solitons (top panels) and their z-propagations (in corresponding bottom panels) obtained from direct numerical diagonalization and integration of Eq. (14.1). The soliton in the top left panel has $\Omega_R = -2.68251$ located below the linear real band at the center ($k = 0$) of the BZ. The corresponding z-propagation is depicted in the bottom left panel. Parameter values for this case are fixed as: $\Gamma = 1.0, \gamma_1 = -0.1, \gamma_3 = -2.847313757 + 0.3i$, $\gamma_5 = -0.6i$. The soliton in the top right panel has $\Omega_R = 2.72421$ located above the linear real band at the edge ($k = \pi$) of the BZ. The corresponding z-propagation is shown in the bottom right panel. Parameter values for this case are fixed as: $\Gamma = 1.0 - 0.01i, \gamma_1 = -0.447102453, \gamma_3 = 2.52 + 0.3i$, $\gamma_5 = 0.6 - 0.28i$. In top panels the continuous black lines with diamonds, blue dashed lines with dots, and red dotted lines with squares, correspond to the modulo square, and real and imaginary parts of ψ_n, respectively

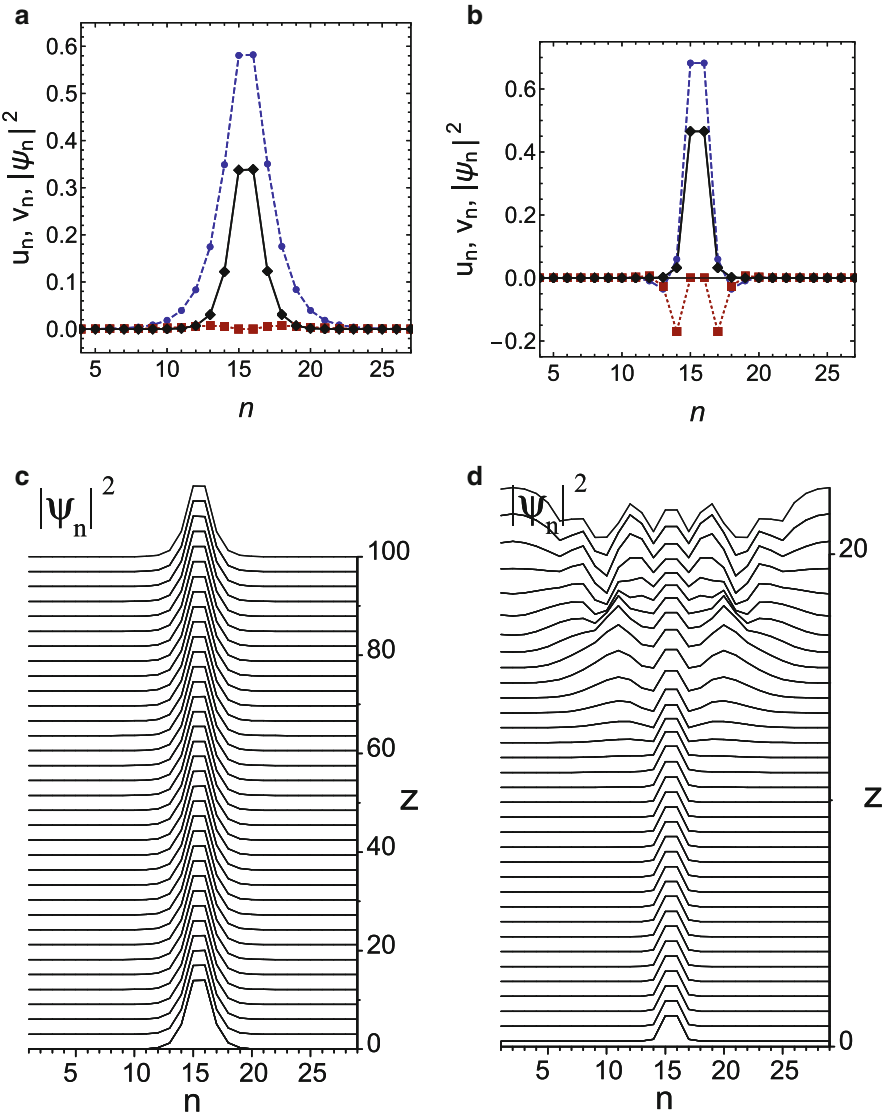

Fig. 14.4 Same as in Fig. 14.3 but for inter-site symmetric dissipative solitons. Parameter are fixed for the left panels as: $\Gamma = 1.0, \gamma_1 = -0.4573, \gamma_3 = -3.8 + 0.3i, \gamma_5 = 2.6 - 0.4i$, and for the right panels as $\Gamma = 0.1 - 0.5i, \gamma_1 = -0.312325, \gamma_3 = -4.0 - 0.6i, \gamma_5 = -0.5 - 0.1i$. In both cases the solitons have real part of the propagation wave-number below the bottom edge of the linear Ω_R band at $k = 0$

$$f_d(x) = -\delta + \frac{g}{1+x} - \frac{a}{1+bx}, \tag{14.4}$$

while the function $f_{is}(x)$ and the strength Q are related to the inter-site Kerr nonlinear refractive index (see [23, 24] for details). The parameters δ describe the linear non resonant losses while g, a are the strengths of the saturable gain and absorption, respectively, and b is the ratio between the gain and absorption saturation intensities. For simplicity in the following we restrict to the case $Q = 0$, $b = 1$ and rewrite Eq. (14.3) in the form

$$i\frac{d\psi_n}{dz} = -\Gamma(\psi_{n+1} + \psi_{n-1}) + i\gamma_1\psi_n + \gamma_3\frac{|\psi_n|^2}{1+\mu|\psi_n|^2}\psi_n, \tag{14.5}$$

where we replaced the Kerr nonlinearity with the saturable nonlinearity, and denoted $\gamma_1 = \delta$ and μ the parameter controlling the nonlinearity saturation (note that in Eq. (14.3) the field ψ_n is normalized according to the gain saturation intensity and the strength, while in Eq. (14.5) the nonlinearity saturation has been made explicit). Moreover, without loss of generality, we fix $\Gamma = 1 - i\alpha$, $\gamma_3 = -\nu + i\gamma$.To study the MI we notice that Eq. (14.5) supports nonlinear plane wave solutions of the form $\psi_n = A\ \exp\ (i(kn - \omega t))$, with amplitude A, wave numbers k and frequency ω satisfying the following nonlinear dispersion relation:

$$A^2 = -\frac{\delta + 2\alpha\cos(k)}{\delta\mu + \gamma + 2\mu\alpha\cos(k)}, k \neq \pm\arccos\left(\frac{\delta\mu+\gamma}{2\mu\alpha}\right) \pm \pi,$$
$$\omega = 2\cos(k)\left(\frac{\nu\alpha}{\gamma} - 1\right) + \frac{\nu\delta}{\gamma}. \tag{14.6}$$

For $\omega > 0$ there are two possibilities for plane wave existence, e.g. i) for $\nu/\mu > 0$, the frequency must vary in the interval $2 - \nu/\mu < \omega < 2$; ii) for $\nu/\mu < 0$, the frequency must vary in the interval $2 < \omega < 2 + \ |\nu/\mu|$. In the case $\omega < 0$ we find that the frequency must be varied in the interval $2 - \nu/\mu < \omega < 0$, with $\nu/\mu > 2$. Taking into account that ω is defined by Eq. (14.6), one can easily derive restriction on parameters for the existence of plane waves at special points of k-space: at $k = 0$ (unstaggered solution) and at $k = \pi$ (staggered solution). For the staggered solution we find the restriction $\delta \leq 2\alpha$, while for the unstaggered $k = 0$ solution we find that $\nu(2\alpha + \delta)/\gamma \leq 4$ must be satisfied.

To analyze MI in Eq. (14.5) we look for solutions of the form

$$\phi_n(z) = (A + \phi_n(z))\exp(i(kn - \omega z)), \phi \ll A. \tag{14.7}$$

By substituting into Eq. (14.5) we get

$$i\phi_{n,t} + (1 - i\alpha)\left(\phi_{n+1}e^{ik} + \phi_{n-1}e^{-ik} - 2\cos(k)\phi_n\right) + (\nu - i\gamma)\frac{A^2}{\left(1+\mu A^2\right)^2}\left(\phi_n + \phi_n^*\right) = 0. \tag{14.8}$$

By looking for solutions of Eq. (14.8) of the form

$$\phi_n = Be^{i(Qn-\Omega t)} + C^* e^{-i(Qn-\Omega^* t)}, \tag{14.9}$$

with B, C, Ω complex numbers, one readily obtains the following dispersion relation is obtained

$$\Omega^2 - \Lambda_1\Omega - \Lambda_2 = 0, \tag{14.10}$$

where

$$\Lambda_1 = 2(2S + i(2\alpha\Delta + \gamma D)),$$
$$\Lambda_2 = 4\left(1+\alpha^2\right)\left(\Delta^2 - S^2\right) + 4D\Delta(\nu + \alpha\gamma) + 4i(\alpha\nu - \gamma)DS, \tag{14.11}$$

and

$$\Delta = \cos(k)(\cos(Q) - 1), D = \frac{A^2}{\left(1+\mu A^2\right)^2}, S = \sin(k)\sin(Q).$$

From these equations the MI gain $g(Q,k) = \mathrm{Im}[\Omega(Q,k)]$, is readily obtained as

$$g(Q,k) = \left| (2\alpha\Delta + \gamma D) + \frac{1}{\sqrt{2}}\sqrt{-F + \sqrt{G^2 + F^2}}\right|, \tag{14.12}$$

with the functions F, G given by

$$F = \left(4S^2 - (2\alpha\Delta + \gamma D)^2\right) + 4\left(1+\alpha^2\right)\left(\Delta^2 - S^2\right) + 4D\Delta(\nu + \alpha\gamma),$$
$$G = 4S\alpha(2\Delta + \nu D). \tag{14.13}$$

In Fig. 14.5 we show typical dependence of the MI gain on wavevectors Q, k for the focusing case. Notice that the white open regions visible in the figures correspond to the lines $k = \pm\cos^{-1}\left(\frac{\gamma+\delta\mu}{2\alpha\mu}\right) + \pi$ on which the wavevector k is not defined (see Eq. (14.6)). From this analysis the existence of nonlinear localized and extended solutions of Eq. (14.5) is expected. In the next section we shall confirm the existence of dissipative solitons and cnoidal wave solutions by providing few exact solutions and by investigating their stability by means of numerical integrations.

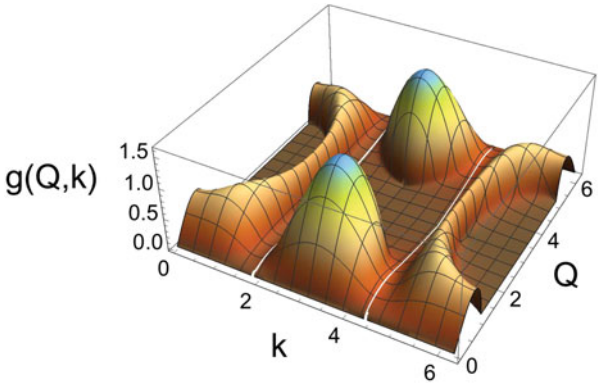

Fig. 14.5 MI gain $g(Q, k)$ in Eq. (14.12) versus wavenumbers Q, k for parameter values $\nu = -3$, $\mu = 1$, $\alpha = 0.01/3$, $\delta = -0.01$, $\gamma = 0.012$. Reprinted from Ref. [18]

14.5 Exact Dissipative Discrete Soliton Solutions

Exact dissipative discrete soliton solutions of different types were obtained in [18] by assuming specific ansatzes that involve elliptic functions [50]. Few of them are listed below.

(i) Single dissipative discrete soliton. It can be search in the form

$$\psi_n = \frac{\sinh(\beta)}{\cosh(\beta n)} e^{-i\omega z}. \tag{14.14}$$

Using the relation

$$\operatorname{sech}(a+\beta) + \operatorname{sech}(a-\beta) = 2\frac{\cosh(a)\cosh(\beta)}{\cosh^2(a) + \sinh^2(\beta)}, \tag{14.15}$$

we obtain that it is the exact solution of Eq. (14.5) if

$$\beta = \cosh^{-1}\left(\frac{\gamma}{2\alpha}\right), \omega = -\frac{\gamma}{\alpha}, \mu = 1, \omega = -\nu, \gamma = -\delta. \tag{14.16}$$

Nonlinear periodic solution. We assume the ansatz form

$$\psi_n = \frac{\mathrm{sn}(\beta, m)}{\mathrm{cn}(\beta, m)} e^{i\omega z} \mathrm{dn}(\beta n, m). \tag{14.17}$$

Taking into account the relation for the cnoidal functions

$$\mathrm{dn}(a+\beta) + \mathrm{dn}(a-\beta) = 2\frac{\mathrm{dn}(a)\mathrm{dn}(\beta)}{1 - m^2\mathrm{sn}^2(a)\mathrm{sn}^2(\beta)}, \tag{14.18}$$

we find that the solution parameters should be taken as:

$$\omega = \frac{\delta}{\alpha} = -\nu, \qquad \frac{\mathrm{dn}\beta}{\mathrm{cn}^2(\beta)} = \frac{\gamma}{2\alpha}, \qquad \gamma = -\delta. \tag{14.19}$$

A second type of the nonlinear periodic solution can be obtained from the ansatz

$$\psi_n = \sqrt{m}\,\frac{\mathrm{sn}(\beta, m)}{\mathrm{dn}(\beta, m)}\mathrm{cn}(\beta n)e^{i\omega z}. \tag{14.20}$$

Taking into account the relation

$$\mathrm{cn}(a+\beta) + \mathrm{cn}(a-\beta) = 2\frac{\mathrm{cn}(a)\mathrm{cn}(\beta)}{m\mathrm{cn}^2(a)\mathrm{sn}^2(\beta) + \mathrm{dn}^2(\beta)}. \tag{14.21}$$

we find that in this case the parameters must satisfy

$$\omega = \frac{\delta}{\alpha} = -\nu, \qquad \frac{\mathrm{cn}\beta}{\mathrm{dn}^2(\beta)} = \frac{\gamma}{2\alpha}, \qquad \gamma = -\delta. \tag{14.22}$$

We remark that for the periodic solutions the above parameter relations must be complemented with the periodicity condition $\beta N_p = X_p$ where N_p is the number of points per spatial period ($X_p = 2K(m)$ for Eq. (14.17) and $X_p = 4K(m)$ for Eq. (14.20), with $K(m)$ the complete elliptic integral of first kind).

The stability of the above exact solutions dissipative can be checked by direct numerical integrations of Eq. (14.5) taking as initial conditions the exact solutions with a small noise component added in order to accelerate the emergence of eventual instabilities. In the top left panel of Fig. 14.6 we show the time evolution of the periodic dissipative soliton trains in Eqs. (14.17) and (14.20). We see that while the *cn* solution remains stable over a long time, the *dn* solution display modulational instability at the propagation length $z \approx 200$ out of which two single humps dissipative solitons are created.

Note from the top right panel of Fig. 14.6 that the *dn* solution is unstable. This correlates with the fact that it can be seen as an uniform $k = 0$ background with superimposed a plane wave of wavenumber $Q = 0.628$ in correspondence of which the analysis of the previous section predicts instability with a MI gain of $\approx$0.561. Moreover, we see that out of the instability emerge bright solitons as it is expected for attractive (focusing) nonlinearity.

In the left bottom panel of Fig. 14.6 we show the propagation of the single hump dissipative soliton in Eq. (14.14) which is the limit of an infinite period ($m \to 1$) of the soliton trains in Eqs. (14.17) and (14.20). We see that this soliton is also very stable under long propagation distances. We remark that this soliton can exist only due to the perfect balance between the linear damping ($\delta < 0$) and the nonlinear amplification a condition which can be realized only in the stationary case.

As soon as one deviate from stationarity, as for example is the case when external forces or potentials try to put the soliton in motion, the soliton may become dynamically unstable under time evolution. To investigate this dynamical instability

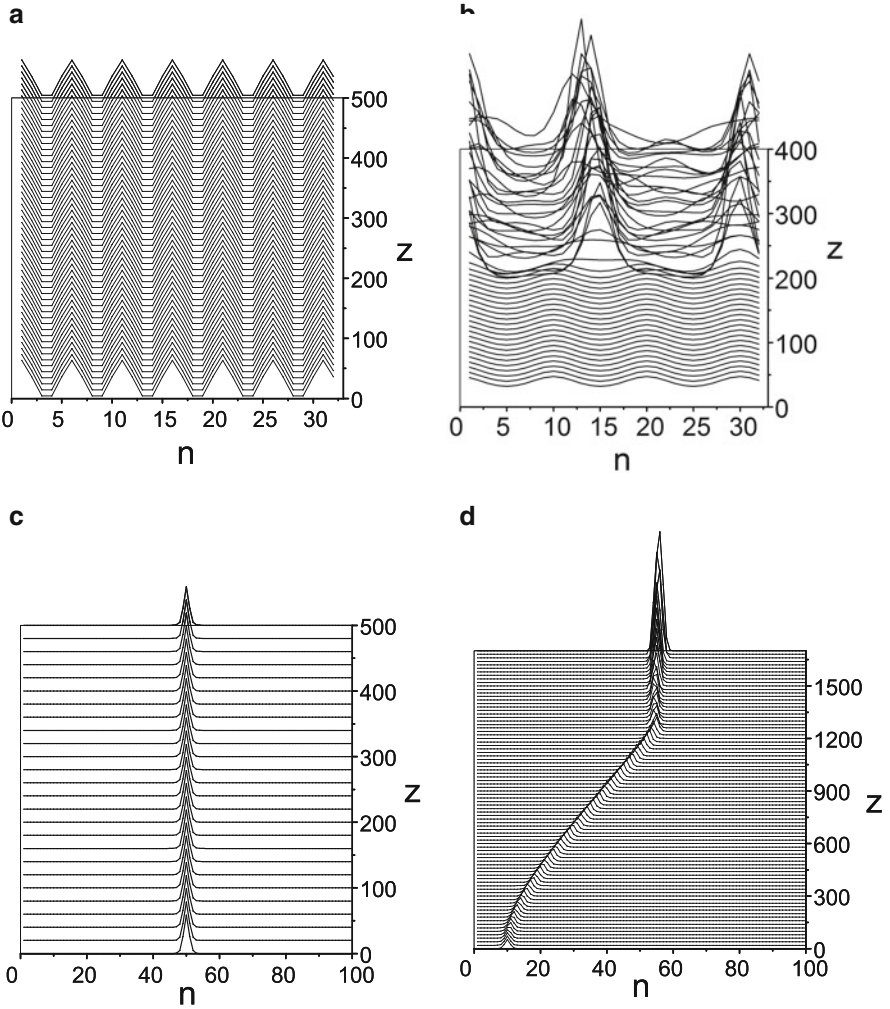

Fig. 14.6 **Top panels**. Z-propagation of the modulo square of the periodic dissipative soliton trains in Eq. (14.20) (top left) and in Eq. (14.17) (top right) as obtained from direct numerical integration of Eq. (14.5). Parameter values are fixed as in Eq. (14.22) with $\alpha = 0.001$, $m = 0.5$, $\beta = 2K(m)/N_p$ for the top left panel and as in Eq. (14.19) with $\alpha = 0.01$, $m = 0.32$, $\beta = 4K(m)/N_p$ for the top right panel. In both cases the number of lattice points per period is $N_p = 10$ and the total number of points along the line is 30. The cn-solution remain stable and dn-solution display MI. **Bottom left panel**. Time evolution of the modulo square of the dissipative soliton in Eq. (14.14) as obtained from direct numerical integration of Eq. (5), for parameter values $\gamma = 0.01$, $\nu = 3$, $\delta = -0.01$. Other parameters are derived from Eq. (14.16) as $\beta = 0.962424$, $\alpha = 0.01/3$. **Bottom right panel**. Time evolution of a dissipative soliton of Eq. (14.5) in presence of a linear ramp potential $\epsilon n \psi_n$ of strength $\varepsilon = 0.0002$. Other parameters are fixed as in bottom left panel. Reprinted from Ref. [18]

we add a linear ramp potential of the type $\epsilon n \psi_n$ in the right hand side of Eq. (14.5) which can be implemented in an optical context through curved optical fibers. The resulting dynamics of the dissipative soliton is depicted in the bottom right panel of Fig. 14.6. We see that, a part for small oscillations, the soliton can survives for a long time the acceleration process without significative changes in its shape. By reducing the strength of the linear potential, pinning phenomena can also become possible, this occurring in the figure at $z \approx 1200$. In this case the onsite symmetric soliton becomes pinned to a lattice site in a state for which the perfect balance between damping and amplification is not realized, this leading to the instability of the state.

14.6 Conclusion

In this chapter we have reviewed some of the linear and nonlinear properties of localized and extended dissipative states of the discrete complex Ginzburg-Landau equation. In particular, we discussed the linear band structure in presence of gain and loss and the existence of onsite and inter-site symmetric discrete solitons for specific and typical parameters. The modulational instability problem of the nonlinear plane waves in the presence of a saturable nonlinearity was also considered and analytical expressions for exact localized and periodic solitons in the (cnoidal waves) derived. It was shown that in the region of the parameter space where the MI gain is positive, generation of solitons and nonlinear periodic wave structures is possible. By taking specific parameters in these regions we found that while discrete soliton and cnoidal waves of cn-type are stable, solutions of dn-types on finite backgrounds are modulationally unstable. We also considered the effect of a linear ramp on a stable localized dissipative soliton and showed that the soliton could propagate under such a disturbance for relatively long distances.

References

1. Y. Kuramoto, Chemical Oscillations, Waves and Turbulence, (Springer, Berlin, 1984).
2. M. C. Cross and P. C. Hohenberg, Rev. Mod. Phys. **65**, 851 (1993).
3. P. Manneville, *Dissipative Structures and Weak Turbulence*, (Academic, San Diego, 1990).
4. I. S. Aranson and L. Kramer, Rev. Mod. Phys. **74**, 99 (2002).
5. N. Akhmediev and A. Ankiewicz (Eds.), *Dissipative Solitons*, Lect. Notes Phys. **661** (Springer, Berlin Heidelberg, 2005).
6. N. Akhmediev and A. Ankiewicz, in *Spatial solitons*, S. Trillo, W. Torruellas (Eds.) (Springer, Berlin Heidelberg New York, 2001), pp. 311–339.
7. N. R. Pereira and L. Stenflo, Phys. Fluids **20**, 1733 (1976).
8. L. A. Ostrovsky, in *Nonlinear deformation waves*, IUTAM Symposium, Tallin, U. Nigul, J. Engelbrecht (Eds.), (Springer, Berlin Heidelberg New York 1983), pp. 32–43.
9. F. Kh. Abdullaev, V. V Konotop, M. Salerno, and A. V Yulin, Phys. Rev. E **82**, 056606 (2010).
10. D. N. Christodoulides and R. I. Joseph, Opt. Lett. **13**, 794 (1988).
11. D. N. Christodoulides, F. Lederer and Y. Silberberg, Nature **424**, 817 (2003).
12. F. Kh. Abdullaev, A. A. Abdumalikov, and B. A. Umarov, Phys. Lett. A **305**, 371 (2002).

13. N. K. Efremidis, and D. N. Christodoulides, Phys. Rev. E **67**, 026606 (2003).
14. K. Maruno, A. Ankiewicz, and N. Akhmediev, Opt. Commun. **221**, 199 (2003); Phys. Lett. A **347**, 231 (2005).
15. U. Peschel, O. Egorov, and F. Lederer, Opt. Lett. **29**, 1909 (2004).
16. O. A. Egorov, F. Lederer, and Yu. S. Kivshar, Opt. Express **15**, 4149 (2007).
17. J. Garnier, F. Kh. Abdullaev, and M. Salerno, Phys. Rev. E **75**, 016615 (2007).
18. F. Kh. Abdullaev and M. Salerno, Phys. Rev. E **97**, 052208 (2018)
19. S. Wang, and H. G. Winful, Appl. Phys. Lett. **52**, 1174 (1998).
20. A. A. Tikhomirov, O. I. Kanakov, B. L. Altshuler, M. V. Ivanchenko, Eur. Phys. J. B **88**, 7 (2015).
21. H. Willaime, O. Cardoso and P. Tabeling, Phys. Rev. Lett. **67**, 3247 (1991).
22. A. Mohamadou, Journal of Modern Phys. **3**, 438 (2012).
23. M. Johansson, J. E. Prilepsky, and S. A. Derevyanko, Phys. Rev. E **89**. 042912 (2014).
24. AL. S. Kiselev, AN. S. Kiselev, and N.N. Rosanov, Optics and spectroscopy, **105**, 547 (2008).
25. N. V. Vysotina, N. N. Rosanov, V. E. Semenov, S. V. Feodorov, and A. N. Shatsev, Opt. Spectrosc. **105**, 436 (2008).
26. C. Mejia-Cortes, J. M. Soto-Crespo, R. A. Vicencio and M. I. Molina, Phys. Rev. A **83**, 043837 (2011).
27. F. Kh. Abdullaev, in *Dissipative solitons*, N. Akhmediev and A. Ankiewicz (Eds.), Springer-Verlag (2005), pp. 50–60.
28. J. Cuevas, J. C. Eilbeck, and N. I. Karachalios, Discr. and Contin. Dynam. Systems, **21**, 445 (2008).
29. M. Stepic, C. E. Ruter, D. Kip, A. Maluckov, and L. Hadzievski, Opt. Commun. **267**, 229 (2006).
30. F. Kh. Abdullaev, A. Bouketir, A. Messikh, and B. A. Umarov, Physica D **232**, 54 (2007).
31. B. Baizakov, A. Bouketir, A. Messikh, and B. A. Umarov, Phys. Rev. E **79**, 046605 (2009).
32. A. Khare, K. O. Rasmussen, M. Salerno, M. Samuelsen, and A. Saxena, Phys. Rev. E **74**, 16607 (2006).
33. R. Conte and K. W. Chow, J. Non. Math. Phys. **15**, 398 (2008).
34. L. Hadzievski, A. Malukov, M. Stepic, and D. Kip, Phys. Rev. Lett. **93** 033901 (2004); Phys. Rev. E **69**, 066618 (2004).
35. R. A. Van Gorder, A. L. Krause, F. Brosa Planella, A. M. Burton, Ann. Physics **396**, 397 (2018).
36. S. Champeaux and L. Bergé, Phys. Rev. E **71**, 046604 (2005).
37. S. Champeaux, L. Bergé, D. Gordon, A. Ting, J. Peãno, and P. Sprangle, Phys. Rev. E **77**, 036406 (2008).
38. N. W. Ashcroft, N. D. Mermin, Solid State Physics (Saunders Collrge, Philadelphia, 1975).
39. K. Otsuka, *Nonlinear dynamics in optical complex systems*, (KTK Scientific Publishers, Tokyo, 1999).
40. E. A. Ultanir, G. I. Stegeman, and D. N. Christodoulides, Opt. Lett. **29**, 845 (2004).
41. A. Trombettoni and A. Smerzi, Phys. Rev. Lett. **86**, 2353 (2001).
42. F. Kh. Abdullaev, B. B. Baizakov, S. A. Darmanyan, V. V. Konotop, and M. Salerno, Phys. Rev. A, **64**, 043606 (2001).
43. V. Konotop and M. Salerno, Phys. Rev. A **65**, 021602(R) (2002).
44. M. Salerno, Laser Physics, Vol. 15, No. 4, pp. 620 (2005).
45. F. Kh. Abdullaev, S. A. Darmanyan, and J. Garnier, Prog. in Optics, **44**, 31 (2004).
46. Y. S. Kivshar and M. Salerno, Phys. Rev. E **49**, 3543 (1994); **44**, 31 (2002).
47. J. Meier, G. I. Stegeman, D. N. Christodoulides, Y. Silberberg, R. Morandotti, H. Yang, G. Salamo, M. Sorel, and J. S. Aitchison, Phys. Rev. Lett. **92**, 163902 (2004).
48. M. Stepic, C. Wirth, C. E. Rueter, and D. Kip, Opt. Lett. **31**, 247 (2006).
49. N.N. Rosanov, *Spatial Hysteresis and Optical Patterns* (Springer, Berlin, 2002)
50. M. Abramowitz and I. A. Stegun (Eds.), *Handbook of Mathematical Functions*, (Dover, New York, 1965).

Chapter 15
Noise-Like Pulses in Mode-Locked Fiber Lasers

Grzegorz Soboń

Abstract The noise-like pulse (NLP) regime is one of the most fascinating phenomena occurring in mode-locked fiber lasers. Observed over two decades ago, still arouses the interest of scientists because of its complexity and chaotic nature. The Chapter reviews the most recent and important research on NLP lasers, with emphasis on the existing hypotheses explaining the formation mechanism of this phenomenon, the dynamics of noisy pulses, and the reported applications of NLP lasers.

Keywords Noise-like pulse lasers · Fiber lasers · Mode-locked laser · Nonlinear optics · Ultrafast phenomena

15.1 Introduction

Mode-locked fiber lasers might operate in a variety of regimes, depending on the chromatic dispersion and nonlinearities of the resonator. One can distinguish three fundamental regimes occurring in anomalous, normal and near-zero dispersion: conventional solitons, dissipative solitons (DS), and stretched-pulses [1], respectively. Among more exotic regimes one should mention like self-smilaritons [2], dissipative soliton resonances (DSR) [3], quartic solitons [4], and others. One of the interesting and not yet fully understood mechanisms is so-called noise-like pulse (NLP) generation, which may occur in the presence of both normal and anomalous dispersion.

In the NLP regime the laser generates sub-nanosecond-long packets of randomly spaced sub-picosecond pulses, with random and uncontrollable duration and peak power. The packets are equally spaced in time (resulting from the cavity round-trip time), like in conventionally mode-locked lasers. Nevertheless, the internal structure of the bunch is incoherent and unstable. Such laser behavior was firstly reported in

G. Soboń (✉)
Faculty of Electronics, Photonics and Microsystems, Wrocław University of Science and Technology, Wrocław, Poland
e-mail: grzegorz.sobon@pwr.edu.pl

M. F. S. Ferreira (ed.), *Dissipative Optical Solitons*, Springer Series in Optical Sciences 238, https://doi.org/10.1007/978-3-030-97493-0_15

1997 by Horowitz et al. [5]. Interestingly, the presence of NLPs was observed in many different types of lasers, regardless of their emission wavelength, cavity net dispersion, or mode-locking mechanism.

In general, the NLP regime manifests itself by several characteristic features: (1) A broad and smooth optical spectrum, very often even broader than the gain bandwidth of the medium (e.g., 120 nm width in an Erbium-doped fiber laser [6]); (2) Intensity autocorrelation of the pulse consisting of a very narrow peak (usually tens/hundreds of femtoseconds) located on top of a much longer pedestal (tens of picoseconds) [7]; (3) A radio-frequency (RF) spectrum with a significant noise pedestal and a significantly worse signal-to-noise ratio in comparison to a stable mode-locked laser [8]; (4) Output pulse train with a high pulse-to-pulse amplitude variation [9]. Usually, all these four features observed in a laser behavior suggest operation in the NLP regime. Due to the smooth and broad spectrum, owing a short coherence length, such sources have found several applications in optical imaging, spectroscopy, metrology, and nonlinear optics, which will be described later in this chapter.

Figure 15.1 illustrates examples of an optical spectrum (a), pulse autocorrelation (b), RF spectrum (c), and oscilloscope trace (d) of a laser generating NLPs. In this example, the laser was a Tm-doped fiber laser with a graphene-based saturable absorber [10]. The optical spectrum (a), has a broad and smooth shape (sharp

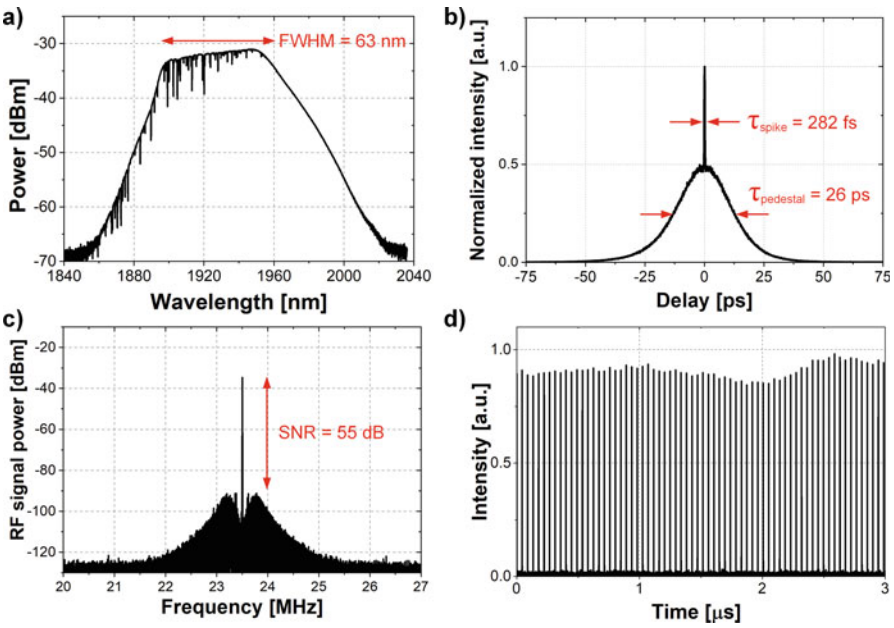

Fig. 15.1 Typical NLP laser output: (**a**) a very broad optical spectrum (the visible sharp dips result from the water vapor absorption lines in air); (**b**) pulse autocorrelation with an ultrashort coherent artifact on top of a wide pedestal; (**c**) radio frequency spectrum with a pronounced noise pedestal and low signal to noise ratio; (**d**) unstable pulse train with significantly varying pulse amplitudes

peaks represent the water absorption lines present in this spectral region). The full width at half maximum (FWHM) width is 63 nm, which is much broader than in typical, conventionally mode-locked, stable Tm-doped fiber lasers. The intensity autocorrelation shown in (b) consists of a broad pedestal with a sharp spike. Here, the FWHM widths of the pedestal and spike are 26 ps and 282 fs, respectively. There were multiple numerical and experimental studies on the autocorrelation characteristics of NLPs. The short spike (often called the "coherent artifact") originates from the short non-random coherent component of the unstable pulse train (i.e., the average duration of the ultrashort sub-pulses in the bunch), while the broad background results from the average overall bunch length [11]. It has been shown that increasing the number of sub-pulses in the NLP bunch leads to a smaller spike-to-pedestal intensity ratio in the AC trace, but without a noticeable change in their width [12]. One of the most characteristic features of NLP lasers is their spectrum in the radio frequency domain, containing a significant noise pedestal around the harmonics. As shown in Fig. 15.1c, the signal to noise ratio (SNR) in the RF signal is at the level of 55 dB, which is significantly less than in the case of stable mode-locking of fiber lasers (where SNR >70 dB is easily achievable at any dispersive regime [1, 8]). The origin of the noise visible in the RF spectrum is mostly the amplitude noise (i.e., fluctuation of the pulse amplitude) and frequency modulation due to the variation of the temporal spacing between the sub-pulses in the bunch. The amplitude fluctuation can be nicely visualized with a fast oscilloscope (d). In the presented case, the amplitude fluctuation is larger than 10% while observing only 60 consecutive pulses, while conventionally mode-locked lasers (even without any active stabilization) achieve output power stability better than 1%.

15.2 Examples of NLP Lasers

The design of a NLP laser is exactly the same as a typical, state-of-art mode-locked fiber laser. The majority of the reported NLP lasers were based on nonlinear polarization rotation (NPR) mode-locking mechanism, in which the cavity transmittance might be easily tuned. It is very often underlined that it is possible to achieve both stable mode-locking (e.g., soliton) and NLPs in the same cavity, but under different pumping conditions or different settings of the polarization controller/waveplates of the NPR. Figure 15.2 illustrates a Thulium-doped fiber laser mode-locked via NPR, which could operate in both dissipative soliton and NLP regime, as reported by Soboń et al. [8]. The laser consisted of the following components: a hybrid component which comprises an output coupler, isolator, and wavelength division multiplexer in one integrated package, a polarization controller (PC), a polarization beam splitter (PBS), the gain fiber (TDF), and a segment of dispersion compensating fiber (DCF). The laser was pumped by an amplified 1566 nm laser diode. The net dispersion of the resonator was normal (0.021 ps^2). At a pump power of 900 mW the laser generated dissipative solitons, with characteristic steep-edged

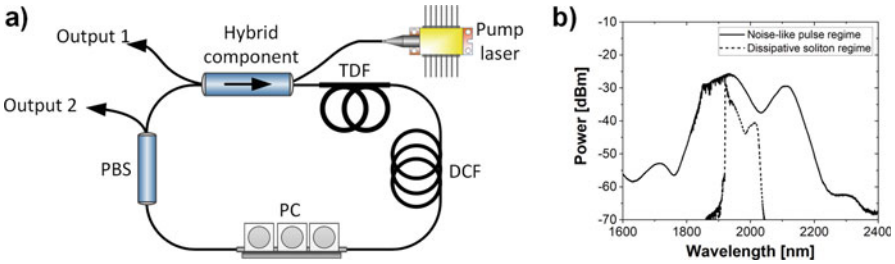

Fig. 15.2 Example of a Thulium-doped fiber laser operating in both dissipative soliton and NLP regime. Experimental setup (**a**) and generated spectra (**b**) [8]

optical spectrum, plotted with dashed line in Fig. 15.2b. If the pump power was increased to 1.1 W, the laser switched to NLP, and emitted extremely broad spectra (solid line in Fig. 15.2b), much broader compared to the DS regime.

Since the first demonstration in 1997 [5], there have been numerous reports on NLP generation from lasers with various cavity architectures. Table 15.1 summarizes the recent achievements in the field of NLP lasers, indicating the wavelength (and used gain medium), net cavity dispersion, mode-locking mechanism, the NLP pulse duration (both the spike and pedestal), and the spectral width. The summary takes into account lasers operating at the most common wavelengths: 1 μm, 1.55 μm, 2.0 μm and 2.1 μm, based on Ytterbium-, Erbium-, Holmium-, and Thulium-doped fibers as gain media, respectively. The NLP lasers reported in the literature used different mode-locking mechanisms: nonlinear polarization rotation (NPR), nonlinear optical loop mirror (NOLM), nonlinear amplifying loop mirror (NALM), and saturable absorbers: graphene, single-walled carbon nanotubes (SWCNTs), semiconductor saturable absorber mirror (SESAM), and molybdenum disulfide (MoS_2). Highlighting the most prominent and record-breaking results: the broadest optical spectrum (considering FWHM) generated from an NLP laser to date was 203 nm by X. Wang et al. [13]. The shortest spike duration of 14.5 fs was reported by R.Q. Xu [7], while the shortest pedestal of 920 fs was achieved by C. Xu et al. [14]. Amplification of NLPs was also reported, with the highest power so far of 13.1 W [15].

15.3 Mechanisms of NLP Formation

The summary shown in the previous section shows that NLPs can be obtained from lasers with completely different resonator architectures (ring, linear, figure-eight, both PM and non-PM), mode-locking mechanism (NPR, NOLM, NALM, saturable absorber: SESAM, graphene, CNTs, MoS_2), net cavity dispersion (anomalous, normal, near-zero), and gain medium (Yb-, Er-, Tm-, and Ho-doped fibers). Therefore, what is the mechanism responsible for such laser behavior? There are several hypotheses explaining this phenomenon, and they will be briefly introduced in this chapter.

Table 15.1 Examples of NLP lasers reported in the literature

No.	Gain medium and wavelength	Cavity dispersion	Mode-locking mechanism	Pulse duration	Spectral width	Refs.
1	Yb:fiber 1070 nm	Normal (+4.6 ps^2)	NPR	τ_{spike} = 100 fs $\tau_{pedestal}$ = 100 ps	35 nm	[16]
2	Yb:fiber 1070 nm	Near-zero	NPR	τ_{spike} = 30 fs $\tau_{pedestal}$ = 4.6 ps	131 nm	[17]
3	Yb:fiber 1100 nm	Normal (+1.5 ps^2)	NOLM	τ_{spike} = 100 fs $\tau_{pedestal}$ = 57 ps	165 nm	[18]
4	Yb:fiber 1100 nm	Normal	NPR	τ_{spike} = 92 fs $\tau_{pedestal}$ = 63 ps	42 nm	[19]
5	Er:fiber 1585 nm	Anomalous	NPR	τ_{spike} = 63 fs $\tau_{pedestal}$ > 50 ps	120 nm	[6]
6	Er:fiber 1560 nm	Anomalous	SESAM	τ_{spike} = N/A $\tau_{pedestal}$ = 62 ps	4.8 nm	[20]
7	Er:fiber 1570 nm	Normal (+0.33 ps^2)	SWCNT	τ_{spike} = N/A $\tau_{pedestal}$ = 34.8 ps	15.6 nm	[21]
8	Er:fiber 1560 nm	Anomalous	NPR	τ_{spike} = 450 fs $\tau_{pedestal}$ > 200 ps	15 nm	[22]
9	Er:fiber 1560 nm	Anomalous	NPR	τ_{spike} = 383 fs $\tau_{pedestal}$ = 51.8 ps	13 nm	[15]
10	Er:fiber 1590 nm	Anomalous	NPR	τ_{spike} = N/A $\tau_{pedestal}$ = 750 ps	203 nm	[13]
11	Er:fiber 1580 nm	Near-zero (+0.004 ps^2)	NPR	τ_{spike} = 92 fs $\tau_{pedestal}$ = 2 ps	75 nm	[23]
12	Tm:fiber 1955 nm	Anomalous	NPR	τ_{spike} = N/A $\tau_{pedestal}$ > 120 ps	60 nm	[24]
13	Tm:fiber 1925 nm (tunable)	Anomalous	SESAM	τ_{spike} = 378 fs $\tau_{pedestal}$ = 250 ps	18.9 nm	[25]
14	Tm:fiber 1977 nm	Anomalous	NPR	τ_{spike} = 260 fs $\tau_{pedestal}$ > 100 ps	15 nm	[26]
15	Tm:fiber 2017 nm	Anomalous (−13.09 ps^2)	NOLM	τ_{spike} = 498 fs $\tau_{pedestal}$ > 150 ps	20.7 nm	[27]
16	Tm:fiber 1948 nm	Normal (+1.63 ps^2)	SWCNT	τ_{spike} = N/A $\tau_{pedestal}$ = 150 ps	5.1 nm	[28]
17	Tm:fiber 1930 nm	Normal (+0.011 ps^2)	Graphene	τ_{spike} = N/A $\tau_{pedestal}$ = N/A	63 nm	[10]
18	Tm:fiber 2000 nm	Normal (+0.021 ps^2)	NPR	τ_{spike} = 130 fs $\tau_{pedestal}$ = 5 ps	120 nm	[8]
19	Tm:fiber 1900 nm	Anomalous	NPR	τ_{spike} = 227 fs $\tau_{pedestal}$ = 272 ps	23.46 nm	[29]
20	Tm:fiber 1990 nm	Anomalous (−0.991 ps^2)	NALM	τ_{spike} = 672 fs $\tau_{pedestal}$ = >200 ps	14.48 nm	[30]
21	Tm:fiber 2003.2 nm	Anomalous (−1.425 ps^2)	NPR	τ_{spike} = 406 fs $\tau_{pedestal}$ = >250 ps	23.2 nm	[31]

(continued)

Table 15.1 (continued)

No.	Gain medium and wavelength	Cavity dispersion	Mode-locking mechanism	Pulse duration	Spectral width	Refs.
22	Tm:fiber 1950 nm	Anomalous (-3.82 ps^2)	MoS_2	$\tau_{spike} = 2.7$ ps $\tau_{pedestal} = >160$ ps	4.2 nm	[32]
23	Tm:fiber 1993.6 nm	Anomalous (-0.711 ps^2)	NALM (PM)	$\tau_{spike} = 232$ fs $\tau_{pedestal} =$ N/A	32.6 nm	[33]
24	Ho:fiber 2133 nm	Anomalous	NPR	$\tau_{spike} = 3.5$ ps $\tau_{pedestal} = 370$ ps	18.3 nm	[34]
25	Ho:fiber 2075 nm	Anomalous	NOLM	$\tau_{spike} =$ N/A $\tau_{pedestal} > 200$ ps	15 nm	[35]

15.3.1 Effect of Cavity Birefringence

In their early work, Horowitz et al. explained the formation of unstable pulses by an interplay of large normal dispersion and high birefringence of the fiber cavity [5]. Their numerical calculations confirmed that strong birefringence induces a large polarization-dependent delay (PDD), which prevents from formation of stable ultrashort pulses. The only stable solution in such system is the formation of noise-like bursts composed of pulses with varying widths and peak intensities. Such explanation was somewhat confirmed by further experiments: note that most of NLPs are generated from long-cavity lasers (>10 m), usually based on nonlinear polarization rotation mechanism. An NPR-based laser always contains a polarization-sensitive component and a set of polarization controllers. Such arrangement favors the formation of a birefringent filter inside the cavity, which in combination with a large anomalous dispersion might lead to formation of noisy pulses. However, it was found later that the birefringence does not play a crucial role in the formation of NLPs.

15.3.2 Soliton Collapse Due to Reverse Saturable Absorption

A more general explanation was proposed in 2005 by D. Y. Tang et al. [36], valid for lasers with weak birefringence. The formation of NLPs might be caused by the soliton collapse effect combined with an effect called by the authors "positive cavity feedback" of the laser. The "positive cavity feedback" means that the losses of the cavity decrease with the peak power of the pulses, which is true in pulsed lasers with a saturable absorber. The "negative cavity feedback regime" means the opposite (and happens if there is reverse saturable absorption in the laser). A typical NPR transmittance curve has a sinusoidal shape and can be described by a function [37]:

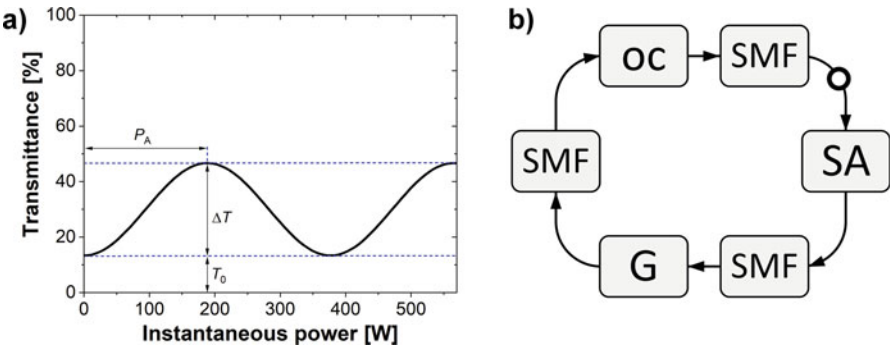

Fig. 15.3 (**a**) Typical transmittance curve of the NPR according to [37]; (**b**) typical model of a NLP fiber laser used for numerical modeling

$$T(P) = T_0 + \Delta T \sin^2\left(\frac{\pi}{2}\frac{P}{P_A} + \varphi\right), \tag{15.1}$$

where T_0 denotes the transmittance offset (linear transmittance of the NPR), ΔT is the modulation depth (difference between the minimum and maximum transmittance), P is the instantaneous peak power inside the cavity, φ is the phase bias, and P_A is a parameter which can be referred to saturable power, i.e., power required to fully saturate the NPR. An example of an NPR transmittance curve with zero phase bias is plotted in Fig. 15.3a. At low powers (i.e., lower than P_A), it behaves similarly to a conventional real saturable absorber (providing positive cavity feedback). Above the critical point (instantaneous power of P_A), the transmittance rolls over, resulting in a negative cavity feedback. Further increase of the pump power will eventually lead to peak power clamping and pulse break-up. The newly formed multiple pulses are then amplified and they break up again. Multiple of such processes occurring sequentially lead to the formation of a NLP. The phase bias might be introduced by changing the setting of the waveplates in the nonlinear polarization rotation setup. Therefore, in a properly designed cavity it is possible to switch between stable mode-locking and NLP by tuning the waveplates. A typical schematic of a modeled NLP laser for numerical simulation purposes is depicted in Fig. 15.3b. The laser roundtrip starts at an arbitrarily chosen point (here marked with a circle). The cavity consists of three main components: the saturable absorber (SA), the gain fiber (G) and the output coupler (OC), each separated with a segment of single-mode fiber (SMF).

The soliton collapse was predicted years earlier by Chernykh and Turitsyn [38]. They have found a solution of the Haus model [39], in which a quasi-stable train of pulses is formed due to the limited response of the saturable absorber at high pulse intensities. As an interplay of the gain, loss, saturable absorption, and a proper cavity phase delay bias, the solitons in the laser are constantly generated and collapsed. Under strong pumping, multiple of such process might coexist without any synchronization, which is observed as noise-like pulse operation [36]. Further

works confirmed the role of soliton collapse in the formation of NLPs [40]. Nevertheless, since a soliton is a phenomenon typical for all-anomalous dispersion lasers (as a balance of negative GVD and nonlinearities), the soliton collapse model still did not explain how NLPs are formed in all-normal dispersion lasers [8, 10, 16, 18, 19] where solitons do not exist.

Z. Cheng et al. [37] performed numerical simulations on dissipative soliton, dissipative soliton resonance and NLP generation in fiber lasers mode-locked with NPR. It was found that all three regimes might be obtained in exactly the same cavity configuration, while switching between different modes is possible only by tuning the polarization controller in the laser cavity (i.e., changing the transmittance of the saturable absorber) and the pump power (i.e., changing the laser gain). It was also observed that NLP can be generated under similar cavity conditions as DSR. However, NLP is the dominant regime in systems with high gain saturation energy, which activates the reverse saturable absorption and leads to pulse break-up [37]. This observation directly proves that the main mechanism behind NLP formation is related to peak power clamping of the pulse [41, 42] and its break-up caused by reverse saturable absorption at high intensities. The role of reverse saturable absorption and peak power clamping in NLP formation was later confirmed by another studies, in both anomalous and normal-dispersion fiber lasers [43, 44].

15.3.3 Raman-Driven NLP

Another but completely different mechanism of NLP formation can be observed in long-cavity lasers as a consequence of Stimulated Raman Scattering (SRS). The SRS can destabilize the laser leading to NLP generation, but might also assist in obtaining ultra-broad bandwidths.

The phenomenon of Raman-assisted NLP formation was firstly observed and reported by C. Aguergaray et al. in 2013 [45] in an 200-m-long ytterbium-doped fiber mode-locked laser. They have shown that the output of the laser might be destabilized by the emergence of a frequency-downshifted Stokes signal, leading to the formation of NLPs. The Stokes signal present in the spectrum is downshifted by 13 THz from the pump and originates from SRS, which is additionally strengthened by the amount of single-mode fiber in the cavity (200 m). Right after the demonstration of the presented Yb-doped fiber laser, Raman-induced NLPs were observed in an Er-doped fiber laser with anomalous dispersion as well [46]. Proper cavity design with the use of optical fibers favoring SRS led to various record-breaking results in terms of spectral bandwidth (like 200 nm-broad NLP generation by X. Wang [13]). The bandwidth was maximized by a tailored cavity design based on dispersive fibers supporting strong SRS.

SRS-assisted NLP generation usually requires long (>100 m) cavities. [13, 45–48], since the power threshold for SRS (P_{th}) directly depends on the fiber length, according to formula [49]:

$$P_{\text{th}} = \frac{16 A_{\text{eff}}}{g_{\text{R}} L_{\text{eff}}}, \tag{15.2}$$

where A_{eff} is the effective mode area of the fiber, g_{R} is the Raman gain coefficient, and L_{eff} is the effective length of the optical fiber. However, in the presence of high gain and small mode-field area fibers it is possible to obtain broadband SRS-assisted NLP generation even without any specialty fibers or additional SMF. For example, 61 nm broad spectra were generated from an Yb-doped fiber laser with an all-normal dispersion cavity [50], based on standard single-mode fibers, with only 11.7 m length.

15.3.4 NLP Formation in Amplifiers

Interestingly, noise-like pulses may be formed not only in oscillators but also in amplifiers [7, 51]. This very intriguing and non-intuitive phenomenon was firstly reported in 2018 [7] and is also related to SRS and Stokes wave generation. In the experiment done by R.-Q. Xu et al., a conventional Yb-doped fiber amplifier was seeded by a ring-cavity Yb-doped fiber laser. The seed operated in the all-normal dispersion regime, and generated dissipative solitons at 1036 nm wavelength with approx. 12 ps duration. When these dissipative solitons were injected into the amplifier, pulse break-up into NLPs was observed. The autocorrelation of the generated pulse had a very narrow coherent spike of 108 fs on top of a 19.5 ps envelope. The pulses were afterwards compressed down to 14.5 fs and 3.7 ps spike and pedestal duration, respectively. A very detailed mathematical description of the transformation of dissipative solitons into noise-like pulses during amplification is provided in [7]. The formation of NLPs is connected with the generation of a noisy Stokes wave during nonlinear amplification of the 1036 nm seed pulses. The Stokes wave originates from white noise, which later evolves into spontaneously scattered Raman noise and is amplified into pulse bundles. These bundles collapse into sub-pulses forming a NLP. Interestingly, the NLPs might be easily compressed using a standard grating-based compressor. Further studies have shown the possibility of pedestal compression down to 920 fs [51].

15.4 Dynamics, Coherence and Stability of NLP Lasers

Typical characterization techniques like optical spectrum analysis or intensity autocorrelation measurements provide only averaged information about the spectral shape and temporal profile of NLPs. They do not give any insight into the statistics and dynamics of the NLP generation process. Investigation of so-called “shot-to-shot” dynamics of NLPs was the subject of several numerical [52] and experimental

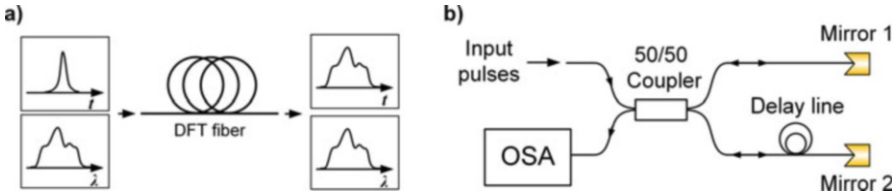

Fig. 15.4 Two experimental techniques allowing for direct characterization of NLP dynamics and coherence: (**a**) the dispersive Fourier transform for shot-to-shot retrieval of the spectral shape, (**b**) unequal-path Michelson interferometer for pulse-to-pulse coherence measurement

studies [9, 22, 53]. Measurements of real-time fluctuations of NLPs generated from fiber lasers have provided significant insights into fundamental aspects of NLP dynamics, statistics, and coherence.

A very convenient method of investigating the shot-to-shot spectral fluctuations of laser sources is the Dispersive Fourier Transform (DFT) technique, firstly proposed by D.R. Solli et al. to characterize of spectral fluctuations in nonlinear processes [54]. Later this technique was widely implemented for the characterization of shot-to-shot stability of supercontinuum sources [55–57] and mode-locked oscillators [22]. In the DFT setup, schematically depicted in Fig. 15.4a, the ultrashort pulses from a laser are transmitted through a highly dispersive medium, e.g., a long piece of optical fiber, and recorded in the time domain using a photodiode and a fast oscilloscope [55–57]. Due to the dispersion of the fiber, the pulses are significantly stretched (e.g., to several nanoseconds). The temporal profile of the stretched pulse directly corresponds to its spectral shape. Since an oscilloscope measurement is intrinsically single-shot, the DFT setup can be considered as an ultrafast, single-shot-resolved optical spectrum analyzer. The temporal signal can be afterward easily re-mapped to the wavelength domain by knowing the dispersion of the used stretching fiber. The resolution of the measurement is directly related to the stretching factor (i.e., more dispersion – better resolution). The DFT is, therefore a powerful tool for detailed diagnostics of the pulse-to-pulse spectral shape stability and statistics. However, DFT measurement provides only information about the temporal stability without any information about the phase coherence. The pulse-to-pulse phase coherence can be retrieved by another simple measurement technique based on so-called unequal-path Michelson interferometer, in which the interference between two consecutive pulses of the train is observed [22]. The setup illustrated in Fig. 15.4b comprises a simple fiber-based Michelson interferometer, in which one of the arms is longer by half of the pulse spacing. The interference is observed on the optical spectrum analyzer (OSA). The visibility of the amplitude modulation in the interference signal directly corresponds to the degree of coherence of the measured pulses [57, 58]. The fringe visibility function $V(\lambda)$ is defined as:

$$V(\lambda) = \frac{I_{\max}(\lambda) - I_{\min}(\lambda)}{I_{\max}(\lambda) + I_{\min}(\lambda)}, \tag{15.3}$$

where I_{max} and I_{min} are the maximum and minimum intensities in the spectral interference signal, respectively. Visibility equal to 1 suggests perfect degree of coherence, while no visible modulation suggests no phase coherence between two consecutive pulses generated by the laser.

Both techniques were used to analyze the coherence and shot-to-shot fluctuations of a noise-like pulse laser [22]. The measurements revealed absolutely no phase correlations between consecutive pulses in the NLP train. The NLP laser was compared to a conventionally mode-locked laser in the soliton regime, in which fringe visibility of >0.98 was observed across the entire spectrum, suggesting almost total pulse-to-pulse coherence. Figure 15.5 presents the DFT measurement results

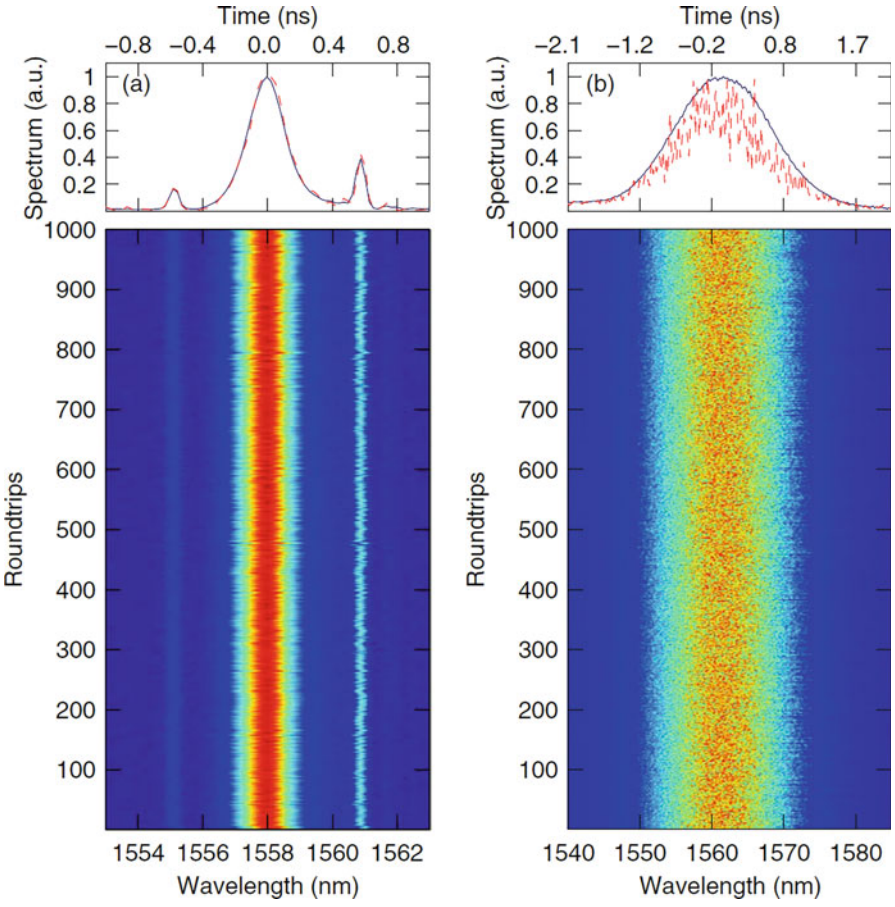

Fig. 15.5 Results of DFT analysis of a soliton (left) and NLP (right) laser performed by A. F. J. Runge et al. Top panel: solid curves represent the mean spectrum from the DFT measurement and the dashed curve shows a single-shot spectrum. Bottom panel: single-shot spectra over 1000 consecutive laser roundtrips plotted as a density map. Reprinted with permission from [22] © The Optical Society

obtained by A. F. J. Runge et al. [22]. In this measurement, 1000 consecutive pulses were analyzed when the laser operated in the soliton and NLP regime. It can be clearly seen that each individual NLP spectrum is structured, and the spectral shape varies from pulse to pulse. The red dashed line represents a single shot spectrum (picked up arbitrarily from the 1000 recorded shots). The mean spectrum calculated from the averaging of all 1000 DFT spectra is in good agreement with the measurement performed with the optical spectrum analyzer. However, if the OSA scan takes, for example, one second, then the measured spectrum is averaged over millions of pulses (assuming a ~ MHz-level repetition rate). We can conclude that the OSA measurement is insufficient to characterize an NLP laser fully. A quantitative analysis done by A. F. J. Runge et al. revealed that the spectral with (defined as FWHM) of NLPs fluctuates 25 times more than the solitons.

A similar analysis, leading to the same observations, was performed by Lecaplain and Grelu [9]. Additionally, they extended their study to a more quantitative analysis of the spectral peak intensity distribution in the NLP train, depending on the net dispersion sign of the laser. Surprisingly, it was found that the statistical distributions are non-Gaussian, regardless of the dispersion regime of the laser. However, the histograms showing the peak spectral intensity distribution demonstrated a more substantial deviation from Gaussian statistics for the anomalous dispersion cavity. The obtained heavy-tailed statistics, exceeding the Gaussian distribution, suggests extreme fluctuations of the spectral peaks. Moreover, Lecaplain and Grelu suggested a clear relationship between the NLPs and rogue waves [59]. It is even suggested that such NLP events should be called "spectral rogue waves" [9]. Such behavior was later also confirmed numerically by Donovan [52].

The investigations presented above focused on the statistics or single-shot spectrum of the whole NLP bunch. The question is: what is the distribution of the ultrashort sub-pulses inside the bunch? O. Pottiez et al. proposed a new technique of statistical characterization of the internal structure of NLPs based on a so-called nonlinear optical loop mirror (NOLM) [53]. So far, NOLM has been used as an artificial saturable absorber for mode-locking of fiber laser, since it manifests a power-dependent transmission [60]. The study revealed a strongly asymmetric, heavy-tailed distribution of the peak intensity of the ultrashort sub-pulses. This suggests the existence of highly-intense sub-pulses in the NLP bunch, which confirms the connection between NLPs and rogue waves.

From the presented research on the dynamics of NLP lasers, we can conclude that: (1) the spectral intensity distribution in the NLP wave packet is randomized and unstable, and the distribution of the peak intensity represents a non-Gaussian statistics, regardless of the cavity dispersion regime; (2) some of the NLP events might be considered as optical rogue waves; (3) the internal structure of the NLP bunch is also non-uniform, and shows a non-Gaussian distribution of the peak intensities inside the bunch; (4) the NLPs are incoherent, and there is no fixed phase relationship between consecutive pulses in the train.

15.5 Applications of NLP Lasers

Despite the great number of reports on NLP lasers, they still did not find many real-life applications. The architecture of a NLP laser is exactly the same as any other mode-locked laser. The NLP state might be often obtained in the same cavity, sometimes as an unwanted side-effect. Significantly more real-life applications benefit from a stable mode-locked laser output, with well-defined, phase-coherent ultrashort pulses. Nevertheless, NLPs might be considered as a substitution of broadband ASE sources, Globars, or superluminescent sources in applications that do not require a high coherence or perfect pulse-to-pulse stability. These include microscopy, optical coherence tomography (OCT), fiber-based sensors, metrology, component testing, or Fourier-transform infrared spectroscopy (FTIR). For example, reported Tm-doped NLP sources around 2 μm [8, 10, 23–33] nicely overlap with the strong absorption bands of trace gases like NO, H_2O, NH_3, CO_2 and HCl, while 1.55 μm Er-doped NLP lasers might be used for targeting CO_2, HCN, or C_2H_6. This paragraph summarizes the recent reports on applications of NLP lasers.

15.5.1 Metrology

In [61], Keren and Horowitz presented a method for real-time interrogation of fiber Bragg gratings (FBGs) using a NLP laser, based on low-coherence spectral interferometry. The laser source delivered NLPs with 70 nm of bandwidth and a pulse bunch duration of 2 ns. The method enables the detection of non-uniform regions inside tested gratings and characterization of both uniform and chirped gratings. Later, the same NLP source was used for optical data storage and reconstruction in optical fibers [62], with the predicted maximum theoretical reconstruction rate of 10 Tbit/s, and for real-time monitoring of the temperature profile in an optical fiber [63].

15.5.2 Spectroscopy

NLP lasers have also been used for laser-induced breakdown spectroscopy (LIBS). It is a spectroscopic technique that enables non-contact measurement of atomic composition of different materials (e.g., iron ores, chemicals, archeological artifacts, etc.). In [64], the authors used an Yb-doped fiber laser delivering 70 ps noise-like clusters, consisting of 50–100 fs-short sub-pulses, with 35 nm of spectral bandwidth centered at 1070 nm. The laser was successfully used in a LIBS spectrometer for the determination of the chemical composition of metals (brass, copper, aluminum alloys) and rocks [64] with excellent sensitivity using a low pulse energy (320 nJ).

15.5.3 Spectral Broadening and Supercontinuum Generation

Supercontinuum generation is a phenomenon in which an interplay of multiple nonlinear effects occurring in the medium (like self-phase modulation and four-wave mixing) causes significant spectral broadening of the input light. One of the most straightforward approaches is to use highly nonlinear optical fibers as medium and ultrashort (femtosecond) pulses as pump light. NLPs, despite their varying length and unstable amplitude, can be used for the generation of broadband, incoherent supercontinuum in optical fibers [23, 65–69], leading to significant spectral broadening even up to one octave width [68].

J. C. Hernandez-Garcia et al. [65] studied the spectral broadening of 50-nm-wide noise-like pulses generated from an Er-doped fiber laser, after propagation in long segments of single-mode fiber. They observed the generation of a continuum spanning up to 1750 nm. Next, A. Zaytsev et al. demonstrated SC generation by NLPs originating from an Yb-doped fiber laser operating at 1070 nm. The NLPs were propagating through a 100 m-long segment of single-mode fiber with normal dispersion, resulting in a flat SC spanning over 1050–1250 nm [66]. Much wider spectral coverage was achieved using highly nonlinear fibers (HNLFs) instead of SMFs. S.-S. Lin et al. pumped a 1-m long HNLF with noise-like pulses from an Erbium-doped fiber laser with 202 mW of average power. As a result, supercontinuum spanning from 1200 to 2100 nm was generated [67] (see Fig. 15.6).

In further experiments, the power of the NLPs was boosted to 13 W via two-stage amplification, which enabled the generation of SC spanning from 950 to 2500 nm and 3.62 W of average power [69]. Interestingly, the SC width obtained with NLP pumping was comparable to that obtained while pumping using well-defined, stable pulses.

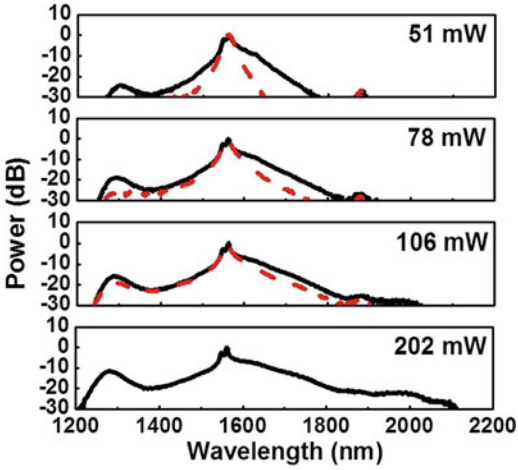

Fig. 15.6 Optical spectra of supercontinuum generated in a highly nonlinear fiber pumped by amplified NLPs, measured at different power settings. (Reprinted with permission from [67] © The Optical Society)

15.5.4 Optical Coherence Tomography

Optical coherence tomography (OCT) is a technique that uses low-coherence light sources for optical imaging of scattering media, e.g., biological samples. So far, a variety of light sources were used for OCT, e.g., superluminescent diodes [70], supercontinuum [71, 72] or Fourier-domain mode-locked lasers (FDMLs) [73, 74]. The low coherence and broad spectral coverage of NLP sources make them useful in OCT, as demonstrated by C.-L. Pan et al. [75, 76]. In their experiment, NLPs from an Yb-doped fiber laser with an average power of 200 mW were amplified to 4.5 W and launched into a 50-m-long piece of standard SMF. A flat SC at central wavelength of 1320 nm with a spectral bandwidth of 420 nm and average power of 560 mW was generated. Such pulses were then used to image different biological samples using the spectral-domain OCT (SD-OCT) technique with a theoretical axial resolution limit of 1.8 μm [75]. The performance was comparable to that obtained with a commercially-available swept-source OCT (SS-OCT) system [76].

15.5.5 Nonlinear Microscopy

A 1.3 μm NLP source based on cascaded Raman scattering was used for photoluminescence measurements [47]. The laser delivered NLPs with either 1212.1 or 1304.2 nm central wavelength and 106.1 and 108.5 nm of bandwidth, respectively. The duration of the coherent spikes were 174 and 167 fs, respectively. Due to the near-infrared wavelength, the source enabled three-photon absorption (3PA) luminescence measurement of the $CH_3NH_3PbBr_3$ perovskite with improved penetration depth compared to one-photon absorption [47].

15.6 Summary

The noise-like pulse regime is undoubtedly one of the most fascinating and surprising regimes occurring in mode-locked fiber lasers. Its uniqueness comes from the fact that it might be observed in almost every laser configuration, regardless the wavelength, dispersion, and mode-locking mechanism. Besides a number of reports on NLP lasers, there have been several comprehensive numerical and advanced experimental studies on the formation, dynamics, and statistics of NLPs, which enabled an almost complete understanding of this regime. Most of the studies treated the NLP bunch as a whole, but there were also studies on its internal structure. They confirmed the existence of highly-intense sub-pulses in the NLP bunch, which suggests a clear connection between NLPs and optical rogue waves. Despite a two-decade history of the NLP regime, there are still some aspects that need to be solved, e.g., the temporal structure of the sub-pulses (i.e., real-time measurement of the duration of single sub-pulses inside the NLP bunch).

References

1. R. Lindberg, J. Bogusławski, I. Pasternak, A. Przewłoka, F. Laurell, V. Pasiskevicius, J. Sotor, "Mapping Mode-Locking Regimes in a Polarization-Maintaining Er-Doped Fiber Laser," *IEEE J. Sel. Top. Quantum Electron.* 24, 1–9 (2018).
2. B. Oktem, C. Ülgüdür, and F. Ömer Ilday, "Soliton–similariton fibre laser," Nat. Photonics 4, 307–311 (2010).
3. E. Ding, Ph. Grelu, and J. N. Kutz, "Dissipative soliton resonance in a passively mode-locked fiber laser," Opt. Lett. 36, 1146–1148 (2011).
4. A. F. J. Runge, D. D. Hudson, K. K. K. Tam, C. M. de Sterke, A. Blanco-Redondo, "The pure-quartic soliton laser," Nat. Photonics 14, 492–497 (2020).
5. M. Horowitz, Y. Barad, and Y. Silberberg, "Noiselike pulses with a broadband spectrum generated from an erbium-doped fiber laser," Opt. Lett. 22, 799–801 (1997).
6. L. M. Zhao, D. Y. Tang, T. H. Cheng, H. Y. Tam, and C. Lu, "120 nm Bandwidth noise-like pulse generation in an erbium-doped fiber laser," Opt. Commun. 281, 157–161 (2008).
7. R. Q. Xu, J. R. Tian, and Y. R. Song, "Noise-like pulses with a 14.5 fs spike generated in an Yb-doped fiber nonlinear amplifier," Opt. Lett. 43, 1910–1913 (2018).
8. G. Sobon, J. Sotor, T. Martynkien, and K. M. Abramski, "Ultra-broadband dissipative soliton and noise-like pulse generation from a normal dispersion mode-locked Tm-doped all-fiber laser," Opt. Express 24, 6156–6161 (2016).
9. C. Lecaplain and Ph. Grelu, "Rogue waves among noiselike-pulse laser emission: An experimental investigation," Phys. Rev. A 90, 013805 (2014).
10. G. Sobon, J. Sotor, A. Przewolka, I. Pasternak, W. Strupinski, and K. Abramski, "Amplification of noise-like pulses generated from a graphene-based Tm-doped all-fiber laser," Opt. Express 24, 20359–20364 (2016).
11. J. Ratner, G. Steinmeyer, T. Chun Wong, R. Bartels, and R. Trebino, "Coherent artifact in modern pulse measurements," Opt. Lett. 37, 2874–2876 (2012).
12. X. Jin, L. Li, J. Luo, Y. Ge, Q. Zhang, and L. Zhao, "Numerical Study on Autocorrelation of Noise-Like Pulse in Fiber Lasers," Laser & Optoelectronics Progress 52, 121902 (2015).
13. X. Wang, A. Komarov, M. Klimczak, L. Su, D. Tang, D. Shen, L. Li, and L. Zhao, "Generation of noise-like pulses with 203 nm 3-dB bandwidth," Opt. Express 27, 24147–24153 (2019).
14. C. Xu, J.-R. Tian, R. Xu, Y. Wu, L. Fan, J. Guo, and Y.-R. Song, "Generation of noise-like pulses with a 920 fs pedestal in a nonlinear Yb-doped fiber amplifier," Opt. Express 27, 1208–1216 (2019).
15. S.-S. Lin, S.-K. Hwang, and J.-M. Liu, "High-power noise-like pulse generation using a 1.56-μm all-fiber laser system," Opt. Express 23, 18256–18268 (2015).
16. B. Nie, G. Parker, V. V. Lozovoy, and M. M. Dantus "Energy scaling of Yb fiber oscillator producing clusters of femtosecond pulses," Opt. Eng. 53, 051505 (2013).
17. M. Suzuki, R. A. Ganeev, S. Yoneya, and H. Kuroda, "Generation of broadband noise-like pulse from Yb-doped fiber laser ring cavity," Opt. Lett. 40, 804–807 (2015).
18. H. Chen, S. Chen, Z. Jiang, and J. Hou, "0.4 μJ, 7 kW ultrabroadband noise-like pulse direct generation from an all-fiber dumbbell-shaped laser," Opt. Lett. 40, 5490–5493 (2015).
19. E. Aghayari and K. Jamshidi Ghaleh, "High-power supercontinuum generation by noise-like pulse amplification in Yb-doped fiber amplifier operating in a nonlinear regime," Appl. Opt. 58, 4020–4024 (2019).
20. P. Polynkin, A. Polynkin, D. Panasenko, N. Peyghambarian, M. Mansuripur, and J. Moloney, "All-fiber passively mode-locked laser oscillator at 1.5 μm with watts-level average output power and high repetition rate," Opt. Lett. 31, 592–594 (2006).
21. Y. Cui, "Bandwidth-tunable dissipative soliton and noise-like pulse in normal dispersion fiber laser with a dual-scale saturable absorber," J. Opt. 18, 105503 (2016).
22. A. F. J. Runge, C. Aguergaray, N. G. R. Broderick, and M. Erkintalo, "Coherence and shot-to-shot spectral fluctuations in noise-like ultrafast fiber lasers," Opt. Lett. 38, 4327–4330 (2013).

23. K. Qian, Z. Gu, J. Xu, X. Dong, W. Yu, Z. Yu, H. Liao, D. Ren, "Noise-like pulse erbium-doped fiber laser for supercontinuum generation," Optik 158, 215–219 (2018).
24. X. He, A.Luo, Q. Yang, T. Yang, X. Yuan, S.Xu, Q. Qian, D. Chen, Z. Luo, W. Xu, and Z. Yang, "60 nm Bandwidth, 17 nJ Noiselike Pulse Generation from a Thulium-Doped Fiber Ring Laser," Appl. Phys. Express 6, 112702 (2013).
25. Y. Mashiko, E. Fujita, and M. Tokurakawa, "Tunable noise-like pulse generation in mode-locked Tm fiber laser with a SESAM," Opt. Express 24, 26515–26520 (2016).
26. Q. Wang, T. Chen, B. Zhang, A. P. Heberle, and K. P. Chen, "All-fiber passively mode-locked thulium-doped fiber ring oscillator operated at solitary and noiselike modes," Opt. Lett. 36, 3750–3752 (2011).
27. J. Li, Z. Zhang, Z. Sun, H. Luo, Y. Liu, Z. Yan, C. Mou, L. Zhang, and S. K. Turitsyn, "All-fiber passively mode-locked Tm-doped NOLM-based oscillator operating at 2-μm in both soliton and noisy-pulse regimes," Opt. Express 22, 7875–7882 (2014).
28. Q. Wang, T. Chen, M. Li, B. Zhang1, Y. Lu, and K. P. Chen, "All-fiber ultrafast thulium-doped fiber ring laser with dissipative soliton and noise-like output in normal dispersion by single-wall carbon nanotubes," Appl. Phys. Lett. 103, 011103 (2013).
29. V. Voropaev, A. Donodin, A. Voronets, D. Vlasov, V. Lazarev, M. Tarabrin, and A. Krylov, "Generation of multi-solitons and noise-like pulses in a high-powered thulium-doped all-fiber ring oscillator," Sci Rep 9, 18369 (2019).
30. S. Liu, F.-P. Yan, L.-N. Zhang, W.-G. Han, Z.-Y. Bai, and H. Zhou, "Noise-like femtosecond pulse in passively mode-locked Tm-doped NALM-based oscillator with small net anomalous dispersion," J. Opt. 18, 015508 (2016).
31. S. Liu, F. Yan, Y. Li, L. Zhang, Z. Bai, H. Zhou, and Y. Hou, "Noise-like pulse generation from a thulium-doped fiber laser using nonlinear polarization rotation with different net anomalous dispersion," Photon. Res. 4, 318–321 (2016).
32. P. Wang, D. Hu, K. Zhao, L. Jiao, X. Xiao, and C. Yang, "Dissipative rogue waves among Noise-Like pulses in a Tm fiber laser mode locked by a monolayer MoS_2 saturable absorber," IEEE J. Sel. Topics Quantum Electron. 24, 1800207 (2018).
33. M. Michalska, and J. Swiderski, "Noise-Like Pulse Generation Using Polarization Maintaining Mode-Locked Thulium-Doped Fiber Laser With Nonlinear Amplifying Loop Mirror," IEEE Photonics J. 11, 1504710 (2019).
34. G. Liu, K. Yin, L. Yang, Z. Cai, B. Zhang, and J. Hou, "Noise-like pulse generation from a Ho-doped fiber laser based on nonlinear polarization rotation," Proc. SPIE 10619,1061908 (2018).
35. J. Wang, J. Han, J. He, C. Liao, and Y. Wang, "High-energy mode-locked holmium-doped fiber laser operating in noise-like pulse regime," Opt. Lett. 44, 4491–4494 (2019).
36. D. Y. Tang, L. M. Zhao, and B. Zhao, "Soliton collapse and bunched noise-like pulse generation in a passively mode-locked fiber ring laser," Opt. Express 13, 2289–2294 (2005).
37. Z. Cheng, H. Li, and P. Wang, "Simulation of generation of dissipative soliton, dissipative soliton resonance and noise-like pulse in Yb-doped mode-locked fiber lasers," Opt. Express 23, 5972–5981 (2015).
38. A. I. Chernykh and S. K. Turitsyn, "Soliton and collapse regimes of pulse generation in passively mode-locking laser systems," Opt. Lett. 20, 398–400 (1995).
39. H. A. Haus, "Theory of mode locking with a fast saturable absorber," J. Appl. Phys. 46, 3049 (1975).
40. S. Smirnov, S. Kobtsev, S. Kukarin, and A. Ivanenko, "Three key regimes of single pulse generation per round trip of all-normal-dispersion fiber lasers mode-locked with nonlinear polarization rotation," Opt. Express 20, 27447–27453 (2012)
41. Z. Dong, J. Tian, R. Li, Y. Cui, W. Zhang, Y. Song, "Conventional Soliton and Noise-Like Pulse Generated in an Er-Doped Fiber Laser with Carbon Nanotube Saturable Absorbers," Appl. Sci.10, 5536 (2020).

42. D. Y. Tang, L. M. Zhao, B. Zhao, and A. Q. Liu, "Mechanism of multisoliton formation and soliton energy quantization in passively mode-locked fiber lasers," Phys. Rev. A 72, 043816 (2005).
43. Y. Jeong, L. Alonso Vazquez-Zuniga, S. Lee, Y. Kwon, "On the formation of noise-like pulses in fiber ring cavity configurations," Opt. Fiber Technol. 20, 575–592 (2014).
44. X. Li, S. Zhang, M. Han, and J. Liu, "Fine-structure oscillations of noise-like pulses induced by amplitude modulation of nonlinear polarization rotation," Opt. Lett. 42, 4203–4206 (2017).
45. C. Aguergaray, A. Runge, M. Erkintalo, and N. G. R. Broderick, "Raman-driven destabilization of mode-locked long cavity fiber lasers: fundamental limitations to energy scalability," Opt. Lett. 38, 2644–2646 (2013).
46. T. North and M. Rochette, "Raman-induced noiselike pulses in a highly nonlinear and dispersive all-fiber ring laser," Opt. Lett. 38, 890–892 (2013).
47. J.-H. Lin, T.-Y. Liao, C.-Y. Yang, D.-G. Zhang, C.-Y. Yang, Y.-W. Lee, S. Das, A. Dhar, and M. Chandra Paul, "Noise-like pulse generation around 1.3-μm based on cascaded Raman scattering," Opt. Express 28, 12252–12261 (2020).
48. W.-C. Chang, J.-H. Lin, T.-Y. Liao, and C.-Y. Yang, "Characteristics of noise-like pulse with broad bandwidth based on cascaded Raman scattering," Opt. Express 26, 31808–31816 (2018).
49. G. P. Agrawal, Nonlinear Fiber Optics, 5th ed. (Academic Press, 2013).
50. D. Li, D. Shen, L. Li, H. Chen, D. Tang, and L. Zhao, "Raman-scattering-assistant broadband noise-like pulse generation in all-normal-dispersion fiber lasers," Opt. Express 23, 25889–25895 (2015).
51. C. Xu, J.-R. Tian, R. Xu, Y. Wu, L. Fan, J. Guo, and Y.-R. Song, "Generation of noise-like pulses with a 920 fs pedestal in a nonlinear Yb-doped fiber amplifier," Opt. Express 27, 1208–1216 (2019).
52. G. M. Donovan, "Dynamics and statistics of noise-like pulses in modelocked lasers," Physica D 309, 1–8 (2015).
53. O. Pottiez, R. Paez-Aguirre, J. L.Cruz, M. V.Andrés, E. A.Kuzin, "Statistical characterization of the internal structure of noiselike pulses using a nonlinear optical loop mirror," Opt. Commun. 377, 41–51 (2016).
54. D. R. Solli, G. Herink, B. Jalali, and C. Ropers, "Fluctuations and correlations in modulation instability," Nat. Photonics 6, 463–468 (2012).
55. K. Goda, and B. Jalali, "Dispersive Fourier transformation for fast continuous single-shot measurements," Nat. Photonics 7, 102–112 (2013).
56. T. Godin, B. Wetzel, T. Sylvestre, L. Larger, A. Kudlinski, A. Mussot, A. Ben Salem, M. Zghal, G. Genty, F. Dias, and J. M. Dudley, "Real time noise and wavelength correlations in octave-spanning supercontinuum generation," Opt. Express 21, 18452–18460 (2013).
57. K. Tarnowski, T. Martynkien, P. Mergo, J. Sotor, and G. Soboń, "Compact all-fiber source of coherent linearly polarized octave-spanning supercontinuum based on normal dispersion silica fiber," Sci. Rep. 9, 12313 (2019).
58. S. Kim, J. Park, S. Han, Y.-J. Kim, and S.-W. Kim, "Coherent supercontinuum generation using Er-doped fiber laser of hybrid mode-locking," Opt. Lett. 39, 2986 (2014).
59. D. R. Solli, C. Ropers, P. Koonath, and B. Jalali, "Optical rogue waves," Nature 450, 1054–1057 (2007).
60. Irl N. Duling III (Ed.), Compact Sources of Ultrashort Pulses (Cambridge University Press, 1995).
61. S. Keren and M. Horowitz, "Interrogation of fiber gratings by use of low-coherence spectral interferometry of noiselike pulses," Opt. Lett. 26 (2001) 328–330.
62. S. Keren, E. Brand, Y. Levi, B. Levit, M. Horowitz, "Data storage in optical fibers and reconstruction by use of low-coherence spectral interferometry," Opt. Lett. 27, 125–127 (2002).
63. V. Goloborodko, S. Keren, A. Rosenthal, B. Levit, and M. Horowitz, "Measuring temperature profiles in high-power optical fiber components," Appl. Opt. 42, 2284–2288 (2003).

64. G. J. Parker, D. E. Parker, B. Nie, V. Lozovoy, M. Dantus, "Laser-induced Breakdown Spectroscopy and ablation threshold analysis using a megahertz Yb fiber laser oscillator," Spectrochim. Acta B 107, 146–151 (2015).
65. J. C. Hernandez-Garcia, O. Pottiez, J. M. Estudillo-Ayala, "Supercontinuum generation in a standard fiber pumped by noise-like pulses from a figure eight fiber laser," Laser Phys. 22, 221–226 (2012).
66. A. Zaytsev, C.-H. Lin, Y.J. You, C.-C. Chung, C.L. Wang, C.L. Pan, "Supercontinuum generation by noise-like pulses transmitted through normally dispersive standard single-mode fibers," Opt. Express 21, 16056–16062 (2013).
67. S.-S. Lin, S.-K. Hwang, and J.-M. Liu, "Supercontinuum generation in highly nonlinear fibers using amplified noise-like optical pulses," Opt. Express 22, 4152–4160 (2014).
68. E. Aghayari and K. Jamshidi Ghaleh, "High-power supercontinuum generation by noise-like pulse amplification in Yb-doped fiber amplifier operating in a nonlinear regime," Appl. Opt. 58, 4020–4024 (2019).
69. K.-Y. Chang, W.-C. Chen, S.-S. Lin, S.-K. Hwang, and J.-M. Liu, "High-power, octave-spanning supercontinuum generation in highly nonlinear fibers using noise-like and well-defined pump optical pulses," OSA Continuum 1, 851–863 (2018).
70. D. Huang, E. A. Swanson, C. P. Lin, J. S. Schuman, W. G. Stinson, W. Chang, M. R. Hee, T. Flotte, K. Gregory, C. A. Puliafito, and J. G. Fujimoto, "Optical coherence tomography," Science 254, 1178–1181 (1991).
71. I. Hartl, X. D. Li, C. Chudoba, R. K. Ghanta, T. H. Ko, J. G. Fujimoto, J. K. Ranka, and R. S. Windeler, "Ultrahigh-resolution optical coherence tomography using continuum generation in an air–silica microstructure optical fiber," Opt. Lett. 26, 608–610 (2001).
72. Y. Wang, Y. Zhao, J. S. Nelson, Z. Chen, and R. S. Windeler, "Ultrahigh-resolution optical coherence tomography by broadband continuum generation from a photonic crystal fiber," Opt. Lett. 28, 182–184 (2003).
73. M. Wojtkowski, T. Bajraszewski, P. Targowski, and A. Kowalczyk, "Real-time in vivo imaging by high-speed spectral optical coherence tomography," Opt. Lett. 28, 1745–1747 (2003).
74. M. Wojtkowski, A. Kowalczyk, R. Leitgeb, and A. F. Fercher, "Full range complex spectral optical coherence tomography technique in eye imaging," Opt. Lett. 27, 1415–1417 (2002).
75. Y. You, C. Wang, P. Xue, A. Zaytsev, and C. Pan, "Supercontinuum Generated by Noise-like Pulses for Spectral-domain Optical Coherence Tomography," in CLEO: 2015, OSA Technical Digest (online) (Optical Society of America, 2015), paper JW2A.94.
76. C.-L. Pan, A. Zaytsev, Y.-J. You and C.-H. Lin, "Fiber-laser-generated Noise-like Pulses and Their Applications," in "Fiber Laser", M. Chandra Paul (Ed.) (InTech Open, 2016).

Chapter 16
Dissipative Rogue Waves

Lei Gao

Abstract In this chapter, the history and main characteristics of rogue waves in the oceans are introduced. Due to phenomenological and physical analogies between extreme events in optics and hydrodynamics, the concept of optical rogue waves is extended into optics, associated with a long-tailed intensity histogram in the long-wavelength range of fiber optical supercontinuum spectra. Then, we discuss the real-time techniques for observing optical rogue waves. Namely, the well-known dispersive-Fourier-transform-based ultrafast spectroscopy and the time magnifier based on space-time duality. Further, the optical rogue waves in dissipative systems that often referred as open systems far away from the thermodynamic equilibrium, are reviewed briefly, including ultrafast lasers, microresonators, extended systems, and optical polarization rogue waves. These dissipative optical systems can be described by the Ginzburg-Landau equations, and various dynamical processes of fluctuation, pulsing, bifurcation, turbulence, and chaos are expected to be observed. Finally, two possible interpretations, and the predictabilities of dissipative rogue waves are also discussed.

Keywords Rogue waves · Optical rogue waves · Dispersive Fourier transformation · Time-lens · Dissipative rogue waves · Ultrafast lasers · Microresonators · Optical polarization rogue waves · Breather · Soliton · Predictability

L. Gao (✉)
Key Laboratory of Optoelectronic Technology & Systems (Ministry of Education), Chongqing University, Chongqing, China
e-mail: gaolei@cqu.edu.cn

M. F. S. Ferreira (ed.), *Dissipative Optical Solitons*, Springer Series in Optical Sciences 238, https://doi.org/10.1007/978-3-030-97493-0_16

16.1 Introduction

16.1.1 Rogue Waves in the Oceans

Rogue waves (RWs) are known as extremely large amplitude waves, which propagate in open oceans. Such rare events emerge with unexpectedly large probabilities, deviating from the power law wave-amplitude statistics which are typical for random processes, and leave without a trace [1–7]. As depicted in Fig. 16.1, these events constitute water walls as high as 20–30 m, which impose a threat for ships and ocean liners. From both the matters of physics and industrial applications, huge efforts have been devoted to explore the rogue waves.

RWs can be experimentally identified by the presence of heavy-tailed statistics, typically L-shaped, describing the appearance of rare events [9]. Several models have been developed based on the weak nonlinear interactions between thousands of waves, through the nonlinear Schrödinger equations (NLSEs), where both numerical simulation and analytical solutions such as breathers or turbulence have been carried out. Different RWs mechanisms have been proposed so far: from the simple linear random superposition of independent weak waves, to nonlinear effects such as modulation instability (MI) and the subsequent formation of localized breathers. When the coherence of a physical system is deteriorated, RWs with diverse parameters may occur in different dimensions [10–12]. However, the steep profile during the extreme events seems to be too freak to be captured. Other efforts have been devoted to the experimental observations on the directional oceans or laboratory. The debate about the origin of rogue waves continues, and, in my opinion, it will be long as far as concerning the great gulf between the theory and experiments.

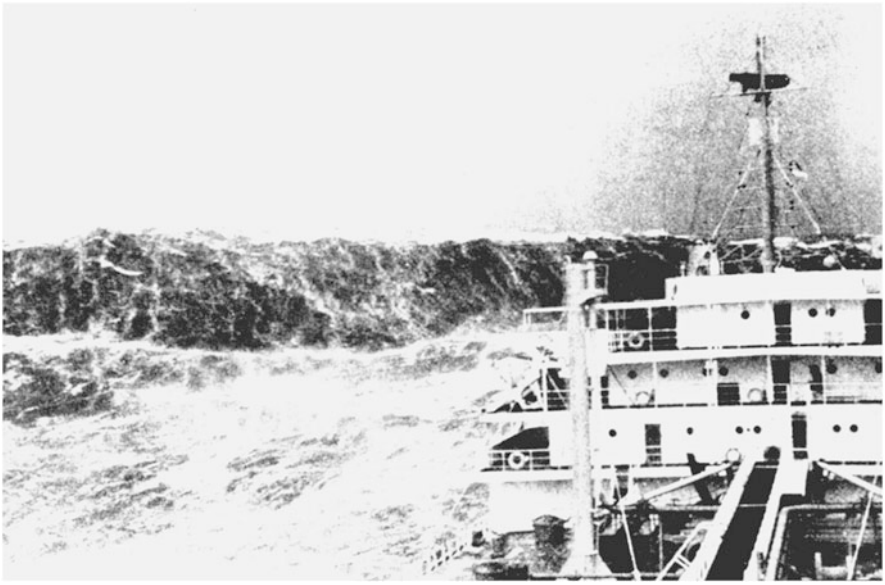

Fig. 16.1 Huge wave on the Bay of Biscay. (Reproduced from NOAA Photo Library) [8]

16.1.2 Introduction of Optical Rogue Waves

Given the harsh conditions, studying RWs in their natural environment is problematic. The term of RWs has been expanded to other domains. Examples include: the fluence profiles of multi-filaments, liquid helium, and high intensity pulses in supercontinuum generation in optical fibers [13–18]. In 2007, due to phenomenological and physical analogies between extreme events in optics and hydrodynamics, D. R. Solli et al. introduced the concept of optical RWs, associated with a long-tailed intensity histogram in the long-wavelength range of fiber optical supercontinuum spectra [14]. As shown in Fig. 16.2, using a real-time detection based on dispersive Fourier transformation (DFT), they observe optical RWs in soliton-fission supercontinuum based on a micro-structured optical fiber. Their results high light the energy coupling between the solitons and other wave packets, and the characteristic lifetime during the formation of optical RWs.

Since then, much effort has been dedicated to finding RW solutions of the nonlinear Schrödinger equation in different physical systems: various kinds of breathers have been proposed as examples of optical RWs [15, 19–21]. Recently, real-time detection techniques, such as the DFT and time-lens, have been utilized to identify the presence of coherent pulses with extremely high intensities. An abrupt phase change across the pulse profile was found to be associated with optical RWs [22, 23]. The presence of a RWs is identified by a trough-to-crest height larger than

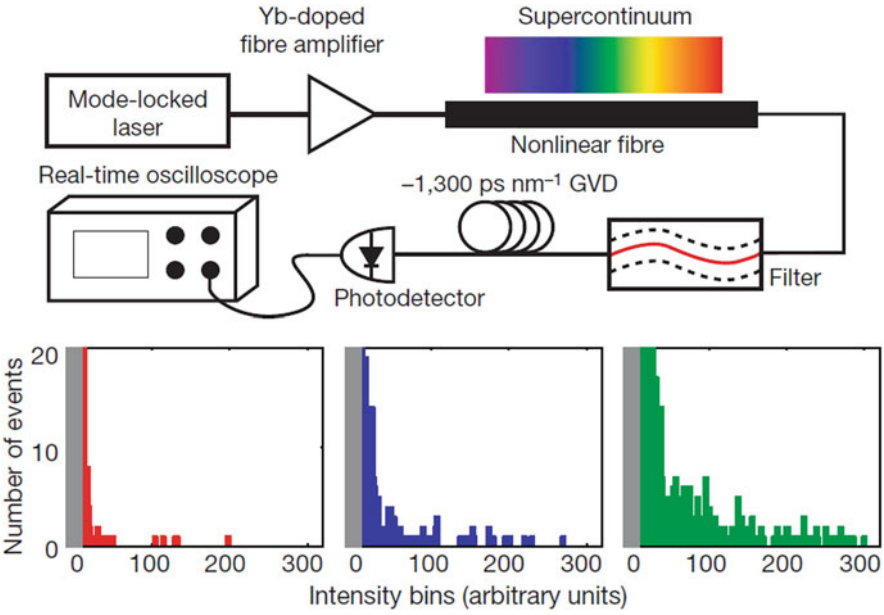

Fig. 16.2 (**a**) Schematic of experimental setup. (**b**) Histograms of filtered intensities for average power of 0.8μW (red), 3.2μW(blue), and 12.8μW(green) [14]

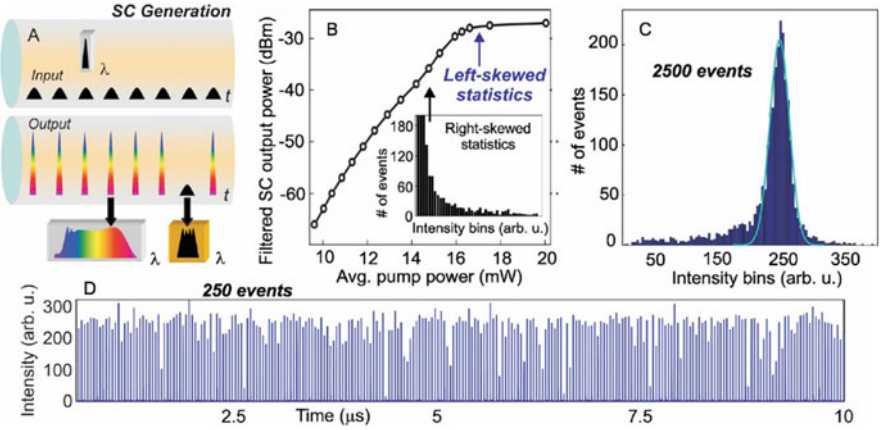

Fig. 16.3 The dark RWs in the depth of dark pulses [27]

2 times the significant wave height (SWH). Moreover, the occurrence of RWs in optics can be identified in different domains: for example, in the pulse intensity for the time domain [14], in the spectral width for the frequency domain [24], in the spatial intensity in a two-dimensional camera image [13, 25], the depth of dark pulses [26], and the presence of spectrally narrowband pulses with a right-skewed distribution [27]. One example is given in Fig. 16.3, where the concept of rogue rather than the intensities is taken seriously. For a comprehensive investigation of optical RWs, additional dimensions can be introduced.

16.1.3 Real-Time Techniques for Observing Optical Rogue Waves

For capturing the ultrafast and transient rogue waves, there are two fundamental challenges within any real-time techniques. One is the trade-off between the speed and the detection sensitivity of the optoelectronic detectors because fewer photons are collected during the short integration time [28]. The other is the trade-off between the measured dynamic range and the speed of the real-time analog-to-digital converter. The two shortcomings restrict the direct characterization of optical ultrafast pulses with durations in picosecond and sub-picosecond order. Specially, for these non-repetitive and transient RWs events, the insufficient sampling rate and detecting bandwidth distort the measured optical signals. Until now, two kinds of real-time characterization of ultrafast pulse have been well developed, namely, the dispersive-Fourier-transform-based ultrafast spectroscopy [29], and the time-lens-based time magnifier [30].

16.1.3.1 Dispersive-Fourier-Transform-Based Ultrafast Spectroscopy

The DFT technology stems from the spatiotemporal duality [31]: the transmission of a temporal pulse in a dispersive element with a sufficiently large dispersion is analogous to the diffraction of a beam passing through a lens in the far-field approximation. The frequency-domain spectral information of the pulse is thus mapped into the temporal pulse waveform, and the stretched light pulse has the same shape as the spectral intensity envelope, as shown in Fig. 16.4. According to NLSE, the amplitude envelope evolution of output pulse from the dispersion component without the consideration of gain and loss can be expressed by [32]:

$$|u(z,T)|^2 = \frac{1}{4\pi^2}\left|\int_{-\infty}^{+\infty} \tilde{u_s}\,(0,\omega-\omega_0)e^{i\frac{\beta_2 z_0}{2}\left(\omega-\omega_0-\frac{T}{\beta_2 z_0}\right)^2} d\omega\right|^2, \tag{16.1}$$

where $\tilde{u_s}$ represent the amplitude envelope of the tested device and pulse source, respectively. ω is the light frequency, ω_0 is the center frequency, β_2 is the second-order dispersion coefficient, z is the propagation distance, and T is the time in the reference frame of the pulse propagating with the group velocity given by T-$(\omega) = \beta_2 z(\omega - \omega_0)$ the intensity profile of the temporally dispersed pulse then becomes proportional to:

$$|u(z,T)|^2 = \frac{2}{\pi\beta_2 z}\left|\tilde{u_s}\left(0,\frac{T}{\beta_2 z}\right)\right|^2, \tag{16.2}$$

Therefore, the wavelengths and stretched time relation, $\Delta\tau = |D|z\Delta\lambda$, where D denotes the total amount of temporal dispersion, $\Delta\tau$ is the stretched time duration into which the optical spectrum is mapped. Via this technique the sub-picosecond pulses are stretched into nanoseconds. However, such real-time ultrafast spectroscopy technology can only obtain the spectrum information of a single pulse. It is impossible to clearly and accurately measure the time when the RWs appear.

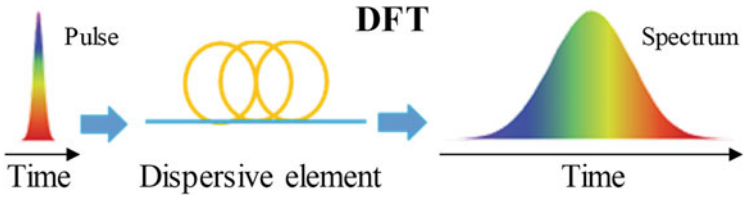

Fig. 16.4 Principle of dispersive Fourier transform

16.1.3.2 Time Magnifier

Inspired by space-time duality and temporal imaging [33], the narrow-band dispersion (time domain) of a plane-wave light in a dielectric medium exhibits a behavior similar to the paraxial diffraction (space) of a monochromatic beam in free space. Mathematically, the propagation distance in the space domain is a direct analog of group delay dispersion (GDD) in the time domain. The ideal time imaging system requires GDD to be independent of frequency. The following Fig. 16.5 shows the principle of time magnifier.

Analogous to the space-lens magnification system, in time-lens based time magnifier system, the temporal imaging condition satisfy the following formula [30]:

$$\frac{-1}{\varphi_1''} + \frac{1}{\varphi_2''} = \frac{1}{\varphi_f''}, \tag{16.3}$$

Where the φ_1'', φ_2'' and φ_f'' are the GDD of input output and time lens. Herein, the function of time-lens part of Fig. 16.6a is to induce quadratic spatial phase modulation to input pulse. Such the temporal phase modulation can be expressed as [30]:

$$\varnothing(t) = \frac{t^2}{2\varphi_f''}, \tag{16.4}$$

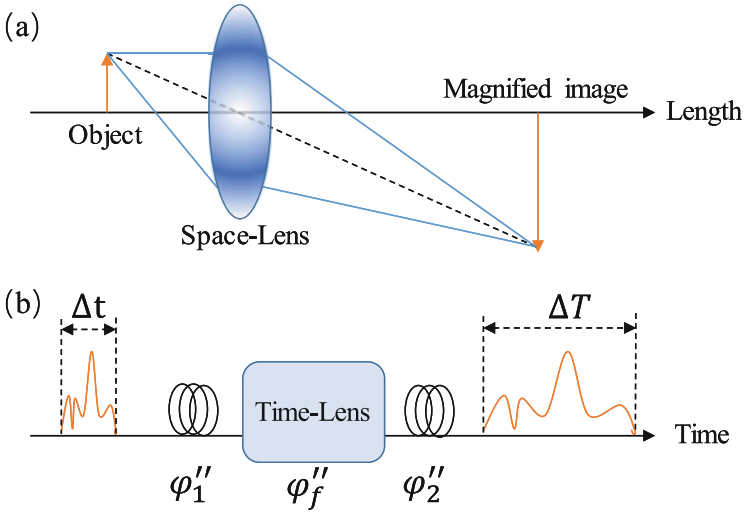

Fig. 16.5 Principle of time magnifier. (**a**) Spatial analog of time magnifier. (**b**) Schematic diagram of a time magnifier

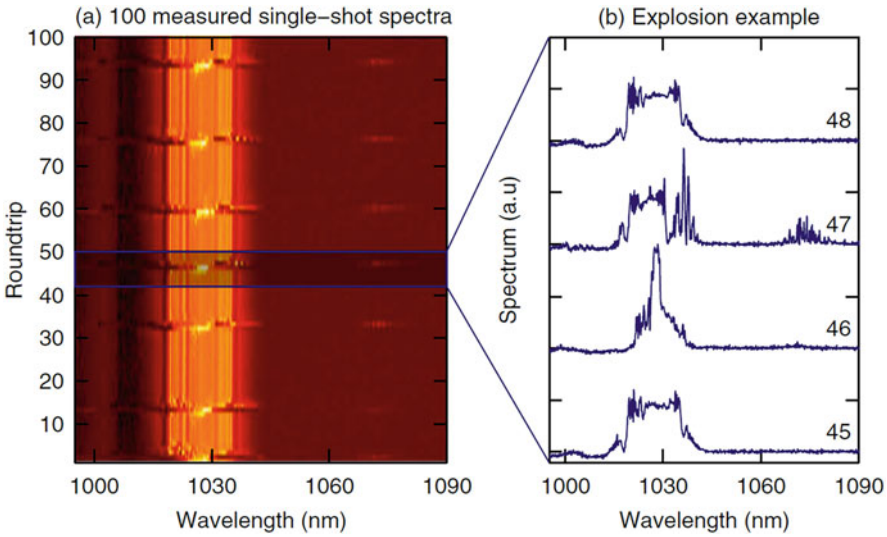

Fig. 16.6 (**a**) The single-shot spectra of 100 consecutive pulses with the laser operating in the transition regime. (**b**) Example spectra for a particular explosion event [40]. (Reprinted with permission from Ref. [40] © The Optical Society)

Where the focal GDD φ_f'' can be induced by phase modulator [34] or nonlinear parametric process [35]. Therefore, a magnifier ultrafast pulse replica will be generated from the input waveform with a magnification ratio:

$$M = \left|\frac{\varphi_2''}{\varphi_1''}\right|, \tag{16.5}$$

Eventually, combining a real-time oscilloscope and high-speed photodetector, the round-trip evolution of ultrafast temporal structures will be experimentally resolved at sub-ps resolution, and RWs can be identified [36], directly.

16.2 Dissipative Rogue Waves

16.2.1 Rogue Waves in Dissipative Systems

Considering both the fundamental and possible industrial applications, the RWs in optical systems have been under huge investigations. Examples include the MI, supercontinuum. All those freak events appear in the conservative and integrable systems, which can be described by the nonlinear Schrödinger equations.

In fact, all the real physical systems tend to be dissipative. A dissipative system is often referred as an open system that far away from the thermodynamic equilibrium,

while its balance can be sustained via exchanges of energy, matter, or entropy. Ultrafast laser system is a typical dissipative optical system, where sustained energy supply and dissipation factors, such as loss, are continuously undergo within the resonator. Together with the nonlinearity, dispersion, et al., such a kind of dissipative optical system can be described by the Ginzburg-Landau equations.

$$\frac{\partial A}{\partial z} = \left(\frac{g}{\omega_g^2} - j\frac{\beta_2}{2}\right)\frac{\partial^2 A}{\partial t^2} + \left(g + j\gamma A^2\right)A \tag{16.6}$$

Where A is the field envelope, z is the propagating distance, t is the frame time moving at the signal velocity, β_2 is the GVD parameter, γ is the self phase modulation coefficient, g is the saturated gain coefficient, and ω_g is the gain bandwidth. Depending on the specific parameters of the optical dissipative systems, one would expect to observe the dynamical processes of fluctuation, pulsing, bifurcation, turbulence, and chaos. RWs, which are extremely sensitive to initial conditions and perturbations, are always anticipated in those dynamics. They are identified in ultrafast laser systems, microresonator, or other extended systems, utilizing the single-shot techniques based on DFT and Time-lens effects.

16.2.2 Dissipative Rogue Waves in Ultrafast Lasers

The coherent structures and patterns are generally arising from the composite balance between conservative and dissipative effects in various areas of physics, ranging from quantum mechanics to astrophysics. Therein, the dissipative solitons are highly coherent solutions of nonlinear wave equations, and provide an ideal platform for study of nonlinear optical dynamics. So far, numerous striking soliton dynamics have been investigated in dissipative soliton fiber lasers, including dissipative soliton molecules [37], dissipative soliton rain [38], noise-like pulses (NLPs) [39], dissipative soliton explosions [40], buildup of dissipative solitons [41] and so on. All of these nonlinear processes are frequently accompanied by energy oscillation in laser cavity, as well as the generation of high amplitude waves.

Thanks to the development of real-time measurement, which offers a powerful tool to characterization the transient nonlinear dynamics in ultrafast laser. In 2015, researchers from university of Auckland identify clear explosion signatures of a Yb-doped mode-locked fiber laser that is operating in a transition regime between stable and noise-like emission [40]. This transition between these two regimes can be achieved by increasing the pump power. Meanwhile, in the noise-like regime the Raman scattering is stimulated by the huge energy oscillations during soliton explosions process. The single-shot experimental results are shown in following figure. Where after, two groups have identified the optical rogue waves during soliton explosions in coherent and incoherent dissipative ultrafast laser cavity [42, 43].

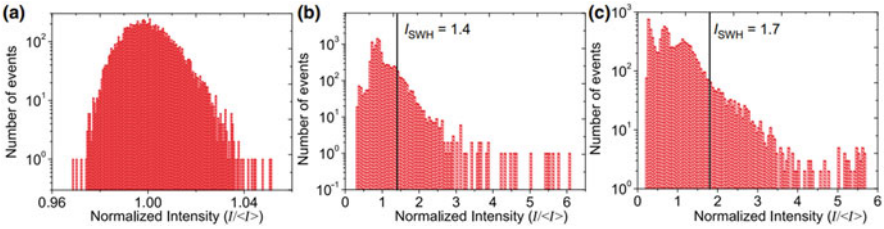

Fig. 16.7 Intensity histograms of the three mode-locking regimes. (**a**) Stable dissipative solitons. (**b**) Breathing dissipative solitons. (**c**) Breathing dissipative soliton explosions. The black line denotes the SWH [44]

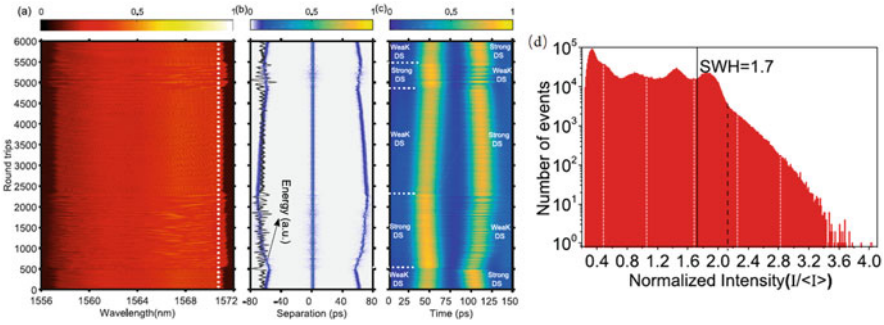

Fig. 16.8 (**a**) Real-time spectra of soliton molecules. (**b**) The field autocorrelation trace calculated from the spectra. (**c**) The corresponding temporal intensity evolutions measured by a photodetector. (**d**) Spectral intensity histogram of the soliton molecule [45]. (Reprinted with permission from Ref. [45] © The Optical Society)

One more interesting found is that the researchers have discovered that akin to solitons, breathing dissipative solitons can also exhibit explosions. And such breathing dissipative solitons and breathing dissipative solitons explosions also induce optical rogue waves, as shown in following Fig. 16.7 [44].

The soliton molecules may also excite RWs. In 2019, a group in China have experimentally investigated the dynamics of soliton molecules in the normal-dispersion regime [45]. They show that the separation between two bound dissipative solitons (DSs) evolves aperiodically. An additional modulation on the spectra is observed suggesting that the DSs split aperiodically. Such a splitting occurs when the DSs exchange energy. Moreover, rogue waves are present in the soliton molecule (Fig. 16.8).

For characterizing the rogue waves among the noise-like pulses or soliton rain, the dispersive Fourier transform based single-shot measurement is not accurate enough. As the rogue waves appear among the pulses cluster more randomly, the DFT based real-time spectroscopy to hardly capture the intensity peaks of pulse waveform. The time magnifier based on time-lens effect has been utilized to capture the temporal waveform for NLPs or soliton rain [36]. To enable self-triggering, a

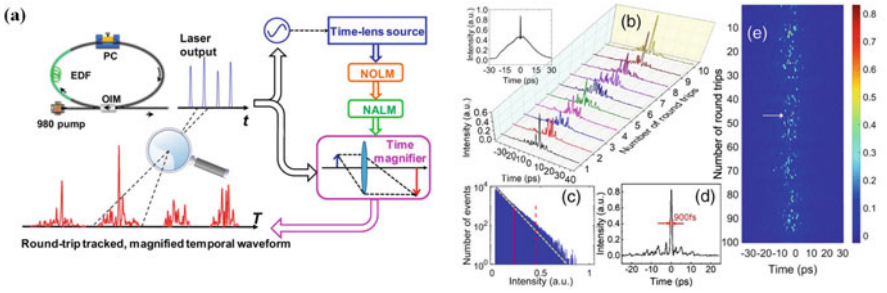

Fig. 16.9 (**a**) Schematic diagram of synchronized time magnifier for NLPs. (**b**) Detailed temporal structure of the NLPs. (**c**) Pulse intensity histogram of the NLPs waveforms. (**d**) A Typical example of a rogue event. (**e**) Pulse evolution over 100 consecutive round trips [36]. (Reprinted with permission from Ref. [36] © The Optical Society)

pump signal is produced from the signal under test. As can be seen in Fig. 16.9, the NLPs output from laser cavity is broaden spectrally and amplified. The reproduced the synchronous pump laser undergoes parametric process with signal, thereby achieving a self-triggered time magnifier with sub-picosecond resolution. Using this powerful technique, real-time observation of NLPs structures has been realized, and RWs were also observed under a sub-ps timescale. The ORWs in NLPs might have been resulted from the interaction of noise-like temporal structures and the energy convergence toward a single coherent pulse [36].

16.2.3 Dissipative Rogue Waves in Microresonators

In addition to the ultrafast laser systems, in recent years, RWs in microresonators have been also extensively reported [46–50]. The whispering-gallery-mode (WGM) resonator can be made from a glass microsphere, a crystal disk, or an integrated resonator. Dissipative RWs appear in WGM resonators, due to the chaotic interplay between Kerr nonlinearity and anomalous group-velocity dispersion. Researchers have observed freak events associated with non-Gaussian statistics, and theoretical evidence of RWs in WGM resonators by investigating the nonlinear dynamics in the resonator with the Lugiato-Lefever equation (LLE), resulting from the collision of soliton breathers in the process of hyperchaotic Kerr comb generation.

Figure 16.10 depicts the evolution of the optical field in the WGM resonator pumped by a continuous-wave laser via the evanescent field of a tapered fiber [46]. This figure displays a snapshot of the numerical simulations that shows a rogue wave, which is characterized by extreme amplitude and very rare occurrence. For the color-coded map of the evolution of the field intensity with time, for $F^2 = 6$ and 8, stable solitons and soliton breathers emerge. As the pump is increased to $F^2 = 10$ and 20, rare, and extremely high amplitude waves are encountered.

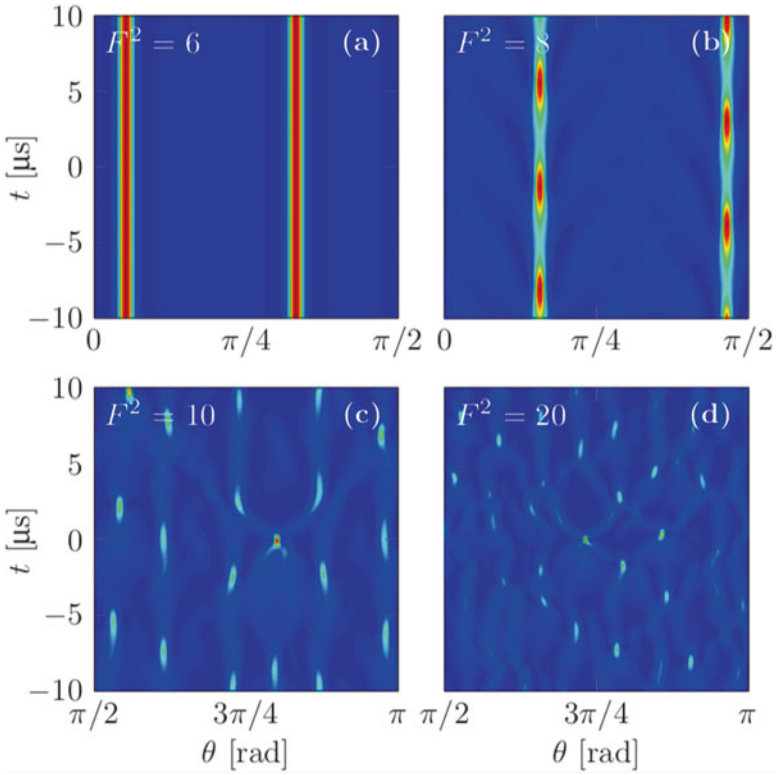

Fig. 16.10 The evolution of the optical field in the WGM resonator. F^2 denotes the square of the dimensionless pump term F in the LLE, which is proportional to the laser power [46]

The corresponding spatial distribution of the optical field along the azimuthal direction of the cavity is in the left column of Fig. 16.11. In the right column, the statistical distribution of the wave heights is shown with a logarithmic scale. For higher pump powers ($F^2 = 10$), the soliton breathers start to interact with one another. And the statistical distribution of the peak heights becomes continuous. The feature of an exponential decay of the distribution characterizes the threshold value, the SWH. When wave height is at least twice the SWH, a rogue wave occurs.

16.2.4 Dissipative Rogue Waves in Extended Systems

Apart from the systems mentioned above, rogue waves can be observed in other extended systems, including nonlinear optical cavity [47, 51–53] or even linear regime [25, 54], where RWs with non-Gaussian probability distribution occur. Take the multimode optical fiber for example, RWs result from interference between multiple transverse modes.

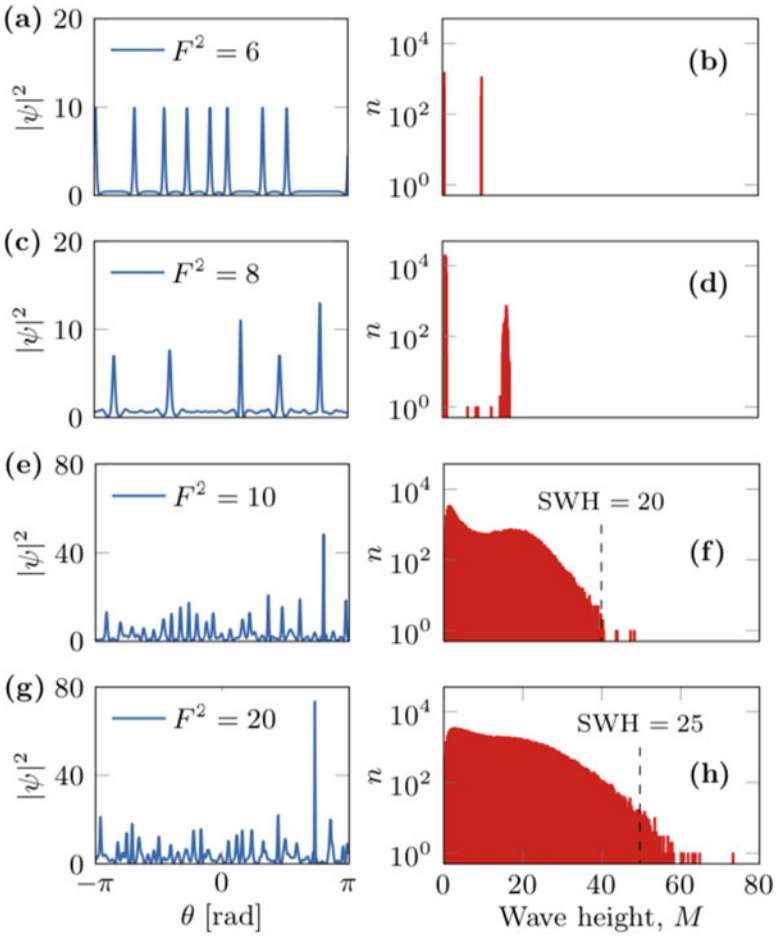

Fig. 16.11 Left column: Spatial distribution of the optical intensity in the cavity when the highest wave occurs for different pump powers. Right column: The intensity histograms of the optical pulses for different F^2 [46]

Figure 16.12 also depicts a ring cavity consists of three high-reflectivity dielectric mirrors, together with a liquid crystal light valve (LCLV) composed of a liquid crystal cell with one of the walls made of a slice of the photorefractive crystal. The LCLV is pumped by a plane-wave optical beam provided by a solid-state laser at 532 nm. The light amplification in the cavity is based on wave mixing with the pump beam. The PDFs of the cavity field intensity are obtained from large number of images and thereafter the histograms of the intensity value are performed. It is known that an exponential trend corresponds to a Gaussian statistics for the field amplitude. In other words, an exponential intensity PDF is characteristic of a speckles pattern, where many uncoupled modes independently contributed to each

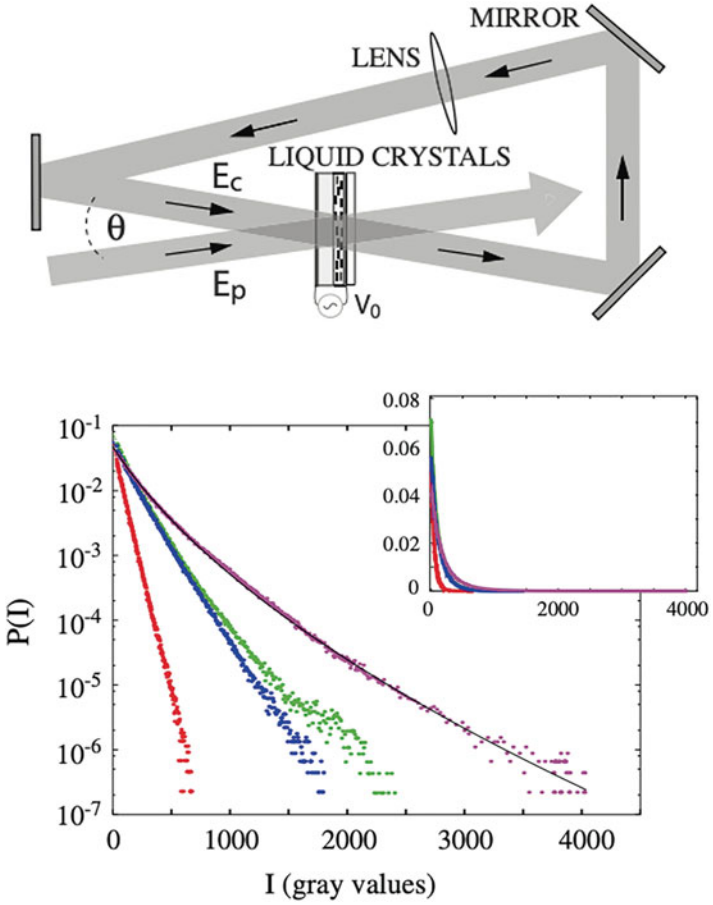

Fig. 16.12 (**a**) schematic of the experimental setup. (**b**) PDF of the cavity field intensity with different pump intensities [53].

point. At low pump, the behavior is Gaussian. However, when the pump increases, the increasing nonlinear coupling results in a complex space-time dynamic. When PDF exhibits a large deviation from Gaussian distribution, rogue events occur.

16.2.5 Optical Polarization Rogue Waves

Until now, all the RWs are identified based on the probability distributions of the temporal intensities within specific filtered wavelength range, or the integrated intensities of the obtained single-shot spectra. Namely, the RWs are identified in the temporal and in the spatial domains based on the SWH method. Yet another

inherently fundamental parameter of the laser emission, its state of polarization (SOP), has received relatively less attention [43, 55, 56]. In particular, the dynamics of the laser SOP has not been fully demonstrated. Yet, the corresponding SOPs would behavior rather complex trajectories, especially in the dissipative laser systems.

Figure 16.13 depicts the evolving SOP distributions for a filtered wavelength in the laminar-turbulent transition of the PMLs at different pump powers [57]. It is clear that the corresponding SOPs for wavelengths far away from the laser center line bifurcate into a cross-like shape on the Poincaré sphere. The multiple wave mixing processes generate new frequencies with separately evolving output SOP azimuth and ellipticity angles, resulting in perpendicular lines aligning with either a meridian or a parallel curve on the Poincaré sphere, respectively. The onset of SOP turbulence is accompanied by the loss of system coherence. Irregular polarization states locating outside of the main polarization directions emerge when the pump power exceeds 250 mW. This scattering of SOPs aggravates when the intracavity power is further increased. This result seems natural when we consider the usual road map for chaos, resulting from a cascade of successive period-doubling bifurcations. Whenever the pump power is larger than 600 mW, the cascaded four wave mixing (FWM) leads to a fully developed turbulent evolution, and the SOPs of filtered wavelengths appears as totally random.

The irregular polarization state of laser emission is associated with the emergence of a new kind of optical rogue waves in randomly-driven mode-locking systems, namely optical rogue waves in polarization domain. Different from the temporal or spatial rogue waves, RWs in polarization domain are vector, and a new method is introduced for their characterization. The SOPs can be expressed as $\hat{\mathrm{S}} = (s_1, s_2, s_3)$. Therefore, the relative distance, r, between two SOPs is defined by

$$\begin{aligned} r &= |S_m - S_n| \\ &= 2\sin^{-1}\left(\sqrt{(S_{m1} - S_{n1})^2 + (S_{m2} - S_{n2})^2 + (S_{m3} - S_{n3})^2}/2\right) \end{aligned} \tag{16.7}$$

The probabilities of the distance between various SOPs under different pump powers for filtered wavelengths are depicted in Fig. 16.14 [58]. A mere cross-like bifurcation of the SOP results in a distorted Gaussian function, while that for the total turbulence trends to be Gaussian shaped. During the laminar-turbulence transition of the SOP, L-shaped probability density function (PDF) distributions deviating from the Gaussian statistics prove that photons with large excursions of their SOP obey their own PDF, which is a characteristic property of extreme events in the polarization domain rather than the temporal or spectral domains. Considering the similarities, we referred it as polarization rogue waves (PRWs).

The PRWs is a phenomenon that is universal in any nonlinear dissipative optical systems undergo coherence deterioration. It is attributed to the stochastic mixing of its longitudinal modes, where vector FWM cascades with nonlinear chaotic phase-matching conditions. In fact, even for a high coherent ultrafast laser system, when

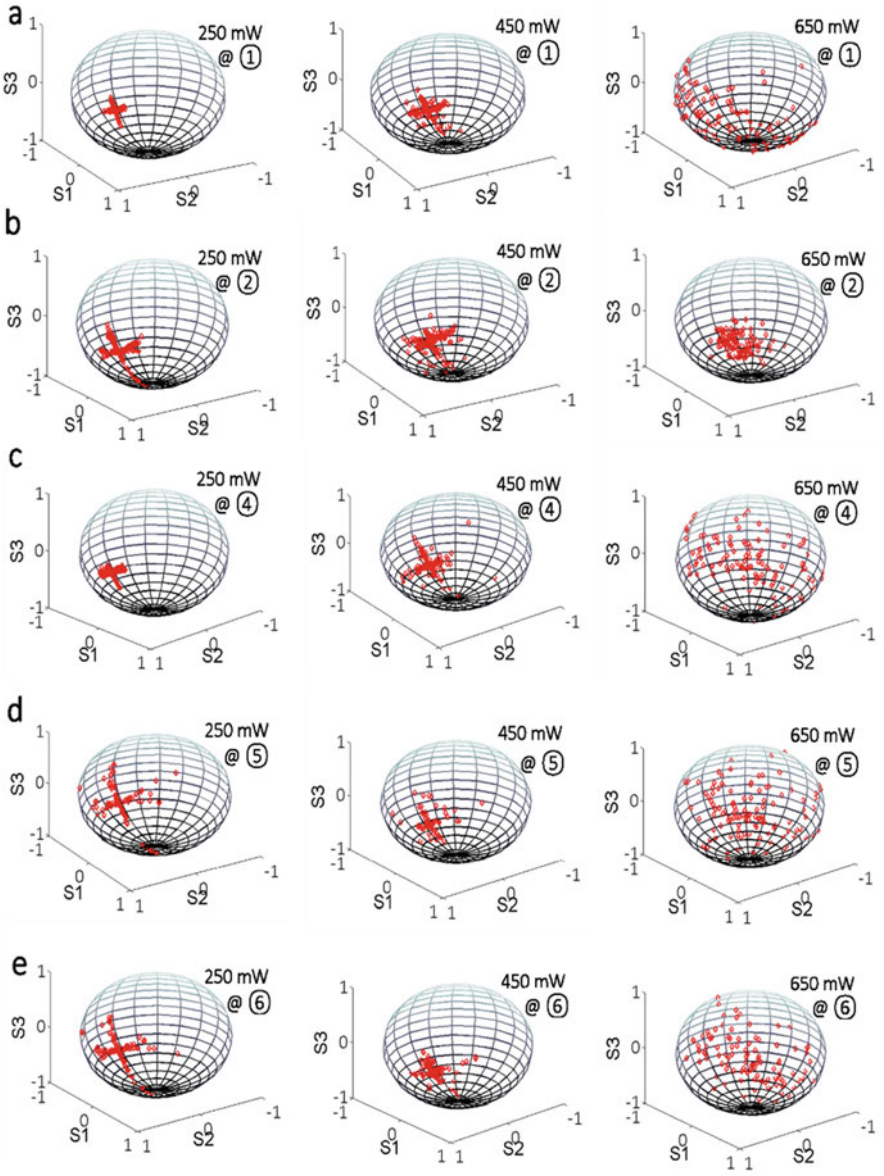

Fig. 16.13 Experimentally measured polarization states for filtered wavelengths under various pump powers for PMLs [57]

perturbated by excessive energy or phase, new frequencies with freak SOPs can be excited by the possible FWMs. Figure 16.15 schematically shows a normal-dispersioned fiber ring cavity mode-locked by a saturable absorbing film made by single-wall-carbon-nanotubes, where dissipative solitons (DSs) are produced. DSs

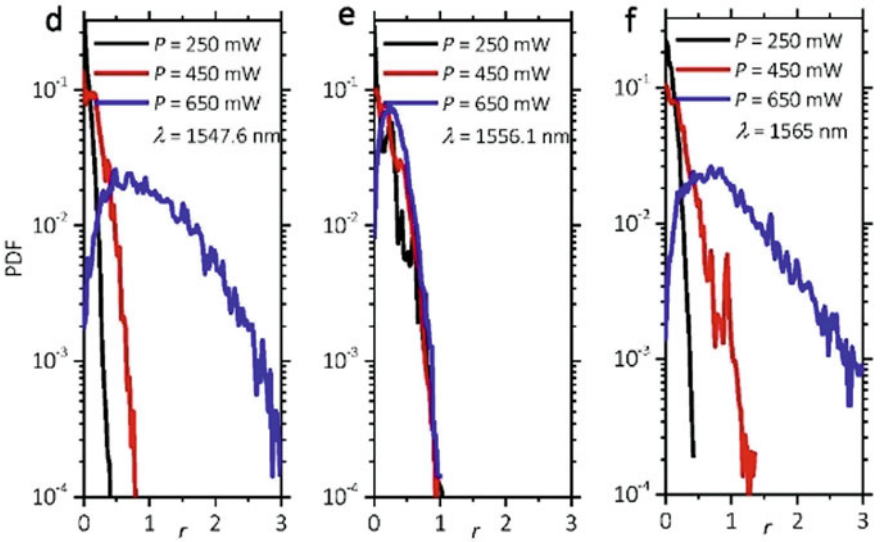

Fig. 16.14 Optical polarization rogue waves in the polarization laminar-turbulent transition for NLPs [58]. (Reprinted with permission from Ref. [58] © The Optical Society)

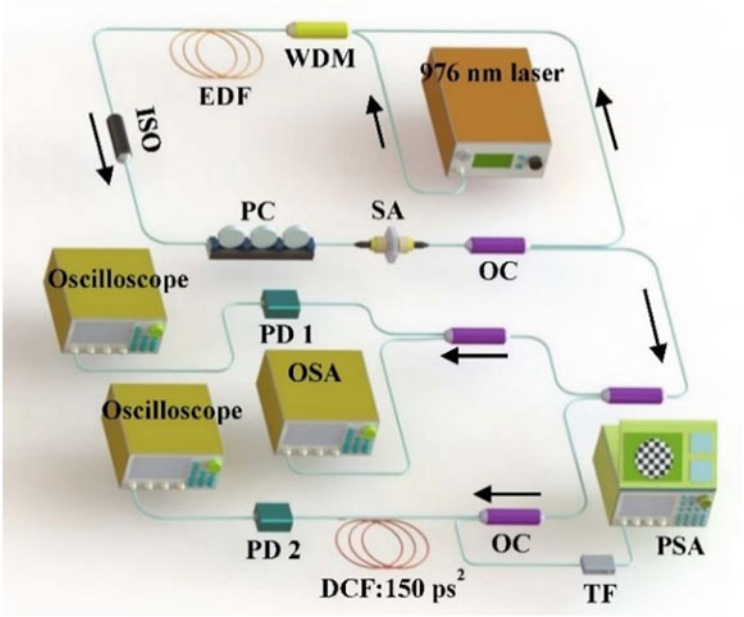

Fig. 16.15 Schematic of the fiber laser cavity and measurement methods [59]

are high coherent solutions of nonlinear wave equations, and arise from a balance between nonlinearity, dispersion, and loss/gain. At variance with NLSE solitons in integrable fiber systems operating in the anomalous dispersion regime, DSs in dissipative fiber laser systems operating in the normal dispersion regime exhibit extremely complex and striking dynamics.

For such a laser cavity, stable DS can be observed with a pump power threshold of 55 mW, where the rectangle-shaped optical spectrum with a FWHM of 13.6 nm is shown. For pump powers between 55 mW and 65 mW, the laser operates in a stable DS regime. For a pump power of 70 mW, regular DSs with neatly rectangle-shaped optical spectra are frequently detected. Yet, much broader optical spectra persisting near the square spectrum may also be occasionally encountered, exhibiting two extremely high peaks. This DS explosion. For soliton explosions, the balance of nonlinearity, dispersion, and loss/gain for the DS is perturbed by the surplus cavity gain at large pump powers. Part of the DS energy dissipates into CWs via the explosion, and the DS maintains its property of a highly coherent pulse.

The PRWs are identified during the DS explosion. Figure 16.16 illustrates the corresponding SOP distributions. It is clear from the distribution of points on the Poincaré sphere that the corresponding SOPs for each wavelength are evolving from a random cloud into a fixed narrow domain as the pump power grows larger. When a stable DS is formed, a well-defined SOP trajectory vs. frequency is observed on the Poincaré sphere. Whereas for pump powers above 66 mW, the SOPs of unstable DSs exhibit fluctuations (Fig. 16.16d). For even stronger pump powers (Fig. 16.16e), these intense fluctuations trend to be spreading more on the Poincaré sphere, especially for frequencies locating on the two spectral edges. The instability and fluctuations of SOPs on the two edges of the spectrum reveal a new aspect of the complex dynamics in DS formation, which so far has been largely unnoticed.

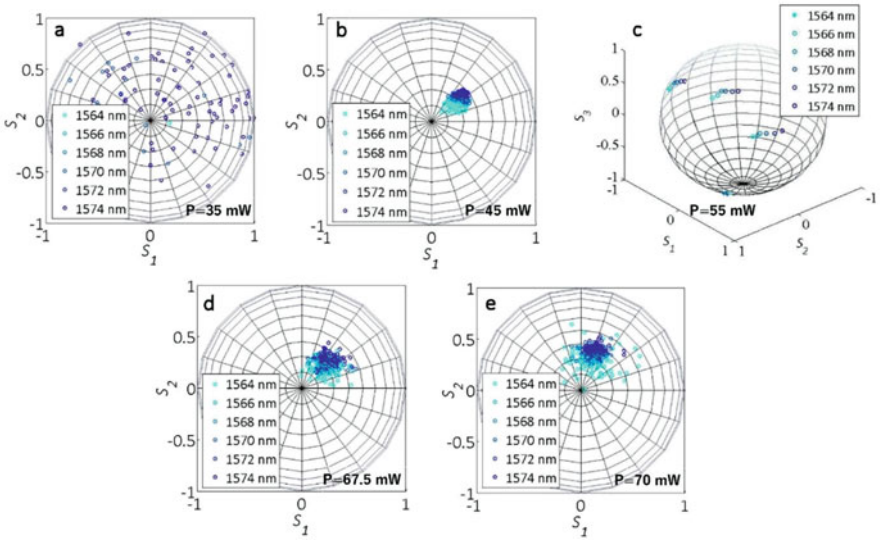

Fig. 16.16 Evolution of SOPs for various filtered wavelengths and different pump powers [59]

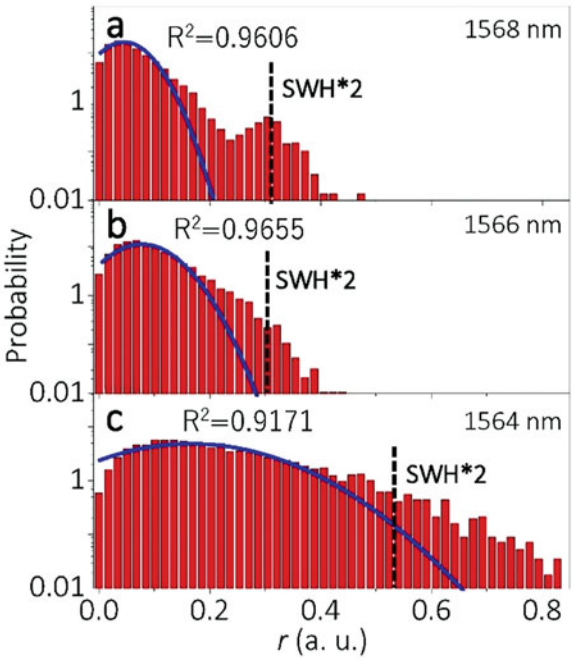

Fig. 16.17 Histograms of the relative distance between points on the Poincaré sphere for 70 mW pump power [59]

Figure 16.17 depicts the PDF of r when the DS is deteriorated at high pump powers. As can be seen, the PDF has a quasi-Gaussian shape at the 1568 nm wavelength (in the center region of the DS spectrum). Howbeit, for wavelengths far away from the DS spectral center, a trend develops towards the generation of L-shaped PDFs, which characterize the emergence of extreme events in the polarization domain, rather than in time or frequency domains. In other words, the irregular SOP of a deteriorated DS is associated with the emergence of a new type of optical rogue waves in the polarization dimension, namely PRWs. Such rogue events appear with both unexpected SOP values and relatively large probabilities of occurrence. From a statistical point of view, the occurrence of polarization rogue waves can be testified by the emergence of a heavy tail in the measured histogram. As shown for the 1568 nm wavelength, 1.8% of the events have a value that is larger than the twice of the SWH. Whereas rogue events represent about 3.8% of the events at the 1564 nm wavelength.

Similarly, the PRWs can be identified by any supercontinuum generation under nonlinear optical processes. The DS from Fig. 16.15 is compressed and amplified by a commercial high gain erbium-doped fiber amplifier, and injected into 20 m of highly nonlinear fiber with zero dispersion at 1550 nm. The commercially available ZDF has an effective diameter of 3.86μm and a nonlinear coefficient of 10 W^{-1} km^{-1}. Such a fiber facilitates phase matching of FWM over an ultra-broad frequency range, and octave-spanning spectrum can be easily obtained. In our experiment, primary sidebands are generated by MI. Next, new frequencies are

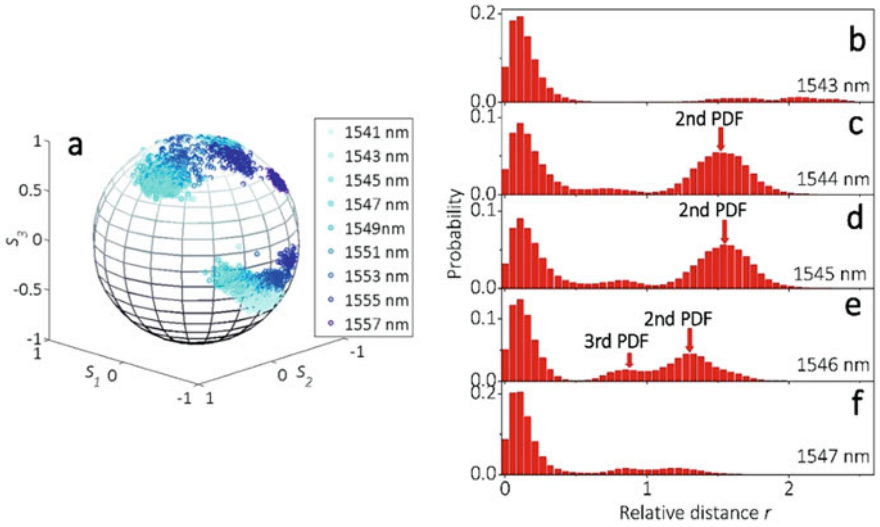

Fig. 16.18 SOPs and histograms at the pump power of 100 mW [60]. (Reprinted with permission from Ref. [60] © The Optical Society)

generated by cascaded FWM among those sidebands and the DS spectrum. Namely, all FWM procedures are possible. Primarily, we observe the MI with a degenerate FWM process. During supercontinuum generation (SCG), a transition from high to low spectral coherence may be controlled by varying the pump pulse peak power. Consequently, RWs in temporal, spectral, and polarization domains emerge in the SCG process.

To characterize the emergence of PRWs in SCG, we calculate the PDFs of SOP for wavelengths ranging from 1541 nm to 1557 nm. Figure 16.18a illustrates their SOPs values, for a fixed pump power of 100 mW. As can be seen, SOPs emerging at 1557 nm are scattered within a single domain. Whereas, as the wavelength is blue-shifted, the SOPs evolve into two separate domains. For wavelengths situated even farther away from the DS pump, the corresponding SOPs scatter within three different domains, which are continuously interchanging their energy. Those wavelengths are generated by vector FWM processes, which occur among all possible polarization interactions in a nonpolarization maintaining fiber. For wavelengths between 1543 nm and 1547 nm, the corresponding histograms in Fig. 16.18b–f clearly denote the existence of optical PRWs. The histograms are highly sensitive to the specific filtered wavelength. For example, at 1543 nm and 1547 nm, SOPs with rogue positions are observed on the Poincaré sphere, as denoted by the heavy tails at large r values. However, double PDFs, and even triple PDFs may appear, depending on the wavelength selected.

Polarization rogue waves are quite different from the intensity distributions for conventional RWs. Quantitatively, PRWs are identified based on the PDF of relative distance, r, between any two points on the Poincaré sphere for the single frequency,

while conventional RWs denote the emergence of ultrahigh intensities within wide frequencies. The corresponding temporal intensities for PRWs may not be large enough, even may be ultrasmall when we consider the forming procedure. The PRWs are more than the polarization aspect of the conventional RWs. However, we also believe that there is a connection between the PRWs and conventional RWs, as they are both formed only under high nonlinear process. A more convincing and reliable investigation between them requires single-shot measurement of the intensity and polarizations simultaneously, together with more rigorous theoretical analysis.

16.3 Generating Mechanisms of Dissipative Rogue Waves

16.3.1 Two Interpretations

The recent years have witnessed a growing interest for RWs in optics. While great debates on the classification of different kinds of RWs are clear in this community. In the pioneer works, the optical filtering has been taken seriously by the following researchers [14, 17, 24]. Based on different experimental systems, there are mainly two possible interpretations have been, not completely, partially accepted. While the two groups both admit the two main phenomenological features. The first one is the deviations of wave amplitude statistics from the Gaussian behavior. The other is the coherent build up in an extended spatio-temporal system. For optical fibers, the parameter is mainly limited to the dispersion, where time-frequency structures are formed. While for spatially extended optical systems, the two-dimensional structures are formed on the transverse wave front. Therefore, a reliable model should be described by partially differential equations, where either dispersion or nonlinearity leads to a coherent build-up of giant waves [9]. While, we have to admit that the chaotic behaviors or noise-induced intermittency, which described by ordinary equations, have to be considered for the RWs classification [61]. The later care about the probability of the RWs, which arise a fundamental question: the predictability of RWs. The researchers found that the RWs do not necessarily appear without a warning, but often preceded by a short phase of relative order [62–64]. The predictability can only be understood by the turbulence language.

The well-known theoretical model is the breathers for high nonlinear optical system. In fact, it lies on the ocean-optics analogy. Both the dynamics of ocean waves and pulse propagation in optical fibers can be modeled by the NLSE. For a more complex system, an extended version for the Ginzburg-Landau equation. For optics, the NLSE describes the pulse envelope modulating an electric field, while for water it represents the envelope modulating surface waves. Certain analogy does exist. Yet, such an analogy shall not be extended for the different higher order perturbations.

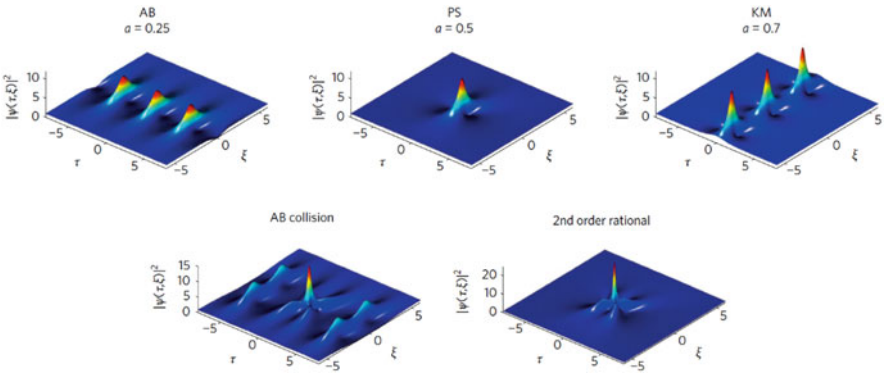

Fig. 16.19 Various kinds of solitons and breathers [15]

The most interesting phenomenon associated with the RWs in optical fibers are the formation of breathers [65–70]. These high coherent structures can be regards as a kind of solitons on finite background. They have certain analytical solutions. This is easy to understand: the optical system always tends to be loss, and the pure soliton is out-of-balanced by the mismatch of nonlinearity and dispersion. There are several kinds of breathers: the Akhmediev breathers, the Kuznetsov-Ma solitons, the Peregrine soliton. More higher orders of solutions are possible with even stronger localization and higher intensities. Figure 16.19 shows the properties of the breathers with spatial and temporal localization structures. These different breathers are frequently be used as the interpretation of RWs, both in the MI, the fiber resonator, or supercontinuum generation.

Despite of the success in interpreting RWs as a coherent structure, either in the soliton or breather, controversy still exists. This originate the experiment observation of incoherent soliton, which firstly found in photorefractive crystals [71]. It results from the spatial self-trapping of incoherent light in a highly noninstantaneous response nonlinear medium. The noninstantaneous photorefractive nonlinearity averages field fluctuations when its response time is much longer than the correlation time of the beam. More achievements have been made, such as, the existence of incoherent dark solitons [72], the modulation instability of incoherent waves [73, 74], the incoherent solitons in resonant interactions [75], or spectral incoherent solitons in optical fibers [76]. For all the statistical nonlinear optics, the kinetic waves theory provides a nonequilibrium thermodynamic description of turbulence. Recent experiments provide general physical insights of the RWs in the optical turbulence [77]. Depending on the amount of incoherence, different regimes are identified. Figure 16.20 depicts the probabilities for three regimes: the coherent rogue quasi-solitons, the intermittent-like rogue quasi-solitons that appear and disappear erratically, and the sporadic RWs that emerge from the turbulent fluctuations.

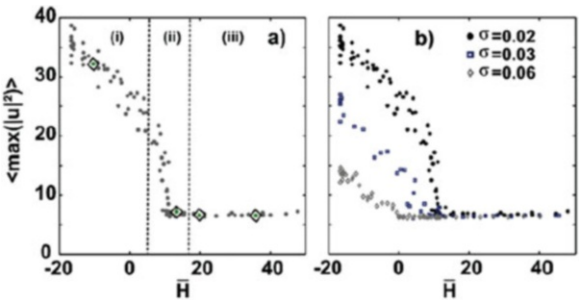

Fig. 16.20 Average of the maximum intensity peak as a function of the Hamiltonian density [77]

16.3.2 Are the Dissipative Rogue Waves Predictable?

As soon as the discovery of RWs, a fundamental question arises: Are the RWs predictable? The answers are just controversial as the interpretations of the RWs. When we follow the first explanation: RWs are rare extreme localized waves, which can be modeled by high order solitons, breathers, or their continuously coupling superpositions, and exact analytical solutions of NLSE with perturbations can be founded at prescribed conditions [62]. In this sense, predictable RWs are rational. One example is the second-order breathers based on NLSEs with a quadratic potential modulated spatially [78]. By controlling the modal parameter or spatial frequencies, the giant waves can be manipulated by overlapping the Kuznetsov-Ma breathers and Peregrine soliton, as depicted by Fig. 16.21. For this case, the simulations hold true, although partially, as both the boundary conditions and simulation accuracy will deteriorate their predictabilities.

While another question occurs: are the RWs formed in dissipative systems predictable? After all, the basic nature of dissipative system is the spontaneous formation of symmetry breaking and complex, even chaotic structures. The dissipative factors make the NLSE unsuitable for describing unintegrable systems, but only Ginzburg-Landau equations. And in most cases, there are only numerical simulations, and analytical solutions are hard to find as the dissipative dynamics are extremely sensitive to the initial perturbations. This behavior resembles to the very beginning of "disappearing without the slightest trace" of RWs [14], thus challenging the prediction of dissipative RWs. This is especially true in highly nonlinear optical systems, such as the PRWs in PML, or supercontinuum generation: the probabilities of finding freak SOP is decreasing when the coherence is deteriorated. In this sense, the prediction of RWs in dissipative systems is similar to the prediction of trajectory of system undergoing from laminar to turbulence, you can find the difference when the fluctuations and even bifurcations occur, yet it is far away to figure it out when the system is fully chaotic.

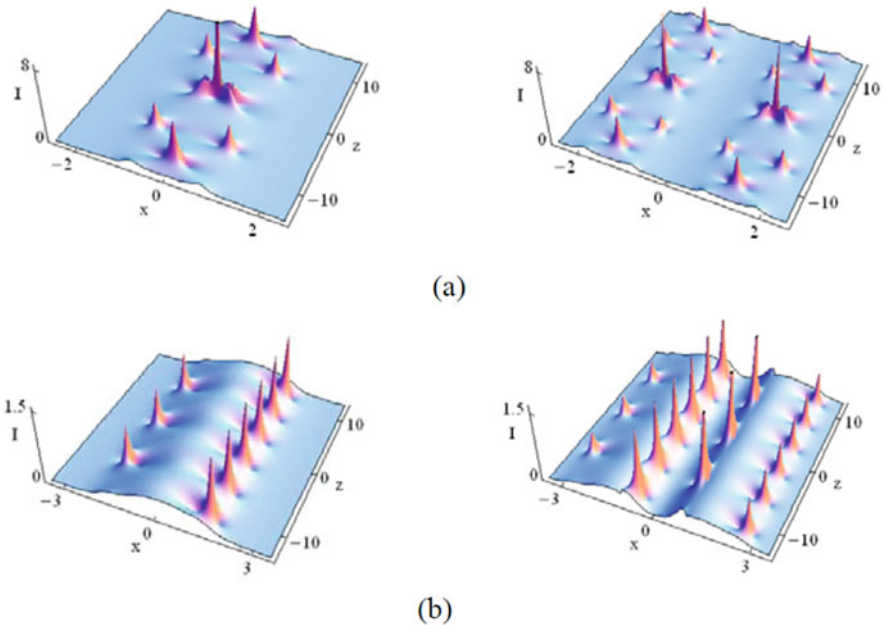

Fig. 16.21 RWs as second-order breathers, which are superpositions of Kuznetsov-Ma breathers and Peregrine solitons [78]. (Reprinted with permission from Ref. [78] © The Optical Society)

References

1. C. Kharif, E. Pelinovsky. Physical mechanisms of the rogue wave phenomenon. European Journal of Mechanics, B/Fluids, 2003, 22(6):603–634.
2. B. White, B. Fornberg. On the chance of freak waves at sea. Journal of Fluid Mechanics, 1998, 355:113–138.
3. N. Akhmediev, E. Pelinovsky. Discussion & debate: Rogue waves – towards a unifying concept?. European Physical Journal – Special Topics, 2010, 185(1):1–266.
4. M. Onorato, A. Osborne, M. Serio, and S. Bertone. Freak waves in random oceanic sea states. Phys. Rev. Lett. 2001, 86(25):5831–5834.
5. J.S.-C.N. Akhmediev, A. Ankiewicz. Extreme waves that appear from nowhere: On the nature of rogue waves. Physics Letters A, 2009, 373(25):2137–2145.
6. A. Dyachenko, V. Zakharov. On the formation of freak waves on the surface of deep water. Jetp Letters, 2008, 88(5):307–311.
7. K. B. Dysthe, H. E. Krogstad, H. Socquet-Juglard, K. Trulsen. Freak waves, rogue waves, extreme waves and ocean wave climate. 2005. http://www.math.uio.no/∼karstent/waves/indexen.html.
8. https://photolib.noaa.gov/Collections/National-Weather-Service/Meteorological-Monsters/Surfs-Up/emodule/634/eitem/3318.
9. M. Onorato, S. Residori, U. Bortolozzo, A. Montina, and F. T. Arecchi. Rogue waves and their generating mechanisms in different physical contexts. Physics Reports, 2013, 528(2):47–89.
10. C. Fochesato, S. Grilli, F. Dias. Numerical modeling of extreme rogue waves generated by directional energy focusing. Wave Motion, 2007, 44(5):395–416.

11. G. Clauss. Dramas of the sea: episodic waves and their impact on offshore structures. APPLIED OCEAN RESEARCH, 2002, 24(3):147–161.
12. M. Brown, A. Jensen. Experiments on focusing unidirectional water waves. Journal of Geophysical Research, 2001, 106(C8):16917.
13. S. Birkholz, E. T. J. Nibbering, C. Brée, S. Skupin, A.Demircan, G. Genty, and G. Steinmeyer. Spatiotemporal Rogue Events in Optical Multiple Filamentation. Physical Review Letters, 2013, 111(24):243903.
14. D. R. Solli, C. Ropers, P. Koonath, and B. Jalali. Optical rogue waves. Nature, 2007, 450(7172):1054.
15. J. M. Dudley, F. Dias, M. Erkintalo, and G. Genty. Instabilities, breathers and rogue waves in optics. Nature Photonics, 2014, 8(10):755–764.
16. C. Lecaplain, P. Grelu, J. M. Soto-Crespo, and N. Akhmediev. Dissipative Rogue Waves Generated by Chaotic Pulse Bunching in a Mode-Locked Laser. Physical Review Letters, 2012, 108(23):233901.
17. Z. Liu, S. Zhang, and F. W. Wise. Rogue waves in a normal-dispersion fiber laser. Optics Letters, 2015, 40(7):1366.
18. J.-P. Eckmann. Roads to turbulence in dissipative dynamical systems. Reviews of Modern Physics, 1981, 53(4):643–654.
19. N. Akhmediev, J. M. Dudley, D. R. Solli, and S. K. Turitsyn. Recent progress in investigating optical rogue waves. Journal of Optics, 2013, 15(6):060201.
20. M. Erkintalo, G. Genty, and J. M. Dudley. On the statistical interpretation of optical rogue waves. European Physical Journal Special Topics, 2010, 185(1):135–144.
21. A. Zaviyalov, O. Egorov, R. Iliew, and F. Lederer. Rogue waves in mode-locked fiber lasers. Phys. Rev. A, 2012, 85:013828.
22. P. Suret, R. E. Koussaifi, A. Tikan, C. Evain, S. Randoux, C. Szwaj, and S. Bielawski. Single-shot observation of optical rogue waves in integrable turbulence using time microscopy. Nature Communications, 2016, 7:13136.
23. M. Närhi, B. Wetzel, C. Billet, S. Toenger, T. Sylvestre, J. Merolla, R. Morandotti, F. Dias, G. Genty, and J. M. Dudley. Real-time measurements of spontaneous breathers and rogue wave events in optical fibre modulation instability. Nature Communications, 2016, 7:13675.
24. J. M. Dudley, G. Genty, and B. J. Eggleton. Harnessing and control of optical rogue waves in supercontinuum generation. Optics Express, 2008, 16(6):3644–51.
25. F. T. Arecchi, U. Bortolozzo, A. Montina, and S. Residori. Granularity and inhomogeneity are the joint generators of optical rogue waves. Physical Review Letters, 2011, 106(15):153901.
26. B. Frisquet, B. Kibler, P. Morin, F. Baronio, M. Conforti, G. Millot, and S. Wabnitz. Optical Dark Rogue Wave. Sci Rep, 2016, 6(1):20785.
27. D. R. Solli, C. Ropers, and B. Jalali. Rare frustration of optical supercontinuum generation. Applied Physics Letters, 2010, 96(15):151108.
28. A. Mahjoubfar, D. V. Churkin, S. Barland, N. Broderick, S. K. Turitsyn and B. Jalali. Time Stretch and its applications. Nature Photonics, 2017, 11:341.
29. G. Herink, B. Jalali, C. Ropers, D.R. Solli. Resolving the build-up of femtosecond mode-locking with single-shot spectroscopy at 90 MHz frame rate. Nat. Photon, 2016, 10:321–326.
30. R. Salem, M. A. Foster, and A. L. Gaeta. Application of space–time duality to ultrahigh-speed optical signal processing. Adv. Opt. Photonics, 2013, 5(3):274–317.
31. K. Goda and B. Jalali. Dispersive Fourier transformation for fast continuous single-shot measurements. Nat. Photon, 2013, 7:102–112.
32. Y. Li, Y. Cao, L. Gao, L. Huang, H. Han, I. P. Ikechukwu, and T. Zhu. Fast Spectral Characterization of Optical Passive Devices Based on Dissipative Soliton Fiber Laser Assisted Dispersive Fourier Transform. Physical Review Applied, 2020, 14:024074.
33. B. H. Kolner. Space-time duality and the theory of temporal imaging. IEEE J. Quantum Electron, 1994, 30(8):1951–1963.
34. Y Wei, B Li, P Feng, J Kang, K.K.Y. Wong. Broadband dynamic spectrum characterization based on gating-assisted electro-optic time lens. Applied Physics Letters, 2019, 114(2):021105.

35. B. Li, S. Huang, Y. Li, C. W. Wong and K. K. Y. Wong. Panoramic-reconstruction temporal imaging for seamless measurements of slowly-evolved femtosecond pulse dynamics. Nature Communications, 2017, 8:61.
36. B. Li, J. Kang, S. Wang, Y. Yu, P. Feng, K. K. Y Wong. Unveiling femtosecond rogue-wave structures in noise-like pulses by a stable and synchronized time magnifier. Optics Letters, 2019, 44(17):4351–4354.
37. A. Zavyalov, R. Iliew, O. Egorov, and F. Lederer. Dissipative soliton molecules with independently evolving or flipping phases in mode- locked fiber lasers. Phys. Rev. A, 2009, 80:043829.
38. S. Chouli and P. Grelu. Rains of solitons in a fiber laser. Opt. Express, 2009, 17: 11776–11781.
39. Y. Cao, L. Gao, Y. Li, H. Ran, L. Kong, Q. Wu, L. Gang, W. Huang and T. Zhu. Polarization-dependent pulse dynamics of mode-locked fiber laser with near-zero net dispersion. Applied Physics Express, 2019, 12:112001.
40. A. F. J. Runge, N. G. R. Broderick, and M. Erkintalo. Observation of soliton explosions in a passively mode-locked fiber laser. Optica, 2015, 2:36.
41. H. Chen, et al. Buildup dynamics of dissipative soliton in an ultrafast fiber laser with net-normal dispersion. Optics Express, 2018, 26(3):2972–2982.
42. L. Meng, et al. Dissipative rogue waves induced by soliton explosions in an ultrafast fiber laser. Optics letters, 2016, 41(17):3912–3915.
43. K. Krupa, K. Nithyanandan and P. Grelu. Vector dynamics of incoherent dissipative optical solitons. Optica, 2017, 4(10):1239–1244.
44. J. Peng, and H. Zeng. Experimental observations of breathing dissipative soliton explosions. Physical Review Applied, 2019, 12(3):034052.
45. J. Peng, and H. Zeng. Dynamics of soliton molecules in a normal-dispersion fiber laser. Optics Letters, 2019, 44(11):2899–2902.
46. A. Coillet, J. Dudley, G. Genty, L. Larger, Y. K. Chembo. Optical rogue waves in whispering-gallery-mode resonators. Physical Review A, 2014, 89(1).
47. G. R. Kol. Controllable rogue waves in lugiato–lefever equation with higher-order nonlinearities and varying coefficients. Optical & Quantum Electronics, 2016, 48(9):419.
48. S. Coulibaly, M. Taki, A. Bendahmane, G. Millot, B. Kibler, M. G. Clerc. Turbulence-induced rogue waves in kerr resonators. Physical Review X, 2019, 9(1).
49. G.R. Kol, S.T. Kingni, P. Woafo. Rogue waves in Lugiato-Lefever equation with variable coefficients. Centr. Eur. J. Phys, 2014, 12, 767–772.
50. A. K. Vinod, W. Wang, S. W. Huang, J. Yang, B. Li, C. W. Wong. Persistence of extreme events in microresonators. CLEO, 2020.
51. A. Montina, U. Bortolozzo, S. Residori, F.T. Arecchi. Non-Gaussian statistics and extreme waves in a nonlinear optical cavity. Physical Review Letters, 2009, 103 (17):173901.
52. U. Bortolozzo, A. Montina, F.T. Arecchi, J.P. Huignard, S. Residori. Spatiotemporal pulses in a liquid crystal optical oscillator. Physical Review Letters, 2007, 99 (2):3–6.
53. A. Montina, U. Bortolozzo, S. Residori, J. P. Huignard, F.T. Arecchi. Complex dynamics of a unidirectional optical oscillator based on a liquid-crystal gain medium. Physical Review A, 2007, 76(3):399–406.
54. R. Höhmann, U. Kuhl, H.-J. Stöckmann, L. Kaplan, E.J. Heller. Freak waves in the linear regime: a microwave study. Physical Review Letters, 2010, 104 (9):093901.
55. S. A. Kolpakov, H. Kbashi, and S. V. Sergeyev. Dynamics of vector rogue waves in a fiber laser with a ring cavity. Optica, 2016, 3 (8):870–875.
56. V. Kalashnikov, S. V. Sergeyev, G. Jacobsen, S. Popov, S. K. Turitsyn. Multi-scale polarisation phenomena. Light: Science & Applications, 2016, 5(1):e16011.
57. L. Gao, T. Zhu, S. Wabnitz, M. Liu, and W. Huang. Coherence loss of partially mode-locked fiber laser. Sci. Rep, 2016, 6:24995.
58. L. Gao, T. Zhu, S. Wabnitz, Y. Li, X. S. Tang, and Y. L. Cao. Optical puff mediated laminar-turbulent polarization transition. Optics Express, 2018, 26(5):6103–6113.

59. L. Gao, Y. Cao, S. Wabnitz, H. Ran, L. Kong, Y. Li, W. Huang, L. Huang, D. Feng, and T. Zhu. Polarization evolution dynamics of dissipative soliton fiber lasers. Photonics Research, 2019, 7(11): 1331–1339.
60. L. Gao, L. Kong, Y. Cao, S. Wabnizt, H. Ran, Y. Li, W. Huang, L. Huang, M. Liu, and T. Zhu. Optical polarization rogue waves from supercontinuum generation in zero dispersion fiber pumped by dissipative soliton. Optics Express, 2019, 27(19): 23830–23838.
61. A. Picozzi, J. Garnier, T. Hansson, P. Suret, S. Randoux, G. Millot, and D. N. Christodoulides. Optical wave turbulence: Towards a unified nonequilibrium thermodynamic formulation of statistical nonlinear optics. Physics Reports, 2014, 542(1):1–132.
62. S. Birkholz, C. Brée, A. Demircan, and G. Steinmeyer. Predictability of rogue events. Physical Review Letters, 2015, 114(21):213901.
63. M.-R. Alam. Predictability Horizon of Oceanic Rogue Waves. Geophysical Research Letters, 2014, 41(23):8477–8485.
64. N. Akhmediev, A. Ankiewicz, J. M. Soto-Crespo, and J. M. Dudley. Rogue wave early warning through spectral measurements?. Physics Letters A, 2011, 375(3):541–544.
65. B. Kibler, J. Fatome, C. Finot, G. Millot, F. Dias, G. Genty, N. Akhmediev, and J. M. Dudley. The Peregrine soliton in nonlinear fibre optics. Nature Physics, 2010, 6(10):790–795.
66. K. B. Dysthe, K. Trulsen. Note on Breather Type Solutions of the NLS as Models for Freak-Waves. Physica Scripta, 1999, T82(1):48.
67. N. Akhmediev, A. Ankiewicz. Solitons: Non-linear Pulses and Beams (Chapman & Hall, 1997).
68. K. Tai, A. Hasegawa, and A. Tomita. Observation of modulational instability in optical fibers. Physical Review Letters, 1986, 56(2):135–138.
69. J. M. Dudley, G. Genty, and S. Coen. Supercontinuum generation in photonic crystal fiber. REVIEWS OF MODERN PHYSICS, 2006, 78(4):1135–1184.
70. D. R. Solli, G. Herink, B. Jalali, and C. Ropers. Fluctuations and correlations in modulation instability. Nature Photonics, 2012, 6(7):463–468.
71. M. Mitchell, Z. Chen, M. Shih, M. Segev. Self-Trapping of Partially Spatially Incoherent Light. Physical Review Letters, 1996, 77(3):490–493.
72. Z. Chen, M. Mitchell, M. Segev, T.H. Coskun, D.N. Christodoulides. Self-Trapping of Dark Incoherent Light Beams. Science, 1998, 280(5365):889–892.
73. M. Soljacic, M. Segev, T. Coskun, D. Christodoulides, A. Vishwanath. Modulation Instability of Incoherent Beams in Noninstantaneous Nonlinear Media. Physical Review Letters, 2000, 84(3):467–470.
74. D. Kip, M. Soljacic, M. Segev, E. Eugenieva, D. Christodoulides. Modulation Instability and Pattern Formation in Spatially Incoherent Light Beams. Science, 2000, 290(5491):495–498.
75. A. Picozzi, M. Haelterman, S. Pitois, G. Millot. Incoherent Solitons in Instantaneous Response Nonlinear Media. Physical Review Letters, 2004, 92(14):143906.
76. B. Kibler, C. Michel, A. Kudlinski, B. Barviau, G. Millot, A. Picozzi. Emergence of spectral incoherent solitons through supercontinuum generation in photonic crystal fibers. Physical Review E Statistical Nonlinear & Soft Matter Physics, 2011, 84(2):066605.
77. K. Hammani, B. Kibler, C. Finot, and A. Piozzi. Emergence of rogue waves from optical turbulence. Physics Letters A, 2010, 374(34):3585–3589.
78. W. P. Zhong, M. Belic, and Y. Zhang. Second-order rogue wave breathers in the nonlinear Schrodinger equation with quadratic potential modulated by a spatially-varying diffraction coefficient. Optics Express, 2015, 23:3708.